Physics of Atomic Nuclei, Vol. 65, No. 3, 2002, pp. 393–399. From Yadernaya Fizika, Vol. 65, No. 3, 2002, pp. 419–425.

NUCLEI
Experiment

Forward-Angle Yields of $2 \leq Z \leq 11$ Isotopes in the Reaction of ^{18}O(35A MeV) with ^{9}Be*

A. G. Artukh[1], G. F. Gridnev[1], M. Gruszecki[1),2)], F. Koscielniak[1),2)], A. G. Semchenkov[1),3)], O. V. Semchenkova[1),3)], Yu. M. Sereda[1),3)], J. Szmider[1),2)], and Yu. G. Teterev[1)]

Received January 25, 2000; in final form, April 28, 2001

Abstract—A systematic investigation of the forward-angle inclusive yields of $2 \leq Z \leq 11$ isotopes produced in collisions of ^{18}O projectile nuclei with a ^{9}Be target in the Fermi energy region (35A MeV) is performed. The measurements were based on the use of the COMBAS double achromatic kinematical separator in the spectrometry mode at the Flerov Laboratory of Nuclear Reactions at the Joint Institute for Nuclear Research, FLNR (JINR, Dubna). The velocity, isotopic, and element distributions are presented. There is no unique mechanism that would explain the total set of results obtained in this experiment. A dominant role of low-energy reaction mechanisms is observed. The intensity of secondary beams of halolike nuclei ^{11}Li, ^{12}Be, and ^{14}Be is determined. © *2002 MAIK "Nauka/Interperiodica".*

1. INTRODUCTION

The availability of heavy ions in the intermediate-energy region offers a unique opportunity for detailed studies of the transition-energy region [1] between low-energy nuclear collisions [2] and high-energy multifragmentation processes [3]. In the transition region (20 to 100A MeV), the projectile velocities are commensurate with the characteristic velocities in nuclear matter such as the velocity of sound and the Fermi velocity of nucleons inside nuclei. Overcoming these threshold velocities, one can hope to encounter qualitatively new phenomena. There still remains the open question of how fast reaction mechanisms of the binary type (characteristic of the low-energy regime) evolve in the multifragmentation disintegration of colliding partners (characteristic of the high-energy regime). The possible influence of the neutron excess $(N/Z)_p$ in the projectile and $(N/Z)_t$ in the target on the cross section for the production of unstable nuclei also remains unknown. It is well known that weakly bound drip-line isotopes are synthesized with maximum yields in nucleus–nucleus collisions at intermediate energies [4, 5]. What reaction mechanisms are dominant in processes that produce "cold" drip-line isotopes at intermediate energies?

Presently, there are many experimental data concerning the investigation of reaction mechanisms in the region of intermediate energies, but the main sample of data was obtained in large-angle measurements [1, 6–11]. As a rule, fragments emitted outside the zero-angle region (large angles) are produced in nucleus–nucleus collisions involving high traverse-momentum transfers (large losses of kinetic energy) or in multifragmentation processes. Such experiments are not sensitive to the "quasielastic" production of weakly bound (drip-line) isotopes.

To fill the gap in our knowledge, it is necessary to study the evolution of the mechanisms of reactions producing weakly bound nuclei versus projectile energy in nucleus–nucleus collisions with different entry mass and charge asymmetry. Moreover, experimental information to be obtained is of paramount importance for choosing the optimal energy and projectile–target combination needed to synthesize unknown drip-line nuclei and to form intense secondary radioactive beams.

This study is aimed at exploring the yields of charged reaction products with reference to the production of near-drip-line nuclei in collisions between ^{18}O projectiles in the Fermi energy domain (35A MeV) and a light ^{9}Be target efficiently used in the synthesis of drip-line nuclei and at determining the intensity of secondary radioactive beams of halo-like ^{11}Li, ^{12}Be, and ^{14}Be nuclei.

Considering that weakly bound neutron-drip-line isotopes could survive only when they are involved in "soft" peripheral nuclear collisions with a minimum transverse-momentum transfer (minimum excitation

*This article was submitted by the authors in English.

[1)]Joint Institute for Nuclear Research, Moscow oblast, Dubna, 141980 Russia.
[2)]Henryk Niewodniczanski Institute of Nuclear Physics, Cracow, Poland.
[3)]Institute for Nuclear Research, National Academy of Sciences, pr. Nauki 47, Kiev, 252028 Ukraine.

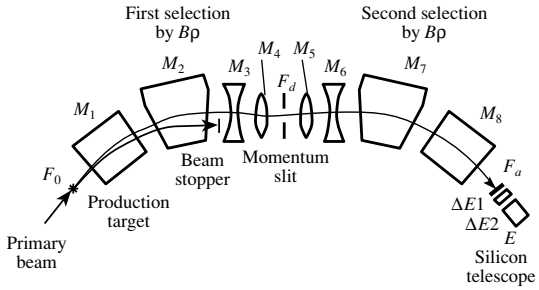

Configuration	ΔΩ, msr	$\Delta p/p$, %	Bρ, T m	$R_{p/\Delta p}$	L, m
$M_1\,M_2\,M_3\,M_4\,F_d\,M_5\,M_6\,M_7\,M_8\,F_a$	6.4	±10	4.5	4360	14.5

Fig. 1. Layout of the COMBAS secondary-beam facility. The main ion-optics parameters of the COMBAS kinematic separator are presented in the table.

energy), we used the COMBAS kinematical separator in zero-angle spectrometry of charged reaction products [12].

2. EXPERIMENTAL CONDITIONS

A 14-mg/cm^2 ^{9}Be target foil was irradiated with a 35A-MeV ^{18}O beam of (electric) intensity up to 2 μA from the U-400M cyclotron installed at the Flerov Laboratory of Nuclear Reactions, Joint Institute for Nuclear Research (JINR, Dubna). The target was placed at the entrance focus of the COMBAS separator (Fig. 1). The diameter of the beam spot on the target did not exceed 3 mm.

Nuclear products emitted at forward angles within a COMBAS solid angle (6.4 msr) were separated from the intense beam of bombarding particles by magnetic rigidity and identified by the mass number A and atomic number Z with a (ΔE, E) telescope [13, 14] placed at the exit achromatic focus of the COMBAS separator. The yields of isotopes were measured by scanning the range of magnetic rigidities covering the velocity distributions of the $2 \le Z \le 11$ light-element isotopes studied here. The magnetic fields of all eight magnets of the separator were measured with Hall probes. The ^{18}O primary beam was transmitted along the ion-optics axis of the separator in order to determine the beam magnetic rigidity and to use it as a momentum reference in measuring momentum distributions (or velocity distributions) of charged products. The thickness of the Be target was controlled by the primary-beam magnetic rigidity with the installed target and without it. Proportional counters were placed behind the target on both sides of the beam axis to monitor the beam intensity and beam position on the target. The target was also used to measure the beam current.

In the F_d dispersive focal plane, the 2-mm slit on the ion-optics axis of the separator was positioned to restrict the momentum acceptance within 0.15% and to reduce the load of the electronics and readout system near the beam magnetic rigidity. In the same F_d plane, a thin stripping 24-μm Mylar foil was installed to remove products whose ionic charge differed from the nuclear charge. The proximity to the beam magnetic rigidity was restricted by the ratios $B\rho/B\rho_{\rm beam} = 0.98$ and $B\rho/B\rho_{\rm beam} = 1.01$. The products were detected in the achromatic focus F_a by a telescope consisting of silicon detectors—$\Delta E1$ (0.38 mm, 60 × 60 mm^2), $\Delta E2$ (3.5 mm, ∅60 mm), and E (7.5 mm, ∅60 mm)—and were identified by the nuclear charge and by the mass number by combining two methods: magnetic rigidity and (ΔE, E):

$$E = (B\rho)^2 \times Z^2/A, \quad (1)$$

$$\Delta E \approx A \times Z^2/E. \quad (2)$$

Here, A, Z, and E are, respectively, the mass number, the atomic number, and the energy of the detected product.

The yields of all of the isotopes are presented in relative units after the normalization of the recorded isotopic events to the monitor detector counting.

3. EXPERIMENTAL RESULTS

3.1. Forward-Angle Inclusive Velocity Distributions of Products

The inclusive forward-angle velocity distributions of $2 \le Z \le 11$ isotopes produced in the reaction of 35A-MeV ^{18}O nuclei on a ^{9}Be target are shown in Figs. 2–5. The isotopic velocity V is referred to that of the projectile, $V_{\rm projectile}$. The existence of different reaction mechanisms can be observed from the evolution of the shape of the isotopic velocity distributions with increasing number of transferred nucleons.

Figure 2 displays the velocity distributions for the two extreme cases of a small nucleon transfer (a) and a multinucleon transfer (b) corresponding to weakly bound nuclei produced near the neutron drip-line. Nuclear-reaction products of mass close to the mass of the projectile (^{16,17,19}O, ^{17,18}N, ^{16}C) are characterized (see Fig. 2a) by a narrow bell-like shape with a maximum close to the projectile velocity. The visual shift of the velocity maxima of the ^{18}N and ^{19}O isotopes produced in the neutron-pickup reaction is of a kinematical origin (see below). Gaussian-like velocity distributions of such a shape are observed in small-nucleon-transfer reactions at low energies (quasielastic transfer). The shape of the velocity distributions in the region of smaller velocities (Fig. 2a) shows a bend at a level of more than 100 below the maximum yield; then, a slower exponential fall is observed. The contribution of this slower fall component

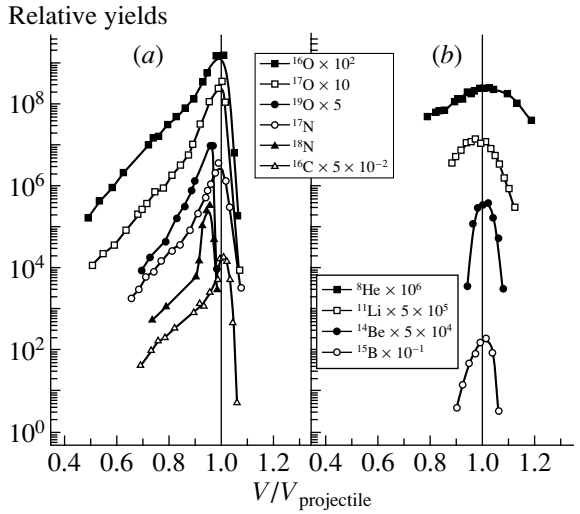

Fig. 2. Forward-angle inclusive velocity distributions (relative yields) of isotopes produced in (*a*) small-nucleon-transfer reactions and (*b*) proton-stripping reactions. The isotope velocity V is referred to the projectile velocity $V_{\text{projectile}}$. The numbers near the isotopic symbols (within the frame) show the factors by which the experimental yields are multiplied.

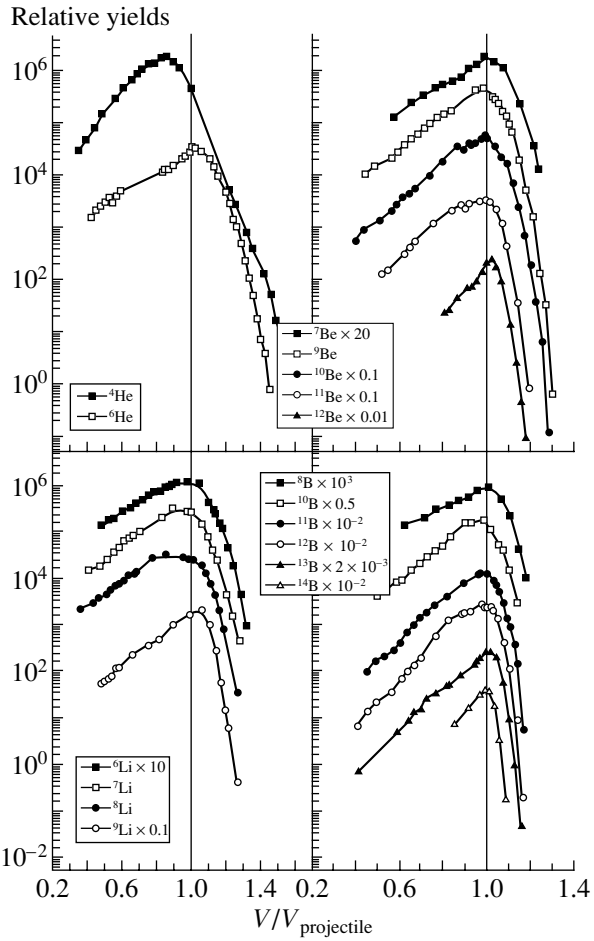

Fig. 3. Forward-angle inclusive velocity distributions (relative yields) of He, Li, Be, and B isotopes. The isotope velocity V is referred to the projectile velocity $V_{\text{projectile}}$. The numbers near isotopes (within the frame) show the factors by which the experimental yields are multiplied.

(inelastic portion of the spectrum) to the total yield of the isotope increases noticeably with increasing number of transferred nucleons.

The group of weakly bound isotopes (Fig. 2*b*) is characterized by a Gaussian-like single-component shape that is symmetrically concentrated around the projectile velocity. The widths of the velocity distributions for those isotopes tend to increase with increasing number of transferred nucleons. The shape of the velocity distributions of those weakly bound nuclei is close to the shape of the quasielastic component in the yields of isotopes obtained in the case of small nucleon transfer (Fig. 2*a*). As can be seen from Fig. 2*b*, there is no inelastic component in the yields of these nuclei, despite the fact that they are produced through a massive nucleon transfer. Evidently, this is due to the decay of weakly bound nuclei produced in inelastic processes with a noticeable excitation energy.

More complicated velocity distributions are observed for the intermediate case of massive nucleon transfers (Figs. 3–5). The isotopes around the stability line and proton-rich isotopes produced in a more massive stripping of nucleons are characterized by asymmetric shapes. The maximum yields are concentrated near the projectile velocity (with exception of the alpha-particle distribution), and there is a trend toward the broadening of the distributions with increasing number of transferred nucleons. The contribution of inelastic components (low-velocity sides) increases appreciably as the number of transferred nucleons increases (the tails are flattened). This growing contribution of the exponential tails from the low-velocity side to the total yields of these isotopes demonstrates the increasing role of dissipative processes and of secondary deexcitation processes.

The velocity distributions of isotopes produced in nucleon-pickup or nucleon-exchange reactions ($^{19-21}$F, $^{18-22}$Ne, ^{17,18}C, ^{18}N, ^{19}O) are similar in shape to those of the intermediate group, with the exception of the positions of maxima. The maxima of these distributions are concentrated at velocities less than the projectile velocity, showing a tendency toward a systematic shift as the number of pickup protons and neutrons increases. These phenomena are of a kinematical origin and are due to a decrease in the velocity of isotopes with the pickup of nucleons. The growing contribution of the low-energy tails, with increasing number of pickup nucleons, demonstrates the increasing role of dissipative processes in the production of nuclei.

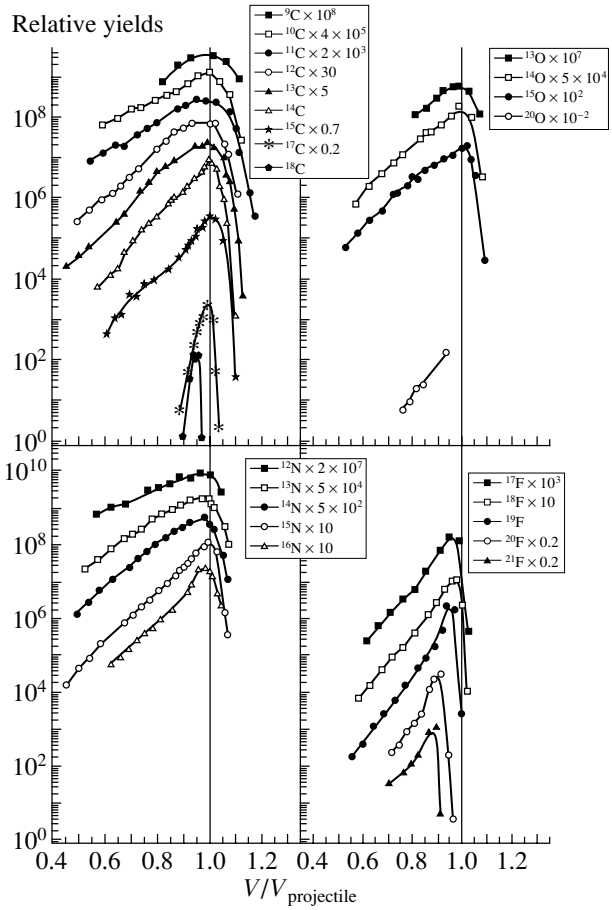

Fig. 4. As in Fig. 3, but for C, N, O, and F isotopes.

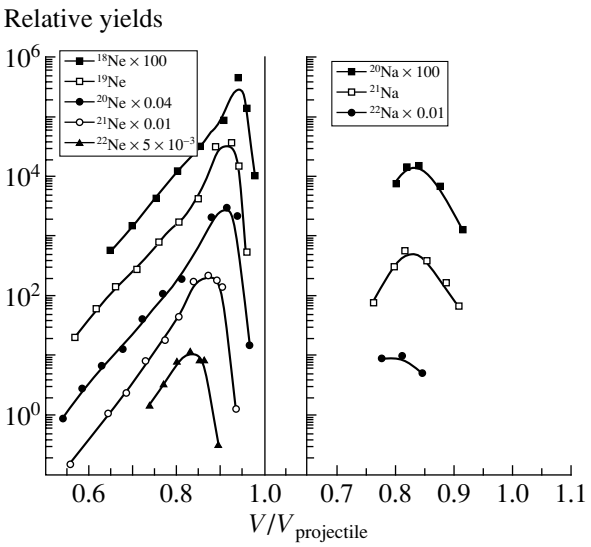

Fig. 5. As in Fig. 3, but for Ne and Na isotopes.

3.2. Isotopic Distribution of Reaction Products

To produce isotopic distributions, the velocity distributions were integrated over the measured region of velocities (Fig. 6*a*). In the oxygen isotopic distribution, the yield of the ^{18}O isotope was excluded because it was impossible to separate the reaction yield of ^{18}O from ^{18}O projectiles.

For each element, the isotopic distributions are similar to bell-like shapes; this is not so only for the He and Li distributions. The most probable yields correspond to masses around the stability-line isotopes. A sharp exponential decrease in the yields of heavy isotopes for each element is observed. The light-isotope side of the distributions increases with the number of stripping protons. The isotopic distributions of Li and He elements produced with a maximum number of stripping protons and neutrons degenerate into an exponential shape. An accumulation of the lightest isotopes (proton-rich ones) for each element, especially for the lightest elements, is affected by the contributions of evaporative lightest particles. This correlates with the behavior of growing contributions of the low-energy part of velocity distributions of these isotopes.

3.3. Element Distributions of Reaction Products

The element distributions (Z distributions) were obtained by integrating the isotopic distributions (Fig. 6*b*). The yield of the $Z = 8$ element (projectile) is underestimated because of the unknown yield of ^{18}O reaction products.

For the products of Z greater than the Z value of the projectile, the production yields decrease with increasing Z. A weak odd–even effect (enhancement of carbon) is also visible in the Z distribution. A striking feature of the resulting Z distribution is that, within a factor of five, all the elements from $Z = 2$ to $Z = 7$ are equally produced. A sharply increasing yield of the lightest elements (with $Z \leq 2$) is observed.

4. DISCUSSION OF THE RESULTS

The evolution of the velocity and isotopic distributions obtained in forward-angle measurements versus the number of transferred nucleons suggests the existence of different reaction mechanisms.

In the Fermi energy domain (35A MeV), the velocity distribution of isotopes close to the projectile demonstrates a dominant role of direct peripheral reactions like the binary processes of stripping and pickup of a few nucleons in the low-energy region [2, 15]. The main contribution of these reactions is observed in the yields of all isotopes including isotopes produced in reactions involving a massive transfer of nucleons. In the production of the weakly bound nuclei of ^{8}He, ^{11}Li, ^{12}Be, ^{14}Be, and ^{15}B, the peripheral

binary reactions also play a dominant role. These drip-line nuclei are produced in nuclear reactions with the maximum number of the transferred protons.

The analysis of the velocity distributions of detected fragments within the simple fragmentation model showed that there is disagreement with the experimental data obtained in forward-angle measurements.

A naive picture of geometric fragmentation predicts a regular decrease in the velocity of isotopes with increasing number of removed nucleons [1, 6]:

$$V/V_p = \left[(35A - (A_p - A) \times 8)/(35A_p)\right]^{1/2} \times (A_p/A)^{1/2}, \quad (3)$$

where A_p and A are the mass numbers of the ^{18}O projectile with $35A$ MeV and the isotope, respectively, while V_p and V are their velocities; 8 MeV is the mean energy of a single removed nucleon. As can be seen from Fig. 2*b*, the experiment has not confirmed the systematic shift of the maximum of the velocity distributions toward lower velocities with increasing number of removed protons as predicted by the fragmentation model.

For example, the relative yields of Be isotopes according to the calculation by the LISE code based on the fragmentation hypothesis [16] are presented in Fig. 7. There is no agreement between the prediction and the experimental data in the shape and, especially, in the position of the maximum. The discrepancy between the predicted shape of the magnetic-rigidity distributions and the experimental data increases for heavier isotopes. For the drip-line isotope ^{14}Be, the widest distribution is predicted and the centroid is considerably shifted toward smaller values of the magnetic rigidity. The observed discrepancy in the shape and position of the maximum for the drip-line nuclei should be taken into account in the experiments being planned, especially when a low-momentum-acceptance fragment separator is used. Figure 6*a* illustrates the degree of agreement between the fit calculated by the LISE code and the experimental data on the isotopic yields.

In addition, the production of $Z > Z_{\text{projectile}}$ isotopes (F, Ne, and Na) is not conceptually assumed within the projectile-fragmentation hypothesis. In Fig. 6*a*, the experimental points for these isotopes are connected by dotted curves to guide the eye.

It is well known from [17] that, in the low-energy region, the yields of isotopes produced in stripping reactions can be approximated by a simple exponential function of Q_{gg},

$$y = C \exp(Q_{gg}/T), \quad (4)$$

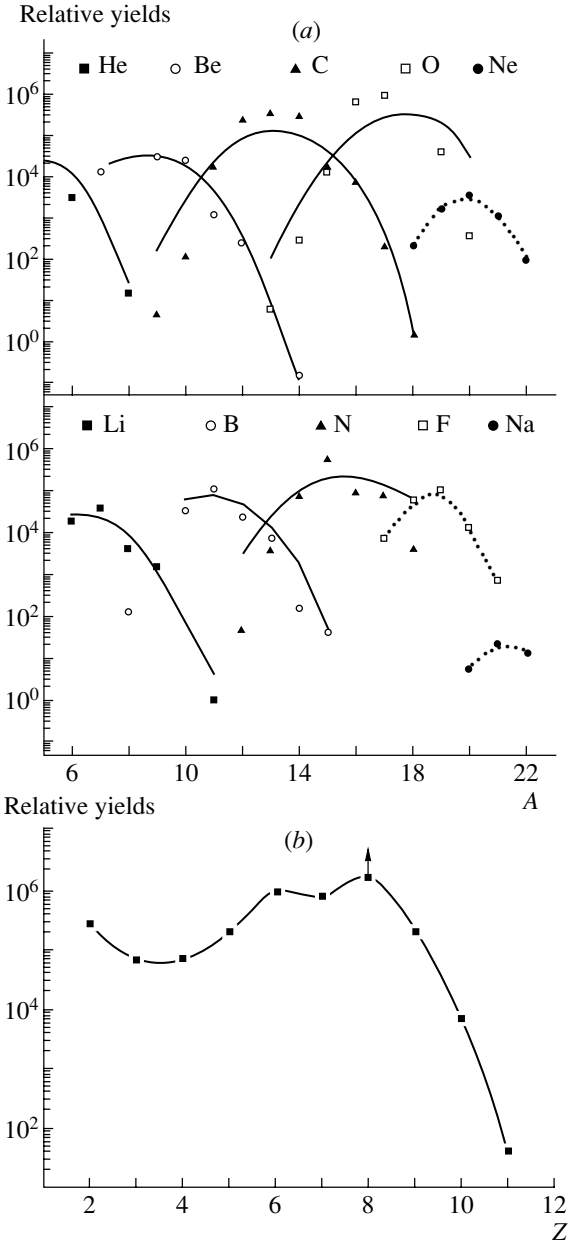

Fig. 6. (*a*) Isotopic distributions that were obtained by integration of velocity distributions versus the detected mass A. The yield of the ^{18}O isotope is excluded because ^{18}O reaction products could not be separated from ^{18}O projectiles. The solid curves present the LISE code fit (see main body of the text). The dotted curves for the F, Ne, and Na isotopic distributions induced in the proton-pickup reactions are drawn through the experimental yields for visual convenience. (*b*) Element distributions (Z distributions) versus the atomic number. The yield of the $Z = 8$ element (projectile) is underestimated because of unknown yields of ^{18}O reaction products.

where T is the parameter (measured in MeV) determining the slope of the exponential and C is a constant.

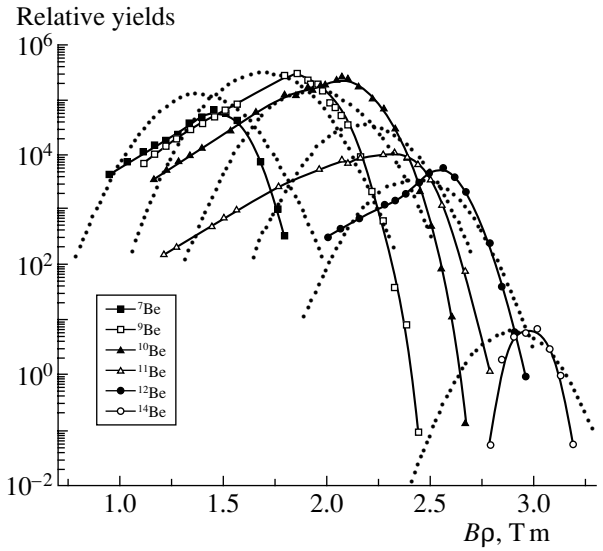

Fig. 7. Yield distributions of Be isotopes versus the magnetic rigidity $B\rho$. The solid curves are drawn through the experimental points for visual convenience. The dotted curves represent the LISE code fit (see main body of the text).

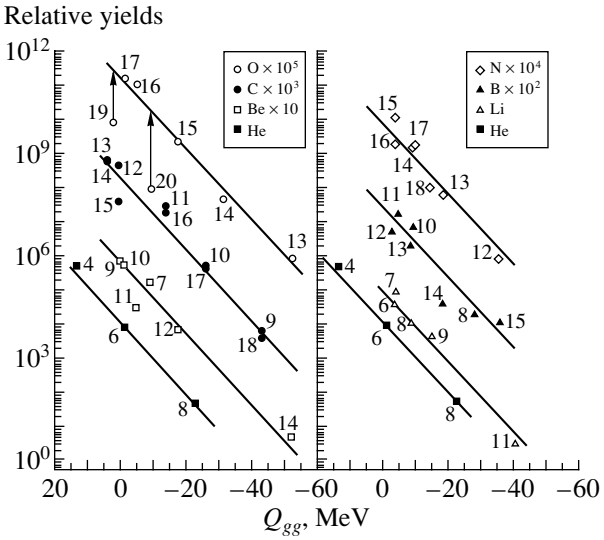

Fig. 8. Isotopic yields of $2 \leq Z \leq 8$ elements versus Q_{gg} (Q_{gg} systematics), where Q_{gg} is $(M_p + M_t) - (M_{\rm det} + M_{\rm undet})$, with M_p, M_t, $M_{\rm det}$, and $M_{\rm undet}$ being the ground-state masses of the projectile, the target, the detected isotope, and the undetected isotope (the partner of the detected isotope in the exit channel of the reaction), respectively. The arrows for the ^{19}O and ^{20}O isotopes show the decrease in the yields of the isotopes as the possible consequence of deexcitation effects. The numbers near isotopes (in frame) show the factors by which the experimental yields are multiplied for visual convenience.

The Q_{gg} systematics characterizing the binary type of isotopic production is given in Fig. 8. In calculating Q_{gg}, it is assumed that there are two particles (projectile and target) in the entrance channel and two particles (the detected fragment and an undetected residue of the compound system) in the exit channel. The Q_{gg} value is determined by the difference of the ground-state masses of the partners before and after the collision event being considered.

It can be seen from Fig. 8 that the simple exponential approximation realized by the Q_{gg} systematics describes the total yield of the isotopes produced in nucleon-stripping reactions with large negative Q_{gg} values. The uniqueness of the Q_{gg} systematics consists in a satisfactory description of the isotopic yields of all elements by the same simple exponential over a range of more than five orders. The Q_{gg} systematics is a powerful tool for correctly predicting the expected yields of unknown drip-line nuclei in experimental searches. As can be seen from Fig. 8, the decrease in the yields of the detected isotopes in relation to the averaged Q_{gg} exponential is observed in the region of small negative or positive Q_{gg} values. The largest discrepancy is observed for the heavy isotopes of ^{19}O and ^{20}O produced in the neutron-pickup reactions. It is well known that each nucleon-pickup event deposits an excitation energy in a nuclear acceptor. That is why the observed decrease in the yields for nuclei originating from neutron-pickup reactions can be due to deexcitation effects. The reduction of the detected yields of single-neutron-halo isotopes of ^{11}Be, ^{14}B, and ^{15}C can be caused by their low binding energies favoring disintegration.

The experiment was also carried out to estimate the production rates for halolike nuclei of ^{11}Li (6×10^3 pps), ^{12}Be (3×10^5 pps), and ^{14}Be (5×10^2 pps) generated by a 630-MeV ^{18}O beam on a 200-mg/cm^2 ^{9}Be target. The primary-beam current at the target reached 10 μAe. The COMBAS achromatic spectrometer was used with a total momentum ($\pm 10\%$) acceptance and a total solid angle (6.4 msr).

5. CONCLUSION

The production of $4 \leq A \leq 22$, $2 \leq Z \leq 11$ isotopes that is induced in the inverse-kinematics reaction ^{18}O + ^{9}Be in the Fermi energy domain ($35A$ MeV) has been studied in forward-angle measurements by using the COMBAS double achromatic kinematical separator.

No evidence has been found for any dramatic change in the reaction mechanism for peripheral reactions in relation to that in the low-energy range. In the beam direct selection of isotopes produced in the interaction of a light projectile and a light target, the dominant role of stripping, pickup, and exchange nuclear reactions has been observed. Considerable

contributions from dissipative processes have been found for isotopes around the stability line. A unified exponential approximation using the Q_{gg} systematics of isotopic distributions for all detected elements has confirmed the binary type of the reaction producing neutron-rich isotopes. The simple exponential approximation realized by the Q_{gg} systematics is a powerful tool for correctly predicting the expected yields of unknown drip-line nuclei.

It has been shown that the LISE code underestimates the yields and incorrectly predicts the characteristics of the velocity distributions of the drip-line isotopes (the width and the position of the maximum), and this fact should be taken into account in experiments aimed at synthesizing unknown drip-line isotopes by using a fragment separator with small momentum acceptances. The observed intense production of isotopes with atomic numbers larger than that of the projectile ($Z > 8$) contradicts the projectile-fragmentation hypothesis.

The production rates have been determined for exotic nuclei of ^{9}Li, ^{11}Li, ^{11}Be, ^{12}Be, and ^{14}Be, which could be used for secondary radioactive beams of halolike nuclei.

It would be very important to continue studying the evolution of reaction mechanisms versus the projectile energy and the target neutron excess $(N/Z)_t$.

ACKNOWLEDGMENTS

We are indebted to Prof. Yu.Ts. Oganessian for stimulating discussions and support of this study. We also thank A.V. Solodovnikov for his assistance during the run and V.E. Zhuchko and V.S. Salamatin for the data-acquisition and processing programs.

This work was supported in part by INTAS (grant no. 93-496) and by the Russian Foundation for Basic Research (project no. 96-02-17214).

REFERENCES

1. B. Borderie, M. F. Rivet, and L. Tassan-Got, Ann. Phys. (Paris) **15**, 287 (1990).
2. M. Lefort and Ch. Ngo, Ann. Phys. (Paris) **3**, 5 (1978).
3. A. S. Goldhaber and H. H. Heckman, Annu. Rev. Nucl. Part. Sci. **28**, 161 (1978).
4. D. Guillemaud-Mueller, Yu. E. Penionzhkevich, R. Anne, *et al.*, Z. Phys. A **332**, 189 (1989).
5. H. Sakurai, N. Aoi, D. Beaumel, *et al.*, in *Proceedings of 4th International Conference on Radioactive Nuclear Beams, Omiya, 1996,* Ed. by S. Kubono, T. Kobayashi, and I. Tanihata (Elsevier, Amsterdam, 1997), p. 311.
6. V. Borrel, D. Guerreau, J. Galin, *et al.*, Z. Phys. A **314**, 191 (1983).
7. Y. Blumenfeld, Ph. Chomaz, N. Frascaria, *et al.*, Nucl. Phys. A **455**, 357 (1986).
8. V. Borrel, B. Gatty, D. Guerreau, *et al.*, Z. Phys. A **324**, 205 (1986).
9. M. C. Mermaz, V. Borrel, D. Guerreau, *et al.*, Z. Phys. A **324**, 217 (1986).
10. D. Bazin, D. Guerreau, R. Anne, *et al.*, GANIL Report P89-22 (1989).
11. Ch. O. Bacri, P. Roussel, V. Borrel, *et al.*, Nucl. Phys. A **555**, 477 (1993).
12. A. G. Artukh, G. F. Gridnev, M. Grushezki, *et al.*, Nucl. Instrum. Methods Phys. Res. A **426**, 605 (1999).
13. A. G. Artukh, G. F. Gridnev, V. L. Mikheev, and V. V. Volkov, Nucl. Phys. A **137**, 348 (1969).
14. A. G. Artukh, V. V. Avdeichikov, J. Ero, *et al.*, Nucl. Instrum. Methods **83**, 72 (1970).
15. A. G. Artukh, G. F. Gridnev, V. L. Mikheev, *et al.*, Nucl. Phys. A **215**, 91 (1973).
16. D. Bazin and O. Sorlin, private communications; http://www.nscl.msu.edu/~bazin/LISE/html; modified version: http://dnr080.jinr.ru/LISE/html.
17. A. G. Artukh, V. V. Avdeichikov, J. Ero, *et al.*, Nucl. Phys. A **160**, 511 (1971).

Physics of Atomic Nuclei, Vol. 65, No. 3, 2002, pp. 400–408. Translated from Yadernaya Fizika, Vol. 65, No. 3, 2002, pp. 426–434.

NUCLEI
Theory

Interaction of Neutrons with Nanoparticles

V. V. Nesvizhevsky*

Institute Laue-Langevin, Grenoble, France

Received February 13, 2001; in final form, October 5, 2001

Abstract—Two hypotheses concerning the interaction of neutrons with nanoparticles and having applications in the physics of ultracold neutrons (UCN) are considered. In 1997, it was found that, upon reflection from the sample surface or spectrometer walls, UCN change their energy by about 10^{-7} eV with a probability of 10^{-7}–10^{-5} per collision. The nature of this phenomenon is not clear at present. Probably, it is due to the inelastic coherent scattering of UCN on nanoparticles or nanostructures weakly attached at the surface, in a state of Brownian thermal motion. An analysis of experimental data on the basis of this model allows one to estimate the mass of such nanoparticles and nanostructures at 10^7 a.u. The proposed hypothesis indicates a method for studying the dynamics of nanoparticles and nanostructures and, accordingly, their interactions with the surface or with one another, this method being selective in their sizes. In all experiments with UCN, the trap-wall temperature was much higher than a temperature of about 1 mK, which corresponds to the UCN energy. Therefore, UCN increased their energy. The surface density of weakly attached nanoparticles was low. If, however, the nanoparticle temperature is lower than the neutron temperature and if the nanoparticle density is high, the problem of interaction of neutrons with nanoparticles is inverted. In this case, the neutrons of initial velocity below 10^2 m/s can cool down, under certain conditions, owing to their scattering on ultracold heavy-water, deuterium, and oxygen nanoparticles to their temperature of about 1 mK, with the result that the UCN density increases by many orders of magnitude. © *2002 MAIK "Nauka/Interperiodica".*

1. INTRODUCTION

A long storage of ultracold neutrons (UCN, $V_{\mathrm{UCN}} \sim 5$ m/s, $E_{\mathrm{UCN}} \sim 10^{-7}$ eV) in traps is useful in fundamental-physics experiments. This application of UCN motivates continuing attempts at eliminating their extra losses in the trap wall. Let us recall how the interaction of UCN with a surface is described: UCN are reflected from a uniform potential barrier, which is formed upon averaging strong neutron–nucleon interaction, with a critical energy E_{lim} and the corresponding critical velocity V_{lim}. One observes total reflection if $V_{\mathrm{UCN}} < V_{\mathrm{lim}}$, but UCN can be lost with a small probability because of their absorption by nuclei in the trap walls or because of their upscattering in the trap walls to the energy region around kT, where k is the Boltzmann constant and T is the trap-wall temperature. UCN may penetrate inside if $V_{\mathrm{UCN}} > V_{\mathrm{lim}}$. If the surface is immobile in the laboratory frame, collisions are elastic. Otherwise, UCN may change their energy.

An additional kind of UCN escape mechanism from gravitational spectrometers [1] due to their scattering on surfaces of beryllium, copper, stainless steel, and liquid fomblin oil was found and investigated in 1997. The phenomenon consists in a small increase in UCN energy owing to their interaction with the surface. By analogy with the usual evaporation process, such events will be referred to as the formation of VUCN (Vaporizing UCN). The measured characteristic probability of VUCN generation was $P_{\mathrm{VUCN}} \sim 10^{-7}$–$10^{-5}$ per collision. If the resulting neutron energy is higher than the wall potential barrier, then the neutron can penetrate into the wall material, where it will be absorbed or upscattered; if the wall is sufficiently thin, then it may penetrate through it, as this was measured in [2]. A permanent generation of VUCN prevents a spectrum shaping such that all above-barrier neutrons are removed. The new escape channel, described below in detail, is in line with the general hypothesis proposed in [3] to explain anomalous UCN losses [4].

At the liquid-fomblin-oil surface, where the probability P_{VUCN} has the highest value among all measured materials, this process was independently found and studied in [5] and in other publications of this group. Other research groups are expected to publish their papers later that also confirm the existence of small changes in UCN energy in fomblin-oil-coated traps. It is straightforward to assume that the phenomenon of a small decrease in the UCN energy—it was found in [6] at a liquid-fomblin-oil surface and

*e-mail: nesvizhevsky@ill.fr

in [1] at a solid-stainless-steel surface—has the same nature as the aforementioned phenomenon of a small increase in the UCN energy.

Thus, UCN were expected to be upscattered on surfaces to energies in the region around kT (that is, about 10^{-2} eV at room temperature or at liquid nitrogen temperature). Such upscattering was actually measured in [7, 8] and in other experiments. The total probability of this process is usually 10^{-5}–10^{-4} per collision with the surface. The "tail" of such an energy distribution at energies of about 10^{-7} eV has to be negligible. In all models, the probability of such a scattering process is much lower than 10^{-10}. However the probability of upscattering to this energy region appeared to be surprisingly high ($P_{\mathrm{VUCN}} \sim 10^{-7}$–$10^{-5}$), commensurate with the probability of normal upscattering to the energies around kT. The nature of this phenomenon has to be clarified. Moreover, a simultaneous investigation of VUCN generation and UCN anomalous losses is of interest, since these two phenomena have similar experimental manifestations.

These small changes in the energy of UCN, which occur in their interaction with trap walls, are probably due to the thermal motion of nuclei forming the wall potential. However, the mechanism that is responsible for the transformation of this thermal motion into the spreading of the UCN spectrum is not clear. The point is that the interaction of neutrons with nuclei is a quantum process, and the corresponding potential results from the interaction of neutrons with a large number of nuclei even when these nuclei are at rest. When the nuclei move, we have a quantum problem of many interacting bodies, and even methods for solving such a problem are still under discussion.

The reflection of UCN from a flat surface was considered in a series of theoretical studies of Barabanov and Belyaev [9]. The changes in the energy of UCN in their quasielastic reflections from the surface corresponded to values measured in experiments. However the probability of VUCN generation due to the reflection of UCN from a flat surface was estimated to be much lower than that measured in experiments.

In Section 2, we consider the hypothesis that VUCN are generated owing to the inelastic coherent scattering of UCN on nanoparticles or nanostructures weakly attached at the surface in a state of thermal motion. In this case, the problem is much simpler because of the assumption that the interaction of UCN with surface nanoparticles involved in the thermal motion is the dominant mechanism of transformation of the thermal motion of atomic nuclei in walls into small changes in the UCN energy. As a result, the problem becomes equivalent to the well-known quantum-mechanical problem of two bodies—that is, to the problem of a neutron–nanoparticle collision that is elastic in the c.m. frame of the colliding particles. General ideas of additional UCN losses due to small particles at the surface were formulated earlier, for instance, in [10, 11]. In [10], clusters of molecules were considered. In [11], it was indicated that UCN could aid in identifying a new particle with a long-range potential and a weak coupling to the surface. In any case, the nanoparticle temperature is obviously equal to the trap temperature T in the range 10^1–10^3 K. The UCN energy corresponds to $T_{\mathrm{UCN}} \sim 1$ mK. Ultracold neutrons increase preferentially their energy in collisions with such "warm" nanoparticles. The probability of such inelastic UCN scattering on the surface is small, since the surface density of such weakly attached nanoparticles is small.

However, the mathematical problem of neutron–nanoparticle interaction can in principle be inverted: the interaction of "warm" neutrons with ultracold nanoparticles of temperature about 1 mK can cool down the neutrons. If the density of weakly attached nanoparticles is high (not only do these nanoparticles cover the surface, but they also fill the volume) and if, during cooling of neutrons, the probability of their absorption and β decay is low, then the neutron density increases. This process can allow, for the first time, the equilibrium cooling of neutrons down to UCN temperature. It is analyzed in Section 3.

In order to produce UCN, one first uses nuclear fission in nuclear reactors, which releases neutrons of energy about 10^7 eV. The energy of neutrons in pulsed sources based on proton accelerators is commensurate with that in reactors. However, the cooling of neutrons by a factor of about 10^8(!) is achieved just owing to a few tens of their collisions with nuclei in reactor moderators (hydrogen, deuterium). The energy transfer is very efficient, and the neutron losses during the cooling process are low because the mass of moderator nuclei is equal to (or about) the neutron mass. However, a further cooling does not occur: the lower the neutron energy, the larger the neutron wavelength. When it becomes commensurate with the distances between the nuclei of the moderator, the neutrons do not "see" individual nuclei any longer—they are just affected by the average optical potential of the medium. The neutron energy becomes lower than the binding energy of atoms in the medium. A further cooling of the neutrons due to their interaction with collective degrees of freedom (such as phonons) is less efficient than the moderation of the neutrons due to their collisions with nuclei. However, it allows the cooling of the neutrons to the energy range of cold neutrons (about 10^{-3} eV). But this is insufficient for the cooling of the main portion of the neutrons

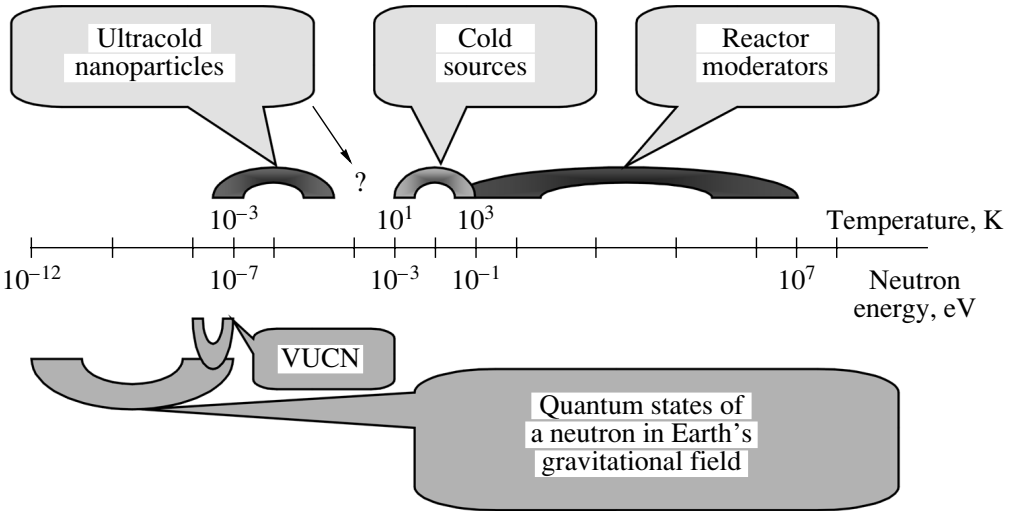

Fig. 1. Neutron energy and temperature ranges that correspond to various moderators, along with a few examples of physical phenomena involving UCN and even slower neutrons.

to the UCN energy region [12–15]. The idea of neutron cooling on ultracold nanoparticles as proposed in Section 3 in this article consists in reproducing the principle of neutron cooling in reactor moderators via multiple collisions. However, the scale is different: the sizes are greater by a factor of about 10^2, which increases the energy range of application of this mechanism by a few orders of magnitude. The energy and the temperature scales that correspond to the mechanisms being considered are shown in Fig. 1. It should be noted that such a UCN source is based on the principle of UCN density accumulation as in a superthermal source [13] but not on the use of UCN flux from a source in the flow-through mode.

In conventional sources used to select UCN, thermal equilibrium is not achieved. Sources are much hotter than UCN. Only a very small portion of the neutrons are used—other neutrons are lost. Actually, these are sources of cold or very cold neutrons (VCN), and experimentalists have to select a narrow fraction of a broad energy spectrum. For instance, the most intense flux of UCN is now produced in a liquid-deuterium source placed within the core of the high-flux reactor at the Institute Laue-Langevin (ILL) [12]. It increases the UCN flux by a factor of about 10^2 in relation to that available anyway in a reactor in the thermal equilibrium spectrum. Only a fraction of the neutron flux of about 10^{-9} is actually used then. On the other hand, the cooling of neutrons on ultracold nanoparticles could provide a further neutron cooling in a significant energy range, thereby increasing the neutron density available for experiments.

2. ARE VUCN PRODUCED ON SURFACE NANOPARTICLES?

2.1. Description of the Model

Let us assume that inelastic coherent UCN scattering on nanoparticles or nanostructures that are weakly attached at the surface and which are permanently in a state of random thermal motion is the dominant mechanism through which the energy of UCN undergoes small changes in their interaction with the surface. In contrast to the general quantum-mechanical problem of UCN reflection from many moving nuclei, this model allows a radical simplification, which reduces the general problem to that of a UCN collision with a moving nanoparticle, this collision being elastic in the c.m. frame of the two particles. In contrast to the general problem, the proposed model does not obviously describe any features of UCN interaction with the surface other than the aforementioned mechanism of small changes in the UCN energy.

Within the proposed model, no assumptions about the size distribution for such objects at the surface is needed for explaining experimental results. The nature of the interaction itself provides a selection of the particle size d that is important in experiments and which corresponds to the neutron wavelength $\lambda\!\!\!^{-}_n$, which is related to the neutron velocity V_n as

$$\lambda\!\!\!^{-}_n[\mathrm{nm}] = \frac{63}{V_n[\mathrm{m/s}]} \text{ or } \lambda\!\!\!^{-}_{\mathrm{UCN}}[\mathrm{nm}] = \frac{63}{V_{\mathrm{UCN}}[\mathrm{m/s}]}. \quad (1)$$

Thus, we conclude that, if, on one hand, $d \gg \lambda\!\!\!^{-}_{\mathrm{UCN}}$, then such particles are too slow; therefore, the

change in UCN velocity, ΔV_{UCN}, is too low and can hardly be measured. If, on the other hand, $d \ll \lambda\!\!\!^{-}_{\mathrm{UCN}}$, then such particles are too small; therefore, the probability of their interaction with neutrons P_{VUCN} is too low, since neutrons diffract around such nanoparticles. Only if

$$d \approx \lambda\!\!\!^{-}_{\mathrm{UCN}}, \tag{2}$$

then corresponding VUCN can easily be measured, both owing to their relatively high energy and owing to the high probability of such a process.

Moreover, we do not need any hypothesis about special features of the interaction of nanoparticles with the surface. The probability of inelastic UCN scattering on strongly bound particles (or merely on a flat surface) is too small because of the smallness of their vibration amplitudes. In a rather general case, VUCN are produced on rigid small objects weakly attached to the surface. Nanoparticles can move along surface and (or) oscillate about equilibrium points with a large amplitude. Weak coupling of nanoparticles to the surface is natural because, usually, only a few atoms in nanoparticles interact simultaneously with the surface: the interatomic interaction is small at distances longer than about one angstrom, and any actual surface is rough on a nanometer scale.

Upon formulating the model, we will now justify its statements and estimate its parameters.

2.2. Justification of the Model and Estimation of Its Parameters

(i) Let us show that the thermal motion of nanoparticles or surface nanozones of diameter d equal to the UCN wavelength $\lambda\!\!\!^{-}_{\mathrm{UCN}}$ at a characteristic velocity of $V_{\mathrm{UCN}} \approx 3$ m/s, $d \approx \lambda\!\!\!^{-}_{\mathrm{UCN}} \approx 20$ nm, just corresponds to a change of $\Delta V_{\mathrm{UCN}} \sim 1$ m/s in the UCN velocity, a value that was measured in [1, 5, 6].

In thermodynamic equilibrium at a temperature T, the mean energy of about $kT/2$ is associated with each degree of freedom of a particle. For a nanoparticle of mass M, this allows one to estimate its mean velocity component $\overline{V_M}$ parallel to the momentum-transfer direction:

$$\overline{V_M} \approx \sqrt{kT/M}. \tag{3}$$

The mass of a spherical particle of density ρ is

$$M \approx \frac{\rho d^3}{2}. \tag{4}$$

The change in UCN energy is equal to the doubled nanoparticle velocity:

$$\Delta V_{\mathrm{UCN}} = 2V_M. \tag{5}$$

Thus, the mean change in the UCN velocity is

$$\overline{\Delta V_{UCN}} \approx 2\sqrt{\frac{2kT}{\rho d^3}}; \tag{6}$$

that is, it is just about 1 m/s.

(ii) How large is the mass of the particles that are responsible for the measured phenomenon? Equations (3), (5), and (6) give the mass of $M \approx kT/\overline{V_M^2} \approx 10^7$ a.u.

(iii) Let us show how the nanoparticle diameter that is of importance in experiments is chosen. If $d \ll \lambda\!\!\!^{-}_{\mathrm{UCN}}$, then the scattering probability is too low and depends strongly on the nanoparticle diameter:

$$P_{\mathrm{VUCN}} \sim \left(\frac{d}{\lambda\!\!\!^{-}_{\mathrm{UCN}}}\right)^6. \tag{7}$$

This is so because neutron scattering on a nanoparticle is a coherent process; therefore, the scattering cross section is proportional to the square of the number of nuclei in the nanoparticle, this number in turn being proportional to the cube of the nanoparticle size.

Equation (6) shows that, if $d \gg \lambda\!\!\!^{-}_{\mathrm{UCN}}$, the change in UCN velocity is too low, so that such VUCN can hardly be measured.

(iv) Let us show that the scattering of UCN on strongly bound nanoparticles corresponds to a low probability P_{VUCN}. The limiting case is that of a piece of material belonging to a flat uniform surface and having a total mass M and a diameter of $d \approx \lambda\!\!\!^{-}_{\mathrm{UCN}}$. In the Debye approximation, the quantum zero-point mean-square displacement of such a particle as a discrete unit in the direction perpendicular to the surface plane is

$$\langle X^2\rangle^0_\perp = \frac{\hbar}{8\pi^2 M}\int_0^{\nu_D}\frac{g(\nu)}{\nu}d\nu = \frac{3\hbar}{16\pi^2 M\nu_D}, \tag{8}$$

where $g(\nu) = \dfrac{3\nu^2}{\nu_D^3}$ is the phonon density of states and ν_D is the Debye cutoff frequency. Evidently, we have $\sqrt{\langle X_\perp^2\rangle^0} < 10^{-4}$ Å. At a finite temperature T, the surface displacement (Debye–Waller factor) is larger, but it is still at least as small as $\sqrt{\langle X_\perp^2\rangle^T} < 10^{-3}$ Å. Since $\sqrt{\langle X_\perp^2\rangle^T} \ll \lambda\!\!\!^{-}_{\mathrm{UCN}}$ and since the vibration frequency is much higher than the characteristic frequency of about 10^8 Hz, which is equal to the reciprocal quantum-mechanical time of UCN interaction with the surface, the interaction is of quantum

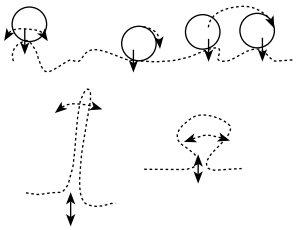

Fig. 2. Interaction of nanoparticles with the surface. The points of attraction of nanoparticles to the surface are indicated by solid arrows. The directions of motion are shown by dotted arrows.

nature: it is mainly elastic (in the absence of trivial vibrations of the walls), but, with a low probability, inelastic. The probability of such inelastic reflection can be estimated as the square of the ratio of the amplitude of wall vibrations to the neutron wavelength [16, 10]. Evidently, the corresponding value P_{VUCN} is much less than the measured probabilities; therefore, thermal vibrations of strongly bound nanostructures cannot produce the experimentally observed phenomenon.

(v) The opposite case is that of a free nanoparticle (a particle of mass about 10^7 a.u. at room temperature can ascend at an altitude of about 3 cm in Earth's gravitational field) or that of a weakly attached nanoparticle (it may diffuse along the surface or oscillate with a frequency of about 10^8 Hz and with an amplitude commensurate with its size). In this limit, the interaction cross section is nearly equal to the geometric cross section of the nanoparticle if the condition in (2) is satisfied. In all these cases, the probability P_{VUCN} can be estimated as the relative area coated with such "active" nanoparticles. One "active" nanoparticle of size about 20 nm on a square area of size about 20 μm provides the value of P_{VUCN} that was measured in [1]. Under such collisions, UCN change the energy of nanoparticles by a negligible value of $\Delta E_{\mathrm{UCN}} \approx 10^{-7}$ eV $\sim \Delta E_M$. Figure 2 illustrates the phenomenon under discussion in an idealized way.

(vi) In an intermediate case of slightly stronger binding ($\nu_{\mathrm{osc}} > 10^8$ Hz and $\sqrt{\langle X^2\rangle_\perp^T} < \lambda\!\!\!^{-}_{\mathrm{UCN}}$), the population of such objects at the surface must be higher than the probability P_{VUCN} of VUCN generation in order to fit measured P_{VUCN} values. It should be noted that the population of such "active" particles seems to have a reasonable value, since the population of any nanostructures, structural irregularities, or nanoparticles of the required size on an actual surface is much higher than that. These were measured with an atomic-force microscope at the surfaces of all samples that were actually used in the experiments reported in [1].

(vii) Let us analyze the predictions of this model.

As follows from Eq. (6), $\Delta V_{\mathrm{UCN}} \sim T^{1/2}$; therefore, $\Delta E_{\mathrm{UCN}} \sim T$ if $V_M < V_{\mathrm{UCN}}$. These dependences are better satisfied for smaller velocities of the thermal motion of nanoparticles and larger values of the UCN wavelength.

The probability P_{VUCN} depends on the number of active weakly attached nanoparticles. The dependence $P_{\mathrm{VUCN}}(T)$ is smooth if the coupling in the direction of large-amplitude motion (along the surface) is small.

Equation (6) also indicates that $\Delta V_{\mathrm{UCN}} \sim \rho^{-1/2}$; that is, the smaller the nanoparticle density, the larger the change in the UCN velocity. By the way, the density ρ can be calculated by using experimental data or can be obtained by comparing experimental data with a calibration measurement involving nanoparticles of known density.

In addition, $\Delta V_{\mathrm{UCN}} \sim d^{-3/2}$; for the optimal ratio of the nanoparticle diameter to the UCN wavelength [see Eq. (2)], this yields $\Delta V_{\mathrm{UCN}} \sim V_{\mathrm{UCN}}^{3/2}$.

Equation (6) estimates the upper boundary of the VUCN spectrum due to the wave properties of neutrons as they tunnel "around" overly small nanoparticles. The penetration of neutrons "through" nanoparticles above their potential barrier provides an alternative upper boundary of the VUCN spectrum. Known values of the critical velocity for various materials can provide additional information for verifying the present hypothesis or for identifying the particle material if the validity of the present model would be established. The actual value of ΔV_{max} is the smallest value of these two. Of course, a quantitative analysis of experiments within the present model requires more careful calculations than the above estimations.

2.3. Qualitative Analysis of Experimental Results

This hypothesis assumes a universal reason for VUCN generation at surfaces of different materials; in fact, relevant measurements were performed for the surfaces of stainless steel, fomblin oil, beryllium, and copper [1, 5], with the generation probability being scattered by one to two orders of magnitude.

From [1], it follows that, at solid surfaces, the generation probability $P_{\mathrm{VUCN}}(T)$ at a temperature of 400 K is not considerably higher than that at a temperature of 300 K. New data [17] showed a rather smooth temperature dependence $P_{\mathrm{VUCN}}(T)$ for beryllium and copper samples in the temperature range 100–300 K. On the other hand, the mobility of any nanoobjects at fomblin-oil surfaces (and, accordingly, the P_{VUCN} value) must be much higher than that at solid surfaces. Also, P_{VUCN} must increase

strongly at higher temperatures owing to a decrease in the oil viscosity.

The present model is compatible with the measured values for the low energy transfer of $\Delta E_{\rm UCN} \sim 10^{-7}$ eV.

It assumes higher values of $\Delta E_{\rm UCN}$ for greater initial values of $E_{\rm UCN}$. Such a trend was actually found in [1] for a stainless-steel surface.

The Doppler shift in energy could be either positive or negative. A negative shift was in fact found in [6, 1]. The probability of such a process depends on the phase space available to VUCN. As might have been expected, measurements showed a much higher probability for heating than for cooling.

It is often stated that, if UCN gain in energy owing to any thermal motion, the energy scale around kT is involved. This is not true in our case since UCN leave traps just after the first event(s) of increase in energy, when no thermal equilibrium of UCN with walls has been achieved so far. The energy change depends on the nanoparticle velocity, which is small since it is associated with a relatively massive object of energy about kT.

A few factors complicate experiments of this kind. If $V_{\rm UCN} - V_M > V_{\rm lim}$, then $P_{\rm VUCN}$ is low. If $\Delta E_{\rm UCN}$ is too low, such VUCN could hardly be distinguished from UCN because of a finite energy resolution of spectrometers. If $\Delta E_{\rm UCN}$ is too high, then a poor storage time for such VUCN in spectrometers reduces significantly the detection efficiency. If $E_{\rm UCN} + \Delta E_{\rm UCN} > E_{\rm lim}$, the efficiency is negligible. These reasons make difficult quantitative analysis of many previous experiments with UCN. Therefore, a dedicated study of small changes in the UCN energy in a well-optimized spectrometer is required.

3. CAN COOLING ON NANOPARTICLES PRODUCE UCN?

A new method for producing UCN consists in the equilibrium cooling of VCN owing to their many collisions with ultracold nanoparticles made from low-absorbing materials (D_2O, D_2, O_2, etc.) down to the temperature of these nanoparticles of about 1 mK during the diffusion motion of these neutrons in a macroscopically large ensemble of nanoparticles. The principle of equilibrium cooling allows an increase in the neutron phase-space density in contrast to the method of discrimination of a narrow energy range out of a warmer neutron spectrum. The use of nanoparticles provides a sufficiently large cross section for coherent interaction and an inhomogeneity of the moderator density on a spatial scale of about the neutron wavelength; they also shift the energy-transfer range far below a value of about 10^{-3} eV, a characteristic limit for liquid and solid moderators. Many collisions are needed since the nanoparticle mass is much higher than the neutron mass; therefore, the energy transfer to nanoparticles and nanostructures is difficult. A large number of collisions constrains the choice of materials: only low-absorbing ones are appropriate. The nanoparticle temperature should correspond to such a minimal neutron energy down to which neutrons can still be cooled by this method. The diffusion motion of neutrons in the ensemble of nanoparticles allows one to minimize the thermalization length and, accordingly, to increase the achievable UCN density. The cooling itself is provided by the interaction of neutrons with individual degrees of freedom of weakly bound or free nanoparticles, as well as by the excitation of collective degrees of freedom in ensembles of nanoparticles, such as vibrations and rotations, and also by the breaking of internanoparticle bonds.

Upon formulating our main ideas, we will now proceed to justify them within the simple model of free nanoparticles and to estimate the model parameters.

3.1. Model of Free Nanoparticles and Estimation of Parameters

(i) Let us estimate the loss of neutrons due to their capture in nuclei during their cooling in a gas of free molecules. At low temperatures, all gases become liquid (helium) or solid. Therefore, a consideration of neutron scattering on free molecules at temperature of about 1 mK is only the first step in analyzing neutron interaction with nanoparticles. From the theory of neutron cooling in reactor moderators, it follows that, for an isotropic angular distribution of scattered neutrons in the c.m. frame, the cooling of neutrons in gases of free atoms (or molecules) with an atomic mass A is efficient if

$$\frac{\sigma_{\rm coh}}{A\sigma_{\rm abs}} > \ln\left(\frac{V_i}{V_f}\right), \qquad (9)$$

where V_i is the initial neutron velocity and V_f is the final neutron velocity. It should be noted that the coherent-scattering cross section $\sigma_{\rm coh}$ is independent of the neutron velocity, while the absorption cross section $\sigma_{\rm abs}$ is proportional to the reciprocal neutron velocity:

$$\sigma_{\rm abs}(V_n) \sim \sigma_{\rm abs}(V_0)V_0/V_n. \qquad (10)$$

This circumstance limits the minimal velocity $V_{\rm min}$ that can be achieved owing to the cooling of neutrons in a free molecular gas even at zero temperature. On the other hand, the losses of neutrons are negligible when the neutron velocity is higher than this "dangerous" limit. The condition in (9) constrains the list of candidates to a very few: deuterium, oxygen, probably

Estimates of the minimal velocity to which neutrons can be cooled down in a gas of free atoms, molecules, or nanoparticles of various materials $\left[\frac{\sigma_{\rm coh}}{A\sigma_{\rm abs}(V_{\rm min})} = 1\right]$

Molecule/atom	$V_{\rm min}$, m/s
D, D_2	~ 0.4
D_2O	~ 1.0
O, O_2	~ 2.4
CO_2	~ 10.0
C	~ 16.0
Be	~ 20.0

carbon, or a combination of these species. The table compares different materials for nanomoderators. The cooling of neutrons down to velocities even lower than that presented in the table is not efficient, but, fortunately, such neutrons have already been cooled sufficiently in order to trap them.

(ii) Evidently, a decrease in the thermalization length increases the density of cooled neutrons. This condition requires a significant increase in the neutron-scattering cross section in moderators; this may be achieved by assembling molecules (or atoms) into nanoparticles. The cross section for the interaction of neutrons with nanoparticles is proportional to the square of the number of molecules in a nanoparticle, while the absorption cross section is in direct proportion to the number of molecules in a nanoparticle. (If $T \sim 10^{-3}$ K, then absorption is supposed to be the only alternative to the cooling of neutrons. This assumption is surely correct if the low-energy upscattering of UCN [1, 5] is actually responsible for anomalous losses of UCN [4] and if other unknown phenomena are not involved.) With increasing the nanoparticle size, there arise two factors that compensate each other. (A) The number of collisions needed for cooling neutrons is proportional to the nanoparticle mass M. (B) The ratio of the coherent-scattering cross section to the absorption cross section is also proportional to the nanoparticle mass, $\sigma^M_{\rm coh}/\sigma^M_{\rm abs} \sim M$. Therefore, the condition in (9) for the efficiency of cooling is valid until the nanoparticle size becomes so great that scattering proves to be anisotropic; that is, if $d < \lambda\!\!\!^{-}_n$, then

$$\frac{\sigma^M_{\rm coh}}{M\sigma^M_{\rm abs}} \approx \frac{\sigma_{\rm coh}}{A\sigma_{\rm abs}}. \qquad (11)$$

If the neutron velocity is higher or if the nanoparticle size exceeds these limits (or if both these conditions are satisfied), the angular distribution of scattered neutrons is directed forward. This change in the angular distribution of scattered neutrons increases the relative importance of absorption. The condition in (11) is not valid in this case, since the coherent-scattering cross section increases more slowly than in proportion to N^2; also, the energy transfer per collision decreases. Therefore, the velocity range for neutrons that can still be cooled down is restricted from above by some velocity $V_{\rm max}$.

(iii) Thus, the neutron velocity range $V_{\rm min}$–$V_{\rm max}$ in which the cooling at ultracold nanoparticles is efficient is restricted from both sides: the minimal velocity $V_{\rm min}$ is restricted by neutron absorption in the nuclei of a nanoparticle material, while the maximal velocity $V_{\rm max}$ is restricted by a decrease both in the interaction cross section and in the energy transfer. The broader this range of acceptable velocities, the greater the resulting increase in the neutron phase-space density.

(iv) Let us show that the range of acceptable neutron velocities in the model of free nanoparticles is broad. An estimate of $V_{\rm min}$ is independent of the nanoparticles size, since the condition in (11) is always valid if $d < \lambda\!\!\!^{-}_n$. But the neutron wavelength is proportional to the reciprocal neutron velocity (1) and, in the low-velocity limit, is just large at the last stage of cooling. Thus, only the nanoparticle material specifies the value of $V_{\rm min}$, which can be estimated as

$$\frac{\sigma_{\rm coh}}{A\sigma_{\rm abs}(V_{\rm min})} = 1; \qquad (12)$$

that is, it can be as low as about 1 m/s (see table).

On the other hand, the quantum-mechanical problem of neutron interaction with a nanoparticle must be solved in order to estimate $V_{\rm max}$. This is beyond the scope of the present study, but I am going to address the problem in a forthcoming publication. However, $V_{\rm max}$ can be estimated. Let us use the following model: The distance between nanoparticles is three times greater than the nanoparticle diameter; that is, the relative volume of about 1.6% is occupied by nanoparticles. Therefore, neutrons can resolve the variation in the density of nuclei in such a moderator. The macroscopic scattering length in such a moderator is

$$\Delta l \approx \frac{1}{N^M\sigma^M_{\rm coh}} \approx \frac{(3d)^3A^2m_n^2}{\sigma_{\rm coh}M^2} \approx \frac{108A^2m_n^2}{\sigma_{\rm coh}\rho^2d^3}. \qquad (13)$$

Under the assumption of an isotropic angular distribution of scattered neutrons, the thermalization length L is greater by a factor equal to the square root of the number of scattering events needed for thermalization:

$$L \approx \Delta l\sqrt{\frac{M}{m_n}} \approx \frac{80A^2m_n^{3/2}}{\sigma_{\rm coh}\rho^{3/2}d^{3/2}}. \qquad (14)$$

The thermalization length for heavy-water nanoparticles in this simplified model is

$$L^{D_2O}[\text{cm}] \approx \frac{40}{(d[\text{nm}])^{3/2}}. \quad (15)$$

A reasonable moderator size of 10 cm corresponds to the nanoparticle diameter of about 2.5 nm or [see Eq. (2)] to the initial neutron velocity of about 25 m/s. The efficiency of neutron thermalization is still significant for an initial neutron velocity a few times higher than that; therefore, the maximal neutron velocity of interest is about 10^2 m/s.

4. DISCUSSION

(i) In actual nanoparticle moderators at ultralow temperatures, nanoparticles are not free. However, the interaction between them is very weak sometimes. By way of example, we indicate that, if one takes nanoparticles of needed size and material (D_2O, D_2, O_2, etc.) and drops them into superfluid ^{4}He (not absorbing neutrons and just providing heat transfer), they are immediately coated with a thin layer of solidified helium. This layer screens the nanoparticles from one another and reduces the interaction between neighboring nanoparticles [18, 19]. An important problem to be studied in experiments is that of the conditions under which nanoparticles move rather independently in their collisions with neutrons. Does the interaction of nanoparticles in such gels leave sufficient freedom for them? Their independent interaction with neutrons is of crucial importance, since, otherwise, the effective mass of nanoparticles increases, with the result that the energy transfer decreases dramatically. On the other hand, additional degrees of freedom (vibrations, rotations, breaking of interparticles bonds) in such gels provide probably an even more efficient cooling of neutrons than collisions, and they should be considered specially.

(ii) In actual moderators, in contrast to the simplified model of free nanoparticles, it is necessary to take into account neutron-optics effects due to finite distances between nanoparticles. As soon as the neutron energy becomes sufficiently low (the neutron wavelength becomes sufficiently large), the neutron wavelength covers simultaneously a few nanoparticles; therefore, the effect of coherent upward scattering of neutrons in the ensemble of nanoparticles takes place. This results in the following: (A) The energy transfer decreases, and the cooling process becomes less efficient. (B) The depth of extraction of such neutrons increases, and the moderator becomes more transparent for such low-energy neutrons. In this case, UCN can diffuse out to the moderator surface from its total depth, and this simplifies their extraction.

(iii) The technical feasibility of such a moderator should be carefully studied. The use of ultralow temperatures does not permit placing it in the vicinity of the reactor core. It can be installed at the exit of an optimized VCN neutron guide. A detailed experimental and theoretical study of the feasibility of the proposed neutron moderator using ultracold nanoparticles is to be performed in the framework of the project described in [20].

5. CONCLUSION

The proposed hypothesis on the nature of VUCN generation explains small changes in the UCN energy in traps in terms of their coherent scattering on nanoparticles weakly bound to surface or just on nanostructures of a rough surface for which large oscillation amplitudes are allowed. UCN change their energy in such a scattering process because nanoparticles and nanostructures are always in a state of thermal motion. This model is qualitatively compatible with available experimental data. Such weakly attached nanoparticles or nanostructures could be selected in a direct measurement (for instance, with an atomic-force microscope) or in future UCN experiments (for instance, by a selective action on a surface nanostructure with a simultaneous control of VUCN generation). This model provides guidelines for experimental studies, but it cannot yet be proven or rejected on the basis of already known results. On the other hand, this hypothesis provides a sensitive method for studying the dynamics of specially introduced nanoparticles or nanostructures and, as a result, their interactions with the surface or with one another.

In addition, a new concept for increasing the UCN density has been proposed. This concept is based on the cooling of neutrons on ultracold nanoparticles of heavy water, deuterium, or oxygen in superfluid helium. This method can be applied at initial neutron energies in the range from 10^{-8}–10^{-7} eV to 10^{-5}–10^{-4} eV. It differs from traditional methods for UCN selection by a high efficiency of employing the initial neutron flux. Detailed theoretical and experimental study of such a cooling process, as well as reliable estimations of UCN density gain and the maximal neutron energy at which such a process is still efficient, is required.

ACKNOWLEDGMENTS

I am grateful to my colleagues for criticism and discussions, especially to H. Börner, V.K. Ignatovich, R.U. Khafizov, E.V. Lychagin, A.V. Muzychka, J.M. Pendlebury, and A.V. Strelkov.

REFERENCES

1. V. V. Nesvizhevsky, A. V. Strelkov, P. Geltenbort, and P. S. Iaydjiev, ILL Annual Report (1997), p. 62; Eur. J. Appl. Phys. **6**, 151 (1999); Yad. Fiz. **62**, 832 (1999) [Phys. At. Nucl. **62**, 776 (1999)]; A. V. Strelkov, V. V. Nesvizhevsky, P. Geltenbort, *et al.,* Nucl. Instrum. Methods Phys. Res. A **440**, 695 (2000).
2. P. Geltenbort, A. G. Kharitonov, V. V. Nesvizhevsky, *et al.,* ILL Preprint 97GE5051 (1997).
3. A. V. Strelkov, in *Proceedings of IV School on Neutron Physics, Alushta, Russia, 1990*, p. 325.
4. V. P. Alfimenkov, V. V. Nesvizhevsky, A. P. Serebrov, *et al.*, Pis'ma Zh. Éksp. Teor. Fiz. **55**, 92 (1992) [JETP Lett. **55**, 84 (1992)].
5. L. N. Bondarenko, P. Geltenbort, E. I. Korobkina, *et al.*, Yad. Fiz. **65**, 13 (2002) [Phys. At. Nucl. **65**, 11 (2002)].
6. L. N. Bondarenko, E. I. Korobkina, V. I. Morozov, *et al.,* Pis'ma Zh. Éksp. Teor. Fiz. **68**, 663 (1998) [JETP Lett. **68**, 691 (1998)]; in *Proceedings ISINN-6, JINR, Dubna, Russia, 1998,* p. 101.
7. A. V. Strelkov and M. Hetzelt, Zh. Éksp. Teor. Fiz. **74**, 23 (1978) [Sov. Phys. JETP **47**, 11 (1978)].
8. A. D. Stoica, A. V. Strelkov, and M. Hetzelt, Z. Phys. B **29**, 349 (1978).
9. S. T. Belyaev and A. L. Barabanov, Nucl. Instrum. Methods Phys. Res. A **440**, 704 (2000); A. L. Barabanov and S. T. Belyaev, Yad. Fiz. **62**, 824 (1999) [Phys. At. Nucl. **62**, 769 (1999)]; Eur. Phys. J. B **15**, 59 (2000).
10. V. K. Ignatovich, *The Physics of Ultracold Neutrons* (Clarendon, Oxford, 1990).
11. J. M. Pendlebury, Annu. Rev. Nucl. Part. Sci. **43**, 687 (1993).
12. A. Steyerl *et al.,* Phys. Lett. A **116**, 347 (1986); P. Ageron, P. De Beaucourt, H. D. Harig, *et al.*, Cryogenics **9**, 42 (1969).
13. R. Golub and J. M. Pendlebury, Phys. Lett. A **62A**, 337 (1977).
14. I. S. Altarev, N. V. Borovikova, A. P. Bulkin, *et al.*, Pis'ma Zh. Éksp. Teor. Fiz. **44**, 269 (1986) [JETP Lett. **44**, 344 (1986)].
15. A. P. Serebrov, V. A. Mityukhlyaev, A. A. Zakharov, *et al.*, Pis'ma Zh. Éksp. Teor. Fiz. **59**, 728 (1994) [JETP Lett. **59**, 757 (1994)].
16. L. D. Landau and E. M. Lifshitz, *Course of Theoretical Physics,* Vol. 3: *Quantum Mechanics: Non-Relativistic Theory* (Nauka, Moscow, 1989, 4th ed.; Pergamon, New York, 1977, 3rd ed.).
17. E. V. Lychagin, A. Yu. Muzychka, V. V. Nesvizhevsky, *et al.*, Yad. Fiz. **63**, 609 (2000) [Phys. At. Nucl. **63**, 548 (2000)].
18. L. T. Mezhov-Deglin and A. M. Kokotin, Pis'ma Zh. Éksp. Teor. Fiz. **70**, 744 (1999) [JETP Lett. **70**, 756 (1999)].
19. S. I. Kiselev, V. V. Khmelenko, and D. M. Lee, J. Low Temp. Phys. **121**, 671 (2000).
20. V. V. Nesvizhevsky, ILL Millenium Program (2000), p. 30.

Translated by V. Nezvishevsky

Physics of Atomic Nuclei, Vol. 65, No. 3, 2002, pp. 409–412. Translated from Yadernaya Fizika, Vol. 65, No. 3, 2002, pp. 435–440.

NUCLEI
Theory

Stopping Kinetics of Fast Protons in Oriented Crystal Targets

V. V. Balashov, L. L. Balashova*, and I. V. Bodrenko**

Institute of Nuclear Physics, Moscow State University, Vorob'evy gory, Moscow, 119899 Russia

Received January 16, 2001

Abstract—A method is proposed for theoretically studying the energy distributions of fast protons traversing oriented crystal targets. The method combines the use of kinetic equations for the distribution of channeled and dechanneled particles with a Monte Carlo computer simulation of their propagation. Specific calculations were performed for 1-MeV protons traversing a silicon target along the ⟨100⟩ axis.

1. INTRODUCTION

Special features of the transmission of charged particles through oriented crystals is of great interest for various realms of investigations—from high-energy physics (the transportation of accelerated particles by using bent single crystals [1–3]) to atomic physics (the resonance coherent excitation of multiply charged ions in channeling [4–7]). However, there are still obscure questions in the theory of the transmission process itself. In particular, this concerns the description of energy losses of particles in channeling. Even at the early stages of investigating this phenomenon, there arose the question of how the spectra of particles ejected from a target can be broken down into the contribution from those that travel the entire path as channeled ones and the contribution from dechanneled particles moving as if being in a nonoriented target. These dechanneled particles, which are in a medium where the electron density is higher than that inside the channel, lose, on average, a much greater amount of energy than channeled particles. On the other hand, dechanneling, which is caused, according to Lindhard [8], by multiple random collisions between the traveling particle and the electrons of the medium and by thermal vibrations of the crystal lattice, is a stochastic process. The combination of these factors results in that the superposition of the loss spectra of channeled and dechanneled particles generates a nontrivial picture of total loss spectra at the output of the target (see, for example, [9]), and reliable methods for quantitatively describing these spectra have yet to be developed. The recent experiments reported in [10], which seem to produce results where the contributions from the channeled and the dechanneled component to the observed loss spectrum are separated, and their interpretation in [11] on the basis of a Monte Carlo computer simulation rekindled interest in this long-standing problem. In this study, we consider it within an approach that combines the Monte Carlo method and the method of kinetic equations for the distribution of channeled and dechanneled particles. Our quantitative calculations are performed with an eye to the conditions of the experiment described in [10], where a 1-MeV proton beam traverses a silicon target 3.8 μm thick in directions close to the ⟨100⟩ axis.

2. KINETIC EQUATIONS FOR THE STOPPING PROCESS AND DECHANNELING

We introduce the distributions $F_{\rm ch}(\Delta, z)$ and $F_{\rm dec}(\Delta, z)$ of the energy losses $\Delta = E_0 - E$ for channeled and dechanneled particles at a given distance z from the input of the target. In general, the stopping kinetics of charged particles is described by a set of coupled differential or integral equations if multiple transitions from one state to another are taken into account. We consider the equations for partial (for a specific charge state $\langle k\rangle$ of a particle) energy distributions $F_k(\Delta, z)$ that were proposed in [12] for describing, within the diffusion approach, ion stopping accompanied by charge exchange. In the differential form, these equations can be represented as

$$\frac{\partial F_k(\Delta,z)}{\partial z} = -\lambda_k^{\rm tot} F_k(\Delta,z) - S_k\frac{\partial F_k(\Delta,z)}{\partial \Delta} + \frac{\Omega_k^2}{2}\frac{\partial^2}{\partial \Delta^2}F_k(\Delta,z) + \sum_l \lambda_{kl} F_l(\Delta-\Delta_{lk},z), \quad k=1,\ldots,N, \tag{1}$$

where S_k and Ω_k^2 are, respectively, the stopping power and the straggling parameter in the state $\langle k\rangle$; λ_{kl} are

*e-mail: balash@anna19.npi.msu.su
**e-mail: bodrenko@anna19.npi.msu.su

the partial rates of transitions from the state $\langle k\rangle$ to various states $\langle l\rangle$; $\lambda_k^{\rm tot} = \sum_l \lambda_{kl}$ is the corresponding total rate of transitions; and Δ_{lk} is the average energy loss in an event of the charge-exchange process leading from the state $\langle l\rangle$ to the state $\langle k\rangle$. In the dechanneling problem, the structure of the set of coupled equations is considerably simplified because the transition from one state under consideration to the other proceeds only in one direction—from channeling to dechanneling—and the additional energy loss in a dechanneling event is negligible under the conditions of a transmission experiment.

We denote by $\lambda_{\rm dec}(z)$ the dechanneling rate (that is, the inverse length of dechanneling) at a distance z from the input of the target; by $S_{\rm ch}$ and $S_{\rm dec}$ the stopping powers for, respectively, the channeled and the dechanneled component of the particle beam; and by $\Omega^2_{\rm ch}$ and $\Omega^2_{\rm dec}$ the corresponding straggling parameters. The set of kinetic equations for the distributions $F_{\rm ch}(\Delta, z)$ and $F_{\rm dec}(\Delta, z)$ that follows from (1) has the form

$$\frac{\partial F_{\rm ch}}{\partial z} = -\lambda_{\rm dec}F_{\rm ch} - S_{\rm ch}\frac{\partial F_{\rm ch}}{\partial \Delta} + \frac{\Omega^2_{\rm ch}}{2}\frac{\partial^2}{\partial \Delta^2}F_{\rm ch}, \quad (2a)$$

$$\frac{\partial F_{\rm dec}}{\partial z} = \lambda_{\rm dec}F_{\rm ch} - S_{\rm dec}\frac{\partial F_{\rm dec}}{\partial \Delta} + \frac{\Omega^2_{\rm dec}}{2}\frac{\partial^2}{\partial \Delta^2}F_{\rm dec}. \quad (2b)$$

We also specify initial conditions as

$$F_{\rm ch}(\Delta, z=0) = F^0_{\rm ch}(\Delta), \quad (3)$$
$$F_{\rm dec}(\Delta, z=0) = F^0_{\rm dec}(\Delta).$$

Solving the first equation with these initial conditions at fixed parameters $S_{\rm ch}$ and $\Omega^2_{\rm ch}$, we obtain

$$F_{\rm ch}(\Delta, z) = \exp\left(-\int_0^z \lambda_{\rm dec}(z')dz'\right) \quad (4)$$
$$\times \int F^0_{\rm ch}(\Delta - \Delta')\frac{\exp(-(\Delta' - S_{\rm ch}z)^2/(2\Omega^2_{\rm ch}z))}{\sqrt{2\pi\Omega^2_{\rm ch}z}}d\Delta'.$$

This solution has the form of a convolution of a Gaussian distribution decaying in amplitude and the initial distribution $F^0_{\rm ch}$. In this case, the fraction of channeled particles is

$$P_{\rm ch}(z) = \int F_{\rm ch}(\Delta, z)d\Delta \quad (5)$$
$$= P_{\rm ch}(0)\exp\left(-\int_0^z \lambda_{\rm dec}(z')dz'\right).$$

In order to obtain the loss spectrum of dechanneled particles, we solved the second equation in (2) numerically.

3. STATISTICAL SIMULATION ACCORDING TO THE MONTE CARLO METHOD

A Monte Carlo computer simulation of proton channeling in a silicon crystal was carried out here by using the ASTRA code described in [13, 14]. The basic physical approximations underlying the code are as follows. Incident-beam particles entering the channel with an initial energy E_0 are assumed to move independently of one another along classical trajectories. The deflecting force $\mathbf{F}_{\rm sc}(\mathbf{r}) = -{\rm grad}U(x, y)$ acting from crystal-lattice atoms is calculated by using the continuous Lindhard potential $U(x, y)$, which in turn is obtained by averaging the sum of the potentials representing the interaction between a proton and individual atoms ordered along the chains forming the channel. For these potentials, we take the known Molière–Erginsoy form [15]. The contributions from the electrons of outer and inner shells of medium atoms are assumed to be additive. To calculate moderation due to the interaction with valence electrons, we use the local-density approximation. The dependence of energy losses on the impact parameter in the interaction of propagating particles with the electrons of inner shells is computed according to [16]. We take into account multiple collisions with electrons of the medium and with thermal vibrations of the lattice.

The trajectory of each particle is traced until its angle of inclination ψ with respect to the channel axis exceeds the critical angle $\psi_{\rm max}$ for which we take the Lindhard angle $\psi_{\rm L} = (2Ze^2/E_0d)^{1/2}$, where d is the lattice parameter. In the case under consideration, where a 1-MeV proton travels along the $\langle 100\rangle$ channel of a silicon crystal, the critical angle $\psi_{\rm max}$ is 0.49°. A particle is considered to be dechanneled if the condition $\psi < \psi_{\rm max}$ is violated at some point $\mathbf{r}$ of its trajectory or if the particle approaches the channel chain at a distance less than a critical value $r_{\rm cr}$ that is specified by the amplitude of thermal vibrations of lattice atoms. The energy E' of the particle and the slope θ' of its trajectory are fixed at this point; from this instant on, its energy E and the scattering angle θ at the output of the target are calculated on the basis of the standard formulas of stopping theory and the multiple scattering of particles traveling in disordered media [17] (the mean values of the required parameters for proton energies in the interval from 0.8 to 1.0 MeV are $S_{\rm dec} = 40$ keV/μm and $\Omega^2_{\rm dec} = 26$ keV^2/μm).

In each series of calculations that corresponds to a given target thickness, we considered 20 000 trajectories. As in [10], we took the value of FWHM = 19.5 keV for the particle-energy spread in the incident beam; the initial angular spread in the beam was characterized by the parameter $\Delta(\psi_{\rm in}) = 0.025°$.

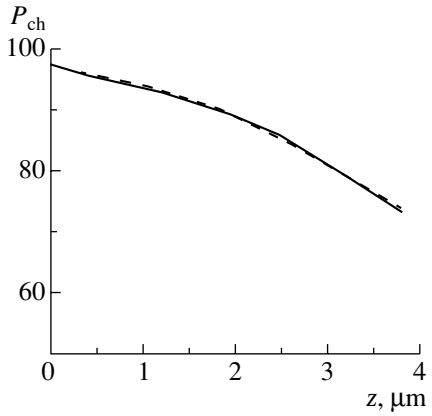

Fig. 1. Fraction of channeled particles in a proton beam having an initial energy of 1 MeV and traversing a silicon crystal along the ⟨100⟩ axis: (solid curve) results of a Monte Carlo calculation and (dashed curve) results of the calculation by formula (5).

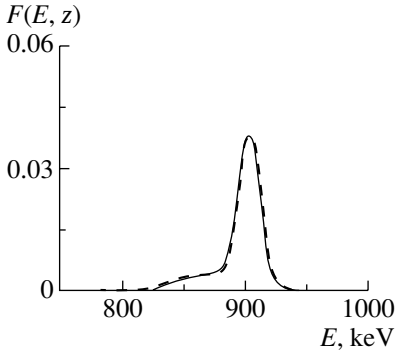

Fig. 2. Energy distribution of protons of initial energy 1 MeV upon traversing a 3.8-μm silicon target along the ⟨100⟩ axis: (solid curve) result obtained by solving Eq. (2) and (dashed curve) result of a Monte Carlo calculation.

4. RESULTS OF THE CALCULATIONS AND DISCUSSION

The parameters S_{ch}, Ω^2_{ch}, and λ_{dec}, which are necessary for solving the set of Eqs. (2), depend on the dynamics of channeled-particle interaction with lattice atoms and electrons of the medium. In this study, we take them from the results of a Monte Carlo computer simulation of the process under consideration. The first two parameters proved to be $S_{ch} = 25$ keV/μm and $\Omega^2_{ch} = 1.55$ keV^2/μm. Data on the dechanneling rate

$$\lambda_{dec}(z) = -\frac{dP_{ch}/dz}{P_{ch}}$$

and on its dependence on the path traveled by the particle are taken from the Monte Carlo calculation of the fraction of channeled particles.

For a 1-MeV proton beam incident on a silicon crystal along the ⟨100⟩ axis, Fig. 1 shows the results of Monte Carlo calculations illustrating the variation of the channeled-particle fraction $P_{ch}(z)$ in the beam as it traverses the target. Some fraction of protons (about 3%) occur outside the channel immediately upon entering the target. As the channeled particles propagate into the target, the rate of their dechanneling grows steadily. In the thickness interval $z = 0$–3.8 μm considered here, this growth can be taken to be linear. The dashed curve shows the fraction of channeled particles that was calculated by formula (5) with the aid of the linear approximation $\lambda_{dec}(z) = 0.032z + 0.012$: $P_{ch}(0) = 0.966$.

In order to obtain the spectra of channeled and dechanneled particles (and the total spectra together with them) at various distances from the input of the target by using the set of Eqs. (2), we adopt the above linear approximation for $\lambda_{dec}(z)$. Figure 2 shows the total energy distributions of channeled and dechanneled protons according to Monte Carlo calculations (the dashed curve) and according to calculations based on solving Eqs. (2) with the param-

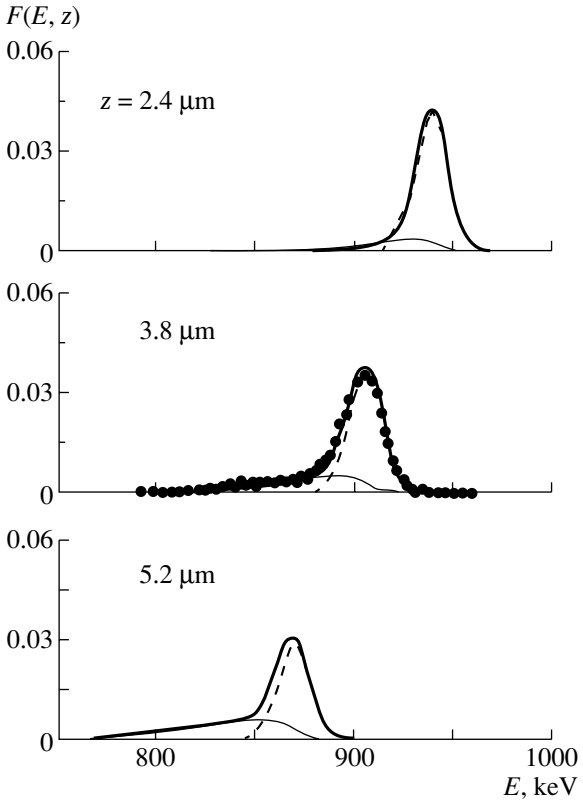

Fig. 3. Energy distribution of protons of initial energy 1 MeV upon traversing silicon targets of various thicknesses z along the ⟨100⟩ axis (thick solid curves). The dashed and thin solid curves represent the contributions from, respectively, channeled and dechanneled particles. Points correspond to experimental data from [10].

eters chosen in the way indicated above. That the two curves are virtually coincident suggests that the basic statistical approximations underlying the set of Eqs. (2) are adequate to the dynamics of particle-beam propagation through the target as simulated by the Monte Carlo procedure.

The results of the calculations for the thickness values of $z = 2.4$, 3.8, and 5.2 μm are displayed in Fig. 3. For the second value, they can be compared with experimental data from [10]. Separately, we show the contributions from channeled and from dechanneled particles. The spectra of channeled protons have a Gaussian shape. The shape of the spectrum of dechanneled protons is more complicated and is determined by the fact that part of their path lies in the region of low-electron density within the channel, while the part after dechanneling occurs in the region of high-electron density. It should be emphasized that the spectrum of dechanneled particles at the output of the target is not Gaussian, so that a Gaussian fit to such spectra, which is used in practice (in particular, in [10]), drastically simplifies the situation.

5. CONCLUSION

An approach combining the method of kinetic equations borrowed from the theory of propagation of multicomponent beams of charged particles through a medium with a Monte Carlo computer simulation supplements the theory of channeling with a procedure for calculating the energy-loss spectra of charged particles in targets of various thicknesses that admits a simple implementation and which is physically clear. In this study, we have presented an example of such a calculation with reference to the problem of separating the contributions from channeled and dechanneled particles to their energy distribution at the output from the target. Good agreement with available experimental data has been obtained without using adjustable parameters. In the future, the approach proposed here will be extended with the aim of including, in the consideration, not only energy spectra, but also angular characteristics of channeling and dechanneling.

ACKNOWLEDGMENTS

This work was supported by the Russian Foundation for Basic Research, project no. 00-02-17207.

REFERENCES

1. E. N. Tzyganov, Preprint Fermilab TM-684 (Batavia, 1976).
2. W. M. Gibson, I. J. Kim, M. Pisharody, *et al.*, Nucl. Instrum. Methods Phys. Res. B **2**, 54 (1984).
3. S. I. Baker, R. A. Carrigan, C. Crawford, *et al.*, Phys. Lett. B **137B**, 129 (1984).
4. V. V. Okorokov, D. L. Tolchenkov, I. S. Khizhnyakov, *et al.*, Phys. Lett. A **43A**, 485 (1973).
5. V. V. Okorokov, Yad. Fiz. **2**, 1009 (1965) [Sov. J. Nucl. Phys. **2**, 719 (1966)].
6. S. Datz, C. D. Moak, O. H. Crawford, *et al.*, Phys. Rev. Lett. **40**, 843 (1978).
7. T. Ito, Y. Takabayashi, K. Komaki, *et al.*, Nucl. Instrum. Methods Phys. Res. B **164**, 68 (2000).
8. J. Lindhard, K. Dan. Vidensk. Selsk. Mat. Fys. Medd. **34** (14) (1965).
9. B. R. Appleton, C. Erginsoy, and W. M. Gibson, Phys. Rev. **161**, 330 (1967).
10. Z. Y. Zhao, A. M. Arrale, S. L. Li, *et al.*, Phys. Rev. A **57**, 2742 (1998).
11. L. L. Balashova, Vestn. Mosk. Univ., Ser. 3: Fiz., Astron., No. 1, 58 (2001).
12. V. V. Balashov, A. V. Bibikov, and I. V. Bodrenko, Zh. Éksp. Teor. Fiz. **111**, 2226 (1997) [JETP **84**, 1215 (1997)].
13. K. Lenkeit, Ch. Trikalinos, L. L. Balashova, *et al.*, Phys. Status Solidi B **161**, 513 (1990).
14. Ch. Trikalinos, N. M. Kabachnik, L. L. Balashova, *et al.*, Nucl. Instrum. Methods Phys. Res. B **94**, 218 (1994).
15. Y.-H. Ohtsuki, *Charged Beam Interaction with Solids* (Taylor and Francis, London, 1983; Mir, Moscow, 1985).
16. L. L. Balashova, N. M. Kabachnik, and V. N. Kondratiev, Phys. Status Solidi B **161**, 113 (1990).
17. H. H. Andersen and J. F. Ziegler, *Hydrogen Stopping Powers and Ranges*, in *All Elements* (Pergamon, New York, 1977).

Translated by V. Bukhanov

Physics of Atomic Nuclei, Vol. 65, No. 3, 2002, pp. 413–425. Translated from Yadernaya Fizika, Vol. 65, No. 3, 2002, pp. 441–452.

NUCLEI
Theory

Mean Single-Particle Potentials and Single-Particle Energies in a Microscopic Model of the Nucleus

A. I. Steshenko

Bogolyubov Institute for Theoretical Physics, National Academy of Sciences of Ukraine, Metrologicheskaya ul. 14b, Kiev, 242153 Ukraine

Received June 2, 2000; in final form, December 13, 2000

Abstract—A method for calculating mean single-particle potentials and the corresponding single-particle energy levels in nuclei is presented. Specific formulas for these quantities are written for Slater determinant wave functions in the case of polarized orbitals and a central exchange nucleon–nucleon potential featuring a Gaussian radial dependence. The resulting theoretical estimates of single-particle properties of the nuclei considered in the present study are in satisfactory agreement with relevant experimental data. © *2002 MAIK "Nauka/Interperiodica".*

1. INTRODUCTION

The objective of a traditional microscopic theory of the nucleus is to construct nuclei on the basis of the nonrelativistic Schrödinger equation for a system of A interacting particles. In this case, the nucleon–nucleon potential plays the role of the main link in the chain that makes it possible to relate various nuclear properties within the algorithm of the model and to understand special features of their behavior versus variations in relevant physical parameters. In view of well-known difficulties, the nuclear many-body problem is solved approximately. An approximate theory (microscopic model) is constructed in such a way as to meet the following requirements: (i) It must be sufficiently simple from the mathematical point of view. (ii) It must describe satisfactorily the measured properties of actual nuclei.

At the first stage, it seems natural to describe a nuclear system in terms of individual particle states by representing the multinucleon wave function Ψ_A of the nucleus as the antisymmetrized product of single-particle orbitals $\phi_i(j)$ (Hartree–Fock approximation). By applying then the variational principle to the energy functional, one can derive [1], for $\phi_i(j)$, an equation that is interpreted as the Schrödinger equation for the corresponding particle moving in a self-consistent (mean or single-particle) nuclear field.

Owing to the explicit dependence of the wave function Ψ_A on the coordinates of all A intranuclear nucleons, it is possible to estimate, within multiparticle models, almost all nuclear quantities. However, microscopic calculations on the basis of model variational wave functions are usually performed only for collective (multinucleon) nuclear properties (binding energies, root-mean-square radii, spectra of the lowest energy levels, probabilities of $E2$ transitions, and so on), virtually no attention being given to single-particle features of nuclei. In an attempt at filling this gap to some extent, mean single-particle potentials and single-particle energies are considered in the present study on the basis of a microscopic model involving a pair exchange nucleon–nucleon potential.

The approach proposed here combines the following three equations: (i) an equation for the variational total-nuclear-energy functional, (ii) the Hartree–Fock equation for single-particle orbitals $\phi_i(j)$, and (iii) the well-known equation relating the total energy E of a nucleus to the sum of single-particle energies ε_λ. These equations are used to derive general formulas for mean single-particle potentials and mean single-particle energies. On the basis of these formulas, a dedicated package of codes is developed that makes it possible to calculate the aforementioned single-particle features for almost all nuclei (both spherical and deformed ones). For some light and medium-mass nuclei, specific calculations, which illustrate the efficiency of the approach proposed here, are performed for a few central exchange nucleon–nucleon forces that are often used in the literature.

2. SINGLE-PARTICLE POTENTIALS

In the model of deformed oscillator shells, the multiparticle wave function of a nucleus is represented as the Slater determinant

$$\Psi_A(1,2,\ldots,A) = \frac{1}{\sqrt{A!}}\det[\phi_i(j)] \qquad (1)$$

formed by the single-particle orbitals

$$\phi_i(j) = \psi_{\mathbf{n}_i}(\mathbf{r}_j)\chi_{\sigma_i\tau_i}(j) \equiv \psi_{n_i^x}(x_j/a_i) \qquad (2)$$

1063-7788/02/6503-0413$22.00

$$\times \psi_{n_i^y}(y_j/b_i)\psi_{n_i^z}(z_j/c_i)\chi_{\sigma_i\tau_i}(j),$$

where $\psi_n(x/a)$ are well-known functions for a one-dimensional harmonic oscillator (the oscillator-length parameter a is related to the frequency ω_x by the equation $a=\sqrt{\hbar/m\omega_x}$) and $\chi_{\sigma_i\tau_i}(j)$ is the spin–isospin function for the jth nucleon. The oscillator lengths $\{a_i,b_i,c_i\}$ are taken here for variational parameters. The variational functional for the total nuclear energy is defined as the expectation value of the multiparticle Hamiltonian for the functions in (1); that is,

$$E(\{a_i,b_i,c_i\})=\langle\Psi_A|\hat{H}|\Psi_A\rangle/\langle\Psi_A\Psi_A\rangle. \quad (3)$$

The Hamiltonian $\hat{H}$ of the system under consideration includes a central exchange nucleon–nucleon potential, whose radial dependence can be represented, without loss of generality, as the sum of Gaussian functions,

$$\hat{V}_{ij}(r)=\sum_{S,T=0,1}\sum_{\nu=1}^{\nu_{\rm pot}}V^{[\nu]}_{2S+1,2T+1} \quad (4)$$
$$\times\exp\left\{-\frac{r^2}{\mu_\nu^2}\right\}\hat{P}_{S,T}(i,j),\quad r\equiv|\mathbf{r}_i-\mathbf{r}_j|,$$

where $\hat{P}_{S,T}(i,j)$ are well-known projection operators [2], which, in the wave function Ψ_A, cut states corresponding to the total spin S and isospin T of the (i,j) pair of interacting nucleons. Owing to this choice of the radial dependence of the nucleon–nucleon potential, all matrix elements required for determining the functional in (3) can be calculated in terms of elementary functions. In this connection, it is convenient to represent the Coulomb interaction of intranuclear protons in the integral form

$$\hat{U}_{\rm Coul}=\sum_{i>j=1}^{Z}\frac{e^2}{|\mathbf{r}_i-\mathbf{r}_j|} \quad (5)$$
$$=\frac{2e^2}{\sqrt{\pi}}\sum_{i>j=1}^{Z}\int_0^1 e^{-\frac{(\mathbf{r}_i-\mathbf{r}_j)^2}{\mu_c^2}}\frac{d\tau}{(1-\tau^2)^{3/2}},$$
$$\mu_c\equiv\frac{1}{\tau}\sqrt{1-\tau^2}.$$

In the following, we consider only even–even light and medium-mass nuclei, in which case the matrix $\|B\|\equiv\|b_{ij}\|$ formed by the overlap integrals $b_{ij}=\langle\phi_i\phi_j\rangle$ of single-particle functions has a diagonal form. Upon summation over spin–isospin variables, the functional in (3) for the total nuclear energy will then be given by [3]

$$E=\langle\Psi_A|-\frac{\hbar^2}{2m}\sum_{i=1}^{A}\Delta_i-\hat{T}_{\rm c.m.}|\Psi_A\rangle \quad (6)$$
$$+\int_{-\infty}^{\infty}\int_{-\infty}^{\infty}d\mathbf{r}_1d\mathbf{r}_2\frac{3V_{33}+V_{13}}{2\times4}F(\mathbf{n};\mathbf{r}_1,\mathbf{r}_1)F(\mathbf{n};\mathbf{r}_2,\mathbf{r}_2)$$
$$-\int_{-\infty}^{\infty}\int_{-\infty}^{\infty}d\mathbf{r}_1d\mathbf{r}_2\frac{3V_{33}-V_{13}}{2\times4}F^2(\mathbf{n};\mathbf{r}_1,\mathbf{r}_2)$$
$$+\int_{-\infty}^{\infty}\int_{-\infty}^{\infty}d\mathbf{r}_1d\mathbf{r}_2\frac{3V_{33}+V_{13}}{2\times4}\Phi(\mathbf{m};\mathbf{r}_1,\mathbf{r}_1)\Phi(\mathbf{m};\mathbf{r}_2,\mathbf{r}_2)$$
$$-\int_{-\infty}^{\infty}\int_{-\infty}^{\infty}d\mathbf{r}_1d\mathbf{r}_2\frac{3V_{33}-V_{13}}{2\times4}\Phi^2(\mathbf{m};\mathbf{r}_1,\mathbf{r}_2)$$
$$+\int_{-\infty}^{\infty}\int_{-\infty}^{\infty}d\mathbf{r}_1d\mathbf{r}_2\frac{3V_{33}+3V_{31}+V_{13}+V_{11}}{2\times4}$$
$$\times F(\mathbf{n};\mathbf{r}_1,\mathbf{r}_1)\Phi(\mathbf{m};\mathbf{r}_2,\mathbf{r}_2)$$
$$-\int_{-\infty}^{\infty}\int_{-\infty}^{\infty}d\mathbf{r}_1d\mathbf{r}_2\frac{3V_{33}-3V_{31}-V_{13}+V_{11}}{2\times4}$$
$$\times F(\mathbf{n};\mathbf{r}_1,\mathbf{r}_2)\Phi(\mathbf{m};\mathbf{r}_1,\mathbf{r}_2)$$
$$+\frac{e^2}{\sqrt{\pi}}\int_0^1\frac{d\tau}{(1-\tau^2)^{3/2}}$$
$$\times\left(\int_{-\infty}^{\infty}\int_{-\infty}^{\infty}d\mathbf{r}_1d\mathbf{r}_2F(\mathbf{n};\mathbf{r}_1,\mathbf{r}_1)F(\mathbf{n};\mathbf{r}_2,\mathbf{r}_2)e^{-\frac{|\mathbf{r}_1-\mathbf{r}_2|}{\mu_c^2}}\right.$$
$$\left.-\frac{1}{2}\int_{-\infty}^{\infty}\int_{-\infty}^{\infty}d\mathbf{r}_1d\mathbf{r}_2F^2(\mathbf{n};\mathbf{r}_1,\mathbf{r}_2)e^{-\frac{|\mathbf{r}_1-\mathbf{r}_2|}{\mu_c^2}}\right),$$

where the two-particle density matrices for the proton and neutron distributions,

$$F(\mathbf{n};\mathbf{r}_1,\mathbf{r}_2)=\sum_{i=1}^{Z}\psi_{\mathbf{n}_i}(\mathbf{r}_1)\psi_{\mathbf{n}_i}(\mathbf{r}_2), \quad (7)$$
$$\Phi(\mathbf{m};\mathbf{r}_1,\mathbf{r}_2)=\sum_{j=1}^{N}\psi_{\mathbf{m}_j}(\mathbf{r}_1)\psi_{\mathbf{m}_j}(\mathbf{r}_2),$$

now depend only on the spatial coordinates $\mathbf{r}_1$ and $\mathbf{r}_2$. The quantities V_{33}, V_{31}, V_{13}, and V_{11} are the corresponding spin–isospin components of the exchange potential (4); that is,

$$V_{2S+1,2T+1}=\sum_{\nu=1}^{\nu_{\rm pot}}V^{[\nu]}_{2S+1,2T+1}\exp\left\{-\frac{r^2}{\mu_\nu^2}\right\}. \quad (8)$$

The total nuclear energy E and the sum of the single-particle energies ε_λ are related by the equa-

tion [4]

$$E = \sum_{\lambda=1}^{A} \varepsilon_\lambda - \frac{1}{2}\left[\sum_{\lambda=1}^{A}\int d\mathbf{r}\psi_\lambda(\mathbf{r})V_d(\mathbf{r})\psi_\lambda(\mathbf{r}) + \sum_{\lambda=1}^{A}\int\int d\mathbf{r}_1 d\mathbf{r}_2 \psi_\lambda(\mathbf{r}_1)V_{\rm ex}(\mathbf{r}_1,\mathbf{r}_2)\psi_\lambda(\mathbf{r}_2)\right] - \langle T_{\rm c.m.}\rangle, \quad (9)$$

where $V_d(\mathbf{r})$ and $V_{\rm ex}(\mathbf{r}_1,\mathbf{r}_2)$ are, respectively, the so-called direct and the so-called exchange potential, which appear in the Hartree–Fock equation for the orbitals $\psi_\lambda(\mathbf{r})$; that is,

$$-\frac{\hbar^2}{2m}\Delta\psi_\lambda(\mathbf{r}) + V_d(\mathbf{r})\psi_\lambda(\mathbf{r}) + \int d\mathbf{r}' V_{\rm ex}(\mathbf{r},\mathbf{r}')\psi_\lambda(\mathbf{r}') = \varepsilon_\lambda\psi_\lambda(\mathbf{r}). \quad (10)$$

The expressions for the potentials $V_d(\mathbf{r})$ and $V_{\rm ex}(\mathbf{r},\mathbf{r}')$ follow from Eqs. (6), (9), and (10). By way of example, we indicate that, for protons, these expressions are

$$V_d(\mathbf{r}_1) = \frac{1}{4}\int d\mathbf{r}_2(3V_{33}+V_{13})F(\mathbf{n};\mathbf{r}_2,\mathbf{r}_2) + \frac{1}{8}\int d\mathbf{r}_2(3V_{33}+3V_{31}+V_{13}+V_{11})\Phi(\mathbf{m};\mathbf{r}_2,\mathbf{r}_2) + \int d\mathbf{r}_2\frac{e^2}{|\mathbf{r}_1-\mathbf{r}_2|}F(\mathbf{n};\mathbf{r}_2,\mathbf{r}_2), \quad (11)$$

$$V_{\rm ex}(\mathbf{r}_1,\mathbf{r}_2) = -\frac{1}{4}(3V_{33}-V_{13})F(\mathbf{n};\mathbf{r}_1,\mathbf{r}_2) - \frac{1}{8}(3V_{33}-3V_{31}-V_{13}+V_{11})\Phi(\mathbf{m};\mathbf{r}_1,\mathbf{r}_2) - \frac{e^2}{2|\mathbf{r}_1-\mathbf{r}_2|}F(\mathbf{n};\mathbf{r}_1,\mathbf{r}_2).$$

In the case of neutrons, it is necessary to make the substitutions $F(\mathbf{n};\ldots)\to\Phi(\mathbf{m};\ldots)$ and $\Phi(\mathbf{m};\ldots)\to F(\mathbf{n};\ldots)$ in (11) and discard the Coulomb terms.

It should be noted that the expressions in (11) for $V_d(\mathbf{r})$ and $V_{\rm ex}(\mathbf{r}_1,\mathbf{r}_2)$ are not, strictly speaking, solutions to the Hartree–Fock equation, but they represent an approximation (possibly, a rough one) to the self-consistent nuclear field of the nucleus. Here, the accuracy of the approximation is determined by the precision of the variational calculation within the multiparticle problem being considered for specific nucleon–nucleon forces. In other words, the self-consistent field calculated by formulas (11) will be close to the actual mean field of the nucleus only if the chosen multiparticle variational function reproduces adequately the most important modes of the motion of nucleons.

As is well known, the self-consistent field of a fermion system is nonlocal and depends on the state of a particle that occurs in this field. Formally, the nonlocal potential being considered can be replaced by the local potential

$$V^{\rm loc}_{[\lambda]}(\mathbf{r})\psi_\lambda(\mathbf{r}) \equiv V_d(\mathbf{r})\psi_\lambda(\mathbf{r}) + \int d\mathbf{r}' V_{\rm ex}(\mathbf{r},\mathbf{r}')\psi_\lambda(\mathbf{r}'), \quad (12)$$

where λ stands for the set of quantum numbers that are necessary for fully characterizing the single-particle functions ψ_λ. For the first time, such a replacement was made by Slater [5] for electrons as far back as 1951. At some point $\mathbf{r}_i > 0$, the local potential introduced in (12) can have a singularity if the single-particle function ψ_λ has a node at this point.

It was mentioned above that, in our model, the single-particle orbitals ψ_λ are approximated by the functions of a deformed three-dimensional harmonic oscillator; that is,

$$\psi_\lambda \equiv \psi_{\mathbf{n}}(\mathbf{r}) \equiv \psi_{n_i^x}(x_j/a_i)\psi_{n_i^y}(y_j/b_i)\psi_{n_i^z}(z_j/c_i).$$

For the case of an even–even nucleus, the general expression for the mean local potential describing the interaction of the λ proton with the A nucleus can be found by taking into account the explicit form of the oscillator functions $\psi_n(\ldots)$ and by using the formulas presented above. The result is

$$V^{\rm loc}_{[\lambda]}(\mathbf{r}) = \sum_{\nu=1}^{\nu_{\rm pot}}\left\{\frac{1}{4}\sum_{i=1}^{Z}\left[(3V^\nu_{33}+V^\nu_{13})\,f_{n_i^x}(x;a_i,\mu_\nu)f_{n_i^y}(y;b_i,\mu_\nu)f_{n_i^z}(z;c_i,\mu_\nu)\right.\right. \quad (13)$$
$$-(3V^\nu_{33}-V^\nu_{13})\tilde f_{n_\lambda^x n_i^x}(x;a_\lambda,a_i,\mu_\nu)\tilde f_{n_\lambda^y n_i^y}(y;b_\lambda,b_i,\mu_\nu)\tilde f_{n_\lambda^z n_i^z}(z;c_\lambda,c_i,\mu_\nu)]$$
$$+\frac{1}{8}\sum_{j=1}^{N}\left[(3V^\nu_{33}+3V^\nu_{31}+V^\nu_{13}+V^\nu_{11})\,f_{m_j^x}(x;a'_j,\mu_\nu)f_{m_j^y}(y;b'_j,\mu_\nu)f_{m_j^z}(z;c'_j,\mu_\nu)\right.$$
$$\left.\left.-(3V^\nu_{33}-3V^\nu_{31}-V^\nu_{13}+V^\nu_{11})\tilde f_{n_\lambda^x m_j^x}(x;a_\lambda,a'_j,\mu_\nu)\tilde f_{n_\lambda^y m_j^y}(y;b_\lambda,b'_j,\mu_\nu)\tilde f_{n_\lambda^z m_j^z}(z;c_\lambda,c'_j,\mu_\nu)\right]\right\}$$

$$+\frac{e^2}{\sqrt{\pi}}\int_0^1\frac{d\tau}{(1-\tau^2)^{3/2}}\sum_{i=1}^{Z}[2\,f_{n_i^x}(x;a_i,\mu_c)f_{n_i^y}(y;b_i,\mu_c)f_{n_i^z}(z;c_i,\mu_c)$$
$$-\tilde{f}_{n_\lambda^x n_i^x}(x;a_\lambda,a_i,\mu_c)\tilde{f}_{n_\lambda^y n_i^y}(y;b_\lambda,b_i,\mu_c)\tilde{f}_{n_\lambda^z n_i^z}(z;c_\lambda,c_i,\mu_c)],$$

where the functions $f_n(\ldots)$ and $\tilde{f}_{n_\lambda n}(\ldots)$ are the incomplete partial overlap integrals of single-particle orbitals and the Gaussian component of the nucleon–nucleon potential (4). The explicit expressions for these overlap integrals are presented in Appendix A [see Eqs. (A.1) and (A.2)]. As can be seen from Eq. (13), the mean single-particle potential depends on the parameters of the nucleon–nucleon potential (specifically, on the strengths $V^{[\nu]}_{2S+1,2T+1}$ and on the ranges μ_ν) and on the set of variational parameters in the total wave function Ψ_A.

We note that a specific calculation must be performed in the following order: (i) The first step consists in a variational calculation aimed at minimizing the total-nuclear-energy functional (6) in the hyperspace of nonlinear parameters ($\{a_i, b_i, c_i\}$, $i = 1, 2, \ldots, Z$, for protons and $\{a'_j, b'_j, c'_j\}$, $j = 1, 2, \ldots, N$, for neutrons). (ii) Given the numerical values of these parameters for the optimal configurations of protons ($\{n_i^x, n_i^y, n_i^z\}$, $i = 1, 2, \ldots, Z$) and neutrons ($\{m_j^x, m_j^y, m_j^z\}$, $j = 1, 2, \ldots, N$), the mean single-particle potential (13) of the $A = Z + N$ nucleus is calculated at the second step. If there is a neutron in the field of a nucleus, the corresponding mean potential $V^{\rm loc}_{[\lambda]}(\mathbf{r})$ is also calculated by formulas (13), where the obvious substitutions $Z \to N$, $f_n(\ldots) \to f_m(\ldots)$, $\tilde{f}_{n_\lambda n}(\ldots) \to \tilde{f}_{n_\lambda m}(\ldots)$, and $\{a_i, b_i, c_i\} \to \{a'_j, b'_j, c'_j\}$ are made and where the Coulomb terms are discarded.

3. SINGLE-PARTICLE ENERGIES

In order to calculate the single-particle energies, it is necessary to solve the Schrödinger equation with the local potential $V^{\rm loc}_{[\lambda]}$ given by Eq. (13). This is almost always not a simple problem, with the exception of the case of a magic nucleus, where $V^{\rm loc}_{[\lambda]}$ depends only on the absolute value of the vector $\mathbf{r}$. The difficulty in question can be sidestepped if the orbitals ψ_λ determined in a variational calculation are sufficiently close to exact solutions to the corresponding set of the Hartree–Fock equations over the important region of $\mathbf{r}$. The single-particle energy for the λ proton can then be roughly estimated with the aid of the relation

$$\varepsilon_\lambda = \left\langle \psi_{\mathbf{n}_\lambda} \left| -\frac{\hbar^2}{2m}\Delta \right| \psi_{\mathbf{n}_\lambda} \right\rangle \qquad (14)$$

$$+\frac{1}{8}\sum_{\nu=1}^{\nu_{\rm pot}}\int\int d\mathbf{r}_1 d\mathbf{r}_2\,\{\psi^2_{\mathbf{n}_\lambda}(\mathbf{r}_1)[2(3V^\nu_{33}+V^\nu_{13})$$
$$\times F(\mathbf{n};\mathbf{r}_2,\mathbf{r}_2)+(3V^\nu_{33}+3V^\nu_{31}+V^\nu_{13}+V^\nu_{11})$$
$$\times\Phi(\mathbf{m};\mathbf{r}_2,\mathbf{r}_2)]-\psi_{\mathbf{n}_\lambda}(\mathbf{r}_1)\psi_{\mathbf{n}_\lambda}(\mathbf{r}_2)[2(3V^\nu_{33}-V^\nu_{13})$$
$$\times F(\mathbf{n};\mathbf{r}_1,\mathbf{r}_2)+(3V^\nu_{33}-3V^\nu_{31}-V^\nu_{13}+V^\nu_{11})$$
$$\times\Phi(\mathbf{m},\mathbf{r}_1;\mathbf{r}_2)]\}\exp\left(-\frac{|\mathbf{r}_1-\mathbf{r}_2|^2}{\mu_\nu^2}\right)$$
$$+\frac{1}{2}\int\int d\mathbf{r}_1 d\mathbf{r}_2[2\psi^2_{\mathbf{n}_\lambda}(\mathbf{r}_1)F(\mathbf{n};\mathbf{r}_2,\mathbf{r}_2)$$
$$-\psi_{\mathbf{n}_\lambda}(\mathbf{r}_1)\psi_{\mathbf{n}_\lambda}(\mathbf{r}_2)F(\mathbf{n};\mathbf{r}_1,\mathbf{r}_2)]\frac{e^2}{|\mathbf{r}_1-\mathbf{r}_2|}.$$

By taking into account the explicit form of the functions $F(\mathbf{n},\mathbf{r}_1,\mathbf{r}_2)$, $\Phi(\mathbf{m};\mathbf{r}_1.\mathbf{r}_2)$, and $\psi_{\mathbf{n}_\lambda}(\mathbf{r})$ appearing in the above relation, we obtain the general formula

$$\varepsilon_\lambda=\frac{\hbar^2}{2m}\left(\frac{n_\lambda^x+1/2}{a_\lambda^2}+\frac{n_\lambda^y+1/2}{b_\lambda^2}+\frac{n_\lambda^z+1/2}{c_\lambda^2}\right)$$
$$+\frac{1}{8}\sum_{\nu=1}^{\nu_{\rm pot}}\left\{2\sum_{i=1}^{Z}[(3V^\nu_{33}+V^\nu_{13})f'_{n_\lambda^x n_i^x}(a_\lambda,a_i,\mu_\nu)\right.$$
$$\times f'_{n_\lambda^y n_i^y}(b_\lambda,b_i,\mu_\nu)f'_{n_\lambda^z n_i^z}(c_\lambda,c_i,\mu_\nu)$$
$$-(3V^\nu_{33}-V^\nu_{13})f''_{n_\lambda^x n_i^x}(a_\lambda,a_i,\mu_\nu) \qquad (15)$$
$$\times f''_{n_\lambda^y n_i^y}(b_\lambda,b_i,\mu_\nu)f''_{n_\lambda^z n_i^z}(c_\lambda,c_i,\mu_\nu)]$$
$$+\sum_{j=1}^{N}[(3V^\nu_{33}+3V^\nu_{31}+V^\nu_{13}+V^\nu_{11})f'_{n_\lambda^x m_j^x}(a_\lambda,a'_j,\mu_\nu)$$
$$\times f'_{n_\lambda^y m_j^y}(b_\lambda,b'_j,\mu_\nu)f'_{n_\lambda^z m_j^z}(c_\lambda,c'_j,\mu_\nu)$$
$$-(3V^\nu_{33}-3V^\nu_{31}-V^\nu_{13}+V^\nu_{11})f''_{n_\lambda^x m_j^x}(a_\lambda,a'_j,\mu_\nu)$$
$$\left.\times f''_{n_\lambda^y m_j^y}(b_\lambda,b'_j,\mu_\nu)f''_{n_\lambda^z m_j^z}(c_\lambda,c'_j,\mu_\nu)]\right\}$$

$$+\frac{e^2}{\sqrt{\pi}}\int\limits_0^1\frac{d\tau}{(1-\tau^2)^{3/2}}\sum_{i=1}^{Z}[2f'_{n_\lambda^x n_i^x}(a_\lambda,a_i,\mu_c)$$
$$\times f'_{n_\lambda^y n_i^y}(b_\lambda,b_i,\mu_c)f'_{n_\lambda^z n_i^z}(c_\lambda,c_i,\mu_c)$$
$$-f''_{n_\lambda^x n_i^x}(a_\lambda,a_i,\mu_c)f''_{n_\lambda^y n_i^y}(b_\lambda,b_i,\mu_c)f''_{n_\lambda^z n_i^z}(c_\lambda,c_i,\mu_c)],$$

where the functions $f'_{n_\lambda n}(...)$ and $f''_{n_\lambda n}(...)$, in contrast to the functions $f_n(...)$ and $\tilde{f}_{n_\lambda n}(...)$ appearing in Eq. (13), are expressed in terms of complete partial overlap integrals of single-particle orbitals and the Gaussian component of the nucleon–nucleon potential (4). The definition of these functions and the explicit expressions for them are given in Appendix A [see Eqs. (A.3), (A.4)]. In order to derive a similar formula for the case of the λ neutron, it is necessary to make the simple substitutions $Z \to N$, $f'_{n_\lambda n}(\ldots) \to f'_{n_\lambda m}(\ldots)$, $f''_{n_\lambda n}(\ldots) \to f''_{n_\lambda m}(\ldots)$, and $\{a_i,b_i,c_i\} \to \to \{a'_j,b'_j,c'_j\}$ in (15) and to discard the Coulomb integral [the last term in Eq. (15)].

^{4}He *and* ^{16}O *Nuclei*

To illustrate the use of the above formulas, we consider two first magic nuclei, ^{4}He and ^{16}O. We take the determinant functions (1) of maximum $SU(3)$ symmetry for the wave functions describing the ground states (0^+) of the aforementioned nuclei. We employ one variational parameter a_0 (common to the proton and the neutron s orbital) in Ψ_A for ^{4}He and as many as four parameters in Ψ_A for ^{16}O. In the latter case, two parameters (a and b) correspond to the proton s and p orbitals, while the remaining two (a' and b') correspond to the neutron s and p orbitals. From the general formula (13), we can then find the mean local potential describing the interaction of the s proton [$\psi_{s\text{-state}} = \psi_0(x/a_\lambda)\psi_0(y/a_\lambda)\psi_0(z/a_\lambda)$] with the ^{4}He nucleus. The result is

$$V^{\rm loc}_{s\text{-state}}(\mathbf{r}) = \frac{1}{4}\sum_{\nu=1}^{\nu_{\rm pot}}\left[(9V^\nu_{33}+3V^\nu_{31}+3V^\nu_{13}+V^\nu_{11})\right. \tag{16}$$
$$\times\left(1+\frac{a_0^2}{\mu_\nu^2}\right)^{-3/2}\exp\left(-\frac{r^2}{a_0^2+\mu_\nu^2}\right)$$
$$-(9V^\nu_{33}-3V^\nu_{31}-3V^\nu_{13}+V^\nu_{11})$$
$$\times\left(\frac{1}{2}+\frac{a_0^2}{2a_\lambda^2}+\frac{a_0^2}{\mu_\nu^2}\right)^{-3/2}$$
$$\left.\times\exp\left\{-\frac{r^2}{\tilde{a}_0^2+\mu_\nu^2}-\left(\frac{1}{a_0^2}-\frac{1}{a_\lambda^2}\right)\frac{r^2}{2}\right\}\right]$$
$$+2\frac{e^2}{r}\mathrm{erf}\left(\frac{r}{a_0}\right)-\left(\frac{1}{2}+\frac{a_0^2}{2a_\lambda^2}\right)^{-3/2}$$
$$\times\exp\left\{-\frac{r^2}{2}\left(\frac{1}{a_0^2}-\frac{1}{a_\lambda^2}\right)\right\}\frac{e^2}{r}\mathrm{erf}\left(\frac{r}{\tilde{a}_0}\right),$$
$$\tilde{a}_0^{-2}\equiv\frac{1}{2a_0^2}+\frac{1}{2a_\lambda^2}.$$

In the case of $a_0 = a_\lambda$, expression (16) is simplified to become

$$V^{\rm loc}_{s\text{-state}}(\mathbf{r}) = \frac{3}{2}\sum_{\nu=1}^{\nu_{\rm pot}}\left[(V^\nu_{31}+V^\nu_{13})\left(1+\frac{a_0^2}{\mu_\nu^2}\right)^{-3/2}\right. \tag{17}$$
$$\left.\times\exp\left(-\frac{r^2}{a_0^2+\mu_\nu^2}\right)\right]+\frac{e^2}{r}\mathrm{erf}\left(\frac{r}{a_0}\right).$$

The analogous formulas for the ^{16}O nucleus are given by

$$V^{\rm loc}_{s(p)\text{-state}}(\mathbf{r}) = \sum_{\nu=1}^{\nu_{\rm pot}}\left\{\frac{1}{2}(3V^\nu_{33}+V^\nu_{13})\Phi_0(r;a,b,\mu_\nu)\right. \tag{18}$$
$$+\frac{1}{4}(3V^\nu_{33}+3V^\nu_{31}+V^\nu_{13}+V^\nu_{11})\Phi_0(r;a',b',\mu_\nu)$$
$$-\frac{1}{2}(3V^\nu_{33}-V^\nu_{13})\Phi_{s(p)}(r;a_\lambda,a,b,\mu_\nu)$$
$$-\frac{1}{4}(3V^\nu_{33}-3V^\nu_{31}-V^\nu_{13}+V^\nu_{11})$$
$$\left.\times\Phi_{s(p)}(r;a_\lambda,a',b',\mu_\nu)\right\}+V^{\rm C}(r)-W^{\rm C}_{s(p)}(r),$$

where the explicit expressions for the functions $\Phi_0(\ldots)$, $\Phi_{s(p)}(\ldots)$, $V^{\rm C}(r)$, and $W^{\rm C}_{s(p)}(r)$ are presented in Appendix B [see Eqs. (A.5)–(A.10)]. If all the parameters involved are equal, $a = b = a' = b' = a_\lambda$, expressions (18) reduce to

$$V^{\rm loc}_{s\text{-state}}(\mathbf{r}) = \frac{1}{4}\sum_{\nu=1}^{\nu_{\rm pot}}\left(1+\frac{a^2}{\mu_\nu^2}\right)^{-3/2} \tag{19}$$
$$\times\left\{(9V^\nu_{33}+3V^\nu_{31}+3V^\nu_{13}+V^\nu_{11})\right.$$
$$\left.\times\left[1+3\left(1+\frac{a^2}{\mu_\nu^2}\right)^{-1}+2\frac{a^2r^2}{\mu_\nu^4}\left(1+\frac{a^2}{\mu_\nu^2}\right)^{-2}\right]\right.$$
$$-(9V^\nu_{33}-3V^\nu_{31}-3V^\nu_{13}+V^\nu_{11})$$

$$\times\left[1+2\frac{r^2}{\mu_\nu^2}\left(1+\frac{a^2}{\mu_\nu^2}\right)^{-1}\right]\Bigg\}\exp\left(-\frac{r^2}{a^2+\mu_\nu^2}\right)$$
$$+\frac{e^2}{r}\left(7-\frac{a^2}{2r^2}\right)\mathrm{erf}\left(\frac{r}{a}\right)$$
$$-\frac{e^2}{a\sqrt{\pi}}\left(4-\frac{a^2}{r^2}\right)\exp\left(-\frac{r^2}{a^2}\right),$$

$$V^{\mathrm{loc}}_{p\text{-state}}(\mathbf{r})-V^{\mathrm{loc}}_{s-\mathrm{state}}(\mathbf{r})=\frac{1}{2}\sum_{\nu=1}^{\nu_{\mathrm{pot}}}\left[\left(1+\frac{a^2}{\mu_\nu^2}\right)^{-5/2}\right. \tag{20}$$
$$\times(9V^\nu_{33}-3V^\nu_{31}-3V^\nu_{13}+V^\nu_{11})\left(\frac{r^2}{a^2+\mu_\nu^2}\right)$$
$$\left.\times\exp\left(-\frac{r^2}{a^2+\mu_\nu^2}\right)\right]+2\frac{e^2}{a\sqrt{\pi}}\left(1+\frac{a^2}{r^2}\right)$$
$$\times\exp\left(-\frac{r^2}{a^2}\right)-\frac{e^2a^2}{r^3}\mathrm{erf}\left(\frac{r}{a}\right).$$

For the single-particle energies ε_λ, the expressions obtained with the aid of (15) are presented immediately below.

(i) For the s state of the ^{4}He nucleus, we have

$$\varepsilon_{\mathrm{s\text{-}state}}=\frac{3\hbar^2}{4ma_\lambda^2} \tag{21}$$
$$+\frac{1}{4}\sum_{\nu=1}^{\nu_{\mathrm{pot}}}\Bigg\{(9V^\nu_{33}+3V^\nu_{31}+3V^\nu_{13}+V^\nu_{11})$$
$$\times\left(1+\frac{a^2}{\mu_\nu^2}+\frac{a_\lambda^2}{\mu_\nu^2}\right)^{-3/2}$$
$$-(9V^\nu_{33}-3V^\nu_{31}-3V^\nu_{13}+V^\nu_{11})$$
$$\times\left[\left(\frac{1}{2}+\frac{a^2}{2a_\lambda^2}\right)\left(\frac{1}{2}+\frac{a_\lambda^2}{2a^2}+2\frac{a_\lambda^2}{\mu_\nu^2}\right)\right]^{-3/2}\Bigg\}$$
$$+\sqrt{\frac{2}{\pi}}e^2\sqrt{\frac{2}{a^2+a_\lambda^2}}\left[2-\left(\frac{2aa_\lambda}{a^2+a_\lambda^2}\right)^2\right].$$

(ii) For the s and p states of the ^{16}O nucleus, the results are

$$\varepsilon_{s\text{-state}}=\frac{3\hbar^2}{4ma_\lambda^2} \tag{22}$$
$$+\sum_{\nu=1}^{\nu_{\mathrm{pot}}}\left[\frac{1}{2}(3V^\nu_{33}+V^\nu_{13})F_d(a_\lambda,a,b,\mu_\nu)\right.$$
$$+\frac{1}{4}(3V^\nu_{33}+3V^\nu_{31}+V^\nu_{13}+V^\nu_{11})F_d(a_\lambda,a',b',\mu_\nu)$$
$$-\frac{1}{2}(3V^\nu_{33}-V^\nu_{13})F_{\mathrm{ex}}(a_\lambda,a,b,\mu_\nu)$$
$$\left.-\frac{1}{4}\left(3V^\nu_{33}-3V^\nu_{31}-V^\nu_{13}+V^\nu_{11}\right)F_{\mathrm{ex}}(a_\lambda,a',b',\mu_\nu)\right]$$
$$+\frac{2e^2}{\sqrt{\pi}}\left\{\frac{2}{\sqrt{a^2+a_\lambda^2}}+\frac{2}{\sqrt{b^2+a_\lambda^2}}\left(2+\frac{a_\lambda^2}{b^2+a_\lambda^2}\right)\right.$$
$$-\frac{1}{2\sqrt{2}a_\lambda}\left[2\left(\frac{1}{2}+\frac{a_\lambda^2}{2a^2}\right)^{-1}\left(\frac{1}{2}+\frac{a^2}{2a_\lambda^2}\right)^{-3/2}\right.$$
$$\left.\left.+\left(\frac{1}{2}+\frac{a_\lambda^2}{2b^2}\right)^{-1}\left(\frac{1}{2}+\frac{b^2}{2a_\lambda^2}\right)^{-5/2}\right]\right\},$$

$$\varepsilon_{p\text{-state}}=\frac{5\hbar^2}{4ma_\lambda^2} \tag{23}$$
$$+\sum_{\nu=1}^{\nu_{\mathrm{pot}}}\left[\frac{1}{2}(3V^\nu_{33}+V^\nu_{13})F^1_d(a_\lambda,a,b,\mu_\nu)\right.$$
$$+\frac{1}{4}(3V^\nu_{33}+3V^\nu_{31}+V^\nu_{13}+V^\nu_{11})F^1_d(a_\lambda,a',b',\mu_\nu)$$
$$-\frac{1}{2}(3V^\nu_{33}-V^\nu_{13})F^1_{\mathrm{ex}}(a_\lambda,a,b,\mu_\nu)$$
$$\left.-\frac{1}{4}(3V^\nu_{33}-3V^\nu_{31}-V^\nu_{13}+V^\nu_{11})F^1_{\mathrm{ex}}(a_\lambda,a',b',\mu_\nu)\right]$$
$$+\frac{4e^2}{\sqrt{\pi}}\left[\frac{1}{\sqrt{a^2+a_\lambda^2}}\left(1-\frac{1}{3}\frac{a_\lambda^2}{a^2+a_\lambda^2}\right)\right.$$
$$\left.+\frac{1}{\sqrt{b^2+a_\lambda^2}}\left(2+\frac{b^2a_\lambda^2}{(b^2+a_\lambda^2)^2}\right)\right]$$
$$-\frac{e^2}{3\sqrt{2\pi}a_\lambda}\left[\frac{a^2}{a_\lambda^2}\left(\frac{1}{2}+\frac{a_\lambda^2}{2a^2}\right)^{-1}\left(\frac{1}{2}+\frac{a^2}{2a_\lambda^2}\right)^{-5/2}\right.$$
$$\left.+\frac{11}{2}\left(\frac{1}{2}+\frac{a_\lambda^2}{2b^2}\right)^{-2}\left(\frac{1}{2}+\frac{b^2}{2a_\lambda^2}\right)^{-5/2}\right].$$

The definitions of the functions $F_d(\ldots)$, $F_{\mathrm{ex}}(\ldots)$, $F^1_d(\ldots)$, and $F^1_{\mathrm{ex}}(\ldots)$ appearing in formulas (22) and (23) are given in Appendix B [see Eqs. (A.11)–(A.14)]. The neutron single-particle energies are calculated by formulas (21)–(23), where it is necessary to make the substitution $a,b\leftrightarrow a',b'$ and discard the Coulomb terms.

In the case of $a=b=a'=b'=a_\lambda$, expressions (21)–(23) are simplified.

(a) For the ^{4}He nucleus, we then have

$$\varepsilon_{s\text{-state}}=\frac{3\hbar^2}{4ma^2} \tag{24}$$

$$+\frac{3}{2}\sum_{\nu=1}^{\nu_{\rm pot}}(V_{31}^{\nu}+V_{13}^{\nu})\left(1+2\frac{a^2}{\mu_\nu^2}\right)^{-3/2}+\sqrt{\frac{2}{\pi}}\frac{e^2}{a}.$$

(b) For the ^{16}O nucleus, the corresponding results are

$$\varepsilon_{s\text{-state}}=\frac{3\hbar^2}{4ma^2}+\frac{11}{\sqrt{2\pi}}\frac{e^2}{a}+\sum_{\nu=1}^{\nu_{\rm pot}}\left(1+2\frac{a^2}{\mu_\nu^2}\right)^{-3/2}\times\left\{\tilde{V}_\nu\left[1+3\left(1+\frac{a^2}{\mu_\nu^2}\right)\left(1+2\frac{a^2}{\mu_\nu^2}\right)^{-1}\right]-\tilde{W}_\nu\left[1+3\frac{a^2}{\mu_\nu^2}\left(1+2\frac{a^2}{\mu_\nu^2}\right)^{-1}\right]\right\},$$

$$\varepsilon_{p\text{-state}}=\frac{5\hbar^2}{4ma^2}+\frac{61}{6\sqrt{2\pi}}\frac{e^2}{a}+\sum_{\nu=1}^{\nu_{\rm pot}}\left(1+2\frac{a^2}{\mu_\nu^2}\right)^{-5/2}\times\left\{\tilde{V}_\nu\left[4+\frac{a^2}{\mu_\nu^2}+5\frac{a^4}{\mu_\nu^4}\left(1+2\frac{a^2}{\mu_\nu^2}\right)^{-1}\right]-\tilde{W}_\nu\left[1+\frac{a^2}{\mu_\nu^2}+5\frac{a^4}{\mu_\nu^4}\left(1+2\frac{a^2}{\mu_\nu^2}\right)^{-1}\right]\right\},\quad(25)$$

$$\tilde{V}_\nu\equiv\frac{1}{4}(V_{33}^{\nu}+3V_{31}^{\nu}+3V_{13}^{\nu}+V_{11}^{\nu}),$$

$$\tilde{W}_\nu\equiv\frac{1}{4}(V_{33}^{\nu}-3V_{31}^{\nu}-3V_{13}^{\nu}+V_{11}^{\nu}).$$

4. RESULTS OF NUMERICAL CALCULATIONS AND CONCLUSIONS

In order to perform specific numerical calculations, dedicated computer codes were developed on the basis of the general formulas (13) and (15) for the mean single-particle potentials and for the single-particle energies, respectively. For exchange central nucleon–nucleon forces, we chose known central nucleon–nucleon potentials having a Gaussian radial dependence [6, 7].

Let us first consider the results obtained within the $SU(3)$ microscopic nuclear model, where the highest weight function (or the function characterized by a maximally compact filling) involving only one variational parameter $a=\sqrt{\hbar/m\omega}$ is taken for the wave function. In this case, the single-particle potentials for the ^{4}He and ^{16}O nuclei can easily be calculated by using the simple formulas (17) and (19). The results obtained by calculating the potential $V^{\rm loc}(r)$ for the ^{4}He nucleus are presented in Fig. 1 for the Brink–Boecker [6] (BBI) and the Volkov [7] (VI) version of the nucleon–nucleon potential. In order to calculate $V^{\rm loc}(r)$ by these formulas, it is necessary to know, in addition to the parameters of the nucleon–nucleon potential, that value of the variational parameter a which minimizes the total-nuclear-energy functional for a chosen nucleon–nucleon potential. The variational calculations of the bound-state energies for light and medium-mass nuclei within the $SU(3)$ nuclear model were performed by many authors (see, for example, [8]). According to [9], the optimal value of the variational parameter a for the ^{4}He nucleus is 1.40 fm for the BBI potential and 1.38 fm for the VI potential. Figure 1 also displays the potential of proton interaction with the ^{4}He nucleus (curve *3*). It was reconstructed in [10] on the basis of data on proton scattering by the ^{4}He nucleus at low energies (up to 23 MeV inclusive). From Fig. 1, we can see that, in the most important region of the argument r, the single-particle potentials under investigation behave consistently.

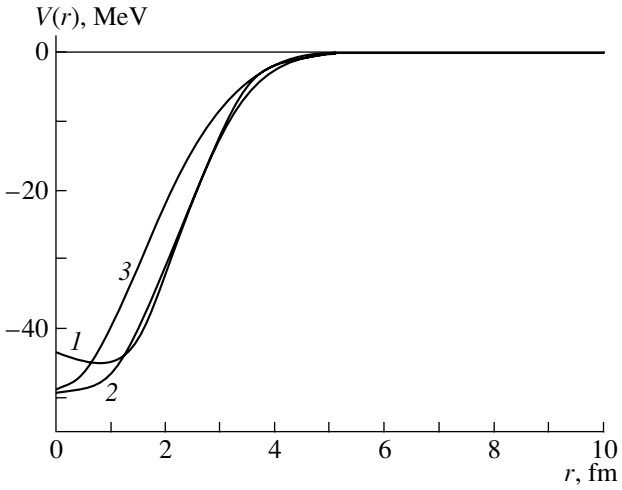

Fig. 1. Mean single-particle potential in the ^{4}He nucleus for protons according to the calculation by formula (17) with the nucleon–nucleon potential in the (curve *1*) BBI or the (curve *2*) VI form. Curve *3*, which represents the potential of proton interaction with the ^{4}He nucleus, was borrowed from [10].

For neutrons in the ^{16}O nucleus, the results of similar calculations for the single-particle potentials are shown in Fig. 2. Here, curves *1* and *2* were calculated for the s and the p state, respectively, by using formulas (19) and (20) with the BBI nucleon–nucleon potential (the corresponding optimal value of the variational parameter is $a=1.79$ fm), while curves *1′* and *2′* represent phenomenological analogs of the potentials $V^{\rm loc}(r)$ for the ^{16}O nucleus in the

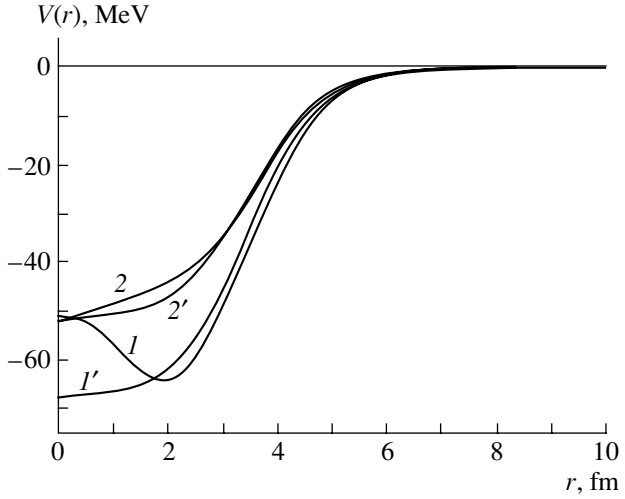

Fig. 2. Mean single-particle potentials for neutrons in the ^{16}O nucleus according to the calculation by formulas (19) and (20) with the BBI nucleon–nucleon potential for (curve *1*) the s and (curve *2*) the p state. Curves *1′* and *2′* represent the corresponding phenomenological potentials from [11].

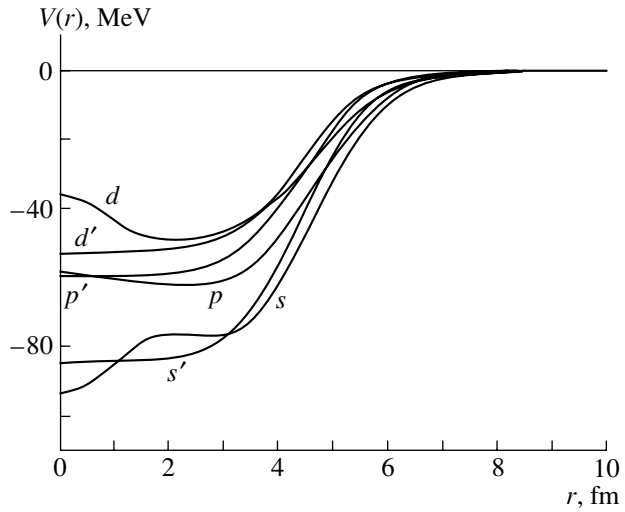

Fig. 3. As in Fig. 2, but for the ^{40}Ca nucleus. The calculated s, p, and d single-particle potentials are associated with the s, p, and d states; the curves labeled with the symbols s', p', and d' represent their phenomenological analogs from [11].

Woods–Saxon form from the study of Elton and Swift [11].

The potentials $V^{\rm loc}(r)$ for neutrons in the ^{40}Ca nucleus according to the theoretical calculation with the BBI nucleon–nucleon potential (the equilibrium value of the oscillator parameter is $a = 1.97$ fm) is displayed in Fig. 3, along with the phenomenological analogs of these potentials from [11] (curves s', p', and d'). From Fig. 2, it can be seen that the potentials $V^{\rm loc}(r)$ calculated here are in satisfactory agreement with the phenomenological single-particle potentials from [11].

Figures 4 and 5 illustrate the effect of Coulomb forces on the behavior of the mean single-particle potentials $V^{\rm loc}(r)$ in the ^{16}O and ^{40}Ca nuclei, respectively. As can be seen from these figures, the proton single-particle potentials nearly replicate the behavior of the corresponding neutron potentials, but there is some Coulomb shift, which, in the interval $1 \le r \le 2$ fm, is $\Delta \approx 4$ MeV for the ^{16}O nucleus and $\Delta \approx 9$ MeV for the ^{40}Ca nucleus. The coincidence of the s and p single-particle potentials at the point $r = 0$ (in Fig. 4) follows from formula (20) determining the difference of the potentials being considered. Figure 4 also displays the mean single-particle potential for protons that was calculated by the folding method as

$$V_{\rm fold}(r) = \int d\mathbf{r}' V_{pp}(|\mathbf{r}-\mathbf{r}'|) F(\mathbf{n};\mathbf{r}',\mathbf{r}') + \int d\mathbf{r}' V_{pn}(|\mathbf{r}-\mathbf{r}'|)\Phi(\mathbf{n};\mathbf{r}',\mathbf{r}') + \int d\mathbf{r}' \frac{e^2}{|\mathbf{r}-\mathbf{r}'|} F(\mathbf{n};\mathbf{r}',\mathbf{r}'), \quad (26)$$

where the proton and the neutron density matrix [$F(\ldots)$ and $\Phi(\ldots)$, respectively] were defined in Eq. (7) (see above). The potentials V_{pp} and V_{pn} were constructed from the components of the nucleon–nucleon potential (4) as

$$V_{pp}(r) = V_{nn}(r) = \frac{1}{4}(3V_{33}+V_{13}) - \frac{1}{4}(3V_{33}-V_{13}) = \frac{1}{2}V_{13}(r), \quad (27)$$

$$V_{pn}(r) = \frac{1}{8}(3V_{33}+3V_{31}+V_{13}+V_{11}) - \frac{1}{8}(3V_{33}-3V_{31}-V_{13}+V_{11}) = \frac{1}{4}\left[3V_{31}(r)+V_{13}(r)\right].$$

(The same combinations of the components of this potential appear in the direct and exchange integrals for the total energy of the nucleus.) For the ^{16}O nucleus treated on the basis of the $SU(3)$ model being considered, it can be found with the aid of expressions (26) and (27) that

$$V_{\rm fold}(r) = \frac{3}{2}\sum_{\nu=1}^{\nu_{\rm pot}} \left\{ (V_{31}^{\nu}+V_{13}^{\nu}) \left(1+\frac{a^2}{\mu_\nu^2}\right)^{-3/2} \times \left[1+3\left(1+\frac{a^2}{\mu_\nu^2}\right)^{-1} + 2\frac{a^2r^2}{\mu_\nu^4}\left(1+\frac{a^2}{\mu_\nu^2}\right)^{-2}\right] \times \exp\left(-\frac{r^2}{a^2+\mu_\nu^2}\right)\right\} + \frac{8e^2}{r}\,\mathrm{erf}\left(\frac{r}{a}\right) \quad (28)$$

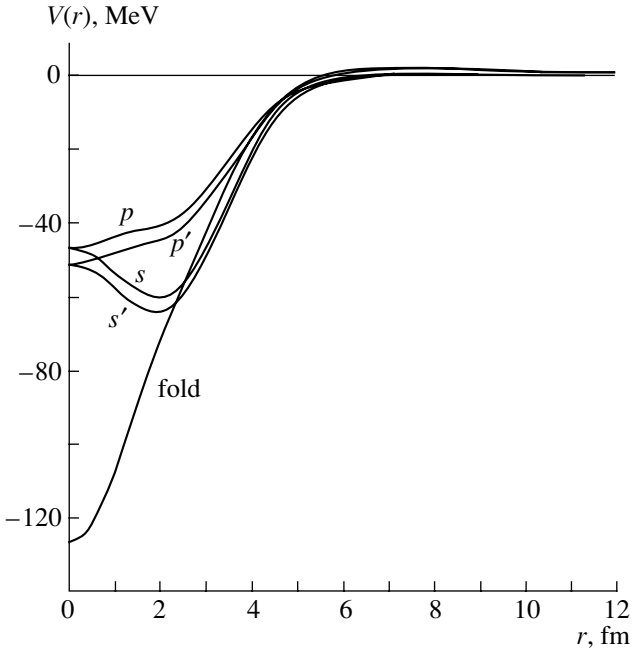

Fig. 4. Proton (curves s, p) and neutron (curves s', p') single-particle potentials $V^{\rm loc}(r)$ for the s and p states in the ^{16}O nucleus according to the calculations with the BBI potential. The curve labeled with the symbol "fold" represents the folding potential.

$$-\frac{4e^2}{a\sqrt{\pi}}\exp\left(-\frac{r^2}{a^2}\right),$$

where, for the BBI potential, the equilibrium value of the variational parameter a is $a = 1.79$ fm.

As is well known, a drawback of folding potentials is that the Pauli exclusion principle is ignored in constructing them. This is the reason why, for $r \leq 2$ fm (see Fig. 4), the potential $V_{\rm fold}(r)$ can significantly differ from actual single-particle potentials. Nevertheless, it is folding potentials that are often used to describe scattering data. In all probability, this is justified at low energies, in which case the main contribution comes from the periphery of $V_{\rm fold}(r)$—the point is that, there, the potential $V_{\rm fold}(r)$ can be close to the potential of the actual mean field of the nucleus (see Fig. 4).

So far, we have demonstrated the results obtained with the simple one-parameter function of the $SU(3)$ model of the nucleus, in which case, the potentials $V^{\rm loc}(r)$ are central. If we consider a more complicated model or a nonmagic nucleus, the potential $V^{\rm loc}$ will be, in general, a function of all three Cartesian coordinates x, y, and z. As a nontrivial example, the potential $V^{\rm loc}(\mathbf{r})$ for the proton p state in the ^{11}Be nucleus is displayed in Fig. 6. This potential was calculated on the basis of the general formula (13)

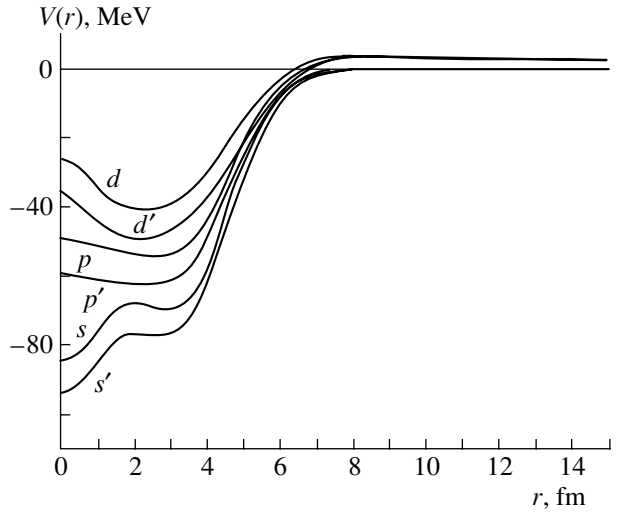

Fig. 5. As in Fig. 4, but for the ^{40}Ca nucleus and for the s, p, and d states.

by using the wave function of the polarized-orbital model and the nucleon–nucleon potential from [12], where it was constructed in terms of five Gaussian functions. The relevant variational calculation of the energies of the ^{11}Be nucleus was performed in [12], where, among other things, all optimum values of the variational parameters $\{a_i, b_i, c_i\}$ of the wave function for the ground ($1/2^+$) state of the ^{11}Be nucleus [they are necessary for calculating $V^{\rm loc}(\mathbf{r})$] are presented in Table 3. The complicated surface in Fig. 6 represents the potential $V^{\rm loc}$ as a function of two Cartesian coordinates x and z at a fixed value of the third coordinate ($y = 0$). A similar (but not equivalent) pattern is obtained in terms of the coordinates y and z at a fixed value of x ($x = 0$).

Further, we proceed to consider single-particle energies. In order to determine these quantities, it is necessary solve the corresponding Schrödinger equation, which can generally involve nontrivial objects, such as the potential $V^{\rm loc}(\mathbf{r})$ displayed in Fig. 6. For nuclear problems, however, which are characterized by a rather poor accuracy (in relation to the accuracy of the results in some atomic problems) in view of the special features of nucleon–nucleon forces, one can use an approximate solution for single-particle energies. Within our approach, such solutions are given by Eq. (15). The required quantities ε_λ can easily be calculated if we know the optimum values of the variational parameters for the single-particle state being considered and the parameters of the nucleon–nucleon potential that was used in a specific variational calculation of the total energy of the nucleus.

In the table, we present the theoretical values of ε_λ for the ^{16}O and ^{4}He nuclei according to the calculation by formulas (25) and (24) with the BBI nucleon–

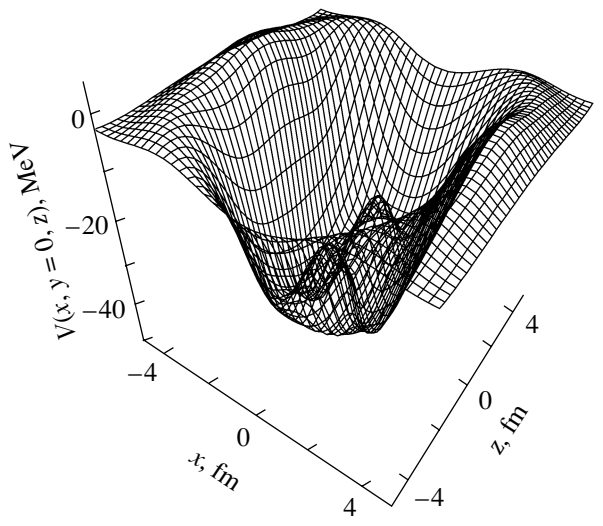

Fig. 6. Single-particle potential for the proton p state in the ^{11}Be nucleus as a function of the coordinates x and z at the fixed value of $y = 0$.

nucleon potential. As can be seen from the table, the theoretical values of ε_λ are in satisfactory agreement with experimental estimates even in the case where use is made of the functions of the simplest $SU(3)$ model.

As was noted above, the mean single-particle potential calculated in this way may prove to be not a rigorously self-consistent (in the sense of Hartree–Fock theory) potential. The accuracy of our approximation can probably be estimated in terms of the normalized difference of single-particle energies, $\delta \equiv (\varepsilon_\lambda - \varepsilon'_\lambda)/\varepsilon'_\lambda$, where ε'_λ is the value that represents the same single-particle energy as ε_λ does, but which follows from a precise numerical solution to the Schrödinger equation with the corresponding single-particle potential (13) rather than from a calculation by formula (15). For this, such numerical solutions to the Schrödinger equation with the potential (13) were found here for neutrons in the ^{16}O and ^{4}He nuclei. Specifically, the s states in the single-particle potential $V^{\rm loc}(r)$ were calculated with the parameters corresponding to the BBI nucleon–nucleon potential. In the calculation, use was made of the special Fortran code presented in [14]. This code makes it possible to choose the most efficient method for numerically solving the radial Schrödinger equation among those that are known in the literature. The calculation yielded two s states at $\varepsilon_1 = -47.652$ MeV and $\varepsilon_2 = -15.411$ MeV in the potential $V^{\rm loc}_{s\text{-state}}(r)$ for the ^{16}O nucleus and only one s state at $\varepsilon = -22.461$ MeV in the potential $V^{\rm loc}_{s\text{-state}}(r)$ for the ^{4}He nucleus. By comparing these values of ε_λ with the corresponding theoretical values from the table, we see that the parameter δ introduced above to characterize the accuracy of the proposed approximation is $\delta \approx 0.95\%$ for the ^{16}O nucleus and $\delta \approx 1.92\%$ for the ^{4}He nucleus. Therefore, we can conclude that, in nuclear problems, the accuracy of the single-particle energies ε_λ calculated by formula (15) is quite acceptable. This is especially important for complicated potentials $V^{\rm loc}(\mathbf{r})$, in which case a precise determination of ε_λ requires dealing with the three-dimensional Schrödinger equation. The extremely difficult problem involving the three-dimensional Schrödinger equation obviously arises in the case of the model that was considered in [12] and which takes into account, in addition to deformations, the polarization of single-particle orbitals.

Single-particle energies (in MeV) calculated theoretically and obtained from the experimental data reported in [13] for the ^{16}O and ^{4}He nuclei

State	Nucleus			
	^{16}O		^{4}He	
	Neutrons	Protons	Neutrons	Protons
s (theor.)	−47.197	−45.029	−22.029	−21.208
s (expt.)	−47.0	-40 ± 8	–	–
p (theor.)	−19.783	−16.520	–	–
p (expt.)	−20.36	−16.30	–	–

In conclusion, we note that this study have not been aimed at describing experimental data on the single-particle properties of a large number of nuclei (specific systematic calculations and their comparative analysis have yet to be performed). Moreover, we have not considered here potentials $V^{\rm loc}_{s\text{-state}}(\mathbf{r})$ featuring singularities in the region $\mathbf{r} > 0$ (the use of such potentials in calculating physical quantities involves considerable mathematical difficulties). We have deliberately restricted our consideration to the simplest nuclei (with the exception of ^{11}Be) and the $SU(3)$ model in order to represent the formulas for $V^{\rm loc}(\mathbf{r})$ and ε_λ in the most concise form and to provide the reader with the simplest possibility of assessing the efficiency of this approach to obtaining the single-particle properties of the nucleus in the case of other versions of nucleon–nucleon forces.

APPENDIX A

The incomplete partial overlap integrals $f_n(\ldots)$ and $\tilde{f}_{n_\lambda n}(\ldots)$ appearing in Eq. (13) are given by

$$f_n(x;a,\mu) \equiv \int\limits_{-\infty}^{\infty} dx' \psi_n^2(x'/a) \exp\left\{-\frac{(x-x')^2}{\mu^2}\right\} \tag{A.1}$$

$$= \exp\left\{-\frac{x^2}{a^2+\mu^2}\right\}\left(1+\frac{a^2}{\mu^2}\right)^{-1/2} \times \sum_{k=0}^{n} \frac{n!}{2^{n-k}k![(n-k)!]^2}\left(\frac{a^2}{a^2+\mu^2}\right)^{n-k} \times H_{2(n-k)}\left(\frac{x}{\sqrt{a^2+\mu^2}}\right);$$

$$\tilde{f}_{n_\lambda n}(x;a_\lambda,a,\mu) \equiv [\psi_n(x/a)/\psi_{n_\lambda}(x/a_\lambda)] \tag{A.2}$$

$$\times \int\limits_{-\infty}^{\infty} dx' \psi_n(x'/a)\psi_{n_\lambda}(x'/a_\lambda) \exp\left\{-\frac{(x-x')^2}{\mu^2}\right\}$$

$$= 2^{n_\lambda} n_\lambda! \left(\frac{1}{\sqrt{\alpha}}\right)\left[\frac{H_n(x/a)}{H_{n_\lambda}(x/a_\lambda)}\right] \times \exp\left\{-\frac{x^2}{a^2+\mu^2} - \frac{x^2}{2}\left(\frac{1}{a^2}-\frac{1}{a_\lambda^2}\right)\right\} \times \sum_{l=0}^{[n_\lambda/2]} \frac{(-1)^l}{4^l l!(n_\lambda-2l)!}\left(\frac{\mu}{a_\lambda}\right)^{n_\lambda-2l}$$

$$\times \sum_{k=0}^{[\frac{n}{2}]} \frac{(-1)^k}{4^k k!(n-2k)!}\left(\frac{\mu}{a}\right)^{n-2k} \sum_{m=0}^{\left[\frac{n_\lambda+n}{2}-k-l\right]} \left(\frac{a^2}{\mu^2}\right)^m \times \frac{(n_\lambda+n-2k-2l)!}{(4\alpha)^m m!(n_\lambda+n-2k-2l-2m)!} \times \left(\frac{1}{\alpha}\frac{x\mu}{a^2}\right)^{n_\lambda+n-2k-2l-2m},$$

where $H_n(x)$ are Hermitian polynomials, $[X]$ is the integral part of the number X, and $\alpha \equiv 1/2 + a^2/2a_\lambda^2 + a^2/\mu^2$.

In the case of $n, n_\lambda = \{0,1\}$, we can find from (A.1) and (A.2) that

$$f_0(x;a,\mu) = \exp\left\{-\frac{x^2}{a^2+\mu^2}\right\}\left(1+\frac{a^2}{\mu^2}\right)^{-1/2}, \tag{A.1a}$$

$$f_1(x;a,\mu) = f_0(x;a,\mu) \times \left[1+2\frac{x^2a^2}{\mu^4}\left(1+\frac{a^2}{\mu^2}\right)^{-1}\right]\left(1+\frac{a^2}{\mu^2}\right)^{-1};$$

$$\tilde{f}_{00}(x;a_\lambda,a,\mu) = \frac{1}{\sqrt{\alpha}} \times \exp\left\{-\frac{x^2}{\tilde{a}^2+\mu^2} - \frac{x^2}{2}\left(\frac{1}{a^2}-\frac{1}{a_\lambda^2}\right)\right\} \equiv \tilde{f}_{00}, \tag{A.2a}$$

$$\tilde{a}^{-2} \equiv \frac{1}{2a^2} + \frac{1}{2a_\lambda^2}, \quad \tilde{f}_{10}(x;a_\lambda,a,\mu) = \tilde{f}_{00}\frac{a^2}{\alpha\mu^2},$$

$$\tilde{f}_{01}(x;a_\lambda,a,\mu) = \tilde{f}_{00}\frac{2x^2}{\alpha\mu^2},$$

$$\tilde{f}_{11}(x;a_\lambda,a,\mu) = \tilde{f}_{00}\frac{1}{\alpha}\left(1+\frac{2x^2a^2}{\alpha\mu^4}\right).$$

The complete partial overlap integrals $f'_{n_\lambda n}(\ldots)$ and $f''_{n_\lambda n}(\ldots)$ determining the single-particle energies in (15) have the form

$$f'_{n_\lambda n}(a_\lambda,a,\mu) \equiv \int\limits_{-\infty}^{\infty} dx_1 \int\limits_{-\infty}^{\infty} dx_2 \psi_{n_\lambda}^2\left(\frac{x_1}{a_\lambda}\right) \times \psi_n^2\left(\frac{x_2}{a}\right)\exp\left\{-\frac{(x_1-x_2)^2}{\mu^2}\right\} \tag{A.3}$$

$$= n_\lambda! n! \left(1+\frac{a_\lambda^2+a^2}{\mu^2}\right)^{-1/2} \times \sum_{l=0}^{n_\lambda}\sum_{k=0}^{n}(-1)^{n+k+l} C_{lk}^{n_\lambda n} \frac{a_\lambda^{2l} a^{2(n-k)}}{(\mu^2+a_\lambda^2+a^2)^{n+l-k}},$$

$$C_{lk}^{n_\lambda n} \equiv \frac{(2l-1)!!(2n-2k-1)!!}{k!(n-k)!l!(n_\lambda-l)!} \times \sum_{i=0}^{\min(l,n-k)} \frac{2^i}{(n-k-i)!(l-i)!i!(2i-1)!!};$$

$$f''_{n_\lambda n}(a_\lambda,a,\mu) \equiv \int\limits_{-\infty}^{\infty} dx_1 \int\limits_{-\infty}^{\infty} dx_2 \psi_{n_\lambda}\left(\frac{x_1}{a_\lambda}\right) \tag{A.4}$$

$$\times \psi_{n_\lambda}\left(\frac{x_2}{a_\lambda}\right)\psi_n\left(\frac{x_1}{a}\right)\psi_n\left(\frac{x_2}{a}\right) \times \exp\left\{-\frac{(x_1-x_2)^2}{\mu^2}\right\} = \frac{1}{n_\lambda! n!}\frac{a_r^2}{a_\lambda a} \times \left(1-\frac{a_r^4}{\mu^4}\right)^{-1/2} \sum_{k_1=0}^{[n_\lambda/2]} C_{n_\lambda}^{k_1} \sum_{l_1=0}^{[n_\lambda/2]} C_{n_\lambda}^{l_1}$$

$$\times \sum_{k_2=0}^{[n/2]} C_n^{k_2} \sum_{l_2=0}^{[n/2]} C_n^{l_2} \sum_{m=0}^{[n_r/2]} \frac{n_r!}{2^m m!} \times \frac{[n_\lambda+n+n_r-2(l_1+l_2+m)-1]!!}{(n_r-2m)!} \times \left(\frac{a_r^2}{a_\lambda^2}\right)^{n_\lambda-k_1-l_1}\left(\frac{a_r^2}{a^2}\right)^{n-k_2-l_2}$$

$$\times \left(\frac{a_r^2}{\mu^2}\right)^{n_r-2m} \left(\frac{\mu^4}{\mu^4-a_r^4}\right)^{n_r+k_1+k_2-l_1-l_2-m},$$

$$C_n^k \equiv \frac{(-1)^k n!}{2^k k!(n-2k)!}, \quad \frac{1}{a_r^2} \equiv \frac{1}{\mu^2} + \frac{1}{2a_\lambda^2} + \frac{1}{2a^2},$$

$$n_r \equiv n_\lambda + n - 2k_1 - 2k_2.$$

In the case of $n, n_\lambda = \{0,1\}$, expressions (A.3) and (A.4) reduce to

$$f'_{00}(a_\lambda, a, \mu) = \left(1 + \frac{a_\lambda^2 + a^2}{\mu^2}\right)^{-1/2} \equiv f'_{00}, \quad \text{(A.3a)}$$

$$f'_{10}(a_\lambda, a, \mu) = f'_{00}\frac{a^2+\mu^2}{a^2+\mu^2+a_\lambda^2},$$

$$f'_{01}(a_\lambda, a, \mu) = f'_{00}\frac{a_\lambda^2+\mu^2}{a_\lambda^2+\mu^2+a^2},$$

$$f'_{11}(a_\lambda, a, \mu) = f'_{00}\left(1 + \frac{a_\lambda^2 + a^2}{\mu^2}\right)^{-1}$$

$$\times \left[1 + 3\frac{a_\lambda^2 a^2}{\mu^4}\left(1 + \frac{a_\lambda^2 + a^2}{\mu^2}\right)^{-1}\right];$$

$$f''_{00}(a_\lambda, a, \mu) = \frac{a_r^2}{a_\lambda a}\left(1 - \frac{a_r^4}{\mu^4}\right)^{-1/2} \equiv f''_{00}, \quad \text{(A.4a)}$$

$$f''_{10}(a_\lambda, a, \mu) = \frac{a^2}{\mu^2}(f''_{00})^3,$$

$$f''_{01}(a_\lambda, a, \mu) = \frac{a_\lambda^2}{\mu^2}(f''_{00})^3,$$

$$f''_{11}(a_\lambda, a, \mu) = \left[1 + 3\frac{a_\lambda^2 a^2}{\mu^4}(f''_{00})^2\right](f''_{00})^3.$$

APPENDIX B

The functions appearing in the definition of the local potential (18) are given by

$$\Phi_0(r; a, b, \mu) = \left(1 + \frac{a^2}{\mu^2}\right)\exp\left\{-\frac{r^2}{a^2+\mu^2}\right\} \quad \text{(A.5)}$$

$$+ \left(1 + \frac{b^2}{\mu^2}\right)^{-5/2}\exp\left\{-\frac{r^2}{b^2+\mu^2}\right\}$$

$$\times \left[3 + 2\frac{b^2 r^2}{\mu^4}\frac{1}{1+\frac{b^2}{\mu^2}}\right],$$

$$\Phi_s(r; a_\lambda, a, b, \mu_)) = \left(\frac{1}{2} + \frac{a^2}{2a_\lambda^2} + \frac{a^2}{\mu^2}\right)^{-3/2} \quad \text{(A.6)}$$

$$\times \exp\left\{-\frac{r^2}{\tilde{a}^2+\mu^2} - \left(\frac{1}{a^2} - \frac{1}{a_\lambda^2}\right)\frac{r^2}{2}\right\}$$

$$+ 2\frac{r^2}{\mu^2}\left(\frac{1}{2} + \frac{b^2}{2a_\lambda^2} + \frac{b^2}{\mu^2}\right)^{-5/2}$$

$$\times \exp\left\{-\frac{r^2}{\tilde{b}^2+\mu^2} - \left(\frac{1}{b^2} - \frac{1}{a_\lambda^2}\right)\frac{r^2}{2}\right\},$$

$$\Phi_p(r; a_\lambda, a, b, \mu_)) = \frac{a^2}{\mu^2}\left(\frac{1}{2} + \frac{a^2}{2a_\lambda^2} + \frac{a^2}{\mu^2}\right)^{-5/2} \quad \text{(A.7)}$$

$$\times \exp\left\{-\frac{r^2}{\tilde{a}^2+\mu^2} - \left(\frac{1}{a^2} - \frac{1}{a_\lambda^2}\right)\frac{r^2}{2}\right\}$$

$$+ \left[1 + 2\frac{b^2 r^2}{\mu^4}\left(\frac{1}{2} + \frac{b^2}{2a_\lambda^2} + \frac{b^2}{\mu^2}\right)^{-1}\right]$$

$$\times \left(\frac{1}{2} + \frac{b^2}{2a_\lambda^2} + \frac{b^2}{\mu^2}\right)^{-5/2}$$

$$\times \exp\left\{-\frac{r^2}{\tilde{b}^2+\mu^2} - \left(\frac{1}{b^2} - \frac{1}{a_\lambda^2}\right)\frac{r^2}{2}\right\},$$

$$V^{\mathrm{C}}(r) = 2\frac{e^2}{r}\mathrm{erf}\left(\frac{r}{a}\right) \quad \text{(A.8)}$$

$$+ 6\frac{e^2}{r}\mathrm{erf}\left(\frac{r}{b}\right) - 4\frac{e^2}{b\sqrt{\pi}}\exp\left(-\frac{r^2}{b^2}\right),$$

$$W_s^{\mathrm{C}}(r) = \left(\frac{\tilde{a}}{a}\right)^3 \quad \text{(A.9)}$$

$$\times \exp\left\{-\frac{r^2}{2}\left(\frac{1}{a^2} - \frac{1}{a_\lambda^2}\right)\right\}\frac{e^2}{r}\mathrm{erf}\left(\frac{r}{\tilde{a}}\right)$$

$$+ \left(\frac{\tilde{b}}{b}\right)^5 \exp\left\{-\frac{r^2}{2}\left(\frac{1}{b^2} - \frac{1}{a_\lambda^2}\right)\right\}$$

$$\times \frac{e^2 b^2}{2r^2}\left[\frac{1}{r}\mathrm{erf}\left(\frac{r}{\tilde{b}}\right) - \frac{2}{\tilde{b}\sqrt{\pi}}\exp\left(-\frac{r^2}{\tilde{b}^2}\right)\right],$$

$$W_p^{\mathrm{C}}(r) = \left(\frac{\tilde{a}}{a}\right)^5 \quad \text{(A.10)}$$

$$\times \exp\left\{-\frac{r^2}{2}\left(\frac{1}{a^2} - \frac{1}{a_\lambda^2}\right)\right\}\frac{e^2 a^2}{2r^3}\mathrm{erf}\left(\frac{r}{\tilde{a}}\right)$$

$$- \left(\frac{\tilde{a}}{a}\right)^4 \frac{ae^2}{r^2\sqrt{\pi}}\exp\left(-\frac{r^2}{a^2}\right)$$

$$+ \left(\frac{\tilde{b}}{b}\right)^5 \exp\left\{-\frac{r^2}{2}\left(\frac{1}{b^2} - \frac{1}{a_\lambda^2}\right)\right\}$$

$$\times \frac{e^2}{r}\left(1 + \frac{\tilde{b}^2}{r^2}\right)\mathrm{erf}\left(\frac{r}{\tilde{b}}\right)$$

$$-\left(\frac{\tilde{b}}{b}\right)^4 \frac{2e^2}{b\sqrt{\pi}}\left(1+\frac{\tilde{b}^2}{r^2}\right)\exp\left(-\frac{r^2}{b^2}\right),$$

where we have used the notation

$$\tilde{a}^{-2} \equiv \frac{1}{2a^2}+\frac{1}{2a_\lambda^2}, \quad \tilde{b}^{-2} \equiv \frac{1}{2b^2}+\frac{1}{2a_\lambda^2}.$$

In formulas (22) and (23) for the single-particle energies of the ^{16}O nucleus, the following notation has been introduced:

$$F_d(a_\lambda,a,b,\mu) \equiv \left(1+\frac{a^2+a_\lambda^2}{\mu^2}\right)^{-3/2} + 3\left(1+\frac{a_\lambda^2}{\mu^2}\right)\left(1+\frac{b^2+a_\lambda^2}{\mu^2}\right)^{-5/2}, \tag{A.11}$$

$$F_{\rm ex}(a_\lambda,a,b,\mu) \equiv \left[\left(\frac{1}{2}+\frac{a^2}{2a_\lambda^2}\right)\left(\frac{1}{2}+\frac{a_\lambda^2}{2a^2}+2\frac{a_\lambda^2}{\mu^2}\right)\right]^{-3/2} + 3\frac{a_\lambda^2}{\mu^2}\left[\left(\frac{1}{2}+\frac{b^2}{2a_\lambda^2}\right)\left(\frac{1}{2}+\frac{a_\lambda^2}{2b^2}+2\frac{a_\lambda^2}{\mu^2}\right)\right]^{-5/2}, \tag{A.12}$$

$$F_d^1(a_\lambda,a,b,\mu) \equiv \left(1+\frac{a^2}{\mu^2}\right)\left(1+\frac{a^2+a_\lambda^2}{\mu^2}\right)^{-5/2} + \left[3+5\frac{b^2a_\lambda^2}{\mu^4}\left(1+\frac{b^2+a_\lambda^2}{\mu^2}\right)^{-1}\right] \times \left(1+\frac{b^2+a_\lambda^2}{\mu^2}\right)^{-5/2}, \tag{A.13}$$

$$F_{\rm ex}^1(a_\lambda,a,b,\mu) \equiv \frac{a^2}{\mu^2}\left[\left(\frac{1}{2}+\frac{a^2}{2a_\lambda^2}\right)\left(\frac{1}{2}+\frac{a_\lambda^2}{2a^2}+2\frac{a_\lambda^2}{\mu^2}\right)\right]^{-5/2} + \left[1+5\frac{b^2a_\lambda^2}{\mu^4}\left(\frac{1}{2}+\frac{b^2}{2a_\lambda^2}\right)^{-1} \times\left(\frac{1}{2}+\frac{a_\lambda^2}{2b^2}+2\frac{a_\lambda^2}{\mu^2}\right)^{-1}\right] \times\left[\left(\frac{1}{2}+\frac{b^2}{2a_\lambda^2}\right)\left(\frac{1}{2}+\frac{a_\lambda^2}{2b^2}+2\frac{a_\lambda^2}{\mu^2}\right)\right]^{-5/2}. \tag{A.14}$$

REFERENCES

1. B. I. Barts, Yu. L. Bolotin, E. V. Inopin, and V. Yu. Gonchar, *Hartree–Fock Method in the Theory of the Nucleus* (Naukova Dumka, Kiev, 1982).
2. J. M. Eisenberg and W. Greiner, *Microscopic Theory of the Nucleus* (North-Holland, Amsterdam, 1972; Atomizdat, Moscow, 1976).
3. A. I. Steshenko and G. F. Filippov, Yad. Fiz. **14**, 715 (1971) [Sov. J. Nucl. Phys. **14**, 403 (1972)].
4. H. A. Bethe, Phys. Rev. **103**, 1353 (1956).
5. J. C. Slater, Phys. Rev. **81**, 385 (1951).
6. D. M. Brink and E. Boecker, Nucl. Phys. A **91**, 1 (1967).
7. A. B. Volkov, Nucl. Phys. **74**, 33 (1965).
8. M. Harvey, Adv. Nucl. Phys. **1**, 67 (1968).
9. I. P. Okhrimenko and A. I. Steshenko, Preprint ITF-82-96R (Institute for Theoretical Physics, Kiev, 1982).
10. S. G. Cooper and R. S. Mackintosh, Phys. Rev. C **43**, 1001 (1991).
11. L. R. B. Elton and A. Swift, Nucl. Phys. A **94**, 52 (1967).
12. A. I. Steshenko, Yad. Fiz. **60**, 599 (1997) [Phys. At. Nucl. **60**, 520 (1997)].
13. H. F. Boersma and R. Malfliet, Phys. Rev. C **49**, 1495 (1994).
14. L. G. Ixaru, *Numerical Methods for Differential Equations and Applications* (Academiei, Bucharest, 1984).

Translated by A. Isaakyan

Physics of Atomic Nuclei, Vol. 65, No. 3, 2002, pp. 426–436. Translated from Yadernaya Fizika, Vol. 65, No. 3, 2002, pp. 453–463.

NUCLEI
Theory

Excited States of Deformable Nonaxial Odd Nuclei

Sh. Sharipov and M. J. Ermamatov

Institute of Nuclear Physics, Uzbek Academy of Sciences, pos. Ulughbek, Tashkent, 702132 Republic of Uzbekistan

Received February 28, 2001

Abstract—Rotationally single-particle and vibrational excitations of deformable nonaxial odd nuclei are investigated with allowance for the interaction of collective and single-particle states. The ratios of excitation energies, of reduced probabilities of $E2$ transitions, and of quadrupole moments for deformed nonaxial odd nuclei are calculated up to high-spin states. © *2002 MAIK "Nauka/Interperiodica".*

1. INTRODUCTION

By convention, low-lying excited states of deformable nuclei can be broken down into the group of single-particle states and the group of collective states [1–3]. The latter in turn can be divided into β- and γ-vibrational levels and rotational levels [2]. The partition of excitations into single-particle and collective ones is legitimate for even–even nuclei, because their spectrum of the single-particle excitations is separated from the ground state by a gap of 1 to 2 MeV. In odd nuclei, the energy of single-particle excitations is on the same order of magnitude as the rotational energy and the energy of vibrations of the nuclear surface; therefore, the separation of single-particle excitations from the total excitation of a nucleus is not very well justified [3, 4].

The theory of collective quadrupole-type excitations that takes into account the coupling of single-particle and collective motion and which was developed in [3–7] makes it possible to explain some regularities observed in the excitation spectra of deformable odd nuclei.

Investigation of heavy-ion reactions furnished information about high-spin high-lying excited states of nuclei [8, 9]—in particular, information about the energy levels of the ground-state rotationally single-particle, anomalous rotationally single-particle, rotationally single-particle γ-vibrational, and rotationally single-particle β-vibrational bands, which is in good agreement with theoretical predictions [3–7].

The arrangement of energy levels, the probabilities of electric quadrupole transitions between excited levels, and quadrupole moments of excited states change significantly upon taking into account the deformability of nuclei [4]. Below, the effect of the deformability of the shape of an odd nucleus on its energy spectra, on the reduced probabilities of $E2$ transitions, and on the quadrupole moments of excited states of nonaxial odd nuclei is investigated in the nonadiabatic approximation up to high-spin states.

2. ENERGY OF LEVELS AND WAVE FUNCTIONS

It is well known that, in the case of strong coupling, the general theory of quadrupole excitations in nonspherical odd nuclei featuring one external nucleon is determined by a Hamiltonian that involves five collective dynamical variables β, γ, θ_1, θ_2, and θ_3, (where β and γ are the variables of, respectively, longitudinal and transverse vibrations and θ_1, θ_2, and θ_3 are Euler angles) and the external-nucleon coordinates x, y, and z [1] and which can be represented in the form

$$\hat{H} = \frac{\hbar^2}{2B}\left[\hat{T}_\beta + \frac{1}{\beta^2}\left(\hat{T}_\gamma + \hat{T}_{\rm rot}\right)\right] + V(\beta,\gamma) + \hat{H}_p - T\beta\left[\cos\gamma\left(3\hat{j}_3^2 - \hat{\mathbf{j}}^2\right) + \sqrt{3}\sin\gamma\left(j_1^2 - j_2^2\right)\right]. \quad (1)$$

Here, B is the mass parameter;

$$\hat{T}_\beta = -\frac{1}{\beta^4}\frac{\partial}{\partial\beta}\left(\beta^4\frac{\partial}{\partial\beta}\right),$$

$$\hat{T}_\gamma = -\frac{1}{\sin 3\gamma}\frac{\partial}{\partial\gamma}\left(\sin 3\gamma\frac{\partial}{\partial\gamma}\right),$$

$$\hat{T}_{\rm rot} = \frac{1}{4}\sum_{\kappa=1}^{3}\frac{(\hat{I}_\kappa - \hat{j}_\kappa)^2}{\sin^2\left(\gamma - \kappa\frac{2\pi}{3}\right)};$$

I_κ and j_κ are the projections of the operators of, respectively, the total nuclear spin $\hat{\mathbf{I}}$ and the angular momentum $\hat{\mathbf{j}}$ of the external nucleon onto the principal axes of the nucleus; $V(\beta,\gamma)$ is the potential energy of β and γ vibrations; H_p is the spherically

1063-7788/02/6503-0426$22.00

symmetric part of the Hamiltonian of the external nucleon; and T_β is a quantity that characterizes the interaction of the nucleon with the nonspherical part of the nuclear-core field. The eigenfunctions Ψ of the operator in (1) are defined in the space of the variables $\beta > 0,\ 0 < \gamma < \pi/3,\ 0 < \theta_1 < 2\pi,\ 0 < \theta_2 < \pi,\ 0 < \theta_3 < 2\pi,\ -\infty < x < \infty,\ -\infty < y < \infty$, and $-\infty < z < \infty$, the relevant volume element being

$$d\tau = \beta^4 |\sin 3\gamma|\, d\beta d\gamma d\theta_1 \sin\theta_2 d\theta_2 d\theta_3 dx dy dz. \quad (2)$$

It is very difficult to solve the Schrödinger equation with the operator in (1). A general solution to this equation has not yet been found. Only some particular cases have been considered so far [2–7]. Suppose that the potential energy has the form

$$V(\beta,\gamma) = V(\beta) + \frac{\beta_0^4}{\beta^2}V(\gamma) + \left(\frac{\beta}{\beta_0} - \frac{\beta_0^2}{\beta^2}\right)\beta_0^2 V(\gamma). \quad (3)$$

At low excitation energies, the eigenvalues and eigenfunctions of the operator in (1) can then be found by perturbation theory in the third term of the potential-energy operator (3),

$$H' = \left(\frac{\beta}{\beta_0} - \frac{\beta_0^2}{\beta^2}\right)\beta_0^2 V(\gamma). \quad (4)$$

For the Hamiltonian of the zero-order approximation, the Schrödinger equation can be represented as

$$\left[\frac{\hbar^2}{2B}\left(\hat{T}_\beta + \frac{2B}{\hbar^2}V(\beta) + \frac{\Lambda(\beta,\gamma)}{\beta^2}\right)\right]\Psi = (E - \varepsilon_j)\Psi, \quad (5)$$

where

$$\Lambda(\beta,\gamma) = \hat{T}_\gamma + \hat{T}_{\rm rot} + \frac{2B\beta_0^4}{\hbar^2}V(\gamma) \quad (6)$$
$$- \frac{2BT\beta^3}{\hbar^2}\left[(3\hat{j}_3^2 - \hat{\mathbf{j}}^2)\cos\gamma + \sqrt{3}(\hat{j}_1^2 - j_2^2)\sin\gamma\right],$$

$$\hat{H}_p\Psi_p = \varepsilon_j\Psi_p, \quad (7)$$

with Ψ_p being the eigenfunctions of the spherically symmetric part of the Hamiltonian for the external nucleon. In Eq. (5), we replace the operator $\Lambda(\beta,\gamma)$ by the operator $\Lambda(\beta_0,\gamma)$ and seek a solution to Eq. (5) in the form

$$\Psi = F(\beta)\Phi(x,y,z,\gamma,\theta_i), \quad i = 1,2,3. \quad (8)$$

Upon separating the variable β, the Schrödinger equation (5) reduces to a set of two coupled equations:

$$\left[-\frac{\hbar^2}{2B}\frac{d^2}{d\beta^2} - \frac{2\hbar^2}{B\beta}\frac{d}{d\beta} + V(\beta) + \frac{\hbar^2\Lambda_0}{2B\beta^2}\right. \quad (9)$$
$$\left. + \frac{\hbar^2(\Lambda - \Lambda_0)}{2B\beta^2} - (E - \varepsilon_j)\right]F(\beta) = 0,$$

$$\left\{\frac{1}{\sin 3\gamma}\frac{\partial}{\partial\gamma}\left(\sin 3\gamma\frac{\partial}{\partial\gamma}\right) - \frac{1}{4}\sum_{\kappa=1}^{3}\frac{(\hat{I}_\kappa - \hat{j}_\kappa)^2}{\sin^2\left(\gamma - \kappa\frac{2\pi}{3}\right)}\right. \quad (10)$$
$$- \frac{2B\beta_0^4 V(\gamma)}{\hbar^2} + \frac{2BT\beta_0^3}{\hbar^2}\left[(3\hat{j}_3^2 - \hat{\mathbf{j}}^2)\cos\gamma\right.$$
$$\left.\left. + \sqrt{3}(\hat{j}_1^2 - \hat{j}_2^2)\sin\gamma\right] + \Lambda\right\}\Phi(x,y,z,\gamma,\theta_i) = 0.$$

The constant Λ_0 is chosen in such a way that it coincides with the minimum value of Λ determined by Eq. (10).

In order to take into account transverse γ vibrations, we expand the operator

$$\hat{X}(\gamma) = \frac{1}{4}\sum_{\kappa=1}^{3}\frac{(\hat{I}_\kappa - \hat{j}_\kappa)^2}{\sin^2\left(\gamma - \kappa\frac{2\pi}{3}\right)} + \frac{2BT\beta_0^3}{\hbar^2} \quad (11)$$
$$\times\left[(3\hat{j}_3^2 - \hat{\mathbf{j}}^2)\cos\gamma + \sqrt{3}(\hat{j}_1^2 - \hat{j}_2^2)\sin\gamma\right]$$

in Eq. (10) in a series around the equilibrium ground-state deformation γ_0:

$$\hat{X}(\gamma) = \hat{X}(\gamma_0) + \left.\frac{\partial\hat{X}(\gamma)}{\partial\gamma}\right|_{\gamma=\gamma_0}(\gamma - \gamma_0) \quad (12)$$
$$+ \left.\frac{\partial^2\hat{X}(\gamma)}{\partial\gamma^2}\right|_{\gamma=\gamma_0}(\gamma - \gamma_0)^2 + \ldots.$$

In order to find the wave functions $\Phi(x,y,z,\gamma,\theta_i)$ and the eigenvalues Λ, we make use of perturbation theory. In the zeroth order of the expansion of the operator $\hat{X}(\gamma)$, Eq. (10) has the form

$$\left\{\frac{1}{\sin 3\gamma}\frac{\partial}{\partial\gamma}\left(\sin 3\gamma\frac{\partial}{\partial\gamma}\right) - \frac{1}{4}\sum_{\kappa=1}^{3}\frac{(\hat{I}_\kappa - \hat{j}_\kappa)^2}{\sin^2\left(\gamma_0 - \kappa\frac{2\pi}{3}\right)}\right. \quad (13)$$
$$- \frac{2B\beta_0^4 V(\gamma)}{\hbar^2} + \frac{2BT\beta_0^3}{\hbar^2}\left[(3\hat{j}_3^2 - \hat{\mathbf{j}}^2)\cos\gamma_0\right.$$
$$\left.\left. + \sqrt{3}(\hat{j}_1^2 - \hat{j}_2^2)\sin\gamma_0\right] + \Lambda\right\}\Phi(x,y,z,\gamma,\theta_i) = 0.$$

The variables are then separated; that is,

$$\Phi(x,y,z,\gamma,\theta_i) = \chi(\gamma)\varphi(x,y,z,\theta_i). \quad (14)$$

After that, Eq. (13) reduces to the set of two equations

$$\left\{\frac{1}{4}\sum_{\kappa=1}^{3}\frac{(\hat{I}_\kappa - \hat{j}_\kappa)^2}{\sin^2\left(\gamma_0 - \kappa\frac{2\pi}{3}\right)} - \frac{2BT\beta_0^3}{\hbar^2}\right. \quad (15)$$

$$\times \left[(3\hat{j}_3^2 - \hat{\mathbf{j}}^2)\cos\gamma_0 + \sqrt{3}(\hat{j}_1^2 - \hat{j}_2^2)\sin\gamma_0\right] - \varepsilon_{I\tau}\Bigg\}$$
$$\times \varphi(x, y, z, \theta_i) = 0,$$
$$\left\{\frac{1}{\sin 3\gamma}\frac{\partial}{\partial\gamma}\left(\sin 3\gamma\frac{\partial}{\partial\gamma}\right)\right. \quad (16)$$
$$\left. - \frac{2B\beta_0^4 V(\gamma)}{\hbar^2} + \Lambda - \varepsilon_{I\tau}\right\}\chi(\gamma) = 0,$$

where $\varepsilon_{I\tau}$ are the eigenvalues of a rigid nonaxial rotor and τ numbers wave functions that are associated with identical I. The terms that are disregarded in Eq. (12) are not expected to have a pronounced effect on the results of our calculations [5].

Solutions to Eq. (15) are well known [3]. In order to solve Eq. (16), we introduce the function

$$\chi(\gamma) = \frac{Y(\gamma)}{\sqrt{\sin 3\gamma}}, \quad (17)$$

whereupon Eq. (16) reduces to the form

$$-\frac{\hbar^2}{2B}\frac{d^2Y(\gamma)}{d\gamma^2} + \left[W(\gamma) + \frac{\hbar^2}{2B}(\varepsilon_{I\tau} - \Lambda)\right]Y(\gamma) = 0, \quad (18)$$

where

$$W(\gamma) = \beta_0^4 V(\gamma) - \frac{9\hbar^2}{8B}\frac{1 + \sin^2 3\gamma}{\sin^2 3\gamma}. \quad (19)$$

For the first time, an equation having the form (18) appeared in the Davydov–Chaban model [3]; this equation can be solved for an oscillatory-type potential. In this case, the quantum number of β vibrations will be noninteger. Equation (18) is similar to the equation for β vibrations in [10], where the potential for β vibrations is chosen in such a way that the quantum number of β vibrations is integral. Since γ_0 is the equilibrium position for transverse vibrations, the effective potential energy $W(\gamma)$ has a minimum at $\gamma = \gamma_0$ and can be represented in the form

$$W(\gamma) = V(\gamma_0)\left(\frac{\gamma}{\gamma_0} - \frac{\gamma_0}{\gamma}\right)^2. \quad (20)$$

The eigenvalues and eigenfunctions of Eq. (18) are then given by

$$\Lambda = \Lambda_{n_\gamma Ij\tau} = (4n_\gamma + 2p + 3)\frac{\sqrt{2g_{\gamma_0}}}{\gamma_0^2} - \frac{4g_{\gamma_0}}{\gamma_0^2} + \varepsilon_{I\tau}, \quad (21)$$

$$Y(\gamma) = C_{\gamma_0}\gamma^{p+1}\exp\left(-\frac{\gamma^2}{2b_{\gamma_0}}\right)L_{n_\gamma}^{p+1/2}\left(-\frac{\gamma^2}{2b_{\gamma_0}}\right), \quad (22)$$

where $n_\gamma = 1, 2, \ldots$ is the quantum number of γ vibrations, $p = \frac{1}{2}\left(-1 + \sqrt{1 + 8g_{\gamma_0}}\right)$, $g_{\gamma_0} = \frac{BV(\gamma_0)\gamma_0^2}{\hbar^2}$ is a dimensionless parameter of the theory, $V(\gamma_0)$ is a parameter appearing in the theory and having dimensions of energy, $b_{\gamma_0} = \gamma_0[2g_{\gamma_0}]^{-1/4}$, $L_{n_\gamma}^{p+1/2}\left(-\frac{\gamma^2}{2b_{\gamma_0}}\right)$ are Laguerre polynomials, and C_{γ_0} is the normalization factor.

We will now solve Eq. (9) by making use of the zero-order solution (21) to Eq. (10). Since β_0 is the equilibrium position for longitudinal vibrations, the effective potential energy

$$W(\beta) = V(\beta) + \frac{\hbar^2\Lambda_0}{2B\beta^2} \quad (23)$$

has a minimum at $\beta = \beta_0$ and can be represented in the form

$$W(\beta) = \frac{V(\beta_0)}{\beta^2}(\beta - \beta_0)^2. \quad (24)$$

For the potential (24), the eigenvalues and eigenfunctions of Eq. (9) are given by

$$E_{n_\beta} = -1 \quad (25)$$
$$+ \frac{2g_{\beta_0}}{\left[n_\beta + 0.5 + (2.25 + \Lambda - \Lambda_0 + 2g_{\beta_0})^{1/2}\right]^2} - \frac{\varepsilon_j}{V_0},$$

$$F_{n_\beta}(\beta) = N_\beta\exp\left(-\frac{x}{2}\right)F(-n_\beta, 2s + 4, x), \quad (26)$$

where n_β is the quantum number of β vibrations,

$$x = \frac{2g_{\beta_0}}{n_\beta + 0.5 + (2g_{\beta_0} + \Lambda - \Lambda_0 + 2.25)^{1/2}}\frac{\beta}{\beta_0},$$

$g_{\beta_0} = \frac{BV(\beta_0)\beta_0^2}{\hbar^2}$ is a dimensionless parameter of the theory, $V(\beta_0)$ is a parameter appearing in the theory and having dimensions of energy, $s = \sqrt{2.25 + \Lambda - \Lambda_0 + 2g_{\beta_0}} - 1.5$, $F(-n_\beta, 2s + 4, x)$ is a confluent hypergeometric function, and

$$N_\beta = \frac{4}{\sqrt{n_\beta + s + 2}} \quad (27)$$
$$\times\left\{\frac{4g_{\beta_0}}{\beta_0\left(n_\beta + 0.5 + \sqrt{2.25 + \Lambda - \Lambda_0 + 2g_{\beta_0}}\right)}\right\}^{5/2}$$
$$\times\frac{1}{\Gamma(2s + 4)}\sqrt{\frac{\Gamma(n_\beta + 2s + 4)}{\Gamma(n_\beta + 1)}}$$

is the normalization factor.

According to expressions (21) and (25), the energy of an excited level of an odd nucleus is specified the quantum numbers n_β, n_γ, I, j, and τ:

$$\Delta E_{n_\beta n_\gamma I I_0 \tau} = E_{n_\beta n_\gamma I I_0 \tau} - E_{00 I_0 I_0 1} = \frac{2g_{\beta_0}}{\left[0.5 + (2.25 + 2g_{\beta_0})^{1/2}\right]^2} \tag{28}$$

$$- \frac{2g_{\beta_0}}{\left[n_\beta + 0.5 + \left(2.25 + 4n_\gamma \frac{\sqrt{2g_{\gamma_0}}}{\gamma_0^2} + \varepsilon_{I\tau}(\xi, \gamma_0) + \varepsilon_{I_0 1}(\xi, \gamma_0) + 2g_{\beta_0}\right)^{1/2}\right]^2}.$$

Here, $\xi = \dfrac{\hbar^2}{6BT\beta_0^3}$ is a dimensionless parameter that takes into account the relationship between rotation and single-particle motion.

It is convenient to consider the ratio of the excitation energy to the energy of the first excited level,

$$R = \frac{\Delta E_{n_\beta n_\gamma I I_0 \tau}}{\Delta E_{00 I_0 + 1 I_0 1}}. \tag{29}$$

By way of example, the calculated ratios of the excitation energy to the energy of the first excited level in the ground-state rotationally single-particle ($I_0 = 5/2$, $n_\beta = n_\gamma = 0$), the first rotationally single-particle β-vibrational ($I_0 = 5/2$, $n_\beta = 1$, $n_\gamma = 0$), and the first rotationally single-particle γ-vibrational ($I_0 = 5/2$, $n_\beta = 0$, $n_\gamma = 1$) band (at the parameter values of $\xi = 1$, $\gamma_0 = 10^\circ$, and $g_{\gamma_0} = 1$) versus the parameter g_{β_0} are displayed in Fig. 1 for deformable nonaxial odd nuclei whose ground-state spin is 5/2. In the figure, each bandhead is indicated by the quantum numbers (n_β, n_γ).

From Fig. 1, it can be seen that, at fixed values of ξ, γ_0, and g_{γ_0}, the energies of levels in all bands increase with increasing g_{β_0} and that, for $g_{\beta_0} \to 0$ and fixed values of ξ, γ_0, and g_{γ_0}, the levels in all the aforementioned bands descend considerably on the energy scale and are mixed, becoming equidistant, which corresponds to spherical nuclei. As the parameter g_{β_0} grows, the equidistant structure of the spectrum is gradually violated and the levels in the first rotationally single-particle β-vibrational and the first rotationally single-particle γ-vibrational band ascend noticeably on the energy scale with respect to the level of the ground-state rotationally single-particle band, as in the case of even–even [11] and deformable nonaxial odd [5] nuclei (only the excitation energies for a different potential for β vibrations were calculated in [5]). In this case, low-lying energy levels of deformable odd nonaxial nuclei will be purely rotationally single-particle ones, and this corresponds to the spectra of deformed odd nuclei.

Therefore, the shape of a deformable nonaxial odd nucleus changes from a spherical to an ellipsoidal one in response to changes in the parameters ξ, γ_0, g_{γ_0}, and g_{β_0}. There arises the possibility of describing, in a unified way, the spectrum of levels of excited states in the spherical, transition, and deformable odd nuclei in terms of four parameters ξ, γ_0, g_{γ_0}, and g_{β_0}, which can be determined by fitting the theoretical values of energy to their experimental counterparts.

The theoretical and experimental energies of the excited levels in the odd nuclei ^{161}Dy, ^{163}Dy, and ^{167}Er are quoted in Table 1.

The calculated energy levels better reproduce experimental data on the ^{163}Dy and ^{167}Er nuclei; for the energy levels of the ^{161}Dy nucleus, there is a considerable deviation from experimental values at high spins. All experimentally observed levels appear in the theory. However, the nonadiabatic theory developed in this study for nonaxial odd nuclei predicts many other levels that have not yet been observed experimentally.

3. REDUCED PROBABILITIES OF $E2$ TRANSITIONS

In order to calculate the reduced probabilities of $E2$ transitions, we represent the $E2$-transition operator in the form [3]

$$\Re(E2) = e_{\text{eff}} r^2 \sum_q D^2_{\mu q} Y_{2q}(\theta, \varphi) \tag{30}$$

$$+ \sqrt{\frac{5}{16\pi}} Q_{2\mu}(\beta, \gamma_0),$$

where e_{eff} is the effective charge of the external nucleon; $D_{\mu q}$ is a Wigner function; $q = 0, \pm 1, \pm 2$ is the projection of the angular momentum of the external nucleon in the coordinate frame associated with it; and

$$Q_{2\mu}(\beta, \gamma_0) = Q_0 \frac{\beta}{\beta_0} \tag{31}$$

$$\times \left\{ D^2_{\mu 0} \cos\gamma_0 + [D^2_{\mu 2} + D^2_{\mu,-2}] \frac{\sin\gamma_0}{\sqrt{2}} \right\}.$$

Here, Q_0 is the internal quadrupole moment of the odd nucleus being considered. By substituting the operator from (30) and the wave functions (8) into the expression

$$B(E2; i \to f) \tag{32}$$

Table 1

Theory		Experiment		Theory		Experiment	
I	R	I	R	I	R	I	R
^{161}Dy $\xi = 0.3$, $g_{\beta_0} = 418$, $\gamma_0 = 7°$ [16]				^{163}Dy $\xi = 0.3$, $g_{\beta_0} = 418$, $\gamma_0 = 7°$ [14]			
5/2	0	5/2	0	5/2	0	5/2	0
7/2	1	7/2	1	7/2	1	7/2	1
9/2	2.27	9/2	2.29	9/2	2.27	9/2	2.28
11/2	3.83	11/2	4.21	11/2	3.82	11/2	3.83
13/2	5.61	13/2	6.11	13/2	5.60	13/2	5.65
3/2	6.52	–	–	3/2	7.34	–	–
5/2	6.93	–	–	15/2	7.67	15/2	7.74
15/2	7.74	15/2	9.29	5/2	7.79	–	–
7/2	8.20	–	–	7/2	8.97	–	–
9/2	8.55	–	–	9/2	9.41	–	–
1/2	9.30	–	–	17/2	9.90	17/2	10.07
17/2	9.93	17/2	11.60	1/2	10.44	–	–
5/2	10.16	–	–	5/2	11.22	–	–
11/2	11.11	–	–	11/2	11.76	–	–
13/2	11.22	–	–	13/2	12.03	–	–
3/2	11.25	–	–	3/2	12.36	–	–
19/2	12.66	19/2	16.41	19/2	12.48	19/2	12.67
9/2	12.76	–	–	9/2	13.66	–	–
7/2	14.32	–	–	1/2	14.14	–	–
17/2	15.07	–	–	3/2	14.55	–	–
21/2	15.16	21/2	18.86	9/2	14.56	–	–
15/2	15.23	–	–	21/2	15.06	21/2	15.48
13/2	16.78	–	–	5/2	15.20	–	–
23/2	18.53	23/2	25.53	7/2	15.29	–	–
11/2	18.57	–	–	15/2	15.67	–	–
21/2	20.07	–	–	17/2	15.71	–	–
17/2	20.45	–	–	11/2	16.03	–	–
25/2	21.21	25/2	27.90	7/2	16.18	–	–
17/2	21.98	–	–	9/2	17.31	–	–
15/2	23.90	–	–	13/2	17.45	–	–
27/2	25.25	27/2	36.56	13/2	17.76	–	–
25/2	26.16	–	–	23/2	18.14	23/2	18.56
23/2	26.67	–	–	11/2	18.62	–	–
29/2	28.02	29/2	36.56	11/2	19.57	–	–
21/2	28.17	–	–	15/2	19.73	–	–
1/2	28.95	–	–	21/2	20.42	–	–

Table 1. (Contd.)

Theory		Experiment		Theory		Experiment	
I	R	I	R	I	R	I	R
3/2	29.32	–	–	13/2	20.43	–	–
9/2	29.39	–	–	19/2	20.59	–	–
5/2	29.93	–	–	25/2	20.98	25/2	21.79
19/2	30.16	–	–	1/2	21.15	–	–
11/2	30.75	–	–	7/2	21.24	–	–
7/2	30.77	–	–	3/2	21.46	–	–
9/2	31.86	–	–	17/2	21.94	–	–
13/2	32.34	–	–	5/2	22.00	–	–
31/2	32.74	31/2	39.34	9/2	22.26	–	–
11/2	33.17	–	–	17/2	22.34	–	–
29/2	33.18	–	–	7/2	22.74	–	–
27/2	33.75	–	–	11/2	23.47	–	–
15/2	34.16	–	–	9/2	23.76	–	–
13/2	34.71	–	–	5/2	24.29	–	–
1/2	34.76	–	–	19/2	24.38	–	–
7/2	34.85	–	–	17/2	24.49	–	–
3/2	35.05	–	–	27/2	24.53	27/2	25.29
25/2	35.23	–	–				
33/2	35.50	33/2	51.05				
^{167}Er $\xi = 0.7, g_{\beta_0} = 330, \gamma_0 = 5^\circ$ [15]							
7/2	0	7/2	0	1/2	8.68	–	–
9/2	1	9/2	1	17/2	8.91	17/2	9.74
11/2	2.20	11/2	2.24	11/2	8.95	–	–
13/2	3.63	13/2	3.72	9/2	9.64	–	–
5/2	3.97	–	–	7/2	10.48	–	–
7/2	4.54	–	–	5/2	11.29	–	–
15/7	5.21	15/7	5.48	19/2	11.34	19/2	12.04
9/2	5.59	–	–	17/2	11.80	–	–
11/2	6.13	–	–	19/2	11.92	–	–
3/2	6.29	–	–	15/2	12.37	–	–
7/2	6.86	–	–	13/2	13.11	–	–
17/2	7.09	17/2	7.40	23/2	13.26	23/2	15.05
5/2	7.33	–	–	11/2	14.00	–	–
3/2	8.14	–	–	9/2	14.93	–	–
13/2	8.19	–	–	25/2	16.33	25/2	17.56
15/2	8.51	–	–				

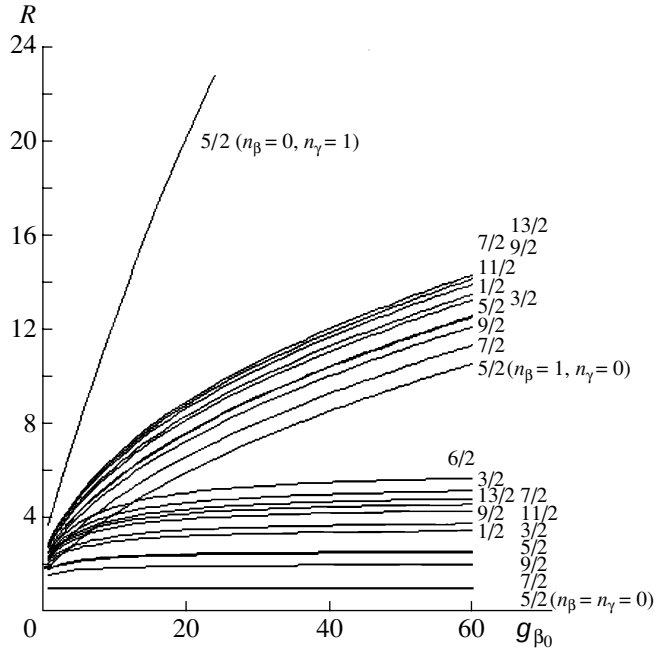

Fig. 1. Ratios R of the excitation energies of levels to the energy of the first excited level in the ground-state rotationally single-particle, the first rotationally single-particle β-vibrational, and the first rotationally single-particle γ-vibrational band versus g_{β_0} at $\gamma_0 = 10^\circ$, $\xi = 1$, and $g_{\gamma_0} = 1$.

$$= \sum_{MM'\mu} \left| \left\langle \Psi_{n_\beta n_\gamma I j \tau} \left| \Re(E2) \right| \Psi_{n'_\beta n'_\gamma I' j' \tau'} \right\rangle \right|^2,$$

we find for transitions between the $i \equiv \{n_\beta n_\gamma I j \tau\}$ and $f \equiv \left\{ n'_\beta n'_\gamma I' j' \tau' \right\}$ states that

$$B(E2; i \to f) = \left| \sqrt{\frac{5}{16\pi}} Q_0 \left\{ \sum_{KK'\Omega} A^{I\tau'}_{K'\Omega} A^{I\tau}_{K\Omega} (I2K2|I'K) \cos\gamma_0 \right.\right.$$
$$+ \sum_{KK'\Omega} A^{I\tau'}_{K'\Omega} A^{I\tau}_{K\Omega} [(I2K2|I'K+2) + (I2K,-2|I'K-2)] \frac{\sin\gamma_0}{\sqrt{2}}$$
$$\left.\left. + \sum_{KK'\Omega} A^{I\tau'}_{K'\Omega} A^{I\tau}_{K\Omega} (I2,-K2|I'2-K) \frac{\sin\gamma_0}{\sqrt{2}} \right\} S_{if} \right. \qquad (33)$$
$$+ s(l2\,j/2; r) \sum_{KK'\Omega} [A^{I\tau'}_{K'\Omega} A^{I\tau}_{K\Omega} (j2\Omega, K'-K|j\Omega)(I2K, K'-K|I'K')$$
$$\left. + (-1)^{I-j} A^{I\tau}_{K',\Omega} A^{I\tau}_{K\Omega} (j2,-\Omega, K'+K|j'\Omega)(I2,-K, K'+K|I'K')] \right|^2,$$

where

$$s(l2\,j/2; r) = (-1)^{j+l-1/2} e_n \langle f_{nl}| r^2_{nl} |f_{nl}\rangle \qquad (34)$$
$$\times \sqrt{\frac{5}{16\pi}(2j+1)(2l+1)}(2l00|l0) W(jljl; 1/2\,2).$$

Here, $\langle f_{nl}| r^2_{nl} |f_{nl}\rangle$ is the mean-square radius of an individual nucleon, $W(jljl; 1/2\,2)$ are Racah coefficients, l is the orbital angular momentum of the external nucleon, and $A^{I\tau}_{K\Omega}$ is the coefficient in the expansion of the wave function $\varphi(x,y,z,\theta)$ in terms of the eigenfunctions of the axially symmetric nucleus [3]. The factor S_{if} takes into account the deformability of the nucleus and has the integral form

$$S_{if} = \int_0^\infty F_f(\beta) \frac{\beta}{\beta_0} F_i(\beta) \beta^4 d\beta. \qquad (35)$$

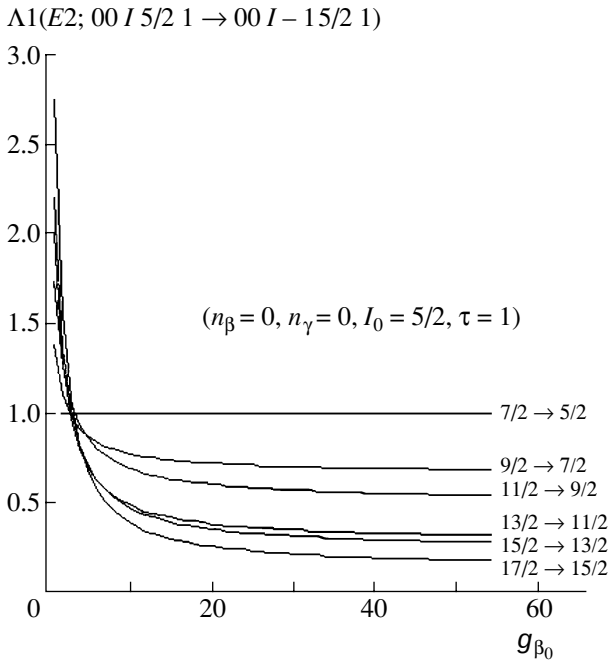

Fig. 2. Ratios of the reduced probabilities (39) the $E2$ transitions within the ground-state rotationally single-particle bands versus g_{β_0} at $\gamma_0 = 10^\circ$ and $\xi = 1$.

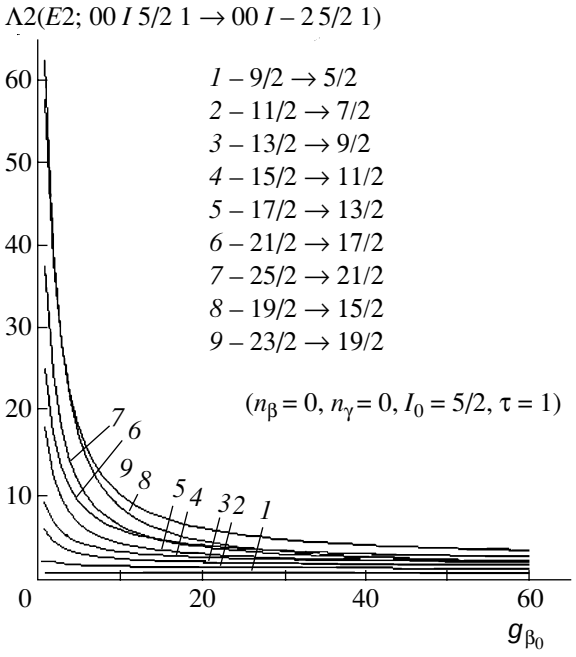

Fig. 3. Ratios of the reduced probabilities (40) of $E2$ transitions within the ground-state rotationally single-particle band versus g_{β_0} at $\gamma_0 = 10^\circ$ and $\xi = 1$.

The general expression for the matrix elements (35) is very cumbersome. For this reason, we consider the particular cases of $n_\beta = n_\gamma = 0$ and $n_\beta = 1$, $n_\gamma = 0$. For the matrix element (35), we then obtain

$$S_{00Ij1;00I'j'1} = \frac{2^{s'+s+3}}{g_{\beta_0}} \times \frac{(s+2)^{s'+3}(s'+2)^{s+3}}{(s'+s+4)^{s'+s+6}} \frac{\Gamma(s'+s+6)}{\sqrt{\Gamma(2s'+4)\Gamma(2s+4)}} \quad (36)$$

within the ground-state rotationally single-particle band,

$$S_{10Ij1;00I'j'1} = \frac{2^{s'+s+3}}{g_{\beta_0}} \times \frac{(s+3)^{s'+3}}{(s'+s+5)^{s'+s+6}} \sqrt{\frac{2s+4}{\Gamma(2s'+4)\Gamma(2s+4)}} \times \Gamma(s'+s+6)\left\{1 - \frac{(s'+s+6)(s'+2)}{(s'+s+5)(s+2)}\right\} \quad (37)$$

between the first and the ground-state rotationally single-particle β-vibrational band, and

$$S_{10Ij1;10I'j'1} = \frac{2^{s'+s+4}}{g_{\beta_0}} \frac{(s'+3)^{s+3}(s+3)^{s'+3}}{(s'+s+6)^{s'+s+6}} \times \Gamma(s'+s+6)\sqrt{\frac{(s'+2)(s+2)}{\Gamma(2s'+4)\Gamma(2s+4)}} \times \left\{1 + \frac{(s'+s+7)(s'+3)(s+3)}{(s'+s+6)(s'+2)(s+2)} - \frac{s+3}{s'+2} - \frac{1}{s+2}\right\} \quad (38)$$

within the first rotationally single-particle β-vibrational band. By using expressions (33) and (36), we can calculate the following ratios of the reduced probabilities of $E2$ transitions:

$$\Lambda 1(E2; 00Ij1 \to 00I - 1j1) = \frac{B(E2; 00Ij1 \to 00I - 1j1)}{B(E2; 00I_0 + 1j1 \to 00I_0 j1)}, \quad (39)$$

$$\Lambda 2(E2; 00Ij1 \to 00I - 2j1) = \frac{B(E2; 00Ij1 \to 00I - 2j1)}{B(E2; 00I_0 + 2j1 \to 00I_0 j1)}. \quad (40)$$

For heavy nuclei, the effect of the first (single-particle) term in the operator given by (30) can be neglected [3]. The ratios of the reduced probabilities of $E2$ transitions in (39) and (40) depend only on the parameters g_{β_0}, ξ, and γ_0, which also appear in the formula for the ratio of the excitation energy to the energy of the first excited level.

For transitions within the ground-state rotationally single-particle band, the results of the calculations for the ratios in (39) and (40) at $\xi = 1$ and $\gamma_0 = 10^\circ$ are displayed in Figs. 2 and 3, respectively, versus the parameter g_{β_0}. As the parameter g_{β_0} grows, these

ratios decrease at different rates. Only for $g_{\beta_0} \to 0$ do we obtain the results corresponding to a rigid rotor [12]. As the spin of nuclear levels grows at fixed values of the parameters ξ, γ_0, and g_{β_0}, the ratio in (39) decreases, while the ratio in (40) increases similarly to what was observed in the experiments reported in [13–15].

For the ^{161}Dy, ^{163}Dy, and ^{167}Er nuclei, Table 2 presents the theoretical and experimental ratios of the reduced probabilities of $E2$ transitions.

Just like in the case of the energy levels, the maximal discrepancy is observed for the ^{161}Dy nucleus, since the energy levels and the probabilities for $E2$ transitions are calculated at the same parameter values.

4. ELECTRIC QUADRUPOLE MOMENTS

Let us now consider the effect of nuclear-shape deformability on the mean values of the electric quadrupole moments of excited states of deformable nonaxial odd nuclei. These mean values are determined by the relevant diagonal matrix elements

$$\langle Q_2 \rangle_{n_\beta n_\gamma I j \tau} = \left\langle \Psi_{n_\beta n_\gamma I j \tau} \left| \Re(E2) \right| \Psi_{n_\beta n_\gamma I j \tau} \right\rangle . \tag{41}$$

If use is made of the operator in (30), the mean values of the electric quadrupole moments of a nonaxial odd nucleus can be represented as

$$\langle Q_2 \rangle_{00Ij1} = \sqrt{\frac{I(2I-1)}{(I+1)(2I+3)}} \left\{ \frac{(2s+4)(2s+5)}{8 g_{\beta_0}} \sqrt{\frac{5}{16\pi}} Q_0 \left[\sum_{K\Omega} A^{I\tau'}_{K\Omega} A^{I\tau}_{K\Omega} (I2K0|IK) \cos\gamma_0 \right. \right. \tag{42}$$

$$\left. + \sum_{K\Omega} A^{I\tau'}_{K\Omega} A^{I\tau}_{K\Omega} [(I2K2|IK+2) + (I2K,-2|IK-2) + (I2,-K2|I2-K)] \frac{\sin\gamma_0}{\sqrt{2}} \right]$$

$$+ s(l2\,1/2j;r) \sum_{KK'\Omega} [A^{I\tau'}_{K'\Omega} A^{I\tau}_{K\Omega} (I2K, K'-K|IK)(j2\Omega, K'-K|j\Omega)$$

$$\left. + (-1)^{I-j} A^{I\tau'}_{K'\Omega} A^{I\tau}_{K\Omega} (I2,-K,K'+K|I,\Omega)(j2,-\Omega,K'+K|j\Omega)] \right\}$$

for the ground state rotationally single-particle β-vibrational band and as

$$\langle Q_2 \rangle_{10Ij1} = \sqrt{\frac{I(2I-1)}{(I+1)(2I+3)}} \left\{ \frac{(s+2)^2(2s+5)}{2 g_{\beta_0} (s+3)^4} \right. \tag{43}$$

$$\times \left[1 + \frac{(2s+7)(s+3)}{2(s+2)^2} - \frac{s+4}{s+2} \right] \sqrt{\frac{5}{16\pi}} Q_0 \left[\sum_{K\Omega} A^{I\tau'}_{K\Omega} A^{I\tau}_{K\Omega} (I2K0|IK) \cos\gamma_0 \right.$$

$$\left. + \sum_{K\Omega} A^{I\tau'}_{K\Omega} A^{I\tau}_{K\Omega} [(I2K2|IK+2) + (I2K,-2|IK-2) + (I2,-K2|I2-K)] \frac{\sin\gamma_0}{\sqrt{2}} \right]$$

$$+ s(l2\,1/2j;r) \sum_{KK'\Omega} [A^{I\tau'}_{K'\Omega} A^{I\tau}_{K\Omega} (I2K, K'-K|IK')(j2\Omega K'-K|j\Omega)$$

$$\left. + (-1)^{I-j} A^{I\tau'}_{K'\Omega} A^{I\tau}_{K\Omega} (I2,-K,K'+K|IK')(j2-\Omega,K'+K|j\Omega)] \right\}$$

for the first rotationally single-particle β-vibrational band.

For heavy nuclei, the effect of the first (single-particle) term in the operator given by (30) can be neglected, in which case the ratios of the electric quadrupole moments of excited levels to the quadrupole moment of the first excited state depend on three parameters: g_{β_0}, ξ, and γ_0.

For the ground-state rotationally single-particle β- and γ-vibrational bands of deformed nonaxial odd nuclei, the calculated ratio of the mean electric quadrupole moment to the quadrupole moment of the spin-9/2 excited state at the fixed parameter values of

Table 2

Spin	$\Lambda 1(E2; n_\beta n_\gamma\ I\ 5/2\ \tau \to 00\ I\ 15/2\ 1)$		$\Lambda 2(E2; n_\beta n_\gamma\ I\ 5/2\ \tau \to 00\ I\ 25/2\ 1)$	
	Theory	Experiment	Theory	Experiment
^{161}Dy $\xi = 0.3, g_{\beta_0} = 418, \gamma_0 = 7^\circ$ [13]				
7/2	1	1		
9/2	0.79	0.75(41)	1	1
11/2	0.58	0.45(45)	1.54	1.63(12)
13/2	0.43	0.21(14)	1.85	1.71(11)
15/2	0.33	0.28(15)	2.06	1.94(12)
17/2	0.26	0.03(06)	2.16	2.42(12)
19/2	0.21	0.09(07)	2.30	2.60(14)
21/2	0.16	0.03(07)	2.29	2.83(14)
23/2	0.14	0.04(06)	2.48	2.54(13)
25/2	0.11	0.01(07)	2.32	3.75(35)
^{163}Dy $\xi = 0.25, g_{\beta_0} = 418, \gamma_0 = 10^\circ$ [14]				
7/2	1	1		
9/2	0.80	0.75(18)	1	1
11/2	0.59	0.50(12)	1.55	1.63(11)
13/2	0.44	0.44(35)	1.85	2.04(44)
15/2	0.34	0.33(16)	2.07	2.80(31)
17/2	0.26	0.17(11)	2.15	2.44(18)
19/2	0.22	0.12(14)	2.33	2.6(4)
21/2			2.23	2.44(24)
23/2			2.51	2.28(35)
^{167}Er $\xi = 0.7, g_{\beta_0} = 330, \gamma_0 = 5^\circ$ [16]				
9/2	1	1		
11/2	0.95	1.9(20)	1	1
13/2	0.78	0.6(11)	1.76	2.29(20)
15/2	0.61	0.35(68)	2.28	2.34(28)
17/2	0.49	0.54(61)	2.67	3.39(20)
19/2	0.37	0.25(48)	2.93	3.44(32)
21/2	0.31	0.14(19)	3.18	4.29(43)
23/2	0.23	0.10(22)	3.33	3.15(33)

$\xi = 1$ and $\gamma_0 = 10^\circ$ is displayed in Fig. 4 versus the parameter g_{β_0}.

It can be seen that the ratios of the quadrupole moments of the levels in the rotationally single-particle β- and γ-vibrational bands decrease at different rates as the parameter g_{β_0} increases and, at large values of g_{β_0}, tend to constant values. At a fixed value of g_{β_0}, the ratios of the quadrupole moments of the levels in the above bands increase with increasing spin of nuclear levels.

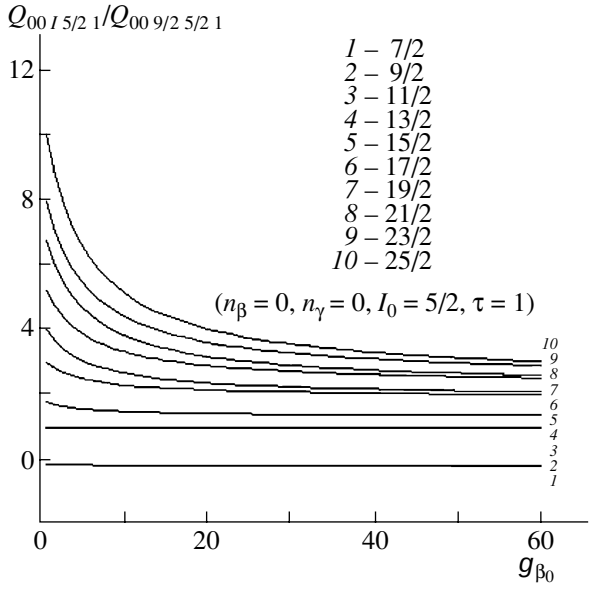

Fig. 4. Ratio of quadrupole moments to the quadrupole moment of the spin-9/2 excited level of the rotationally single-particle band as a function of g_{β_0} at $\gamma_0 = 10°$ and $\xi = 1$.

5. CONCLUSION

The observed regularities in the behavior of the ratios of energy levels, in the behavior of the reduced probabilities of $E2$ transitions, and in the behavior of electric quadrupole moments as functions of the parameter g_{β_0} demonstrate that the shape of a deformable nonaxial odd nucleus changes from a spherical to an ellipsoidal one. There arises the possibility of constructing a unified description of the spectrum of energy levels, the reduced probabilities of $E2$ transitions, and electric quadrupole moments for excited states of spherical, transition, and deformed nonaxial odd nuclei in terms of four parameters: g_{β_0}, g_{γ_0}, ξ, and γ_0. From the above comparison of the theoretical results and experimental data (Tables 1 and 2), it can be seen that the model describes satisfactorily, at the same values of the parameters g_{β_0}, ξ, and γ_0, the ratios of the energies of levels and the ratios of the reduced probabilities of $E2$ transitions within the ground-state rotationally single-particle band of nonaxial odd nuclei.

REFERENCES

1. A. Bohr, K. Dan. Vidensk. Selsk. Mat. Fys. Medd. **26** (14) (1952).
2. A. Bohr and B. R. Mottelson, *Nuclear Structure*, Vol. 2: *Nuclear Deformations* (Benjamin, New York, 1975; Mir, Moscow, 1977).
3. A. S. Davydov, *Excited States of Nuclei* (Atomizdat, Moscow, 1967).
4. Sh. Sharipov, Author's Abstract of Doctoral Dissertation (Tashkent, 1990).
5. Sh. Sharipov and M. J. Ermamatov, Uzb. Fiz. Zh., No. 3, 5 (1996).
6. Sh. Sharipov and M. J. Ermamatov, Uzb. Fiz. Zh., No. 1, 17 (1997).
7. Sh. Sharipov and M. J. Ermamatov, Ukr. Fiz. Zh. **44**, 1069 (1999).
8. *Table of Isotopes,* Ed. by C. M. Lederer and V. S. Shirley (Wiley, New York, 1978).
9. E. Browne, Nucl. Data Sheets **52**, 127 (1987).
10. P. F. Skorobogatov, Yad. Fiz. **15**, 220 (1972) [Sov. J. Nucl. Phys. **15**, 124 (1972)].
11. Sh. Sharipov, Izv. Akad. Nauk UzSSR, Ser. Fiz.-Mat. Nauk **5**, 50 (1988).
12. R. A. Sardaryan, Vestn. Mosk. Univ., Ser. 3: Fiz., Astron. **4**, 18 (1968).
13. M. Oshima, E. Minehaka, S. Ichikawa, *et al.*, Phys. Rev. C **37**, 2578 (1988).
14. M. Oshima, E. Minehaka, S. Kicuchi, *et al.*, Phys. Rev. C **39**, 645 (1989).
15. M. Oshima, E. Minehaka, M. Ishii, *et al.*, Nucl. Phys. A **436**, 518 (1985).
16. R. G. Helmer, Nucl. Data Sheets **59**, 1 (1990).

Translated by A. Isaakyan

Physics of Atomic Nuclei, Vol. 65, No. 3, 2002, pp. 437–441. Translated from Yadernaya Fizika, Vol. 65, No. 3, 2002, pp. 464–468.

NUCLEI
Theory

Excitation of the Δ Resonance in Inclusive *ed* Scattering

E. L. Kuplennikov

Institute for Physics and Technology, Akademicheskaya ul. 1, Kharkov, 310108 Ukraine

Received November 25, 1999; in final form, December 16, 2000

Abstract—The parameters of the pion-electroproduction peak in the cross section for inclusive electron scattering on ^{1}H and d target nuclei are determined for various kinematical conditions of measurements. It is shown that, for low 4-momentum transfers, $0.030 \le Q^2 \le 0.086$ $(\mathrm{GeV}/c)^2$, the Q^2 dependence of the shift of the pion-electroproduction peak in the πN invariant mass for a deuteron target with respect to that for a free proton does not exhibit a universal behavior that is characteristic of complex nuclei.

1. INTRODUCTION

The energy spectrum of high-energy electrons inelastically scattered by nuclei for energy transfers (ω) from the pion-electroproduction threshold to about 500 MeV is dominated by a wide peak [1], which is associated with the electroexcitation and decay of the first pion–nucleon resonance, Δ(1232), in nuclear matter. Under specific conditions, the pion-electroproduction peak can determine almost completely the structure of the energy spectrum; therefore, it is attractive for experimental and theoretical investigations.

A great body of experimental data on the inclusive scattering of electrons near the Δ(1232) resonance on light, medium-mass, and heavy nuclei have already been accumulated (see, for example, [1–4]). Measurements cover a wide range of 4-momentum transfers [$0.09 \le Q^2 \le 0.52$ $(\mathrm{GeV}/c)^2$]. An analysis of the $A(e, e')$ differential cross sections revealed a number of regularities. The cross-section values per nucleon, $(d^2\sigma/d\omega d\Omega)/A$, at the maximum of the pion-electroproduction peak virtually coincide for different nuclei and are systematically smaller than the cross section for a free-proton target [1, 2]. The FWHM of the pion-electroproduction peak for nuclear targets (FWHM^A) differs considerably from the peak width for a hydrogen target (FWHM$^{\mathrm{H}}$) and from the quasifree-peak width [1]. An extraordinary 4-momentum-transfer dependence of the position of the pion-electroproduction peak in the energy spectrum with respect to the peak for a free proton was found [3].

A comprehensive analysis revealed [2] that, within the experimental errors, the πN invariant mass W^A corresponding to the maximum of the pion-electroproduction peak in the double-differential cross section near the Δ(1232) resonance undergoes no changes from ^{4}He to ^{184}W nuclei. This quantity depends only on the square of the 4-momentum transfer (Q^2). At the same time, the πN invariant mass corresponding to the maximum of the pion-electroproduction peak for a free proton is independent of the kinematical conditions of measurements and is equal to $W^{\mathrm{H}} \sim 1220$ MeV [2]. The πN invariant mass was calculated as [3]

$$W^2 = M^2 - Q^2 + 2M\omega, \qquad (1)$$

where M is the nucleon mass, while $Q = [4E_1E_2\sin^2(\theta/2)]^{1/2}$ and $\omega = E_1 - E_2$ (E_1 and E_2 are the energies of, respectively, the incident and the detected electron) are, respectively, the momentum and the energy transfer from the electron to the target nucleus.

From an analysis of the Q^2 dependence of W^A for $A = 4$–184 nuclei, it was found [2] that $W^A(Q^2)$ for $Q^2 < 0.13$ $(\mathrm{GeV}/c)^2$ is less than the corresponding value for a free proton. For $Q^2 \sim 0.13$ $(\mathrm{GeV}/c)^2$, the W values for complex nuclei are approximately equal to that for a proton. As the momentum transfer increases further [$Q^2 > 0.13$ $(\mathrm{GeV}/c)^2$], $W^A(Q^2)$ grows smoothly with respect to W^{H}. Under certain conditions, the difference can be as great as a few tens of MeV [2]. The reasons behind this behavior of the pion-electroproduction peak for complex nuclei with respect to the peak for a free proton have not been established conclusively. The observed dependence may carry an imprint of the properties of the resonance itself [5]. Problems in interpreting the dependence $W^A(Q^2)$ are partly due to the fact that the final state of the system in inclusive (e, e') scattering on nuclei is not specified completely—the pion-electroproduction peak receives contributions from

1063-7788/02/6503-0437$22.00

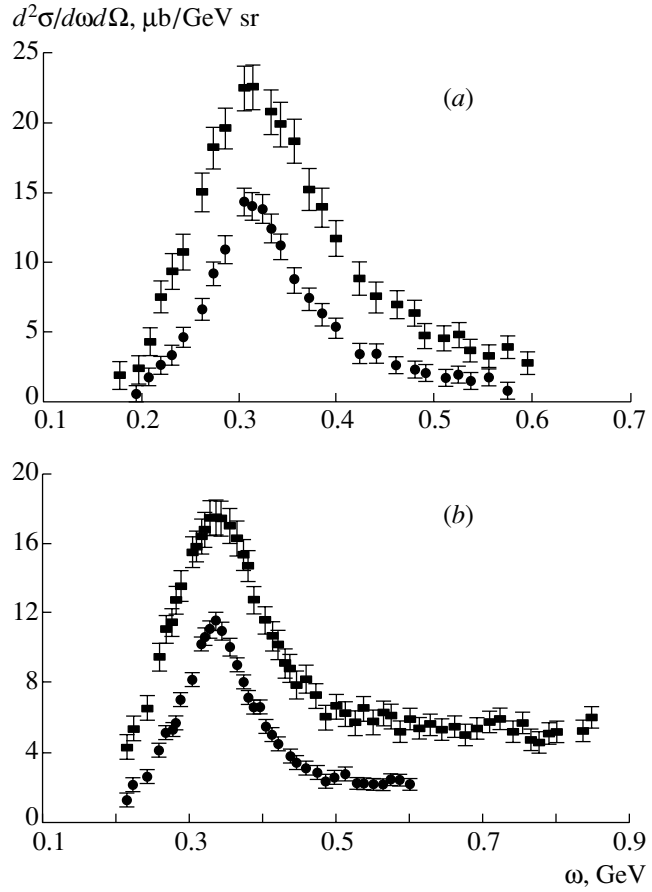

Fig. 1. Differential cross sections for the reactions (•) ^{1}H(e, e') and (■) $d(e, e')$ versus the energy transfer for a scattering angle of 14° and initial energies of (*a*) 0.888 and (*b*) 1.385 GeV.

all physical processes possible under the kinematical conditions of reaction being considered. These background processes are not associated with the resonance, but their contribution to the cross section can in principle change the basic parameters of the pion-electroproduction peak [2–4].

The cross section for inclusive electron–deuteron scattering near the first nucleon resonance has received considerably less adequate study. Systematic experimental data were obtained in [6, 7]. The cross section for $\Delta(1232)$ production on a neutron in the range $0.1 \leq Q^2 \leq 0.5$ (GeV/c)^2 was extracted in [6]. For squared momentum transfers in the range 0.16–0.38 (GeV/c)^2, the transition form factors $G*$ for the $\gamma^* n\Delta^0$ and γ^*pΔ^+ vertices were determined in [7]. The theoretical calculations performed in [6, 7] describe quite well the differential cross section for the reaction $d(e, e')$ near the Δ resonance and the position of the pion-electroproduction peak over a wide kinematical range. Discrepancies were observed only in the regions of the low- and the high-energy tails of the pion-electroproduction peak.

This article presents systematic experimental data on high-energy inelastic (e, e') scattering on hydrogen and deuteron targets near the first nucleon resonance. The energy spectra were measured at low momentum transfers $[0.030 \leq Q^2 \leq 0.086$ (GeV/c)$^2]$, where one observes the largest distinction between the πN invariant masses W^A and $W^{\rm H}$ for complex nuclei and for a free proton [2]. The basic parameters of the pion-electroproduction peak were determined for various kinematical conditions of measurements. The results are compared with the results of other experiments.

2. DESCRIPTION OF THE EXPERIMENT

The double-differential cross sections for the inelastic reactions ^{1}H(e, e') and $d(e, e')$ were measured at a 2-GeV linear electron accelerator for incident electron energies of $E_1 = 0.888$, 0.990, 1.191, and 1.385 GeV and a scattering angle of $\theta = 14°$. The experiment was conducted at a facility for studying the electromagnetic structure of nuclei and nucleons [8]. A three-target hydrogen–deuterium cryostat

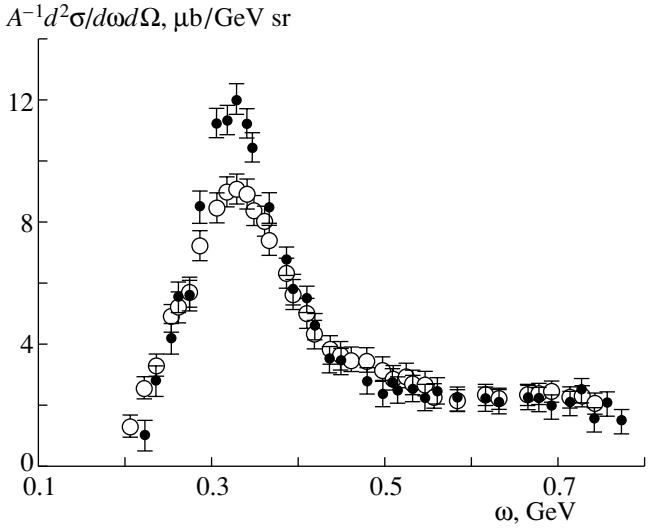

Fig. 2. Differential cross sections per nucleon for the reactions (•) $^1\mathrm{H}(e,e')$ and (○) $d(e,e')$ versus the energy transfer for a scattering angle of 14° and an incident energy of 1.191 GeV.

was used for a target [9]. Three operating targets were situated at an angle of 120° to each other and were remotely exposed to a beam. Electrons scattered on hydrogen, deuterium, or an empty target, which was employed for measuring the background, were momentum-analyzed by a uniform-field double-focusing magnetic spectrometer and were detected by a counter telescope.

Each spectrum was measured for a negative and a positive polarity of the spectrometer. Assuming that the numbers of the product electron–positron pairs are identical for all spectra, we subtracted the background events from the electron spectrum. The intensity of the primary electron beam was measured by a secondary emission monitor. For the absolute normalization of the double-differential cross section, the cross section for elastic *ep* scattering was measured under identical kinematical conditions. The contributions from processes where an electron interacting with target nuclei emits real or virtual photons were taken into account by introducing radiative corrections in the differential cross section. These corrections were calculated and introduced in the inclusive (e,e') cross section by means of the standard procedure proposed in [10].

3. ANALYSIS OF DATA AND DISCUSSION OF THE RESULTS

Figure 1 displays the corrected differential cross sections for hydrogen and deuterium targets in the region of the pion-electroproduction peak. These data were obtained for a scattering angle of $\theta = 14°$ and incident electron energies of $E_1 = 0.888$ and 1.385 GeV. Wide peaks above the pion-electroproduction threshold are attributed to the transition of an intranuclear nucleon to the first excited state Δ(1232), which is predominantly formed by two contributions, that from the electroproduction of $\Delta^+(1232)$ and that from the electroproduction of $\Delta^0(1232)$.

Figure 1 demonstrates that, in contrast to what occurs for complex nuclei, the pion-electroproduction peak is not noticeably shifted with respect to the peak for a free proton at low momentum transfers [0.030 and 0.086 $(\mathrm{GeV}/c)^2$]. Above the Δ(1232) region (for $\omega \gg \omega^{\max}$, where $\omega^{\max}$ is the energy transfer corresponding to the maximum of the pion-electroproduction peak), the differential cross section does not vanish and is virtually independent of the energy transfer. At the same time, the ratio of the cross section in the region of the high-energy tail to that at the maximum of the pion-electroproduction peak takes different values under different kinematical conditions of measurements—it is about 27 and 30% at, respectively, $Q^2 = 0.061$ and $0.086\,(\mathrm{GeV}/c)^2$ for the reaction $d(e,e')$ and is about 18% at $Q^2 = 0.086\ (\mathrm{GeV}/c)^2$ for the reaction $^1\mathrm{H}(e,e')$. For a moderate value of the momentum transfer [$Q^2 = 0.302\ (\mathrm{GeV}/c)^2$] at $E_1 = 1.215$ GeV and $\theta = 35°$, the cross section in the region $\omega \gg \omega^{\max}$ is one-half as large as that at the maximum of the pion-electroproduction peak [7]. The effect observed in the energy-spectrum section under investigation is thought to be due to the contributions from higher resonances and deep-inelastic electron scattering [1–3].

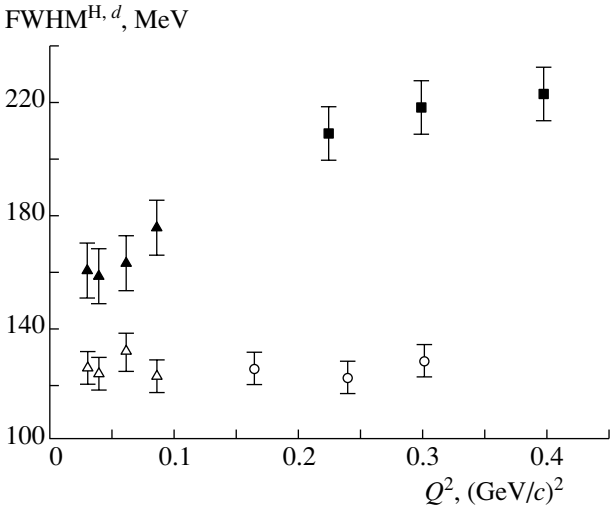

Fig. 3. FWHM of the pion-electroproduction peak versus the square of the 4-momentum transfer: (▲) and (△) data obtained in this study for the reactions $d(e,e')$ and $^1\mathrm{H}(e,e')$, respectively, and (■) and (○) results obtained from an analysis of the energy spectra for the reactions $d(e,e')$ [6] and $^1\mathrm{H}(e,e')$ [7], respectively.

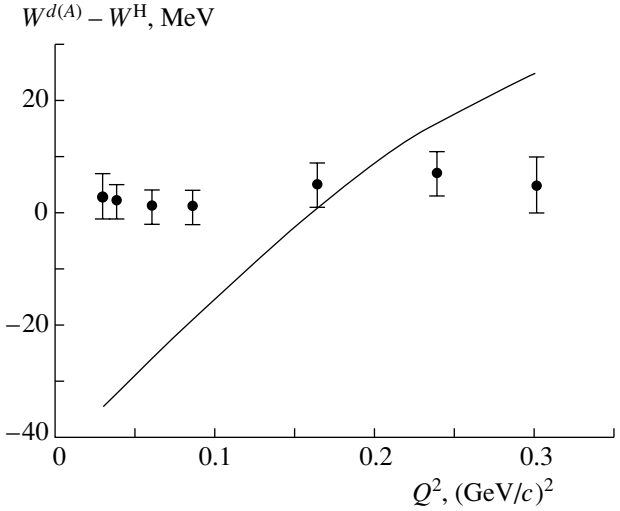

Fig. 4. Difference of the πN invariant masses at the maximum of the pion-electroproduction peak for deuteron and hydrogen targets versus the square of the 4-momentum transfer. Three points at high values in the range $Q^2 = 0.165$–0.302 (GeV/c)^2 were determined from an analysis of the energy spectra presented in [7]. The solid curve was obtained for nuclear data taken from [2].

The differential cross sections per nucleon for deuteron and hydrogen targets, $(d^2\sigma/d\omega d\Omega)^d/A$ and $(d^2\sigma/d\omega d\Omega)^{\mathrm{H}}$, are shown in Fig. 2 for the region of the $\Delta(1232)$ resonance. The energy spectra were measured for an incident electron energy of 1.191 GeV and a scattering angle of 14°. It can be seen that the cross section for a proton at the maximum of the pion-electroproduction peak is larger than $(d^2\sigma/d\omega d\Omega)^d/A$; the excess is about 29% for $Q^2 \leq 0.061$ (GeV/c)^2. This difference may be due to the nuclear-medium effect. A theoretical calculation of the inclusive cross section near the $\Delta(1232)$ resonance for complex nuclei within the most consistent isobar–hole model [11] revealed [1] that the nuclear-medium effect reduces the pion-electroproduction cross section and increases the width of its peak.

The FWHM of the pion-electroproduction peak for the reactions $^1\mathrm{H}(e,e')$ and $d(e,e')$ as a function of the square of the momentum transfer is displayed in Fig. 3, along with data taken from [6, 7]. As can be seen, the FWHM^d increases smoothly from 160 ± 9 to 228 ± 12 MeV in the range $0.030 \leq Q^2 \leq 0.4$ (GeV/c)^2. The experimental width of the pion-electroproduction peak for a deuteron is larger than that for a free proton. Within the measurement errors, FWHM$^{\mathrm{H}}$ is virtually independent of the momentum transfer, its mean value in the range studied here being 126 ± 7 MeV. For the sake of comparison, we indicate that the experimental values obtained in [1] for the width of the pion-electroproduction peak at $Q^2 = 0.103$ (GeV/c)^2 for a free nucleon and for $A =$ 4, 9, 12, and 16 nuclei are FWHM$^{\mathrm{H}} = 120 \pm 5$ MeV and FWHM$^A \sim 250$ MeV. The quasifree-peak width, which is almost entirely due to the Fermi motion of nucleons, is about 100 to 120 MeV. An additional FWHM^A (squared) is about 185 MeV. The value of FWHM$^{\mathrm{H}} = 120 \pm 5$ MeV agrees reasonably well with our data.

To analyze the position of the pion-electroproduction peak in the energy spectrum, the double-differential cross sections for the reactions $^1\mathrm{H}(e,e')$ and $d(e,e')$ are expressed here in terms of the invariant mass W according to Eq. (1). The $W^{\mathrm{H},\,d}$ values corresponding to the peak maximum are then determined by fitting a smooth polynomial curve to experimental data near the maximum of the pion-electroproduction peak. Representing the data in this form, one can easily compare the invariant masses $W^d(Q^2)$, $W^A(Q^2)$ [2], and W^{H} for a deuteron, complex nuclei, and a free proton, respectively; determine the shift of peaks; and analyze the dependence of this shift on the kinematical conditions of measurements.

The shift of the maximum of the pion-electroproduction peak for a deuteron with respect to that for a free proton was defined as $\epsilon^d(Q^2) = W^d(Q^2) - W^{\mathrm{H}}$. For $A \geq 4$ nuclear data [2], the corresponding quantity was roughly estimated as $\epsilon^A(Q^2) = W^A(Q^2) - W^{\mathrm{H}} = W^A(Q^2) - 1220$ MeV. Since experimental data on $W^A(Q^2)$ for numerous nuclei agree within the

experimental errors, the experimental points for $A \geq 4$ [2] were approximated by a smooth curve $W^A(Q^2)$. The results are shown in Fig. 4, where it can be seen that $\epsilon^d(Q^2)$ differs from $\epsilon^A(Q^2)$ both in absolute value and in Q^2 dependence. The quantity $\epsilon^d(Q^2)$ is positive; that is, the pion-electroproduction peak for a deuteron (in contrast to what occurs for complex nuclei) is systematically shifted toward higher energies with respect to that for a hydrogen target over the entire momentum transfer range under investigation. In principle, this is not surprising, since it is natural to assume that the formation of a resonance on a bound nucleon requires additional energy.

4. CONCLUSIONS

The energy spectra for the reactions $^1\mathrm{H}(e,e')$ and $d(e,e')$ in the region of $\Delta(1232)$ excitation have been measured at a 2-GeV linear electron accelerator for low momentum transfers $[0.030 \leq Q^2 \leq 0.086\ (\mathrm{GeV}/c)^2]$.

An analysis of experimental data has led to the following conclusions:

(i) The differential cross section per nucleon for the reaction $d(e,e')$ at the maximum of the pion-electroproduction peak is systematically smaller than that for a free-proton target. For high energy transfers (above the resonance region), the cross section does not vanish and is virtually independent of the energy transfer. The ratio of the cross section for the reaction $d(e,e')$ in the region of the high-energy tail ($\omega \gg \omega^{\max}$) of the pion-electroproduction peak to that at the maximum depends on Q^2, changing from about 27 to about 50% in the range $0.061 \leq Q^2 \leq 0.302\ (\mathrm{GeV}/c)^2$.

(ii) In the range $0.030 \leq Q^2 \leq 0.4\ (\mathrm{GeV}/c)^2$, the width of the pion-electroproduction peak for a deuteron increases from 160 ± 9 to 228 ± 12 MeV with increasing Q^2. The analogous width for a free proton is independent of Q^2 within the experimental errors. The mean value is $\mathrm{FWHM}^{\mathrm{H}} = 126 \pm 7$ MeV.

(iii) On the scale of the πN invariant mass, the pion-electroproduction peak for a deuteron occurs systematically higher (in contrast to that for complex nuclei) than the peak for a free proton over the entire momentum-transfer range studied here.

ACKNOWLEDGMENTS

I am grateful to Prof. Yu.N. Ranyuk and A.S. Omelaenko for assistance in the study and stimulating discussions.

REFERENCES

1. J. S. O'Connell, W. R. Dodge, J. W. Lightbody, *et al.,* Phys. Rev. C **35**, 1063 (1987).
2. R. M. Sealock, K. L. Giovanetti, S. T. Thornton, *et al.,* Phys. Rev. Lett. **62**, 1350 (1989).
3. P. Barreau, M. Bernheim, J. Duclos, *et al.*, Nucl. Phys. A **402**, 515 (1983).
4. Z. E. Meziani, P. Barreau, M. Bernheim, *et al.,* Phys. Rev. Lett. **54**, 1233 (1985).
5. J. S. O'Connell and B. Schroder, Phys. Rev. C **38**, 2447 (1988).
6. J. Bleckwenn, H. Klein, J. Moritz, *et al.,* Nucl. Phys. B **33**, 475 (1971).
7. R. V. Akhmerov, A. S. Omelaenko, E. V. Stepula, and Yu. I. Titov, Yad. Fiz. **21**, 113 (1975) [Sov. J. Nucl. Phys. **21**, 57 (1975)].
8. N. G. Afanas'ev, V. A. Gol'dshteĭn, and S. V. Dementiĭ, Prib. Tekh. Éksp., No. 5, 146 (1967).
9. V. A. Gol'dshteĭn, V. V. Lubyanyĭ, and A. I. Germanov, Prib. Tekh. Éksp., No. 4, 37 (1972).
10. L. W. Mo and Y. S. Tsai, Rev. Mod. Phys. **41**, 205 (1969).
11. J. H. Koch and N. Ohtsuka, Nucl. Phys. A **435**, 765 (1981).

Translated by R. Tyapaev

Physics of Atomic Nuclei, Vol. 65, No. 3, 2002, pp. 442–455. Translated from Yadernaya Fizika, Vol. 65, No. 3, 2002, pp. 469–482.

NUCLEI
Theory

Charge-Exchange Reaction $pd \to n(pp)$ within the Bethe–Salpeter Approach

S. M. Dorkin[1)], L. P. Kaptari, B. Kämpfer[2)], and S. S. Semikh

Joint Institute for Nuclear Research, Dubna, Moscow oblast, 141980 Russia

Received October 6, 2000; in final form, January 23, 2001

Abstract—The charge-exchange reaction $pd \to n(pp)$ at low momentum transfers and low excitation energies of the pp pair is considered within the Bethe–Salpeter approach. The method is proposed for calculating observables in the case where the pp pair is in the $^1S_0$ state. The results of methodological numerical calculations for the differential cross sections and the tensor analyzing power T_{20} are presented. The possibility of using the reaction in question as a basic reaction for creating a deuteron tensor polarimeter at high energies and for obtaining additional information about the elementary amplitude for nucleon–nucleon charge-exchange is predicted. © *2002 MAIK "Nauka/Interperiodica"*.

1. INTRODUCTION

Investigation of polarization features in hadron and lepton scattering on light nuclei furnishes detailed information both about the reaction mechanism and about the structure of the nucleon–nucleon potential and of nuclear wave functions. In addition, the quasielastic scattering of polarized light nuclei on heavy targets makes it possible to investigate exotic excitations of heavy nuclei, such as the excitation of anomalous-parity levels and the separation of $\Delta T = 0$ and $\Delta T = 1$ isospin admixtures in spin-flip transitions (see, for example, [1, 2]). At present, the programs of experimental investigations (at COSY, TJNAF, etc.) into elastic and quasielastic scattering in electromagnetic [3, 4] and hadronic processes [5] on polarized deuterons are being actively deployed. By way of example, we indicate that, in order to understand the electromagnetic structure of the deuteron, it is necessary to determine three deuteron form factors: the magnetic, the electric, and the quadrupole one. In unpolarized elastic ed scattering, it is possible to investigate only the magnetic form factor and some function that depends on the momentum transfer, $A(Q^2)$, and which is a combination of all three of them. In order to isolate the charge form factor and investigate all form factors individually, one needs experiments measuring polarization features of a reaction— for example, the tensor polarization T_{20} of the recoil deuteron in elastic ed scattering. This would make it possible to determine the deuteron charge form factor G_c at high momentum transfers. This is an important problem, since it is the form factor G_c that is sensitive to models of the NN interaction at short internucleon distances [3, 4, 6]. Various reactions, including elastic scattering at large angles [7], inclusive reactions [8], and exclusive processes [9], are investigated in the realm of hadron–deuteron scattering, and all of the possible polarization observables are measured in such processes. It should be noted that, in hadron processes, it is quite feasible to perform experiments that admit a complete experimental reconstruction of the reaction amplitude (for example, the amplitude for backward elastic pd scattering [10–12]). Here, however, it is also necessary to measure the polarizations of recoil deuterons, as in the case of determination of G_c. Thus, we arrive at the general conclusion that, in polarization experiments, it is of paramount importance to measure the polarization features of reaction products. It is obvious that any process where one measures final polarizations represents a double-scattering experiment where the final deuteron being investigated undergoes scattering in a secondary reaction in a polarimeter. Therefore, it is necessary that the cross section for the secondary reaction and its analyzing powers be sufficiently large—otherwise, the efficiency of the polarimeter will be low. For the secondary reaction, it is common practice to use the process $^3\mathrm{He}(d,p)\,^4\mathrm{He}$ at low energies (a few tens of MeV) [13] and elastic dp scattering [14] at relativistic energies (a few GeV and higher). Along with these processes, it is of great interest to study the potential of the exclusive reaction $p\vec{d} \to (pp)n$ where the pp pair of very low excitation energy is observed. Bugg and Wilkin [15] proposed using this reaction as a

[1)]Far Eastern State University, ul. Sukhanova 8, Vladivostok, 690600 Russia.

[2)]Research Center Rossendorf, Institute for Nuclear and Hadron Physics, Germany.

deuteron tensor polarimeter at relatively low energies (a few hundred MeV) [16]. They noticed that, at low momentum transfers and low relative energies in the pp pair, the reaction $p\vec{d} \to n(pp)$ predominantly proceeds via the elementary charge-exchange process suffered by the incident proton on the neutron of the deuteron, the remaining proton playing the role of a spectator. In this case, the nonrelativistic model proposed in [15] and based on the spectator mechanism predicts, for this reaction, zero vector analyzing power and a rather large tensor analyzing power, the reaction cross section being sufficiently large for efficiently studying the process in experiments. More recent investigations of this process [1, 17–19] at low energies completely confirmed the validity of these predictions. Thus, this reaction can serve, for example, as a means for measuring T_{20} in the reaction $pp \to d\pi^+$ [20] in investigating $NN\pi$ systems or for exploring $\Delta T = 0$, $\Delta S = 1$ isoscalar transitions [2] in inelastic $(\vec{d}, \vec{d}')$ reactions on heavy nuclei. Along with the possibility of using the process $p\vec{d} \to n(pp)$ for an effective polarimeter, its investigation is of interest for some other reasons. First, it was shown in [15] that the cross section for this reaction is directly related to the partial amplitudes for nucleon–nucleon charge exchange. Using this circumstance, together with nucleon–nucleon data, one can deduce experimental information for completely reconstructing the $pn \to np$ amplitude [21]. Second, it is possible to investigate the impact of nuclear effects on the elementary amplitude of charge-exchange nuclear reactions [22, 23] and also to obtain directly the probability of spin flip in quasielastic deuteron scattering on nuclei [1]. Third, interest in this reaction is quickened by the experiments that are being performed and planned at COSY [5, 9] for the region of relativistic energies.

In the present study, we propose a theoretical analysis of the reaction $p\vec{d} \to n(pp)$ at relativistic energies (Dubna, COSY) and, as in the case of the nonrelativistic analysis from [15], consider the possible applications of this reaction in the relativistic case. The proposed approach relies on the relativistic Bethe–Salpeter formalism and invokes a numerical solution to the homogeneous Bethe–Salpeter equations with a realistic interaction kernel [24, 25]. On this basis, all partial spin amplitudes of the process are calculated in a covariant form; this makes it possible to determine any spin observables of the reaction. By way of example, we present calculations of the differential cross section and the tensor analyzing power T_{20} and compare our results with available experimental data.

The ensuing exposition is organized as follows. In Section 2, we introduce basic kinematical quantities and a general expression for the differential cross section and determine the most general form of the spin structures of the amplitude and of the observables for the reaction being considered. In Section 3, we describe the dynamical model of the reaction within the Bethe–Salpeter approach, calculate analytically the matrix element of the process, and discuss the approximations adopted in this section. The results of our numerical calculations, along with their analysis and comparison with experimental data, are presented in Section 4, which also contains basic conclusions drawn from this study. Some cumbersome formulas and notation can be found in the Appendices.

2. KINEMATICS AND NOTATION

In this study, we consider the exclusive reaction induced by collisions of protons with polarized deuterons at intermediate and high energies that leads to the production of three nucleons in the final state. Of all possible kinematically different processes, we choose those that, in the deuteron c.m. frame, correspond to the formation of a slow correlated pair of two protons and one fast neutron—that is, to a reaction of the type

$$p + \vec{d} = n + (p_1 + p_2). \qquad (1)$$

A feature peculiar to process (1) is that the momentum transfer from the proton to the neutron is low; therefore, the main mechanism of this reaction can be described in terms of charge transfer from the incident proton to the target neutron, the remaining proton of the deuteron playing the role of a spectator. It is well known from [26] that the differential cross section for the elementary charge-exchange process $pn \to np$ has a sharp peak at zero momentum transfer. It follows that, if process (1) is indeed due to the charge-exchange subprocess, the resulting pp pair will be characterized by low values of the total and the relative momentum. Such reactions can be reliably extracted against the background of other possible processes and comprehensively studied in experiments. The diagram for such processes is depicted in Fig. 1, where the following notation is adopted: $p = (E_p, \mathbf{p})$ and $n = (E_n, \mathbf{n})$ are the 4-momenta of the initial proton and the final neutron, respectively, and P' is the total 4-momentum of the pp pair—that is, the sum of the proton momenta $p_1 = (E_1, \mathbf{p}_1)$ and $p_2 = (E_2, \mathbf{p}_2)$, $P' = p_1 + p_2$. The invariant square of the pp-pair mass is denoted by s_f, $s_f = P'^2 = (2m + E_x)^2$, where m is the nucleon mass and E_x is the excitation energy of the pair. According to the above assumptions about the reaction mechanism, the excitation energy E_x is low; here, we consider its range between zero and a few MeV ($E_x \sim$ 0–8 MeV). At such low values of E_x, the pp pair occurs predominantly in the $^1S_0$ state [18]. Hereafter,

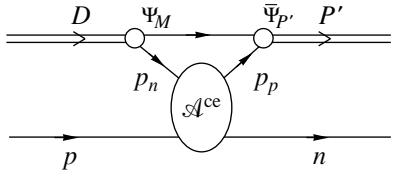

Fig. 1. Diagram for the process $pd \to n(pp)$ under the assumption that it proceeds through charge transfer from the initial proton to the target neutron.

we therefore assume that the contribution of higher partial waves is much smaller than the contribution of the $^1S_0$ component. The problem of corrections from higher waves will be discussed in a separate publication.

In the case of standard normalizations adopted here, the Dirac spinors

$$u(\mathbf{p}, r) = \sqrt{m+\epsilon}\begin{pmatrix} \chi_r \\ \dfrac{\boldsymbol{\sigma}\cdot\mathbf{p}}{m+\epsilon}\chi_r \end{pmatrix} \qquad (2)$$

are normalized by the condition $\bar{u}(p)u(p) = 2m$ and the differential cross section for reaction (1) is given by

$$d^9\sigma = \frac{1}{2\sqrt{\lambda(p,D)}}|M_{fi}|^2(2\pi)^4\delta(P_f - P_i) \qquad (3)$$
$$\times \frac{d^3n}{2E_n(2\pi)^3}\frac{1}{2}\prod_{k=1}^{2}\frac{d^3p_k}{2E_k(2\pi)^3},$$

where $\lambda(p, D)$ is the flux factor, M_{fi} is the invariant amplitude for process (1), and the statistical factor of $1/2$ corresponds to two identical particles (protons) in the final state. In expression (3), it is convenient to go over from the momenta $\mathbf{p}_{1,2}$ to the relative momentum in the pair and its total momentum, whereupon integration with respect to the total momentum and the absolute value of the relative momentum is removed by the δ function. The resulting four-dimensional differential cross section can once again be integrated in view of the fact that, in the case where the pair is in the $^1S_0$ state, the matrix element M_{fi} is independent of the angles specifying the direction of the relative momentum. As a result, we arrive at

$$d^3\sigma = \frac{1}{16\pi\sqrt{\lambda(p,D)}}\sqrt{1-\frac{4m^2}{s_f}}|M_{fi}|^2 \qquad (4)$$
$$\times \frac{d^3n}{2E_n(2\pi)^3}\frac{1}{2}.$$

This is a general expression for the invariant differential cross section describing process (1) under the assumption that the final-state protons are in the $^1S_0$ state. For the ensuing calculations, we choose the deuteron rest frame and present all subsequent arguments in it. In this frame, the z axis (quantization axis) is taken to be aligned with the direction of the incident-proton momentum $\mathbf{p}$ (the directions of the x and y axes are specified below). Defining the momentum transfer as $q = n - p$, we go over, in (4), to the invariant variables $t = q^2$ and $s_f = (D-q)^2$, whereupon the cross section takes the form

$$\frac{d^2\sigma}{dtds_f} = \frac{1}{2}\frac{1}{64\pi\lambda(p,D)}\sqrt{1-\frac{4m^2}{s_f}} \qquad (5)$$
$$\times \int \frac{d\phi}{(2\pi)^3}|M_{fi}|^2,$$

where ϕ is the azimuthal angle of final-neutron emission. In the following, we consider only the case where the primary proton and the final neutron are unpolarized and where the deuteron density matrix ρ_d is axisymmetric with respect to the $z||\mathbf{p}$ axis; that is,

$$\rho_d = \frac{1}{3}\mathbf{1} + p_v\hat{T}_{10} + p_t\hat{T}_{20},$$

with p_v and p_t being, respectively, the vector and the tensor polarization parameter. It can then easily be shown that, in (5), there is no dependence on the angle ϕ, so that we finally have

$$\frac{d^2\sigma}{dtds_f} = \frac{1}{2}\frac{1}{64\pi\lambda(p,D)}\sqrt{1-\frac{4m^2}{s_f}}\frac{1}{(2\pi)^2}|M_{fi}|^2, \quad (6)$$

where the amplitude $|M_{fi}|^2$ can be calculated at an arbitrary value of ϕ—for example, at $\phi = 0$. In order to determine the amplitude M_{fi}, we can in principle calculate directly the diagram in Fig. 1 and obtain expression (6) for the cross section. This, however, obscures the final results and hampers the interpretation of spin observables. In order to avoid this, we adopt here a procedure for computing observables that consists of a few steps (see also [12])—namely, we (i) write the most general spin structure of the amplitude M_{fi} in the form of an expansion in partial invariant amplitudes and independent spin factors and define observables of the process in terms of these partial amplitudes, (ii) calculate the diagram in Fig. 1 and rearrange the resulting theoretical expression for the amplitude M_{fi} in such a way as to obtain the spin structure in a general form, and (iii) determine the explicit form of the partial spin amplitudes from a comparison of the theoretical expression for the amplitude and its general structure and evaluate the observables numerically.

By virtue of the assumption that the total angular momentum of the pp pair is zero, reaction (1) is of the $1/2 + 1 = 1/2 + 0$ spin type, in which case there are only six independent complex amplitudes because of parity conservation. The choice of representation

for these amplitudes is dictated by considerations of convenience and can be different for different particular cases (for example, the partial amplitudes can be defined in the helicity basis or in the representation of a specific spin projection onto the z axis in the c.m. frame of the particles involved). In this study, the general form of the amplitude M_{fi} is specified as follows [27]. The initial ($|i\rangle$) and the final ($|f\rangle$) state of the system will be characterized, apart from other quantum numbers, by specific values of the spin projection onto the quantization axis. In the matrix element M_{fi}, we write the spin dependence explicitly, isolating, in the $|i\rangle$ and $|f\rangle$ states, the deuteron polarization 3-vector and the two-component spinors of free nucleons. In the deuteron rest frame ($\mathbf{D} = \mathbf{0}$), we introduce the basis formed by the vectors

$$\mathbf{c} = \frac{\mathbf{p}}{|\mathbf{p}|}, \quad \mathbf{b} = \frac{[\mathbf{p}\times\mathbf{n}]}{|[\mathbf{p}\times\mathbf{n}]|}, \quad \mathbf{a} = [\mathbf{b}\times\mathbf{c}]. \quad (7)$$

The amplitude M_{fi} can then be represented in the form

$$M_{fi} \equiv \mathcal{T}^M_{r'r} = [\chi^+_{r'}]_\alpha \left(\mathcal{M}_{\alpha\beta}\boldsymbol{\xi}_M\right)[\chi_r]_\beta, \quad (8)$$
$$\alpha,\beta = 1,2,$$

where r', r, and M are the projections of, respectively, the neutron, the proton, and the deuteron spin onto the z axis, while the amplitude $\mathcal{M}_{\alpha\beta}$, which is simultaneously a vector in coordinate space and a matrix in spinor space, can be expanded in the basis vectors (7) and the Pauli matrices σ_i ($i = x, y, z$) as

$$\mathcal{M}_{\alpha\beta} = i\mathcal{A}\mathbf{b}\delta_{\alpha\beta} + \mathcal{B}\mathbf{b}(\boldsymbol{\sigma}\cdot\mathbf{b})_{\alpha\beta} + \mathcal{C}\mathbf{a}(\boldsymbol{\sigma}\cdot\mathbf{a})_{\alpha\beta} \quad (9)$$
$$+\mathcal{D}\mathbf{a}(\boldsymbol{\sigma}\cdot\mathbf{c})_{\alpha\beta} + \mathcal{E}\mathbf{c}(\boldsymbol{\sigma}\cdot\mathbf{a})_{\alpha\beta} + \mathcal{F}\mathbf{c}(\boldsymbol{\sigma}\cdot\mathbf{c})_{\alpha\beta}.$$

In expression (8), $\boldsymbol{\xi}_M$ denotes the polarization vector of the deuteron in its rest frame:

$$\boldsymbol{\xi}_{+1} = -\frac{1}{\sqrt{2}}\begin{pmatrix}1\\ i\\ 0\end{pmatrix}, \quad \boldsymbol{\xi}_{-1} = \frac{1}{\sqrt{2}}\begin{pmatrix}1\\ -i\\ 0\end{pmatrix}, \quad (10)$$

$$\boldsymbol{\xi}_0 = \begin{pmatrix}0\\ 0\\ 1\end{pmatrix}.$$

Although expressions (8) and (9) are noncovariant, this form of the amplitude is the most general one and is valid both in the nonrelativistic and in the relativistic approach. This can easily be verified by noticing that, in any reference frame, the deuteron polarization 4-vector ξ_M can be expressed in terms of the vector $\boldsymbol{\xi}_M$ as

$$\xi_M = \left[\frac{\mathbf{D}\cdot\boldsymbol{\xi}_M}{M_d}, \boldsymbol{\xi}_M + \mathbf{D}\frac{\mathbf{D}\cdot\boldsymbol{\xi}_M}{M_d(E_d+M_d)}\right],$$

where M_d and E_d are the deuteron mass and total energy, respectively, and that, in the covariant matrix elements, we can always go over from the spinors in (2) to the two-component spinors χ_r.

As was mentioned above, the z axis is aligned with the vector $\mathbf{c}$. For the sake of convenience, the y and x axes are chosen to be directed along the vectors $\mathbf{b}$ and $\mathbf{a}$, respectively; this choice is justified by the fact that the azimuthal angle of the neutron emission, ϕ, can be assumed to be zero. The invariant amplitudes $\mathcal{A}, \mathcal{B}, \ldots, \mathcal{F}$ depend only on three variables; for these, we can take the total initial energy, the square of the momentum transfer (t), and the invariant mass of the pp pair (s_f). These amplitudes are related to the partial spin amplitudes $\mathcal{T}^M_{r'r}$ by the equations

$$\mathcal{A} = (\mathcal{T}^1_{-\frac{1}{2}-\frac{1}{2}} + \mathcal{T}^1_{\frac{1}{2}\frac{1}{2}})/\sqrt{2}, \quad (11)$$
$$\mathcal{B} = -(\mathcal{T}^1_{\frac{1}{2}-\frac{1}{2}} - \mathcal{T}^1_{-\frac{1}{2}\frac{1}{2}})/\sqrt{2},$$
$$\mathcal{C} = -(\mathcal{T}^1_{\frac{1}{2}-\frac{1}{2}} + \mathcal{T}^1_{-\frac{1}{2}\frac{1}{2}})/\sqrt{2},$$
$$\mathcal{D} = (\mathcal{T}^1_{-\frac{1}{2}-\frac{1}{2}} - \mathcal{T}^1_{\frac{1}{2}\frac{1}{2}})/\sqrt{2},$$
$$\mathcal{E} = \mathcal{T}^0_{\frac{1}{2}-\frac{1}{2}}, \quad \mathcal{F} = \mathcal{T}^0_{\frac{1}{2}\frac{1}{2}}.$$

The amplitudes $\mathcal{A}$, $\mathcal{B}$, ..., $\mathcal{F}$ make it possible to calculate any spin observables for process (1). Specifically, the expectation value of a physical quantity associated with a spin operator $\mathcal{O}$ is given by

$$\langle\mathcal{O}\rangle = 6\frac{\mathrm{tr}\,(\mathcal{M}\mathcal{O}\mathcal{M}^+)}{\mathrm{tr}\,(\mathcal{M}\mathcal{M}^+)}, \quad (12)$$

where the denominator corresponds to the cross section for process (1) in the case of unpolarized particles,

$$\frac{1}{6}\mathrm{tr}\left(\mathcal{M}\mathcal{M}^+\right) = \frac{1}{3}(\mathcal{A}\mathcal{A}^* + \mathcal{B}\mathcal{B}^*$$
$$+\mathcal{C}\mathcal{C}^* + \mathcal{D}\mathcal{D}^* + \mathcal{E}\mathcal{E}^* + \mathcal{F}\mathcal{F}^*).$$

For example, the tensor analyzing power $\langle T_{20}\rangle$ is given by

$$\langle T_{20}\rangle = 6\frac{\mathrm{tr}\left(\mathcal{M}\hat{T}_{20}\mathcal{M}^+\right)}{\mathrm{tr}\,(\mathcal{M}\mathcal{M}^+)} = \frac{\sqrt{2}}{\mathrm{tr}\,(\mathcal{M}\mathcal{M}^+)} \quad (13)$$
$$\times(\mathcal{A}\mathcal{A}^* + \mathcal{B}\mathcal{B}^* + \mathcal{C}\mathcal{C}^* + \mathcal{D}\mathcal{D}^* - 2[\mathcal{E}\mathcal{E}^* + \mathcal{F}\mathcal{F}^*]).$$

It should be noted that the representation of the amplitude M_{fi} in the form specified by Eqs. (8) and (9) is valid in the case where the initial and the final state can be described by wave functions—that is, where these are pure states. In the case of mixed states, all of the aforesaid remains valid except that,

in squaring the amplitude M_{fi}, it is necessary to sum all spin projections by using the density matrices

$$\rho_N = \frac{1}{2}\sum_r |r\rangle\langle r|, \quad \rho_d = \frac{1}{3}\sum_M |M\rangle\langle M|.$$

Thus, the problem consists in calculating first the amplitudes $\mathcal{T}^M_{r'r}$ and then the observables of process (1) by using relations (11)–(13). It should be emphasized once again that objective of this study is to perform methodological calculations of a predictive character for planned experiments at high initial energies under the conditions where, in any reference frame, either the initial deuteron or the final *pp* pair moves. In order to describe correctly a moving two-nucleon system at high energies, covariant approaches are preferable where the procedure of Lorentz boosts is defined for states of the system. The Bethe–Salpeter formalism, within which it is possible to describe self-consistently both the bound state (deuteron) and the scattering states of the *pp* pair, is quite appropriate for our purposes. The effects of Lorentz boosts of a two-nucleon state are taken into account automatically in this approach [12]. It is also possible to use, for example, the approach based on the Gross equation [28]. It is very close to the Bethe–Salpeter formalism—as a matter of fact, this is the Bethe–Salpeter equation in the approximation where one nucleon is on the mass shell. We prefer to avoid this additional simplification; therefore, we employ the numerical solution to the Bethe–Salpeter equation from [24, 25], where this solution was constructed for the case, in which the deuteron, with its two nucleons, is off the mass shell. Moreover, a detailed comparison of our solution and the solution to the Gross equation [29] revealed that, up to the relative momenta of $|\mathbf{k}| \sim 1.5$ GeV/c, these two approaches yield virtually identical results.

In the present study, the amplitude $\mathcal{T}^M_{r'r}$ is determined within the Bethe–Salpeter formalism directly on the basis of the diagram in Fig. 1. In the following, we assume that the initial energy of the reaction is so high that the initial-state proton–deuteron interaction and the final-state interaction between the neutron and the *pp* pair can be neglected. This means that the initial and final three-particle states can be treated as the direct product of the relativistic spinor of a fast nucleon and the states of a nucleon–nucleon system that are described by the homogeneous (deuteron) or the nonhomogeneous (a *pp*-pair state in the continuous spectrum) Bethe–Salpeter equation.

3. REACTION AMPLITUDE WITHIN THE BETHE–SALPETER APPROACH

As was mentioned above, we consider here process (1) at intermediate and high energies and low momentum transfers. Under these conditions, the main reaction mechanism is that of charge exchange between the initial proton and the target neutron. Following the technique of Mandelstam [30], we represent the covariant reaction matrix element corresponding to the diagram in Fig. 1 (spinor indices are retained) in the form

$$\mathcal{T}^M_{r'r} = \bar{u}^{r'}_\gamma(n)u^r_\delta(p)\int d^4k\bar{\Phi}_{P'}\left(\frac{q}{2}+k\right)_{\alpha\beta} \times \left(\frac{\hat{D}}{2}+\hat{k}-m\right)_{\alpha\mu}\Phi_M(k)_{\mu\nu}\mathcal{A}^{\rm ce}_{\beta\gamma,\delta\nu}, \quad (14)$$

where Φ_M is the Bethe–Salpeter deuteron amplitude, which is a solution to the homogeneous Bethe–Salpeter equation for the deuteron, and $\bar{\Phi}_{P'}$ is the conjugate Bethe–Salpeter amplitude for the *pp* pair (it is a solution to the nonhomogeneous Bethe–Salpeter equation for the pair in the continuum spectrum). The charge-exchange vertex $\mathcal{A}^{\rm ce}$ corresponds to the four-point Green's function for the process $pn \to np$ where the initial neutron and the final proton are generally off the mass shell. In Eq. (14), it is convenient to go over from the direct product of the spinors and the amplitudes to the matrix product. For this, the Bethe–Salpeter amplitudes are redefined as [31]

$$\Phi(k) \equiv \Psi(k)U_C, \quad \bar{\Psi}(k) = \gamma_0\Psi^\dagger(k)\gamma_0,$$

where $U_C = i\gamma_2\gamma_0$ is the charge-conjugation matrix. The new amplitudes $\Psi(k)$ can then be considered as ordinary 4×4 matrices acting in spinor space, and the Bethe–Salpeter equations for the new amplitudes are matrix integral equations. In order to solve these equations numerically, the amplitudes $\Psi(k)$ are usually expanded in some complete set of 4×4 matrices, whereby a set of integral equations for the coefficients in this expansion is obtained. These coefficients are known in the literature as Bethe–Salpeter partial amplitudes. It is obvious that the form of partial amplitudes depends on the specific choice of basis for the aforementioned expansion, different bases being related by a unitary transformation. In [24, 25], the set of Bethe–Salpeter equations for deuteron partial amplitudes with a realistic interaction kernel (sum of exchanges of $\pi, \omega, \rho, \sigma, \eta$, and δ mesons) was solved numerically in the representation of the complete set of 16 Dirac matrices. This representation is convenient for obtaining a numerical solution; however, clarity is lost here in calculating observables for specific processes, and the interpretation of the results derived in this way becomes complicated. From the physical point of view, it is more convenient to use the so-called ρ-spin classification of partial amplitudes that is obtained in the basis of spin–angular harmonics [32], where partial amplitudes can be interpreted

in terms of states characterized by specific values of the spin and of the total angular momentum. In particular, this makes it possible to find their nonrelativistic analogs. By way of example, we indicate that, for the deuteron, the amplitude Ψ_M consists of eight components, which can be divided into three groups: (i) two components that are the largest in magnitude and which are characterized by positive ρ spins (they correspond to the S and the D wave in the nonrelativistic pattern of the deuteron), (ii) four so-called P waves (which are small in relation to the S and D waves) having one positive and one negative ρ spin, and (iii) two negligibly small components whose ρ spins are both negative (for more details, see [33]). In the present study, all analytic calculations are performed in the ρ-spin representation, while numerical results are derived by using the solution presented in [24, 25]. The explicit form of the unitary transformation from the expansion in the Dirac matrices to the expansion in spin–angular harmonics can be found in [33]. Below, we disregard the contribution of the partial amplitudes having at least one negative ρ-spin value. This means that the Bethe–Salpeter amplitude for the deuteron can be represented in the form (see also Appendix A)

$$\Psi_M(k) = \Psi^M_{S^{++}}(k) + \Psi^M_{D^{++}}(k). \qquad (15)$$

It should be noted that, for a two-nucleon system (deuteron or *pp* pair), the inclusion of only the leading partial components of the Bethe–Salpeter amplitude does not mean a rejection of the relativistic description of the reaction, but it is a well-justified approximation within the general relativistic formalism.

In order to determine the vertex $\mathcal{A}^{\rm ce}$, we can expand it in the complete set of matrices—in just the same way as in solving the Bethe–Salpeter equations—and determine the expansion coefficients from an experiment studying nucleon–nucleon charge exchange. However, this procedure is not quite consistent since all nucleons are not real in this case. Obviously, additional theoretical arguments and dedicated theoretical models are required for estimating off-shell-mass effects in $\mathcal{A}^{\rm ce}$. Moreover, the excitation energies and momentum transfers are comparatively low in the reaction being considered; therefore, the nucleons of the *pp* pair are close to the mass shell, so that off-mass-shell corrections can be neglected. The quantity $\mathcal{A}^{\rm ce}$ can then be directly expressed in terms of the amplitudes $f_{r's',sr}$ for the real charge-exchange process $p + p_n = p_p + n$, where all particles are on the mass shell; that is, we have

$$f_{r's',sr} = \bar{u}^{s'}_\alpha(p_p)\bar{u}^{r'}_\beta(n)\mathcal{A}^{\rm ce}_{\alpha\beta,\gamma\delta}u^r_\gamma(p)u^s_\delta(p_n). \qquad (16)$$

By using Eq. (16), we obtain

$$\mathcal{T}^M_{r'r} = \sum_{ss'}\frac{1}{(2m)^2}\int d^4k f_{r's',sr}\bar{u}^s(p_n)\Psi_M(k) \qquad (17)$$
$$\times(\hat{D}/2 - \hat{k} + m)\bar{\Psi}_{P'}(k - q/2)u^{s'}(p_p).$$

The amplitude in (17) now becomes the main subject of a further analysis. It can be seen that it possesses a manifest Lorentz covariance.

The problem of taking into account the interaction in the $^1S_0$ final state of this reaction is equivalent to the analogous problem in describing the deuteron-electrodisintegration process $ed \to e'(pn)$; therefore, we will follow [31] in our approach. According to the ρ classification, the Bethe–Salpeter amplitude in the $^1S_0$ state has four components whose quantum numbers are $^1S_0^{++}$, $^1S_0^{--}$, $^3P_0^{+-}$, and $^3P_0^{-+}$; in the following, these components are denoted by ϕ_1, …, ϕ_4, respectively. As in the case of the deuteron, we will disregard, in the final expressions, all components whose ρ spin is negative—that is, we will retain only the leading (++) component (ϕ_1). It should be noted that the expansion in spin–angular harmonics is constructed in the rest frame of the *pp* pair. In order to derive the amplitude in any other reference frame, we must make a Lorentz boost (see, for example, [33]). However, the cumbersome procedure of performing the boost explicitly can be sidestepped by noticing that the amplitude $\bar{\Psi}_{P'}$ can be written in the covariant form [31]

$$\sqrt{4\pi}\bar{\Psi}_{P'}(p) = -b_1\gamma_5 - b_2\frac{1}{m}(\gamma_5\hat{p}_1 + \hat{p}_2\gamma_5) \qquad (18)$$
$$- b_3\left(\gamma_5\frac{\hat{p}_1 - m}{m} - \frac{\hat{p}_2 + m}{m}\gamma_5\right) - b_4\frac{\hat{p}_2 + m}{m}\gamma_5\frac{\hat{p}_1 - m}{m},$$

where $p_{1,2} = P'/2 \pm p$, p being the relative 4-momentum, and where the functions $b_i \equiv b_i(P'p, p^2)$ are Lorentz-invariant. It is now sufficient to express them in terms of the ρ-spin components $\phi_i \equiv \phi_i(r_0, |\mathbf{r}|)$, $i = 1, \ldots, 4$, whereby the effects of the Lorentz boost are automatically taken into account (see also [12]). The relation between b_i and ϕ_i is presented in Appendix A.

Following the above method for calculating observables, we substitute Eqs. (18) and (15) into (17) and obtain an expression for the integrand matrix element in terms of two-component spinors and 3-vectors, that is,

$$f_{r's',sr}\bar{u}^s(p_n)\Psi_M(k)(\hat{D}/2 - \hat{k} + m) \qquad (19)$$
$$\times\,\bar{\Psi}_{P'}(k - q/2)u^{s'}(p_p) = f_{r's',sr}\Big\{\chi^\dagger_s(\boldsymbol{\sigma}\cdot\boldsymbol{\xi}_M)$$
$$\times\chi_{s'}(\psi_S - \psi_D/\sqrt{2})C_1 + \chi^\dagger_s(\boldsymbol{\sigma}\cdot\mathbf{k})\chi_{s'}(\mathbf{k}\cdot\boldsymbol{\xi}_M)\psi_D C_2$$
$$+ [-\chi^\dagger_s(\boldsymbol{\sigma}\cdot\mathbf{q})\chi_{s'}(\mathbf{k}\cdot\boldsymbol{\xi}_M)(\psi_S + \sqrt{2}\psi_D)$$
$$+ \chi^\dagger_s(\boldsymbol{\sigma}\cdot\mathbf{k})\chi_{s'}(\mathbf{q}\cdot\boldsymbol{\xi}_M)(\psi_S - \psi_D/\sqrt{2})$$
$$+ \chi^\dagger_s\chi_{s'}i([\mathbf{q}\times\mathbf{k}]\cdot\boldsymbol{\xi}_M)(\psi_S - \psi_D/\sqrt{2})]C_3\Big\},$$

where the scalar coefficients C_1, C_2, and C_3, which were introduced for the sake of brevity, depend on the kinematical variables of the process and on the partial wave functions $\phi_1, \ldots, \phi_4$ for the $^1S_0$ final states, but they are independent of the spin variables. The explicit expressions for them are presented in Appendix A. From formula (19), it is clear how one can calculate the amplitude $\mathcal{T}^M_{r'r}$ at specific values of the spin indices r', r, and M and, hence, determine the invariant amplitudes $\mathcal{A}$, $\mathcal{B}$, ..., $\mathcal{F}$ (11) and the observables given by (12) and (13).

In order to determine ϕ_i, it is necessary, in principle, to use the same NN-interaction model as for the deuteron, but this model must be supplemented with the electromagnetic interactions of protons. By way of example, we indicate that, in the simplest case, where only the pseudoscalar pion–nucleon interaction is taken into account, the nonhomogeneous Bethe–Salpeter equation for $\bar{\Psi}_{P'}(p)$ has the form [34]

$$\bar{\Psi}_{P'}(p) = \bar{\Psi}^0_{P'}(p) + ig^2_{\pi NN} \times \int \frac{d^4p'}{(2\pi)^4}\Delta(p-p')\tilde{S}(p_2)\gamma_5\bar{\Psi}_{P'}(p')\gamma_5 S(p_1), \tag{20}$$

where Δ and S are the propagators for the scalar and the spinor field, respectively; $\tilde{S} \equiv U_C S U_C^{-1}$; and $\bar{\Psi}^0_{P'}(p)$ is the relativistic plane wave corresponding to the motion of two noninteracting protons. A solution to Eq. (20) can be represented, for example, in the form of a Neumann series, its first term being $\bar{\Psi}^0_{P'}(p)$. Symbolically, this can be represented as

$$\bar{\Psi}_{P'}(p) = \bar{\Psi}^0_{P'}(p) + \bar{\Psi}^i_{P'}(p). \tag{21}$$

The second term, which is determined by the interaction, can be referred to by convention as a diverging wave. In the rest frame of the pp pair, we find for the $^1S_0$ state that [31]

$$\bar{\Psi}^0_{P'}(r)|_{P'=(\sqrt{s_f},\mathbf{0})} = \phi^0_1(r_0,|\mathbf{r}|)\Gamma_{^1S_0^{++}}(\hat{\mathbf{r}}),$$
$$\phi^0_1(r_0,|\mathbf{r}|) = 2(2\pi)^4\frac{1}{\sqrt{4\pi}}\frac{1}{|\mathbf{r}^*|^2}\delta(r_0)\delta(|\mathbf{r}|-|\mathbf{r}^*|),$$

where $r = (r_0, \mathbf{r})$ is the relative 4-momentum (argument of the amplitude), $|\mathbf{r}^*| = \sqrt{s_f/4 - m^2}$ is the real (measured experimentally) relative 3-momentum in the pair, and $\Gamma_{^1S_0^{++}}(\hat{\mathbf{r}})$ is a spin–angular harmonic (see Appendix A). In order to determine the diverging wave in (21), it is necessary to solve an equation of the type in (20). This, however, involves considerable difficulties—in particular, such equations do not admit the Wick rotation procedure [35], so that it is necessary to solve them directly in Minkowski space, but there are presently no regular methods for this. One possible way to estimate $\bar{\Psi}^i_{P'}$ is to invoke the so-called one-iteration approximation described in [31], where it was shown that the corrections from the second term in expansion (21) are similar to meson-exchange currents in nonrelativistic approaches. A detailed investigation of the contribution from the second term in (21) will be performed in a subsequent publication. As a natural initial step in developing a model for reaction (1), we will retain here only the first term in expansion (21); that is,

$$\phi_1(r_0,|\mathbf{r}|) = \phi^0_1(r_0,|\mathbf{r}|), \qquad \phi_2 = 0, \quad \phi_3 = 0, \quad \phi_4 = 0. \tag{22}$$

For the specific kinematical situation considered in our study [see Eq. (17)],

$$\delta(r_0) = \delta[(P', k - q/2)/\sqrt{s_f}], \tag{23}$$

$$\delta(|\mathbf{r}| - |\mathbf{r}^*|) = \delta\left(\sqrt{-(k-q/2)^2} - \sqrt{s_f/4 - m^2}\right), \tag{24}$$

and we finally have

$$\phi^0_1(r_0,|\mathbf{r}|) = 2(2\pi)^4\frac{1}{\sqrt{4\pi}}\frac{1}{E|\mathbf{k}||\mathbf{q}|} \times \sqrt{\frac{s_f}{s_f/4-m^2}}\delta(k_0 - [M_d/2 - E]) \times \delta\left(\cos\theta_{kq} + \frac{s_f - 2E(M_d - q_0)}{2|\mathbf{k}||\mathbf{q}|}\right), \tag{25}$$

where θ_{kq} is the angle between the vectors $\mathbf{k}$ and $\mathbf{q}$. In the approximation specified by Eqs. (22)–(25), which is also known as the relativistic impulse approximation, the matrix element (17) assumes the form

$$\mathcal{T}^M_{r'r} = \sum_{ss'}\int\limits_{|\mathbf{k}|_{\min}}^{|\mathbf{k}|_{\max}} d|\mathbf{k}|F_k\int\limits_0^{2\pi} d\phi_k f_{r's',sr} \times \left\{\chi^\dagger_s(\boldsymbol{\sigma}\cdot\boldsymbol{\xi}_M)\chi_{s'}\left(G_S - \frac{G_D}{\sqrt{2}}\right)\left(\frac{s_f}{2} + mP'_0\right) + \chi^\dagger_s(\boldsymbol{\sigma}\cdot R_q\mathbf{k})\chi_{s'}(\boldsymbol{\xi}_M\cdot R_q\mathbf{k})\frac{3}{\sqrt{2}}G_D\frac{P'_0}{E-m} - \chi^\dagger_s(\boldsymbol{\sigma}\cdot\mathbf{q})\chi_{s'}(\boldsymbol{\xi}_M\cdot R_q\mathbf{k})(G_S + \sqrt{2}G_D) + \chi^\dagger_s(\boldsymbol{\sigma}\cdot R_q\mathbf{k})\chi_{s'}(\mathbf{q}\cdot\boldsymbol{\xi}_M)\left(G_S - \frac{G_D}{\sqrt{2}}\right) + \chi^\dagger_s\chi_{s'}i([\mathbf{q}\times R_q\mathbf{k}]\cdot\boldsymbol{\xi}_M)\left(G_S - \frac{G_D}{\sqrt{2}}\right)\right\}, \tag{26}$$

$$F_k = \frac{1}{(4\pi)^{3/2}} \times \frac{|\mathbf{k}|}{|\mathbf{q}|E(M_d-2E)\sqrt{(s_f/4-m^2)(E+m)(p^0_p+m)}}, \tag{27}$$

where we have introduced, instead of the Bethe–Salpeter amplitudes, the corresponding vertex functions $G_{S,D}$ (see Appendix A); R_q is the matrix describing the rotation about the y axis through the angle θ (the angle between the vector $\mathbf{q}$ and the z axis),

$$R_q = \begin{pmatrix} \cos\theta & 0 & \sin\theta \\ 0 & 1 & 0 \\ -\sin\theta & 0 & \cos\theta \end{pmatrix};$$

and the limits of integration with respect to $|\mathbf{k}|$ are

$$|\mathbf{k}|_{\max,\min} = \left| \sqrt{1+\frac{\mathbf{q}^2}{s_f}}\sqrt{\frac{s_f}{4}-m^2} \pm \frac{|\mathbf{q}|}{2} \right|.$$

By using expressions (10) and the explicit form of the Pauli matrices, we can now calculate $\mathcal{T}^M_{r'r}$ for specific values of the indices and obtain numerically the amplitudes $\mathcal{A}, \mathcal{B}, \ldots, \mathcal{F}$ with the aid of expressions (11). It is only necessary to explain how one can perform calculations with the charge-exchange amplitudes $f_{r's',sr}$. In addition to the spin indices, they also depend on two Mandelstam variables: the total energy of the charge-exchange subprocess, $s_{pn} = (D/2+k+p)^2$ (where p is the primary-proton momentum), and the momentum transfer squared $t = (n-p)^2$ (this variable is common to the subprocess and the reaction as a whole). Under the kinematical conditions being considered, the neutron in the deuteron (it plays the role of the primary neutron in the elementary subprocess) and the final proton possess the 4-momenta $D/2+k$ and $P'/2+k-q/2$, respectively; in general, these particles are off the mass shell. In the relativistic impulse approximation, however, we have $p_p = P'/2+k-q/2$ after integration with the δ functions, so that only the neutron in the deuteron remains off the mass shell. It was indicated in [26] that the amplitude for the NN charge exchange depends only slightly on the total energy; in view of the smallness of the neutron binding energy in the deuteron, we can neglect the off-mass-shellness of the neutron. Additionally, the amplitude $f_{r's',sr}$ can be taken outside the sign of the integral with respect to ϕ_k to a high precision, whereby the calculations are significantly simplified. These arguments are commonly accepted in the literature devoted to evaluating diagrams for proton–deuteron scattering in the impulse approximation, where the off-mass-shell amplitude of the subprocess is replaced by the on-shell nucleon–nucleon amplitude, which is directly measured in experiments [15, 36–38].

4. RESULTS AND CONCLUSIONS

In numerical calculations, we have used the elementary charge-exchange amplitudes in the form of the analytic parametrization from [26] or in the form of numerical results deduced by various groups of authors [41, 42] from partial-wave analyses:[3)]

$$f_1 = \langle ++|\mathcal{A}^{\rm ce}|++\rangle, \quad (28)$$
$$f_2 = \langle ++|\mathcal{A}^{\rm ce}|--\rangle, \quad f_3 = \langle +-|\mathcal{A}^{\rm ce}|+-\rangle,$$
$$f_4 = \langle +-|\mathcal{A}^{\rm ce}|-+\rangle, \quad f_5 = \langle ++|\mathcal{A}^{\rm ce}|+-\rangle.$$

Here, f_i are the helicity amplitudes for NN charge exchange that are normalized by the condition

$$\frac{d\sigma^{\rm ce}}{dt} = \frac{1}{32\pi s(s-4m^2)}\left\{\sum_{i=1}^{4}|f_i|^2 + 4|f_5|^2\right\}. \quad (29)$$

In the matrix element (26), the amplitudes $f_{r's',sr}$ are spin (not helicity) amplitudes, on one hand, and are defined in the deuteron rest frame, on the other hand. It follows that, in numerical calculations, one must first perform the Lorentz boost in (28) along the vector $\mathbf{p}+\mathbf{k}$ from the c.m. frame of the pn system to the laboratory frame and then, by means of a Wigner rotation, go over from particle helicities to spin projections onto the z axis. Considering that the Lorentz boost procedure leads to a rotation of the helicities [43], two rotations of the spin state are needed for each particle (see Appendix B).

The partial amplitudes in (28) versus the momentum transfer $|\mathbf{q}|$ are shown in Fig. 2 at the energy value corresponding to the primary-nucleon momentum of $|\mathbf{p}| = 2.5$ GeV/c in the laboratory frame. The solid curves represent the results of the partial-wave analysis presented in [40, 42], while the dashed curves correspond to the parametrization proposed in [26]. It can be seen that the partial-wave amplitudes obtained by different groups of authors differ significantly, and it is difficult to give preference from the outset to one result or another. In order to obtain unambiguous results for the phenomenological amplitudes in (28), it is necessary to have a great number (approximately ten) of independent polarization experiments, and the most accurate fit to experimental data is a basic criterion here. If the existing data are insufficient, there remain ambiguities in determining the partial amplitudes in (28). In this connection, an investigation of the process in (1) can significantly supplement available information about the amplitude for the elementary event of nucleon–nucleon charge exchange, and this was already indicated, for example, in [21].

For the case of polarized deuterons, Figs. 3 and 4 display the differential cross section $d\sigma/dt$ and the

[3)] These amplitudes are freely available in the on-line regime (see, for example, [39, 40]).

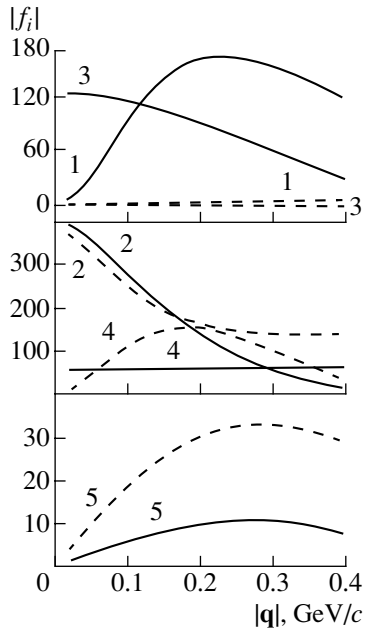

Fig. 2. Absolute values of the amplitudes in (28), which correspond to the primary-nucleon momentum of $|\mathbf{p}| = 2.5$ GeV/c in the laboratory frame: (solid curves) SAID parametrization of the charge-exchange subprocess [40, 42] and (dashed curve) parametrization from [26]. The amplitudes in question are dimensionless, as follows from (29).

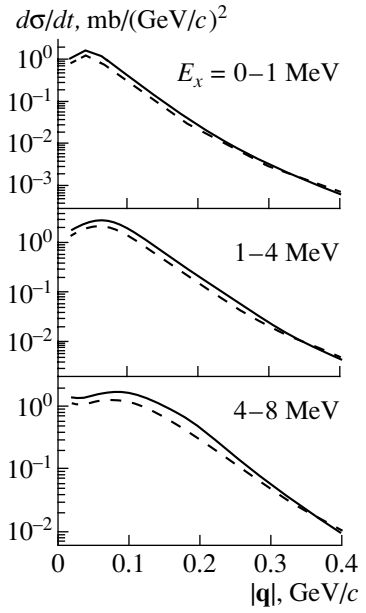

Fig. 3. Unpolarized differential cross section (30) at the primary-proton momentum of $|\mathbf{p}| = 2.5$ GeV/c (in the laboratory frame) for the excitation-energy intervals (31)–(33): (solid curves) results for the SAID parametrization of the charge-exchange subprocess [40, 42] and (dashed curves) results for the parametrization from [26].

tensor analyzing power T_{20} for process (1) at the primary momentum of $|\mathbf{p}| = 2.5$ GeV/c that were calculated with (solid curves) the partial-wave amplitudes from [40, 42] and (dashed curves) the amplitudes from [26]. The above differential cross section $d\sigma/dt$ is obtained by integrating the double-differential cross section (6) over the intervals of the excitation energy of the pair, E_x, that correspond to the actual experimental condition; that is,

$$\left(\frac{d\sigma}{dt}\right)_k = \frac{1}{(8\pi)^3\lambda}\int\limits_{R_k} ds_f \sqrt{1-\frac{4m^2}{s_f}}\,|M_{fi}|^2, \quad (30)$$

$$k = 1, 2, 3, \ldots,$$

where k numbers the experimentally accessible intervals of the energy E_x. By way of example, we indicate that, at the SATURN-II facility [19], reaction (1) was investigated in detail at the initial energies corresponding to the proton momenta of $|\mathbf{p}| = 0.444$ GeV/c and $|\mathbf{p}| = 0.599$ GeV/c. The pair-excitation-energy intervals studied there are

$$R_1: \quad 0 \le E_x \le 1 \text{ MeV}, \quad (31)$$

$$R_2: \quad 1 \le E_x \le 4 \text{ MeV}, \quad (32)$$

$$R_3: \quad 4 \le E_x \le 8 \text{ MeV}, \quad (33)$$

with the variable t taking values from 0 to 0.16 (GeV/c)^2. For the convenience of comparison, we will everywhere quote the results of our calculations for precisely these kinematical intervals of E_x and t.

It can be seen from Fig. 3 that, as might have been expected, the differential cross section is not sensitive to the choice of parametrization for the elementary charge-exchange cross section, since the elementary cross section (29) itself does not depend on the details of the choice of form for the partial amplitudes (28). A totally different pattern is observed in the results of the calculation of the polarization features (12), where the contribution of the partial-wave amplitudes is off-diagonal. Inspecting Fig. 4, one can conclude that the behavior of the tensor analyzing power (13) depends greatly on the choice of parametrization for the elementary amplitude—in principle, an experimental investigation of T_{20} can furnish information about the relative contribution of the elementary partial-wave amplitudes and about the quality of the chosen parametrization. There are presently no experimental data on the polarization features of reaction (1) at high energies. However, it was mentioned above that, at initial energies of about a few hundred MeV, this reaction was thoroughly investigated at the SATURN-II facility [19] for two values of the primary momentum $|\mathbf{p}|$ (0.444 and 0.599 GeV/c). Although these

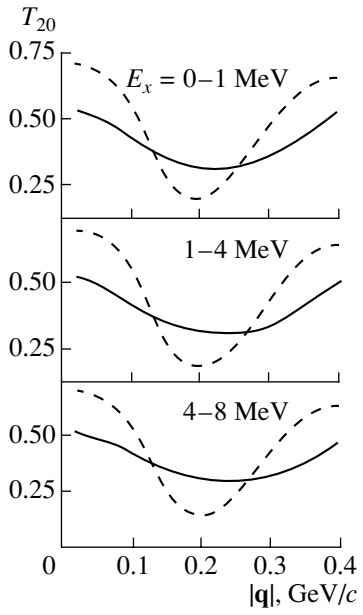

Fig. 4. Tensor analyzing powers T_{20} (13) corresponding to the same conditions as those adopted for Fig. 3.

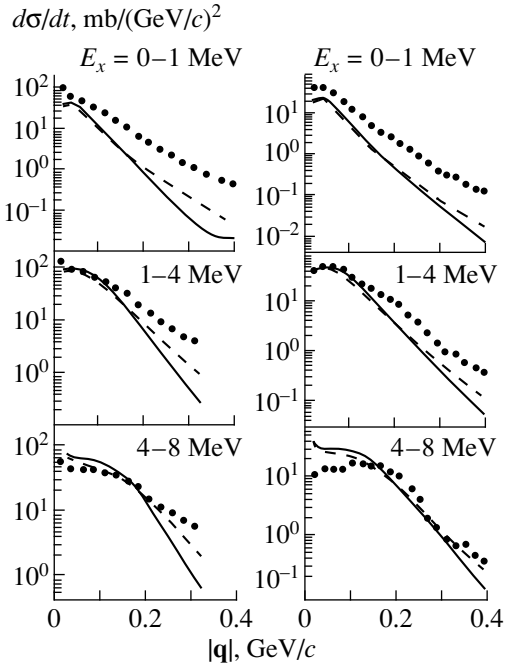

Fig. 5. Unpolarized differential cross section (30) at the primary-proton momenta of $|\mathbf{p}| = 0.444$ GeV/c and $|\mathbf{p}| = 0.599$ GeV/c for the excitation-energy intervals (31)–(33): results of the calculations with (solid curves) the SAID parametrization [40, 42] of the charge-exchange process and (dashed curves) the parametrization from [26]. The experimental data displayed here were borrowed from [19].

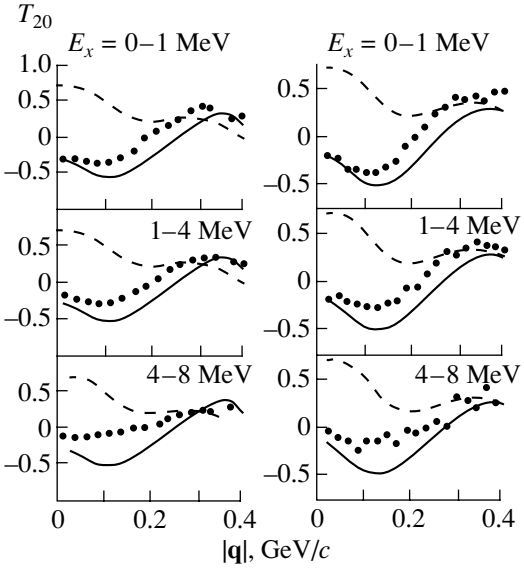

Fig. 6. Tensor analyzing power T_{20} (13) calculated under the same conditions as those adopted for Fig. 5.

energies are insufficiently high for the impulse approximation adopted here to be valid and for effects of initial- and final-state interaction to be negligible, a comparison of the theoretical results and experimental data is informative.

Figures 5 and 6 present the differential cross section (30) and the tensor analyzing power T_{20} (13) computed by using formulas (26) and (27). The solid and the dashed curves correspond to the parametrizations of the helicity amplitudes from [40, 42] and [26], respectively. From Fig. 5, it can be seen that the behavior of the cross section is in reasonable agreement with experimental data at low values of the momentum transfer $|\mathbf{q}|$ up to about 0.2 GeV/c and in the pair-excitation-energy interval $1 \leq E_x \leq 4$ MeV. In other intervals of E_x and at higher values of $|\mathbf{q}|$, the agreement of the results of the calculations with the experimental data is poorer. From here, one can immediately conclude that, at very low excitation energies ($E_x \sim 0$), the final-state interaction of two protons (strong Coulomb repulsion) plays a significant role, so that the disregard of these effects is illegitimate here at any initial energies. As the excitation energy of the pair grows, the final-state interaction becomes less important, so that the use of the impulse approximation becomes more justified. With increasing primary energy and momentum transfer, the agreement with experimental data is improved, which seems to validate the assumption that the pp pair is detected in the $^1S_0$ state.

The same conclusions are suggested by the analysis of the results presented in Fig. 6 for T_{20} . It can be seen that only if use is made of the partial-wave amplitudes from [40, 42] (solid curves) are the results of the calculations in qualitative agreement with ex-

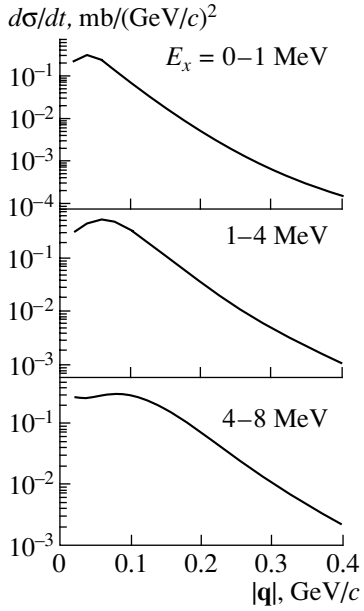

Fig. 7. Unpolarized differential cross section (30) at the primary-proton momentum of $|\mathbf{p}| = 5$ GeV/c. The amplitudes for nucleon–nucleon charge exchange were taken from [26].

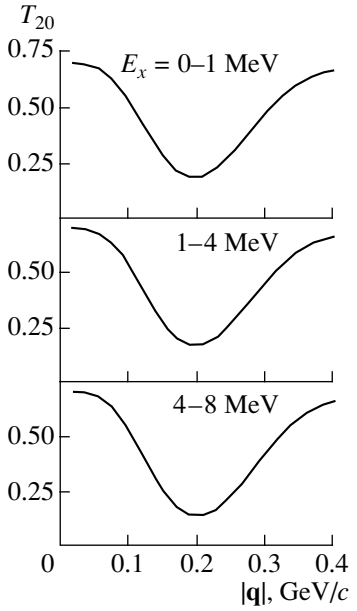

Fig. 8. Tensor analyzing power T_{20} (13) under the same conditions as those adopted for Fig. 7.

perimental data over the entire interval of momentum transfers for all values of the pair excitation energy. The calculation with the amplitudes from [26] leads to a qualitatively different behavior of T_{20} and even to a wrong sign of it. This indicates that preference should be given to the results from [40, 42]. Since T_{20} is determined by the ratio of two quantities [see Eq. (13)], the contribution from the effects of final-state interaction is expected to be suppressed here in relation to that in the differential cross section. Therefore, the agreement with experimental data must be of approximately the same qualitative character in all intervals of the excitation energy E_x, and this is indeed observed in Fig. 6. The quantitative discrepancy seen here indicates that, in all probability, it is necessary to take into account the contribution from higher partial waves (in particular, from the triplet states) to the final state of the proton pair [15]. In the region of energies realized at COSY and in Dubna (2–5 GeV), which is the subject of our prime interest, the contribution of higher partial waves is not expected to be sizable (see, for example, [21]). It should be noted that, in all previous calculations, the vector analyzing power was rigorously equal to zero. Thus, we can conclude that, in the excitation-energy interval $1 \leq E_x \leq 4$ MeV and at relatively low momentum transfers $|\mathbf{q}|$, the proton pair is detected in the $^1S_0$ state. Both in the nonrelativistic and in the relativistic approach, the reaction mechanism can be reliably described in terms of nucleon charge exchange in the impulse approximation, the accuracy of this approximation becoming higher with increasing primary energy. Within this approach, we have found that the differential cross sections are sufficiently large for experimentally studying the polarization features of reaction (1). Owing to this, one can obtain, among other things, additional information about elementary partial charge-exchange amplitudes. On the other hand, the observation of a proton pair originating from this process with a low excitation energy and having simultaneously zero vector analyzing power and significant tensor analyzing power may furnish unambiguous information about the character of initial deuteron polarization. In other words, this reaction may serve as a good polarimeter not only at low initial energies [15], but also at intermediate and relativistic initial energies. For the sake of completeness, the cross sections and tensor analyzing powers expected at the energies of the Dubna synchrophasotron are displayed in Figs. 7 and 8.

5. SUMMARY

Within the covariant approach based on the Bethe–Salpeter formalism, it has been shown that the reaction $\vec{d}(p,n)pp$ producing a proton pair of low excitation energy can be used as an efficient deuteron polarimeter at intermediate energies attainable at COSY and in Dubna and as a source of information about the amplitude for nucleon–nucleon charge exchange.

ACKNOWLEDGMENTS

We are grateful to A.I. Titov and Yu.N. Uzikov for stimulating discussions and support. L.P. Kaptari and S.S. Semikh gratefully acknowledge the hospitality extended to them at Institute for Nuclear and Hadron Physics (Rossendorf Research Center, Germany), where part of this study was performed.

This work was supported by grant nos. BMBF 06 DR 829/1 and WTZ RUS 98/678 and by the Heisenberg–Landau program (JINR–Germany). The work of S.S. Semikh was also supported by the Russian Foundation for Basic Research (project no. 00-15-96737).

APPENDIX A

Bethe–Salpeter Amplitudes

1. In the laboratory frame (rest frame), the components of the Bethe–Salpeter amplitude for the deuteron that appear in Eq. (15) are given by [33]

$$\Psi^M_{S^{++}}(k) = \mathcal{N}(\hat{k}_1 + m) \times \frac{1+\gamma_0}{2}\hat{\xi}_M(\hat{k}_2 - m)\psi_S(k_0, |\mathbf{k}|), \tag{A.1}$$

$$\Psi^M_{D^{++}}(k) = -\frac{\mathcal{N}}{\sqrt{2}}(\hat{k}_1 + m)\frac{1+\gamma_0}{2} \times \left(\hat{\xi}_M + \frac{3}{2|\mathbf{k}|^2}(\hat{k}_1 - \hat{k}_2)(k\xi_M)\right) \times (\hat{k}_2 - m)\psi_D(k_0, |\mathbf{k}|),$$

where $\xi_M = (0, \boldsymbol{\xi}_M)$; $k_{1,2}$ are 4-vectors on the mass shell,

$$k_1 = (E, \mathbf{k}), \quad k_2 = (E, -\mathbf{k}), \quad k = (k_0, \mathbf{k}), \quad E = \sqrt{\mathbf{k}^2 + m^2}; \tag{A.2}$$

and $\hat{k}_{1,2} \equiv k^\mu_{1,2}\gamma_\mu$. The quantities $\psi_{S,D}(k_0, |\mathbf{k}|)$ are partial amplitudes related to the partial vertex functions by the equations

$$\psi_{S,D}(k_0, |\mathbf{k}|) = \frac{G_{S,D}(k_0, |\mathbf{k}|)}{(M_d/2 - E)^2 - k_0^2}.$$

In formulas (A.1), the normalization factor is $\mathcal{N} = \frac{1}{\sqrt{8\pi}}\frac{1}{2E(E+m)}$.

2. The invariant functions b_i appearing in expansion (18) are related to the partial amplitudes $\phi_i \equiv \phi_i(r_0, |\mathbf{r}|)$ in the expansion in spin–angular harmonics by the equations [31]

$$b_1 = -\frac{\sqrt{2}}{16}a_1[D_1^-\phi_1 - D_1^+\phi_2] - \frac{1}{8}a_1a_2D_2\phi_3 + \frac{1}{\sqrt{s_f}}a_2r_0\phi_4,$$

$$b_2 = -\frac{1}{4}a_2\phi_4,$$

$$b_3 = \frac{\sqrt{2}}{2}a_1m^2[\phi_1 - \phi_2] - \frac{1}{2}a_1a_2(e^2 - 2m^2)\phi_3 + \frac{1}{2\sqrt{s_f}}a_2r_0\phi_4,$$

$$b_4 = -\frac{\sqrt{2}}{4}a_1m^2[\phi_1 - \phi_2] - a_1a_2m^2\phi_3,$$

where

$$a_1 = 1/(\sqrt{s_f}e), \quad a_2 = m/|\mathbf{r}|,$$
$$D_1^\pm = (\sqrt{s_f} \pm 2e)^2 - 4(4m^2 + r_0^2),$$
$$D_2 = s_f + 12e^2 - 16m^2 - 4r_0^2.$$

Here,

$$r_0 = \frac{(P', p)}{\sqrt{s_f}}, \quad |\mathbf{r}| = \sqrt{r_0^2 - p^2}, \qquad e = \sqrt{\mathbf{r}^2 + m^2}, \tag{A.3}$$

where p is the relative 4-momentum in (18). It is obvious from (A.3) that the 4-vector $r = (r_0, \mathbf{r})$ is the relative 4-momentum in the pp pair in its rest frame; throughout the present article, we adopt this notation. By analogy with (A.1) and (A.2), we define 4-vectors on the mass shell as

$$r_1 = (e, \mathbf{r}), \quad r_2 = (e, -\mathbf{r}).$$

The spin–angular harmonic for the $++$ component of the amplitude $\bar{\Psi}_{P'}$ can be represented in the form [31]

$$\Gamma_{^1S_0^{++}}(\hat{\mathbf{r}}) = \frac{1}{\sqrt{8\pi}(e+m)}(m - \hat{r}_2)\frac{1-\gamma_0}{2}\gamma_5(m + \hat{r}_1).$$

3. The explicit expressions for the scalar coefficients C_1, C_2, and C_3 appearing in Eq. (19) are

$$C_1 = B[(\mathbf{p}_p \cdot \mathbf{k})(d_1 - d_2) - (E+m)(p_p^0 + m) \times (d_1 + d_2) - (\mathbf{q} \cdot \mathbf{k})(p_p^0 + m)(d_3 + d_4) - (\mathbf{q} \cdot \mathbf{p}_p)(E+m)(d_3 - d_4)],$$

$$C_2 = \frac{3B}{\sqrt{2}(E-m)}[d_1(E - p_p^0 - 2m) - d_2(p_p^0 + E) + (d_4 - d_3)(2\mathbf{k} - \mathbf{q} \cdot \mathbf{q})],$$

$$C_3 = B[d_1 - d_2 + d_3(p_p^0 - E) + d_4(p_p^0 + E + 2m)],$$

where

$$B = 2m\mathcal{N}(M_d/2 - k_0 - E)\frac{1}{\sqrt{4\pi}}\sqrt{\frac{E+m}{p_p^0 + m}}, \qquad d_1 = -b_1 - 2b_2 + 2b_3 \tag{A.4}$$

$$+ (1 + [P_0'(p_1^0 - p_p^0) - p_1^2]/m^2)b_4,$$

$$d_2 = [(P_0' - 2[p_1^0 - p_p^0])b_2 - P_0'b_3]/m, \quad \text{(A.5)}$$

$$d_3 = (b_2 - b_3)/m, \quad \text{(A.6)}$$

$$d_4 = (p_1^0 - p_p^0)b_4/m^2. \quad \text{(A.7)}$$

Here, we have introduced the 4-vectors p_1 [see Eq. (18)] and p_p, the latter being on the mass shell; that is,

$$p_1 = \frac{P'}{2} + k - \frac{q}{2} = (p_1^0, \mathbf{p}_p),$$

$$p_p = (p_p^0, \mathbf{p}_p), \quad p_p^0 = \sqrt{m^2 + \mathbf{p}_p^2}, \quad \mathbf{p}_p = \mathbf{k} - \mathbf{q}.$$

In the plane-wave approximation, we have $p_1^0 = p_p^0$, and formulas (A.4)–(A.7) can be significantly simplified.

APPENDIX B

Helicity Wick Rotations

By definition, the state characterized by a momentum $\mathbf{p}$ and a helicity λ in some reference frame $\mathcal{O}$ can be obtained from the state characterized by the spin projection s_z with the aid of the Lorentz transformation from the rest frame $\mathcal{O}_{\text{rest}}$ to $\mathcal{O}$; that is,

$$|\mathbf{p};\lambda\rangle \equiv |\overset{0}{p}, s, s_z\rangle_{\mathcal{O}},$$

where $\overset{0}{p} = (m, 0, 0, 0)$. The Lorentz transformation $h(\mathbf{p})$ involves two operations performed consecutively: (i) the boost $l_z(v)$ along the z axis, where v is the particle velocity in the reference frame $\mathcal{O}$, and (ii) rotation in the direction from the z axis to $\mathbf{p}$—that is, $\mathcal{O} = r^{-1}(\phi, \theta, 0)l_z^{-1}(v)\mathcal{O}_{\text{rest}}$.

Let us now assume that there exists a state $|\mathbf{p};\lambda\rangle$ specified in the reference frame $\mathcal{O}$, and it is necessary find out how it is transformed upon the transition to another reference frame $\mathcal{O}'$ that is related to $\mathcal{O}$ by a Lorentz transformation l:

$$|\mathbf{p};\lambda\rangle_{\mathcal{O}'} = U(l^{-1})|\mathbf{p};\lambda\rangle.$$

According to the definition of helicity states, we have

$$U(l^{-1})|\mathbf{p};\lambda\rangle = U(l^{-1})U[h(\mathbf{p})]|\overset{0}{p};\lambda\rangle, \quad \text{(A.8)}$$

where $h(\mathbf{p})$ is the corresponding Lorentz transformation $\overset{0}{p} \to p$. Multiplying (A.8) by unity represented as $U[h(\mathbf{p}')]U^{-1}[h(\mathbf{p}')] = 1$, where $h(\mathbf{p}')$ is the transformation leading to the helicity state $|\mathbf{p}';\lambda\rangle = U[h(\mathbf{p}')]|\overset{0}{p},\lambda\rangle$ with the same vector $\mathbf{p}'$ ($\mathbf{p}'$ is obtained from $\mathbf{p}$ upon the transition from $\mathcal{O}$ to $\mathcal{O}'$), we obtain

$$U(l^{-1})|\mathbf{p};\lambda\rangle = U[h(\mathbf{p}')]\mathcal{R}|\overset{0}{p},\lambda\rangle,$$

where the operation $\mathcal{R} = U^{-1}[h(\mathbf{p}')]U(l^{-1})U[h(\mathbf{p})]$ can be represented as the succession of the transformations $\overset{0}{p} \to p \to p' \to \overset{0}{p}$, which is nothing but a three-dimensional rotation. We then have

$$|\mathbf{p},\lambda\rangle_{\mathcal{O}'} = D^{(s)}_{\lambda\lambda'}(\omega)|\mathbf{p}',\lambda'\rangle,$$

where ω is the set of Euler angles describing this rotation. In the case where the Lorentz transformation in question is an ordinary boost along the z axis with the velocity β, ω is a single angle of rotation about the y axis; that is,

$$\cos\omega = \cos\theta'\cos\theta + \gamma\sin\theta'\sin\theta,$$

where, as usual, $\gamma = 1/\sqrt{1-\beta^2}$ and θ and θ' are the polar angles of the vector $\mathbf{p}$ in the reference frames $\mathcal{O}$ and $\mathcal{O}'$, respectively. This operation is known as the Wick rotation of helicities, in contrast to the canonical Wigner rotation of spins. In our case, the z axis for the boost is directed along the vector $\mathbf{k} + \mathbf{p}$.

REFERENCES

1. S. Ishida, H. Sakai, H. Okamura, *et al.*, Phys. Lett. B **314**, 279 (1993); H. Sakai, T. Wakasa, T. Nonaka, *et al.*, Nucl. Phys. A **631**, 757 (1998).
2. M. Morlet *et al.*, Phys. Lett. B **247**, 228 (1990).
3. S. Kox and E. J. Beise (spokespersons), TJNAF experiments 94-018 "Measurement of the Deuteron Polarization at Large Momentum Transfers in $d(e,e')d$ Scattering"; http://www.jlab.org/ex_prog
4. E. Tomasi-Gustafsson, in *Proceedings of XIV International Seminar on High Energy Physics Problems,* Preprint No. E1, 2-2000-166, OIYaI (Joint Inst. for Nuclear Research, Dubna, 2000); http://relnp.jinr.ru/ishepp/XIV/
5. I. M. Sitnik *et al.*, JINR Rapid Commun., No. 2[70]-95, 19 (1995).
6. R. G. Arnold, C. E. Carlson, and F. Gross, Phys. Rev. C **23**, 363 (1981).
7. M. P. Rekalo and I. M. Sitnik, Phys. Lett. B **356**, 434 (1995); L. S. Azhgirei *et al.*, Phys. Lett. B **361**, 21 (1995).
8. V. G. Ableev *et al.*, Nucl. Phys. A **393**, 491 (1983); C. F. Perdrisat and V. Punjabi, Phys. Rev. C **42**, 1899 (1990); A. P. Kobushkin, A. I. Syamtomov, C. F. Perdrisat, and V. Punjabi, Phys. Rev. C **50**, 2627 (1994); J. Erö *et al.*, Phys. Rev. C **50**, 2687 (1994); J. Arvieux *et al.*, Nucl. Phys. A **431**, 6132 (1984).
9. V. I. Komarov (spokesman) *et al.*, *COSY proposal #20 "Exclusive Deuteron Break-up Study with Polarized Protons and Deuterons at COSY"*; V. I. Komarov *et al.*, KFA Annual Rep. Jülich (1995), p. 64; A. K. Kacharava *et al.*, Preprint No. E1-96-42, OIYaI (Joint Inst. for Nuclear Research, Dubna, 1996); C. F. Perdrisat (spokesperson) *et al.*, *COSY proposal #68.1 "Proton-to-Proton Polarization Transfer in Backward Elastic Scattering"*.

10. M. P. Rekalo, N. M. Piskunov, and I. M. Sitnik, Few-Body Syst. **23**, 187 (1998); Preprint No. E4-96-328, OIYaI (Joint Inst. for Nuclear Research, Dubna, 1996); Yad. Fiz. **57**, 2170 (1994) [Phys. At. Nucl. **57**, 2089 (1994)].
11. V. P. Ladygin and N. B. Ladygina, J. Phys. G **23**, 847 (1997); V. P. Ladygin, Phys. At. Nucl. **60**, 1238 (1997).
12. L. P. Kaptari, B. Kämpfer, S. M. Dorkin, and S. S. Semikh, Phys. Rev. C **57**, 1097 (1998).
13. W. Grüebler, P. A. Schmelzbach, and V. König, Phys. Rev. C **22**, 2243 (1980).
14. J. Yonnet *et al.*, in *Proceedings of XIII International Seminar on High-Energy Physics Problems,* Preprint No. E1,2-98-154, JINR (Dubna, 1998).
15. D. V. Bugg and C. Wilkin, Phys. Lett. B **152B**, 37 (1985); Nucl. Phys. A **467**, 575 (1987).
16. S. Kox *et al.*, Nucl. Instrum. Methods Phys. Res. A **346**, 527 (1994).
17. T. Motobayashi *et al.*, Phys. Lett. B **233**, 69 (1989).
18. J. Carbonell, M. Barbaro, and C. Wilkin, Nucl. Phys. A **529**, 653 (1991).
19. S. Kox *et al.*, Nucl. Phys. A **556**, 621 (1993).
20. D. V. Bugg, A. Hasan, and R. L. Shypit, Nucl. Phys. A **477**, 546 (1988); C. Furget *et al.*, Nucl. Phys. A **631**, 747 (1998).
21. B. S. Aladashvili *et al.*, Nucl. Phys. B **86**, 461 (1975).
22. D. E. Greiner *et al.*, Phys. Rev. Lett. **35**, 152 (1975).
23. L. P. Kaptari and A. I. Titov, Yad. Fiz. **39**, 612 (1984) [Sov. J. Nucl. Phys. **39**, 387 (1984)].
24. A. Yu. Umnikov, L. P. Kaptari, and F. C. Khanna, Phys. Rev. C **56**, 1700 (1997); A. Yu. Umnikov, L. P. Kaptari, K. Yu. Kazakov, and F. C. Khanna, Phys. Lett. B **334**, 163 (1994).
25. A. Yu. Umnikov, Z. Phys. A **357**, 333 (1997).
26. A. Bouquet and B. Diu, Nuovo Cimento A **35**, 157 (1976).
27. P. W. Keaton, Jr., J. L. Gammel, and G. G. Ohlsen, Ann. Phys. (N.Y.) **85**, 152 (1974).
28. F. Gross, Phys. Rev. **186**, 1448 (1969).
29. C. Ciofi degli Atti, D. Faralli, A. Yu. Umnikov, and L. P. Kaptari, Phys. Rev. C **60**, 034 003 (1999).
30. S. Mandelstam, Proc. R. Soc. London, Ser. A **233**, 123 (1955).
31. S. G. Bondarenko, V. V. Burov, M. Beyer, and S. M. Dorkin, Phys. Rev. C **58**, 3143 (1998).
32. J. J. Kubis, Phys. Rev. D **6**, 547 (1972).
33. L. P. Kaptari, A. Yu. Umnikov, S. G. Bondarenko, *et al.*, Phys. Rev. C **54**, 986 (1996).
34. A. Yu. Korchin and A. V. Shebeko, Preprint No. 88-56, KFTI (Kharkov, 1988).
35. G. C. Wick, Phys. Rev. **96**, 1124 (1954).
36. V. M. Kolybasov and N. Ya. Smorodinskaya, Phys. Lett. B **37B**, 272 (1971).
37. L. P. Kaptari, B. Kämpfer, S. M. Dorkin, and S. S. Semikh, Few-Body Syst. **27**, 189 (1999).
38. L. P. Kaptari, B. Kämpfer, S. M. Dorkin, and S. S. Semikh, Phys. Lett. B **404**, 8 (1997).
39. http://nn-online.sci.kun.nl
40. http://said.phys.vt.edu
41. V. G. J. Stoks, R. A. M. Klomp, M. C. M. Rentmeester, and J. J. de Swart, Phys. Rev. C **48**, 792 (1993).
42. R. A. Arndt, I. I. Strakovsky, and R. L. Workman, nucl-th/0004039; Phys. Rev. C (in press).
43. C. Bourrely, E. Leader, and J. Soffer, Phys. Rep. **59**, 95 (1980).

Translated by A. Isaakyan

Physics of Atomic Nuclei, Vol. 65, No. 3, 2002, pp. 456–461. Translated from Yadernaya Fizika, Vol. 65, No. 3, 2002, pp. 483–488.

NUCLEI
Theory

Effect of Tensor Nucleon–Nucleon Forces on the Nucleon–Nucleus Optical Potential

S. M. Kravchenko

Institute for Applied Physics, National Academy of Sciences of Ukraine, Sumy, Ukraine

Received September 19, 2000; in final form, February 5, 2001

Abstract—In the approximation of unpolarized nuclear matter, the optical potential for nucleon–nucleus scattering is calculated on the basis of the effective Skyrme interaction with allowance for tensor nucleon–nucleon forces. It is shown that the tensor Skyrme forces make a significant contribution to the imaginary part of the optical potential. The effect of tensor nucleon–nucleon forces on the radial distribution of the imaginary part of the optical potential is investigated by considering the example of elastic neutron scattering by ^{40}Ca nuclei at scattering energies of about a few tens of MeV. © *2002 MAIK "Nauka/Interperiodica".*

1. In the approximation of nuclear matter, the nucleon–nucleus optical potential obtained by calculating the mass operator for the single-particle Green's function [1, 2] is considered here for the effective density-dependent nucleon–nucleon Skyrme interaction [3–5].

It is well known [5, 6] that the effective nucleon–nucleon Skyrme interaction involves components describing tensor interaction between intranuclear nucleons. However, tensor nucleon–nucleon forces are usually disregarded in studying the structure of nuclei and various collective phenomena in them [7], as well as nucleon–nucleus scattering [8–10]. It should also be noted that the disregard of tensor nucleon–nucleon forces is characteristic of various calculations based on Skyrme forces or on other effective nucleon–nucleon interactions [7]. In many cases, this is justified, since any density-dependent effective nucleon–nucleon interaction, including the Skyrme interaction, takes partly into account the contribution of tensor forces [11]. For example, the effect of tensor Skyrme forces on the single-particle spectra of some even–even nuclei was analyzed in [5], where it was shown that the contribution of these forces is not decisive for the features of these spectra.

The optical potential for the interaction of nucleons with even–even nuclei was investigated in [12] without taking into account tensor forces. As was shown in [13], however, the tensor component of the effective Skyrme interaction makes a significant contribution to the central and the tensor spin–spin potential for the interaction of nucleons with odd nuclei.

Hence, it is of particular interest to investigate the effect of tensor Skyrme forces on the optical potential for the interaction of nucleons with even nuclei.

In the present study, the nucleon–nucleus optical potential is analyzed on the basis of a calculation of the mass operator for the single-particle Green's function [8–10, 12], this calculation being performed with allowance for the tensor component of the effective Skyrme nucleon–nucleon interaction. It is shown, among other things, that, in the Hartree–Fock approximation (within the method used here, this is the zero-order approximation [12]), the tensor nucleon–nucleon interaction does not contribute to the mass operator—that is, to the real part of the optical potential. In this mass operator, the expression that determines the imaginary part of the optical potential develops, however, in the second order of perturbation theory in the effective nucleon–nucleon interaction [12], additional terms that are quadratic in the parameters of the tensor Skyrme interaction. The effect of the tensor Skyrme forces on the radial dependence of the optical potential is analyzed here by considering the example of neutron scattering by ^{40}Ca nuclei.

2. Let us represent the effective Skyrme nucleon–nucleon interaction in the form [4, 5]

$$v = v_1 + v_2(\rho) + v_{\rm te} + v_{\rm to}, \qquad (1)$$

where v_1 and $v_2(\rho)$ are the components that are, respectively, independent of and dependent on the density ρ, while $v_{\rm te}$ and $v_{\rm to}$ are, respectively, the even and the odd component of the tensor interaction. The terms appearing in expression (1) are given by

$$v_1 = t_0(1 + x_0P_\sigma)\delta(\mathbf{r}) + \frac{1}{2}t_1(1 + x_1P_\sigma) \qquad (2)$$
$$\times \left[\mathbf{k}'^2\delta(\mathbf{r}) + \delta(\mathbf{r})\mathbf{k}^2\right] + t_2(1 + x_2P_\sigma)\mathbf{k}'\delta(\mathbf{r})\mathbf{k}$$
$$+ iW_0\left[\mathbf{k}' \times \delta(\mathbf{r})\mathbf{k}\right](\boldsymbol{\sigma}_1 + \boldsymbol{\sigma}_2),$$

1063-7788/02/6503-0456$22.00

$$v_2(\rho) = \frac{1}{6}t_3(1+x_3P_\sigma)\rho^\gamma(\mathbf{R})\delta(\mathbf{r}) \quad (3)$$
$$+\frac{1}{2}t_4(1+x_4P_\sigma)\left[\mathbf{k}'^2\rho(\mathbf{R})\delta(\mathbf{r})+\delta(\mathbf{r})\rho(\mathbf{R})\mathbf{k}^2\right]$$
$$+t_5(1+x_5P_\sigma)\mathbf{k}'\rho(\mathbf{R})\delta(\mathbf{r})\mathbf{k},$$

$$v_{\rm te} = \frac{1}{2}T \quad (4)$$
$$\times\left\{\left[(\boldsymbol{\sigma}_1\cdot\mathbf{k}')(\boldsymbol{\sigma}_2\cdot\mathbf{k}')-\frac{1}{3}(\boldsymbol{\sigma}_1\cdot\boldsymbol{\sigma}_2)\mathbf{k}'^2\right]\delta(\mathbf{r})\right.$$
$$\left.+\delta(\mathbf{r})\left[(\boldsymbol{\sigma}_1\cdot\mathbf{k})(\boldsymbol{\sigma}_2\cdot\mathbf{k})-\frac{1}{3}(\boldsymbol{\sigma}_1\cdot\boldsymbol{\sigma}_2)\mathbf{k}^2\right]\right\},$$

$$v_{\rm to} = U\left\{(\boldsymbol{\sigma}_1\cdot\mathbf{k}')\delta(\mathbf{r})(\boldsymbol{\sigma}_2\cdot\mathbf{k})\right. \quad (5)$$
$$\left.-\frac{1}{3}(\boldsymbol{\sigma}_1\cdot\boldsymbol{\sigma}_2)(\mathbf{k}'\cdot\delta(\mathbf{r})\mathbf{k})\right\},$$

where the notation used is identical to that in [4, 5, 7, 9, 10].

In the approximation of unpolarized nuclear matter (that is, for even–even nuclei), the real part of the optical potential $U_{\alpha\alpha}$ based on the interaction in (1) with $v_{\rm te} = v_{\rm to} = 0$ was calculated in [12]. The corresponding expression for $U_{\alpha\alpha}$ is presented in the Appendix.

Since the potential $U_{\alpha\alpha}$ is determined by the antisymmetrized diagonal matrix elements of the interaction in (1) [7, 12], the tensor nucleon–nucleon interaction specified by Eqs. (4) and (5) does not contribute to the real part of the optical potential in the approximation of unpolarized nuclear matter.

In the second order of perturbation theory in the effective nucleon–nucleon interaction, the imaginary part of the mass operator for the single-particle Green's function is given by [8–10, 12]

$$M_{\alpha\alpha}(\varepsilon) = -\pi\sum_{\lambda\mu\nu}\langle\alpha\nu|v|\lambda\mu\rangle\langle\lambda\mu|v(1-P)|\alpha\nu\rangle \quad (6)$$
$$\times(1-n_\lambda)(1-n_\mu)n_\nu\delta(\varepsilon+\varepsilon_\nu-\varepsilon_\lambda-\varepsilon_\mu),$$

where α,ν (λ,μ) are quantum numbers that characterize states of two interacting nucleons, ε_μ stands for single-particle energies, n_μ are occupation numbers, and P is the operator executing the permutations of spatial, spin, and isospin variables.

Substituting the Skyrme interaction specified by Eqs. (1)–(5) into (6) and replacing single-particle wave functions by plane waves, we represent the imaginary part of the optical potential in the form

$$W_{\alpha\alpha}(r) = -\frac{1}{64\pi^5}\sum_{i=1}^{7}W_i, \quad (7)$$

$$W_1 = \left(2g_{00}+\frac{1}{18}g_{33}\rho^{2\gamma}+\frac{2}{3}g_{03}\rho^\gamma\right) \quad (8)$$
$$\times[I_1(\tau_\alpha,n)+I_1(\tau_\alpha,p)]$$
$$-\left(2h_{00}+\frac{1}{18}h_{33}\rho^{2\gamma}+\frac{2}{3}h_{03}\rho^\gamma\right)I_1(\tau_\alpha,\tau_\alpha),$$

$$W_2 = \left(2g_{01}+2g_{04}\rho+\frac{1}{3}g_{13}\rho^\gamma+\frac{1}{3}g_{34}\rho^{\gamma+1}\right) \quad (9)$$
$$\times[I_2(\tau_\alpha,n)+I_2(\tau_\alpha,p)]$$
$$-\left(2h_{01}+2h_{04}\rho+\frac{1}{3}h_{13}\rho^\gamma+\frac{1}{3}h_{34}\rho^{\gamma+1}\right)I_2(\tau_\alpha,\tau_\alpha),$$

$$W_3 = \left(\frac{1}{2}g_{11}+\frac{1}{2}g_{44}\rho^2+g_{14}\rho+\frac{1}{3}T^2\right) \quad (10)$$
$$\times[I_3(\tau_\alpha,n)+I_3(\tau_\alpha,p)]$$
$$-\left(\frac{1}{2}h_{11}+\frac{1}{2}h_{44}\rho^2+h_{14}\rho+\frac{1}{3}T^2\right)I_3(\tau_\alpha,\tau_\alpha),$$

$$W_4 = 2\left(2g_{02}+2g_{05}\rho+\frac{1}{3}g_{23}\rho^\gamma+\frac{1}{3}g_{35}\rho^{\gamma+1}\right) \quad (11)$$
$$\times[I_4(\tau_\alpha,n)+I_4(\tau_\alpha,p)],$$

$$W_5 = 2\left(g_{12}+g_{15}\rho+g_{24}\rho+g_{45}\rho^2+\frac{2}{3}UT\right) \quad (12)$$
$$\times[I_5(\tau_\alpha,n)+I_5(\tau_\alpha,p)],$$

$$W_6 = 2\left(g_{22}+g_{55}\rho^2+2g_{25}\rho+\frac{2}{3}U^2\right) \quad (13)$$
$$\times[I_6(\tau_\alpha,n)+I_6(\tau_\alpha,p)]$$
$$+2\left(h_{22}+h_{55}\rho^2+2h_{25}\rho+\frac{2}{3}U^2\right)I_6(\tau_\alpha,\tau_\alpha),$$

$$W_7 = (4W_0^2+U^2-T^2)[I_7(\tau_\alpha,n)+I_7(\tau_\alpha,p)]$$
$$+(4W_0^2+U^2+T^2)I_7(\tau_\alpha,\tau_\alpha), \quad (14)$$

where $\rho=\rho(r)$; $g_{ij} = t_it_j\left(1+x_ix_j+\frac{x_i+x_j}{2}\right)$; $h_{ij} = t_it_j\left(x_i+x_j+\frac{1+x_ix_j}{2}\right)$, $i,j=0,1,\ldots,5$; and

$$I_i(\tau_\alpha,\tau_\mu) \quad (15)$$
$$=\int d\mathbf{K}_\mu d\mathbf{K}_\lambda d\mathbf{K}_\nu f_i(\mathbf{K}_\alpha,\mathbf{K}_\mu,\mathbf{K}_\lambda,\mathbf{K}_\nu)$$
$$\times\delta(E+\varepsilon_\mu-\varepsilon_\lambda-\varepsilon_\nu)\delta(\mathbf{K}_\alpha+\mathbf{K}_\mu-\mathbf{K}_\lambda-\mathbf{K}_\nu)$$
$$\times n_\mu(1-n_\lambda)(1-n_\nu), \quad i=1,\ldots,7.$$

In expression (15), τ_μ is the isospin index of the μ state ($\tau_\mu = n$ for neutrons and $\tau_\mu = p$ for protons) with $\tau_\lambda = \tau_\alpha$ and $\tau_\nu = \tau_\mu$, while the functions

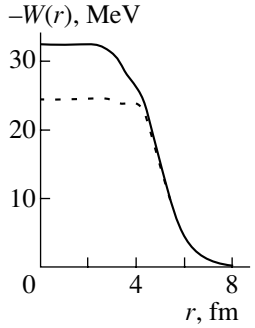

Fig. 1. Radial distribution of the imaginary part of the optical potential for the elastic scattering of 50-MeV neutrons by ^{40}Ca nuclei according to the calculation (solid curve) with and (dashed curve) without allowance for the tensor Skyrme forces (SkM^* parametrization).

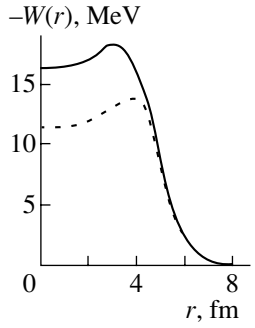

Fig. 2. As in Fig. 1, but for the *Ska* parametrization.

$f_i(\mathbf{K}_\alpha, \mathbf{K}_\mu, \mathbf{K}_\lambda, \mathbf{K}_\nu)$ $(i = 1, \ldots, 7)$ are given by [8]

$$f_1 = 1, \quad f_2 = \mathbf{K}_{\alpha\mu}^2 + \mathbf{K}_{\lambda\nu}^2, \tag{16}$$

$$f_3 = \left(\mathbf{K}_{\alpha\mu}^2 + \mathbf{K}_{\lambda\nu}^2\right)^2, \quad f_4 = \mathbf{K}_{\alpha\mu} \cdot \mathbf{K}_{\lambda\nu},$$

$$f_5 = \left(\mathbf{K}_{\alpha\mu}^2 + \mathbf{K}_{\lambda\nu}^2\right)(\mathbf{K}_{\alpha\mu} \cdot \mathbf{K}_{\lambda\nu}),$$

$$f_6 = (\mathbf{K}_{\alpha\mu} \cdot \mathbf{K}_{\lambda\nu})^2, \quad f_7 = (\mathbf{K}_{\alpha\mu} \times \mathbf{K}_{\lambda\nu})^2,$$

where $\mathbf{K}_{\alpha\mu} = (\mathbf{K}_\alpha - \mathbf{K}_\mu)/2$ and $\mathbf{K}_{\lambda\nu} = (\mathbf{K}_\lambda - \mathbf{K}_\nu)/2$.

The integrals in (15) can be calculated analytically [8]. For the case of symmetric nuclear matter (that is, for nuclear matter consisting of an equal number of neutrons and protons) considered below, the corresponding expressions are presented in the Appendix.

Thus, we see that, in expressions (10) and (12)–(14), which determine the imaginary part of the nucleon–nucleus optical potential, there arise terms describing the contribution of the tensor nucleon–nucleon interaction [recall that it is specified by Eqs. (4) and (5)], which are quadratic in the parameters T and U of this interaction.

3. For the example of neutron scattering by ^{40}Ca nuclei, in which case the approximation of unpolarized symmetric nuclear matter is valid, we further consider the effect of tensor nucleon–nucleon forces on the radial distribution of the imaginary part of the optical potential.

As was mentioned above, virtually no parametrizations that are currently used for the effective Skyrme interaction include the parameters T and U, which characterize the strength of tensor forces. They were taken into account only in [5, 6]; it should be noted that three-particle velocity-dependent Skyrme forces were used in [6], whereas a two-particle density-dependent effective interaction is employed here.

Two approaches to parametrizing tensor Skyrme forces were proposed in [5]. The first approach reduces to calculating the parameters T and U on the basis of a specific realistic potential for free nucleon–nucleon scattering, while the second one consists in fitting these parameters on the basis of an analysis of the single-particle spectra of the ^{48}Ca, ^{56}Ni, and ^{208}Pb nuclei.

In [13], both these parametrizations of the tensor forces were used in studying the real part of the optical potential for the interaction of nucleons with odd nuclei. As a result, it was shown that the second approach is preferable in describing experimental data on elastic nucleon–nucleus scattering. In this study, we therefore use the T and U values that were obtained from the analysis of the single-particle nuclear spectra.

According to [5], the admissible values of the parameters T and U [under the condition that the remaining parameters of the effective interaction (1) are preset] are constrained as

$$\alpha_0 + \beta_0 \geqslant 0, \quad -80 \leqslant \alpha_0 \leqslant 0, \quad 0 \leqslant \beta_0 \leqslant 80, \tag{17}$$

where

$$\alpha_0 = \frac{5}{12}U + \frac{1}{8}(t_1 - t_2) - \frac{1}{8}(t_1 x_1 + t_2 x_2), \tag{18}$$

$$\beta_0 = \frac{5}{24}(T + U) - \frac{1}{8}(t_1 x_1 + t_2 x_2). \tag{19}$$

In the particular case of $\alpha_0 = \beta_0 = 0$, we obtain $T = -U = 163.5$ MeV fm^5 for the SkM^* parametrization [14] and $T = -U = 191.574$ MeV fm^5 for the *Ska* parametrization [15].

The results obtained by numerically calculating the imaginary part of the optical potential for elastic neutron scattering by ^{40}Ca nuclei are displayed in Figs. 1 and 2. In this calculation, the empirical Negele formula [16] was used to describe the nucleon-density distribution in the ^{40}Ca nucleus.

Figures 1 and 2 show the radial distributions of the imaginary part of the optical potential for neutron scattering at $E = 50$ MeV that were calculated

Table 1. Volume integrals and root-mean-square radii of the imaginary part of the optical potential for elastic neutron scattering by ^{40}Ca nuclei according to the calculation performed with $[W(r)]$ and without $[W_0(r)]$ allowance for the tensor Skyrme forces; {also presented are the analogous results for the phenomenological optical potential $\tilde{W}(r)$ [18]}

Forces	Potential	J_W, MeV fm^3		r_W, fm	
		$E = 0$	$E = 50$ MeV	$E = 0$	$E = 50$ MeV
SkM^*	$W(r)$	75.40	462.40	4.03	4.39
	$W_0(r)$	71.31	414.89	4.08	4.50
Ska	$W(r)$	43.91	268.48	4.06	4.34
	$W_0(r)$	40.75	230.27	4.12	4.48
$S3m$	$W(r)$	57.99	374.59	3.90	4.18
	$W_0(r)$	55.08	312.34	3.94	4.27
$S4$	$W(r)$	25.93	170.76	4.05	4.20
	$W_0(r)$	23.68	141.54	4.11	4.31
$S5$	$W(r)$	22.29	155.97	4.09	4.20
	$W_0(r)$	20.18	127.36	4.15	4.29
	$\tilde{W}(r)$	52.20	81.64	4.84	4.35

with or without allowing for the tensor nucleon–nucleon forces obtained on the basis of the SkM^* and Ska parametrizations, respectively. As can be seen from these figures, the inclusion of the tensor Skyrme forces leads to the noticeable increase in the depth of $W(r)$ in the interior of the nucleus (approximately by a factor of 1.3 for the SkM^* forces and by a factor of 1.4 for the Ska forces), but this does not affect the behavior of the imaginary part of the optical potential in the surface region.

In order to characterize the radial distribution of $W(r)$, the values of the volume integrals J_W,

$$J_W = -\frac{1}{A}\int d^3r W(r), \qquad (20)$$

where A is the number of intranuclear nucleons, and the values of the root-mean-square radii r_W,

$$r_W^2 = \frac{\int d^3r r^2 W(r)}{\int d^3r W(r)}, \qquad (21)$$

are listed in Table 1. We note that the inclusion of the tensor Skyrme forces leads to an increase in the volume integrals and to a decrease in the root-mean-square radii, the relative contribution of the tensor forces becoming greater at higher scattering energy.

It is also worth noting that the T and $|U|$ values obtained from the condition $\alpha_0 = \beta_0 = 0$ are minimal in the region specified by (17). Therefore, a variation of the parameters α_0 and β_0 leads to a further increase in the depth of $W(r)$.

Table 1 also displays the values of J_W and r_W for the $S3m$, $S4$, and $S5$ forces [17] and for the phenomenological optical potential (last row in the table) that was obtained from an analysis of experimental data on elastic nucleon–nucleus scattering [18]. The best agreement is achieved if we use the $S4$ and $S5$ forces (up to 50 MeV) and the Ska and $S3m$ forces (up to 20 MeV). At the same time, the best description of the real part of the optical potential (A.1) is obtained with the $S3m$, Ska, and SkM^* Skyrme forces (see Table 2).

In Table 2, the quantities J_U and r_U are defined in the same way as the quantities J_W (20) and r_W

Table 2. Volume integrals and root-mean-square radii of the real part of the optical potential for elastic neutron scattering by ^{40}Ca nuclei according to the calculation that employs various parametrizations of the Skyrme forces (given additionally in the last row are the analogous results for the phenomenological optical potential from [18])

Forces	J_U, MeV fm^3		r_U, fm	
	$E = 0$	$E = 50$ MeV	$E = 0$	$E = 50$ MeV
SkM^*	498.75	426.93	3.91	3.98
Ska	464.29	315.05	3.89	4.01
$S3m$	463.15	374.59	3.82	3.88
$S4$	431.01	206.92	3.86	4.02
$S5$	420.47	145.30	3.87	4.05
	500.67	373.75	4.06	4.06

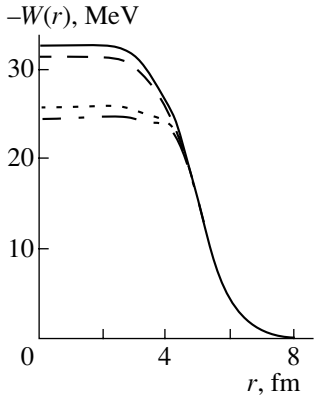

Fig. 3. As in Fig. 1, but either (solid curve) with or (dash-dotted curve) without allowance for the tensor Skyrme forces, as well as with allowance for only (long-dashed curve) odd ($T = 0$) or (short-dashed curve) even ($U = 0$) component of these forces.

(21) and the values in the last row correspond to the phenomenological optical potential from [18].

Further, we investigate the partial contributions of the tensor Skyrme forces acting in the even and in the odd states of the relative motion of two nucleons. Figure 3 shows the radial distribution of $W(r)$ at $E = 50$ MeV for the SkM^* parametrization according to the calculation allowing only for the even or only for the odd component of the tensor forces. As can be seen from this figure, the contribution to the imaginary part of the optical potential from the odd component (at the center of nucleus) considerably exceeds the contribution from the even component:

$$\frac{W_{\rm odd}(0) - W_0(0)}{W_{\rm even}(0) - W_0(0)} \approx 5.4. \qquad (22)$$

This is a consequence of the antisymmetrization of the matrix elements of the effective interaction that determine the imaginary part of the optical potential. Indeed, it can be seen from formulas (10) and (14) that, at $\tau_\alpha = n$ (neutron scattering), the terms proportional to T^2 cancel partly, in contrast to the terms proportional to U^2 [see formulas (13), (14)].

4. Thus, we have demonstrated that the tensor nucleon–nucleon forces determine, to a considerable extent, the imaginary part of the optical potential for nucleon–nucleus scattering, the main contribution coming from the component of the tensor forces that corresponds to the interaction of two nucleons in odd states of their relative motion.

The present analysis has revealed that, at least for $E < 20$ MeV, the optical potential for nucleon–nucleus scattering can be calculated by using the $S3m$ and Ska forces. In order to achieve better agreement between the microscopic optical potential and phenomenological ones, it seems necessary to calculate simultaneously the basic properties of nuclei and the relevant optical potentials. Preliminary calculations show that even a small (smaller than 5%) variation in the parameters t_0 and t_3 of the Skyrme forces makes it possible to improve considerably the accuracy in describing elastic nucleon–nucleus scattering, basic properties of bound nuclear states concurrently undergoing only minor changes (within 1%).

Another way to improve the results obtained here consists in studying more comprehensively and consistently taking into account those components of the Skyrme forces that are proportional to the parameters t_4 and t_5. These terms make a dominant contribution to the Hartree–Fock potential (and, hence, to the optical potential) only near the nuclear surface and, in principle, enable one to describe better the smearing of the surface nuclear layer.

ACKNOWLEDGMENTS

I am grateful to A.P. Soznik for an enlightening discussion on the results obtained in this study.

APPENDIX

In the approximation of unpolarized nuclear matter, the real part of the optical potential is given by [12]

$$U_{\alpha\alpha}(r,E) = \frac{m^*_\alpha}{m_\alpha}\Bigg\{ g_0\rho - h_0\rho_\alpha + \frac{1}{4}\kappa[g_1 + g_2 + (g_4+g_5)\rho] - \frac{1}{4}\kappa_\alpha[h_1 - h_2 + (h_4-h_5)\rho] + \frac{1}{6}\rho^\gamma(g_3\rho - h_3\rho_\alpha) + \frac{1}{4}(g_4+g_5)\rho\kappa - \frac{1}{4}(h_4-h_5)\sum_q \rho_q\kappa_q + \frac{1}{12}\gamma\rho^{\gamma-1} \times \left(g_3\rho^2 - h_3\sum_q \rho_q^2\right)\Bigg\} + \left(1 - \frac{m^*_\alpha}{m_\alpha}\right)\frac{M}{M+m_\alpha}E, \qquad (A.1)$$

where m_α is the mass of the incident nucleon; M is the target-nucleus mass; E is the scattering energy; $\alpha = \{n,p\}$ is the isospin index; $g_i = t_i(1 + x_i/2)$ and $h_i = t_i(1/2 + x_i)$ with $i = 0, 1, \ldots, 5$; $\kappa = \frac{3}{5}\left(3\pi^2\rho/2\right)^{2/3}\rho$; $\kappa_\alpha = \frac{3}{5}(3\pi^2\rho_\alpha)^{2/3}\rho_\alpha$; and m^*_α is an effective mass that satisfies the relation

$$\frac{m_\alpha}{m^*_\alpha} = 1 + \frac{1}{4}\frac{2m_\alpha}{\hbar^2}\{[g_1 + g_2 + (g_4+g_5)\rho]\rho - [h_1 - h_2 + (h_4-h_5)\rho]\rho_\alpha\}. \qquad (A.2)$$

In the approximation of symmetric nuclear matter, we have $\rho_n = \rho_p = \rho/2$ and $m_n^* = m_p^* = m^*$, while the integrals in (15) become [8]

$$I_1 = \frac{2m^*}{\hbar^2}\frac{2\pi^2}{15K_\alpha}\left[(5K_\alpha^2 - 7K_\mathrm{F}^2)K_\mathrm{F}^3 + 2(2K_\mathrm{F}^2 - K_\alpha^2)^{5/2}\theta(2K_\mathrm{F}^2 - K_\alpha^2)\right], \quad \text{(A.3)}$$

$$I_2 = \frac{2m^*}{\hbar^2}\frac{\pi^2}{105K_\alpha}[(35K_\alpha^4 - 14K_\alpha^2K_\mathrm{F}^2 - 45K_\mathrm{F}^4)K_\mathrm{F}^3 + 4(K_\alpha^2 + 5K_\mathrm{F}^2) \times (2K_\mathrm{F}^2 - K_\alpha^2)^{5/2}\theta(2K_\mathrm{F}^2 - K_\alpha^2)], \quad \text{(A.4)}$$

$$I_3 = \frac{m^*}{\hbar^2}\frac{\pi^2}{945K_\alpha}[(315K_\alpha^6 + 441K_\alpha^4K_\mathrm{F}^2 - 747K_\alpha^2K_\mathrm{F}^4 - 473K_\mathrm{F}^6)K_\mathrm{F}^3 - 8(5K_\alpha^4 - 20K_\alpha^2K_\mathrm{F}^2 - 43K_\mathrm{F}^4)(2K_\mathrm{F}^2 - K_\alpha^2)^{5/2}\theta(2K_\mathrm{F}^2 - K_\alpha^2)], \quad \text{(A.5)}$$

$$I_4 = I_5 = 0, \quad \text{(A.6)}$$

$$I_6 = \frac{m^*}{4\hbar^2}\frac{\pi^2}{945K_\alpha}[(105K_\alpha^6 - 189K_\alpha^4K_\mathrm{F}^2 + 711K_\alpha^2K_\mathrm{F}^4 - 803K_\mathrm{F}^6)K_\mathrm{F}^3 - 16(2K_\alpha^2 - 13K_\mathrm{F}^2) \times (2K_\mathrm{F}^2 - K_\alpha^2)^{7/2}\theta(2K_\mathrm{F}^2 - K_\alpha^2)], \quad \text{(A.7)}$$

$$I_7 = I_3 - I_6, \quad \text{(A.8)}$$

where $\theta(x)$ is a theta function, $K_\mathrm{F} = \left(3\pi^2\rho/2\right)^{1/3}$ is the Fermi momentum, and

$$K_\alpha^2 = \frac{2m_\alpha}{\hbar^2}\left(\frac{M}{M+m_\alpha}E - U_{\alpha\alpha}\right). \quad \text{(A.9)}$$

REFERENCES

1. J. S. Bell and E. J. Squires, Phys. Rev. Lett. **3**, 96 (1959).
2. D. A. Kirzhnits, *Field Theoretical Methods in Many-Body Systems* (Gosatomizdat, Moscow, 1963; Pergamon, Oxford, 1967).
3. T. H. R. Skyrme, Nucl. Phys. **9**, 615 (1958/1959).
4. S. Krewald, V. Klemt, J. Speth, and A. Faessler, Nucl. Phys. A **281**, 166 (1977).
5. Fl. Stancu, D. M. Brink, and H. Flocard, Phys. Lett. B **68B**, 108 (1977).
6. Keh-Fei Liu, Hongde Luo, Zhongyu Ma, *et al.*, Nucl. Phys. A **534**, 1 (1991).
7. B. I. Barts, Yu. L. Bolotin, E. V. Inopin, and V. Yu. Gonchar, *Hartree–Fock Method in the Theory of the Nucleus* (Naukova Dumka, Kiev, 1982).
8. Qingbiao Shen, Jingshang Zhang, Ye Tian, *et al.*, Z. Phys. A **303**, 69 (1981).
9. Lingxiao Ge, Yizhong Zhuo, and N. Wolfgang, Nucl. Phys. A **459**, 77 (1986).
10. Guo-Qiang Li, Jian-Qing Shi, and Qin Gao, Nucl. Phys. A **515**, 273 (1990).
11. H. A. Bethe, Phys. Rev. **167**, 879 (1968).
12. S. M. Kravchenko, V. I. Kuprikov, and A. P. Soznik, Int. J. Mod. Phys. E **7**, 465 (1998).
13. S. M. Kravchenko and A. P. Soznik, Int. J. Mod. Phys. E **8**, 137 (1999).
14. J. Bartel, P. Quentin, M. Brack, *et al.*, Nucl. Phys. A **386**, 79 (1982).
15. H. S. Köhler, Nucl. Phys. A **258**, 301 (1976).
16. J. W. Negele, Phys. Rev. C **1**, 1260 (1970).
17. M. Beiner, H. Flocard, N. van Giai, and P. Quentin, Nucl. Phys. A **238**, 29 (1975).
18. G. M. Honoré, W. Tornow, C. R. Howell, *et al.*, Phys. Rev. C **33**, 1129 (1986).

Translated by A. Isaakyan

Physics of Atomic Nuclei, Vol. 65, No. 3, 2002, pp. 462–477. Translated from Yadernaya Fizika, Vol. 65, No. 3, 2002, pp. 489–503.

NUCLEI
Theory

Reactions Involving the Flip of the Deuteron Spin and Isospin and Supermultiplet Potential Model for the Interaction of Extremely Light Clusters

V. M. Lebedev, V. G. Neudatchin, and B. G. Struzhko[1)]

Institute of Nuclear Physics, Moscow State University, Vorob'evy gory, Moscow, 119899 Russia

Received December 22, 2000

Abstract—On the basis of the Migdal–Watson approximation, various data on the double- and triple-differential cross sections for the processes $d + p \to np + p$ and $d + t(h) \to np + t(h)$ or $d + t \to nn + h$ are recast into a unified form of the angular dependences of the differential cross section for the production of singlet nucleon–nucleon pairs. The results are compared with those produced by the supermultiplet potential model for the interaction of extremely light nuclei. For $d + t(h)$ scattering, where the power of the potential $V^{[41]}(r)$ is 50% higher than the power of the potential $V^{[32]}(r)$ ($[f] = [41]$ and $[f] = [32]$ are orbital Young diagrams), the theory in question is able to provide a quantitative description of both the experimental data being discussed and experimental data on elastic scattering. For $d + p$ scattering, where the difference of the powers of the potentials for $[f] = [3]$ and $[f] = [21]$ is not more than 20%, the agreement with the data on the deuteron-spin-flip reaction leading to the singlet final state is only qualitative. It would be of interest to investigate, by means of triple coincidences, the process $d + d \to d_s + d_s$, where the difference of the corresponding powers for $[f] = [4]$ and $[f] = [22]$ amounts to about 300%. © *2002 MAIK "Nauka/Interperiodica".*

1. INTRODUCTION

Theoretical investigations of extremely light clusters formed by nucleons employ three main approaches.

The first is developed within the theory of three-body systems [1], which is based on the set of Faddeev–Yakubovsky equatons for coupled antisymmetrized wave functions corresponding to all possible partitions of the nucleon system being considered into subsystems. With the aid of these equations, involving a nucleon–nucleon (NN) interaction that is assumed to be known, specific nuclear reactions of various types are analyzed by means of unwieldy numerical calculations (this unwieldiness is due to taking completely into account a virtual continuum in the set of coupled equations). Somewhat simplified versions of this theory are also used [2].

The second is the resonating-group method (RGM) [3], where, for a fixed composition of nucleon clusters, a full antisymmetrization is performed and where a specific version of NN interaction is embedded, but where no account is taken of a virtual continuum. The method is used to determine the E- and L-dependent interaction of the clusters involved and to calculate relevant phase shifts, reactions of photodisintegration into clusters, etc.

The third is based on the potential model of cluster interaction [4]. Conceptually, the model relies on a rich experience gained in microscopically studying cluster degrees of freedom in light nuclei within the multiparticle-shell model [5]. This makes it possible, among other things, to take effectively into account the Pauli exclusion principle through the introduction of deep attractive potentials involving forbidden states [4–6]. On this basis, a good description can be obtained both for $\alpha + \alpha$, $\alpha + d$, $\alpha + t$, and $t + h$ cluster scattering and for relevant photonuclear reactions [7], the phenomenological parameters being eventually fixed within rather narrow corridors. By thus combining an investigation of the on-shell scattering matrix with an investigation of the off-shell scattering matrix, the validity of the above attractive potentials was reliably confirmed; that is, it was proven that all phase shifts for them are positive. In contrast to the extensively used RGM, this approach unveils a simple physics of the scattering process; in addition, it provides a fresh view of cluster–cluster interaction and is quite simple in numerical calculations. We foresee seminal possibilities in combining the potential model with the aforementioned theory of few-body systems, whereby one could perform, for example, an ab initio determination of cluster-interaction potentials being

[1)]Institute for Nuclear Research, National Academy of Sciences of Ukraine, pr. Nauki 47, Kiev, 252028 Ukraine.

1063-7788/02/6503-0462$22.00

discussed, taking into account a virtual continuum. A specific analysis of various reactions will then be performed by using these cluster–cluster potentials without invoking, each time, the whole machinery of numerical calculations within this theory. From the general point of view, such an approach is quite in line with a common practice of using conventional optical potentials of nucleon–nucleus interaction, which effectively reproduce the microscopic multinucleon pattern.

In the 1980s and 1990s, the potential model of cluster interactions was generalized to cover cluster systems like $d+p$, $d+d$, $t+p$, and $d+t$ that had previously defied any attempt at describing them within potential models. This became possible as soon as an important step that is absolutely necessary in dealing with channels characterized by a minimum total spin S and which consists in taking into account the interference of two potential amplitudes corresponding to two different Young diagrams $[f]$ (this is a supermultiplet potential model also known as SPM) was made in [8]. Some applications of this approach were discussed in [8–11]. In particular, an interesting possibility within the supermultiplet potential model was indicated there: a superposition of potential amplitudes for different $[f]$ leads to the emergence of the inelastic channel where the deuteron spin and isospin are flipped (in particular, charge-exchange channel) [10]. In other words, the respective differential cross section can be expressed in terms of the elastic-scattering phase shifts $\delta_L^{[f]}(E)$ determined experimentally, provided that the phase shifts $\delta_{L,S}(E)$ corresponding to different values of the total spin S of the system have been measured. Moreover, a superposition of Young diagrams proved to be a very useful concept in analyzing photonuclear reactions in the region of extremely light nuclei as well [11, 12].

The formalism being discussed is characterized by an extensive use of multiparticle spin–isospin fractional-parentage coefficients [5, 13].

So far, $[f]$-dependent potentials have not been used in studies (with the exception of those that were reported in [11]) devoted to the theory of few-body systems, since the spectra of such systems begin to display spectacular features associated with Majorana nucleon–nucleon interaction and Young diagrams behind it from the atomic weights of 4 and 5, in which case rows of maximum length appear in a Young diagram: $[f]=[4]$ and $[f]=[41]$ for ^{4}He and ^{5}He–^{5}Li nuclei, respectively. The energy ΔE associated with the excitation of a closed quartet of Young diagrams, $[f]=[4]\to[f]=[31]$ or $[f]=[41]\to[f]=[32]$, is especially high here: $\Delta E\simeq 15$–20 MeV (see below).

Experimental data accumulated over the past few decades for reactions involving light nuclei and proceeding either through charge-exchange channels (which lead to the production of nn or pp pairs of zero total spin) or through channels where the spin and isospin are flipped with the production of a singlet deuteron [14–29] are sufficient for analysis and systematics. The present study is devoted to describing the entire body of these data on the basis of the supermultiplet potential model and to clarifying the predictive power and the applicability range of this model. Naturally, this must be done along with an analysis of data on elastic scattering.

It should be noted that only a few studies (for example, [14, 15, 24, 29]) present experimental angular dependences of the differential cross sections $d\sigma/d\Omega$ for the production of singlet nucleon pairs characterized by low relative energies. In the majority of the cases, these data are represented in the form of various spectra of double- and triple-differential cross sections (in various projections, in various coordinate frames, etc.) or in the form of angular dependences of cross sections at the corresponding maxima of the spectra (for an overview, see, for example, [30]). First of all, we will therefore try to recast such data into a unified form of the angular dependences of the differential cross sections for singlet-pair production. In general, the experimental spectra of double- and triple-differential cross sections involve contributions from sequential decays through various resonances, from the formation of an np pair in the triplet state, and so on. In order to single out the component that is associated with the production of a singlet dinucleon, use was made of the well-known Migdal–Watson approximation [31, 32], which describes the final-state interaction (FSI) of nucleons at energies of their relative motion that are close to the internal energy of a singlet deuteron (dineutron). In the present study, we do not analyze reactions leading to the production of proton–proton pairs, since, in that case, the Coulomb interaction of the protons involved smears the relevant spectra, rendering the results deduced from their analysis less transparent.

Presently, a vast body of experimental data on elastic pd and $dt(h)$ scattering has been accumulated, and we also give here an analysis of these data on the basis of the supermultiplet potential model. Only via a global analysis outlined above can one assess comprehensively the advantages and disadvantages of this model and pinpoint interesting problems requiring a further investigation.

2. FORMALISM OF THE SUPERMULTIPLET POTENTIAL MODEL

Under the assumption of $SU(4)$ symmetry, the expansion of a partial-wave amplitude for $A+B$ scat-

tering (here, A and B stand for some nuclei) can be represented in the form [8–12]

$$T_L = \sum_S T_{L,S} = \sum_{S,\sigma,t,\tau,[f]} (t_A\tau_A, t_B\tau_B|t\tau) \quad (1)$$
$$\times (S_A\sigma_A, S_B\sigma_B|S\sigma)\langle[\widetilde{f}_A]S_At_A, [\widetilde{f}_B]S_Bt_B|[\widetilde{f}]St\rangle$$
$$\times T_L^{[f]}\langle[\widetilde{f}]St|[\widetilde{f}_A]S'_At'_A, [\widetilde{f}]S'_Bt'_B\rangle$$
$$\times (S\sigma|S'_A\sigma'_A, S'_B\sigma'_B)(t\tau|t'_A\tau'_A, t'_B\tau'_B),$$

where S and t are, respectively, the spin and the isospin of the $A+B$ system; $[\widetilde{f}]$ is the corresponding spin–isospin Young diagram; σ and τ are the projections of the spin and the isospin, respectively; $\langle[\widetilde{f}_A]S_At_A,\ [\widetilde{f}_B]S_Bt_B|[\widetilde{f}]St\rangle$ are isoscalar factors in the Clebsch–Gordan coefficients of the $SU(4)$ group (spin–isospin fractional-parentage coefficients) [5, 13]; $T_L^{[f]}$ are partial-wave amplitudes invariant under the transformations of the $SU(4)$ group; and $[f]$ is the orbital Young diagram for the $A+B$ system. Within the supermultiplet potential model, the amplitude $T_{L,S}$ depends on S indirectly through the dependence on the form (signature) of $[f]$, which is the most important. This nontrivial feature of the supermultiplet potential model leads to an economical description of experimental data—the model features no explicit spin–orbit, spin–spin, etc., interactions, but it takes into account the most important effect, a very large (about 15 to 20 MeV) splitting of the levels of extremely light p-shell nuclei ($A \le 9$) in Young diagrams that occurs (see above) in the cases where a closed quartet of four such diagrams is excited ($[f] = [4] \to [f] = [31]$). This is due to strong Majorana forces between the nucleons involved [5]. In the aspect that is of interest to us, there is a similar strong splitting of the cluster–cluster potentials $V^{[f]}(r)$ between Young diagrams of the $[f] = [41]$ and the $[f] = [32]$ type. In other words, the supermultiplet model can be quite workable for the $d + t(h)$ and $p + t(h)$ systems, but it is more questionable whether this is so for the $d + p$ system because the splitting of the levels between the signatures of $[f] = [3]$ and $[f] = [21]$ is one-half as great as that in the preceding case (see a comparison of the powers of the potentials in Tables 1 and 2 below).

The partial-wave amplitudes T_L specify the expansion of the total scattering amplitude $f(\theta)$ in the orbital angular momenta L; that is,

$$f(\theta) = -\frac{i}{2p_0}\sum_L (2L+1)T_L P_L(\cos\theta), \quad (2)$$

where p_0 is the momentum of the relative motion of particles A and B in the c.m. frame.

The quantity obtained by averaging, over the initial orientations of the spins σ_A and σ_B, the cross section for scattering accompanied by the flip of the deuteron spin and isospin and summing the result over final σ'_A and σ'_B (we consider the scattering of unpolarized particles) has the form [11]

$$\frac{d\sigma}{d\Omega}(\theta) = \frac{1}{(2S_A+1)(2S_B+1)} \quad (3)$$
$$\times \sum_{\sigma_A,\sigma_B,\sigma'_A,\sigma'_B} |f(\theta)|^2 = \frac{1}{4p_0^2}\frac{(2S'_A+1)(2S'_B+1)}{(2S_A+1)(2S_B+1)}$$
$$\times (t'_A\tau'_A, t'_B\tau'_B|t\tau)^2 |\sum_L (2L+1)P_L(\cos\theta)$$
$$\times \{\langle[\widetilde{f}_A]S_At_A, [\widetilde{f}_B]S_Bt_B|[\widetilde{f}_1]St\rangle$$
$$\times\langle[\widetilde{f}'_A]S'_At'_A, [\widetilde{f}'_B]S'_Bt'_B|[\widetilde{f}_1]St\rangle T_L^{[f_1]}$$
$$+\langle[\widetilde{f}_A]S_At_A, [\widetilde{f}_B]S_Bt_B|[\widetilde{f}_2]St\rangle$$
$$\times\langle[\widetilde{f}'_A]S'_At'_A, [\widetilde{f}'_B]S'_Bt'_B|[\widetilde{f}_2]St\rangle T_L^{[f_2]}\}|^2,$$

where $S_B = 1$, $S'_B = 0$, $t_B = 0$, $t'_B = 1$, $[\widetilde{f}_B] = [\widetilde{f}'_B] = [\widetilde{2}]$, $S_A = 1/2$, $S'_A = 1/2$, $t_A = 1/2$, $t'_A = 1/2$, $[\widetilde{f}_A] = [\widetilde{f}'_A] = [\widetilde{1}]$ or $[\widetilde{3}]$, $t = 1/2$, $\tau = 1/2$, and $S = 1/2$ for the $p + d$ and the $h + d$ system and $S_A = 1$, $S'_A = 0$, $t_A = 0$, $t'_A = 1$, $[\widetilde{f}_A] = [\widetilde{f}'_A] = [\widetilde{2}]$, $t = 0$, $\tau = 0$, and $S = 0$ for the $d + d$ system. If the deuteron spin and isospin are flipped without charge exchange, we have $\tau'_A = 1/2$ and $\tau'_B = 0$ for the $p + d$ and the $d + h$ system and $\tau'_A = \tau'_B = 0$ for the $d + d$ system; but if charge exchange occurs, then $\tau'_A = 1/2$ and $\tau'_B = 1$ for the $p + d$ and the $d + h$ system and $\tau'_A = 1$ and $\tau'_B = -1$ for the $d + d$ system.

Formulas (1) and (3) demonstrate (it is necessary to substitute there specific values of spin–isospin Clebsch–Gordan coefficients and fractional-parentage coefficients [5, 13]) that, if use is made of the conventional notation

$$S^{\rm el}_{L,S} = \eta_{L,S}\exp(2i\delta_{L,S}) \equiv T_{L,S} + 1, \quad (4)$$

the following relations hold for these systems:

$$\delta_{L,1/2} = \frac{1}{2}\delta_L^{[f_1]} + \frac{1}{2}\delta_L^{[f_2]}, \quad (5)$$
$$\eta_{L,1/2} = |\cos(\delta_L^{[f_1]} - \delta_L^{[f_2]})|;$$
$$\delta_{L,3/2} = \delta_L^{[f_2]}, \quad \eta_{L,3/2} = 1. \quad (6)$$

Here, $[f_1] = [3]$ and $[f_2] = [21]$ for the $d + p(n)$ system, and $[f_1] = [41]$ and $[f_2] = [32]$ for the $d + t(h)$ system, while the phase shift $\delta_L^{[f]}$ characterizes the potential $V_{AB}^{[f]}(r)$ of $A + B$ interaction. These potentials, which are strongly dependent on the signature of

$[f]$—this is a key point of the supermultiplet potential model—are presented in [9–12] (see below).

The nonunitarity of the elastic-scattering amplitude in the doublet channels (5) is due to the inclusion of channels involving the flip of the deuteron spin and isospin, $d+p \to d_s+p$ and $d+h \to d_s+h$, and charge exchange, $d+p \to pp+n$ and $d+h \to pp+t$:

$$S^{\text{flip}}_{L,1/2} = \left(\frac{1}{2}\frac{1}{2}, 10\middle|\frac{1}{2}\frac{1}{2}\right)\left(\frac{1}{2}T^{[f_1]}_L - \frac{1}{2}T^{[f_2]}_L\right), \quad (7)$$

$$S^{\text{ce}}_{L,1/2} = \left(\frac{1}{2} - \frac{1}{2}, 11\middle|\frac{1}{2}\frac{1}{2}\right)\left(\frac{1}{2}T^{[f_1]}_L - \frac{1}{2}T^{[f_2]}_L\right). \quad (8)$$

Obviously, the S matrix is unitary:

$$\left|S^{\text{el}}_{L,1/2}\right|^2 + \left|S^{\text{flip}}_{L,1/2}\right|^2 + \left|S^{\text{ce}}_{L,1/2}\right|^2 = 1, \quad (9)$$

$$\left|S^{\text{el}}_{L,3/2}\right|^2 = 1.$$

As a result, we obtain a simple and informative expression describing the cross section for $p+d$ interaction accompanied by the flip of the deuteron spin and isospin:

$$\frac{d\sigma}{d\Omega}(\theta) = \frac{1}{144p_0^2}\Big|\sum_L (2L+1)P_L(\cos\theta) \times \left[T^{[21]}_L - T^{[3]}_L\right]\Big|^2. \quad (10)$$

For $t+d$ ($^3\text{He}+d$) scattering governed by the same mechanism, we have the analogous expression

$$\frac{d\sigma}{d\Omega}(\theta) = \frac{1}{144p_0^2}\Big|\sum_L (2L+1)P_L(\cos\theta) \times \left[T^{[41]}_L - T^{[32]}_L\right]\Big|^2. \quad (11)$$

In the case of charge exchange, we arrive at expressions that are similar to (10) and (11), but which involve an additional factor of 2 appearing because of different projections τ'_B of the isospin for the deuteron and for the pp and nn pairs in the relevant Clebsch–Gordan coefficient $(t'_A\tau'_A, t'_B\tau'_B|t\tau)$. It should be recalled [11] that these expressions are valid if the collision energy in the c.m. frame is considerably higher than that required for exciting the deuteron to the singlet state (that is, higher than 2.22 MeV).

For elastic proton–deuteron scattering, we similarly obtain

$$\frac{d\sigma}{d\Omega}(\theta) = \frac{1}{12p_0^2}\left\{\Big|\sum_L (2L+1)P_L(\cos\theta) \times \left[\frac{1}{2}T^{[3]}_L + \frac{1}{2}T^{[21]}_L\right]\Big|^2 + 2\Big|\sum_L (2L+1) \times P_L(\cos\theta)T^{[21]}_L\Big|^2\right\}. \quad (12)$$

In describing elastic $dt(h)$ scattering, the substitutions $T^{[3]}_L \to T^{[41]}_L$ and $T^{[21]}_L \to T^{[32]}_L$ must be made in expression (12). For the ensuing analysis, it is important to indicate that the values of the total spin of the system that correspond to the first and the second sum in (12) are $S=1/2$ and $S=3/2$, respectively.

The potentials corresponding to various admissible permutation symmetries $[f]$ can be reconstructed according to the procedure described in detail in [11]. Here, we only note that for the $d+p(n)$ and the $d+h(t)$ system, they are constructed in the form

$$V^{[f]}_L(r) = V_1\exp(-\alpha_1 r^2) + V_2\exp(-\alpha_2 r),$$

where the exponential term $V_2\exp(-\alpha_2 r)$ simulates the attraction at the periphery. The splitting in the orbital angular momentum L is taken into account in constructing the potentials [10, 11]. This significant splitting reflects the important role of nucleon exchange between the subsystems [11]. The potential parameters are given in Tables 1 and 2. The corresponding phase shifts (which are used in the present study) are presented in [10, 11]. Comparing the strongest components of the potentials, we note that the power of the potential $V^{[41]}_{L\text{odd}}(r)$ (it is defined here in the simplest way as $V_0R_0^2$) is 50% higher than that of the potential $V^{[32]}_{L\text{even}}(r)$, but that, for the potentials $V^{[3]}_{L\text{even}}$ and $V^{[21]}_{L\text{odd}}$, this distinction is only 20%. In this way, we can comprehend the important fact that (as will be seen below) the $d \to d_s$ process is described fairly well in the case of $d+t(h)$ scattering, whereas there is only general qualitative agreement between experimental data and the supermultiplet potential model for this process in the case of $d+p$ scattering. Nevertheless, it proved to be possible for the first time to explain, on this basis, a spectacular feature of elastic $d+p$ scattering (see Section 4).

3. TREATMENT OF SPECTRA IN THE MIGDAL–WATSON APPROXIMATION

In order to verify the above theoretical approach, it is necessary to compare the calculated and the experimental differential cross sections $d\sigma/d\Omega$ both for elastic scattering and for the inelastic scattering under discussion in $d+p$ and $d+t(h)$ collisions. For elastic scattering, such a comparison is performed directly; as to the inelastic processes being considered, the experimental cross sections for the formation of singlet dinucleons must be extracted by integrating

Table 1. Potentials of proton–deuteron interaction

[f]	L	V_1, MeV	α_1, fm^{-2}	V_2, MeV	α_2, fm^{-1}	Power, MeV fm^2
[21]	Even	−57.0	0.37	7.2	0.36	−53
[21]	Odd	−8.8	0.06	–	–	−73
[3]	Even	−55.8	0.31	–	–	−90
[3]	Odd	−13.8	0.16	1.6	0.09	−30

Table 2. Potentials of d^3He interaction

[f]	L	V_1, MeV	α_1, fm^{-2}	V_2, MeV	α_2, fm^{-1}	Power, MeV fm^2
[32]	Even	−50.0	0.15	–	–	−167
[32]	Odd	−73.1	0.23	18.1	0.56	−123
[41]	Even	−57.0	0.16	8.4	0.21	−138
[41]	Odd	−69.0	0.14	–	–	−246

the continuous spectra for three-body reactions, since the singlet states of dinucleons are not bound. In order to determine the contribution from the FSI of nucleons, one has naturally to simulate experimental distributions and to take into account the variety of physical processes leading to a specific final state, which include the quasifree scattering of clusters, the formation and decay of resonances in the subsystems, and the triplet interaction in the np final state.

In this section, we will briefly describe the technique used in the present study to obtain the experimental differential cross sections $d\sigma/d\Omega_{ds}$(c.m.) from the spectra presented in the literature for three-body reactions of the type

$$A + B \to N_1 + N_2 + N_3. \qquad (13)$$

The kinematical relations for such reactions are comprehensively described by Olsen [33]; therefore, we will briefly recall only some of them.

The kinematics of the three-particle final state of reaction (13) is specified by three particle momenta $\mathbf{P}_i (i = 1, 2, 3)$, but the number of independent momentum components becomes equal to five (not nine) upon taking into account the laws of energy–momentum conservation:

$$\mathbf{P} = \mathbf{P}_A + \mathbf{P}_B = \mathbf{P}_1 + \mathbf{P}_2 + \mathbf{P}_3, \qquad (14)$$

$$E = E_A + E_B = E_1 + E_2 + E_3. \qquad (15)$$

Kinematically complete experiments record two final products of the three at specific values of the angles θ_1, θ_2, φ_1, and φ_2 and measure their kinetic energies E_1 and E_2. This results in determining six momentum components, their number exceeding that of independent components by one. In accordance with the laws of energy–momentum conservation, the allowed values of the kinetic energies E_1 and E_2 in the laboratory frame are determined by the well-known equation of an ellipse [33] in the $(E_1)^{1/2}(E_2)^{1/2}$ plane. As a result, measurements yield two-dimensional coincidence vectors $N(E_1, E_2)$, where N is the number of coincidences—that is, the number of particles that were detected simultaneously and which had energies in the intervals $[E_1, E_1 + \Delta E_1]$ and $[E_2, E_2 + \Delta E_2]$. In order to perform a comparison with the results of theoretical calculations, the two-dimensional spectra are further reduced, by various methods, to one-dimensional spectra. In the majority of studies, the triple-differential cross sections are represented as a function of the length E_s of the arc s along the kinematical line of the ellipse—that is, the projection onto the kinematical curve. If an experiment records particles N_1 and N_2, we then obtain

$$d^3\sigma/d\Omega_1 d\Omega_2 dE_s = d^3\sigma/d\Omega_1 d\Omega_2 dE_1 \times [1 + (dE_2/dE_1)^2]^{-1/2}. \qquad (16)$$

On the right-hand side, there appears a cross section that can already be compared with theoretical models, where the differential cross section is given by [33, 34]

$$d^3\sigma/d\Omega_1 d\Omega_2 dE_1 = (2\pi/v_0)|T_{fi}|^2 \rho^*_{1l}. \qquad (17)$$

Here, v_0 is the relative velocity of particles A and B; T_{fi} is the reaction amplitude; and the subscript l indicates that the quantity ρ^*_{1l}, which is the well-known phase-space factor whose explicit expression is given in [33], is taken in the laboratory frame.

It is convenient to perform integration of the spectra in the system of Jacobi coordinates, where the shape of the spectrum is described analytically. In the coordinate frame employing the relative momenta (Jacobi momenta), the triple-differential cross section assumes the form

$$d^3\sigma/d\Omega_{1-23} d\Omega_{2-3} dE_{1-23} = (2\pi/v_0)|T_{fi}|^2 \rho_{1c}, \qquad (18)$$

$$\rho_{1c}(E_{1-23}) = [2/(2\pi)^6](m_1m_2m_3/M)^{3/2} \times [E_{1-23}(E^c_{\rm tot} - E_{1-23})]^{1/2}, \quad (19)$$

where $E^c_{\rm tot}$ is the total energy of the three-particle system in the c.m. frame; the indices "2–3" and "1–23" label quantities referring, respectively, to the relative motion of particles N_2 and N_3 and to the motion of particle N_1 with respect to the center of mass of the $N_2 + N_3$ system; and $M = m_1 + m_2 + m_3$. Since the quantity E_{1-23} can be defined as

$$E_{1-23} = E^c_{\rm tot} - E_{2-3}, \quad (20)$$

E_{2-3} can be used in expression (19) instead of E_{1-23}.

In some cases, experimentalists content themselves with measuring the inclusive spectrum of one reaction product. Such experiments are referred to as kinematically incomplete experiments, because only three kinematical parameters (for example, the energy E_1 and the angles θ_1 and φ_1) of five independent ones are then known in the final state. Nonetheless, some features in the behavior of the $N_2 + N_3$ system can be revealed in the cross sections obtained in this way. From the relations

$$E^c_{\rm tot} = Q + [m_A/(m_A + m_B)]E^l_A = E_{1-23} + E_{2-3}, \quad (21)$$
$$E_{1-23} = (m_1 + m_2 + m_3)E^c_1/(m_2 + m_3),$$

where E^c_1 is the energy of particle N_1 in the c.m. frame and Q is the reaction energy, it does indeed follow that the energy E_{2-3} is specified at each point of the inclusive spectrum; however, the dependence of the cross sections on some other parameters (E_{1-2}, E_{1-3}) is not specified (it is integrated out); therefore, the results obtained in this way should be interpreted with caution. By integrating Eq. (18) over the solid angle Ω_{2-3}, we can find that the differential cross section and the matrix element for particle N_1 are related as

$$d^2\sigma/d\Omega_{1-23}dE_{1-23} = (2\pi/v_0)\rho_{1c}(E_{1-23}) \int |T_{fi}|^2 d\Omega_{2-3}. \quad (22)$$

In the laboratory frame, we have

$$d^2\sigma/d\Omega_1 dE^l_1 = (2\pi/v_0)\rho_{1l}(E^l_1) \int |T_{fi}|^2 d\Omega_{2-3}, \quad (23)$$

$$\rho_{1l}(E^l_1)dE^l_1 d\Omega_1 = \frac{2}{(2\pi)^6}\frac{M^{1/2}(m_1m_2m_3)^{3/2}}{(m_2+m_3)} \times \left[E^l_1\left(\frac{m_2+m_3}{M}E^c_{\rm tot} - E^l_1 + 2a_1(E^l_1)^{1/2} - a_1^2\right)\right]^{1/2} dE^l_1 d\Omega_1,$$

where $a_1 = (m_1m_AE^l_1)^{1/2}/(m_A + m_B)$. We note that the last expression for $\rho_{1l}(E^l_1)dE^l_1 d\Omega_1$ differs from that presented in [33], where it is obviously erroneous.

The reaction involving the formation of a singlet dinucleon proceeds in two stages:

$$(i)\ A + B \to N_1 + (N_2 + N_3)^*,$$
$$(ii)\ (N_2 + N_3)^* \to N_2 + N_3.$$

Particle N_1 and an intermediate system—that is, a dinucleon $(N_2 + N_3)^*$—are formed at the first stage. At the second stage, the dinucleon $(N_2 + N_3)^*$ decays into two nucleons. As a rule, the Migdal–Watson model is applied to a subsystem of two nucleons, such as two neutrons or two protons in the singlet $^1S_0$ state, or a neutron–proton pair both in the singlet and in the triplet $^3S_1$ state.

In accordance with this model, the shape of the three-particle spectrum at low relative energies E_{2-3} is determined primarily by a virtual $^1S_0$ level, and the square of the reaction amplitude can be factorized:

$$|T_{fi}|^2 = |F_{NN^*}|^2|F_{\rm FSI}(E_{2-3})|^2. \quad (24)$$

The first factor in (24) is associated with the formation of the dinucleon and is assumed to be smoothly changing; therefore, the shape of the spectrum in the region of the maximum is determined by the amplitude $F_{\rm FSI}(E_{2-3})$. In the following, the square of this amplitude will be represented as the linear combination

$$|F_{\rm FSI}|^2 = c_s|F_s|^2 + c_t|F_t|^2 + c_r|F_r|^2. \quad (25)$$

The amplitudes F_s and F_t describe the FSI of the neutron–proton pair in, respectively, the $^1S_0$ and the $^3S_1$ state [in the case of the nn system, the term F_t drops out from expression (25)]; F_r takes into account the effect of resonances in other subsystems of the type $(N_1 + N_2)^*$ or $(N_1 + N_3)^*$ (by way of example, we indicate that, in the reaction $t + d \to t + p + n$, this is the resonance ^{4}He* in the $t + p$ and ^{3}He $+ n$ subsystems); and c_s, c_t, and c_r are free parameters that are determined from a least squares fit to experimental spectra. In the Migdal–Watson approximation, the amplitudes F_s and F_t are given by [31]

$$F_{s(t)}(k) \sim r_{NN}(k^2 + \alpha^2)/[2(-a^{-1} + r_{NN}k^2/2 - ik)], \quad (26)$$
$$\alpha = [1 + (1 - 2r_{NN}/a)^{1/2}]/r_{NN},$$

where k is the internal momentum in the dinucleon, r_{NN} is the effective range of the interaction, and a is the NN scattering length. In fitting the spectra for the three-body reactions in question, we used here the following values of the parameters a and r_{NN} [35, 36]:

$$a^s_{np} = (-23.748 \pm 0.009)\ {\rm fm},\ r^s_{np} = (2.73 \pm 0.03)\ {\rm fm},$$

$$a^s_{nn} = (-18.7 \pm 0.6)\ \text{fm},\ r^s_{nn} = (2.84 \pm 0.03)\ \text{fm},$$
$$a^t_{np} = (5.411 \pm 0.004)\ \text{fm},\ r^t_{np} = (1.747 \pm 0.004)\ \text{fm}.$$

The amplitude F_r is specified in the form of the Breit–Wigner resonance; that is,

$$F_r(E) \sim (\Gamma/2)(E - E_r + i\Gamma/2),$$

where E is the energy of relative motion in the p^3H pair, E_r is the position of the resonance ^{4}He* over the threshold for the breakup process $^4\text{He} \to p + {}^3\text{H}$, and Γ is its width.

Since, in analyzing the experimental spectra, we are interested only in the region of np or nn FSI where the Migdal–Watson maximum is present, we can henceforth assume that the shape of these spectra in kinematically complete experiments (in the laboratory frame) is given by [see Eqs. (17), (24), and (25)]

$$d^3\sigma/d\Omega_1 d\Omega_2 dE_1 = (2\pi/v_0)(c_s|F_s|^2 + c_t|F_t|^2 + c_r|F_r|^2)\rho^*_{1l}. \quad (27)$$

For the inclusive spectra, we have

$$d^2\sigma/d\Omega_1 dE_1 = (8\pi^2/v_0)(c_s|F_s|^2 + c_t|F_t|^2 + c_r|F_r|^2)\rho_{1l}, \quad (28)$$

where ρ_{1l} is given by expression (23).

The coefficients c_s found in fitting experimental data were then used to determine the cross sections $d\sigma/d\Omega_{d_s}$ in the system of Jacobi coordinates by using relations (18) and (19):

$$d^3\sigma/d\Omega_{1-23} d\Omega_{2-3} dE_{1-23} = (2\pi/v_0) c_s |F_s|^2 \rho_{1c}. \quad (29)$$

Defining $d\Omega_{1-23} = d\Omega_{(N_2N_3)_s}$ and considering that a dinucleon in the $^1S_0$ configuration decays isotropically in relative coordinates, we obtain

$$d^2\sigma/d\Omega_{(N_2N_3)_s} dE_{1-23} = (8\pi^2/v_0) c_s |F_s|^2 \rho_{1c}. \quad (30)$$

Taking into account relation (20) and integrating Eq. (30) with respect to energy, we eventually arrive at the relation

$$d\sigma/d\Omega_{(N_2N_3)_s} = (8\pi^2/v_0) c_s \int_0^{E^m_{2-3}} |F_s|^2 \rho_{1c} dE_{2-3}, \quad (31)$$

where E^m_{2-3} is taken from the interval $(0 - E^c_{\text{tot}})$. Thus, similar computational schemes were used in analyzing the kinematically complete spectra and in analyzing the inclusive spectra, the only distinction of importance being that different expressions were taken for ρ_{1l} in Eqs. (27) and (28). A similar approach to calculating $d\sigma/d\Omega_{(N_2N_3)_s}$ was previously employed in [14, 24]. In [14], use was made of the alternative Phillips–Griffy–Biedenharn model [37], which displays virtually no distinctions from the Migdal–Watson distribution at low values of the relative energy of the nucleons involved; at high energies, however, the cross section within that approach decreases faster.

By way of example, Fig. 1 displays the experimental and the computed inclusive spectra for the reactions $^3\text{H}(d,t)np$ and $^3\text{H}(d,\ ^3\text{He})nn$ at $E_{\text{c.m.}} = 8.31$ MeV [24]. Shown in the figure are the computed contributions to the spectra from the singlet and the triplet component, as well as the contribution from the decays of the ^{4}He resonances at 21.1 and 22.1 MeV. The energy resolution was taken into account. It can be seen that the Migdal–Watson model describes fairly well the experimental data being discussed, whence it follows that this model can indeed be used to reconstruct the differential cross sections for the processes $^3\text{H} + d \to t + d_s$ and $^3\text{H} + d \to\ ^3\text{He} + (nn)_s$ on the basis of inclusive experimental data.

One of the problems to be solved in analyzing experimental spectra is associated with choosing the region of integration with respect to the relative energy E_{2-3} of the nucleons. Obviously, the upper limit of this integration must be bounded by some energy E^m_{2-3}. There is presently no consensus on choosing E^m_{2-3}. The values of E^m_{2-3} that are equal to 150 keV, 700 keV, and 1 MeV, as well as the value of $E^m_{2-3} = E^c_{\text{tot}}$, can be found in the literature [14, 15, 27, 38]. For a criterion in determining E^m_{2-3}, we use here general agreement between the absolute values of the calculated and the experimental angular distributions $d\sigma/d\Omega_{(N_2N_3)_s}$. Figure 2 shows the excitation functions for the reaction $^2\text{H}(p,d_s)p$ at $\theta_{d_s}(\text{lab}) = 25^\circ$ [$\theta_p(\text{c.m.}) = 126^\circ - 129^\circ$ for the reaction $^2\text{H}(p,p)d_s$] that were obtained by integrating the corresponding spectra at $E^m_{2-3} = 1$ MeV and $E^m_{2-3} = E^c_{\text{tot}}$. It can be seen that, on average, the calculated energy dependence of the cross section agrees fairly well with experimental dependence at $E^m_{2-3} = 1$ MeV; at the same time, points corresponding to integration over the entire kinematically allowed region of E_{2-3} lie higher than the computed values by approximately one-half of an order of magnitude. On this basis, we eventually decided on the value of $E^m_{2-3} = 1$ MeV for both types of scattering.

For the sake of comparison, the experimental angular distributions are shown in Figs. 3 and 4 both for $E^m_{2-3} = 1$ MeV and for $E^m_{2-3} = E^c_{\text{tot}}$.

For protons from the reaction $^2\text{H}(p,p)d_s$ leading to the production of a singlet deuteron, Fig. 3 presents the experimental angular distributions obtained in the way outlined above. As has already been mentioned, the experimental data used were borrowed from [14,

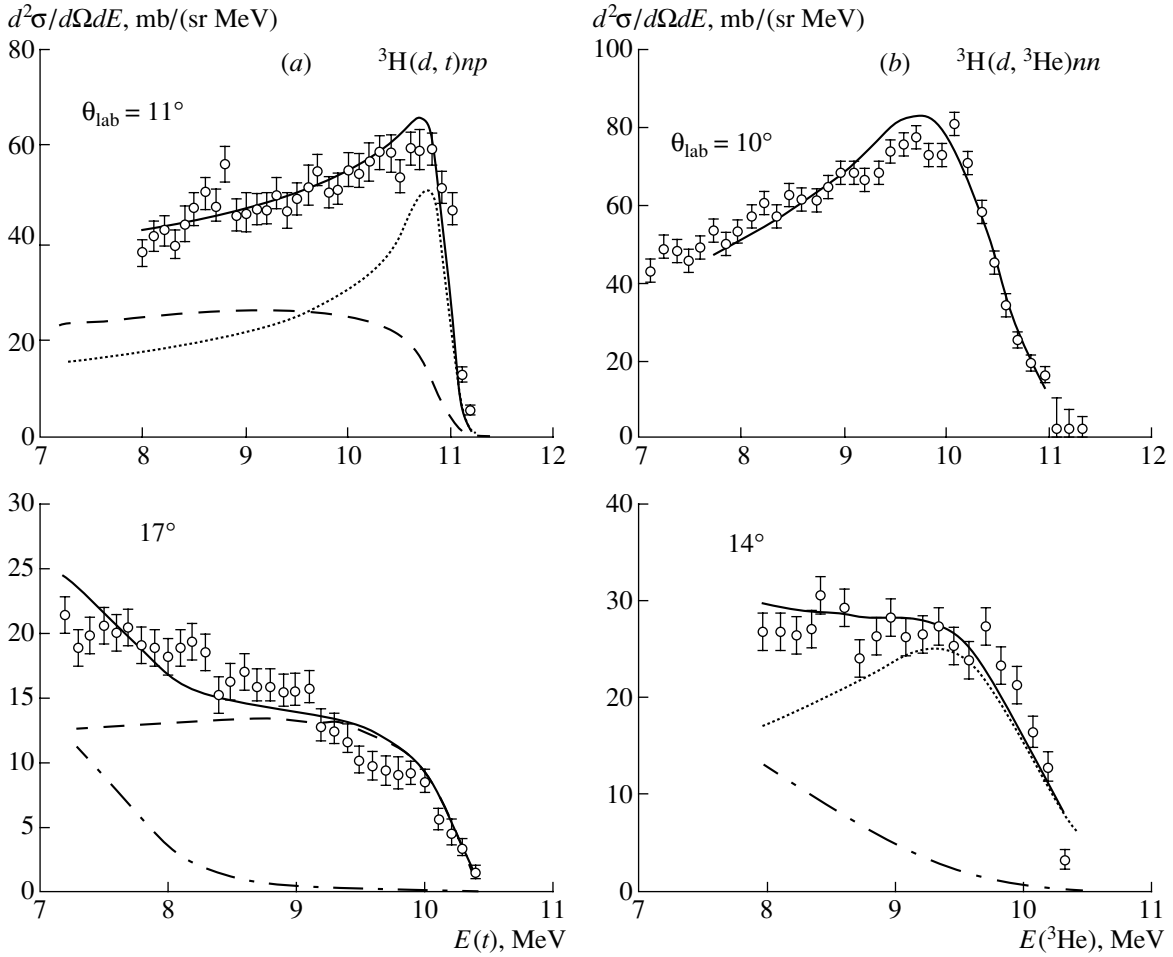

Fig. 1. Inclusive spectra for the reactions (a) ^{3}H$(d,t)np$ and (b) ^{3}H$(d,\ ^3$He$)nn$ at an energy of $E_{\text{c.m.}} = 8.31$ MeV. The experimental points shown here were borrowed from [24] at the particle detection angles θ_{lab} indicated in the figure. The dotted and the dashed curves represent the calculated contributions of the formation of a dinucleon in, respectively, the singlet and the triplet state, while the dash-dotted curves correspond to the contribution from the decay of the resonance of ^{4}He. The total calculated spectra are shown by solid curves.

15], where pn coincidences were measured directly at $E_{\text{c.m.}} = 8.3$, 9.1, 10, and 11.33 MeV. The angular distributions of protons at $E_{\text{c.m.}} = 10.6$ and 20.2 MeV were obtained by fitting and integrating the spectra of pp coincidences from [16, 20] according to the above formulas. Only the regions of Migdal–Watson peaks were processed in the spectra of those studies, and the results obtained in this way were then transformed into the coordinate frame corresponding to the scattering process ^{2}H$(p,p)d_s$. Only the angular distributions of triple-differential cross sections at the maxima of Migdal–Watson peaks are presented in [17, 18]. In those cases, the computed peaks at the maxima were fitted to the corresponding experimental values and were further integrated as usual ($E_{\text{c.m.}} =$ 12.67, 15.3 MeV). Data at $E_{\text{c.m.}} = 17.3$ MeV in the form of integrated cross sections were taken from the article of Van der Weerd *et al.* [15], who used, at this energy value, the results presented in [19]. Also displayed at the energy value of $E_{\text{c.m.}} = 9.1$ MeV, which is indicated in Fig. 3, are the experimental points obtained with the aid of the data from [22], where the inclusive spectrum for $n + {}^2$H scattering was studied at the close energy of $E_{\text{c.m.}} = 9.6$ MeV. A comparison with the results for $E_{\text{c.m.}} = 9.1$ MeV that were obtained from a kinematically complete experiment shows satisfactory agreement.

Figure 4 displays the angular distribution of singlet dinucleons from the reactions ^{3}H(d,d_s), ^{3}He(d,d_s), and ^{3}H(d,nn). These results were deduced from an analysis of experimental data from [23–29]. The inclusive spectra of tritons or ^{3}He nuclei were measured in [23, 24, 29] ($E_{\text{c.m.}} = 6.55$, 8.31, and 18.6 MeV), while the results of kinematically complete experiments (which detected tp or ^{3}Hep coincidences) were presented in [25–28] ($E_{\text{c.m.}} =$

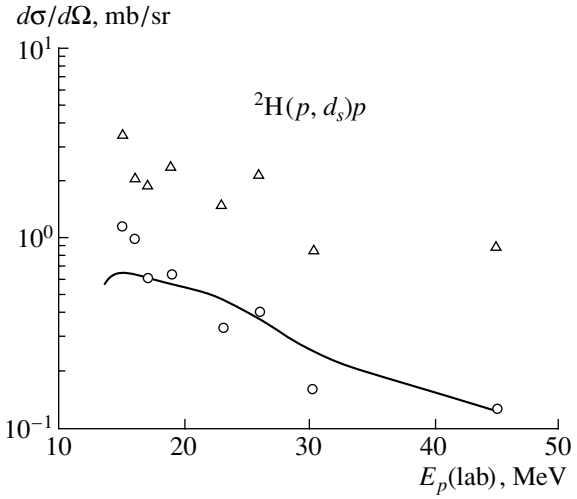

Fig. 2. Excitation functions for the reaction $^2\mathrm{H}(p, d_s)p$ at $\theta_{d_s}(\mathrm{lab}) = 25°$. The solid curve represents the results of the calculation based on the supermultiplet potential model. Points correspond to various upper limits in integration of the spectrum: (circles) $E^m_{2\text{–}3} = 1$ MeV and (triangles) $E^m_{2\text{–}3} = E^c_{\mathrm{tot}}$. The experimental data used were borrowed from [15].

10.2, 13, 13.85, and 14.36 MeV). The cross sections $d\sigma/d\Omega_{d_s}$ were given only in [24, 27, 29] at $E_{\mathrm{c.m.}} =$ 8.31, 13.85, and 18.6 MeV. For the remaining energy values indicated in Fig. 4 ($E_{\mathrm{c.m.}} = 6.55$, 10.2, and 14.36 MeV), the cross sections were determined according to the procedure described above. The results at $E_{\mathrm{c.m.}} = 13$ and 13.85 MeV are not quoted, since they involve only one experimental point at either energy value.

We note that Aleksandrov *et al.* [29] ($E_{\mathrm{c.m.}} =$ 18.6 MeV) integrated the singlet-dinucleon peak in the inclusive spectra, approximating it by a normal Gaussian distribution; obviously, this reduces the absolute cross-section value and distorts the shape of the angular dependence of the cross section in relation to the results that are obtained in the Migdal–Watson approximation. Since we were unable to obtain the required cross sections by processing their spectra with the aid of the Migdal–Watson procedure (these spectra are presented in relative units), we do not employ those data.

A comparison of various experimental angular dependences in Figs. 3 and 4 reveals that there is no significant difference between the cross sections as obtained from kinematically complete spectra and from inclusive spectra.

It should be noted that the above method for deriving differential cross sections made it possible to reconstruct them even in the case where only the cross-section values at the maxima of the spectra are available, whereas the experimental spectra themselves are not presented (such a situation is not rare in the literature).

4. DISCUSSION OF THE RESULTS

We begin a discussion of our results by analyzing experimental data on elastic $p(n) + d$ and $d + {}^3\mathrm{He}(t)$ scattering. These data are presented in Figs. 5 and 6, along with the results of the calculations on the basis of the supermultiplet potential model [formula (12)]. The experimental points in Fig. 5 were borrowed from [39–45] ($E_{\mathrm{c.m.}} = 6.47$ MeV [39]; 9.4 MeV [40]; 10.8, 11.4, 14.7, and 23.3 MeV [41]; 12 MeV [42]; 15.1 MeV [43]; 20.7 MeV [44]; and 30.9 MeV [45]); for Fig. 6, use was made of data from [46–49] ($E_{\mathrm{c.m.}} =$ 6.6 MeV [46]; 7.23, 8.27, 10, 12.22, 13.84, 16.65, and 17.49 MeV [47]; 8.64 MeV [48]; and 23.5 MeV [49]).

The experimental and the theoretical angular dependences of the differential cross section for elastic $p(n)d$ scattering are seen to be in satisfactory agreement (at least in shape) from low energies to $E_{\mathrm{c.m.}} = 15.1$ MeV. There appears a significant discrepancy between these theoretical and experimental results (especially in the backward hemisphere of θ_p) at $E_{\mathrm{c.m.}} = 20.7$ MeV, and it becomes still more pronounced as the energy is increased further.

A better situation is observed for $d + {}^3\mathrm{He}(t)$ scattering (Fig. 6). Here, however, there is also a discrepancy at large values of the angle θ_d from 16.65 MeV; at lower values of $E_{\mathrm{c.m.}}$, the experimental data are described fairly well both at small and at large angles of deuteron emission. For $E_{\mathrm{c.m.}} = 13.84$ MeV, the dotted curve in Fig. 6 represents the theoretical angular dependence obtained in [50] on the basis of the resonating-group method. It can be seen that, in describing experimental data for large scattering angles, this approach also runs into difficulties at the above energy value (at lower energies, the calculations performed in [50] within this framework comply well with the experimental data).

For both types of elastic scattering, poorer agreement with the experimental data in the backward hemisphere of angles for $E_{\mathrm{c.m.}} > 17$–20 MeV is likely to be due to a greater role of the increasing imaginary part of the potential, since it masks supermultiplet effects, rendering the model inefficient.

A comparison of the theoretical results obtained on the basis of the supermultiplet potential model [see Eq. (10)] with experimental angular dependences for inelastic proton scattering on ^{2}H nuclei that leads to the formation of a singlet np pair (Fig. 3) shows that there is only qualitative agreement over the entire energy region subjected to investigation. Better agreement is observed in the backward hemisphere

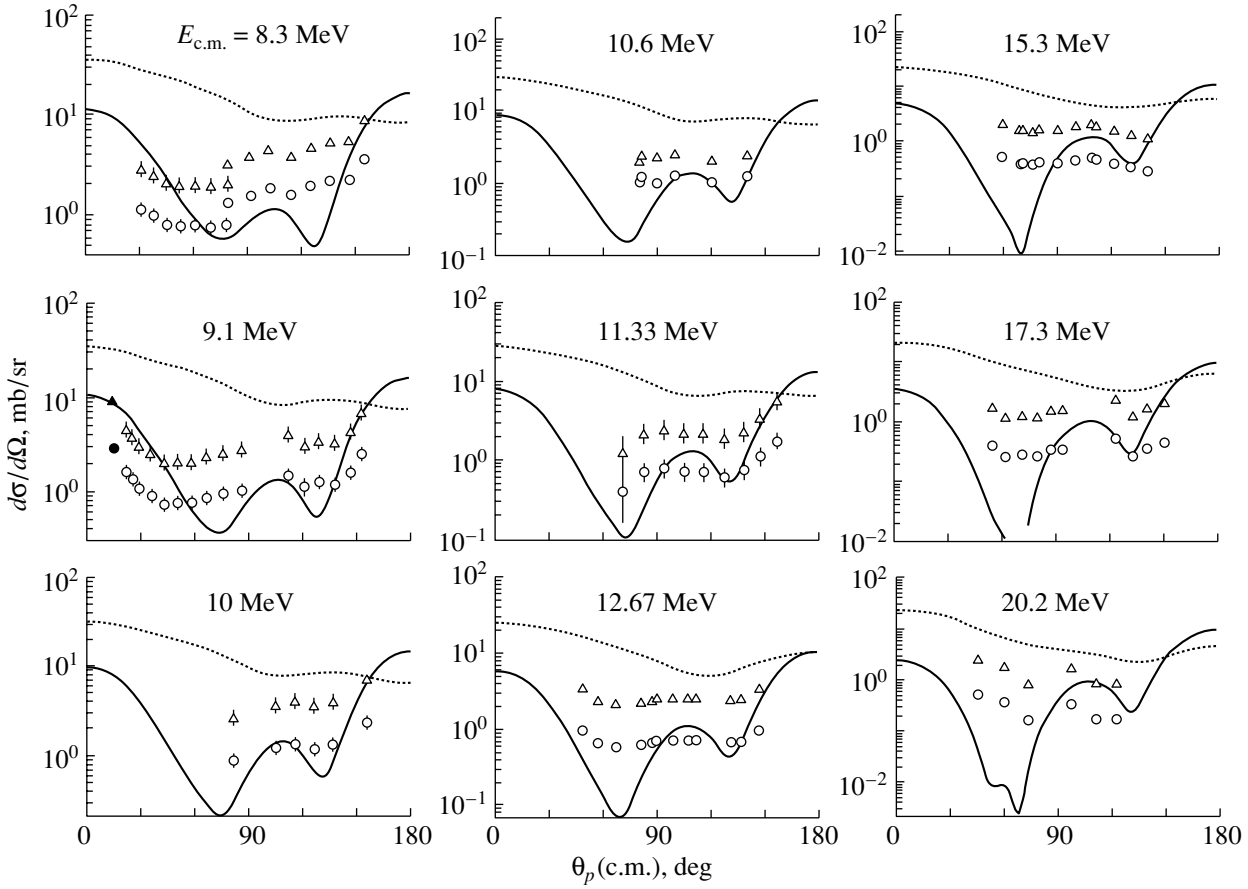

Fig. 3. Experimental angular distributions of protons from the reaction $^2\mathrm{H}(p,p)d_s$ leading to the production of the singlet state of a neutron–proton pair, along with the results of the calculations based on the supermultiplet potential model (solid curves). The notation for the points is identical to that in Fig. 2. References to experimental data are given in the main body of the text. The extreme left points (▲, ●) in the figure at $E_{\mathrm{c.m.}} = 9.1$ MeV were obtained from the inclusive spectrum presented in [22] at $E_{\mathrm{c.m.}} = 9.6$ MeV. The dotted curves represent the results of the calculations for elastic *pd* scattering at the total-spin value of $S = 1/2$.

of the angle θ_p. As to the forward hemisphere, we can state that there is a qualitative agreement here at energies in the range $E_{\mathrm{c.m.}} = 8$–11 MeV, but it is impaired as the energy is increased further. Since there are unfortunately no experimental data at small values of the angle θ_p in the region $E_{\mathrm{c.m.}} > 10$ MeV, we cannot state, with absolute confidence, that the conclusions drawn from the analysis of the results obtained are quite unambiguous.

The theoretical results presented here (even those of a qualitative character) make it possible to understand the spectacular fact (see [11] and references therein) that, in the doublet channels of elastic $d+p$ scattering, there is a significant inelasticity ($\eta_{L,1/2} \leq 0.5$ for $E_{\mathrm{c.m.}} \geq 7$ MeV), whereas, in the quartet channels, there is a nearly exact unitarity: $\eta_{L,3/2} \approx 1$ up to $E_{\mathrm{c.m.}} \simeq 25$ MeV. Obviously, the reason is that the quartet channel is a potential one; as to the doublet channel, it was indicated in Section 2 that two different amplitudes interfere there, which yields a microscopically motivated inelasticity at comparatively low energies. This inelasticity has nothing to do with the imaginary part $iW(r)$ that could be introduced in the potential for the sake of completeness and which would reflect the effect of the three-body continuum proper on the elastic-scattering channel; as was indicated above, the imaginary part in question becomes significant in the region $E_{\mathrm{c.m.}} \geq 20$ MeV. A similar phenomenon must occur for the $d+t(h)$ system as well, but there are presently no necessary data from partial-wave analyses for that case, so that their derivation would be of great value.

As a brief summary of our consideration of the $d+p$ system, we note that the aforementioned 20% difference of the powers of the $d+p$ potentials for the $[f]=[3]$ and $[f]=[21]$ Young diagrams is insufficient for the supermultiplet potential model to be workable at a quantitative level. That this distinction is small is reflected, in particular, in the smallness of the cross section for the $d \to d_s$ process in Fig. 3 in relation to

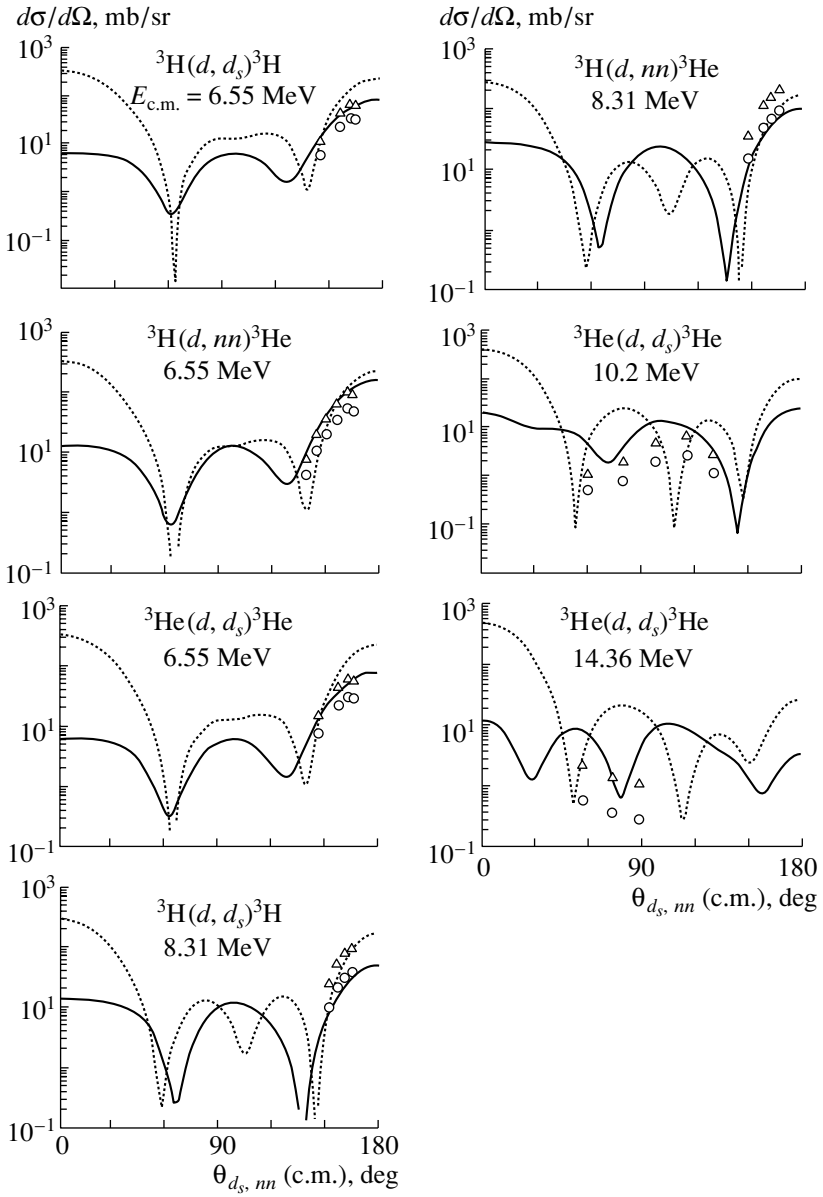

Fig. 4. As in Fig. 3, but for inelastic deuteron scattering on ^{3}H and ^{3}He nuclei.

the cross section for elastic scattering in the $S = 1/2$ channel.

For reactions where the initial state is that of $d + {}^3\mathrm{H}({}^3\mathrm{He})$ (Fig. 4), there are, as a rule, no experimental points for small and medium values of the emission angles of singlet np and nn pairs (it would be desirable to fill this gap), since, in measuring the corresponding inclusive spectra (it is measurements of precisely this type that were predominantly performed), relevant peaks are very rapidly smeared with increasing angle of detection of ^{3}H (^{3}He) nuclei. This can be seen, for example, from Fig. 1 [the experiment in question investigated reactions of the type $^3\mathrm{H}(d,t)d_s$, and the angles are reversed upon the interchange of t and d_s]. The comparison of available experimental data with the results of the calculations on the basis of the supermultiplet potential model [see Eq. (11)] in Fig. 4 demonstrates fairly good agreement up to an energy of 10.2 MeV, at which the theoretical calculations describe well the shape of the experimental angular distribution, but they overestimate the cross section. Unfortunately, data for higher energies are very scanty.

Thus, we conclude that, both for elastic $d + t(h)$ scattering and for the respective inelastic processes leading to the production of singlet np (nn) pairs, the supermultiplet potential model is able to describe satisfactorily the available experimental data in the

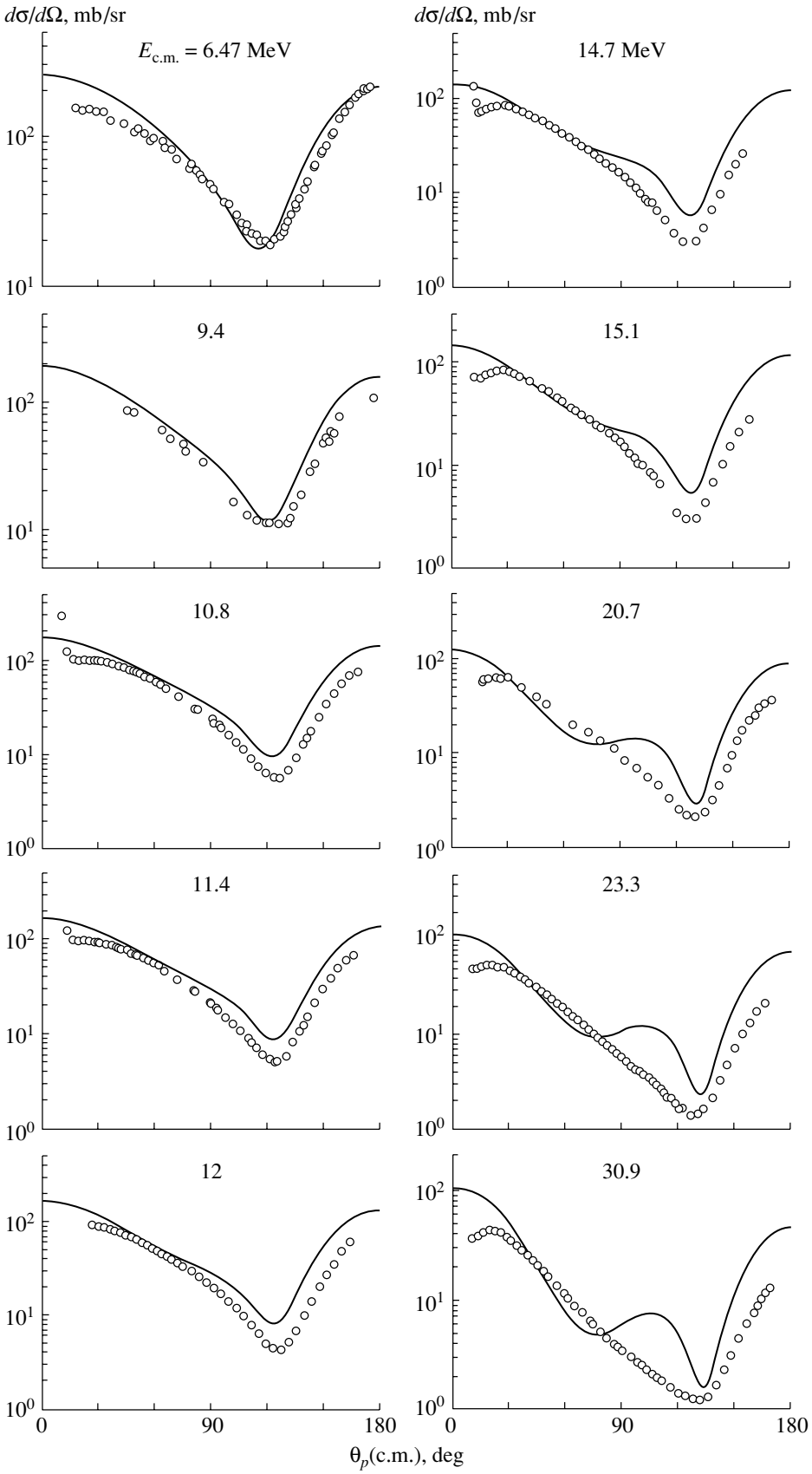

Fig. 5. Experimental angular dependences for elastic *pd* scattering (points) and results of the calculations based on the supermultiplet potential model (solid curves). References to the relevant experimental studies are given in the main body of the text. Data at an energy value of 9.4 MeV are those on *nd* scattering.

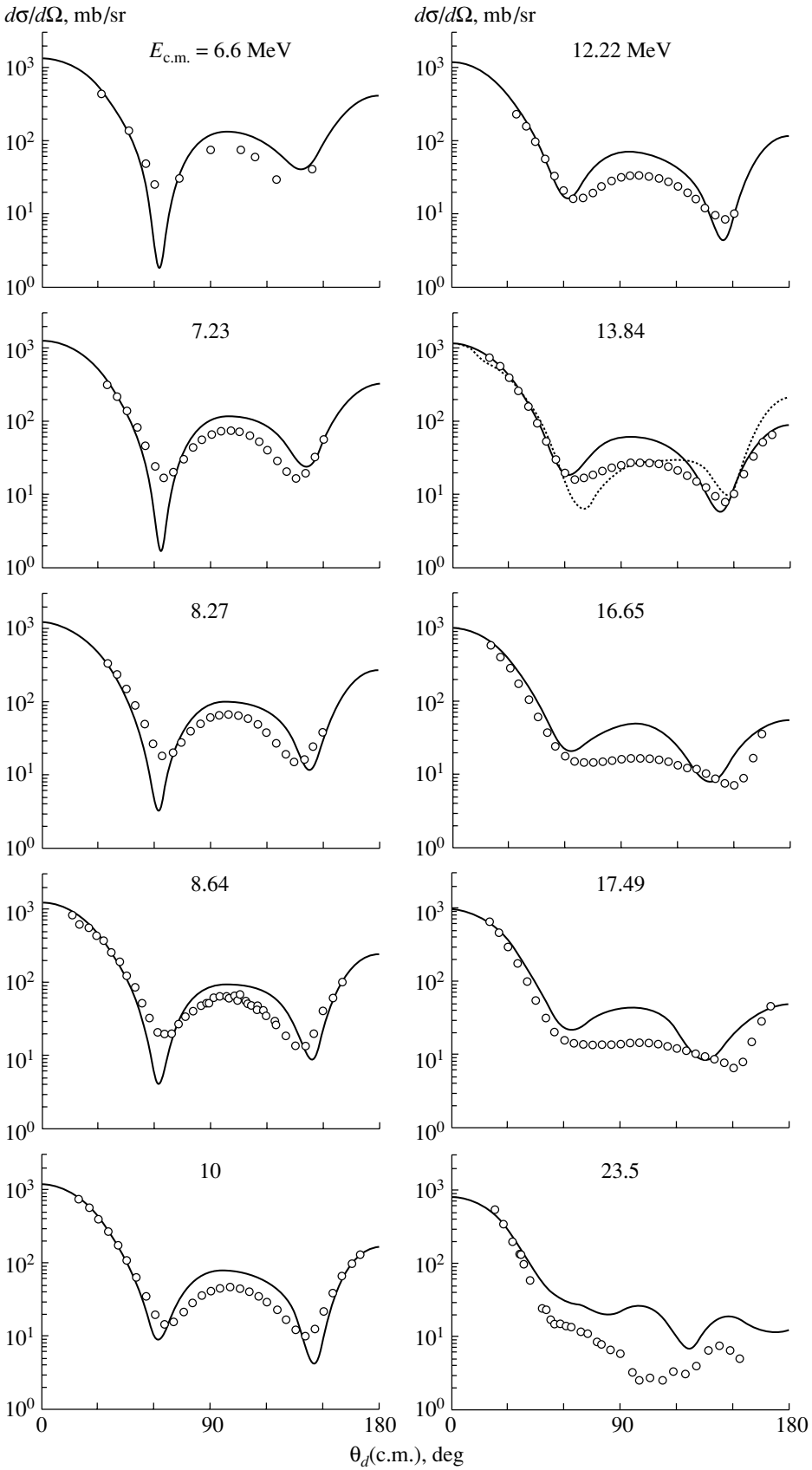

Fig. 6. As in Fig. 5, but for d^3He scattering. The dotted curve represents the results of the calculation based on the resonating-group method [50]. The data presented at an energy value of 6.6 MeV are those for *dt* scattering.

energy range $E_{\text{c.m.}} \simeq 6$–17 MeV and that, as the energy increases further, the agreement fast becomes poorer, which is due to an increase in the imaginary part $iW(r)$ of the potential.

Briefly summarizing our consideration of the $d + t(h)$ system, we can state that even the aforementioned 50% difference of the powers of the $d + t(h)$ potentials for the $[f] = [41]$ and $[f] = [32]$ Young diagrams is sufficient for the supermultiplet potential model to be quantitatively accurate. The significant difference between these potentials in power is manifested, in particular, in that the differential cross sections for elastic scattering in the $S = 1/2$ channel and those for the process $d \to d_s(nn)$ are commensurate in Fig. 4, in contrast to what can be seen in Fig. 3.

The situation for the $d + d$ system, where [with an eye to the process $d + d \to d_s(nn) + d_s(pp)$ in relation to elastic scattering in the $S = 0$ channel] the potentials $V^{[4]}(r)$ and $V^{[22]}(r)$ differ in power by a factor as great as 3 [11], would be extreme. That the process $d + d \to d_s + d_s$ is of paramount importance is suggested even by available results (see [51]). In principle, the above formidable distinction furnishes a sufficient motivation for performing a $^6\text{Li} + d$ experiment [both for elastic scattering and for spin flip into singlets $^6\text{Li}(3.56\ \text{MeV}, 0^+, T = 1) + d_s$] with the interference in the $S = 0$ channel between the amplitudes for the signatures of $[f] = [44]$ and $[f] = [422]$. However, it is very difficult at present to measure phase shifts for this scattering process at various values of the total spin S and the cross sections for the spin-flip process leading to the formation of the above singlets.

5. CONCLUSION

We have systematically investigated the consequences of the fact that, within the supermultiplet potential model, there can arise an inelastic channel where, owing to a superposition of potential amplitudes corresponding to different Young diagrams $[f]$, a deuteron undergoes spin–isospin flip (charge exchange), $d \to d_s(nn)$. The approach to studying the interactions of extremely light nuclei (clusters) that is based on this important possibility makes it possible to express the differential cross sections for the process $d \to d_s(nn)$ in terms of phase shifts $\delta_{L,S}$ at different total spins S for the elastic-scattering process, which is described simultaneously, and provides a clear pattern of the physics behind the scattering process. This approach is also very straightforward in numerical calculations.

Experiments studying reactions that lead to the production of singlet np and nn pairs have been performed over a few decades; however, it turned out that only a small amount of data can be found in the literature that are suitable for directly analyzing them within the supermultiplet potential model; moreover, all of them concern dp and $dt(h)$ scattering. In the present study, we have therefore performed, for the first time, a systematization of these data from the literature and have recast them into a unified form of the angular dependences of the differential cross sections for reactions leading to the production of singlet pairs (this is of value in itself). This procedure was implemented by using the well-known Migdal–Watson approximation, which successfully describes spectra in the region of final-state interaction. For our analysis, we have used data both from kinematically complete experiments and from measurements of inclusive spectra. In either case, the application of the Migdal–Watson approximation has made it possible to perform integration of the spectra quite reliably and to obtain identical results in those cases where the same reaction has been considered by the two methods.

A comparison of the experimental data transformed in this way with theoretical results based on the supermultiplet potential model has revealed that, over quite a broad energy region, this model successfully describes both elastic scattering in the $d + t(h)$ system and reactions involving the flip of the deuteron spin and isospin into a singlet or the production of np and nn pairs (in principle, this must also be so for pp pairs). At the same time, the description of the spin-flip process producing a singlet is only qualitative for the $d + p$ system. The latter is due to the fact that the potentials for the $[f] = [3]$ and $[f] = [21]$ Young diagrams differ in power only by 20%, which is insufficient for the supermultiplet potential model to be valid; for the $[f] = [41]$ and $[f] = [32]$ Young diagrams (which differ by the excitation of a closed nucleon quartet), this distinction is 50%. At the same time, the difference of the powers of the potentials for the signatures of $[f] = [4]$ and $[f] = [22]$ must be as great as 300% for the $d + d$ system. The question associated with this is of importance for describing the process $d + d \to d_s + d_s$, but experimental data required here have yet to be obtained [currently available data on the processes $d + t(h) \to d_s + t(h)$ and $d + t \to nn + h$ cover only the narrow region of small angles]. By and large, the results presented here demonstrate that analyses in terms of Young diagrams, which characterize multiplet symmetry, could be very useful in the theory of few-body systems.

REFERENCES

1. S. P. Merkur'ev and L. D. Faddeev, *Quantum Scattering Theory for Few-Body Systems* (Nauka, Moscow, 1985).

2. W. Gloekle, H. Witala, D. Huber, *et al.*, Phys. Rep. **274**, 107 (1996); G. G. Ellerkman, W. Sandhas, S. A. Sofianos, and H. Fiedeldey, Phys. Rev. C **53**, 2638 (1996); A. C. Fonseca, in *Proceedings of the XV International Conference "Few-Body Problems in Physics," Groningen, 1997*, Ed. by J. C. S. Bacelar *et al.* (Elsevier, Amsterdam, 1998), p. 675.
3. H. Kanada, T. Kaneko, and Y. C. Tang, Phys. Rev. C **34**, 22 (1986); K. K. Q. Lin, Y. C. Tang, and H. Kanada, Few-Body Syst. **12**, 175 (1992); R. S. Mackintosh and S. G. Cooper, Nucl. Phys. A **589**, 377 (1995).
4. V. G. Neudatchin, V. I. Kukulin, V. P. Korennoy, and V. L. Korotkih, Phys. Lett. B **34B**, 581 (1971); V. I. Kukulin, V. G. Neudatchin, and Yu. F. Smirnov, Nucl. Phys. A **245**, 429 (1975); V. I. Kukulin, V. G. Neudachin, and Yu. F. Smirnov, Fiz. Élem. Chastits At. Yadra **10**, 1236 (1979) [Sov. J. Part. Nucl. **10**, 492 (1979)].
5. V. G. Neudatchin and Yu. F. Smirnov, *Nucleon Clusters in Light Nuclei* (Nauka, Moscow, 1969); O. F. Nemets, V. G. Neudatchin, A. A. Rudchik, *et al.*, *Nucleon Clustering in Nuclei and Nuclear Reactions of Multinucleon Transfer* (Naukova Dumka, Kiev, 1988).
6. Y. Kundo, F. Michel, and G. Reidemeister, Phys. Lett. B **242**, 340 (1990); F. Michel and G. Reidemeister, Phys. Rev. C **53**, 3032 (1996); M. E. Brandan and G. R. Satchler, Phys. Rep. **285**, 143 (1997).
7. N. A. Burkova and M. A. Zhusupov, Izv. Akad. Nauk SSSR, Ser. Fiz. **51**, 182 (1987); N. A. Burkova, V. V. Denyak, R. A. Eramzhyan, *et al.*, Nucl. Phys. A **586**, 293 (1995); I. V. Kopytin, M. A. Dolgopolov, and A. A. Khuskivadze, Yad. Fiz. **61**, 630 (1998) [Phys. At. Nucl. **61**, 558 (1998)]; I. V. Kopytin, A. S. Kornev, and A. A. Khuskivadze, Izv. Akad. Nauk, Ser. Fiz. **63**, 1005 (1999).
8. W. Iskra, A. I. Mazur, V. G. Neudachin, and Yu. F. Smirnov, Yad. Fiz. **48**, 1674 (1988) [Sov. J. Nucl. Phys. **48**, 1003 (1988)]; V. I. Kukulin, V. G. Neudachin, and V. N. Pomerantsev, Yad. Fiz. **24**, 298 (1976) [Sov. J. Nucl. Phys. **24**, 155 (1976)].
9. V. I. Kukulin, V. G. Neudachin, V. N. Pomerantsev, and A. A. Sakharuk, Yad. Fiz. **52**, 402 (1990) [Sov. J. Nucl. Phys. **52**, 258 (1990)]; S. B. Dubovichenko, V. G. Neudachin, A. A. Sakharuk, and Yu. F. Smirnov, Izv. Akad. Nauk SSSR, Ser. Fiz. **54**, 911 (1990).
10. S. B. Dubovichenko and A. V. Dzhazairov-Kakhramanov, Yad. Fiz. **51**, 1541 (1990) [Sov. J. Nucl. Phys. **51**, 971 (1990)]; Yad. Fiz. **56** (4), 45 (1993) [Phys. At. Nucl. **56**, 447 (1993)].
11. V. G. Neudatchin, V. I. Kukulin, V. N. Pomerantsev, and A. A. Sakharuk, Phys. Rev. C **45**, 1512 (1992); V. G. Neudachin, A. A. Sakharuk, and Yu. F. Smirnov, Fiz. Élem. Chastits At. Yadra **23**, 479 (1992) [Sov. J. Part. Nucl. **23**, 210 (1992)].
12. V. G. Neudatchin, A. A. Sakharuk, and S. B. Dubovitchenko, Few-Body Syst. **18**, 159 (1995).
13. V. G. Neudachin, I. T. Obukhovskiĭ, and Yu. F. Smirnov, Fiz. Élem. Chastits At. Yadra **15**, 1165 (1984) [Sov. J. Part. Nucl. **15**, 519 (1984)].
14. J. P. Burq, J. C. Cabrillat, M. Chemarin, *et al.*, Nucl. Phys. A **179**, 371 (1972).
15. J. C. van der Weerd, T. R. Canada, C. L. Fink, and B. L. Cohen, Phys. Rev. C **3**, 65 (1971).
16. H. Klein, H. Eichner, H. J. Helten, *et al.*, Nucl. Phys. A **199**, 169 (1973).
17. M. Przyborowski, M. Eggert, R. Engels, *et al.*, Phys. Rev. C **60**, 064004 (1999).
18. E. L. Petersen *et al.*, in *Proceedings of the Conference on Few-Body Problems, Quebec, 1974* (North-Holland, Amsterdam, 1974), p. 395.
19. H. Brückman, W. Kluge, M. Matthäy, *et al.*, Bull. Am. Phys. Soc. **15**, 477 (1970).
20. D. J. Margaziotis, M. B. Epstein, I. Šlaus, *et al.*, Phys. Rev. C **8**, 870 (1973).
21. E. L. Petersen, M. I. Haftel, R. G. Allas, *et al.*, in *Proceedings of the VII International Conference on Few-Body Problems in Nuclear and Particle Physics, Delhi, 1976* (North-Holland, Amsterdam, 1976), p. 201.
22. K. Ilakovac, L. H. Kuo, M. Petravić, and I. Šlaus, Phys. Rev. **124**, 1923 (1961).
23. H. T. Larson, A. D. Bacher, K. Nagatani, and T. A. Tombrello, Nucl. Phys. A **149**, 161 (1970).
24. B. G. Struzhko, Izv. Akad. Nauk, Ser. Fiz. **64**, 466 (2000); Ukr. Fiz. Zh. **45**, 1154 (2000).
25. Z. Auer, S. E. Darden, S. Sen, and R. E. Warner, Nucl. Phys. A **562**, 1 (1993).
26. S. E. Darden, O. Karban, C. Blyth, *et al.*, Nucl. Phys. A **486**, 285 (1988).
27. M. Bruno, F. Cannata, M. D. Agostino, *et al.*, J. Phys. G **14**, L235 (1988).
28. R. E. Warner, R. L. Ruyle, W. G. Davies, *et al.*, Nucl. Phys. A **255**, 95 (1975).
29. D. V. Aleksandrov, E. Yu. Nikol'skiĭ, B. G. Novatskiĭ, *et al.*, Pis'ma Zh. Éksp. Teor. Fiz. **67**, 860 (1998) [JETP Lett. **67**, 903 (1998)].
30. H. Kumpf, J. Mösner, K. Möller, and G. Schmidt, Fiz. Élem. Chastits At. Yadra **9**, 412 (1978) [Sov. J. Part. Nucl. **9**, 170 (1978)].
31. A. V. Migdal, Zh. Éksp. Teor. Fiz. **28**, 3 (1955) [Sov. Phys. JETP **1**, 2 (1955)].
32. K. M. Watson, Phys. Rev. **88**, 1163 (1952).
33. G. G. Olsen, Nucl. Instrum. Methods **37**, 240 (1965).
34. M. L. Goldberger and K. M. Watson, *Collision Theory* (Wiley, New York, 1964; Mir, Moscow, 1967).
35. R. Machleidt, Adv. Nucl. Phys. **19**, 189 (1989).
36. W. Tornow, T. S. Carman, Q. Chen, *et al.*, Nucl. Phys. A **631**, 421c (1998).
37. G. C. Phillips, T. A. Griffy, and L. C. Biedenharn, Nucl. Phys. **21**, 327 (1960).
38. A. Niiler, C. Joseph, V. Valcovič, *et al.*, Phys. Rev. **182**, 1083 (1969).
39. J. C. Allred, A. H. Armstrong, R. O. Bondelid, and L. Rosen, Phys. Rev. **88**, 433 (1952).
40. J. C. Allred, A. H. Armstrong, and L. Rosen, Phys. Rev. **91**, 90 (1953).
41. T. A. Cahill, J. Greenwood, H. Willmes, and D. J. Shadoan, Phys. Rev. C **4**, 1499 (1971).

42. K. Sagara, H. Oguri, S. Shimizu, *et al.*, Phys. Rev. C **50**, 576 (1994).
43. W. K. Grüebler, V. Konig, P. A. Schmelzbach, *et al.*, Nucl. Phys. A **398**, 445 (1983).
44. C. C. Kim, S. M. Bunch, D. W. Devins, and H. H. Foster, Nucl. Phys. **58**, 32 (1964).
45. S. N. Bunker, J. M. Cameron, R. F. Carlson, *et al.*, Nucl. Phys. A **113**, 461 (1968).
46. M. Ivanovich, P. G. Young, and G. G. Ohlsen, Nucl. Phys. A **110**, 441 (1968).
47. T. R. King and S. Rodman, Nucl. Phys. A **183**, 657 (1972).
48. J. E. Brolley, Jr., T. M. Putnam, L. Rosen, and L. Stewart, Phys. Rev. **117**, 1307 (1960).
49. R. W. Rutkowski and E. E Gross, Phys. Rev. C **12**, 362 (1975).
50. F. S. Chwieroth, Y. C. Tang, and D. R. Thompson, Phys. Rev. C **9**, 56 (1974).
51. B. G. Struzhko, Izv. Akad. Nauk, Ser. Fiz. **64**, 76 (2000); B. G. Struzhko, J. Phys. Stud. (Lviv, Ukraine) **3**, 431 (1999).

Translated by A. Isaakyan

Physics of Atomic Nuclei, Vol. 65, No. 3, 2002, pp. 478–483. Translated from Yadernaya Fizika, Vol. 65, No. 3, 2002, pp. 504–509.

ELEMENTARY PARTICLES AND FIELDS
Experiment

Mechanism of ^{238}U Disintegration Induced by Relativistic Particles

L. N. Andronenko, A. A. Zhdanov, A. V. Kravtsov, and G. E. Solyakin

Petersburg Nuclear Physics Institute, Russian Academy of Sciences, Gatchina, 188350 Russia

Received July 28, 2000; in final form, June 28, 2001

Abstract—In heavy-nucleus disintegration induced by a relativistic projectile particle, the production of collinear massive fragments accompanied by numerous charged particles and neutrons is explained in terms of the mechanism of projectile-momentum compensation due to the emission of a particle whose mass is greater than the projectile mass. © *2002 MAIK "Nauka/Interperiodica".*

1. INTRODUCTION

The interaction of high-energy particles with nuclei has been analyzed for many years. The prevalent opinion is [1] that, to a first approximation, the interaction with an incident particle whose energy is not less than a few hundred MeV can be broken down into two stages. At the first, fast, stage, the incident particle is scattered on target nucleons a few times, thereby leaving part of its energy in the nucleus. At the second stage—it presumably begins when the incident particle has already escaped from the nucleus—the energy transferred to the nucleus at the first stage is dissipated in this nucleus, which eventually decays. In the case of heavy nuclei, the decay products include two massive fragments accompanied by neutrons and charged particles. The cross sections for the production of two massive fragments are large, which suggests a high fissility of heavy nuclei in the channel of fission induced by relativistic particles. For example, the ratio of the measured total cross section for the production of two massive fragments to the total inelastic cross section, σ_f/σ_{in}, is 0.865 ± 0.036 for the irradiation of ^{238}U nuclei with 1-GeV protons [2].

A detailed analysis of the mechanism of heavy-nucleus disintegration versus the excitation energy is a conventional topic of reviews regularly appearing in the literature. Since the publication of that presented in [3], there have appeared new experimental data that make it possible to refine or even to change our ideas of the process being discussed. In this article, special emphasis is placed on the fact that the motion of two massive fragments is collinear, which is inherent in heavy-nucleus disintegration induced by relativistic particles. This property is at odds with observations of fragments of fission induced by heavy ions, but it is similar to what is observed in spontaneous fission, where there is no momentum transfer to the nucleus undergoing fission.

The objective of this study is to analyze the possible consequences of going over from a branched cascade [1, 3] at the first stage of relativistic-particle interaction with a heavy nucleus to the concept of a single scattering event resulting in projectile-momentum compensation. In [4], we compared the properties of charged particles accompanying two massive fragments in the spontaneous fission of the ^{252}Cf nucleus and in ^{238}U disintegration induced by relativistic particles and collected references to relevant experimental studies. Below, we use experimental data on charged particles from these two processes.

2. ^{238}U DISINTEGRATION INDUCED BY 1-GeV PROTONS AND 2-GeV ^{3}He NUCLEI

In studying heavy-nucleus disintegration into two massive fragments accompanied by charged particles and neutrons, it is important to know the numbers of these charged particles and neutrons and their production rates. Relevant experimental data are presented in [5–8]. Necessary information from those studies for 1-GeV protons is given in Table 1, which displays the production rates (F) for $(2f + n_c)$ disintegration events, where two massive fragments $(2f)$ are accompanied by a preset number n_c of charged particles of lower mass. The experimental probability of the process in which ^{238}U nuclei irradiated with 1-GeV protons undergo coplanar ternary fission into fragments of commensurate masses is quoted in the last column of Table 1. Thus, the irradiation of heavy nuclei with relativistic particles can initiate decays into either three fragments of commensurate masses $(3f)$ or two massive fragments accompanied by a large number of charged particles $(2f + n_c)$. It is noteworthy that, in the case of large n_c, the total mass of all particles, both charged ones and neutrons, can appear to be commensurate with the mass of

1063-7788/02/6503-0478$22.00

Table 1. Production rates (F) for $2f + n_c$ events at various n_c in ^{238}U disintegration induced by 1-GeV protons

n_c	0	1	2	3	4	5	6	7	8	9	10–13	$3f$
F, %	46.3	18.9	14.7	9.5	4.1	3.7	1.4	0.6	0.4	0.2	0.2	$(4.7 \pm 0.5) \times 10^{-2}$

each of the recorded fragments. Naturally, this could imply that the missing mass or a major part of it is associated with a third massive nuclear fragment that is unstable, with a lifetime being commensurate with the time over which the massive fragments fly apart under the effect of their Coulomb repulsion. To confirm or disprove this, it is necessary to measure those parameters of nuclear disintegration that would be sensitive to the motion of the missing mass lost by the initial nucleus. For such a parameter, we can propose the angle θ between the momenta of the massive fragments, which characterizes the recoil momentum caused by the motion of the missing mass.

Measurements of θ for ^{238}U disintegration induced by 1-GeV protons were performed in photoemulsion layers irradiated at the Gatchina synchrocyclotron. The mean angle $\langle\theta\rangle$ as a function of the multiplicity n_c of accompanying charged particles was presented in [9]. Immediately after that, there appeared similar data obtained in Saclay for ^{238}U disintegration induced by 2-GeV ^{3}He ions [10], but those data were presented as a function of the number n_0 of the accompanying neutrons. Calculations of relevant distributions on the basis of the cascade–evaporation model were also presented in [10]. However, the possibility that a third, unstable, nuclear fragment can be formed was disregarded there. Here, we compare these data from the different experiments and analyze the role of unstable nuclear fragments in the mechanism of ^{238}U disintegration induced by relativistic particles.

The experimental dependence of the mean angle $\langle\theta\rangle$ on the multiplicity n_c of accompanying charged particles for ^{238}U disintegration induced by 1-GeV protons is shown in Fig. 1 according to data from [9]. For ^{238}U disintegration induced by 2-GeV ^{3}He ions, the experimental and the calculated results from [10] for the mean angle $\langle\theta\rangle$ as a function of the number n_0 of neutrons accompanying two massive fragments are displayed in Fig. 2. The discrepancy between the experimental data and the cascade–evaporation results, which becomes more pronounced with increasing number n_0 of emitted neutrons, is the most impressive result in Fig. 2. This discrepancy, which is as large as 20° at high n_0 values, indicates that the recoil momentum is strongly overestimated in the calculation. This overestimation is due to adopting an exaggerated value for the excitation energy accumulated in the residual nucleus. The requirement of projectile-momentum compensation needed for the formation of a collinear three-body configuration reduces significantly the excitation energy accumulated in the residual nucleus. A decrease in the energy and momentum per unit of the missing mass can lead to a reduction of the total recoil momentum.

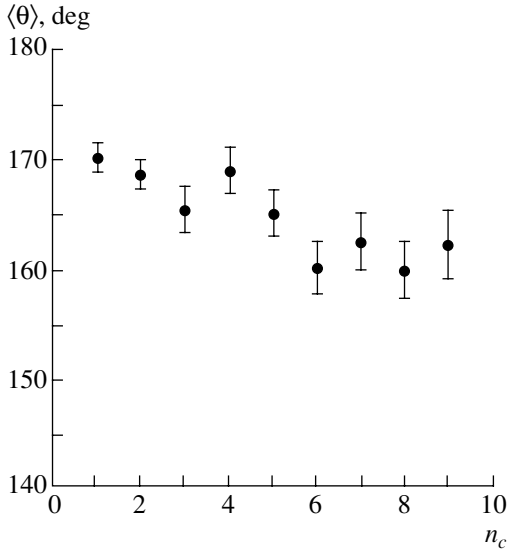

Fig. 1. Experimental dependence of the mean angle $\langle\theta\rangle$ between the momenta of two massive fragments on the number n_c of accompanying charged particles for ^{238}U disintegration induced by 1-GeV protons.

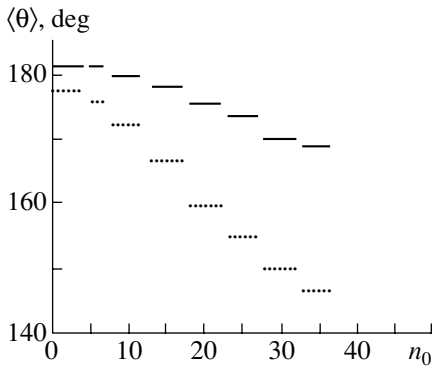

Fig. 2. Experimental (solid straight-line segments) and calculated (dotted straight-line segments) dependences of the mean angle $\langle\theta\rangle$ between the momenta of two fragments on the number n_0 of accompanying neutrons for the ^{238}U disintegration induced by 2-GeV ^{3}He ions. The lengths of the segments correspond to the limits within which the numbers of recorded neutrons varied.

Table 2. Properties of light unstable nuclear fragments

Decay of third (unstable) fragment	Lifetime, s	Energy release Q, MeV
$^5\mathrm{He}(3/2^-) \to {}^4\mathrm{He} + n$	1.1×10^{-21}	0.85
$^7\mathrm{He}(3/2^-) \to {}^6\mathrm{He} + n$	4.1×10^{-21}	0.44
$^8\mathrm{Li}^*(3^+) \to {}^7\mathrm{Li} + n$	2×10^{-20}	0.25
$^7\mathrm{Li}^*(7/2^-) \to {}^4\mathrm{He} + {}^3\mathrm{H}$	7×10^{-21}	2.16
$^6\mathrm{He}^*(2^+) \to {}^4\mathrm{He} + 2n$	6×10^{-21}	0.98

It seems difficult to relate directly the dependence of the angle in question on the multiplicity of charged particles to the dependence of this angle on the number of accompanying neutrons for any multiplicity value. For example, accompanying charged particles can be absent in the case of small n_0. At the same time, one charged particle can accompany two massive fragments both in the case where there are a great number of accompanying neutrons and in the case where their number is small. Nevertheless, there can be a correlation for the maximum measured values of n_0 and n_c, since a high multiplicity of charged particles and a large number of emitted neutrons must correspond to the same disintegration events recorded in different experiments. In order to render a further analysis more illustrative, we deem it appropriate to combine the data presented in Figs. 1 and 2 in the way adopted in Fig. 3. The ordinate remains unchanged, and the bottom and the top abscissa are used for n_c and n_0, respectively. In choosing the axes, we impose the condition $n_0/n_c = 5$, which corresponds to the emission of one charged particle per five neutrons. This choice seems realistic; however, a strict relationship cannot be guaranteed at small values of n_0 and n_c (see above). In principle, we can choose a different scale, but the problem of correlation between n_0 and n_c cannot be solved unambiguously

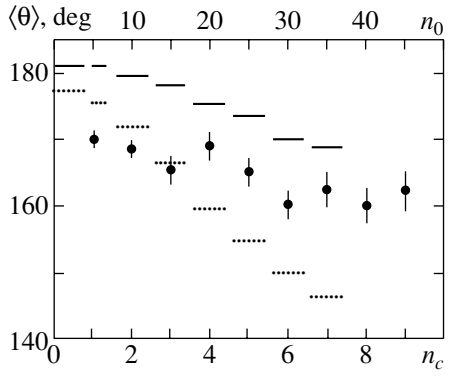

Fig. 3. Combination of the data presented in Figs. 1 and 2.

without additional experimental data. If the $\langle\theta\rangle$ data for all $n_c \geq 7$ are considered as a single experimental point, it turns out that, for the multiplicities from $n_c = 4$ to $n_c \geq 7$, the mean values of the angles $\langle\theta\rangle$ between the momenta of two massive fragments fall just in the middle between the experimental and calculated data obtained for the number n_0 of neutrons from 20 to 35. This means that the recoil momentum in the system of two massive fragments is always higher if the missing mass initially has an electric charge. The motion of this charge as a discrete unit generates a greater recoil effect than the motion of individual nucleons among which neutrons prevail. The motion of a charged nuclear bunch is rather similar to the motion of two fragments at an early stage of Coulomb acceleration, whence it follows that it can be considered as a third fragment. However, this third fragment is unstable; therefore, it does not have time to acquire the total speed and energy, decaying within the time of the Coulomb acceleration of the stable fragments. The very production of these unstable nuclear fragments appears to be possible owing to the collinear three-body configuration, with the excitation energy being concentrated in between two would-be fragments, which, at the initial instant, help to hold excited hadronic matter at rest. As was mentioned above, an overestimation of recoil in the calculation within the cascade–evaporation model at $n_c \geq 4$ is due to the use of a substantially exaggerated value for the accumulated excitation energy, which is concentrated in the entire volume of the residual nucleus. However, the cascade–evaporation mechanism is not completely replaced by the mechanism of the production and subsequent disintegration of a three-body collinear configuration. On the contrary, it remains the basic mechanism in terms of the probability of disintegration leading to small and moderate multiplicities of accompanying particles. This means that the experimental and the calculated values of $\langle\theta\rangle$ must coincide at some value of n_c. In Fig. 3, this occurs at $n_c = 3$. For a different relation between n_0 and n_c, the coincidence would occur at higher or lower values of accompanying charged particles. This uncertainty will be irremovable as long as there are only two sets of experimental data, presented in Fig. 3. Nevertheless, it can be stated that, since the last three calculated values corresponding to the angles of $\langle\theta\rangle = 154.8°$, $149.9°$, and $146.4°$ cannot be correlated with any available experimental data, the dominant role of the collinear three-body configuration is unquestionable for such events of $^{238}\mathrm{U}$ disintegration induced by relativistic particles.

As in the case of $n_c = 3$ in Fig. 3, the agreement between the results of the calculations and experimental data can be considered as the disappearance

of the collinear three-body configuration with its inherent features in the excitation energy and the initial position of the unstable nuclear fragment in between the two recorded fragments. The conventional mechanism considered in [1, 3] then becomes dominant. In this case, the excitation energy is far from its maximum possible value; this is confirmed by the detection of a small or a moderate number of charged or neutral accompanying particles.

For our analysis to be complete, it only remains to find out why the recoil is greater than that which follows from the calculation for $n_c = 1$ and $n_c = 2$ (Fig. 3). Strange as it may seem, the production of light unstable nuclear fragments accompanying two massive fragments is one of the reasons for this. The existence of the spatial and kinematic correlations between charged particles and neutrons and between two charged particles [4] accompanying pair massive fragments of spontaneous fission of ^{252}Cf nuclei was established in different experiments. The experimental data could be explained by the formation of light unstable nuclear fragments and their subsequent disintegration from the ground state or from excited states. Table 2 displays the features of light unstable nuclear fragments known at present. Their lifetimes are commensurate with the time of the Coulomb acceleration of pair massive fragments or exceed it sometimes.

If such neutron-rich nuclei are produced in the spontaneous fission of ^{252}Cf, their production is even more probable in heavy-nucleus disintegration induced by relativistic particles. In particular, disintegration processes starting from excited states are possible; for one, this may be the process $^6\mathrm{He}^*(1.80\ \mathrm{MeV}) \to {}^4\mathrm{He} + 2n$ featuring two neutrons in the final state. Our statement is that the recoil effect associated with the escape of ^{6}He* is always more pronounced than a random combination of recoil effects from three particles. This conclusion remains valid for any disintegration process involving a single charged particle in the final state.

For disintegration processes where the number of accompanying charged particles is $n_c \geq 4$, the diametrically opposite observation of mean angles between the momenta of massive fragments in excess of the calculated ones can also be explained by the disintegration of unstable nuclear fragments. These fragments have higher mass than light fragments in $n_c = 1$ events. A few charged particles are produced in the fission of such fragments, and the direction of motion of the primary fragment is not conserved.

The argument presented in our article is qualitative, because the analysis of the distributions of $\langle\theta\rangle$ was not the main subject in [9, 10]. Nevertheless, this analysis shows that the data on the angles between the momenta of massive fragments may be a direct source of information about the mechanism of nuclear disintegration.

3. COMPENSATION OF THE MOMENTUM OF A RELATIVISTIC PARTICLE INCIDENT ON A HEAVY NUCLEUS

If we go over, as was discussed in the Introduction, from the assumption of a branched cascade at the first stage of the interaction to the single-collision hypothesis, which results in projectile-momentum compensation, the excitation energy W_{ex} accumulated in the nucleus will be given by

$$W_{\mathrm{ex}} = (A_1 - A_2 + m_1)c^2 + T - (m_2^2c^4 + 2m_1c^2T + T^2)^{1/2}, \quad (1)$$

where A_1 and A_2 are the masses of, respectively, the target and the residual nucleus; m_1 and m_2 are the masses of, respectively, the incident and the outgoing particle; c is the speed of light; and T is the kinetic energy of the incident particle. The sum of the last two terms in the radicand is equal to the product of the square of the projectile momentum, $P_1^2 = 2m_1T + (T/c)^2$, and the square of the speed of light. At $m_1 = m_2$, we automatically obtain $A_1 = A_2$ and $W_{\mathrm{ex}} = 0$. This result is usual for the conventional cascade–evaporation model, where the excitation energy of the residual nucleus is related to the longitudinal momentum transfer to the nucleus by a linear equation. Experiments seem to support this result, because an appreciable fraction of all disintegration events (Table 1) are those of low-energy collinear fission not involving outgoing charged particles. However, experimental data also demonstrate that the escape of massive fragments is collinear in high-n_c events when charged particles are recorded [9] and in high-n_0 events when neutrons are recorded [10] as well. This suggests that W_{ex} is not zero. In order to ensure this in formula (1), it is necessary that $m_2 > m_1$, which automatically entails the condition $A_2 < A_1$.

We deem it appropriate to perform specific calculations by formula (1) for the reactions

$$p + {}^{238}\mathrm{U} \to {}^{237}\mathrm{U} + d,$$
$${}^3\mathrm{He} + {}^{238}\mathrm{U} \to {}^{237}\mathrm{U} + {}^4\mathrm{He}.$$

For the first and the second reaction, the solid and the dashed curve in Fig. 4, respectively, illustrate the behavior of the excitation energy W_{ex} versus the kinetic energy T of the incident particle. It can clearly be seen that the excitation energies W_{ex} are quite close for the two reactions when $T_p = 1$ GeV and $T_{^3\mathrm{He}} = 2$ GeV. This justifies the comparison of the experimental data obtained in [9, 10]. In both reactions, the excitation energy W_{ex} tends to the limit ($A_1 -$

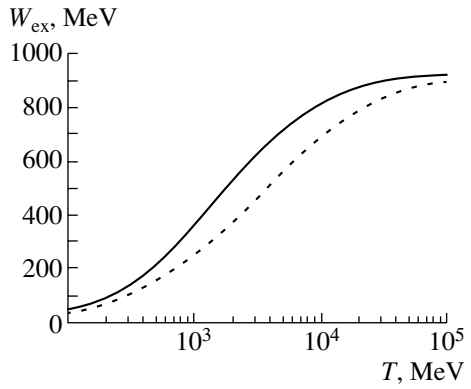

Fig. 4. Excitation energy W_{ex} as a function of the kinetic energy T of the incident particle for the reactions (solid curve) $p + {}^{238}\mathrm{U} \to {}^{237}\mathrm{U} + d$ and (dashed curve) ${}^{3}\mathrm{He} + {}^{238}\mathrm{U} \to {}^{237}\mathrm{U} + {}^{4}\mathrm{He}$ under the assumption of projectile-momentum compensation.

$A_2)c^2$ with increasing T, their difference vanishing in proportion to $(m_2^2 - m_1^2)c^4/2T$.

In the limit $T \ll m_2c^2$, formula (1) reduces to

$$W_{ex} = [(A_1 + m_1) - (A_2 + m_2)]c^2 + T\left(1 - \frac{m_1}{m_2}\right)\left(1 - \frac{T}{2m_2c^2}\right). \quad (2)$$

Here, the second term increases with decreasing m_1. This means that a photon beam must be the most efficient incident beam if the momentum-compensation mechanism is realized in nuclear reactions at low energies. Probably, enhanced yields of some fragments in ${}^{232}\mathrm{Th}$ photofission [11] are a manifestation of a higher photoexcitation energy in relation to what occurs in charged-particle beams.

In considering the mechanism of projectile-momentum compensation, it should be borne in mind that conservation laws also admit the mechanism of overcompensation, in which case the outgoing-particle momentum exceeds the incident-particle momentum, with the result that both massive fragments of the heavy nucleus escape into the backward hemisphere. From the experimental data discussed in [3], it follows that the effect of escape of both fragments into the backward hemisphere ($\theta > 180^\circ$) was sometimes observed. This is also suggested by experimental data presented in [10].

The degree of overcompensation can be characterized by a dimensionless parameter ξ ($\xi = 1$ corresponds to exact compensation). Formula (1) for W_{ex} can then be rewritten as

$$W_{ex} = (A_1 - A_2 + m_1)c^2 + T - [m_2^2c^4 + \xi^2(2m_1c^2T + T^2)]^{1/2} - \frac{(\xi - 1)^2(2m_1c^2T + T^2)}{2A_2c^2}, \quad (3)$$

where the last term takes into account the translational motion of the residual nucleus A_2. For each value of the initial kinetic energy T of the incoming particle m_1, there is some maximum value ξ_{max} specified by (3), provided that the excitation energy is equal to the height of the fission barrier for the heavy nucleus being considered ($W_{ex} = B_f$). In turn, ξ_{max} makes it possible to calculate the limiting angle $\theta_{max} > 180^\circ$ between the momenta of two fragments flying into the backward hemisphere.

4. CONCLUSION

Collinear two- and three-body configurations arising as the result of the primary interaction of an incident particle with a heavy nucleus have enabled us to explain the appearance of events featuring the production of massive fragments accompanied by neutrons and charged particles. An analysis of the experimental distributions with respect to the angle between the momenta of two massive fragments in events characterized by a high multiplicity of accompanying charged particles suggests that the entire missing nuclear mass moves as a discrete unit.

The condition of projectile-momentum compensation considered in this study is the simplest one, because the masses of the incident (m_1) and the outgoing (m_2) particle differ by one mass unit. It is this circumstance that minimizes the excitation energy W_{ex} accumulated in the nucleus undergoing fission. If the mass m_2 differs from m_1 more strongly, the excitation energy W_{ex} will be higher.

ACKNOWLEDGMENTS

We are grateful to M. Mutterer for placing at our disposal information about light unstable nuclear fragments recorded in the spontaneous fission of ${}^{252}\mathrm{Cf}$ nuclei. We also thank H.E. Belovitsky for developing a method for implanting ${}^{238}\mathrm{U}$ nuclei into photoemulsions, which was successfully used in experiments with a 1-GeV proton beam.

REFERENCES

1. J. Cugnon, Nucl. Phys. A **462**, 751 (1987).
2. L. A. Vaishnene, L. N. Andronenko, G. G. Kovshevny, *et al.*, Z. Phys. A **302**, 143 (1981).
3. L. N. Andronenko, L. A. Vaĭshnene, A. A. Kotov, *et al.*, Fiz. Élem. Chastits At. Yadra **18**, 685 (1987) [Sov. J. Part. Nucl. **18**, 289 (1987)].
4. L. N. Andronenko, A. A. Zhdanov, A. V. Kravtsov, and G. E. Solyakin, Preprint No. PNPI-2386 (Petersburg Nuclear Physics Inst., Gatchina, 2000).

5. A. A. Zhdanov, V. I. Zakharov, A. V. Kravtsov, *et al.*, Pis'ma Zh. Éksp. Teor. Fiz. **54**, 311 (1991) [JETP Lett. **54**, 304 (1991)].
6. A. I. Obukhov and G. E. Solyakin, Pis'ma Zh. Éksp. Teor. Fiz. **55**, 548 (1992) [JETP Lett. **55**, 568 (1992)].
7. A. I. Obukhov and G. E. Solyakin, Pis'ma Zh. Éksp. Teor. Fiz. **57**, 73 (1993) [JETP Lett. **57**, 79 (1994)].
8. A. A. Zhdanov, A. I. Obukhov, and G. E. Solyakin, Yad. Fiz. **57**, 1210 (1994) [Phys. At. Nucl. **57**, 1143 (1994)].
9. G. E. Solyakin and A. V. Kravtsov, Phys. Rev. C **54**, 1798 (1996).
10. X. Ledoux, H. G. Bohlen, J. Cugnon, *et al.*, Phys. Rev. C **57**, 2375 (1998).
11. S. A. Karamian, J. Adam, A. G. Belov, *et al.*, Phys. Rev. C **62**, 024601 (2000).

Translated by E. Kozlovskiĭ

Physics of Atomic Nuclei, Vol. 65, No. 3, 2002, pp. 484–496. Translated from Yadernaya Fizika, Vol. 65, No. 3, 2002, pp. 510–522.

ELEMENTARY PARTICLES AND FIELDS
Experiment

Investigation of the Inclusive Spectra of Secondary Protons and Pions of Low Kinetic Energies and of Their Wide Pair Correlations in $\pi^- A$ Interactions at 43 GeV/c

V. G. Kartasheva
The SIGMA–AYAKS Collaboration

Institute for High Energy Physics, Protvino, Moscow oblast, 142284 Russia

Received November 29, 2000

Abstract—The inclusive invariant cross sections for protons produced at angles of $\theta = 90°$ and $60°$ and for positively and negatively charged pions produced at an angle of $\theta = 90°$ are presented for π^-Be, π^-Al, and π^-Cu interactions induced by 43-GeV/c incident π^- mesons. The shape of the inclusive spectra of secondary hadrons, the A dependence of their cross sections, and the correlation functions for pairs of likely charged secondary hadrons at large angles of their divergence are studied. The kinematical region explored in the present article corresponded to kinetic energies of $T \approx 0.16$–0.70 GeV and $T \approx 0.20$–0.76 GeV for secondary protons and secondary pions, respectively. The angles of divergence of hadrons forming a pair, ψ, satisfied the condition $\cos\psi < -0.5$. © *2002 MAIK "Nauka/Interperiodica".*

1. INTRODUCTION

This article is the last one in a series that presents the results obtained by studying data from the most recent run of an experiment performed at the SIGMA–AYAKS facility [1], which was installed at the Institute for High Energy Physics (IHEP, Protvino). Specifically, we consider the results from an investigation of the inclusive spectra of secondary protons produced in π^-Be, π^-Al, and π^-Cu interactions at an incident-negative-pion momentum of $p_{\rm bm} = 43$ GeV/c and recorded at angles of $90°$ and $60°$ and of positively and negatively charged secondary pions that originate from the same interactions at an angle of $90°$. These secondary protons and pions were detected by the double-arm magnetic spectrometer (DAMS) of the facility in the momentum ranges $0.5 < p < 1.5$ GeV/c and $0.3 < p < 1$ GeV/c, respectively. Also presented here are results that were deduced from an analysis of correlations for pairs of likely charged secondary hadrons at large angles of their divergence. The kinematical region explored in this article corresponded to kinetic energies in the ranges $T \approx 0.16$–0.70 GeV and $T \approx 0.20$–0.76 GeV for secondary protons and secondary pions, respectively. That the data of new measurements were obtained in the course of one exposure ensures a high reliability of conclusions that are drawn both from a comparison of the shapes of the inclusive spectra of secondary hadrons and from a comparison of correlation functions for different pairs of hadrons.

The analysis of correlations for some pairs of secondary hadrons originating from hadron–nucleus interactions at incident-positive-pion and incident-proton momenta of $p_{\rm bm} = 3$ and 7.5 GeV/c that was performed at the Institute of Theoretical and Experimental Physics (ITEP, Moscow) revealed [2–4] that the character of wide correlations for pairs of likely charged hadrons (that is, correlations at large angles of divergence of hadrons forming such pairs) is sensitive to the mechanism of their formation, since interference effects and the final-state interaction of particles are immaterial at large angles of divergence, the disregard of such effects and interactions becoming more justified with increasing projectile energy [5]. Therefore, an investigation of wide pair correlations provides an independent check on the concept of hadron-formation processes that is deduced from an analysis of the inclusive spectra of secondary hadrons [2].

Despite a vast body of available experimental data on the generation of secondaries in the region of their cumulative production [6], the mechanism of hadron–nucleus interactions and the effect of nuclear structure on the generation of secondaries in the target-fragmentation region have yet to be understood conclusively. A comparative analysis of inclusive spectra of secondary protons and positively and negatively charged secondary pions recorded at an angle of $90°$ within a single exposure, along with an investigation of correlations for pairs formed by likely charged secondary hadrons that diverge at large angles, furnishes

1063-7788/02/6503-0484$22.00

new information for testing numerous models currently used to describe particle production in nuclear-fragmentation processes.

2. DESCRIPTION OF THE EXPERIMENT AND DATA PROCESSING

The SIGMA–AYAKS facility was arranged at the 2B channel of the accelerator installed at the Institute for High-Energy Physics (IHEP, Protvino). The equipment used in this facility is described in [7, 8]. A beam of 43-GeV/c negatively charged particles that was incident on a target consisted of negative pions, negative kaons, and antiprotons (about 97.9, 1.9, and 0.2%, respectively). Beryllium, aluminum, and copper disks 40 mm in diameter were used for targets, their thicknesses in the beam direction being 70, 23, and 3.86 mm, respectively.

The DAMS of the facility consisted of two arms nearly symmetric with respect to the beam axis. For all targets, the right and the left arm of the DAMS recorded positively charged secondary hadrons of low kinetic energy for emission angles such that $-0.15 < \cos\theta < 0.35$ and $0.30 < \cos\theta < 0.75$ (θ is the angle of secondary-hadron emission in the laboratory frame), respectively, and vice versa for negatively charged secondary hadrons.

For about 60% of statistics, trigger logic selected events where secondaries were emitted into both DAMS arms (an *LR* trigger corresponding to the *LR* correlation sample). About 20% of statistics corresponded to the trigger condition for the actuation of the equipment only in one DAMS arm (*L* and *R* triggers corresponding to *L* and *R* inclusive samples).

Methods for analyzing information from various groups of the tracking detectors of the facility in the exposure being studied, procedures for identifying charged secondaries recorded by the DAMS in the course of the exposure, and results of this identification for π^-Be interactions are described in [7, 9].

In studying the inclusive spectra of secondary hadrons, the efficiencies of particle detection and the momentum and angular resolutions for secondaries were calculated with the aid of the GEANT package [10]. The results of these calculations agree well with the results of analogous calculations performed in studying the facility [7] with the aid of a simplified code that takes into account ionization losses and multiple Coulomb scattering. The inefficiencies of the detectors and of event reconstruction were estimated in [7–9, 11]. For the kinematical region of π^-Be, π^-Al, and π^-Cu interactions that is studied here, the results of GEANT calculations for the kinetic-energy (T) dependence of the accuracy in reconstructing the kinetic energy T of secondary protons and the estimated accuracies in reconstructing T for secondary pions recorded by each DAMS arm were presented in [12].

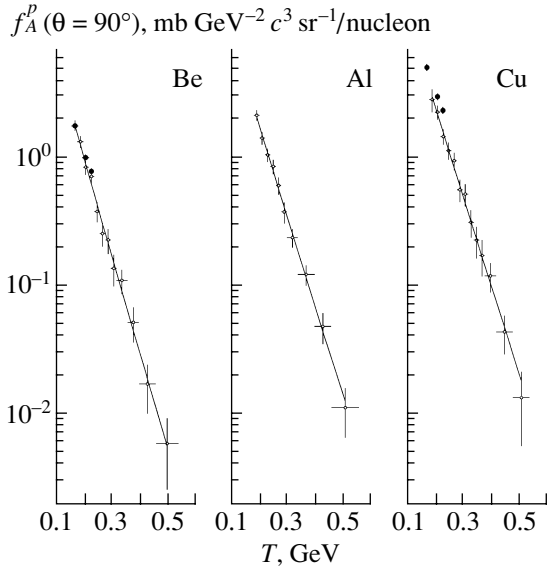

Fig. 1. Inclusive invariant cross sections for (open circles) proton production at an angle of $\theta = 90°$ in π^-Be, π^-Al, and π^-Cu interactions (f_A^p) at a projectile momentum of $p_{\rm bm} = 43$ GeV/c versus the kinetic energy T and (closed circles) results of analogous measurements for π^-Be and π^-Cu interactions at a momentum of $p_{\rm bm} = 5$ GeV/c [15]. The straight line represents the result of a fit.

3. ANALYSIS OF INCLUSIVE SPECTRA OF SECONDARY PROTONS AND PIONS

The contributions to the measured cross sections from cascade processes in the target were calculated by using the FLUKA hadronic-shower generator [13] of the GEANT package [10] (about 20% in π^-Be interactions and about 11 to 15% in π^-Al and in π^-Cu interactions) and were taken into account by introducing correction factors. Statistical errors are displayed in Figs. 1–4, which depict the cross sections for the inclusive production of recorded hadrons. The systematic errors in determining the cross sections for hadron production in π^-Be interactions were estimated at 13 and 16% for protons detected at angles of 90° and 60°, respectively, and at 15% for pions detected at an angle of 90°. An additional systematic error in the production cross section measured by the left DAMS arm for Al and Cu target nuclei did not exceed 5% for protons and 7% for pions. For the cross sections measured by the right DAMS arm, the analogous additional error was 5% for protons and pions produced on Al nuclei; for Cu nuclei, it proved

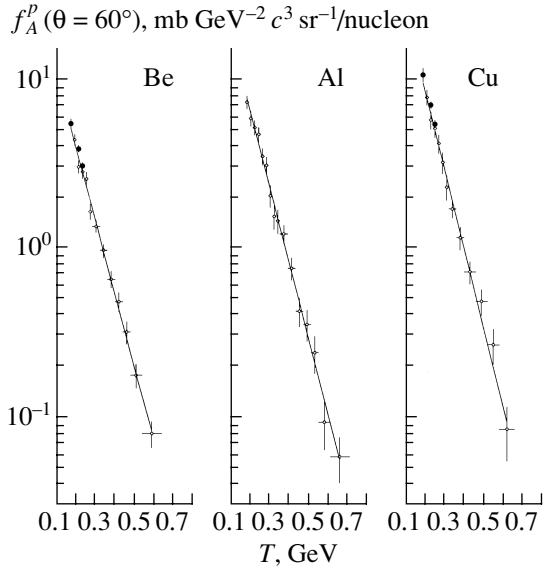

Fig. 2. As in Fig. 1, but for $\theta = 60°$

to be as great as 9% for protons and as great as 15% for pions.

The invariant differential cross sections per target nucleon for the inclusive production of secondary hadrons in $\pi^- A$ interactions were computed by the formula

$$f_A = (E/A)(d^3\sigma/d^3p) = (1/pA)(d^2\sigma/dTd\Omega),$$

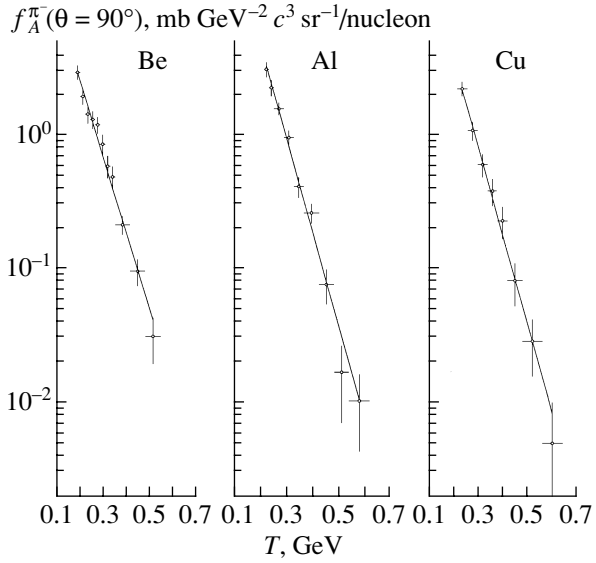

Fig. 3. Inclusive invariant cross sections for negative-pion production at an angle of $\theta = 90°$ in π^-Be, π^-Al, and π^-Cu interactions ($f_A^{\pi^-}$) at a momentum of $p_{\rm bm} = 43$ GeV/c versus the kinetic energy T (open circles). For each type of interaction, the straight line represents the resulting approximation.

where A is the mass number of the target nucleus; E, p, and T are respectively, the energy, the momentum, and the kinetic energy of a secondary particle; σ is the cross section for its production; and Ω is a solid angle.

In calculating f_A, use was made of the cross sections determined experimentally over the angular interval $\Delta\theta$ whose width did not exceed 10°. The cumulative number $n_{\rm cum}$ for secondary hadrons was calculated by the formula $n_{\rm cum} = \big(E - p\cos\theta\big)/M_p$, where E is the energy of a particle whose momentum is p and M_p is the proton mass. By using the MINUIT package [14], the spectra in question were fitted in terms of the function

$$f_A = f_{A0}\exp\left(-T/T_0\right). \qquad (1)$$

Table 1 shows the values of the parameter T_0 that were obtained in studying the shape of the spectra of secondary particles for various regions of their kinetic energies T. The values of T_0 that are labeled with an asterisk in this table were deduced from a fit of the dependence in Eq. (1) to the inclusive spectra of secondary hadrons for the energy-scale binnings shown in Figs. 1–4, where the straight lines represent the resulting approximations. The values of T_0 in Table 1 that are not labeled with an asterisk were obtained from fits constructed by breaking down the range of T under study into the maximum possible number of energy bins having equal widths. In each fit, whose results are quoted in Table 1, the value of χ^2/NDF did not exceed unity.

It should be noted that, although the inclusive production of cumulative hadrons in hadron–nucleus interactions was subjected to extensive experimental studies, data on proton and pion production at angles

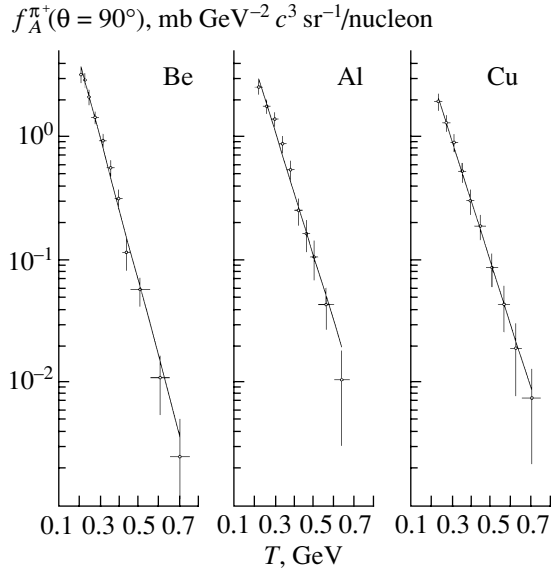

Fig. 4. As in Fig. 3, but for π^+ mesons.

Table 1. Fitted values of the parameter T_0 in the approximation (1) of the invariant differential cross sections for the inclusive production of protons at angles of 90° and 60° and of pions at an angle of 90° in $\pi^- A$ interactions at $p_{\rm bm} = 43$ GeV/c

Be		Al		Cu	
T, GeV	T_0, MeV	T, GeV	T_0, MeV	T, GeV	T_0, MeV
		$\theta_p = 90°$			
0.16–0.54	56.7 ± 2.6*	0.18–0.56	61.7 ± 2.7*	0.18–0.54	62.3 ± 3.0*
0.16–0.54	56.1 ± 2.6	0.18–0.56	59.3 ± 2.6	0.18–0.54	61.4 ± 2.9
0.09–0.23	56.3 ± 1.0 [15]			0.09–0.23	59.0 ± 1.0 [15]
		$\theta_p = 60°$			
0.16–0.64	101.2 ± 2.9*	0.16–0.70	96.9 ± 3.1*	0.16–0.64	92.4 ± 3.8*
0.16–0.64	98.9 ± 2.8	0.16–0.70	94.3 ± 2.9	0.16–0.64	91.3 ± 3.7
0.09–0.23	97.2 ± 2.6 [15]			0.09–0.23	84.9 ± 1.8 [15]
		$\theta_{\pi^-} = 90°$			
0.20–0.54	70.3 ± 3.1*	0.20–0.62	63.9 ± 2.8*	0.22–0.64	64.1 ± 4.0*
0.28–0.54	57.5 ± 4.7	0.28–0.66	58.8 ± 4.6	0.28–0.64	63.2 ± 5.6
		$\theta_{\pi^+} = 90°$			
0.20–0.76	71.4 ± 2.6*	0.20–0.68	83.2 ± 3.7*	0.22–0.76	85.2 ± 4.9*
0.28–0.76	67.6 ± 4.0	0.28–0.68	72.6 ± 5.1	0.28–0.76	77.5 ± 6.4

of $\theta = 90°$ and 60° in $\pi^- A$ interactions have been hitherto unavailable for kinetic energies of secondaries in the range studied here.

The kinetic-energy dependences of the invariant differential cross sections for inclusive proton production that were measured in the experiment by the right DAMS arm at angle of $\theta = 90°$ and by the left DAMS arm at angle of $\theta = 60°$ in π^-Be, π^-Al, and π^-Cu interactions at $p_{\rm bm} = 43$ GeV/c are displayed in Figs. 1 ($\theta = 90°$) and 2 ($\theta = 60°$). Also shown in these figures are the results of analogous measurements at $p_{\rm bm} = 5$ GeV/c [15]. The fitted values of the parameter T_0 in the approximation (1) of the measured inclusive proton spectra in the region $0.09 < T < 0.23$ GeV are quoted in Table 1 [15]. For protons produced at an angle of $\theta = 90°$, the cumulative number $n_{\rm cum}$ changed in the range $n_{\rm cum} \approx 1.1$–1.9 for T varying from 0.16 to 0.54 GeV, while, for protons produced at angle of $\theta = 60°$, it changed in the range $n_{\rm cum} \approx 0.8$–1.1 for T varying from 0.16 to 0.7 GeV. Thus, the protons produced at angle of $\theta = 90°$ were predominantly cumulative. Also, protons formed in the process of deep-inelastic nuclear interaction must constitute a considerable part of the protons produced at angle of $\theta = 60°$ [16]. An investigation of the shape of the inclusive proton spectra has revealed that the experimental spectra of secondary protons are well approximated by the form (1), the values of the parameter T_0 changing only slightly over a broad range of the kinetic energy of these protons.

The agreement between the experimental values of the cross sections for proton production at an angle of $\theta = 90°$ and the corresponding cross sections calculated with the aid of the FLUKA hadronic-shower generator [13] of the GEANT package [10] improved with increasing mass number A of the target nucleus. For the spectra of protons produced at an angle of $\theta = 90°$, the results obtained with the aid of the HEISHA hadronic-shower generator [17] differed considerably in shape and in magnitude both from the experimental spectra and from the spectra calculated with the aid of the FLUKA generator [13], especially for the light target nucleus of Be. For protons generated at an angle of $\theta = 60°$, the results produced by these two generators for the relevant cross sections are closer.[1)]

[1)] On the basis of the FLUKA and the HEISHA hadronic-shower generator (see [13] and [17], respectively) of the GEANT package [10], the cross sections for proton production at angles of $\theta = 90°$ and 60° were calculated in [12] for the propagation of 43-GeV/c negative pions through nuclear targets in the form of disks of radius 1 mm and thickness about 1 mm (0.7 mm) for Be and Al (Cu), in which case effects associated with the target dimensions can be disregarded.

Table 2. Ratio $R_f(\pi^+/\pi^-)$ of the invariant cross sections for inclusive pion production in the region $-0.1 < \cos\theta < 0.1$ for $\pi^- A$ interactions at $p_{\rm bm} = 43$ GeV/c

Be		Al		Cu	
T, GeV	$R_f(\pi^+/\pi^-)$	T, GeV	$R_f(\pi^+/\pi^-)$	T, GeV	$R_f(\pi^+/\pi^-)$
0.20–0.28	1.12 ± 0.09	0.20–0.28	1.00 ± 0.10	0.20–0.28	0.84 ± 0.11
0.22–0.28	1.18 ± 0.11	0.22–0.28	1.07 ± 0.12	0.22–0.28	0.92 ± 0.11
0.28–0.54	1.28 ± 0.10	0.28–0.60	1.63 ± 0.15	0.28–0.60	1.65 ± 0.19

For negatively and for positively charged pions produced at an angle of $\theta = 90°$, the kinetic-energy dependences of the inclusive invariant differential cross sections f_A are displayed in Figs. 3 and 4, respectively. The spectra of negatively (positively) charged pions originating at an angle of $\theta = 90°$ were measured in the experiment by the left (right) DAMS arm. The cumulative number $n_{\rm cum}$ changed from $n_{\rm cum} \approx 0.3$ for $T = 0.2$ GeV pions through $n_{\rm cum} \approx 0.8$ for $T = 0.54$ GeV pions to $n_{\rm cum} \approx 1.1$ for $T = 0.76$ GeV pions. The values of the parameter T_0 that were obtained by fitting the function in (1) to these invariant cross sections are quoted in Table 1.

The cross sections for positive-pion production at an angle of $\theta = 90°$ that were calculated with the aid of the FLUKA hadronic-shower generator [13] similarly to the proton cross sections were approximately twice as large as the corresponding experimental values, but their dependence on the kinetic energy T was close to that observed experimentally. In just the same way as for protons, the agreement between the results of the calculations and the cross sections determined experimentally improved with increasing mass number A of the target nucleus. The results of the analogous calculation of the cross section for negative-pion production at an angle of $\theta = 90°$ showed still more pronounced deviations from experimental data. The calculation of the cross sections for $\pi^{\pm}$-meson production at an angle of $\theta = 90°$ on the basis of the HEISHA hadronic-shower generator [17] could not reproduce even the character of the kinetic-energy dependence of the cross sections determined experimentally.

An investigation of the shape of the inclusive spectra of negative pions produced at an angle of $\theta = 90°$ has revealed that the values of the parameter T_0 for these spectra in π^-Al and π^-Cu interactions are close to the values of T_0 for the spectra of secondary protons in the region of the kinetic energies of these hadrons that was studied here. For energies in excess of $T \simeq 0.28$ GeV, the values of the parameter T_0 for the spectra of negative pions and protons agree within the errors for all targets used in the experiment being discussed.

In the T region studied here, the values of the parameter T_0 for the inclusive spectra of positively charged secondary pions differed from the corresponding values of T_0 both for the spectra of secondary protons and for the spectra of negatively charged secondary pions and increased considerably in going over from the light nucleus of Be to the heavier nuclei of Al and Cu. Statistics of the experiment were not sufficient for studying the dependence of T_0 on T for comparatively high energies of positive pions. Upon an increase in the lower boundary of the T region to 0.28 GeV, the values of T_0 decreased, but they remained about 25% greater than the value of T_0 for the spectra of negatively charged secondary pions in the corresponding region of T, this difference being greater than two measurement errors.

The results of a comparative analysis of the shapes of the inclusive spectra of protons and positive pions produced at an angle of $\theta = 90°$ are in qualitative agreement with the results deduced in [18, 19] from an analysis of the shapes of the inclusive spectra measured with a high statistical accuracy at the ISTRA-3 facility for protons and positively charged pions originating from $\pi^- A$ interactions at a considerably lower momentum of primary negative pions ($p_{\rm bm} = 1.5$ GeV/c) and having kinetic energies on the same order of magnitude as in the experiment being discussed. In particular, it was stated in [18, 19] that, even for $T > 0.4$ GeV, the values of T_0 for the inclusive spectra of positively charged pions produced at an angle of $\theta = 118°$ in $\pi^-{}^{16}$O and π^-Cu interactions were about 12 to 13% greater than the values of T_0 for the inclusive spectra of protons formed at an angle of $\theta = 110°$, this being approximately equal to two measurement errors.

The experimental values of the ratio $R_f(\pi^+/\pi^-)$ of the invariant cross sections for the inclusive production of positively and negatively charged pions for $-0.1 < \cos\theta < 0.1$ are given in Table 2. For π^-Al and π^-Cu interactions, the values of $R_f(\pi^+/\pi^-)$ increased significantly upon going over from pion kinetic energies in the region $T < 0.28$ GeV to those in the region $T > 0.28$ GeV.

It is natural to assume that an increase in the parameter T_0 for the inclusive spectra of positively charged secondary pions originating at an angle of $\theta = 90°$ as the target mass number A becomes greater is associated, to a considerable extent, with the fact that the absorption of $T < 0.4$ GeV positively charged pions by correlated groups of intranuclear nucleons is enhanced with increasing A. The possible effect of such processes on the behavior of the spectra of positively charged secondary pions for $T < 0.4$ GeV is determined by the character of the dependence of the cross section for the process $\pi^+ d \to pp$ on the kinetic energy of the positively charged pion involved (see Fig. 5, where this dependence is plotted on the basis of the compilation of data from [20]). The effect of such processes on the behavior of the spectra of negatively charged pions can be masked by the distinctions between the mechanisms of specific reactions of intranuclear absorption of unlikely charged low-energy pions [21, 22] and by the shift of the negative-pion spectrum with respect to the positive-pion spectrum toward lower energies of the secondaries because of the Coulomb nuclear field (especially for the rather heavy nucleus of Cu) [23].

The results presented in [11] and obtained by studying the experimental data of the exposure in question on the invariant differential cross sections for the inclusive production of positively and negatively charged pions at an angle of $\theta = 60°$ in π^-Be interactions are compatible with the above assumption. The values of the parameter T_0 that were deduced by fitting the function in (1) to these cross sections for $T > 0.4$ GeV were considerably smaller than its values at lower T. The experimental spectra of positively and negatively charged pions that originate at an angle of $\theta = 60°$ from π^-Al and π^-Cu interactions were described much more poorly by the dependence in (1). Statistics of the experiment were not sufficient for studying the structure of these spectra.

For Be, Al, and Cu target nuclei, the ratios of the yields of protons to the yields of positively charged pions, $R(p/\pi^+)$, at identical values of secondary-hadron momenta in the range $0.6 < p < 0.85$ GeV/c at production angles satisfying the condition $-0.10 < \cos\theta < 0.15$, under which secondary hadrons are efficiently recorded by the DAMS, were 12.0 ± 1.9, 14.7 ± 2.5, and 19.1 ± 3.5, respectively.

In the range $0.25 < \cos\theta < 0.30$, the values of the ratio $R(p/\pi^+)$ were less by a factor greater than 2. Thus, the measured value of the ratio $R(p/\pi^+)$ increased sharply with decreasing $\cos\theta$ upon going over to the region $\cos\theta < 0.1$, where the proton cumulative number n_{cum} is greater than unity and where the interaction on a free nucleon is forbidden. That, at identical momenta of secondary hadrons, the yield of pions is suppressed in relation to the yield of cumulative protons is naturally explained within the concept of short-range dynamical correlations between intranuclear nucleons as a source of cumulative hadrons [5]. Dynamical correlations between intranuclear nucleons must arise owing to the experimentally established fact that, at internucleon distances less than some 0.5 fm, the two-nucleon potential features a strong repulsive component [24].

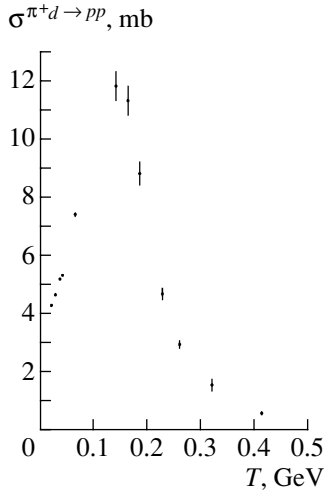

Fig. 5. Cross section for the process $\pi^+ d \to pp$ versus the kinetic energy of the positive pions involved according to the compilation of data from [20] (closed circles).

That processes where slow positively charged pions originating predominantly from the rescattering of secondaries are absorbed by correlated pairs of intranuclear nucleons are essential for the production of cumulative hadrons was demonstrated both for hadron–nucleus [25] and for neutrino–nucleus [26] interactions at projectile energies below 10 GeV. By studying the experimental data of the exposure under discussion on the spectra of secondary pions having low kinetic energies and originating at an angle of $\theta = 90°$ from $\pi^- A$ interactions at a momentum of $p_{\mathrm{bm}} = 43$ GeV/c, some pieces of evidence were obtained for the significance of such processes at higher primary-hadron momenta, in which case the probability of the production of secondary hadrons in projectile interaction with correlated groups of intranuclear nucleons becomes higher [5].

It is interesting to note that the results quoted in Table 2, which were obtained by studying the ratio $R_f(\pi^+/\pi^-)$ at the kinetic-energy values indicated above, are in qualitative agreement with the results deduced in [26] from an analysis of the ratio $R(\pi^+/\pi^-)$ of the yields of $p < 1$ GeV/c positively and negatively charged pions from the interaction of neutrinos with heavy nuclei at the mean energy of primary neutrinos that is equal to 6 GeV. Despite rather

Table 3. Values of $\alpha_{\mathrm{Al/Be}}$, $\alpha_{\mathrm{Cu/Be}}$, and $\alpha_{\mathrm{Cu/Al}}$ determined by formula (3) for the invariant cross sections in the form (2) that characterize the production of secondary protons at angles of $\theta = 90°$ and $60°$ and of secondary pions at an angle of $\theta = 90°$ in $\pi^- A$ interactions at $p_{\mathrm{bm}} = 43$ GeV/c

$\alpha_{\mathrm{Al/Be}}$	$\alpha_{\mathrm{Cu/Be}}$	$\alpha_{\mathrm{Cu/Al}}$
	$\theta_p = 90°$, $T = 0.18$–0.54 GeV	
$1.51 \pm 0.06 \pm 0.05$	$1.48 \pm 0.04 \pm 0.06$	$1.43 \pm 0.09 \pm 0.07$
	$\theta_p = 60°$, $T = 0.18$–0.64 GeV	
$1.36 \pm 0.04 \pm 0.04$	$1.30 \pm 0.03 \pm 0.05$	$1.23 \pm 0.06 \pm 0.06$
	$\theta_{\pi^-} = 90°$, $T = 0.22$–0.54 GeV	
$1.04 \pm 0.08 \pm 0.04$	$1.03 \pm 0.05 \pm 0.05$	$1.02 \pm 0.05 \pm 0.06$
	$\theta_{\pi^+} = 90°$, $T = 0.22$–0.54 GeV	
$1.01 \pm 0.08 \pm 0.04$	$0.94 \pm 0.05 \pm 0.07$	$0.86 \pm 0.12 \pm 0.10$

large experimental errors, it can be stated that the ratio $R(\pi^+/\pi^-)$ measured with the SKAT chamber at IHEP [26] exceeded unity and increased by a factor not less than 1.5 in response to an increase in T in the range $0.28 < T < 0.7$ GeV, this being so both in events featuring no cumulative protons and in events where such protons were recorded. For $T < 0.2$ GeV, this ratio in events where cumulative protons were present sharply decreased to values below unity.

4. INVESTIGATION OF THE A DEPENDENCE OF THE INVARIANT INCLUSIVE CROSS SECTIONS FOR SECONDARY PROTONS AND PIONS

The invariant cross section f ($f = f_A A$) for inclusive hadron production on nuclei as a function of the target mass number is usually expressed in terms of a power-law function featuring an exponent α:

$$f = f_0 A^\alpha. \qquad (2)$$

For each hadron, the values of $\alpha_{\mathrm{Al/Be}}$, $\alpha_{\mathrm{Cu/Be}}$, and $\alpha_{\mathrm{Cu/Al}}$ were determined over the kinetic-energy region that is the most accessible in the cases of all the nuclei under study. This was done by using the formula

$$\alpha_{A_1/A_2} = \ln(f_{A1}/f_{A2})/\ln(A_1/A_2). \qquad (3)$$

The results are quoted in Table 3, along with the statistical and the systematic error of the measurements for each value of α.

In accord with the results of other measurements [15, 27], the values of the exponents in the A dependence (2) of the invariant cross sections for inclusive proton production exceeded unity and increased with increasing angle θ of secondary-proton production and, hence, with increasing cumulative number n_{cum} of secondary protons. Despite the proximity of the values of the parameter T_0 for the inclusive spectra of protons and negatively charged pions originating at an angle of $\theta = 90°$ from $\pi^- A$ interactions, the values of $\alpha \approx 1$ for the invariant cross sections for the inclusive production of negatively charged pions according to the value of their cumulative number n_{cum} were, however, less than the values of α not only for the cross sections for protons produced at the same angle but also for the cross sections for protons produced at an angle of $\theta = 60°$.

Within the errors, the values of α that are presented in Table 3 for protons agree with the estimates of α that were obtained according to data from [15] at $p_{\mathrm{bm}} = 5$ GeV/c. However, the values of α both for protons and for positively charged pions are in excess of the estimates of α from [18, 19] at $p_{\mathrm{bm}} = 1.5$ GeV/c. That, at low energies of the hadron incident on the target nucleus, the growth of the cross sections for the production of cumulative nucleons and pions with increasing A is moderated because of Glauber rescatterings was indicated by Strikman and Frankfurt [5], who analyzed theoretically the scattering of particles on nuclei, relying on the Gribov–Feynman spacetime pattern and on the pair-correlation approximation.

The accuracy of measurements in the experiment being discussed is not sufficient for studying the behavior of α as a function of T in the case of the invariant inclusive cross sections for the production of positively and negatively charged pions at an angle of $\theta = 90°$. It should be noted, however, that, in the case of the invariant cross sections for the inclusive production of negatively charged pions having kinetic energies in excess of 0.28 GeV and arising in the region $-0.1 < \cos\theta < 0.1$, the values of α were nearly identical to those presented in Table 3 for negatively charged pions. At the same time, the values

of α for positively charged pions of kinetic energies higher than 0.28 GeV for $-0.1 < \cos\theta < 0.1$ were greater than those presented in Table 3; for $T = 0.28$–0.64 GeV, they were

$$\alpha_{\mathrm{Al/Be}} = 1.21 \pm 0.07; \quad \alpha_{\mathrm{Cu/Be}} = 1.14 \pm 0.05;$$
$$\alpha_{\mathrm{Cu/Al}} = 1.05 \pm 0.11.$$

The A dependence of the inclusive cross sections for negatively charged pions having momenta in the range 100–500 MeV/c and originating at angles of $\theta = 110°$–$155°$ from π^-Al and π^-Pb interactions at $p_{\mathrm{bm}} = 4.4$ GeV/c was explored at ITEP [28]. As a result, it was shown that α greatly depends on the secondary-pion momentum. For π^--meson momenta in the regions $p \leq 120$ MeV/c and $p \geq 350$ MeV/c ($T \geq 237$ MeV), $\alpha \approx 1$. There is a minimum at the momenta of negatively charged secondary pions in the range 200–250 MeV/c, where $\alpha \approx 0.7$. By comparing their results with the results that were deduced by studying the A dependence of the yields of negatively charged pions at an angle of $\theta = 168°$ from proton–nucleus interactions at $p_{\mathrm{bm}} = 8.9$ GeV/c [29] and which have a similar character, the authors of [28] arrived at the conclusion that the irregularities in the A dependence are determined by the features of a secondary particle.

The results in Table 3 of the present article that were obtained by measuring the A dependence of the inclusive cross sections for negatively charged pions having kinetic energies in excess of 0.22 GeV (the corresponding momenta of negatively charged pions are $p > 330$ MeV/c) and originating at an angle of $\theta = 90°$ from $\pi^- A$ interactions at $p_{\mathrm{bm}} = 43$ GeV/c agree with the results from [28] for the corresponding momenta of negatively charged pions. Further, a comparison with the results presented in [28] reveals that, for the inclusive cross sections describing π^+-meson production at an angle of $\theta = 90°$ that were measured in the exposure under analysis in π^-Al and π^-Cu interactions, the character of the momentum dependence of α is similar to the character of the A dependence of the inclusive cross sections for the production of negatively charged pions of momenta in excess of 200 MeV/c [28]. The region of a minimum in the momentum (or kinetic-energy) dependence of α for positively and negatively charged pions is determined by the region where the processes of secondary-pion absorption are operative. The upper momentum (or kinetic-energy) boundary of this region for negatively charged pions is somewhat shifted toward lower momenta with respect to the corresponding boundary for positively charged pions. It should be noted that the values of $\alpha_{\mathrm{Al/Be}}$ and $\alpha_{\mathrm{Cu/Be}}$ for positively charged pions of kinetic energy in excess of 0.28 GeV are greater than unity, which suggests that, in the kinematical region being considered, the contribution to the cross section for the production of positively charged pions on medium-mass and heavy nuclei from processes of their multiplication is enhanced in relation to the contribution of such processes to the cross section for the formation of negatively charged pions. The behavior of α for pions as a function of kinetic energy corresponded to the behavior of the measured ratio $R_f(\pi^+/\pi^-)$ of the invariant cross sections for the inclusive production of positively and negatively charged pions for $-0.1 < \cos\theta < 0.1$ (see Table 2).

The experimental-data sample quoted above indicates that, in the case where secondary pions of low kinetic energy are produced on medium-mass and heavy nuclei, the special features of their inclusive spectra and the A dependences of the inclusive cross sections are determined by those properties of the intranuclear structure that manifest themselves in the interaction of secondaries with these nuclei.

5. INVESTIGATION OF WIDE CORRELATIONS FOR LIKELY CHARGED PAIRS OF HADRONS

In studying wide correlations for pairs of likely charged hadrons, the correlation function for a pair was defined as [2–4] $R_2^{h_L h_R} = \sigma_{\mathrm{in}} F^{h_L h_R}/(F^{h_L} F^{h_R})$, where the functions F^{h_L} and F^{h_R} are the invariant cross sections for the inclusive production of the hadrons of the pair that were recorded by, respectively, the left and the right DAMS arm and $F^{h_L h_R}$ is the double-inclusive invariant cross section for the production of $h_L h_R$ pairs in those regions of $T_{L,R}$ and $\cos\theta_{L,R}$ where the invariant inclusive cross sections F^{h_L} and F^{h_R} were specified. For the normalization of each function in π^-Be interactions, use is made of the cross section measured at the SIGMA facility [30] for the inelastic interaction of negatively charged pions with Be nuclei at a momentum of 40 GeV/c; in the case of π^-Al and π^-Cu interactions, the cross sections for the inelastic interaction of 60-GeV/c negatively charged pions with the corresponding nuclei were taken for this purpose from [31].

In the following, hadrons that are recorded in the experiment by the left (right) DAMS arm are referred to as left (right) hadrons. The type of a pair is labeled with the index $h_L h_R$—that is, the index of the left hadron always comes first.

It should be noted that, in the region $-0.10 < \cos\theta < 0.25$, the detection efficiencies of the facility are smooth functions showing rather slow variations in magnitude with T and $\cos\theta$ for secondary protons of kinetic energy in the range $0.16 < T < 0.6$ GeV

Table 4. Correlation functions for proton–proton pairs detected in $\pi^- A$ interactions at $p_{\rm bm} = 43$ GeV/c

Target	T_L, GeV	T_R, GeV	R_2^{pp}
Be	0.16–0.64	0.16–0.54	2.00 ± 0.19
	0.16–0.30	0.28–0.54	3.32 ± 0.60
Al	0.16–0.70	0.18–0.60	2.10 ± 0.20
	0.16–0.30	0.28–0.60	2.62 ± 0.48
Cu	0.16–0.70	0.18–0.60	2.71 ± 0.24
	0.16–0.30	0.28–0.60	3.23 ± 0.50

for a Be target and of kinetic energy in the range $0.18 < T < 0.6$ GeV for a Cu target, as well as for secondary pions of kinetic energy in the range $0.20 < T < 0.76$ GeV for a Be target and of kinetic energy in the range $0.22 < T < 0.76$ GeV for a Cu target. The same is true for protons of kinetic energy in the range $0.18 < T < 0.7$ GeV that were recorded at angles satisfying the condition $0.35 < \cos\theta < 0.65$ and for pions of kinetic energy in the range $0.28 < T < 0.76$ GeV that were recorded at angles satisfying the condition $0.35 < \cos\theta < 0.70$ for Be targets and the condition $0.35 < \cos\theta < 0.75$ for the heavier target nucleus. Pairs of likely charged hadrons were recorded at angles of divergence ψ that satisfy the inequality $\cos\psi < -0.5$.

For pairs of likely charged secondary hadrons recorded in $\pi^- A$ interactions, the correlation functions $R_2^{h_L h_R}$ are given in Tables 4–6, which also indicate the domains of the functions in the kinetic energies of the hadrons. For all the samples of hadron pairs under analysis, the emission angles of right protons and positively charged pions and of left negatively charged pions satisfied the condition $-0.15 < \cos\theta < 0.25$. Left protons of the pairs were selected at the values of $\cos\theta$ from the range $0.35 < \cos\theta < 0.65$. In order to enlarge statistics, the pion partners from $\pi^+ p$ and $\pi\pi$ pairs were selected in the range $0.35 < \cos\theta < 0.75$. In response to the reduction of the upper boundary of the angular range to $\cos\theta = 0.70$, the correlation functions for the corresponding samples of $\pi^+ p$ and $\pi\pi$ pairs produced in π^-Be interactions changed insignificantly. Tables 4–6 display the statistical errors in determining the correlation functions. The systematic errors in determining $R_2^{h_L h_R}$, which were associated primarily with the procedure for separating events of hadron-pair production, did not exceed 16%. That inelastic cross sections measured in different experiments and at different momentum values were used to normalize the correlations functions for the various nuclei could lead to a systematic bias of the resulting value of

Table 5. Correlation functions for $p\pi^+$ and $\pi^+ p$ pairs detected in $\pi^- A$ interactions at $p_{\rm bm} = 43$ GeV/c

Target	T_L, GeV	T_R, GeV	$R_2^{h_L h_R}$
		$p\pi^+$	
Be	0.16–0.64	0.20–0.76	1.78 ± 0.21
	0.16–0.64	0.28–0.76	1.92 ± 0.27
Al	0.16–0.70	0.20–0.76	1.76 ± 0.22
	0.16–0.70	0.28–0.76	1.88 ± 0.28
Cu	0.16–0.70	0.22–0.76	2.43 ± 0.32
	0.16–0.70	0.28–0.76	2.58 ± 0.39
		$\pi^+ p$	
Be	0.35–0.70	0.16–0.54	1.32 ± 0.23
	0.40–0.70	0.16–0.54	1.43 ± 0.29
Al	0.35–0.70	0.18–0.60	1.50 ± 0.23
	0.40–0.70	0.18–0.60	1.59 ± 0.28
Cu	0.35–0.70	0.18–0.60	1.43 ± 0.24
	0.40–0.70	0.18–0.60	1.49 ± 0.28

$R_2^{h_L h_R}$ for Al and Cu with respect to Be, but this effect was disregarded here. A comparison of the cross sections for inelastic π^-Cu interactions at a momentum of 60 GeV/c [31] with those at momenta of 40, 50, and 60 MeV/c [30] gives sufficient grounds to believe that the procedure used for a normalization can reduce the correlation functions for Al and Cu by not more than 8%.

The spectra of protons of pp pairs formed in $\pi^- A$ interactions and recorded by the right DAMS arm in the range $-0.15 < \cos\theta < 0.25$ are displayed in Fig. 6 in a form not corrected for the acceptance of the facility. If protons formed upon the dissociation of strongly correlated groups of intranuclear nucleons make a significant contribution to this sample, it follows from [5] that the universality of the spectra must be violated owing to a transition at momenta close to 0.8–0.9 GeV/c (the corresponding values of the kinetic energy T are close to 0.30–0.36 GeV) from the region dominated by pair correlations to the region dominated by triple correlations. It is worth noting that the distributions shown in Fig. 6 are compatible with such a violation. It is of interest to study the behavior of these spectra on the basis of vaster experimental statistics.

The measured values of R_2^{pp} (Table 4) suggest the correlated production of pp pairs formed in the kinematical region of $\pi^- A$ interactions that is studied here, the degree of correlation increasing somewhat

for the heaviest nucleus explored here (Cu). Evidence obtained in the experiment for an increase in R_2^{pp} (it is especially pronounced for the light nucleus of Be) upon selecting pp pairs featuring $T_R \geq 0.28$ GeV right protons and $0.16 \leq T_L \leq 0.30$ GeV left protons is worthy of special note. The selection of such events made it possible to increase, in the resulting sample, the number of events involving a right proton from deep-inelastic interactions, on one hand, and to reject events in which the sum of the cumulative numbers of the protons of the pair, n_{cum}^{pp}, is much greater than 2, on the other hand. A statistically significant observation of such an effect would favor the pair-correlation hypothesis [5], since the presence of two nucleons diverging at a large angle that meet the condition $n_{\text{cum}}^{pp} \leq 2$ can be explained as the result of interaction with a pair correlation. It was indicated in [5] that searches for pair correlations are feasible only for light nuclei, where the mean number of interactions of the incident hadron is small and where the probability of the rescatterings and absorption of secondary nucleons is lower.

The values of the correlation functions $R_2^{p\pi^+}$ for $p\pi^+$ pairs (see Table 5) suggest their correlated production in the kinematical region being studied. Evidence indicating that the correlation functions $R_2^{p\pi^+}$ and R_2^{pp} for hadron pairs featuring identically specified left protons approach each other as the energy of the right pion increases (that is, as we go over to right-pion momenta closer to right-proton momenta) has been obtained, which is an argument in favor of the common mechanism of formation of the bulk of these pairs.

That, for hadron pairs involving identically specified right protons, measurements yield smaller values of the correlation function $R_2^{\pi^+p}$ for π^+p pairs (Table 5) than of R_2^{pp} must correspond to a smaller contribution to the cross sections for π^+-meson production at angles $40^\circ < \theta < 70^\circ$ in the momentum range under study from processes of the correlated production of π^+p pairs in relation to the contribution of processes of the correlated production of two or more protons to the cross section for proton production at the same angles.

Table 6 displays the correlation functions for $\pi^+\pi^+$ and $\pi^-\pi^-$ pairs. For pairs of likely charged pions produced on the light nucleus of Be, the correlation functions $R_2^{\pi^+\pi^+}$ and $R_2^{\pi^-\pi^-}$ measured over the entire kinematical region accessible to investigation are close to unity and take the minimum values among all correlation functions $R_2^{h_Lh_R}$ measured in the experiment being discussed. Upon going over to the heavier target nuclei, the correlation functions $R_2^{\pi\pi}$ increase, which is compatible with the concept suggesting that the relative contribution of deep-inelastic hadron production to the cross sections for the production of hadrons becomes greater with increasing A [16, 32]. In order to compare the mechanisms of the deep-inelastic production of protons and pions, it is necessary to study the correlation functions $R_2^{p\pi^+}$, $R_2^{\pi^+p}$, and $R_2^{\pi\pi}$ at pion kinetic energies in excess of 0.4 GeV—that is, at momenta close to the momenta of protons recorded in the corresponding angular regions. The upper boundary (in $\cos\theta$) of the range $-0.15 < \cos\theta < 0.25$ should be reduced at least to $\cos\theta = 0.15$.

Table 6. Correlation functions for $\pi^+\pi^+$ and $\pi^-\pi^-$ pairs detected in π^-A interaction at $p_{\text{bm}} = 43$ GeV/c

Target	T_L, GeV	T_R, GeV	$R_2^{h_Lh_R}$
		$\pi^+\pi^+$	
Be	0.35–0.70	0.20–0.76	1.27 ± 0.26
	0.35–0.70	0.28–0.76	1.40 ± 0.34
Al	0.35–0.70	0.20–0.76	1.59 ± 0.30
	0.35–0.70	0.28–0.76	1.60 ± 0.36
Cu	0.35–0.70	0.22–0.76	1.77 ± 0.39
	0.32–0.76	0.28–0.76	1.98 ± 0.44
		$\pi^-\pi^-$	
Be	0.30–0.70	0.20–0.76	1.16 ± 0.16
	0.30–0.70	0.28–0.76	1.27 ± 0.33
Al	0.30–0.70	0.20–0.76	1.73 ± 0.23
	0.30–0.70	0.28–0.76	1.77 ± 0.32
Cu	0.30–0.70	0.22–0.76	1.58 ± 0.27
	0.30–0.70	0.28–0.76	1.74 ± 0.36

An analysis revealed that an investigation of wide correlations of proton pairs in π^-Be interactions on the basis of vaster experimental statistics would be the most informative for exploring the mechanism of the deep-inelastic production of proton–proton pairs. The accumulation of such statistics would also be of interest from the point of view of studying the mechanism of production of proton–proton pairs in diffraction-like events of π^-Be interactions, where the forward detector of the facility recorded only a fast negatively charged pion at low values of the square of the momentum transfer to this meson [11]. It is also interesting to collect vaster statistics of events of dp-pair production that were recorded in the exposure being studied. Additionally, it should be noted that a few events featuring the production of dp pairs where the momenta of the left deuteron were higher

Table 7. Correlation functions for pp, $p\pi^+$, and $\pi^+\pi^+$ pairs according to calculations involving a simulation of their production in π^-A interactions at $p_{\rm bm} = 43$ GeV/c on the basis of the FLUKA hadronic-shower generator of the GEANT package

Target	T_L, GeV	T_R, GeV	$\cos\theta_R$	$R_2^{h_L h_R}$
		pp		
Be	0.16–0.70	0.16–0.60	−0.15–0.35	1.20 ± 0.13
	0.16–0.70	0.16–0.60	−0.15–0.25	1.48 ± 0.15
	0.16–0.70	0.16–0.60	−0.15–0.25	1.12 ± 0.12*
	0.16–0.70	0.16–0.60	−0.15–0.15	1.48 ± 0.17
Al	0.16–0.70	0.18–0.60	−0.15–0.35	1.39 ± 0.10
	0.16–0.70	0.18–0.60	−0.15–0.25	1.35 ± 0.10
	0.16–0.70	0.18–0.60	−0.15–0.15	1.36 ± 0.13
Cu	0.16–0.70	0.18–0.60	−0.15–0.35	1.58 ± 0.09
	0.16–0.70	0.18–0.60	−0.15–0.25	1.59 ± 0.10
	0.16–0.70	0.18–0.60	−0.15–0.25	1.53 ± 0.09*
	0.16–0.70	0.18–0.60	−0.15–0.15	1.63 ± 0.11
		$p\pi^+$		
Be	0.16–0.70	0.20–0.76	−0.15–0.25	1.41 ± 0.12
Al	0.16–0.70	0.20–0.76	−0.15–0.25	1.36 ± 0.11
Cu	0.16–0.70	0.22–0.76	−0.15–0.25	1.54 ± 0.12
		$\pi^+\pi^+$		
Be	0.35–0.70	0.20–0.76	−0.15–0.25	0.83 ± 0.09
Al	0.35–0.70	0.20–0.76	−0.15–0.25	1.05 ± 0.09
Cu	0.35–0.70	0.22–0.76	−0.15–0.25	1.20 ± 0.11

than 0.8 GeV/c were recorded among diffraction-like events of π^-Be interactions [13]. In estimating the available resources, it should be borne in mind that the use of a beryllium target in the exposure exclusively would make it possible to enlarge statistics of the correlation sample by a factor of 5, provided that statistics of the L and the R sample were doubled.

The correlation functions for pp, $p\pi^+$, and $\pi^+\pi^+$ pairs were also estimated by simulating, on the basis of the FLUKA hadronic-shower generator [13] of the GEANT package [10], the processes of their production that accompany the passage of 43 GeV/c negatively charged pions through nuclear targets used in the experiment being discussed. The resulting estimates are quoted in Table 7. In order to reduce the machine time in performing this simulation, events of hadron-pair production were specified as those that featured, among its secondaries, two hadrons occurring within the z acceptance of the DAMS and possessing the following properties: (i) their kinetic energies and emission angles with respect to the momentum of the incident negatively charged pion were in the region studied experimentally, and (ii) the difference of the coordinates y of their production vertices in the target were less than 10, 6, and 4 mm for Be, Al, and Cu, respectively, in accordance with the procedures used to reconstruct the tracks of charged particles and to select events of hadron-pair production in π^-A interactions [7, 9]. In addition to the estimates of R_2^{pp} in the angular range $-0.15 < \cos\theta < 0.25$ for recording right protons of pp pairs, which was studied experimentally, Table 7 also displays values of R_2^{pp} calculated for regions containing smaller and larger emission angles ($-0.15 < \cos\theta < 0.35$ and $-0.15 < \cos\theta < 0.15$, respectively) of right protons of these pairs.

The correlation-function values obtained as the result of model calculations are less than those that were determined experimentally. The greatest underestimation is observed for pp and $p\pi^+$ pairs produced

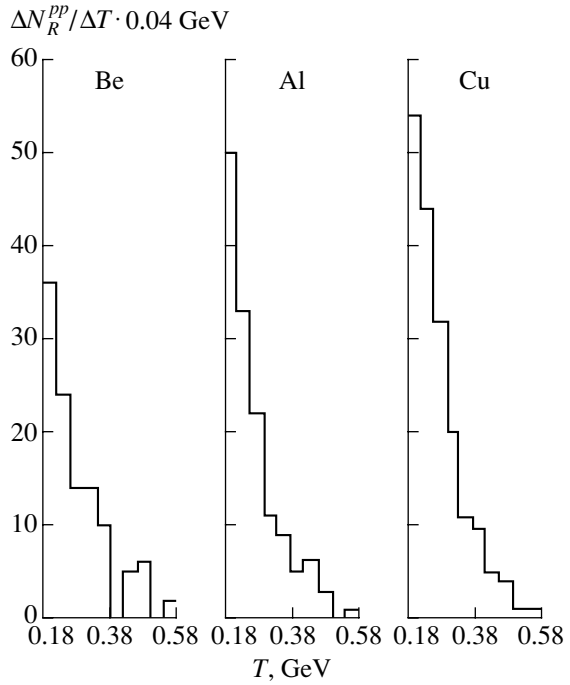

Fig. 6. Spectra of protons that were recorded by the right DAMS arm and which belong to pp pairs formed in π^-Be, π^-Al, and π^-Cu interactions at $p_{\rm bm} = 43$ GeV/c. The emission angles of right (left) protons of these pp pairs satisfied the condition $-0.15 < \cos\theta < 0.25$ ($0.35 < \cos\theta < 0.65$).

in π^-Cu interactions. In Table 7, the estimates of the correlation function R_2^{pp} in π^-Be interactions for a few upper boundaries of the angular range of detection of right protons belonging to pp pairs show an about 25% increase when the upper boundary in question is changed from $\cos\theta_R = 0.35$ to $\cos\theta_R = 0.15$, but these values remain significantly smaller than their experimental counterparts. In the simulation for a beryllium target, the production of pp pairs in the kinematical region corresponding to that which was studied experimentally occurs predominantly in the interactions of secondaries. At the same time, the correlation functions R_2^{pp} obtained for copper targets from a simulation of the production of pp pairs without taking into account the strong interaction of secondaries are consistent, within the errors, with their values computed with allowance for these interactions. The values of R_2^{pp} that were obtained for the case where the mechanism of strong interactions is suppressed for secondaries are labeled with an asterisk in Table 7. In the simulation of π^-A interactions, the calculation of the correlation functions for pairs of secondary hadrons with allowance for all physical effects arising as these hadrons traverse DAMS detectors and an investigation of the dependence of the correlation functions on target dimensions with computers available to the present author would require too much machine time.

6. CONCLUSION

First of all, it should be noted that the results obtained by studying the shapes of the measured inclusive invariant spectra of secondary protons originating at angles of $\theta = 90°$ and 60° from π^-Be, π^-Al, and π^-Cu interactions induced by an incident negatively charged pion of a momentum of 43 GeV/c and the analogous results for negatively and positively charged secondary pions originating at an angle of $\theta = 90°$ from the same interactions, as well as the results of an investigation of the A dependence of the cross sections for their production, are in fairly good agreement with the results of other experiments performed in similar regions of the kinematical variables of secondary hadrons at lower projectile momenta. The results deduced from an analysis of experimental data and presented in this article indicate that, for secondary pions of low kinetic energy that are produced on medium-mass and heavy nuclei, special features in the behavior of their inclusive spectra and of the A dependence of their inclusive cross sections are determined by the properties of the intranuclear structure that are manifested in the interaction of secondaries with these nuclei.

An investigation of wide correlations for pairs of likely charged secondary hadrons has revealed that the production of pp and $p\pi^+$ pairs is correlated, their correlation functions R_2^{pp} and $R_2^{p\pi^+}$ approaching each other with increasing kinetic energy of the pions. This behavior of the correlation functions suggests that the production of the bulk of such pairs is governed by a common mechanism. The correlation functions for pairs of likely charged pions—they were measured over the entire kinematical region accessible to investigation—were close to unity in π^-Be interaction; upon going over to the heavier target nuclei, they increased, which is compatible with the concept that the relative contribution of the deep-inelastic production of hadrons to their cross section increases with increasing mass number A of the target nucleus. In order to compare the mechanisms of the deep-inelastic production of protons and pions, it is necessary to study, on the basis of vaster experimental statistics, wide correlations for proton and pion pairs at kinetic energies of the pions in excess of 0.4 GeV.

From an analysis of experimental data, it follows that an experimental investigation of the interaction of high-energy hadrons with light nuclei is the most informative for studying the mechanism of the deep-inelastic production of proton–proton pairs. It would be of interest to confirm evidence obtained in the

experiment that, in π^-Be interactions, the correlation function R_2^{pp} increases considerably for pp pairs such that the contribution of events where the sum of the cumulative numbers of the protons of the pair satisfies the condition $n_{\text{cum}}^{pp} \leq 2$ is enhanced. An observation of this effect, should it be statistically significant, would be evidence in favor of the pair-correlation hypothesis [5].

ACKNOWLEDGMENTS

I am indebted to Yu.M. Antipov, O.V. Eroshin, I.V. Mandrichenko, and all members of the SIGMA–AYAKS collaboration for placing at my disposal magnetic tapes with packed experimental information, for providing access to the library of data-processing codes for VAX'es, and for consultations on the structural features of the individual detectors of the SIGMA–AYAKS facility. I am also grateful to A.A. Ivanilov for a discussion of this study, advice, and critical comments and to V.F. Obraztsov and V.A. Uvarov for reading the manuscript.

REFERENCES

1. Yu. M. Antipov *et al.*, Preprint No. 90-141, IFVÉ (Institute of High-Energy Physics, Protvino, 1990).
2. Yu. D. Bayukov *et al.*, Yad. Fiz. **50**, 719 (1989) [Sov. J. Nucl. Phys. **50**, 447 (1989)].
3. Yu. D. Bayukov *et al.*, Yad. Fiz. **52**, 480 (1990) [Sov. J. Nucl. Phys. **52**, 305 (1990)].
4. A. V. Vlasov *et al.*, Yad. Fiz. **55**, 2468 (1992) [Sov. J. Nucl. Phys. **55**, 1372 (1992)].
5. M. I. Strikman and L. L. Frankfurt, Fiz. Élem. Chastits At. Yadra **11**, 571 (1980) [Sov. J. Part. Nucl. **11**, 248 (1980)].
6. A. M. Baldin, Kratk. Soobshch. Fiz., No. 1, 35 (1971).
7. V. G. Kartasheva, Preprint No. 95-122, IFVÉ (Institute of High-Energy Physics, Protvino, 1995).
8. V. G. Kartasheva, Preprint No. 97-47, IFVÉ (Institute of High-Energy Physics, Protvino, 1997); Yad. Fiz. **62**, 686 (1999) [Phys. At. Nucl. **62**, 638 (1999)].
9. V. G. Kartasheva, Preprint No. 96-45, IFVÉ (Institute of High-Energy Physics, Protvino, 1996).
10. *GEANT-Detector Description and Simulation Tool—CERNLIB, CERN Program Library Long Writeup W5013* (CERN, Geneva, 1994).
11. V. G. Kartasheva, Preprint No. 98-10, IFVÉ (Institute of High-Energy Physics, Protvino, 1998); Yad. Fiz. **62**, 1451 (1999) [Phys. At. Nucl. **62**, 1370 (1999)].
12. V. G. Kartasheva, Preprint No. 99-46, IFVÉ (Institute of High-Energy Physics, Protvino, 1999).
13. A. Fasso *et al.*, in *Proceedings of the Workshop on Simulating Accelerator Radiation Environment "FLUKA 92," Santa Fe, 1993.*
14. *MINUIT-Function Minimization and Error Analysis—CERNLIB, CERN Program Library Long Writeup D506* (CERN, Geneva, 1992).
15. Yu. D. Bayukov *et al.*, Preprint ITÉF-5 (Institute of Theoretical and Experimental Physics, Moscow, 1985).
16. Yu. D. Bayukov *et al.*, Preprint ITÉF-85 (Institute of Theoretical and Experimental Physics, Moscow, 1982).
17. H. C. Fesefeldt, *Simulation of Hadronic Showers, Physics and Applications,* RWTH Aachen Physikzentrum (Aachen, Germany, 1985).
18. A. E. Bukleĭ *et al.*, Preprint ITÉF-1 (Institute of Theoretical and Experimental Physics, Moscow, 1982).
19. A. E. Bukleĭ *et al.*, Preprint ITÉF-108 (Institute of Theoretical and Experimental Physics, Moscow, 1982).
20. G. Jones, Preprint TRI-PP-81-62 (Vancouver, 1981).
21. V. M. Asaturyan *et al.*, Yad. Fiz. **38**, 684 (1983) [Sov. J. Nucl. Phys. **38**, 408 (1983)].
22. G. R. Gulkanyan *et al.*, Preprint No. 962(12)-87, EFI (Yerevan Physics Institute, Yerevan, 1987).
23. V. S. Barashenkov and V. D. Toneev, *Interactions of High-Energy Particles and Nuclei with Nuclei* (Atomizdat, Moscow, 1972).
24. R. I. Jibuti, *Dynamical Correlations of Nucleons in Atomic Nucleus* (Metsniereba, Tbilisi, 1981).
25. O. B. Abdinov *et al.*, Preprint No. E1-84-421, OIYaI (Joint Inst. for Nuclear Research, Dubna, 1984).
26. V. V. Ammosov *et al.*, Yad. Fiz. **43**, 1186 (1986) [Sov. J. Nucl. Phys. **43**, 759 (1986)].
27. Yu. M. Antipov *et al.*, Yad. Fiz. **53**, 439 (1991) [Sov. J. Nucl. Phys. **53**, 274 (1991)].
28. Yu. D. Bayukov *et al.*, Preprint ITÉF-30 (Institute of Theoretical and Experimental Physics, Moscow, 1979).
29. A. M. Baldin and V. S. Stavinskiĭ, in *Proceedings of V International Workshop on Problems of High-Energy Physics, Dubna, 1978,* D1-2-12036, p. 261.
30. J. V. Allaby *et al.*, Yad. Fiz. **12**, 538 (1970) [Sov. J. Nucl. Phys. **12**, 295 (1971)].
31. A. S. Carrol *et al.*, Phys. Lett. B **80B**, 319 (1979).
32. V. B. Gavrilov and G. A. Leksin, Preprint ITÉF-124 (Institute of Theoretical and Experimental Physics, Moscow, 1983).

Translated by A. Isaakyan

Physics of Atomic Nuclei, Vol. 65, No. 3, 2002, pp. 497–512. From Yadernaya Fizika, Vol. 65, No. 3, 2002, pp. 523–538.

ELEMENTARY PARTICLES AND FIELDS
Theory

Radiative Decays and Quark Content of $f_0(980)$ and $\phi(1020)$*

A. V. Anisovich, V. V. Anisovich, V. N. Markov, and N. A. Nikonov

Petersburg Nuclear Physics Institute, Russian Academy of Sciences, Gatchina, 188350 Russia

Received December 21, 2000; in final form, June 28, 2001

Abstract—The quark structure of $\phi(1020)$ and $f_0(980)$ is studied on the basis of data on the radiative decays $\phi(1020) \to \gamma\pi^0$, $\gamma\eta$, $\gamma\eta'$, $\gamma a_0(980)$, $\gamma f_0(980)$ and $f_0(980) \to \gamma\gamma$. The partial widths are calculated under the assumption that all the mesons under consideration are $q\bar{q}$ states: $\phi(1020)$ is a dominantly $s\bar{s}$ state ($n\bar{n}$ component contributes not more than 1%); η, η', and π^0 are standard $q\bar{q}$ states, $\eta = n\bar{n}\cos\theta - s\bar{s}\sin\theta$ and $\eta' = n\bar{n}\sin\theta + s\bar{s}\cos\theta$ with $\theta \simeq 37°$; and $f_0(980)$ is a $q\bar{q}$ meson with the flavor wave function $n\bar{n}\cos\varphi + s\bar{s}\sin\varphi$. The transition $\phi \to \gamma\pi^0$ specifies the admixture of the $n\bar{n}$ component in the ϕ meson: it is on the order of 0.5%. We argue that this order of $n\bar{n}$ value does not contradict data on the decay $\phi(1020) \to \gamma a_0(980)$. The partial widths calculated for the decays $\phi \to \gamma\eta, \gamma\eta'$ are in reasonable agreement with experimental data. The measured branching-ratio value $\mathrm{Br}(\phi \to \gamma f_0(980)) = (3.4 \pm 0.4\,^{+1.5}_{-0.5}) \times 10^{-4}$ requires $25° \le |\varphi| \le 90°$. For the decay $f_0(980) \to \gamma\gamma$, the agreement with data, $\Gamma(f_0(980) \to \gamma\gamma) = 0.28^{+0.09}_{-0.13}$ keV, is attained at either $\varphi = 85° \pm 8°$ or $\varphi = -46° \pm 8°$. A simultaneous analysis of the decays $\phi(1020) \to \gamma f_0(980)$ and $f_0(980) \to \gamma\gamma$ favors the solution with the negative mixing angle of $\varphi = -48° \pm 6°$, setting $f_0(980)$ very close to the flavor octet ($\varphi_{\mathrm{octet}} = -54.7°$). © *2002 MAIK "Nauka/Interperiodica".*

1. INTRODUCTION

The $f_0(980)$ and $a_0(980)$ resonances are clue particles for the systematics of $q\bar{q}$ states in the range 1000–2300 MeV [1] and for fixing the glueball (see, e.g., [2–5]). The K-matrix analysis of meson spectra [6, 7] on the basis of a combined fit to data of Crystal Barrel [8], GAMS [9], and BNL [10] definitively supports the $q\bar{q}$ origin of $f_0(980)$ and $a_0(980)$. Still, the other possibilities for the origin of these resonances are actively discussed: accordingly, $f_0(980)$ and $a_0(980)$ are exotic states, and such a picture of $f_0(980)$ and $a_0(980)$ is presented in detail in [11] (see the minireview of Spanier and Törnqvist (p. 437) and the list of references).

According to the K-matrix analysis [4, 6, 7], the scalar–isoscalar sector (the $IJ^{PC} = 00^{++}$ wave) is affected by a strong mixing of overlapping resonances. In this way, a decisive role belongs to the *resonance → real mesons* decay processes. In the region 1000–1800 MeV, there exist four comparatively narrow resonances—$f_0(980)$, $f_0(1300)$ {denoted in the PDG compilation in [11] as $f_0(1370)$}, $f_0(1500)$, and $f_0(1750)$—and the broad state $f_0(1530^{+90}_{-250})$. According to the K-matrix analysis, the $f_0(1300)$, $f_0(1500)$, and $f_0(1530^{+90}_{-250})$ resonances are formed as the result of a strong mixing of the lightest scalar gluonium with the $1^3P_0q\bar{q}$ and $2^3P_0q\bar{q}$ states.

As was emphasized in [4, 6, 7], it is reasonable to perform the $q\bar{q}$-nonet classification in terms of the K-matrix, or "bare," poles corresponding to states "before" the mixing that is caused by the *$q\bar{q}$ state → real mesons* transitions.

In terms of f_0^{bare}, the scalar–isoscalar states of the basic $1^3P_0q\bar{q}$ nonet are $f_0^{\mathrm{bare}}(720 \pm 100)$ and $f_0^{\mathrm{bare}}(1260 \pm 30)$; the $f_0^{\mathrm{bare}}(720)$ state is close to the flavor octet—that is, $\varphi \simeq -70°$ [the mixing angle is determined as $f_0 = n\bar{n}\cos\varphi + s\bar{s}\sin\varphi$, where $n\bar{n} = (u\bar{u} + d\bar{d})/\sqrt{2}$], while the $f_0^{\mathrm{bare}}(1260)$ state is close to a singlet ($\varphi \simeq 20°$). The transitions that are due to the decay processes $f_0 \to \pi\pi, K\bar{K}, \eta\eta$ mix the $f_0^{\mathrm{bare}}(720)$ and $f_0^{\mathrm{bare}}(1260)$ states with each other, as well as with the nearby states $f_0^{\mathrm{bare}}(1235 \pm 50)$, $f_0^{\mathrm{bare}}(1600 \pm 50)$, and $f_0^{\mathrm{bare}}(1810 \pm 30)$ (the orthogonality of the coordinate wave functions does not work in the *$(q\bar{q}$ state$)_1$ → real mesons → $(q\bar{q}$ state$)_2$* transition). Two of these states are members of the $2^3P_0q\bar{q}$ nonet, and one is a scalar gluonium—that is either $f_0^{\mathrm{bare}}(1235)$ or $f_0^{\mathrm{bare}}(1600)$; the K-matrix analysis cannot definitively tell us which one. Lattice calculations [12] favor $f_0^{\mathrm{bare}}(1600)$ as a candidate for the glueball. After mixing, we have, in the $IJ^{PC} = 00^{++}$ wave, four comparatively narrow

*This article was submitted by the authors in English.

resonances $[f_0(980), f_0(1300), f_0(1500), f_0(1750)]$ and one rather broad state $f_0(1530^{+90}_{-250})$. The broad state ($\Gamma/2 \simeq 400$–500 MeV) appears as the result of a specific phenomenon that is typical of scalar–isoscalar states in the region 1200–1600 MeV—that is, the accumulation of the widths of overlapping resonances by one of them [13]. A similar phenomenon in nuclear physics was discussed in [14]. A fit to data proves that the main participants of the mixing are the glueball and two $q\bar{q}$ states belonging to the $1^3P_0q\bar{q}$ and $2^3P_0q\bar{q}$ nonets whose flavor wave functions are close to a singlet: the *glueball* $\to q\bar{q}$*(singlet)* transition is allowed, while the *glueball* $\to q\bar{q}$*(octet)* transition is suppressed. The gluonium–$q\bar{q}$ mixture is not suppressed according to the $1/N$-expansion rules [15] (see [16] for details). The glueball descendant is a broad state $f_0(1530^{+90}_{-250})$, which contains about 40–50% of the gluonium component; the rest is almost equally shared by $f_0(1300)$ and $f_0(1500)$.

In addition to the scalar–isoscalar wave, the K-matrix analysis of the scalar–isovector $IJ^P = 10^+$ wave was performed in [7], while the analysis of scalar kaons ($IJ^P = \frac{1}{2}0^+$) was performed in [17]; this allowed one to reconstruct the lightest scalar multiplet $1^3P_0q\bar{q}$ in terms of bare states [7, 17]. It is as follows:

$$a_0^{\rm bare}(960 \pm 30),\ K_0^{\rm bare}\left(1220^{+50}_{-150}\right), \qquad (1)$$
$$f_0^{\rm bare}(720 \pm 100),\ f_0^{\rm bare}(1260 \pm 30),$$
$$\varphi\left[f_0^{\rm bare}(720)\right] = -70^\circ\ {}^{+5^\circ}_{-16^\circ}.$$

According to the K-matrix analysis, the $f_0(980)$ resonance is the descendant of $f_0^{\rm bare}(720 \pm 100)$: the shift of the bare pole into the region around 1000 MeV is due to the transitions of $f_0^{\rm bare}(720 \pm 100)$ into real two-meson states, $\pi\pi$ and $K\bar{K}$. As to its origin, the $f_0(980)$ state is a superposition of the states $q\bar{q}$, $qq\bar{q}\bar{q}$, gluonium, $K\bar{K}$, and $\pi\pi$, and the wave function is to be represented as a Fock column. Concerning the $K\bar{K}$ and $\pi\pi$ components, one should consider that only part of the wave function responds to large meson–meson separations, $r_{\rm meson} > R_{\rm confinement}$; on the contrary, the small interquark separations must be taken into account for the $qq\bar{q}\bar{q}$ state. As to the glueball admixture in $f_0(980)$, the relative suppression of the decay $J/\psi \to \gamma f_0(980)$ [11] tells us that it is not large.

Based on the results of the K-matrix analysis [4, 6, 7], it is natural to check whether the $q\bar{q}$ component dominates $f_0(980)$. In Section 3, we calculate the $\phi(1020) \to \gamma f_0(980)$ decay amplitude, assuming $f_0(980)$ to be a $q\bar{q}$ system: the calculated amplitude describes data for the branching ratio, $\mathrm{Br}(\phi \to \gamma f_0(980)) = (3.4 \pm 0.4\ {}^{+1.5}_{-0.5}) \times 10^{-4}$ [11, 18, 19], with the following mixing angle for the $s\bar{s}$ and $n\bar{n}$ components:

$$\psi_{\rm flavor}\,(f_0(980)) = n\bar{n}\cos\varphi + s\bar{s}\sin\varphi, \qquad (2)$$
$$25^\circ \le |\varphi| \le 90^\circ.$$

The width $\Gamma(\phi \to \gamma f_0(980))$ depends strongly on the radius squared of $f_0(980)$, $R^2_{f_0(980)}$. For $R^2_{f_0(980)} \ge 12\ \mathrm{GeV}^{-2}$ (0.47 fm^2), the data require $|\varphi| \sim 25^\circ$–45°, while, for $R^2_{f_0(980)} \sim 8\ \mathrm{GeV}^{-2}$ (0.32 fm^2), one needs $|\varphi| \sim 40^\circ$–75°.

The estimation of radii of the scalar–isoscalar mesons that was performed by using GAMS data for $\pi^- p \to \pi^0\pi^0 n$ [9] shows that the $q\bar{q}$ component in $f_0(980)$ is comparatively compact, $R^2_{f_0(980)} = 6 \pm 6\ \mathrm{GeV}^{-2}$ [20]. Based on GAMS data, it is therefore reasonable to set

$$6 \le R^2_{f_0(980)} \le 12\ \mathrm{GeV}^{-2}, \qquad (3)$$

which favors large values of the mixing angle.

In what is concerned with the scheme under investigation, it is of prime importance to verify whether the transition $\phi(1020) \to \gamma f_0(980) \to \gamma\pi^0\pi^0$ describes the measured $\pi^0\pi^0$ spectrum within the Flatté formula [21], with the parameters determined by hadronic reactions: in Section 4, we calculate the $\pi^0\pi^0$ spectrum using the parametrization proposed by Bugg, Sarantsev, and Zou [22, 23] and obtain reasonable agreement with data. The calculations of the spectrum indicate the existence of significant systematic errors in the $\phi(1020) \to \gamma f_0(980)$ resonance signal, which are caused by the background contribution.

The radiative decay $f_0(980) \to \gamma\gamma$ provides us with another source of information about the content of $f_0(980)$: the calculation of the $f_0(980) \to \gamma\gamma$ partial width was performed in [24] under the assumption of the $q\bar{q}$ structure of $f_0(980)$. It was emphasized in [25], however, that the extraction of the $f_0(980) \to \gamma\gamma$ signal from the measured $\gamma\gamma \to \pi\pi$ spectra involves a difficulty associated with a strong interference between the resonance and the background, which leads to uncontrollable errors. The partial width $\Gamma(f_0(980) \to \gamma\gamma) = 0.28^{+0.09}_{-0.13}$ keV obtained in [26] is one-half as great as the averaged value reported previously (0.56 ± 0.11 keV [27]). In Section 5, we reanalyze the decay $f_0(980) \to \gamma\gamma$ using the Boglione–Pennington value for the width ($0.28^{+0.09}_{-0.13}$ keV), together with the constraint on the mean radius squared of $f_0(980)$ [20] ($R^2_{f_0(980)} \le 12\ \mathrm{GeV}^{-2}$). This provides two possible intervals for the $n\bar{n}$–$s\bar{s}$ mixing angle:

$$f_0(980) \to \gamma\gamma: \quad \text{i)}\ 80^\circ \le \varphi \le 93^\circ, \qquad (4)$$

ii) $-54^\circ \le \varphi \le -42^\circ$.

In Section 6, we calculate the partial widths with respect to the decays $\phi \to \gamma\eta, \gamma\eta', \gamma\pi^0, \gamma a_0(980)$ on the basis of the same technique as that used for $\phi(1020) \to \gamma f_0(980)$ and with the same parametrization of the ϕ-meson wave function. The calculation of the transition $\phi \to \gamma\pi^0$ allows us to determine the $n\bar{n}$ admixture in the ϕ meson: within the definition $\psi_{\text{flavor}}(\phi(1020)) = s\bar{s}\cos\varphi_V + n\bar{n}\sin\varphi_V$, we have

$$|\varphi_V| \simeq 4^\circ. \tag{5}$$

For the calculation of $\phi(1020) \to \gamma f_0(980)$, we have used the value of $|\varphi_V| = 4^\circ \pm 4^\circ$, which suggests the uncertainty of the quark calculus to be about 3°–5°. The decay $\phi(1020) \to \gamma a_0(980)$ provides us with information about the mixing angle φ_V as well: we argue that the data on the decay $\phi(1020) \to \gamma\pi^0\eta$ [28], which, for $M_{\pi^0\eta} \ge 900$ MeV, include a signal from the $\gamma a_0(980)$ channel, agree quite reasonably with small $|\varphi_V|$.

The reactions $\phi(1020) \to \gamma\eta, \gamma\eta'$, which are determined exclusively by the well-known probabilities of $s\bar{s}$ in η and η', are not sensitive to a small admixture of the $n\bar{n}$ component in the ϕ meson. The calculated partial widths are in reasonable agreement with data, so that the consideration performed for the decays $\phi(1020) \to \gamma\eta, \gamma\eta'$ gives us a strong argument that the applied method for calculating the radiative decays of $q\bar{q}$ mesons is entirely reliable. The need for performing a complete investigation of the radiative decays of ϕ mesons is motivated by a recent discussion on the possible incompatibility of the data on $\phi(1020) \to \gamma f_0(980)$ with the $q\bar{q}$ structure of $f_0(980)$ (see, e.g., [29, 30]).

The constraints on the mixing angle φ that come from a combined analysis of the radiative decays $\phi(1020) \to \gamma f_0(980)$ and $f_0(980) \to \gamma\gamma$ are discussed in Section 8. For negative mixing angles, the combined analysis does not change the constraint in (4),

$$\varphi = -48^\circ \pm 6^\circ, \tag{6}$$

and does not set any constraint on the radius squared $R^2_{f_0(980)}(n\bar{n})$.

For positive mixing angles, the allowed region of $\left(\varphi, R^2_{f_0(980)}(n\bar{n})\right)$ is as follows:

$$\varphi = 86^\circ \pm 3^\circ, \qquad R^2_{f_0(980)}(n\bar{n}) \le 6.8\ \text{GeV}^{-2}. \tag{7}$$

However, the hadronic decays of $f_0(980)$ strongly contradict the almost complete absence of the $n\bar{n}$ component in $f_0(980)$; this gives priority to the solution in (6), according to which $f_0(980)$ is close to the octet state (recall that $\varphi_{\text{octet}} = -54.7^\circ$).

This article is organized as follows.

In Section 2, we write the spin structure of the $V \to \gamma S, \gamma P$ and $S \to \gamma\gamma$ decay amplitudes, where V, S, and P are vector, scalar, and pseudoscalar mesons, respectively.

In Section 3, a method for calculating the decay amplitudes in terms of the spectral integrals with respect to $q\bar{q}$ invariant masses and light-cone variables is presented for the example of $V \to \gamma S$ reactions. The technique that uses double spectral integrals to calculate the transition amplitudes was developed for photon–deuteron interactions [31, 32] and applied to $P \to \gamma\gamma^*(Q^2)$ transition form factors [32]. Using this method, we calculate here the radiative form factors for $\phi(1020) \to \gamma f_0(980)$ (Section 4), $f_0(980) \to \gamma\gamma$ (Section 6), and $\phi(1020) \to \gamma\pi^0, \gamma a_0(980), \gamma\eta, \gamma\eta'$ (Section 7).

The estimation of the $\pi\pi$ spectrum in the decay $\phi(1020) \to \gamma\pi^0\pi^0$ with the Flatté formula is discussed in Section 5. The results are summarized in Section 8. The necessary technique is presented in Appendices A, B, C, and D.

2. SPIN STRUCTURE OF THE $V \to \gamma S$, $V \to \gamma P$, AND $S \to \gamma\gamma$ TRANSITION AMPLITUDES

Here, we present the spin operators for amplitudes under consideration: $\phi(1020) \to \gamma\pi^0$, $\gamma\eta$, $\gamma\eta'$, $\gamma a_0(980)$, $\gamma f_0(980)$, and $f_0(980) \to \gamma\gamma$.

(a) $V \to \gamma S$ transition amplitude. The $V \to \gamma S$ transition amplitude, with V and S being vector and scalar $q\bar{q}$ states, is determined by the final-state orbital angular momenta of $L = 0, 2$. Accordingly, the spin-dependent part of the amplitude, $A_{\mu\nu}$ (the index μ stands for spin of the photon and ν for that of ϕ meson), consists of two terms that are proportional to $g^\perp_{\mu\nu}$ (S wave) and $q^\perp_\mu q^\perp_\nu - q^2_\perp g^\perp_{\mu\nu}/3$ (D wave):

$$A_{\mu\nu} = e\left[g^\perp_{\mu\nu}F_S(q^2) + (q^\perp_\mu q^\perp_\nu - \frac{1}{3}g^\perp_{\mu\nu}q^2_\perp)F_D(q^2)\right]. \tag{8}$$

Here, $q^\perp$ is the projection of the photon momentum, which is orthogonal to the ϕ-meson momentum p, and $g^\perp_{\mu\nu}$ is the metric tensor in the space orthogonal to p:

$$q^\perp_\mu = q_\mu - p_\mu\frac{(qp)}{p^2}, \quad g^\perp_{\mu\nu} = g_{\mu\nu} - \frac{p_\mu p_\nu}{p^2}. \tag{9}$$

The requirement $q_\mu A_{\mu\nu} = 0$ results in the following constraint on the invariant amplitudes $F_S(q^2)$ and $F_D(q^2)$:

$$F_S(q^2) + \frac{2}{3}(qq^\perp)F_D(q^2) = 0. \tag{10}$$

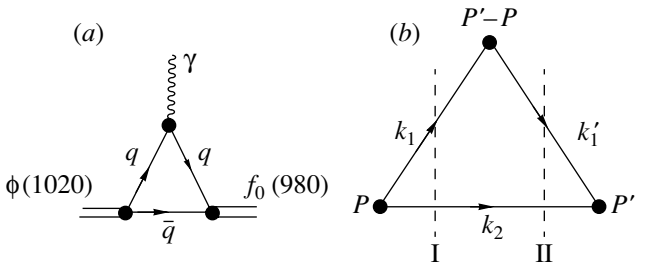

Fig. 1. (*a*) Diagrammatic representation of the transition $\phi(1020) \to \gamma f_0(980)$. (*b*) Three-point quark diagram: dashed lines I and II mark two cuts in the double spectral representation.

Thus, Eq. (8) takes the form

$$A_{\mu\nu} = \frac{3}{2} eF_S(q^2) \left(g^{\perp}_{\mu\nu} - \frac{q^{\perp}_{\mu} q^{\perp}_{\nu}}{q^2_{\perp}} \right) \equiv eA_{V\to\gamma S}(q^2) g^{\perp\perp}_{\mu\nu}. \quad (11)$$

The metric tensor $g^{\perp\perp}_{\mu\nu}$ works in the space orthogonal to p and q (namely, $g^{\perp\perp}_{\mu\nu} p_\nu = 0$ and $g^{\perp\perp}_{\mu\nu} q_\nu = 0$).

(b) $V \to \gamma P$ transition amplitude. Here, the notation for the spin indices and particle momenta is identical to that for $V \to \gamma S$ reactions.

The spin operator for the $V \to \gamma P$ amplitude involves the antisymmetric tensor $\epsilon_{\mu\nu\alpha\beta}$ associated with pseudoscalar-particle production. The only way to construct the spin operator is to contract $\epsilon_{\mu\nu\alpha\beta}$ with two independent momenta p and q. Therefore, the amplitude has the following structure:

$$A_{\mu\nu} = e\epsilon_{\mu\nu\alpha\beta} p_\alpha q_\beta A_{V\to\gamma P}(q^2). \quad (12)$$

(c) $S \to \gamma(q^2)\gamma(q'^2)$ transition amplitude. The $S \to \gamma(q^2)\gamma(q'^2)$ transition amplitude has the same spin structure as the $V \to \gamma S$ amplitude. It has the form

$$A_{\mu\nu} = e^2 A_{S\to\gamma\gamma}(q^2, q'^2) g^{\perp\perp}_{\mu\nu}, \quad (13)$$

where q and q' are the momenta of outgoing photons with spin projections μ and ν, respectively. The metric tensor $g^{\perp\perp}_{\mu\nu}$ works in the space orthogonal to q and q'. It is as follows:

$$g^{\perp\perp}_{\mu\nu} = g_{\mu\nu} - q_\mu q_\nu \frac{q'^2}{D} - q'_\mu q'_\nu \frac{q^2}{D} + (q_\mu q'_\nu + q'_\mu q_\nu) \frac{qq'}{D}, \quad (14)$$

$$D = q^2 q'^2 - (qq')^2.$$

Since $(qq') = \frac{1}{2}(p^2 - q'^2 - q^2)$, where p is the 4-momentum of the scalar particle, the factor D can be expressed in terms of the external momenta squared as

$$D = \frac{1}{4} \left[2q^2(p^2 + q'^2) - (p^2 - q'^2)^2 - q^4 \right]. \quad (15)$$

3. SPECTRAL REPRESENTATION OF THE FORM-FACTOR AMPLITUDES AND THE REACTION $\phi(1020) \to \gamma f_0(980)$

Following the prescription of [32], we present, in this section, the method for calculating the three-point form-factor amplitudes in terms of the spectral representations for intermediate $q\bar{q}$ states. Then, the resulting formulas are applied to the decay $\phi(1020) \to \gamma f_0(980)$.

(a) Double spectral representation of the $V \to \gamma(q^2)S$ form factor. Here, we give a general presentation of the spectral-integral method using $V \to \gamma(q^2)S$ reactions as an example.

Under the assumption of the $q\bar{q}$ structure for the initial (V) and final (S) mesons, the $V \to \gamma S$ coupling constant is determined by $V \to q\bar{q}$ and $q\bar{q} \to S$ processes with the emission of $\gamma(q^2)$ (see Fig. 1*a*). The corresponding three-point loop diagram (see Fig. 1*b*) is calculated by using double spectral representation with respect to intermediate $q\bar{q}$ states (indicated by dashed lines in Fig. 1*b*).

To be illustrative, let us start with the three-point Feynman diagram. For the process in Fig. 1*a*, one has

$$A^{(\text{Feynman})}_{\mu\nu} = \int \frac{d^4k}{i(2\pi)^4} G_V \times \frac{Z^{(q\bar{q})}_{V\to\gamma S} S^{(V\to S)}_{\mu\nu}}{(m^2 - k_1^2)(m^2 - k_1'^2)(m^2 - k_2^2)} G_S. \quad (16)$$

Here, k_1, k_1', and k_2 are quark momenta; m is the quark mass; and G_V and G_S are quark–meson vertices. The quark charges are included in $Z^{(q\bar{q})}_{V\to\gamma S}$. The spin-dependent block has the form

$$S^{(V\to S)}_{\mu\nu} = -\text{tr}\left[(\hat{k}'_1 + m)\gamma^{\perp}_{\mu} \times (\hat{k}_1 + m)\gamma^{\perp}_{\nu}(-\hat{k}_2 + m) \right], \quad (17)$$

where the Dirac matrices $\gamma^{\perp}_{\mu}$ and $\gamma^{\perp}_{\nu}$ are orthogonal to the outgoing momenta: $\gamma^{\perp}_{\mu} q_\mu = 0$ and $\gamma^{\perp}_{\nu} p_\nu = 0$.

To transform the Feynman integral (16) into the double spectral integral with respect to the invariant $q\bar{q}$ masses squared, one should (i) consider the corresponding off-energy-shell diagram, Fig. 1*b*, with $P^2 = (k_1 + k_2)^2 \geq 4m^2$ and $P'^2 = (k'_1 + k_2)^2 \geq 4m^2$ and with a fixed momentum transfer squared $q^2 =$

$(P-P')^2$; (ii) extract the invariant amplitude separating spin operators; and (iii) calculate the discontinuities of the invariant amplitude with respect to intermediate $q\bar{q}$ states indicated in Fig. 1*b* by dashed lines.

The double discontinuity is the integrand of the spectral integral with respect to P^2 and P'^2. Furthermore, we adopt the following notation:

$$P^2 = s, \quad P'^2 = s'. \tag{18}$$

In order to calculate a discontinuity by cutting the relevant Feynman diagram, the pole terms of the propagators are replaced by their residues: $(m^2 - k^2)^{-1} \to \delta(m^2 - k^2)$. Therefore, the particles in the intermediate states indicated by the dashed lines I and II in Fig. 1*b* are on the mass shell, $k_1^2 = k_2^2 = k_1'^2 = m^2$. As a result, integration of the Feynman diagram reduces to integration of the cut diagram states over phase spaces. The corresponding phase space for the three-point diagram is

$$d\Phi(P,P';k_1,k_2,k_1') = d\Phi(P;k_1,k_2) \tag{19}$$
$$\times\, d\Phi(P';k_1',k_2')(2\pi)^3 2k_{20}\delta^{(3)}(\mathbf{k}_2' - \mathbf{k}_2),$$

where the invariant two-particle phase space $d\Phi(P;k_1,k_2)$ has the form

$$d\Phi(P;k_1,k_2) = \frac{1}{2}\,\frac{d^3k_1}{(2\pi)^3 2k_{10}}\,\frac{d^3k_2}{(2\pi)^3 2k_{20}} \tag{20}$$
$$\times\, (2\pi)^4\delta^{(4)}(P - k_1 - k_2).$$

The last step is to single out the invariant component from the spin factor (17). According to (11), the spin factor (17) is proportional to the metric tensor: $S_{\mu\nu}^{(V\to S)} \sim g_{\mu\nu}^{\perp\perp}$. The spin factor $S_{V\to\gamma S}^{(\mathrm{tr})}$ defined as

$$S_{\mu\nu}^{(V\to S)} = g_{\mu\nu}^{\perp\perp} S_{V\to\gamma S}^{(\mathrm{tr})}(s,s',q^2) \tag{21}$$

is then given by

$$S_{V\to\gamma S}^{(\mathrm{tr})}(s,s',q^2) = -2m\Bigg(4m^2 + s - s' \tag{22}$$
$$- \frac{4ss'}{s+s'-q^2}\alpha(s,s',q^2)\Bigg),$$

$$\alpha(s,s',q^2) = \frac{q^2(s+s'-q^2)}{2q^2(s+s') - (s-s')^2 - q^4}.$$

Recall that, in going from (17) to (21), (22), and (23), we have $(k_1k_2) = s/2 - m^2$, $(k_1'k_2) = s'/2 - m^2$, and $(k_1'k_1) = m^2 - q^2/2$. The calculation of the spin factor is presented in more detail in Appendix A.

The spectral integration is performed with respect to the energy squared of quarks in the intermediate states, $s = P^2 = (k_1+k_2)^2$ and $s' = P'^2 = (k_1'+k_2)^2$, at fixed $q^2 = (P'-P)^2$. The spectral representation for the amplitude $A_{V\to\gamma S}(q^2)$ has the form

$$A_{V\to\gamma S}(q^2) = \int\limits_{4m^2}^{\infty}\frac{ds}{\pi} \tag{23}$$
$$\times \int\limits_{4m^2}^{\infty}\frac{ds'}{\pi}\,\frac{G_V(s)}{s-M_V^2}\,\frac{G_S(s')}{s'-M_S^2}$$
$$\times \int d\Phi(P,P';k_1,k_2,k_1')S_{V\to\gamma S}^{(\mathrm{tr})}(s,s',q^2)Z_{V\to\gamma S}^{(q\bar{q})}.$$

The spectral representation of the amplitude $A_{V\to\gamma S}(q^2)$ gives us the invariant part of $A_{\mu\nu}^{(\mathrm{Feynman})}$, Eq. (16), if the vertices are constant: $G_V(s) = \mathrm{const}$ and $G_S(s') = \mathrm{const}$. Generally, energy-dependent vertices can be incorporated into spectral integrals. According to [31, 32], the form factor for a composite system can be obtained by considering the $1+2 \to 1+2$ two-particle partial-wave scattering amplitude, with the same quantum numbers as for the composite system. In this amplitude, the composite system reveals itself as a pole. The amplitude for the emission of a photon by the two-particle-interaction system has two poles associated with the states "before" and "after" electromagnetic interaction, and the two-pole residue of this amplitude provides us with the form factor of the composite system. When a partial-wave scattering amplitude is treated by using the N/D dispersion-relation method, the vertex $G(s)$ is determined by the N function: the vertex, as well as the N function, has left-hand singularities that are determined by the forces between particles 1 and 2.

It is reasonable to refer to the ratios $G_V(s)/(s-m^2)$ and $G_S(s')/(s'-m^2)$ as the wave functions of the vector and the scalar particle, respectively:

$$\frac{G_V(s)}{s-m^2} = \psi_V(s), \quad \frac{G_S(s')}{s'-m^2} = \psi_S(s'). \tag{24}$$

Dealing with Eq. (24), one can either (i) express it in terms of the light-cone variables or (ii) retain the spectral integrals with respect to s and s' and eliminate integrations with respect to quark momenta with the aid of phase-space δ functions.

(b) Light-cone variables. The formulas (18) and (24) allow one to go over to the light-cone variables by using the boost along the z axis. Let us use the reference frame where the initial vector meson moves along the z axis with an infinite momentum:

$$P = (p + \frac{s}{2p}, \mathbf{0}, p), \tag{25}$$
$$P' = (p + \frac{s'+q_\perp^2}{2p}, -\mathbf{q}_\perp, p).$$

In this frame, the two-particle phase space is

$$d\Phi(P;k_1,k_2)=\frac{1}{16\pi^2}\frac{dx_1dx_2}{x_1x_2}d^2k_{1\perp}d^2k_{2\perp} \quad (26)$$
$$\times\,\delta(1-x_1-x_2)\delta^{(2)}(\mathbf{k}_{1\perp}+\mathbf{k}_{2\perp})$$
$$\times\,\delta\left(s-\frac{m^2+k_{1\perp}^2}{x_1}-\frac{m^2+k_{2\perp}^2}{x_2}\right),$$

where $x_i=k_{iz}/p$ and the phase space for the triangle diagram has the form

$$d\Phi(P,P';k_1,k_2,k_1') \quad (27)$$
$$=\frac{1}{16\pi}\frac{dx_1dx_2}{x_1^2x_2}d^2k_{1\perp}d^2k_{2\perp}$$
$$\times\,\delta(1-x_1-x_2)\delta^{(2)}(\mathbf{k}_{1\perp}+\mathbf{k}_{2\perp})$$
$$\times\,\delta\left(s-\frac{m^2+k_{1\perp}^2}{x_1}-\frac{m^2+k_{2\perp}^2}{x_2}\right)$$
$$\times\,\delta\left(s'+q_\perp^2-\frac{m^2+(\mathbf{k}_{1\perp}-\mathbf{q}_\perp)^2}{x_1}-\frac{m^2+k_{2\perp}^2}{x_2}\right).$$

The $V\to\gamma(q^2)S$ amplitude is then given by

$$A_{V\to\gamma(q^2)S}(q^2)=\frac{Z_{V\to\gamma S}^{(q\bar q)}}{16\pi^3}\int\limits_0^1\frac{dx}{x(1-x)^2} \quad (28)$$
$$\times\int d^2k_\perp\psi_V(s)\psi_S(s')S_{V\to\gamma S}^{(\mathrm{tr})}(s,s',q^2),$$

where $x=k_{2z}/p$, $\mathbf{k}_\perp=\mathbf{k}_{2\perp}$, and the $q\bar q$ invariant masses squared are

$$s=\frac{m^2+k_\perp^2}{x(1-x)},\quad s'=\frac{m^2+(\mathbf{k}_\perp+x\mathbf{q}_\perp)^2}{x(1-x)}. \quad (29)$$

(c) Spectral integral representation. In Eq. (23), one can perform integration over the phase space, considering the energies squared s and s' to be fixed. After using the phase-space δ functions, we have

$$A_{V\to\gamma S}(q^2)=\int\limits_{4m^2}^\infty\frac{dsds'}{\pi^2}\psi_V(s)\psi_S(s') \quad (30)$$
$$\times\,\frac{\theta\left(ss'Q^2-m^2\lambda(s,s',Q^2)\right)}{16\sqrt{\lambda(s,s',Q^2)}}$$
$$\times\,Z_{V\to\gamma S}^{(q\bar q)}S_{V\to\gamma S}^{(\mathrm{tr})}(s,s',Q^2),$$

where

$$\lambda(s,s',Q^2)=(s'-s)^2+2Q^2(s'+s)+Q^4. \quad (31)$$

The θ function $\theta(X)$ restricts the integration region for different $Q^2=-q^2$: $\theta(X)=1$ at $X\ge0$ and $\theta(X)=0$ at $X<0$.

In the limit $Q^2\to0$, integration with respect to s' is performed (see Appendix B for details). As a result, we obtain

$$A_{V\to\gamma S}(0)=\int\limits_{4m^2}^\infty\frac{ds}{\pi}\psi_V(s)\psi_S(s) \quad (32)$$
$$\times\left[-\frac{m^3}{2\pi}\ln\frac{\sqrt{s}+\sqrt{s-4m^2}}{\sqrt{s}-\sqrt{s-4m^2}}\right.$$
$$\left.+\,\frac{m}{4\pi}\sqrt{s(s-4m^2)}\right]Z_{V\to\gamma S}^{(q\bar q)}.$$

(d) Meson wave functions. To calculate the form factors, one should define meson wave functions. The simplest parametrization is an exponential one:

$$\psi_V(s)=C_Ve^{-b_Vs},\quad \psi_S(s)=C_Se^{-b_Ss}. \quad (33)$$

The parameters b_V and b_S characterize the size of the system; they are related to the mean radii squared R_V^2 and R_S^2 of the mesons. At fixed R_V^2 and R_S^2, the constants C_V and C_S are determined by the normalization of the wave function; it is given by the meson form factor in an external field, $F_{\mathrm{meson}}(q^2)$. At small q^2, the form factor is

$$F_{\mathrm{meson}}(q^2)\simeq1+\frac{1}{6}R_{\mathrm{meson}}^2q^2. \quad (34)$$

The requirement $F_{\mathrm{meson}}(0)=1$ fixes the constant C_{meson} in (33), while the value R_{meson}^2 is directly related to b_{meson}.

The form factor $F_{\mathrm{meson}}(q^2)$ has the form

$$F_{\mathrm{meson}}(q^2)=\int\limits_{4m^2}^\infty\frac{dsds'}{\pi^2}\psi_{\mathrm{meson}}(s)\psi_{\mathrm{meson}}(s') \quad (35)$$
$$\times\,\frac{\theta\left(ss'Q^2-m^2\lambda(s,s',Q^2)\right)}{16\sqrt{\lambda(s,s',Q^2)}}\,S_{\mathrm{meson}}^{(\mathrm{tr})}(s,s',q^2),$$

where $S_{\mathrm{meson}}^{(\mathrm{tr})}$ is determined by the following traces:

$$2P_\mu^\perp S_S^{(\mathrm{tr})}(s,s',q^2) \quad (36)$$
$$=-\mathrm{tr}\left[(\hat k_1'+m)\gamma_\mu^\perp(\hat k_1+m)(-\hat k_2+m)\right],$$
$$2P_\mu^\perp S_V^{(\mathrm{tr})}(s,s',q^2)$$
$$=-\frac{1}{3}\mathrm{tr}\left[\gamma_\alpha'^\perp(\hat k_1'+m)\gamma_\mu^\perp(\hat k_1+m)\gamma_\alpha^\perp(-\hat k_2+m)\right];$$

the orthogonal components are

$$P_\mu^\perp=P_\mu-q_\mu\frac{(Pq)}{q^2},\quad \gamma_\mu^\perp=\gamma_\mu-q_\mu\frac{\hat q}{q^2}, \quad (37)$$
$$\gamma_\alpha^\perp=\gamma_\alpha-P_\alpha\frac{\hat P}{P^2},\quad \gamma_\alpha'^\perp=\gamma_\alpha-P_\alpha'\frac{\hat P'}{P'^2},$$

and $q = k_1' - k_1$. In determining $S_V^{(\mathrm{tr})}$, we have averaged over three polarizations of the vector meson (the factor of $1/3$).

The functions $S_S^{(\mathrm{tr})}$ and $S_V^{(\mathrm{tr})}$ are given by

$$S_S^{(\mathrm{tr})}(s,s',q^2) = \alpha(s,s',q^2)(s+s'-8m^2-q^2)+q^2, \quad (38)$$

$$S_V^{(\mathrm{tr})}(s,s',q^2) = \frac{2}{3}\left[\alpha(s,s',q^2)(s+s'+4m^2-q^2)+q^2\right].$$

Taking into account (34), one can determine the normalization of the wave function as well as the mean radius squared. For the scalar meson, the normalization condition is

$$1 = \int\limits_{4m^2}^{\infty} \frac{ds}{\pi}\psi_S^2(s)\frac{s-4m^2}{8\pi}\sqrt{\frac{s-4m^2}{s}}, \quad (39)$$

and the mean radius squared is

$$R_S^2 = \int\limits_{4m^2}^{\infty} \frac{ds}{\pi}\psi_S^2(s)\frac{3}{8\pi} \quad (40)$$
$$\times\left(\ln\frac{\sqrt{s}+\sqrt{s-4m^2}}{\sqrt{s}-\sqrt{s-4m^2}} - \frac{s+2m^2}{2s}\sqrt{\frac{s-4m^2}{s}}\right)$$
$$+\int\limits_{4m^2}^{\infty}\frac{ds}{\pi}\left(\psi_S'^2(s)-\psi_S''(s)\psi_S(s)\right)\frac{3(s-4m^2)}{8\pi}$$
$$\times\left(s\ln\frac{\sqrt{s}+\sqrt{s-4m^2}}{\sqrt{s}-\sqrt{s-4m^2}} - 2\sqrt{s(s-4m^2)}\right).$$

For the exponential parametrization of the wave function, the second term in (40) vanishes: $\psi_S'^2(s) - \psi_S''(s)\psi_S(s) = 0$.

Likewise, the normalization condition for vector meson is

$$1 = \int\limits_{4m^2}^{\infty} \frac{ds}{\pi}\psi_V^2(s)\frac{s+2m^2}{12\pi}\sqrt{\frac{s-4m^2}{s}}, \quad (41)$$

and the mean radius squared is given by

$$R_V^2 = \int\limits_{4m^2}^{\infty} \frac{ds}{\pi}\psi_V^2(s)\frac{1}{4\pi} \quad (42)$$
$$\times\left(\ln\frac{\sqrt{s}+\sqrt{s-4m^2}}{\sqrt{s}-\sqrt{s-4m^2}} - \frac{s^2-8m^2s+4m^4}{2s(s-4m^2)}\sqrt{\frac{s-4m^2}{s}}\right)$$
$$+\int\limits_{4m^2}^{\infty}\frac{ds}{\pi}\left(\psi_V'^2(s)-\psi_V''(s)\psi_V(s)\right)\frac{s+2m^2}{4\pi}$$
$$\times\left(s\ln\frac{\sqrt{s}+\sqrt{s-4m^2}}{\sqrt{s}-\sqrt{s-4m^2}} - 2\sqrt{s(s-4m^2)}\right).$$

The meson form factor can also be written in terms of the light-cone variables, whereupon we arrive at a formula similar to (28); that is,

$$F_{\mathrm{meson}}(q^2) = \frac{1}{16\pi^3}\int\limits_0^1 \frac{dx}{x(1-x)^2} \quad (43)$$
$$\times\int d^2k_\perp \Psi_{\mathrm{meson}}(s)\Psi_{\mathrm{meson}}(s')S_{\mathrm{meson}}^{(\mathrm{tr})}(s,s',q^2),$$

where $S_{\mathrm{meson}}^{(\mathrm{tr})}(s,s',q^2)$ is given by (38).

4. $\phi(1020) \to \gamma f_0(980)$: THE DECAY AMPLITUDE AND PARTIAL WIDTH

In this section, we calculate the branching ratio for the decay $\phi \to \gamma f_0(980)$, assuming the $q\bar{q}$ structure of $f_0(980)$.

(a) Partial width. The decay partial width is determined as

$$m_\phi \Gamma_{\phi\to f_0\gamma} = \int \frac{1}{3}|A_{\mu\nu}|^2 d\Phi(p;q,k_f). \quad (44)$$

In (44), the averaging over spin projections of the ϕ meson and summation over those of the photon are performed; $d\Phi$ is the two-particle phase space, which, for the radiative decay $\phi \to \gamma + f_0$, is $\int d\Phi(p;q,k_f) = (m_\phi^2 - m_f^2)/(16\pi m_\phi^2)$.

Summation over photon spin variables results in the metric tensor $g_{\mu\mu'}^{\perp\perp}$:

$$|A_{\mu\nu}|^2 = A_{\nu\mu}^* g_{\mu\mu'}^{\perp\perp} A_{\mu'\nu}, \quad (45)$$

where

$$g_{\mu\mu'}^{\perp\perp} = g_{\mu\mu'} + \frac{4m_\phi^2 q_\mu q_{\mu'}}{(m_\phi^2-m_f^2)^2} + \frac{2(q_\mu p_{\mu'} + p_\mu q_{\mu'})}{m_\phi^2 - m_f^2}. \quad (46)$$

Hence, the partial width is

$$m_\phi\Gamma_{\phi\to f_0\gamma} = \frac{1}{6}\alpha\frac{m_\phi^2-m_f^2}{m_\phi^2}|A_{\phi\to\gamma f_0(980)}(0)|^2, \quad (47)$$

where $\alpha = e^2/4\pi = 1/137$.

(b) Wave functions of $\phi(1020)$ and $f_0(980)$. We write the wave functions of $\phi(1020)$ and $f_0(980)$ as

$$\Psi_\phi(s) = (n\bar{n}\sin\varphi_V + s\bar{s}\cos\varphi_V)\,\psi_\phi(s), \quad (48)$$

$$\Psi_{f_0}(s) = (n\bar{n}\cos\varphi + s\bar{s}\sin\varphi)\,\psi_f(s),$$

assuming the same s dependence for the $n\bar{n}$ and $s\bar{s}$ components. An exponential parametrization is used for $\psi_\phi(s)$ and $\psi_{f_0}(s)$. The radius squared of the $n\bar{n}$ component in the ϕ meson is assumed to be identical to that of the pion ($R_\phi^{(n\bar{n})\,2} \simeq 10.9$ GeV^{-2}), while the radius squared $R_\phi^{(s\bar{s})\,2}$ is slightly less, $R_\phi^{(s\bar{s})\,2} \simeq 9.3$ GeV^{-2} (this corresponds to $b_\phi = 2.5$ GeV^{-2}). As to $f_0(980)$, we vary its radius in the interval $6 \leq R^2_{f_0(980)} \leq 18$ GeV^{-2}.

(c) The result for $\phi(1020) \to \gamma f_0(980)$. The amplitude $A_{\phi\to\gamma f_0}(0)$ is the sum of two terms associated with the $n\bar{n}$ and $s\bar{s}$ components:

$$A_{\phi\to\gamma f_0}(0) = \cos\varphi\sin\varphi_V A^{(n\bar{n})}_{\phi\to\gamma f_0}(0) + \sin\varphi\cos\varphi_V A^{(s\bar{s})}_{\phi\to\gamma f_0}(0). \quad (49)$$

In our estimations, we set $\cos\varphi_V \sim 0.99$ and, correspondingly, $|\sin\varphi_V| \sim 0.1$; for $f_0(980)$, we vary mixing angle in the interval $0^\circ \leq |\varphi| \leq 90^\circ$.

The charge factors for the reaction $\phi(1020) \to \gamma f_0(980)$ are equal to $Z^{(n\bar{n})}_{\phi\to\gamma f_0} = 1/3$ and $Z^{(s\bar{s})}_{\phi\to\gamma f_0} = -2/3$ (see Appendix C).

The results of the calculation are shown in Figs. 2 and 3. In Fig. 2*a*, $A^{(n\bar{n})}_{\phi\to\gamma f_0}(0)$ and $A^{(s\bar{s})}_{\phi\to\gamma f_0}(0)$ are plotted versus the radius squared $R^2_{f_0(980)}$, while the mean radius squared of the ϕ meson is close to that of the pion: $R^2_{\phi(1020)} \simeq 0.4$ fm^2.

In Fig. 3, one can see $\mathrm{Br}(\phi(1020) \to \gamma f_0(980))$ at various values of $\sin|\varphi|$: $\sin|\varphi| = 0.4$, 0.6, 0.8, 0.9, and 0.985. The shaded areas correspond to the variation of φ_V in the interval $-8^\circ \leq \varphi_V \leq 8^\circ$; the lower and upper curves of the shaded area correspond, respectively, to the destructive and to the constructive interference of $A^{(n\bar{n})}_{\phi\to\gamma f_0}(0)$ and $A^{(s\bar{s})}_{\phi\to\gamma f_0}(0)$.

The measurement of the $f_0(980)$ signal in the $\gamma\pi^0\pi^0$ reaction gives the branching ratio $\mathrm{Br}(\phi \to \gamma f_0(980)) = (3.5 \pm 0.3^{+1.3}_{-0.5}) \times 10^{-4}$ [19]; in the analysis of $\gamma\pi^0\pi^0$ and $\gamma\pi^+\pi^-$ channels, it was found that $\mathrm{Br}(\phi \to \gamma f_0(980)) = (2.90 \pm 0.21 \pm 1.5) \times 10^{-4}$ [18]. The averaged value is given in [11]: $\mathrm{Br}(\phi \to \gamma f_0(980)) = (3.4 \pm 0.4) \times 10^{-4}$. Our calculations of the $\pi^0\pi^0$ spectrum with the conventional Flatté formula (Section 5) support the statement of [18, 19] about the presence of large systematic errors associated with the procedure for extracting the $f_0(980)$ signal. In our estimation of the permissible interval for the mixing angle φ, we have used the averaged value given by [11], with the inclusion of systematic errors on the order of those found in [18, 19]: $\mathrm{Br}(\phi \to \gamma f_0(980)) = (3.4 \pm 0.4^{+1.5}_{-0.5}) \times 10^{-4}$.

The calculated values of $\mathrm{Br}(\phi \to \gamma f_0(980))$ agree with experimental data for $|\varphi| \geq 25^\circ$; larger values of mixing angle, $|\varphi| \geq 55^\circ$, correspond to a more compact structure of $f_0(980)$, namely, $R^2_{f_0(980)} \leq 10$ GeV^{-2}, while small mixing angles of $|\varphi| \sim 25^\circ$ are associated with a loosely bound structure, $R^2_{f_0(980)} \geq 12$ GeV^{-2} (recall that, for the pion, $R^2_\pi \simeq 10$ GeV^{-2}).

The evaluation of the radius of $f_0(980)$ was performed in [24] on the basis of GAMS data [9], where the t dependence was measured in the process $\pi^- p \to f_0(980)n$ [t is the square of the momentum transfer to $f_0(980)$]: these data favor a comparatively compact structure of the $q\bar{q}$ component in $f_0(980)$, namely, $R^2_{f_0(980)} = 6 \pm 6$ GeV^{-2}.

5. PARTIAL WIDTH FOR THE REACTION $\phi(1020) \to \gamma\pi^0\pi^0$

In the $\pi^0\pi^0$ spectrum, the $f_0(980)$ resonance is seen as a peak on the edge of the spectrum. It is therefore rather instructive to find the $M_{\pi\pi}$ dependence of $\mathrm{Br}(\phi(1020) \to \gamma\pi^0\pi^0)$ by using the conventional Flatté formula [21].

In hadronic reactions, the $f_0(980)$ resonance is well described by the Flatté formula which takes into account two decay channels, $f_0(980) \to \pi\pi$ and $f_0(980) \to K\bar{K}$; the parameters of the Flatté formula were found by Bugg, Sarantsev, and Zou [22, 23].

In calculating the $\pi\pi$ spectrum, we take into account both the resonance and the background [$B(M^2_{\pi\pi})$] contributions. The partial width $d\Gamma_{\phi\to\gamma\pi\pi}$ is then given by

$$d\Gamma_{\phi\to\gamma\pi\pi} = \Gamma_{\phi\to\gamma f_0(980)} \times \frac{M_f(m_\phi^2 - M^2_{\pi\pi})}{M_{\pi\pi}(m_\phi^2 - M_f^2)} \frac{F^2_{\mathrm{thresh}}(M^2_{\pi\pi})}{F^2_{\mathrm{thresh}}(M_f^2)} \times \left|\frac{1}{M_0^2 - M^2_{\pi\pi} - ig^2_\pi\rho_{\pi\pi} - ig^2_K\rho_{K\bar{K}}} + B(M^2_{\pi\pi})\right|^2 \times g^2_\pi\rho_{\pi\pi}\frac{dM^2_{\pi\pi}}{\pi}. \quad (50)$$

Here, we separate $\Gamma_{\phi\to\gamma f_0(980)}$ and introduce the ratio of the phase spaces for $(\pi\pi) + \gamma$ and $f_0(980) + \gamma$:

$$\frac{d\Phi_{(\pi\pi)\gamma}}{d\Phi_{f_0(980)\gamma}} = \frac{M_f(m_\phi^2 - M^2_{\pi\pi})}{M_{\pi\pi}(m_\phi^2 - M_f^2)}, \quad (51)$$

where $M_f = 0.98$ GeV and M_0 is an adjustable parameter.

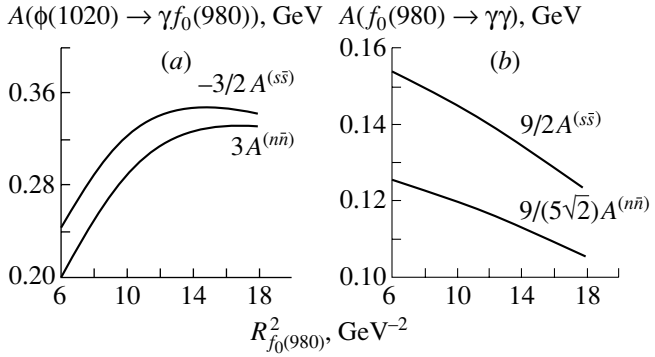

Fig. 2. Amplitudes for strange and nonstrange components, $s\bar{s}$ and $n\bar{n}$, versus the $f_0(980)$ meson radius squared for $\phi(1020) \to \gamma f_0(980)$ and $f_0(980) \to \gamma\gamma$: (*a*) $A^{(n\bar{n})}_{\phi\to\gamma f_0}(0)/Z^{(n\bar{n})}_{\phi\to\gamma f_0}$ and $A^{(s\bar{s})}_{\phi\to\gamma f_0}(0)/Z^{(s\bar{s})}_{\phi\to\gamma f_0}$ and (*b*) $A^{(n\bar{n})}_{f_0\to\gamma\gamma}(0,0)/Z^{(n\bar{n})}_{f_0\to\gamma\gamma}$ and $A^{(s\bar{s})}_{f_0\to\gamma\gamma}(0,0)/Z^{(s\bar{s})}_{f_0\to\gamma\gamma}$.

The factor $F_{\rm thresh}(M^2_{\pi\pi})$ provides the threshold behavior of the amplitude $A_{\phi\to\gamma\pi\pi}$ for $M^2_{\pi\pi} \to m^2_\phi$; we have chosen it to be $F^2_{\rm thresh}(M^2_{\pi\pi}) = 1 - \exp[-(M^2_{\pi\pi} - m^2_\phi)^2/\mu_0^4]$, where μ_0 is the scale parameter (we set $\mu_0 = 2m_\pi$).

The quantities g_π and g_K are the coupling constants for the transitions $f_0(980) \to \pi\pi, K\bar{K}$, respectively. Also, $\rho_{\pi\pi}$ and $\rho_{K\bar{K}}$ are the phase spaces for the $\pi\pi$ and $K\bar{K}$ states: $\rho_{\pi\pi} = \sqrt{M^2_{\pi\pi} - 4m^2_\pi}/(16\pi M_{\pi\pi})$ and $\rho_{K\bar{K}} = \sqrt{M^2_{\pi\pi} - 4m^2_K}/(16\pi M_{\pi\pi})$; recall that, for $M^2_{\pi\pi} < 4m^2_K$, the kaon phase space is imaginary: $\sqrt{M^2_{\pi\pi} - 4m^2_K} = i\sqrt{4m^2_K - M^2_{\pi\pi}}$.

The Bugg–Sarantsev–Zou parametrization of the Flatté formula [22, 23] is

$$g^2_\pi\rho_{\pi\pi} \to (0.12\,\text{GeV})\sqrt{M^2_{\pi\pi} - 4m^2_\pi}, \qquad (52)$$
$$g^2_K\rho_{K\bar{K}} \to (0.27\,\text{GeV})\sqrt{M^2_{\pi\pi} - 4m^2_K},$$
$$M_0 = 0.99 \pm 0.01\ \text{GeV}.$$

The background term is parametrized as $B(M^2_{\pi\pi}) = a + bM^2_{\pi\pi}$, where a and b are complex-valued constants.

The unitarity condition in the $\pi\pi$ channel tells us that the $\phi(1020) \to \gamma\pi\pi$ decay amplitude has a complex phase factor associated with the $\pi\pi$ phase shift in the $(IJ^{PC} = 00^{++})$ channel: $A_{\gamma\pi\pi} = |A_{\gamma\pi\pi}| \exp\left(i\delta^0_0(M_{\pi\pi})\right)$. Therefore, one has

$$\left(\frac{1}{M^2_0 - M^2_{\pi\pi} - ig^2_\pi\rho_{\pi\pi} - ig^2_K\rho_{K\bar{K}}} + B(M^2_{\pi\pi})\right) \times e^{i\Delta\delta^0_0(M_{\pi\pi})} \qquad (53)$$
$$= \left|\frac{1}{M^2_0 - M^2_{\pi\pi} - ig^2_\pi\rho_{\pi\pi} - ig^2_K\rho_{K\bar{K}}} + B(M^2_{\pi\pi})\right| \times e^{i\delta^0_0(M_{\pi\pi})}.$$

We parametrize the phase $\Delta\delta^0_0(M_{\pi\pi})$ as $\Delta\delta^0_0(M_{\pi\pi}) = \Delta_0 + \Delta_1(M_{\pi\pi}/m_0 - 1) + \Delta_2(M_{\pi\pi}/m_0 - 1)^2$ with $m_0 = 1$ GeV. The complex-valuedness of $B(M^2_{\pi\pi})$ is determined by the difference of the phases in the terms for $f_0(980)$ production and the primary background contribution.

To calculate the $\gamma\pi^0\pi^0$ spectrum, one should multiply (50) by the factor associated with the $\pi^0\pi^0$ channel, $d\Gamma_{\phi\to\gamma\pi^0\pi^0} = \frac{1}{3}d\Gamma_{\phi\to\gamma\pi\pi}$. Figure 4 demon-

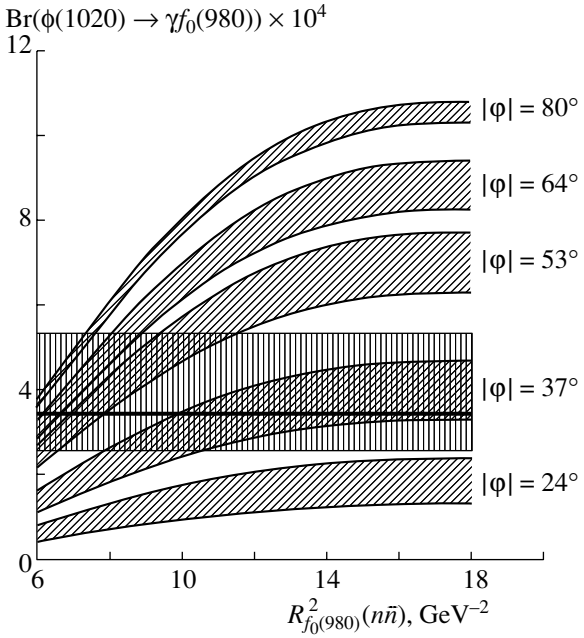

Fig. 3. $\text{Br}(\phi(1020) \to \gamma f_0(980))$ as a function of the radius squared of the $n\bar{n}$ component in $f_0(980)$. The band with vertical shading represents the experimental magnitude; five other bands, with skew shading, correspond to $|\varphi| = 24°, 37°, 53°, 64°, 80°$ at $-8° \le \varphi_V \le 8°$.

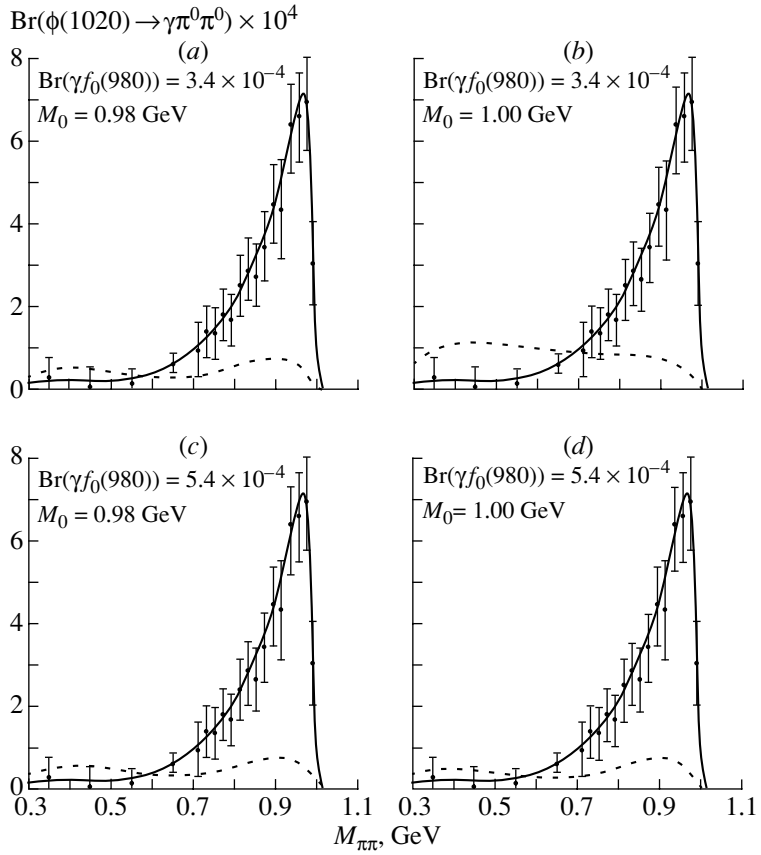

Fig. 4. $\mathrm{Br}(\phi(1020) \to \gamma\pi^0\pi^0)$ calculated by using the Flatté formula (50) and the parametrization given by (54) (solid curves) at different $\mathrm{Br}(\phi(1020) \to \gamma f_0(980))$ and $M_{f_0(980)}$. The background-term contributions are shown by dashed lines. Experimental data were taken from [19].

strates $\mathrm{Br}(\phi(1020) \to \gamma\pi^0\pi^0)$ calculated by Eq. (50) at $\mathrm{Br}(\phi \to \gamma f_0(980)) = 3.4 \times 10^{-4}$, 5.4×10^{-4} and $M_0 = 0.98$, 1.00 GeV. The following parameters (in GeV) are used for the background term $B(M^2_{\pi\pi})$ and the phase $\Delta\delta^0_0(M_{\pi\pi})$:

$$
\begin{gathered}
\text{(a)}\,\mathrm{Br} = 3.4 \times 10^{-4},\ M_0 = 0.98: \\
a = -1.24 + i0.74, \quad b = 1.91 - i0.95, \\
\Delta_0 = 99^\circ, \Delta_1 = 11^\circ, \Delta_2 = 440^\circ; \\
\text{(b)}\,\mathrm{Br} = 3.4 \times 10^{-4}, \quad M_0 = 1.00: \\
a = -1.96 + i0.073, \quad b = 2.37 + i1.8, \\
\Delta_0 = 106^\circ, \Delta_1 = -136^\circ, \Delta_2 = 341^\circ; \\
\text{(c)}\,\mathrm{Br} = 5.4 \times 10^{-4}, \quad M_0 = 0.98: \\
a = -0.84 + i0.91, \quad b = 0.73 - i2.63, \\
\Delta_0 = 98^\circ, \Delta_1 = 203^\circ, \Delta_2 = 735^\circ; \\
\text{(d)}\,\mathrm{Br} = 5.4 \times 10^{-4}, \quad M_0 = 1.00: \\
a = -1.13 + i0.69, \quad b = 1.39 - i1.13, \\
\Delta_0 = 94^\circ, \Delta_1 = 9^\circ, \Delta_2 = 462^\circ.
\end{gathered} \tag{54}
$$

The phase shift $\delta^0_0(M_{\pi\pi})$ for this set of background terms is shown in Fig. 5.

It can be seen that the data from [18] shown in Fig. 4 agree reasonably well with the Flatté parametrization for hadronic reactions given by [22, 23]. A good description of the $\pi^0\pi^0$ spectrum at $\mathrm{Br}(\phi \to \gamma f_0(980)) = 5.4 \times 10^{-4}$ supports the statement of [18, 19] that there were large systematic errors in determining the $\gamma f_0(980)$ signal.

6. RADIATIVE DECAY $f_0(980) \to \gamma\gamma$

The $f_0(980) \to \gamma(q^2 = 0)\gamma(q'^2 = 0)$ decay amplitude is determined as $A_{\mu\nu} = e^2 A_{f_0\to\gamma\gamma}(0,0)\ g^{\perp\perp}_{\mu\nu}$ [see Eq. (13)] with $g^{\perp\perp}_{\mu\nu} q'_\nu = 0$ and $g^{\perp\perp}_{\mu\nu} q_\mu = 0$.

The partial width $\Gamma_{f_0\to\gamma\gamma}$ is

$$
\begin{aligned}
M_f \Gamma_{f_0\to\gamma\gamma} &= \frac{1}{2}\int d\Phi(p; q, k_f) \\
&\times A^*_{\mu\nu} g^{\perp\perp}_{\mu\mu'} g^{\perp\perp}_{\nu\nu'} A_{\mu'\nu'} = \pi\alpha^2 |A_{f_0\to\gamma\gamma}(0,0)|^2,
\end{aligned} \tag{55}
$$

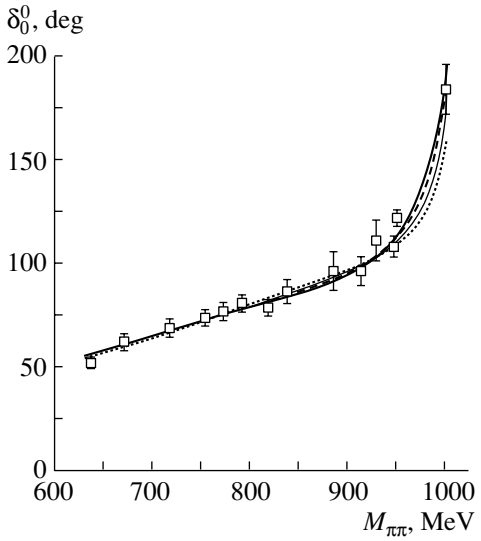

Fig. 5. Phase shifts δ_0^0 determined by (53) for different parametrizations of spectra given by (54). Open squares represent the $\pi\pi$-scattering phase shift δ_0^0 in the 00^{++} wave [17]. The dashed, dotted, thick solid, and thin solid curves stand for solutions *a*, *b*, *c*, and *d*, respectively.

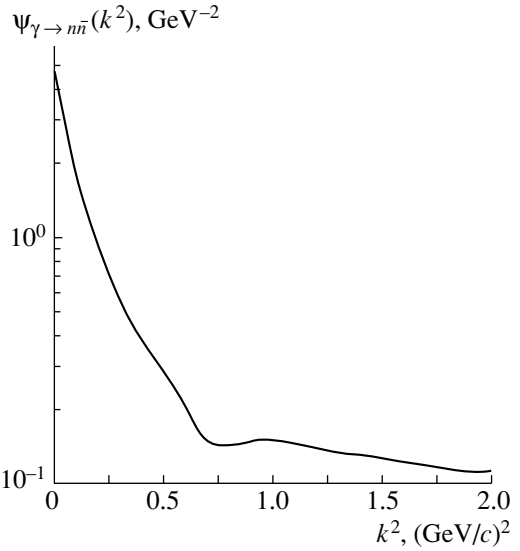

Fig. 6. Photon wave function for nonstrange quarks, $\psi_{\gamma\to n\bar{n}}(k^2) = g_\gamma(k^2)/(k^2+m^2)$, where $k^2 = s/4 - m^2$; the wave function for the $s\bar{s}$ component is $\psi_{\gamma\to s\bar{s}}(k^2) = g_\gamma(k^2)/(k^2+m_s^2)$; the constituent quark masses are $m = 350$ MeV and $m_s = 500$ MeV.

where the factor of $1/2$ is associated with the identity of photons. The amplitude $A_{f_0\to\gamma\gamma}(0,0)$ is determined by the contributions of two flavor components:

$$A_{f_0\to\gamma\gamma}(0,0) = \cos\varphi A^{(n\bar{n})}_{f_0\to\gamma\gamma}(0,0) + \sin\varphi A^{(s\bar{s})}_{f_0\to\gamma\gamma}(0,0). \quad (56)$$

The invariant amplitude for the transition $f_0 \to \gamma(q^2)\gamma$ has the form

$$A^{(q\bar{q})}_{f_0\to\gamma\gamma}(q^2,0) = \sqrt{N_c}\int\limits_{4m^2}^{\infty}\frac{dsds'}{\pi^2}\psi_{f_0}(s)\psi_\gamma(s') \times \frac{\theta(ss'Q^2 - m^2\lambda(s,s',Q^2))}{16\sqrt{\lambda(s,s',Q^2)}} \times Z^{(q\bar{q})}_{f_0\to\gamma\gamma}S^{(\mathrm{tr})}_{f_0\to\gamma\gamma}(s,s',Q^2), \quad (57)$$

where $N_c = 3$ is the number of colors, $Z^{(n\bar{n})}_{f_0\to\gamma\gamma} = 5\sqrt{2}/9$, and $Z^{(s\bar{s})}_{f_0\to\gamma\gamma} = 2/9$ (see Appendix C). The spin factor $S^{(\mathrm{tr})}_{f_0\to\gamma\gamma}(s,s',Q^2)$ is similar to that for $\phi \to \gamma f_0$:

$$S^{(\mathrm{tr})}_{f_0\to\gamma\gamma}(s,s',q^2) = -2m\left(-s+s'+4m^2 - \frac{4ss'}{s+s'-q^2}\alpha(s,s',q^2)\right). \quad (58)$$

The formula for the amplitude $A^{(q\bar{q})}_{f_0\to\gamma\gamma}(q^2,0)$ in terms of the light-cone variables is written in Appendix D.

In the limit $Q^2 \to 0$, the term that makes $S^{(\mathrm{tr})}_{f_0\to\gamma\gamma}(s,s',q^2)$ and $S^{(\mathrm{tr})}_{\phi\to\gamma f_0}(s,s',q^2)$ different vanishes in the integral (57), and we have for $A^{(q\bar{q})}_{f_0\to\gamma\gamma}(0,0)$ an expression similar to (32):

$$A^{(q\bar{q})}_{f_0\to\gamma\gamma}(0,0) = \frac{m\sqrt{N_c}Z^{(q\bar{q})}_{f_0\to\gamma\gamma}}{4\pi} \times \int\limits_{4m^2}^{\infty}\frac{ds}{\pi}\psi_{f_0}(s)\psi_\gamma(s) \times \left[\sqrt{s(s-4m^2)} - 2m^2\ln\frac{\sqrt{s}+\sqrt{s-4m^2}}{\sqrt{s}-\sqrt{s-4m^2}}\right]. \quad (59)$$

The photon wave function was found from an analysis of the $\pi^0 \to \gamma(Q^2)\gamma$, $\eta \to \gamma(Q^2)\gamma$, and $\eta' \to \gamma(Q^2)\gamma$ transition form factors [32]; it is shown in Fig. 6. With this wave function, we have calculated $A^{n\bar{n}}_{f_0\to\gamma\gamma}(0,0)$ and $A^{s\bar{s}}_{f_0\to\gamma\gamma}(0,0)$; these amplitudes plotted versus $R^2_{f_0(980)}$ are shown in Fig. 2*b*.

Figure 7 displays $\Gamma_{f_0\to\gamma\gamma}$ calculated at various $R^2_{f_0(980)}$ and φ, along with the data from [26]. It is possible to describe the experimental data ($\Gamma_{f_0(980)\to\gamma\gamma} = 0.28^{+0.09}_{-0.13}$ keV [26]) by using positive mixing angles or negative ones: $77^\circ \le \varphi \le 93^\circ$ and $-54^\circ \le \varphi \le -38^\circ$. The use of constraint in (3) on

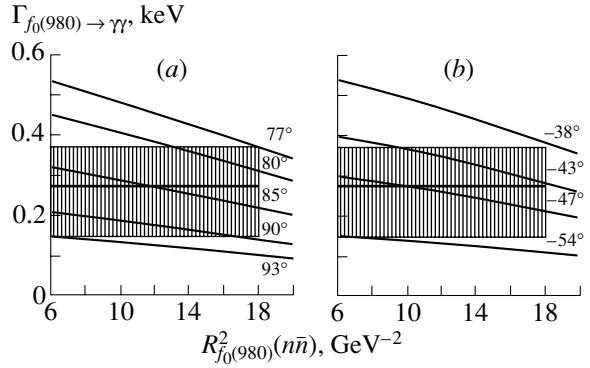

Fig. 7. Partial width $\Gamma_{f_0(980)\to\gamma\gamma}$; experimental data are from [26] (shaded area). Curves are calculated for (*a*) positive mixing angles $\varphi = 77^\circ, 80^\circ, 85^\circ, 90^\circ, 93^\circ$ and (*b*) negative angles $\varphi = -38^\circ, -43^\circ, -47^\circ, -54^\circ$.

the radius constricts slightly the allowed interval of mixing angles [see (4)].

7. RADIATIVE DECAYS $\phi(1020) \to \gamma\eta, \gamma\eta', \gamma\pi^0, \gamma a_0(980)$

The decays $\phi(1020) \to \gamma\eta, \gamma\eta'$ do not provide us with direct information about the quark content of $f_0(980)$ and $\phi(1020)$; yet, calculations and comparison with data are necessary to check the reliability of the method. The decays $\phi(1020) \to \gamma\pi^0$ and $\phi(1020) \to \gamma a_0(980)$ allow us to evaluate the admixture of the $n\bar{n}$ component in the ϕ meson; as was seen in Section 4, this admixture affects significantly $\Gamma_{\gamma f_0(980)}$.

The amplitude for the $\phi \to \gamma P$ reactions, where $P = \eta,\ \eta',\ \pi^0$, has the following structure: $A_{\mu\nu} = eA_{\phi\to\gamma P}(0)\epsilon_{\mu\nu\alpha\beta}p_\alpha q_\beta$ [see Eq. (12)]. The invariant parts of the $\phi \to \gamma\eta,\ \gamma\eta',\ \gamma\pi^0,\ \gamma a_0(980)$ radiative-decay amplitudes are calculated similarly to that of $\phi \to \gamma f_0(980)$ [see Eq. (30)] with necessary substitution of the wave functions, $\psi_S \to \psi_\eta, \psi_{\eta'}, \psi_\pi, \psi_{a_0}$, as well as of the charge and spin factors. The charge factors for the radiative decays being considered are as follows: $Z^{(s\bar{s})}_{\phi\to\gamma\eta} = Z^{(s\bar{s})}_{\phi\to\gamma\eta'} = -2/3$ for the $s\bar{s}$ component in the reactions $\phi \to \gamma\eta, \gamma\eta'$, and $Z_{\phi\to\gamma\pi^0} = Z_{\phi\to\gamma a_0(980)} = 1$ for π^0 and $a_0(980)$ production (see Appendix C).

For the transitions $\phi \to \gamma\eta$ and $\phi \to \gamma\eta'$, we take into account only the dominant $s\bar{s}$ component: $-\sin\theta\, s\bar{s}$ in the η meson and $\cos\theta\, s\bar{s}$ in the η' meson, with $\sin\theta = 0.6$.

The spin factors for pseudoscalar mesons are

$$S^{(\mathrm{tr})}_{\phi\to\gamma\eta}(s, s', q^2) = S_{\phi\to\gamma\eta'}(s, s', q^2) = 4m_s, \quad (60)$$

$$S^{(\mathrm{tr})}_{\phi\to\gamma\pi}(s, s', q^2) = 4m.$$

The formula for the amplitude $A_{\phi\to\gamma P}(q^2)$ is given in Appendix D. For $q^2 \to 0$, one has

$$A_{\phi\to\gamma P}(0) = \frac{mZ^{(q\bar{q})}_{\phi\to\gamma P}}{4\pi} \quad (61)$$
$$\times \int\limits_{4m^2}^{\infty} \frac{ds}{\pi}\psi_\phi(s)\psi_P(s)\ln\frac{\sqrt{s}+\sqrt{s-4m^2}}{\sqrt{s}-\sqrt{s-4m^2}}.$$

For the pion wave function, we have chosen $b_\pi = 2.0\ \mathrm{GeV}^{-2}$, which corresponds to $R^2_\pi = 10.1\ \mathrm{GeV}^{-2}$; the same radius is fixed for the $n\bar{n}$ component in η and η'. As to the strange component in η and η', we took its slope to be the same ($b_{\eta(s\bar{s})} = 2\ \mathrm{GeV}^{-2}$), which leads to the smaller radius of $R^2(s\bar{s}) = 8.3\ \mathrm{GeV}^{-2}$.

The results of the calculations versus branching ratios given by PDG compilation [11] are as follows:

$$\mathrm{Br}(\phi \to \eta\gamma) = 1.46 \times 10^{-2}, \quad (62)$$
$$\mathrm{Br}_{\mathrm{PDG}}(\phi \to \eta\gamma) = (1.30 \pm 0.03) \times 10^{-2},$$
$$\mathrm{Br}(\phi \to \eta'\gamma) = 0.97 \times 10^{-4},$$
$$\mathrm{Br}_{\mathrm{PDG}}(\phi \to \eta'\gamma) = (0.67^{+0.35}_{-0.31}) \times 10^{-4}.$$

The calculated branching ratios agree reasonably well with those given in [11].

For the process $\phi \to \gamma\pi^0$, the compilation [11] gives $\mathrm{Br}(\phi \to \gamma\pi^0) = (1.26 \pm 0.10) \times 10^{-3}$, and this value requires $|\sin\varphi_V| \simeq 0.07$ (or $|\varphi_V| \simeq 4^\circ$), because just with this admixture of the $n\bar{n}$ component in $\phi(1020)$ do we attain agreement with data. However, in estimating the allowed regions for the mixing angle φ (see Fig. 3), we use

$$|\varphi_V| = 4^\circ \pm 4^\circ, \quad (63)$$

considering the accuracy inherent in the quark model to be comparable with the small value obtained for $|\varphi_V|$.

The process $\phi(1020) \to \gamma a_0(980)$ also depends on the mixing angle $|\varphi_V|$: the decay amplitude is proportional to $\sin\varphi_V$, namely, $A_{\phi\to\gamma a_0} = \sin\varphi_V A^{(n\bar{n})}_{\phi\to\gamma a_0}$, and the amplitude $A^{(n\bar{n})}_{\phi\to\gamma a_0}$ is equal to that for the process $\phi \to \gamma f_0$, apart from a numerical factor: $A^{(n\bar{n})}_{\phi\to\gamma a_0}/A^{(n\bar{n})}_{\phi\to\gamma f_0} = Z^{(n\bar{n})}_{\phi\to\gamma a_0}/Z^{(n\bar{n})}_{\phi\to\gamma f_0} = 3$ because $Z^{(n\bar{n})}_{\phi\to\gamma a_0} = 1$ ($3A^{(n\bar{n})}_{\phi\to\gamma f_0}$ is shown in Fig. 2*a*).

For the region $R^2_{a_0(980)} \sim 8$–$12\ \mathrm{GeV}^{-2}$, one has

$$\mathrm{Br}\,(\phi(1020) \to \gamma a_0(980)) \quad (64)$$
$$= \sin^2\varphi_V \cdot (14 \pm 3) \times 10^{-4}$$

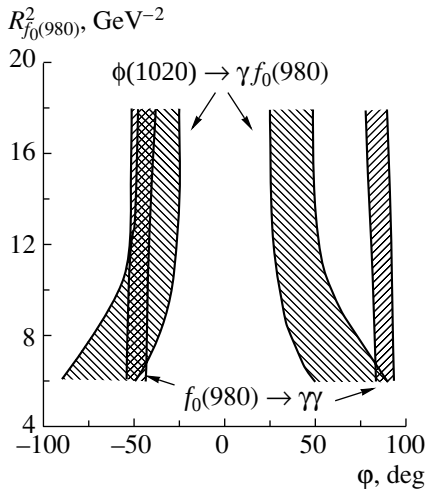

Fig. 8. $(\varphi, R^2_{f_0(980)})$ plot: the shaded areas are allowed for the reactions $\phi(1020) \to \gamma f_0(980)$ and $f_0(980) \to \gamma\gamma$.

with lower values for $R^2_{a_0(980)} \sim 8$ GeV^{-2} and larger ones for $R^2_{a_0(980)} \sim 12$ GeV^{-2}. At $\sin^2\varphi_V = 0.01 \pm 0.01$, we have $\mathrm{Br}(\phi(1020) \to \gamma a_0(980)) = (0.14 \pm 0.14) \times 10^{-4}$.

In [28], the partial width for $\phi(1020) \to \gamma\eta\pi^0$ was measured; the result was $\mathrm{Br}(\phi(1020) \to \gamma\eta\pi^0; M_{\eta\pi} > 900$ MeV$) = (0.46 \pm 0.13) \times 10^{-4}$. If, for $M_{\eta\pi} > 900$ MeV, the resonance-to-background ratio is about unity, which is rather possible, the value found in [28] is in agreement with a small value of $|\varphi_V|$.

8. CONCLUSION

Figure 8 demonstrates the $(\varphi, R^2_{f_0(980)})$ plot, where the allowed areas for the reactions $\phi(1020) \to \gamma f_0(980)$ and $f_0(980) \to \gamma\gamma$ are shown. We see that the radiative decays $\phi(1020) \to \gamma f_0(980)$ and $f_0(980) \to \gamma\gamma$ are well described within the hypothesis of the dominant $q\bar{q}$ structure of $f_0(980)$. The solution with negative φ seems preferable. For this solution, the mixing angle φ for the $n\bar{n}$ and $s\bar{s}$ components $(n\bar{n}\cos\varphi + s\bar{s}\sin\varphi)$ is equal to $\varphi = -48^\circ \pm 6^\circ$; that is, the $q\bar{q}$ component is rather close to the flavor octet ($\varphi_{\mathrm{octet}} = -54.7^\circ$). This proximity to the octet may be due to the following scenario: the broad resonance $f_0(1530^{+90}_{-250})$, which is, according to the K-matrix analysis, the descendant of the lightest scalar glueball, took, after accumulating the widths of neighboring resonances, the singlet component from a predecessor of $f_0(980)$, thus converting $f_0(980)$ into an almost pure octet.

The dominance of the quark–antiquark component does not rule out the existence of other components in $f_0(980)$. The location of the resonance pole near the $K\bar{K}$ threshold definitively points to a certain admixture of the long-range $K\bar{K}$ component in $f_0(980)$. To investigate this admixture, precise measurements of the $K\bar{K}$ spectra in the interval 1000–1150 MeV are necessary: only these spectra could shed light on the role of the long-range $K\bar{K}$ component in $f_0(980)$.

The existence of the long-range $K\bar{K}$ component or that of gluonium in the $f_0(980)$ leads to a decrease in the $s\bar{s}$ fraction in the $q\bar{q}$ component: for example, if the long-range $K\bar{K}$ (or gluonium) admixture is on the order of 15%, the data require either $\varphi = -45^\circ \pm 6^\circ$ or $\varphi = 83^\circ \pm 4^\circ$.

ACKNOWLEDGMENTS

We are grateful to D.V. Bugg, L.G. Dakhno, V.S. Fadin, L. Montanet, and A.V. Sarantsev for stimulating discussions and illuminative information.

This work is supported by the Russian Foundation for Basic Research (project no. 01-02-17861).

APPENDIX A

Spin Factor for $f_0 \to \gamma\gamma$

Here, we calculate the spin factor of the triangle diagram for the transition $f_0 \to \gamma\gamma$. It is determined by the trace

$$S_{\mu\nu}(f_0 \to \gamma\gamma) = -\mathrm{tr}[\gamma_\nu^{\perp\perp}(\hat{k}_1' + m) \times \gamma_\nu^{\perp\perp}(\hat{k}_1 + m)(-\hat{k}_2 + m)]. \quad \text{(A.1)}$$

Here, $\gamma_\mu^{\perp\perp}$ and $\gamma_\nu^{\perp\perp}$ are defined as

$$\gamma_\mu^{\perp\perp} = g_{\mu\mu'}^{\perp\perp}\gamma_{\mu'}, \quad \gamma_\nu^{\perp\perp} = g_{\nu\nu'}^{\perp\perp}\gamma_{\nu'}. \quad \text{(A.2)}$$

$$S_{\mu\nu}(f_0 \to \gamma\gamma) = 4m\left[g_{\mu\nu}^{\perp\perp}((k_1k_1') - (k_1'k_2) + (k_1k_2) - m^2) - 4k_{1\mu}^{\perp\perp}k_{1\nu}^{\perp\perp}\right] = 4m\left[\frac{1}{2}(s - s' - q^2)g_{\mu\nu}^{\perp\perp} - 2k_{\perp\perp}^2 g_{\mu\nu}^{\perp\perp}\right], \quad \text{(A.3)}$$

where

$$k_{\perp\perp}^2 = k_{1\alpha}^{\perp\perp}k_{1\beta}^{\perp\perp}g_{\alpha\beta}^{\perp\perp}. \quad \text{(A.4)}$$

Here, the particle momenta in the dispersion integral are on the mass shell ($k_1^2 = k_1'^2 = k_2^2 = m^2$) but not on the energy shell [$(k_1 + k_2)^2 = s \neq M_f^2$, $(k_1' + k_2)^2 = s' \neq q'^2$]. This means that s and s' are internal variables; we have also used the relations ($k_1 -$

$k_1')^2 = q^2$ and $k_{1\mu}^{\perp\perp} = k_{1\mu}'^{\perp\perp} = -k_{2\mu}^{\perp\perp}$. Owing to integration with respect to the angles, we additionally have $k_{1\mu}^{\perp\perp}k_{1\nu}^{\perp\perp} \to \frac{1}{2}g_{\mu\nu}^{\perp\perp}k_{\perp\perp}^2$.

The simplest way to calculate $k_{\perp\perp}^2$ is to use Eq. (14) directly; therefore,

$$k_{1\mu}^{\perp\perp} = k_{1\mu}'^{\perp\perp} = k'_{1\mu'}g_{\mu\mu'}^{\perp\perp} = k'_{1\mu} + q_\mu\frac{q'^2(q^2+(qq'))}{2D} - q'_\mu\frac{q^2(q'^2+(qq'))}{2D}. \quad \text{(A.5)}$$

Here, we have taken into account the equalities $(k_1'q) = -\frac{1}{2}q^2$ and $(k_1'q') = -\frac{1}{2}q'^2$, which follow from the fact that intermediate particles are on the mass shell: $m^2 = (k_1'+q)^2$ and $m^2 = (-k_1'+q')^2$. The square of Eq. (A.5) has the form

$$k_{\perp\perp}^2 = m^2 - \frac{q^2q'^2}{4D}(q+q')^2, \quad \text{(A.6)}$$

whence it follows that

$$S_{\mu\nu}(f_0 \to \gamma\gamma) = g_{\mu\nu}^{\perp\perp}S_{f_0\to\gamma}(s,s',q^2), \quad \text{(A.7)}$$

where

$$S_{f_0\to\gamma}(s,s',q^2) = -2m\left[s'-s+q^2+4m^2 - \frac{4q^2ss'}{2q^2(s+s')-(s-s')^2-q^4}\right]. \quad \text{(A.8)}$$

APPENDIX B

Spectral Integral for the Form Factor

Considering the scalar- and vector-meson form factors as an example, we write below the spectral integrals with respect to the $q\bar{q}$ mass. Using the variables $s+s' = 2\Sigma$ and $s'-s = \Delta$, we can represent the form factor given by Eq. (35) as

$$F_{\rm meson}(-Q^2) = \int_{4m^2}^{\infty}\frac{d\Sigma}{\pi}\int_{-\infty}^{\infty}\frac{d\Delta}{\pi} \times \psi_{\rm meson}(\Sigma-\frac{1}{2}\Delta)\psi_{\rm meson}(\Sigma+\frac{1}{2}\Delta) \times \frac{\theta\left(Q^2\left(\Sigma^2-\Delta^2/4-4m^2\Sigma\right)-m^2\Delta^2-m^2Q^4\right)}{16\sqrt{\Delta^2+4\Sigma Q^2+Q^4}} \times S_{\rm meson}^{(\rm tr)}(\Sigma+\frac{1}{2}\Delta,\Sigma-\frac{1}{2}\Delta,-Q^2). \quad \text{(A.9)}$$

After the substitution $z = \Delta/Q$, we have

$$F_{\rm meson}(-Q^2) = \int_{4m^2}^{\infty}\frac{d\Sigma}{\pi}\int_{-b}^{b}\frac{dz}{16\pi} \times \psi_{\rm meson}(\Sigma-\frac{1}{2}zQ)\psi_{\rm meson}(\Sigma+\frac{1}{2}zQ) \times \frac{S_{\rm meson}^{(\rm tr)}(\Sigma+\frac{1}{2}zQ,\Sigma-\frac{1}{2}zQ,-Q^2)}{\sqrt{z^2+4\Sigma+Q^2}}, \quad \text{(A.10)}$$

where

$$b = \sqrt{\frac{\Sigma^2-4\Sigma m^2-m^2Q^2}{m^2+Q^2/4}}. \quad \text{(A.11)}$$

In terms of the new variables, the spin factors $S_S^{(\rm tr)}(s,s',q^2)$ and $S_V^{(\rm tr)}(s,s',q^2)$ are rewritten as

$$S_S^{(\rm tr)}(s,s',q^2) = \frac{2\Sigma+Q^2}{z^2+4\Sigma+Q^2}(2\Sigma-8m^2+Q^2)-Q^2 \equiv \frac{a_S(\Sigma,Q^2)}{z^2+4\Sigma+Q^2}+b_S(Q^2), \quad \text{(A.12)}$$

$$S_V^{(\rm tr)}(s,s',q^2) = \frac{2}{3}\left[\frac{2\Sigma+Q^2}{z^2+4\Sigma+Q^2}(2\Sigma+4m^2+Q^2)-Q^2\right] \equiv \frac{a_V(\Sigma,Q^2)}{z^2+4\Sigma+Q^2}+b_V(Q^2). \quad \text{(A.13)}$$

An exponential parametrization for the meson wave function allows one to remove the integration with respect to z. In this case, $\psi_{\rm meson}(\Sigma-\frac{1}{2}\Delta)\psi_{\rm meson}(\Sigma+\frac{1}{2}\Delta) = \psi_{\rm meson}^2(\Sigma)$, and $F_{\rm meson}(q^2)$ takes the form

$$F_{\rm meson}(-Q^2) = \int_{4m^2}^{\infty}\frac{ds}{\pi}\psi_{\rm meson}^2(s) \times \int_{-b}^{b}\frac{dz}{16\pi}\frac{S_{\rm meson}^{(\rm tr)}(s+\frac{1}{2}zQ,s-\frac{1}{2}zQ,-Q^2)}{\sqrt{z^2+4s+Q^2}}. \quad \text{(A.14)}$$

Here, we made the substitution $\Sigma \to s$. The integral with respect to z can easily be calculated, whereupon one has

$$F_{\rm meson}(-Q^2) = \int_{4m^2}^{\infty}\frac{ds}{\pi}\psi_{\rm meson}^2(s) \times \left(a_{\rm meson}(s,Q^2)\,I_1(s,Q^2) + b_{\rm meson}(s,Q^2)\,I_2(s,Q^2)\right), \quad \text{(A.15)}$$

where

$$I_1(s,Q^2) = \frac{1}{4\pi(4s+Q^2)}\sqrt{\frac{s^2-4sm^2-m^2Q^2}{4s^2+4sQ^2+Q^4}}, \quad \text{(A.16)}$$

$$I_2(s,Q^2) \qquad \text{(A.17)}$$
$$= -\frac{1}{16\pi}\ln\frac{2s+Q^2-2\sqrt{s^2-4sm^2-m^2Q^2}}{2s+Q^2+2\sqrt{s^2-4sm^2-m^2Q^2}}.$$

APPENDIX C

Charge Factors

The charge factor for the $n\bar{n}$ component in the transition $\phi\to\gamma f_0$ is defined as

$$Z^{(n\bar{n})}_{\phi\to\gamma f_0} = 2\zeta^{(n\bar{n})}_{\phi\to\gamma f_0}, \qquad \text{(A.18)}$$

where $\zeta^{(n\bar{n})}_{\phi\to\gamma f_0}$ is the convolution

$$\zeta^{(n\bar{n})}_{\phi\to\gamma f_0} = \frac{u\bar{u}+d\bar{d}}{\sqrt{2}}\hat{e}_q\frac{u\bar{u}+d\bar{d}}{\sqrt{2}} = \frac{1}{2}(e_u+e_d) = \frac{1}{6}. \qquad \text{(A.19)}$$

Here, e_u and e_d are the charges of u and d quarks, respectively. The factor of 2 in (A.18) is due to two possibilities for photon emission: the corresponding traces for photon emission by a quark and by an antiquark are equal to each other, namely,

$$\mathrm{tr}\left((\hat{k}_1'+m)\gamma_\mu(\hat{k}_1+m)\gamma_\nu(-\hat{k}_2+m)\right) \qquad \text{(A.20)}$$
$$= \mathrm{tr}\left((-\hat{k}_1'+m)\gamma_\mu(-\hat{k}_1+m)\gamma_\nu(\hat{k}_2+m)\right).$$

Likewise, we have

$$Z^{(s\bar{s})}_{\phi\to\gamma f_0} = 2\zeta^{(s\bar{s})}_{\phi\to\gamma f_0} = 2\,e_s = -\frac{2}{3}. \qquad \text{(A.21)}$$

The charge factors for $s\bar{s}$ in the reactions $\phi\to\gamma\eta$ and $\phi\to\gamma\eta'$ are identical to that for the decay $\phi\to\gamma f_0$:

$$Z^{(s\bar{s})}_{\phi\to\gamma\eta} = Z^{(s\bar{s})}_{\phi\to\gamma\eta'} = Z^{(s\bar{s})}_{\phi\to\gamma f_0}. \qquad \text{(A.22)}$$

For the process $\phi\to\gamma a_0$, one likewise has

$$Z_{\phi\to\gamma a_0} = 2\zeta_{\phi\to\gamma a_0}, \qquad \text{(A.23)}$$
$$\zeta^{(n\bar{n})}_{\phi\to\gamma a_0} = \frac{u\bar{u}+d\bar{d}}{\sqrt{2}}\hat{e}_q\frac{u\bar{u}-d\bar{d}}{\sqrt{2}} = \frac{1}{2}(e_u-e_d) = \frac{1}{2}.$$

The charge factors for $f_0\to\gamma\gamma$ are given by

$$Z^{(n\bar{n})}_{f_0\to\gamma\gamma} = 2\,\frac{e_u^2+e_d^2}{\sqrt{2}}, \quad Z^{(s\bar{s})}_{f_0\to\gamma\gamma} = 2\,e_s^2. \qquad \text{(A.24)}$$

APPENDIX D

Light-Cone Representation for the $f_0\to\gamma(q^2)\gamma$ and $\phi\to\gamma(q^2)P$ Amplitudes

The light-cone representation of the transition amplitudes for the processes $f_0\to\gamma(q^2)\gamma$ and $\phi\to\gamma(q^2)P$ has the form

$$A_{f_0\to\gamma\gamma}(q^2,0) = \frac{Z_{f_0\to\gamma\gamma}\sqrt{N_c}}{16\pi^3} \qquad \text{(A.25)}$$
$$\times\int_0^1\frac{dx}{x(1-x)^2}\int d^2k_\perp\psi_{f_0}(s)\psi_\gamma(s')S_{f_0\to\gamma\gamma}(s,s',q^2),$$

$$A_{\phi\to\gamma P}(q^2) = \frac{Z_{\phi\to\gamma P}}{16\pi^3} \qquad \text{(A.26)}$$
$$\times\int_0^1\frac{dx}{x(1-x)^2}\int d^2k_\perp\psi_\phi(s)\psi_P(s')S_{\phi\to\gamma P}(s,s',q^2),$$

where $s=(m^2+k_\perp^2)/x(1-x)$ and $s'=(m^2+(\mathbf{k}_\perp+x\mathbf{q}_\perp)^2)/x(1-x)$. The factors $Z_{f_0\to\gamma\gamma}$, $Z_{\phi\to\gamma P}$, $S_{f_0\to\gamma\gamma}(s,s',q^2)$, and $S_{\phi\to\gamma P}(s,s',q^2)$ are given in Appendices B and C.

REFERENCES

1. A. V. Anisovich, V. V. Anisovich, and A. V. Sarantsev, Phys. Rev. D **62**, 051502 (2000).
2. S. Narrison, Nucl. Phys. B **509**, 312 (1998).
3. P. Minkowski and W. Ochs, Eur. Phys. J. C **9**, 283 (1999).
4. V. V. Anisovich, Usp. Fiz. Nauk **168**, 481 (1998) [Phys. Usp. **41**, 419 (1998)].
5. R. Ricken, M. Koll, D. Merten, *et al.*, Eur. Phys. J. A **9**, 73 (2000); hep-ph/0008221.
6. V. V. Anisovich, Yu. D. Prokoshkin, and A. V. Sarantsev, Phys. Lett. B **389**, 388 (1996).
7. V. V. Anisovich, A. A. Kondashev, Yu. D. Prokoshkin, *et al.*, Yad. Fiz. **63**, 1489 (2000) [Phys. At. Nucl. **63**, 1410 (2000)].
8. V. V. Anisovich *et al.*, Phys. Lett. B **323**, 233 (1994); C. Amsler *et al.*, Phys. Lett. B **333**, 277 (1994).
9. Yu. D. Prokoshkin *et al.*, Dokl. Akad. Nauk **342**, 473 (1995) [Phys. Dokl. **40**, 266 (1995)]; D. Alde *et al.*, Z. Phys. C **66**, 375 (1995); F. Binon *et al.*, Nuovo Cimento A **78**, 313 (1983); **80**, 363 (1984).
10. S. J. Lindenbaum and R. S. Longacre, Phys. Lett. B **274**, 492 (1992); A. Etkin *et al.*, Phys. Rev. D **25**, 1786 (1982).
11. Particle Data Group (D. E. Groom *et al.*), Eur. Phys. J. C **15**, 1 (2000).
12. G. S. Bali *et al.*, Phys. Lett. B **309**, 378 (1993); J. Sexton, A. Vaccarino, and D. Weingarten, Phys. Rev. Lett. **75**, 4563 (1995); C. J. Morningstar and M. Peardon, Phys. Rev. D **56**, 4043 (1997).
13. V. V. Anisovich, D. V. Bugg, and A. V. Sarantsev, Phys. Rev. D **58**, 111503 (1998).
14. I. Yu. Kobzarev, N. N. Nikolaev, and L. B. Okun, Yad. Fiz. **10**, 864 (1969) [Sov. J. Nucl. Phys. **10**, 499 (1970)]; L. Stodolsky, Phys. Rev. D **1**, 2683 (1970); I. S. Shapiro, Nucl. Phys. A **122**, 645 (1968).
15. G. 't Hooft, Nucl. Phys. B **72**, 161 (1974); G. Veneziano, Nucl. Phys. B **117**, 519 (1976).
16. A. V. Anisovich, V. V. Anisovich, and A. V. Sarantsev, Z. Phys. A **359**, 173 (1997).
17. A. V. Anisovich and A. V. Sarantsev, Phys. Lett. B **413**, 137 (1997).

18. CMD-2 Collab. (R. R. Akhmetshin *et al.*), Phys. Lett. B **462**, 371, 380 (1999).
19. SND Collab. (M. N. Achasov *et al.*), Phys. Lett. B **485**, 349 (2000).
20. V. V. Anisovich, D. V. Bugg, and A. V. Sarantsev, Phys. Lett. B **437**, 209 (1998).
21. W. Flatté, Phys. Lett. B **63B**, 224 (1976).
22. B. S. Zou and D. V. Bugg, Phys. Rev. D **50**, 591 (1994).
23. D. V. Bugg, A. V. Sarantsev, and B. S. Zou, Nucl. Phys. B **471**, 59 (1996); A. V. Sarantsev, private communication.
24. A. V. Anisovich, V. V. Anisovich, D. V. Bugg, and V. A. Nikonov, Phys. Lett. B **456**, 80 (1999).
25. A. V. Anisovich and V. V. Anisovich, Phys. Lett. B **467**, 289 (1999).
26. M. Boglione and M. R. Pennington, Eur. Phys. J. C **9**, 11 (1999).
27. Particle Data Group (C. Caso *et al.*), Eur. Phys. J. C **3**, 1 (1998).
28. SND Collab. (M. N. Achasov *et al.*), Phys. Lett. B **479**, 53 (2000).
29. N. N. Achasov and V. V. Gubin, Phys. Rev. D **56**, 4084 (1997).
30. V. E. Markushin, Eur. Phys. J. A **8**, 389 (2000); E. Marco, S. Hirenzaki, E. Oset, and H. Toki, Phys. Lett. B **470**, 20 (1999).
31. A. V. Anisovich and V. A. Sadovnikova, Yad. Fiz. **55**, 2657 (1992) [Sov. J. Nucl. Phys. **55**, 1483 (1992)]; Eur. Phys. J. A **2**, 199 (1998); V. V. Anisovich, M. N. Kobrinsky, D. I. Melikhov, and A. V. Sarantsev, Nucl. Phys. A **544**, 747 (1992).
32. V. V. Anisovich, D. I. Melikhov, and A. Nikonov, Phys. Rev. D **55**, 2918 (1997); **52**, 5295 (1995).

Physics of Atomic Nuclei, Vol. 65, No. 3, 2002, pp. 513–520. Translated from Yadernaya Fizika, Vol. 65, No. 3, 2002, pp. 539–546.

ELEMENTARY PARTICLES AND FIELDS
Theory

Muon Transverse Polarization in $K_{l2\gamma}$ Decay Due to the Electromagnetic Final-State Interaction

V. V. Braguta, A. A. Likhoded, and A. E. Chalov

Institute for High Energy Physics, Protvino, Moscow oblast, 142284 Russia

Received December 6, 2000; in final form, May 24, 2001

Abstract—For the decay process $K^+ \to \mu^+\nu\gamma$, the effect of muon transverse polarization caused by electromagnetic final-state interaction is analyzed. It is shown that, in the one-loop approximation, the muon transverse polarization varies from -1.3×10^{-3} to zero in the region of the Dalitz plot. The mean value of the muon polarization, $\langle P_T \rangle$, in the kinematical region $E_\gamma \geq 20$ MeV is -5.44×10^{-4}.

1. INTRODUCTION

Investigation of radiative K-meson decays is of interest in connection with searches for effects of new physics beyond the Standard Model of electroweak interactions. Searches for new interactions that may result in CP violation represent one of the most interesting possibilities. In contrast to the Standard Model, where CP violation is caused by the presence of a complex phase in the Cabibbo–Kobayashi–Maskawa matrix, supersymmetry models, for example, may feature CP violation naturally arising owing to the complex-valuedness of the fermionic Yukawa coupling constants of new Higgs bosons [1]. In view of this, it seems interesting to analyze those observables of K-meson decays that are especially sensitive to CP-violation effects. These include the transverse polarization of muons from the decays $K^\pm \to \mu^\pm\nu\gamma$ and $K^\pm \to \pi^0\mu^\pm\nu$ and the T-odd correlation $T = \dfrac{1}{M_K^3}\mathbf{p}_\gamma \cdot [\mathbf{p}_\pi \times \mathbf{p}_l]$ in the process $K^\pm \to \pi^0\mu^\pm\nu\gamma$ [2]. In particular, the muon transverse polarization can amount to $P_T \simeq 7.0 \times 10^{-3}$ in models involving left–right symmetry and one Higgs doublet [3] and to $P_T \simeq 6.0 \times 10^{-2}$ in models involving three Higgs doublets [4].

New possibilities in this realm are being unveiled in connection with the planned OKA experiment [5], which is intended for studying charged-kaon decays. Expected statistics for the decays $K^+ \to \mu^+\nu\gamma$, $K^+ \to \pi^0\mu^+\nu$, and $K^+ \to \pi^0\mu^+\nu\gamma$ are approximately 4.3×10^8, 1.7×10^9, and 7.0×10^5 events, respectively. This gives every reason to hope either to detect new-physics events or to set stringent constraints on the parameters of extended models.

In seeking the new-interaction contribution to the muon transverse polarization, it is of crucial importance to estimate the background contribution of the so-called spurious muon polarization that is due to electromagnetic final-state interaction. For the process $K^+ \to \mu^+\nu\gamma$, the muon transverse polarization caused by electromagnetic final-state interaction was calculated by Efrosinin and Kudenko [6] in the one-loop approximation of minimal QED. They showed that this polarization can vary within the interval $(-0.1–4.0) \times 10^{-3}$. In the present article, we reanalyze the effect of the muon transverse polarization due to final-state interaction. We have revealed disagreement with previous results [6] in calculating the Dalitz plot density ρ_0 and the transverse component ρ_T of muon polarization, which contribute to transverse polarization. This disagreement leads to a change in the interval of values and to a shift of the mean value of the transverse polarization.

The ensuing exposition is organized as follows. In Section 2, we describe the procedure for calculating the transverse polarization with allowance for one-loop diagrams featuring final-state interaction. In Section 3, we present and discuss our numerical results for P_T and $\langle P_T \rangle$. The last section contains a summary and conclusions.

2. TRANSVERSE POLARIZATION OF MUONS IN THE DECAY $K^+ \to \mu^+\nu\gamma$

In the tree approximation, the decay $K^+ \to \mu^+\nu\gamma$ is described by the diagrams in Fig. 1. The diagrams in Figs. 1*b* and 1*c* correspond to bremsstrahlung from the muon and the kaon, respectively, while the diagram in Fig. 1*a* takes into account structural radiation. The amplitude of this process can be represented

1063-7788/02/6503-0513$22.00

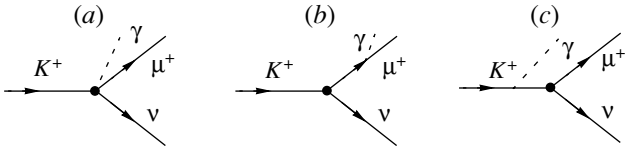

Fig. 1. Feynman diagrams for the decay $K^+ \to \mu^+\nu\gamma$ in the tree approximation.

in the form

$$M = ie\frac{G_\mathrm{F}}{\sqrt{2}}V_{us}^*\varepsilon_\mu^*\left(f_K m_\mu \bar{u}(p_\nu)(1+\gamma_5)\right. \tag{1}$$
$$\left.\times\left(\frac{p_K^\mu}{(p_K q)} - \frac{(p_\mu)^\mu}{(p_\mu q)} - \frac{\hat{q}\gamma^\mu}{2(p_\mu q)}\right)v(p_\mu) - G^{\mu\nu}l_\nu\right),$$

where

$$l_\mu = \bar{u}(p_\nu)(1+\gamma_5)\gamma_\mu v(p_\mu); \tag{2}$$
$$G^{\mu\nu} = iF_v\varepsilon^{\mu\nu\alpha\beta}q_\alpha(p_K)_\beta - F_a(g^{\mu\nu}(p_K q) - p_K^\mu q^\nu);$$

G_F is the Fermi constant; V_{us} is the relevant element of the Cabibbo–Kobayashi–Maskawa matrix; f_K is the leptonic coupling constant of the K meson; p_K, p_μ, p_ν, and q are the 4-momenta of the kaon, the muon, the neutrino, and the photon, respectively; ε_μ is the photon polarization vector; and F_v and F_a are the vector and axial kaon form factors.

That part of the amplitude which is associated with structural radiation and radiation in the initial kaon state and which we will use below in the one-loop calculations has the form

$$M_K = ie\frac{G_\mathrm{F}}{\sqrt{2}}V_{us}^*\varepsilon_\mu^*\left(f_K m_\mu \bar{u}(p_\nu)(1+\gamma_5)\right. \tag{3}$$
$$\left.\times\left(\frac{p_K^\mu}{(p_K q)} - \frac{\gamma^\mu}{m_\mu}\right)v(p_\mu) - G^{\mu\nu}l_\nu\right).$$

The $K^+ \to \mu^+\nu\gamma$ partial decay width in the kaon rest frame can be represented as

$$d\Gamma = \frac{|M|^2}{2m_K}(2\pi)^4\delta(p_K - p_\mu - q - p_\nu) \tag{4}$$
$$\times\frac{d^3q}{(2\pi)^3 2E_q}\frac{d^3p_\mu}{(2\pi)^3 2E_\mu}\frac{d^3p_\nu}{(2\pi)^3 2E_\nu}.$$

Upon introducing a unit vector $\mathbf{s}$ directed along the spin of the muon in its rest frame, where $\mathbf{e}_i$ ($i = L, N, T$) are unit vectors directed along, respectively, the longitudinal, the normal, and the transverse component of the muon polarization, the square of the matrix element for the transition into a pure muon-polarization state takes the form

$$|M|^2 = \rho_0[1 + (P_L\mathbf{e}_L + P_N\mathbf{e}_N + P_T\mathbf{e}_T)\cdot\mathbf{s}], \tag{5}$$

where ρ_0 is the probability density on the Dalitz plot; the unit vectors $\mathbf{e}_i$ are expressed in terms of the 3-momenta of final particles as

$$\mathbf{e}_L = \frac{\mathbf{p}_\mu}{|\mathbf{p}_\mu|}, \quad \mathbf{e}_N = \frac{\mathbf{p}_\mu\times(\mathbf{q}\times\mathbf{p}_\mu)}{|\mathbf{p}_\mu\times(\mathbf{q}\times\mathbf{p}_\mu)|}, \tag{6}$$
$$\mathbf{e}_T = \frac{\mathbf{q}\times\mathbf{p}_\mu}{|\mathbf{q}\times\mathbf{p}_\mu|};$$

and P_T is the muon transverse polarization. Employing the notation introduced in [6],

$$x = \frac{2E_\gamma}{m_K}, \quad y = \frac{2E_\mu}{m_K}, \tag{7}$$
$$\lambda = \frac{x+y-1-r_\mu}{x}, \quad r_\mu = \frac{m_\mu^2}{m_K^2},$$

where E_γ (E_μ) is the photon (muon) energy in the kaon rest frame, we can write the probability density on the Dalitz plot,

$$\rho_0(x,y) = \frac{d^2\Gamma}{dxdy} = \frac{m_K}{256\pi^3}|M|^2, \tag{8}$$

as a function of the variables x and y:

$$\rho_0 = \frac{1}{2}e^2G_\mathrm{F}^2|V_{us}|^2\left(\frac{4m_\mu^2|f_K|^2}{\lambda x^2}(1-\lambda)\right. \tag{9}$$
$$\times\left(x^2 + 2(1-r_\mu)\left(1 - x - \frac{r_\mu}{\lambda}\right)\right)$$
$$+ m_K^6x^2(|F_a|^2 + |F_v|^2)(y - 2\lambda y - \lambda x + 2\lambda^2)$$
$$+ 4\mathrm{Re}(f_K F_v^*)m_K^4 r_\mu\frac{x}{\lambda}(\lambda - 1) + 4\mathrm{Re}(f_K F_a^*)$$
$$\times m_K^4 r_\mu\left(-2y + x + 2\frac{r_\mu}{\lambda} - \frac{x}{\lambda} + 2\lambda\right)$$
$$\left.+2\mathrm{Re}(F_a F_v^*)m_K^6x^2(y - 2\lambda + x\lambda)\right).$$

In calculating the muon transverse polarization, we will henceforth follow the strategies adopted in [7] and assume that the amplitude of the decay under consideration is CP-invariant and that the form factors f_K, F_v, and F_a are real-valued. In the tree approximation, the muon transverse polarization then vanishes: $P_T = 0$. The inclusion of one-loop contributions leads to a nonzero muon transverse polarization owing to the interference between tree diagrams and the imaginary parts of one-loop diagrams generated by electromagnetic final-state interaction.

In order to determine these imaginary parts of the form factors, we employ the unitarity of S matrix [7],

$$S^+S = 1; \tag{10}$$

considering that $S = 1 + iT$, we then arrive at

$$T_{fi} - T_{if}^* = i\sum_n T_{nf}^*T_{ni}, \tag{11}$$

where the indices i, f, and n correspond, respectively, to the initial, to the final, and to the intermediate state of the particle system. Taking into account the T invariance of the matrix element, we obtain

$$\mathrm{Im}\, T_{fi} = \frac{1}{2}\sum_n T^*_{nf} T_{ni}, \tag{12}$$

$$T_{fi} = (2\pi)^4 \delta(P_f - P_i) M_{fi}. \tag{13}$$

The one-loop diagrams that contribute to the muon transverse polarization in the decay $K^+ \to \mu^+\nu\gamma$ are presented in Fig. 2. Applying expression (3), we can write their imaginary parts generating a nonzero contribution to P_T. For the diagrams in Figs. 2*a* and 2*c*, we have

$$\mathrm{Im}\, M_1 = \frac{ie\alpha}{2\pi}\frac{G_\mathrm{F}}{\sqrt{2}} V^*_{us}\bar{u}(p_\nu)(1+\gamma_5) \tag{14}$$
$$\times \int \frac{d^3k_\gamma}{2\omega_\gamma}\frac{d^3k_\mu}{2\omega_\mu}\delta(k_\gamma + k_\mu - P) R_\mu$$
$$\times (\hat{k}_\mu - m_\mu)\gamma^\mu \frac{\hat{q} + \hat{p}_\mu - m_\mu}{(q+p_\mu)^2 - m^2_\mu}\gamma^\delta \varepsilon^*_\delta v(p_\mu).$$

The contribution of the diagrams in Figs. 2*b* and 2*d* is given by

$$\mathrm{Im}\, M_2 = \frac{ie\alpha}{2\pi}\frac{G_F}{\sqrt{2}} V^*_{us}\bar{u}(p_\nu)(1+\gamma_5) \tag{15}$$
$$\times \int \frac{d^3k_\gamma}{2\omega_\gamma}\frac{d^3k_\mu}{2\omega_\mu}\delta(k_\gamma + k_\mu - P) R_\mu$$
$$\times (\hat{k}_\mu - m_\mu)\gamma^\delta \varepsilon^*_\delta \frac{\hat{k}_\mu - \hat{q} - m_\mu}{(k_\mu - q)^2 - m^2_\mu}\gamma^\mu v(p_\mu),$$

where we have introduced the notation

$$R_\mu = f_K m_\mu \left(\frac{(p_K)_\mu}{(p_K k_\gamma)} - \frac{\gamma_\mu}{m_\mu}\right) \tag{16}$$
$$- iF_v \varepsilon_{\mu\nu\alpha\beta}(k_\gamma)^\alpha (p_K)^\beta \gamma^\nu$$
$$+ F_a(\gamma_\mu (p_K k_\gamma) - (p_K)_\mu \hat{k}_\gamma).$$

In order to write the contributions from the diagrams in Figs. 2*e* and 2*f*, we must modify R_μ in expressions (14) and (15) by representing it in the form

$$R_\mu = f_K m_\mu \left(\frac{\gamma_\mu}{m_\mu} - \frac{(k_\mu)_\mu}{(k_\mu k_\gamma)} - \frac{\hat{k}_\gamma \gamma_\mu}{2(k_\mu k_\gamma)}\right). \tag{17}$$

Here, we do not quote the expression for the imaginary part of the diagram in Fig. 2*g* and, in the ensuing calculations, neglect its contribution to the muon transverse polarization, since it is much less than the contributions from other diagrams.

A detailed account of the procedure that we use to calculate the integrals in (14) and (15) and their

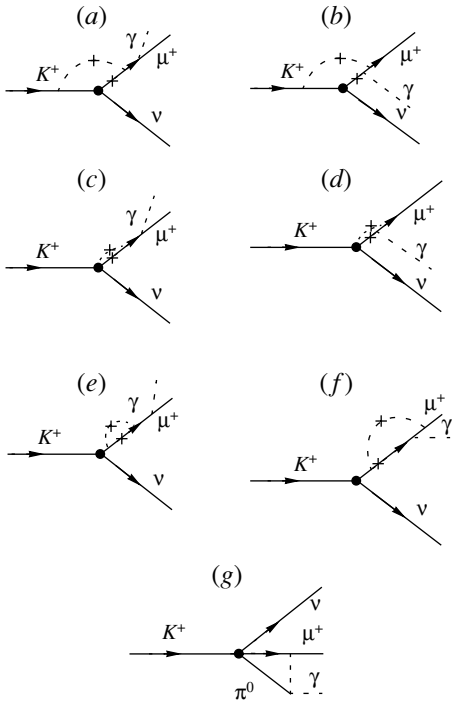

Fig. 2. Feynman diagrams contributing to the muon transverse polarization in the one-loop approximation.

dependences on the kinematical parameters is given in Appendix 1. The expression for the amplitude with allowance for $\mathrm{Im}M_1 + \mathrm{Im}M_2$ has the form

$$M = ie\frac{G_\mathrm{F}}{\sqrt{2}} V^*_{us}\varepsilon^*_\mu \left(\tilde{f}_K m_\mu \bar{u}(p_\nu)(1+\gamma_5)\right. \tag{18}$$
$$\times \left(\frac{p^\mu_K}{(p_K q)} - \frac{(p_\mu)^\mu}{(p_\mu q)}\right) v(p_\mu)$$
$$\left. + \tilde{F}_n \bar{u}(p_\nu)(1+\gamma_5)\hat{q}\gamma^\mu v(p_\mu) - \tilde{G}^{\mu\nu} l_\nu\right),$$

where

$$\tilde{G}^{\mu\nu} = i\tilde{F}_v \varepsilon^{\mu\nu\alpha\beta} q_\alpha (p_K)_\beta - \tilde{F}_a(g^{\mu\nu}(p_K q) - p^\mu_K q^\nu). \tag{19}$$

The form factors $\tilde{f}_K$, $\tilde{F}_v$, $\tilde{F}_a$, and $\tilde{F}_n$ include the one-loop contributions from the diagrams in Figs. 2*a*–2*f*. The choice of these form factors is determined by the decomposition of the matrix element into independent gauge-invariant structures.

We are interested only in the contributions from the imaginary parts, since it is these contributions that lead to the appearance of a nonzero transverse muon polarization. This is the reason why we neglect the real parts of these diagrams, assuming that $\mathrm{Re}\tilde{f}_K$, $\mathrm{Re}\tilde{F}_v$, and $\mathrm{Re}\tilde{F}_a$ coincide with their values in the tree approximation (f_K, F_v, and F_a, respectively) and that $\mathrm{Re}\tilde{F}_n = -f_K m_\mu (p_\mu q)/2$. The expressions

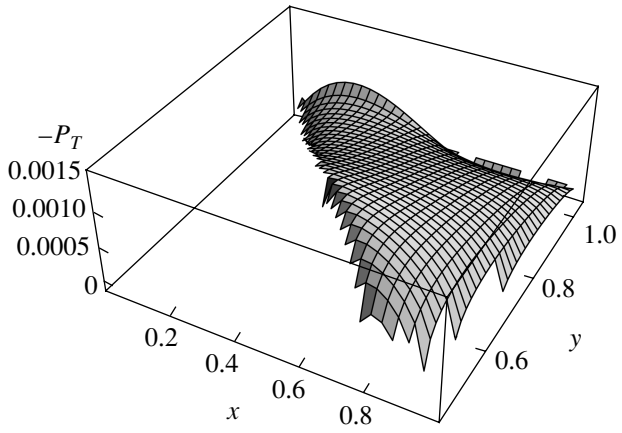

Fig. 3. Three-dimensional Dalitz plot for the muon transverse polarization as a function of the variables $x = 2E_\gamma/m_K$ and $y = 2E_\mu/m_K$.

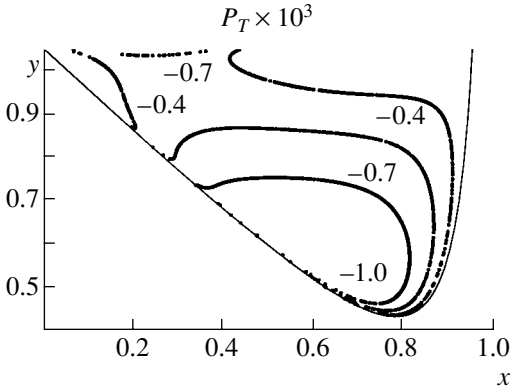

Fig. 4. Level contours on the Dalitz plot for the muon transverse polarization $P_T = f(x, y)$.

for the imaginary parts of the form factors are presented in Appendix 2. The muon transverse polarization can be represented in the form

$$P_T = \rho_T/\rho_0, \tag{20}$$

where

$$\begin{aligned}\rho_T = -2m_K^3 e^2 G_F^2 |V_{us}|^2 x\sqrt{\lambda y - \lambda^2 - r_\mu} \\ \times \left(m_\mu \mathrm{Im}(\tilde{f}_K \tilde{F}_a^*) \left(1 - \frac{2}{x} + \frac{y}{\lambda x}\right) \right. \\ + m_\mu \mathrm{Im}(\tilde{f}_K \tilde{F}_v^*) \left(\frac{y}{\lambda x} - 1 - 2\frac{r_\mu}{\lambda x}\right) \\ + 2\frac{r_\mu}{\lambda x}\mathrm{Im}(\tilde{f}_K \tilde{F}_n^*)(1-\lambda) \\ + m_K^2 x \mathrm{Im}(\tilde{F}_n \tilde{F}_a^*)(\lambda - 1) \\ \left. + m_K^2 x \mathrm{Im}(\tilde{F}_n \tilde{F}_v^*)(\lambda - 1)\right).\end{aligned} \tag{21}$$

3. RESULTS

Before proceeding to discuss our numerical results, we would like to make a few comments.

The above expression for the probability density on the Dalitz plot (ρ_0) differs in the structure of the interference terms from the result presented previously in [6]. In addition, expression (21) differs from the result for ρ_T quoted in [6]. In particular, the expression for ρ_T in [6] does not involve the terms including the imaginary part of the form factor F_n, while the term $\mathrm{Im}(\tilde{f}_K \tilde{F}_a^*)$ has an opposite sign. This is not the whole story, however: in calculating the muon transverse polarization, we have taken here into account the contributions from the diagrams in Figs. 2*e* and 2*f*; these contributions were disregarded in [6], but they are commensurate with the contributions from the other diagrams in Fig. 2. (It should be noted that the expression for ρ_0 was obtained in [8] as well, where all kinematical structures in front of the quadratic and interference terms coincide with those obtained here, but the terms proportional to $\mathrm{Re}(f_K F_v^*)$ and $\mathrm{Re}(F_a F_v^*)$ have opposite signs.) These distinctions lead to considerable discrepancies between the values calculated here and in [6] for the muon transverse polarization.

In performing numerical calculations, we have used the form-factor values [8, 9]

$$f_K = 0.16\ \mathrm{GeV}, \quad F_v = -\frac{0.095}{m_K}, \quad F_a = -\frac{0.043}{m_K}.$$

The value of the form factor f_K is determined from experimental data on kaon decays, while the values of F_v and F_a are calculated within chiral perturbation theory in the one-loop approximation [8].

Figure 3 shows the three-dimensional distribution of the muon transverse polarization calculated in the one-loop approximation of the Standard Model. The behavior of P_T as a function of the parameters x and y is controlled by the additive contributions from the diagrams in Figs. 2*a*–2*f*. The contribution from the diagrams in Figs. 2*a*–2*d* is close in magnitude to that from the diagrams in Figs. 2*e* and 2*f*, but they have opposite signs, so that the total distribution of $P_T(x, y)$ is the difference of these contributions and is an order of magnitude smaller than each of them. Estimations show that, over the entire Dalitz plot, the contribution from the diagram in Fig. 2*g* is an order of magnitude smaller than the total contribution from the other diagrams.

As can be seen from Fig. 3, the absolute value of the muon transverse polarization takes the largest values in two regions of the Dalitz plot: (a) for $0.2 \le x = 2E_\gamma/m_K \le 0.4$ and $y = 2E_\mu/m_K \to 1$; (b) for $0.4 \le x = 2E_\gamma/m_K \le 0.7$ and $0.5 \le y = 2E_\mu/m_K \le 0.7$.

Indeed, an analysis of the behavior of the level contours for the muon transverse polarization versus the parameters x and y (see Fig. 4) shows that the maxima of the absolute value of the transverse polarization are located in the regions of (x, y) around (0.3, 1.0) and (0.6, 0.6). It should be noted that, in this case, the muon transverse polarization is negative over the entire Dalitz plot. The mean muon polarization $\langle P_T^{\mathrm{SM}} \rangle$ can be obtained upon integration over the physical region with allowance for the constraint $E_\gamma > 20$ MeV on the photon energy. The result is

$$\langle P_T^{\mathrm{SM}} \rangle = -5.44 \times 10^{-4} .$$

ACKNOWLEDGMENTS

We are grateful to V.V. Kisilev and A.K. Likhoded for stimulating discussions and enlightening comments.

This work was supported in part by the Russian Foundation for Basic Research (project nos. 99-02-16558 and 00-15-96645).

APPENDIX 1

In calculating the integrals appearing in expressions (14) and (15), we use the notation

$$P = p_\mu + q,$$
$$d\rho = \frac{d^3k_\gamma}{2\omega_\gamma}\frac{d^3k_\mu}{2\omega_\mu}\delta(k_\gamma + k_\mu - P).$$

Below, we present either explicit expressions for corresponding integrals in terms of the parameters introduced above or sets of equations in these parameters, in which case the integrals in question can be calculated by solving these sets of equations.

Thus, we have

$$J_{11} = \int d\rho = \frac{\pi}{2}\frac{P^2 - m_\mu^2}{P^2},$$
$$J_{12} = \int d\rho \frac{1}{(p_K k_\gamma)} = \frac{\pi}{2I}\ln\left(\frac{(Pp_K) + I}{(Pp_K) - I}\right),$$

where

$$I^2 = (Pp_K)^2 - m_K^2 P^2,$$
$$\int d\rho \frac{k_\gamma^\alpha}{(p_K k_\gamma)} = a_{11}p_K^\alpha + b_{11}P^\alpha.$$

Here, the parameters a_{11} and b_{11} are defined as

$$a_{11} = -\frac{1}{(Pp_K)^2 - m_K^2 P^2} \times \left(P^2 J_{11} - \frac{J_{12}}{2}(Pp_K)(P^2 - m_\mu^2)\right),$$

$$b_{11} = \frac{1}{(Pp_K)^2 - m_K^2 P^2} \times \left((Pp_K)J_{11} - \frac{J_{12}}{2}m_K^2(P^2 - m_\mu^2)\right);$$

$$\int d\rho k_\gamma^\alpha = a_{12}P^\alpha,$$
$$\int d\rho k_\gamma^\alpha k_\gamma^\beta = a_{13}g^{\alpha\beta} + b_{13}P^\alpha P^\beta,$$

where

$$a_{12} = \frac{P^2 - m_\mu^2}{2P^2}J_{11},$$
$$a_{13} = -\frac{1}{12}\frac{(P^2 - m_\mu^2)^2}{P^2}J_{11},$$
$$b_{13} = \frac{1}{3}\left(\frac{P^2 - m_\mu^2}{P^2}\right)^2 J_{11};$$

$$J_1 = \int d\rho \frac{1}{(p_K k_\gamma)((p_\mu - k_\gamma)^2 - m_\mu^2)} = -\frac{\pi}{2I_1(P^2 - m_\mu^2)}\ln\left(\frac{(p_K p_\mu) + I_1}{(p_K p_\mu) - I_1}\right),$$

$$J_2 = \int d\rho \frac{1}{(p_\mu - k_\gamma)^2 - m_\mu^2} = -\frac{\pi}{4I_2}\ln\left(\frac{(Pp_\mu) + I_2}{(Pp_\mu) - I_2}\right).$$

Here, we have

$$I_1^2 = (p_K p_\mu)^2 - m_\mu^2 m_K^2, \quad I_2^2 = (Pp_\mu)^2 - m_\mu^2 P^2;$$

$$\int d\rho \frac{k_\gamma^\alpha}{(p_\mu - k_\gamma)^2 - m_\mu^2} = a_1 P^\alpha + b_1 p_\mu^\alpha,$$

where

$$a_1 = -\frac{m_\mu^2(P^2 - m_\mu^2)J_2 + (Pp_\mu)J_{11}}{2((Pp_\mu)^2 - m_\mu^2 P^2)},$$
$$b_1 = \frac{(Pp_\mu)(P^2 - m_\mu^2)J_2 + P^2 J_{11}}{2((Pp_\mu)^2 - m_\mu^2 P^2)}.$$

The following integrals are expressed in terms of the parameters whose values can be obtained by solving the corresponding sets of equations:

$$\int d\rho \frac{k_\gamma^\alpha}{(p_K k_\gamma)((p_\mu - k_\gamma)^2 - m_\mu^2)} = a_2 P^\alpha + b_2 p_K^\alpha + c_2 p_\mu^\alpha,$$

$$\begin{cases} a_2(Pp_K) + b_2 m_K^2 + c_2(p_K p_\mu) = J_2, \\ a_2(Pp_\mu) + b_2(p_K p_\mu) + c_2 m_\mu^2 = -\frac{1}{2}J_{12}, \\ a_2 P^2 + b_2(Pp_K) + c_2(Pp_\mu) = (p_\mu q)J_1; \end{cases}$$

$$\int d\rho \frac{k_\gamma^\alpha k_\gamma^\beta}{(p_K k_\gamma)((p_\mu - k_\gamma)^2 - m_\mu^2)}$$
$$= a_3 g^{\alpha\beta} + b_3(P^\alpha p_K^\beta + P^\beta p_K^\alpha)$$
$$+ c_3(P^\alpha p_\mu^\beta + P^\beta p_\mu^\alpha) + d_3(p_K^\alpha p_\mu^\beta + p_K^\beta p_\mu^\alpha)$$
$$+ e_3 p_\mu^\alpha p_\mu^\beta + f_3 P^\alpha P^\beta + g_3 p_K^\alpha p_K^\beta,$$

$$\begin{cases} 4a_3 + 2b_3(Pp_K) + 2c_3(Pp_\mu) + 2d_3(p_K p_\mu) \\ + g_3 m_K^2 + e_3 m_\mu^2 + f_3 P^2 = 0, \\ c_3(p_K p_\mu) + b_3 m_K^2 + f_3(Pp_K) - a_1 = 0, \\ c_3(Pp_K) + d_3 m_K^2 + e_3(p_K p_\mu) - b_1 = 0, \\ a_3 + b_3(Pp_K) + d_3(p_K p_\mu) + g_3 m_K^2 = 0, \\ b_3(p_K p_\mu) + c_3 m_\mu^2 + f_3(Pp_\mu) = -\frac{1}{2} b_{11}, \\ b_3(Pp_\mu) + d_3 m_\mu^2 + g_3(p_K p_\mu) = -\frac{1}{2} a_{11}, \\ a_3 P^2 + 2b_3 P^2(Pp_K) + 2c_3 P^2(Pp_\mu) \\ + 2d_3(Pp_\mu)(Pp_K) + e_3(Pp_\mu)^2 + f_3(P^2)^2 \\ + g_3(Pp_K)^2 = (p_\mu q)^2 J_1; \end{cases}$$

$$\int d\rho \frac{k_\gamma^\alpha k_\gamma^\beta}{(p_\mu - k_\gamma)^2 - m_\mu^2}$$
$$= a_4 g_{\alpha\beta} + b_4(P^\alpha p_\mu^\beta + P^\beta p_\mu^\alpha) + c_4 P^\alpha P^\beta + d_4 p_\mu^\alpha p_\mu^\beta,$$

$$\begin{cases} a_4 + d_4 m_\mu^2 + b_4(Pp_\mu) = 0, \\ b_4 m_\mu^2 + c_4(Pp_\mu) = -\frac{1}{2} a_{12}, \\ 4a_4 + 2b_4(Pp_\mu) + c_4 P^2 + d_4 m_\mu^2 = 0, \\ a_4 P^2 + 2b_4 P^2(Pp_\mu) + c_4(P^2)^2 \\ + d_4(Pp_\mu)^2 = \frac{(P^2 - m_\mu^2)^2}{4} J_2; \end{cases}$$

$$\int d\rho \frac{k_\gamma^\alpha k_\gamma^\beta k_\gamma^\delta}{(p_\mu - k_\gamma)^2 - m_\mu^2}$$
$$= a_5(g^{\alpha\beta} p_\mu^\delta + g^{\delta\alpha} p_\mu^\beta + g^{\beta\delta} p_\mu^\alpha)$$
$$+ b_5(g^{\alpha\beta} P^\delta + g^{\delta\alpha} P^\beta + g^{\beta\delta} P^\alpha)$$
$$+ c_5 p_\mu^\alpha p_\mu^\beta p_\mu^\delta + d_5 P^\alpha P^\beta P^\delta$$
$$+ e_5(P^\alpha p_\mu^\beta p_\mu^\delta + P^\delta p_\mu^\alpha p_\mu^\beta + P^\beta p_\mu^\delta p_\mu^\alpha)$$
$$+ f_5(P^\alpha P^\beta p_\mu^\delta + P^\delta P^\alpha p_\mu^\beta + P^\beta P^\delta p_\mu^\alpha),$$

$$\begin{cases} 2a_5 + c_5 m_\mu^2 + e_5(Pp_\mu) = 0, \\ a_5 m_\mu^2 + b_5(Pp_\mu) = -\frac{1}{2} a_{13}, \\ b_5 + e_5 m_\mu^2 + f_5(Pp_\mu) = 0, \\ d_5(Pp_\mu) + f_5 m_\mu^2 = -\frac{1}{2} b_{13}, \\ 6a_5 + c_5 m_\mu^2 + 2e_5(Pp_\mu) + f_5 P^2 = 0, \\ 3a_5 P^2(Pp_\mu) + 3b_5(P^2)^2 + c_5(Pp_\mu)^3 \\ + d_5(P^2)^3 + 3e_5 P^2(Pp_\mu)^2 \\ + 3f_5(P^2)^2(Pp_\mu) = \frac{(P^2 - m_\mu^2)^3}{8} J_2. \end{cases}$$

APPENDIX 2

In this appendix, we present expressions for the imaginary parts of the form factors in terms of the parameters calculated in Appendix 1. Specifically, we have

$$\mathrm{Im}\tilde{f}_K = \frac{\alpha}{2\pi} f_K \big(- 4a_3(p_K q) + 4a_2 m_\mu^2(p_K q)$$
$$- 2b_3 m_\mu^2(p_K q) + 4c_2 m_\mu^2(p_K q) - 4c_3 m_\mu^2(p_K q)$$
$$- 2d_3 m_\mu^2(p_K q) - 2e_3 m_\mu^2(p_K q) - 2f_3 m_\mu^2(p_K q)$$
$$+ 4a_2(p_K q)(p_\mu q) - 4b_3(p_K q)(p_\mu q)$$
$$- 4c_3(p_K q)(p_\mu q) - 4f_3(p_K q)(p_\mu q)\big)$$
$$+ \frac{\alpha}{2\pi} F_a \big(8\, a_4(p_K q) - 8a_5(p_K q)$$
$$- 8b_5(p_K q) + 8b_4 m_\mu^2(p_K q)$$
$$+ 4c_4 m_\mu^2(p_K q) - 2c_5 m_\mu^2(p_K q)$$
$$+ 4d_4 m_\mu^2(p_K q) - 2d_5 m_\mu^2(p_K q)$$
$$- 6e_5 m_\mu^2(p_K q) - 6f_5\, m_\mu^2(p_K q)$$
$$+ 12b_4(p_K q)(p_\mu q) + 8c_4(p_K q)(p_\mu q)$$
$$+ 4d_4(p_K q)(p_\mu q) - 4d_5(p_K q)(p_\mu q)$$
$$- 4e_5(p_K q)(p_\mu q) - 8f_5(p_K q)(p_\mu q)\big)$$
$$+ \frac{\alpha}{2\pi} F_v \big(8\, a_4(p_K q) - 8a_5(p_K q)$$
$$- 8b_5(p_K q) + 8b_4 m_\mu^2(p_K q)$$
$$+ 4c_4 m_\mu^2(p_K q) - 2c_5 m_\mu^2(p_K q)$$
$$+ 4d_4 m_\mu^2(p_K q) - 2\, d_5 m_\mu^2(p_K q)$$
$$- 6e_5 m_\mu^2(p_K q) - 6f_5 m_\mu^2(p_K q)$$
$$+ 12b_4(p_K q)(p_\mu q) + 8c_4\,(p_K q)(p_\mu q)$$
$$+ 4d_4(p_K q)(p_\mu q) - 4d_5(p_K q)(p_\mu q)$$
$$- 4e_5(p_K q)(p_\mu q) - 8f_5(p_K q)(p_\mu q)\big);$$

$$\mathrm{Im}\tilde{F}_a = \frac{\alpha}{2\pi} f_K \Big(a_2 m_\mu^2 + 2c_2 m_\mu^2$$

$$
\begin{aligned}
&- c_3 m_\mu^2 - 2d_3 m_\mu^2 - e_3 m_\mu^2 \\
&- \frac{a_1 m_\mu^2}{(p_\mu q)} - \frac{b_1 m_\mu^2}{(p_\mu q)} + \frac{2b_4 m_\mu^2}{(p_\mu q)} + \frac{c_4 m_\mu^2}{(p_\mu q)} + \frac{d_4 m_\mu^2}{(p_\mu q)}\Big) \\
&+ \frac{\alpha}{2\pi} F_v\big(8a_4 - 4a_5 - 12b_5 \\
&- 2a_1 m_\mu^2 + 4b_4 m_\mu^2 + 5c_4 m_\mu^2 \\
&- c_5 m_\mu^2 - d_4 m_\mu^2 - 3d_5 m_\mu^2 \\
&- 5e_5 m_\mu^2 - 7f_5 m_\mu^2 + 2a_1(p_K p_\mu) \\
&- 4b_4(p_K p_\mu) - 4c_4(p_K p_\mu) + 2d_5(p_K p_\mu) \\
&+ 2e_5(p_K p_\mu) + 4f_5(p_K p_\mu) + 2a_1(p_K q) \\
&- 2b_4(p_K q) - 4c_4(p_K q) + 2d_5(p_K q) \\
&+ 2f_5(p_K q) - 4a_1(p_\mu q) + 6b_4(p_\mu q) \\
&+ 10c_4(p_\mu q) - 6d_5(p_\mu q) - 2e_5(p_\mu q) \\
&- 8f_5(p_\mu q)\big) + \frac{\alpha}{2\pi} F_a\big(-6a_4 + 2\,a_5 \\
&+ c_4 m_\mu^2 - d_4 m_\mu^2 - d_5 m_\mu^2 - e_5 m_\mu^2 \\
&- 2f_5 m_\mu^2 + 2a_1(p_K p_\mu) - 4b_4(p_K p_\mu) \\
&- 4c_4(p_K p_\mu) + 2d_5(p_K p_\mu) + 2e_5(p_K p_\mu) \\
&+ 4f_5(p_K p_\mu) + 2a_1(p_K q) - 2b_4(p_K q) \\
&- 4c_4(p_K q) + 2d_5(p_K q) + 2f_5(p_K q) \\
&+ 2c_4(p_\mu q) - 2d_5(p_\mu q) - 2f_5(p_\mu q)\big);
\end{aligned}
$$

$$
\begin{aligned}
\mathrm{Im}\tilde{F}_n = \frac{\alpha}{2\pi} f_K\Big(&4a_1 m_\mu + 2a_3 m_\mu \\
&+ 2b_1 m_\mu + b_{11} m_\mu - 2b_4 m_\mu - 2c_4 m_\mu \\
&- J_{12} m_\mu - 2J_2 m_\mu - b_2 m_K^2 m_\mu \\
&+ g_3 m_K^2 m_\mu - 2a_2 m_\mu^3 - c_2 m_\mu^3 + c_3 m_\mu^3 \\
&+ f_3 m_\mu^3 - 2a_2 m_\mu (p_K p_\mu) - 2b_2 m_\mu (p_K p_\mu) \\
&+ 2b_3 m_\mu (p_K p_\mu) - 2c_2 m_\mu (p_K p_\mu) \\
&+ 2d_3 m_\mu (p_K p_\mu) + 2J_1 m_\mu (p_K p_\mu) + 2b_3 m_\mu (p_K q) \\
&- \frac{a_{12} m_\mu^3}{(p_\mu q)^2} - \frac{J_{11} m_\mu^3}{(p_\mu q)^2} - \frac{a_{12} m_\mu}{(p_\mu q)} - \frac{2a_4 m_\mu}{(p_\mu q)} \\
&+ \frac{J_{11} m_\mu}{(p_\mu q)} - \frac{a_{11} m_K^2 m_\mu}{2(p_\mu q)} + \frac{3\,a_1 m_\mu^3}{(p_\mu q)} + \frac{3\,b_1 m_\mu^3}{(p_\mu q)} \\
&+ \frac{b_{11} m_\mu^3}{2(p_\mu q)} - \frac{2J_2 m_\mu^3}{(p_\mu q)} - \frac{b_{11} m_\mu (p_K p_\mu)}{(p_\mu q)} \\
&+ \frac{J_{12} m_\mu (p_K p_\mu)}{(p_\mu q)} - \frac{b_{11} m_\mu (p_K q)}{(p_\mu q)} + \frac{J_{12} m_\mu (p_K q)}{(p_\mu q)} \\
&- 2a_2 m_\mu (p_\mu q) + 2c_3 m_\mu (p_\mu q) + 2f_3 m_\mu (p_\mu q)\Big) \\
&+ \frac{\alpha}{2\pi} F_v\Big(2a_4 m_\mu - 4a_5 m_\mu + 2b_{13} m_\mu \\
&- 4b_5 m_\mu - 2a_1 m_\mu^3 + c_4 m_\mu^3 \\
&- c_5 m_\mu^3 - d_4 m_\mu^3 - d_5 m_\mu^3 \\
&- 3e_5 m_\mu^3 - 3f_5 m_\mu^3 + 2a_1 m_\mu (p_K p_\mu) \\
&- 2c_4 m_\mu (p_K p_\mu) + 2d_4 m_\mu (p_K p_\mu) \\
&+ 2d_5 m_\mu (p_K p_\mu) + 2e_5 m_\mu (p_K p_\mu) \\
&+ 4f_5 m_\mu (p_K p_\mu) - 2c_4 m_\mu (p_K q) \\
&+ 2d_5 m_\mu (p_K q) + 2f_5 m_\mu (p_K q) \\
&+ \frac{3a_{13} m_\mu}{(p_\mu q)} + \frac{b_{13} m_\mu^3}{(p_\mu q)} \\
&- \frac{b_{13} m_\mu (p_K p_\mu)}{(p_\mu q)} - \frac{b_{13} m_\mu (p_K q)}{(p_\mu q)} \\
&- 2a_1 m_\mu (p_\mu q) + 2c_4 m_\mu (p_\mu q) \\
&- 2d_4 m_\mu (p_\mu q) - 2d_5 m_\mu (p_\mu q) \\
&- 2e_5 m_\mu (p_\mu q) - 4f_5 m_\mu (p_\mu q)\Big) \\
&+ \frac{\alpha}{2\pi} F_a\Big(-6a_4 m_\mu + 8a_5 m_\mu - b_{13} m_\mu \\
&+ 8b_5 m_\mu - 4b_4 m_\mu^3 - 2c_4 m_\mu^3 \\
&+ c_5 m_\mu^3 - 2d_4 m_\mu^3 + d_5 m_\mu^3 + 3e_5 {m_\mu}^3 \\
&+ 3f_5 m_\mu^3 + 2a_1 m_\mu (p_K p_\mu) - 2c_4 m_\mu (p_K p_\mu) \\
&+ 2d_4 m_\mu (p_K p_\mu) + 2d_5 m_\mu (p_K p_\mu) \\
&+ 2e_5 m_\mu (p_K p_\mu) + 4f_5 m_\mu (p_K p_\mu) \\
&- 2c_4 m_\mu (p_K q) + 2d_5 m_\mu (p_K q) + 2f_5 m_\mu (p_K q) \\
&- \frac{3a_{13} m_\mu}{(p_\mu q)} - \frac{b_{13} {m_\mu}^3}{2(p_\mu q)} - \frac{b_{13} m_\mu (p_K p_\mu)}{(p_\mu q)} \\
&- \frac{b_{13} m_\mu (p_K q)}{(p_\mu q)} - 6b_4 m_\mu (p_\mu q) \\
&- 4c_4 m_\mu (p_\mu q) - 2d_4 m_\mu (p_\mu q) \\
&+ 2d_5 m_\mu (p_\mu q) + 2e_5 m_\mu (p_\mu q) + 4f_5 m_\mu (p_\mu q)\Big);
\end{aligned}
$$

$$
\begin{aligned}
\mathrm{Im}\tilde{F}_v = \frac{\alpha}{2\pi} f_K\Big(&a_2 m_\mu^2 + c_3 m_\mu^2 + e_3 m_\mu^2 \\
&+ \frac{a_1 m_\mu^2}{(p_\mu q)} + \frac{b_1 m_\mu^2}{(p_\mu q)} - \frac{2b_4 m_\mu^2}{(p_\mu q)} \\
&- \frac{c_4 m_\mu^2}{(p_\mu q)} - \frac{d_4 m_\mu^2}{(p_\mu q)}\Big) + \frac{\alpha}{2\pi} F_a\big(6a_4 \\
&- 2a_5 - 8b_5 + c_4 m_\mu^2 - d_4 m_\mu^2 \\
&- d_5 m_\mu^2 - e_5 m_\mu^2 - 2f_5 m_\mu^2 \\
&- 2a_1(p_K p_\mu) + 4b_4(p_K p_\mu) + 4\,c_4(p_K p_\mu) \\
&- 2d_5(p_K p_\mu) - 2e_5(p_K p_\mu) - 4f_5(p_K p_\mu) \\
&- 2a_1(p_K q) + 2b_4(p_K q) + 4c_4(p_K q) - 2d_5(p_K q) \\
&- 2f_5(p_K q) + 2c_4(p_\mu q) - 2d_5(p_\mu q) - 2f_5(p_\mu q)\big) \\
&+ \frac{\alpha}{2\pi} F_v\big(-8a_4 + 4a_5 + 4b_5
\end{aligned}
$$

$$
\begin{aligned}
&+ 2a_1 m_\mu^2 - 4b_4 m_\mu^2 - 3c_4 m_\mu^2 \\
&+ c_5 m_\mu^2 - d_4 m_\mu^2 + d_5 m_\mu^2 + 3e_5 m_\mu^2 \\
&+ 3f_5 m_\mu^2 - 2a_1(p_K p_\mu) + 4b_4(p_K p_\mu) \\
&+ 4c_4(p_K p_\mu) - 2d_5(p_K p_\mu) - 2e_5(p_K p_\mu) \\
&- 4f_5(p_K p_\mu) - 2a_1(p_K q) + 2b_4(p_K q) \\
&+ 4c_4(p_K q) - 2d_5(p_K q) - 2f_5(p_K q) \\
&+ 4a_1(p_\mu q) - 6b_4(p_\mu q) - 6c_4(p_\mu q) \\
&+ 2d_5(p_\mu q) + 2e_5(p_\mu q) + 4f_5(p_\mu q)\big).
\end{aligned}
$$

REFERENCES

1. S. Weinberg, Phys. Rev. Lett. **37**, 657 (1976).
2. A. Likhoded, V. Braguta, and A. Chalov, hep-ex/0011033.
3. J. F. Donoghue and B. Holstein, Phys. Lett. B **113B**, 382 (1982); L. Wolfenstein, Phys. Rev. D **29**, 2130 (1984); G. Barenboim *et al.*, Phys. Rev. D **55**, 4213 (1997).
4. M. Kobayashi, T.-T. Lin, and Y. Okada, Prog. Theor. Phys. **95**, 361 (1996); R. Garisto and G. Kane, Phys. Rev. D **44**, 2038 (1991); G. Belanger and C. Q. Cheng, Phys. Rev. D **44**, 2789 (1991).
5. V. F. Obraztsov, hep-ex/0011033 (OKA experiment).
6. V. P. Efrosinin and Yu. G. Kudenko, Yad. Fiz. **62**, 1054 (1999) [Phys. At. Nucl. **62**, 987 (1999)].
7. L. B. Okun' and I. B. Khriplovich, Yad. Fiz. **6**, 821 (1966) [Sov. J. Nucl. Phys. **6**, 598 (1967)].
8. J. Bijnens, G. Ecker, and J. Gasser, Nucl. Phys. B **396**, 81 (1993).
9. Particle Data Group (D. E. Groom *et al.*), Eur. Phys. J. C **15**, (2000).

Translated by O. Chernavskaya

Physics of Atomic Nuclei, Vol. 65, No. 3, 2002, pp. 521–533. Translated from Yadernaya Fizika, Vol. 65, No. 3, 2002, pp. 547–560.

ELEMENTARY PARTICLES AND FIELDS
Theory

Effects of New Neutral Currents at Linear Electron–Positron Colliders

A. A. Pankov

Gomel State Technical University, Gomel, Belarus

Received November 10, 2000; in final form, June 19, 2001

Abstract—Effects that are induced by contact four-fermion interactions in the processes $e^+e^- \to \mu^+\mu^-$, $\bar{b}b$, and $\bar{c}c$ at $\sqrt{s} = 0.5$ TeV linear electron–positron colliders are investigated for the case of longitudinally polarized initial beams. This analysis employs new integrated observables constructed from the polarized cross sections for the scattering of final fermions into the forward (σ_F) and the backward (σ_B) hemisphere in such a way that they single out the helicity cross sections for the processes in question. This property of the observables makes it possible to perform, in the most general form, a model-independent analysis of contact four-fermion interactions and to set constraints on their parameters. It is also shown that the sensitivity of new polarization observables to contact interactions is noticeably higher than the corresponding sensitivity of canonical observables like σ, A_{FB}, A_{LR}, and $A_{LR,FB}$. © *2002 MAIK "Nauka/Interperiodica".*

1. INTRODUCTION

Slightly more than a quarter of a century has passed since the discovery of weak neutral currents at the Gargamelle facility [1]. This discovery, which was one of the first successful applications of the Standard Model (SM), ensured a high phenomenological status of this model and gave impetus to massive efforts aimed at thoroughly verifying every aspect of it in accelerator and nonaccelerator experiments [2–4]. The accuracy of experiments testing the Standard Model has been considerably improved over those years, and impressive advances, which culminated in precision resonance ($\sqrt{s} = M_Z$) and nonresonance ($\sqrt{s} > M_Z$) experiments at the LEP electron–positron collider, the level of precision being 0.1% in the resonance experiments, have been made along this line. Mention should also be made here of recently performed experiments that measured effects of parity violation in cesium atoms (see, for example, [4]) and which are highly sensitive to P-odd effects of nonstandard physics. Processes that are due to neutral currents provide a powerful tool not only for testing the Standard Model but also for seeking the effects of new particles and interactions beyond it.

An observation of deviations from Standard Model predictions in the annihilation production of fermion pairs,

$$e^+ + e^- \to \bar{f} + f\,, \qquad (1)$$

where $f = l$ $(l = \mu, \tau)$ or $f = q$ $(q = u, d, c, s, b)$, would be an unambiguous indication of the existence of new (nonstandard) physics. At low energies, these deviations can be systematically described and investigated on the basis of the formalism of effective Lagrangians. In this approach, an effective Lagrangian is constructed from the matter fields that occur in the Standard Model, so that, at low energies, the symmetry properties of this Lagrangian are identical to those of the Standard Model. The resulting interaction involves the Standard Model interaction as the leading term in a series and higher order terms in the scale parameter $(1/\Lambda^n)$ that are formed by local operators whose dimensions are higher than those in the Standard Model. Thus, effects of nonstandard physics can be observed at energies much lower than Λ in the form of deviations of observables from the values predicted by the Standard Model and can correspond to some effective contact interactions.

The first term in the effective Lagrangian for contact four-fermion interaction has the dimension of $D = 6$ and includes the factor $g^2_{\rm eff}/\Lambda^2$. If we restrict our analysis to the case of fermion currents that conserve helicity and which are diagonal in flavor, the general form of the contact four-fermion $eeff$ interaction invariant under the $SU(3)_C \times SU(2)_L \times U(1)_Y$ symmetry group can be represented in the form [5–12]

$$\mathcal{L} = \sum_f \sum_{\alpha\beta} \eta_{\alpha\beta} \left(\bar{e}_\alpha \gamma_\mu e_\alpha\right) \left(\bar{f}_\beta \gamma^\mu f_\beta\right), \qquad (2)$$

where eight independent coefficients $\eta_{\alpha\beta}$ have dimensions of TeV^{-2} and are usually described in the form $\eta_{\alpha\beta} = g^2_{\rm eff}\epsilon_{\alpha\beta}/\Lambda^2_{\alpha\beta}$, with the strength of interaction being $g^2_{\rm eff} = 4\pi$. The choice of the constant $g_{\rm eff}$ in this form is dictated by considerations according to which the contact interaction becomes strong for $\sqrt{s} \to \Lambda_{\alpha\beta}$. The quantity $\epsilon_{\alpha\beta}$ takes the values of $\epsilon_{\alpha\beta} = 0$ and ± 1. The positive and negative signs correspond to the

1063-7788/02/6503-0521$22.00

Table 1. Models of contact four-fermion interactions

Model	ϵ_{LL}	ϵ_{RR}	ϵ_{LR}	ϵ_{RL}
LL	±1	0	0	0
RR	0	±1	0	0
LR	0	0	±1	0
RL	0	0	0	±1
VV	±1	±1	±1	±1
AA	±1	±1	∓1	∓1
$LL+RR$	±1	±1	0	0
$LR+RL$	0	0	±1	±1

constructive and the destructive interference between the contact interactions and the standard amplitudes describing photon and Z-boson exchanges. In the above expressions, we suppressed the color and the generation indices. The parameters $\eta_{\alpha\beta}\,(\alpha,\beta=L,R)$ determine the chiral structure of the interaction. Interaction terms violating the lepton and the fermion chirality—such as $(\bar{e}_L e_R)(\bar{f}_L f_R)$—are not included in expression (2) for the effective Lagrangian. This is done because available experimental data on the process $\pi^-\to e^-\bar{\nu}$ suggest a significant suppression of scalar and tensor terms of the Lagrangian for a theory that is invariant under the $SU(2)\times U(1)$ transformations.

In composite models of leptons and quarks, contact interactions are considered as a residual manifestation of binding forces acting between their constituent objects (for example, preons). Moreover, various types of nonstandard physics where fermion interactions are characterized by particle exchanges in the s, t, and u channels can be described by an effective contact four-fermion interaction under the condition that the square of the mass of the exchanged particle is much greater than the relevant Mandelstam variables. This concerns, for example, effects induced by the exchange of heavy Z' bosons [13], leptoquarks [14], and sleptons and squarks in supersymmetric theories featuring R-parity violation [15]. The concept of contact interactions is widely used in describing processes that proceed through neutral currents in e^+e^-, ep, and $\bar{p}p$ collisions [8, 9, 16]. Searches for the internal structure of leptons and quarks or for new heavy particles interacting with quarks and gluons are performed in these processes. Thus, contact interactions can be considered as a convenient parametrization of deviations from Standard Model predictions due to some types of nonstandard physics.

The structure of the Lagrangian in (2) is such that, for a given fermion f, there are eight possible types of interaction that correspond to the total number of independent models. This number is determined by the possible number of the helicity combinations $\alpha\beta=LL, LR, RL$, and RR with allowance for arbitrariness in the choice of the signs ($\pm$) of the coupling constants. As a matter of fact, each of these possibilities, which corresponds to one model or another, or any of their combinations can be realized in nature. The list of the models and their parametrizations that are discussed most often in analyzing experimental data in the context of contact four-fermion interactions is presented in Table 1 [3, 8, 17].

We note that the number of independent parameters of the four-fermion interaction can be reduced by imposing additional constraints on the symmetries of the Lagrangian. This results in the appearance of specific relations between the coupling constants.

We will briefly explain this by considering some examples [10]. In the theoretical scheme based on the interaction that is invariant under the transformations of the $SU(2)\times U(1)$ group, leptons and quarks of left-hand helicity form $SU(2)$ doublets; that is, they can be represented as $L=(\nu_L,e_L)$ and $Q=(u_L,d_L)$. The Lagrangian for lepton–quark interactions that is invariant under the transformations of the $SU(2)\times U(1)$ group has the form [10]

$$\begin{aligned}\mathcal{L}_{SU(2)} &= \eta_1(\bar{L}\gamma^\mu L)(\bar{Q}\gamma_\mu Q) \\ &+ \eta_2(\bar{L}\gamma^\mu T^a L)(\bar{Q}\gamma_\mu T^a Q) + \eta_3(\bar{L}\gamma^\mu L)(\bar{u}_R\gamma_\mu u_R) \\ &+ \eta_4(\bar{L}\gamma^\mu L)(\bar{d}_R\gamma_\mu d_R) + \eta_5(\bar{e}_R\gamma^\mu e_R)(\bar{Q}\gamma_\mu Q) \\ &+ \eta_6(\bar{e}_R\gamma^\mu e_R)(\bar{u}_R\gamma_\mu u_R) + \eta_7(\bar{e}_R\gamma^\mu e_R)(\bar{d}_R\gamma_\mu d_R),\end{aligned} \tag{3}$$

where $L=(\nu_L,e_L)$ and $Q=(u_L,d_L)$. In the above expression, the Lagrangian term describing the lepton–quark interaction involving lepton-helicity violation, $(\bar{L}\gamma^\mu Q)(\bar{d}_R\gamma_\mu e_R)$, is discarded. This is done because, upon the Fierz transformation, it becomes equivalent to the interaction of the form $(\bar{L}e_R)(\bar{d}_R Q)$, which, as was mentioned above, is suppressed by virtue of available experimental information about the decay $\pi^-\to e^-\bar{\nu}$. The second term of the Lagrangian in (3) includes the factor $T^a=\sigma^a/2$, where σ^a are the generators of the $SU(2)$ group. There are constraints that $SU(2)$ symmetry imposes on the right-handed electron coupling constants; that is,

$$\eta_{RL}^{eu}=\eta_5=\eta_{RL}^{ed}. \tag{4}$$

Additionally, $SU(2)$ invariance dictates the following relations between the neutrino and the leptonic coupling constants:

$$\begin{aligned}\eta_{LL}^{\nu u} &= \eta_1+\frac{1}{4}\eta_2=\eta_{LL}^{ed}, \\ \eta_{LL}^{\nu d} &= \eta_1-\frac{1}{4}\eta_2=\eta_{LL}^{eu},\end{aligned} \tag{5}$$

$$\eta_{LR}^{\nu u} = \eta_3 = \eta_{LR}^{eu},$$
$$\eta_{LR}^{\nu d} = \eta_4 = \eta_{LR}^{ed}.$$

The breakdown of electroweak symmetry can lead to the removal of degeneracy of the states that form the $SU(2)$ multiplets and to corresponding modification of relations (5). In particular, this may be due to the exchanges of supersymmetric states, such as $\tilde{t}_1$, $\tilde{t}_2$, $\tilde{b}_L$, and $\tilde{b}_R$ [10], in supersymmetric theory involving R-parity violation.

Another example is associated with the symmetry of contact interactions with respect to the $SU(12)$ group. This leads to the relation

$$\eta_{\alpha L}^{eq} = -\eta_{\alpha R}^{eq}. \quad (6)$$

Finally, the vector–vector (VV) character of interactions imposes the following constraints on the coupling constants:

$$\eta_{LL}^{eq} = \eta_{RR}^{eq} = \eta_{LR}^{eq} = \eta_{RL}^{eq} = \eta_{VV}^{eq}. \quad (7)$$

The axial–axial (AA) interactions mediated by a vector boson, which have purely axial-vector coupling constants, yield

$$\eta_{LL}^{eq} = \eta_{RR}^{eq} = -\eta_{LR}^{eq} = -\eta_{RL}^{eq} = \eta_{AA}^{eq}. \quad (8)$$

All these features are reflected in Table 1.

Experimental investigation of contact four-fermion interactions and estimations of constraints on their parameters are based on the analysis of processes that proceed owing to neutral currents. Recently, Barger *et al.* [10] and Zeppenfeld and Cheung [12] performed a global analysis of available experimental data on neutral currents and presented the corresponding constraints on the individual parameters of the contact four-fermion interactions. These data include information about deep-inelastic scattering implemented at the ZEUS and H1 facilities, about parity-violation effects measured at the JILA facility for cesium atoms, about the scattering of polarized electrons on nuclei that was explored at SLAC, about Drell–Yan lepton pairs measured at the Tevatron collider, and about fermion-pair production in electron–positron annihilation at the LEP collider. The absence of signals from nonstandard physics in experiments with leptons and quarks made it possible to set constraints on the parameters $\Lambda_{\alpha\beta}$, the most stringent of these appearing to be at a level of $\Lambda_{\alpha\beta} > 10$–$15$ TeV at a confidence level of 95%. The most stringent constraints on the *eell* lepton interaction follow from data of recent LEP2 experiments at $\sqrt{s} = 130$–202 GeV, which lead to $\Lambda_{\alpha\beta} > 2.0$–$9.8$ TeV, depending on the choice of model [17]. For first-generation quarks, the constraints on lepton–quark parameters of the *eeqq* interaction from LEP2 data appeared to be less stringent (1.5–9.1 TeV). Information about lepton–quark interactions can also be extracted in an alternative way from HERA data on deep-inelastic lepton scattering and from data on hadron–hadron collisions—for example, from the results of measurements of the Drell–Yan process $p(\bar{p}) + p \to l^+l^- + X$ at the Tevatron collider [18]. The lower bound on the parameter $\Lambda_{\alpha\beta}$ from these experiments is close to the constraints following from the LEP2 data. However, the currently most stringent constraints on the contact four-fermion lepton–quark interaction *eeqq* ($\Lambda_{\alpha\beta} > 10$–$15$ TeV [19]) come from experiments that measured parity-violation effects in atoms. At the same time, it should be borne in mind that these experiments can constrain only those parameters of the contact interactions that violate parity.

As soon as the current high-luminosity experimental runs at the Tevatron collider (run II) are completed in the near future, these constraints will be improved to a level of 10 to 30 TeV, a specific value being dependent on the structure of interaction. Should the plans for further increasing the energy and luminosity of the Tevatron collider in the Tripler mode be implemented [20], an improvement in the sensitivity to some parameters of the contact interactions at least by a factor of two are in sight. The expected sensitivity of the hadron supercollider LHC remains the highest, reaching a scale of a few tens of TeV for the majority of the models [20]. Future linear electron–positron colliders (LC) of energy $\sqrt{s} \geq 500$ GeV provide the best possibilities for seeking and investigating effects induced by *eell*, *eebb*, and *eecc* contact interactions in process (1) owing to a high sensitivity of this process at high energies and especially in the case of polarized initial beams [9, 21, 22].

Let us now address an extremely important problem in studying contact four-fermion interactions, that which is associated with a large number (eight) of interaction parameters [5] (see above). In general, the deviations of observables from Standard Model predictions due to contact interactions can indeed depend on a few effective coupling constants (≤ 4). In view of so wide a variety of the parameters, it is rather difficult to separate and determine them empirically either theoretically or experimentally. Obviously, fits to experimental data must take into account all possible versions of contact four-fermion interactions and corresponding coupling constants. In order to simplify relevant analyses or for want of necessary event statistics, however, the authors who studied contact four-fermion interactions (including the authors of the articles quoted above) presented most frequently, for the respective coupling constants, constraints that they obtained by varying only a few (one or two) parameters at zero values of the remaining parameters. Upon simultaneously taking into account the

contributions from a number of chiral coupling constants, there can arise cancellations and, as a result, a reduction of the sensitivity of observables to the parameters $\Lambda_{\alpha\beta}$. In particular, it was indicated in [11] that the constraints can loosen considerably—from a level of $\Lambda_{\alpha\beta} \sim 10$ TeV, which was given in [10] as a typical one-parameter scale, to 3 or 4 TeV—as soon as the dependence of observables on the entire set of parameters is taken fully into account. As a further characteristic example, we can indicate the loosening of constraints in atomic physics from experiments seeking parity-violation effects. It was emphasized in [11] that they become much more lenient upon simultaneously taking into account the contributions to observables from a few sources of different physical origins. From the above examples, it follows that the procedure for setting constraints on the parameters $\Lambda_{\alpha\beta}$ that considers the dependence of observables on an incomplete set of parameters cannot be justified since it leads, as a rule, to obviously exaggerated estimates, which are often by far unrealistic.

An attempt at solving this problem is made in this study. Specifically, a simple and efficient approach is developed here for performing a model-independent analysis of contact four-fermion interactions with allowance for the entire set of interaction parameters treated on equal terms. This approach is based on the use of new integrated observables that are constructed from the cross sections for forward and backward scattering. In [23, 24], Z'-boson effects at the LEP2 collider for the case of unpolarized beams were analyzed in terms of observables similar in structure to those employed here. In contrast to that case, where the initial-beam polarization was impossible, emphasis is placed here, however, on the possibility of using longitudinally polarized beams at linear electron–positron colliders in order to separate different effects and to improve the sensitivity of observables. It is owing to the longitudinal polarization of electron–positron beams that we can isolate here the helicity cross sections for the scattering process (1), thereby solving the problem of separating and extracting the parameters for contact four-fermion interactions. This problem is solved in the most general form—that is, with allowance for the entire set of contact four-fermion coupling constants. A model-independent analysis of contact lepton–lepton ($eell$) and lepton–quark ($eebb$ and $eecc$) interactions in process (1) at a linear electron–positron collider employing longitudinally polarized initial beams is performed here on the basis of this approach.

The ensuing exposition is organized as follows. In Section 2, we discuss canonical unpolarized (σ, A_{FB}) and polarized (A_{LR}, $A_{LR,FB}$) observables and define new integrated variables $\sigma_\pm$. The possibilities for isolating the helicity cross sections with the aid of a longitudinal polarization of initial electron–positron beams are considered further in this section. Section 3 is devoted to analyzing the sensitivity of observables to contact interactions for the cases of unpolarized and polarized positrons. The dependence of the sensitivity of observables on systematic errors is investigated in detail. Here, we also obtain model-independent constraints on $\Lambda_{\alpha\beta}$ from a quantitative analysis of the helicity cross sections and present a comparative analysis of the sensitivities of the canonical and the new observables. The effects of radiative corrections on the resulting constraints are also discussed. The last section summarizes the results obtained in this study and contains concluding comments on them.

2. ISOLATION OF HELICITY CROSS SECTIONS

In the Born approximation that takes into account the exchange of a photon γ and a Z boson and the contribution of the contact four-fermion interactions (2), the differential cross section for the scattering process $e^+e^- \to \bar{f}f$ $(f \neq e, t)$ involving longitudinally polarized electron–positron beams can be represented in the form

$$\frac{d\sigma}{d\cos\theta} = \frac{3}{8}\left[(1+\cos\theta)^2\,\sigma_+ + (1-\cos\theta)^2\,\sigma_-\right], \tag{9}$$

where θ is the fermion emission angle with respect to the direction of the electron beam in the c.m. frame of the $\bar{f}f$ pair. Formula (9) is written in the approximation of $m_f \ll \sqrt{s}$. The functions $\sigma_\pm$ are expressed in terms of the helicity cross sections $\sigma_{\alpha\beta}$ as

$$\sigma_+ = \frac{1}{4}\left[(1-P_e)(1+P_{\bar{e}})\,\sigma_{LL} + (1+P_e)(1-P_{\bar{e}})\,\sigma_{RR}\right] = \frac{D}{4}\left[(1-P_{\text{eff}})\,\sigma_{LL} + (1+P_{\text{eff}})\,\sigma_{RR}\right], \tag{10}$$

$$\sigma_- = \frac{1}{4}\left[(1-P_e)(1+P_{\bar{e}})\,\sigma_{LR} + (1+P_e)(1-P_{\bar{e}})\,\sigma_{RL}\right] = \frac{D}{4}\left[(1-P_{\text{eff}})\,\sigma_{LR} + (1+P_{\text{eff}})\,\sigma_{RL}\right], \tag{11}$$

where P_e and $P_{\bar{e}}$ are the degrees of the longitudinal polarization of the electrons and positrons, respectively;

$$P_{\text{eff}} = \frac{P_e - P_{\bar{e}}}{1 - P_e P_{\bar{e}}} \tag{12}$$

is the effective polarization [25], $|P_{\text{eff}}| \leq 1$; and $D = 1 - P_e P_{\bar{e}}$. It is obvious that, for unpolarized positrons, we have $P_{\text{eff}} \to P_e$ and $D \to 1$. We also note that, for

$P_{\bar{e}} \neq 0$, the quantity $|P_{\rm eff}|$ can be greater than $|P_e|$. Additionally, the helicity cross section is given by

$$\sigma_{\alpha\beta} = N_C\, \sigma_{\rm pt} |\mathcal{M}_{\alpha\beta}|^2, \qquad (13)$$

where $\alpha, \beta = L, R$; N_C is the color factor, which is $N_C \approx 3(1 + \alpha_s/\pi)$ and $N_C = 1$ for quarks and leptons, respectively; and the electromagnetic cross section can be represented as $\sigma_{\rm pt} \equiv \sigma(e^+e^- \to \gamma^* \to l^+l^-) = (4\pi\alpha^2)/(3s)$, with α being the fine-structure constant ($\alpha = e^2/4\pi$). The helicity amplitudes $\mathcal{M}_{\alpha\beta}$ have the form

$$\mathcal{M}_{\alpha\beta} = Q_e Q_f + g^e_\alpha\, g^f_\beta\, \chi_Z + \frac{s}{4\pi\alpha}\eta_{\alpha\beta}, \qquad (14)$$

where $\chi_Z = s/(s - M_Z^2 + iM_Z\Gamma_Z)$ is the propagator for the neutral gauge boson Z, while Γ_Z and M_Z are its total decay width and mass, respectively. The normalization conditions for the chiral coupling constants of fermions in the Standard Model are taken to be $g^f_L = (I^f_{3L} - Q_f\, {\rm s}^2_{\rm W})/\,{\rm s_W\, c_W}$ and $g^f_R = -Q_f\, {\rm s}^2_{\rm W}/\,{\rm s_W\, c_W}$, where ${\rm s}^2_{\rm W} = 1 - {\rm c}^2_{\rm W} \equiv \sin^2\theta_{\rm W}$, Q_f is the electric charge of fermions, and I^f_{3L} is the weak isospin of fermions of left-hand helicity.

A further analysis is based on employing the helicity cross sections for investigating the contact interactions—these cross sections are directly related to the individual coupling constants for the interactions in (2), and it is this property that makes it possible to perform a model-independent analysis of the contact interactions, provided that the helicity cross sections are singled out experimentally. Moreover, the possibility of cancellation of effects that are induced by different parameters of the contact interactions is completely ruled out in this case.

From the practical point of view, it is necessary to perform an experiment at two different sets of polarizations $(P_e, P_{\bar{e}})$ in order to single out the helicity cross sections appearing in expressions (10) and (11). In this way, we would obtain four observables depending on the entire set of parameters of the contact interactions, and this is sufficient for extracting the helicity cross sections. For example, an experiment can be performed at $P_e = \pm P_1$ and $P_{\bar{e}} = \mp P_2$ ($P_{1,2} > 0$), in which case the polarization $P_{\rm eff} = \pm P$ reverses sign, while D does not. Solving the set of Eqs. (10) and (11), we obtain

$$\sigma_{LL} = \frac{1}{D}\left[\frac{1+P}{P}\sigma_+(-P) + \frac{1-P}{-P}\sigma_+(P)\right], \quad (15)$$

$$\sigma_{RR} = \frac{1}{D}\left[\frac{1+P}{P}\sigma_+(P) + \frac{1-P}{-P}\sigma_+(-P)\right], \quad (16)$$

$$\sigma_{LR} = \frac{1}{D}\left[\frac{1+P}{P}\sigma_-(-P) + \frac{1-P}{-P}\sigma_-(P)\right], \quad (17)$$

$$\sigma_{RL} = \frac{1}{D}\left[\frac{1+P}{P}\sigma_-(P) + \frac{1-P}{-P}\sigma_-(-P)\right]. \quad (18)$$

As follows from formulas (15)–(18), the helicity cross sections are expressed in terms of the functions $\sigma_\pm$ taken at two different values of the effective polarization. In turn, the functions $\sigma_\pm$ can be measured with the aid of two integrated cross sections that are determined in different kinematical regions—for example, the cross sections for scattering into the forward and the backward hemisphere (σ_F and σ_B, respectively). In particular, it follows from (9) that

$$\sigma_F(P,D) \equiv \int_0^1 \frac{d\sigma}{d\cos\theta} d\cos\theta = \frac{1}{8}(7\sigma_+ + \sigma_-), \quad (19)$$

$$\sigma_B(P,D) \equiv \int_{-1}^0 \frac{d\sigma}{d\cos\theta} d\cos\theta = \frac{1}{8}(\sigma_+ + 7\sigma_-). \quad (20)$$

With the aid of the equalities in (19) and (20), σ_+ and σ_- can easily be expressed in terms of the directly measurable observables σ_F and σ_B as

$$\sigma_+ = \frac{7}{6}\sigma_F(P,D) - \frac{1}{6}\sigma_B(P,D), \qquad (21)$$

$$\sigma_- = \frac{7}{6}\sigma_B(P,D) - \frac{1}{6}\sigma_F(P,D). \qquad (22)$$

Thus, the above procedure for determining the helicity cross sections is based on the use of the observables σ_F and σ_B, which are directly measurable in experiments. Indeed, the functions σ_+ and σ_- can be estimated on the basis of (21) and (22), while their linear combinations in (15)–(18) will provide information about the helicity cross sections $\sigma_{\alpha\beta}$.

It should be noted that $\sigma_\pm$ can also be expressed in terms of observables that are traditionally measured in experiments—namely, the scattering cross section σ and the forward–backward asymmetry A_{FB}. Specifically, we have

$$\sigma_+ = \frac{1}{2}\sigma(P,D)\left[1 + \frac{4}{3}A_{FB}(P,D)\right] \qquad (23)$$
$$= \frac{1}{2}\sigma(P,D) + \frac{2}{3}\sigma_{FB}(P,D),$$

$$\sigma_- = \frac{1}{2}\sigma(P,D)\left[1 - \frac{4}{3}A_{FB}(P,D)\right] \qquad (24)$$
$$= \frac{1}{2}\sigma(P,D) - \frac{2}{3}\sigma_{FB}(P,D),$$

where

$$\sigma = \sigma_+ + \sigma_- = \frac{D}{4}\left[(1 - P_{\rm eff})(\sigma_{LL} + \sigma_{LR})\right. \qquad (25)$$
$$\left. + (1 + P_{\rm eff})(\sigma_{RR} + \sigma_{RL})\right],$$

$$\sigma_{FB} \equiv \sigma A_{FB} = \sigma_F - \sigma_B = \frac{3}{4}(\sigma_+ - \sigma_-) \quad (26)$$
$$= \frac{3}{16} D\left[(1 - P_{\text{eff}})(\sigma_{LL} - \sigma_{LR}) + (1 + P_{\text{eff}})(\sigma_{RR} - \sigma_{RL})\right].$$

From (19) and (20), it follows that the observables being considered are expressed in terms of the differential cross sections. The energy distributions of these cross sections are considerably modified in shape and magnitude by radiative corrections such as those that are associated with the emission of real photons by initial electrons and positrons. The inclusion of radiative corrections in the investigation of the contact interactions was performed on the basis of the scheme proposed in [26] and realized in the ZEFIT code, which was used simultaneously with the ZFITTER code [27] at $m_t = 175$ GeV and $m_H = 100$ GeV. This code was specially adapted for analyzing the contact four-fermion interactions. In order to enhance the signal from contact four-fermion interactions, it is necessary in addition to exclude events of hard-photon emission. This was done by imposing a constraint on the photon energy, $\Delta = E_\gamma/E_{\text{beam}} = 0.9$ [26], its numerical value corresponding to the energy of a $\sqrt{s} = 0.5$ TeV linear collider.

To conclude this section, we note that there exists an alternative possibility of extracting the helicity cross sections that is based on analyzing the differential cross sections and which was investigated in [28]. However, the observables $\sigma_\pm$ are integrated characteristics and, in the case of not very large statistics, have some advantage over differential variables, yielding mathematically identical results.

3. SENSITIVITY OF OBSERVABLES AND CONSTRAINTS ON $\Lambda_{\alpha\beta}$

As was mentioned in Section 1, the present-day constraints on the scale parameter $\Lambda_{\alpha\beta}$ are about a few TeV; therefore, the contribution of the contact interactions to the amplitude (14) of the process (1) will be suppressed by a factor of $s/\Lambda^2_{\alpha\beta} \ll 1$ at future linear electron–positron colliders of energy $\sqrt{s} = 0.5$ TeV. For this reason, the contact interactions can manifest themselves only indirectly in the form of small deviations of observables from Standard Model predictions. In this case, the sensitivity of the helicity cross sections (15)–(18) for process (1) to the parameters of contact interactions can be defined as the ratio of their deviations from Standard Model predictions, $\Delta\sigma_{\alpha\beta}$, to the corresponding error in measuring the observables:

$$\mathcal{S}(\sigma_{\alpha\beta}) = \frac{|\Delta\sigma_{\alpha\beta}|}{\delta\sigma_{\alpha\beta}}. \quad (27)$$

In the limit $\sqrt{s} \ll \Lambda_{\alpha\beta}$, $\Delta\sigma_{\alpha\beta}$ is determined predominantly by the interference term:

$$\Delta\sigma_{\alpha\beta} \equiv \sigma_{\alpha\beta} - \sigma^{\text{SM}}_{\alpha\beta} \quad (28)$$
$$\simeq 2N_C\,\sigma_{\text{pt}}\left(Q_e\,Q_f + g^e_\alpha\,g^f_\beta\,\chi_Z\right)\frac{s\eta_{\alpha\beta}}{4\pi\alpha}.$$

In (28), $\delta\sigma_{\alpha\beta}$ stands for the error in measuring the helicity cross section; it involves a statistical and a systematic contribution. The expected experimental precision in determining these cross sections can be estimated with the aid of formulas (15)–(18), which determine the helicity cross sections in terms of the directly measurable integrated quantities (21) and (22). By summing the uncertainties in quadratures and neglecting, at this stage, the systematic uncertainty induced by the polarization of the electron and positron beams, we obtain

$$(\delta\sigma_{LL})^2 = \frac{49}{36}\left[\left(\frac{1-P}{PD}\right)^2(\delta\sigma_F(P,D))^2 + \left(\frac{1+P}{PD}\right)^2(\delta\sigma_F(-P,D))^2\right] + \frac{1}{36}\left[\left(\frac{1-P}{PD}\right)^2(\delta\sigma_B(P,D))^2 + \left(\frac{1+P}{PD}\right)^2(\delta\sigma_B(-P,D))^2\right], \quad (29)$$

$$(\delta\sigma_{RR})^2 = \frac{49}{36}\left[\left(\frac{1-P}{PD}\right)^2(\delta\sigma_F(-P,D))^2 + \left(\frac{1+P}{PD}\right)^2(\delta\sigma_F(P,D))^2\right] + \frac{1}{36}\left[\left(\frac{1-P}{PD}\right)^2(\delta\sigma_B(-P,D))^2 + \left(\frac{1+P}{PD}\right)^2(\delta\sigma_B(P,D))^2\right], \quad (30)$$

$$(\delta\sigma_{LR})^2 = \frac{1}{36}\left[\left(\frac{1-P}{PD}\right)^2(\delta\sigma_F(P,D))^2 + \left(\frac{1+P}{PD}\right)^2(\delta\sigma_F(-P,D))^2\right] + \frac{49}{36}\left[\left(\frac{1-P}{PD}\right)^2(\delta\sigma_B(P,D))^2 + \left(\frac{1+P}{PD}\right)^2(\delta\sigma_B(-P,D))^2\right], \quad (31)$$

$$(\delta\sigma_{RL})^2 = \frac{1}{36}\left[\left(\frac{1-P}{PD}\right)^2(\delta\sigma_F(-P,D))^2 + \left(\frac{1+P}{PD}\right)^2(\delta\sigma_F(P,D))^2\right] + \frac{49}{36}\left[\left(\frac{1-P}{PD}\right)^2(\delta\sigma_B(-P,D))^2 + \left(\frac{1+P}{PD}\right)^2(\delta\sigma_B(P,D))^2\right]. \quad (32)$$

It should be noted that the above expressions (29)–(32) for the uncertainties in the helicity cross sections do not take into account the possible correlation between the observables σ_F and σ_B. The inclusion of this correlation would lead to the loss of clarity of the relevant formulas that are required for a further analysis. At the same time, a quantitative comparison of these two cases reveals that results concerning the estimates of the lower bound on $\Lambda_{\alpha\beta}$ remain virtually unchanged.

By summing in quadratures the statistical and systematic errors for $\sigma_{F,B}$, we obtain

$$(\delta\sigma_{F,B})^2 \simeq (\delta\sigma_{F,B}^{\rm SM})^2 = \frac{\sigma_{F,B}^{\rm SM}}{\epsilon\,\mathcal{L}_{\rm int}} + \left(\delta^{\rm syst}\sigma_{F,B}^{\rm SM}\right)^2, \quad (33)$$

where $\mathcal{L}_{\rm int}$ is the integrated luminosity of the collider over the entire experimental time. In the quantitative calculations presented below, the integrated luminosity of the linear collider per year $\mathcal{L}_{\rm int}$ is set to

$$\mathcal{L}_{\rm int} = \int \mathcal{L}dt = 50,\ \ 500\ {\rm fb}^{-1}. \quad (34)$$

Additionally, we assume that, for each value $\pm P$ of the polarization, the relevant luminosity is half of its total value, $\mathcal{L}_{\rm int}/2$.

In the quantitative analysis presented below, the detection efficiency for final fermion states, ϵ, and the systematic errors $\delta^{\rm syst}$ inherent in each fermionic channel [29] are set to $\epsilon = 95\%$ and $\delta^{\rm syst} = 0.5\%$ for l^+l^- leptons pairs, $\epsilon = 60\%$ and $\delta^{\rm syst} = 1\%$ for $\bar{b}b$ quark pairs, and $\epsilon = 35\%$ and $\delta^{\rm syst} = 1.5\%$ for $\bar{c}c$ quark pairs. It is assumed that the systematic errors in the cross sections for forward and backward scattering, σ_F and σ_B, are identical. The planned characteristics of the collider and the detector correspond to the following energy and total interval of scattering angles: $\sqrt{s} = 0.5$ TeV and $|\cos\theta| \le 0.99$.

In order to take into account the effects of systematic uncertainties in measuring the helicity cross sections due to imperfections in measuring the electron and positron polarizations, δP_e and $\delta P_{\bar{e}}$, we must supplement the relevant expressions in formulas (29)–(32). It can be seen from formulas presented in Section 2 that finite values of the quantities δP_e and $\delta P_{\bar{e}}$ will directly affect the accuracy of resulting information about the cross sections $\sigma_{\alpha\beta}$ through the polarization coefficients in equalities (15)–(18), (21), and (22) and through the dependence of $\sigma_{F,B}$ on P and D. All the aforesaid can be represented schematically in the form

$$(\delta\sigma_{\alpha\beta})^2 \to (\delta\sigma_{\alpha\beta})^2 + \left(\delta\sigma_{\alpha\beta}^{\rm pol}\right)^2, \quad (35)$$

where

$$\left(\delta\sigma_{LL}^{\rm pol}\right)^2 = [f(P,D)(1+P_{\bar{e}}P^2) - f(-P,D)(1-P_{\bar{e}}P^2)]^2\left(\frac{\delta P_e}{D^2P^2}\right)^2 + [f(P,D)(1-P_eP^2) - f(-P,D)\times(1+P_eP^2)]^2\left(\frac{\delta P_{\bar{e}}}{D^2P^2}\right)^2, \quad (36)$$

$$\left(\delta\sigma_{LR}^{\rm pol}\right)^2 = [f'(P,D)(1+P_{\bar{e}}P^2) - f'(-P,D)(1-P_{\bar{e}}P^2)]^2\left(\frac{\delta P_e}{D^2P^2}\right)^2 + [f'(P,D)(1-P_eP^2) - f'(-P,D)\times(1+P_eP^2)]^2\left(\frac{\delta P_{\bar{e}}}{D^2P^2}\right)^2,$$

$$\left(\delta\sigma_{RR}^{\rm pol}\right)^2 = [f(P,D)(1-P_{\bar{e}}P^2) - f(-P,D)(1+P_{\bar{e}}P^2)]^2\left(\frac{\delta P_e}{D^2P^2}\right)^2 + [f(P,D)(1+P_eP^2) - f(-P,D)\times(1-P_eP^2)]^2\left(\frac{\delta P_{\bar{e}}}{D^2P^2}\right)^2,$$

$$\left(\delta\sigma_{RL}^{\rm pol}\right)^2 = [f'(P,D)(1-P_{\bar{e}}P^2) - f'(-P,D)(1+P_{\bar{e}}P^2)]^2\left(\frac{\delta P_e}{D^2P^2}\right)^2 + [f'(P,D)(1+P_eP^2) - f'(-P,D)\times(1-P_eP^2)]^2\left(\frac{\delta P_{\bar{e}}}{D^2P^2}\right)^2$$

with

$$f(P,D) = \frac{7}{6}\sigma_F(P,D) - \frac{1}{6}\sigma_B(P,D), \quad (37)$$

$$f'(P,D) = -\frac{1}{6}\sigma_F(P,D) + \frac{7}{6}\sigma_B(P,D). \quad (38)$$

Table 2. Model-independent constraints on the parameter $\Lambda_{\alpha\beta}$ (at a 95% C.L.) that were obtained from the helicity cross sections measured at an $E_{\text{c.m.}} = 0.5$ TeV, $\mathcal{L}_{\text{int}} = 50\,\text{fb}^{-1}$ linear electron–positron collider employing a longitudinally polarized electron beam and an unpolarized positron beam ($P_{\bar{e}} = 0$; $\delta P_e/P_e = 0.5\%$)

Process	P	Λ_{RR}, TeV	Λ_{LL}, TeV	Λ_{RL}, TeV	Λ_{LR}, TeV
$e^+e^- \to \mu^+\mu^-$	1.0	42.6	42.3	38.7	38.0
	0.9	41.3	41.3	37.7	37.0
	0.5	33.4	34.2	30.8	30.5
$e^+e^- \to \bar{b}b$	1.0	48.4	45.1	44.7	34.8
	0.9	44.9	44.6	42.6	34.2
	0.5	31.4	39.5	31.7	29.6
$e^+e^- \to \bar{c}c$	1.0	39.1	36.0	28.9	32.8
	0.9	37.4	35.4	27.3	32.2
	0.5	28.3	30.4	19.1	27.6

Table 3. Model-independent constraints on the parameter $\Lambda_{\alpha\beta}$ (at a 95% C.L.) that were obtained from the helicity cross sections measured at an $E_{\text{c.m.}} = 0.5$ TeV, $\mathcal{L}_{\text{int}} = 500\,\text{fb}^{-1}$ linear electron–positron collider employing a longitudinally polarized electron beam and an unpolarized positron beam ($P_{\bar{e}} = 0$; $\delta P_e/P_e = 0.5\%$)

Process	P	Λ_{RR}, TeV	Λ_{LL}, TeV	Λ_{RL}, TeV	Λ_{LR}, TeV
$e^+e^- \to \mu^+\mu^-$	1.0	61.3	59.8	61.2	59.6
	0.9	59.4	58.4	59.5	58.1
	0.5	47.8	48.6	48.4	47.9
$e^+e^- \to \bar{b}b$	1.0	65.6	54.3	72.4	48.9
	0.9	60.9	53.9	68.5	48.3
	0.5	41.0	49.0	49.7	42.5
$e^+e^- \to \bar{c}c$	1.0	47.3	40.7	42.3	42.4
	0.9	45.0	40.1	39.8	41.8
	0.5	33.3	34.9	28.0	36.6

In our quantitative analysis, the polarization of initial beams was set to $|P_e| = 0.9$ ($\delta P_e/P_e = 0.5\%$) in estimating the constraints on $\Lambda_{\alpha\beta}$. It is precisely the accuracy in the measurement of the electron polarization that was achieved at the SLAC collider [30]. As concerns the positron polarization, two cases will be considered here: (i) that of unpolarized positrons ($|P_{\bar{e}}| = 0$) and (ii) that of longitudinally polarized positrons with $|P_{\bar{e}}| = 0.6$ [31]. We have the effective polarization of $P_{\text{eff}} = P$ in the first case and $P_{\text{eff}} = P = 0.974$ and $D = 1.54$ in the second case. No reliable estimates of the parameter $\delta P_{\bar{e}}$ have been obtained so far—it is only known definitively that it must be poorer than the corresponding electron characteristic. For the above reasons, the value of $\delta P_{\bar{e}}/P_{\bar{e}} = 1\%$ is adopted for the ensuing analysis. In some cases, however, the quantity $\delta P_{\bar{e}}/P_{\bar{e}}$ is varied in a rather wide interval for investigating this dependence more precisely.

In estimating the potential of linear electron–positron colliders in searches for effects of nonstandard physics beyond the Standard Model, such as contact four-fermion interactions, it is important to develop a procedure for treatment and analysis of experimental data. In many respects, it depends on a number of factors associated with details of specific experiments and on the physical and technological characteristics of accelerator facilities and detectors. Even without this experimental information, however, a preliminary estimate can be obtained for the sensitivity of observables of process (1) to the parameters of contact four-fermion interactions. One of the standard procedures for calculations of this kind is based on the analysis of the functions χ^2 defined as [32]

$$\chi^2 = \left(\frac{\Delta\sigma_{\alpha\beta}}{\delta\sigma_{\alpha\beta}}\right)^2, \tag{39}$$

which characterize manifestations of new interactions.

In setting constraints on the parameters of the contact four-fermion interactions, we proceed from the assumption that the results of (future) experiments aimed at measuring observables of process (1) are in agreement with Standard Model predictions within the expected accuracy of measurements. In this case, the requirement imposed on the function in (39) and expressed in the form of the inequality

$$\chi^2 < \chi^2_{\text{C.L.}} \tag{40}$$

makes it possible to determine the allowed region of the parameters of the contact four-fermion interactions. Here, $\chi^2_{\text{C.L.}}$ is a number that is specified by a preset confidence level. As follows from formula (28), the deviation $\Delta\sigma_{\alpha\beta}$ depends only on one effective parameter of the contact interactions; therefore, the value of $\chi^2_{\text{C.L.}} = 3.84$, which corresponds to a confidence level of 95% [32], is adopted in this analysis.

Tables 2 and 3 display model-independent constraints on the scale parameter $\Lambda_{\alpha\beta}$ that were obtained from the processes $e^+e^- \to \mu^+\mu^-$, $e^+e^- \to \bar{b}b$, and $e^+e^- \to \bar{c}c$ with an unpolarized positron beam

at the integrated luminosity of 50 and 500 fb^{-1}, respectively. It can be seen that the helicity cross sections are very sensitive to the parameters of the contact four-fermion interactions. For example, the lower bound on the parameter $\Lambda_{\alpha\beta}$ at $\mathcal{L}_{\rm int} = 500$ fb^{-1} falls within the interval whose width is greater by a factor of 50 to 140 than the energy of the linear collider being considered. The production of $\bar{b}b$ pairs and $e^+e^- \to \bar{c}c$ are processes that exhibit, respectively, the highest and the lowest sensitivity. The decrease in the electron polarization from $P = 1$ to $P = 0.5$ leads to a decrease of 10–40% in the sensitivity, its specific value being dependent on the final state. At the same time, the cross sections σ_{LL} and σ_{LR} for the production of quark pairs are the least prone to such effects.

In the case where the statistical error in measuring observables is much greater than the systematic error, the improvement of the sensitivity in response to the growth of the luminosity from 50 to 500 fb^{-1} obeys the scaling law $\Lambda'_{\alpha\beta} = (\mathcal{L}'_{\rm int}/\mathcal{L}_{\rm int})^{1/4}\Lambda_{\alpha\beta}$, whence it follows that the lower bound on $\Lambda_{\alpha\beta}$ would then increase by a factor of about 1.8. However, a comparison of data in Tables 2 and 3 shows that this rule is satisfied very roughly and only for LR and RL helicity configurations, for which the statistical error is much greater than the systematic one. For the RR and LL combinations, the improvement of the sensitivity to $\Lambda_{\alpha\beta}$ with increasing luminosity $\mathcal{L}_{\rm int}$ is not so significant because of a relatively large contribution of the systematic errors. The dependence of the limiting values of $\Lambda_{\alpha\beta}$ on the energy, integrated luminosity, and statistical and systematic uncertainties can be expressed by the compact formula

$$\Lambda_{\alpha\beta} \sim (\mathcal{L}_{\rm int} \times s)^{1/4}\left[1 + \left(\delta^{\rm syst}/\delta^{\rm stat}\right)^2\right]^{-1/4}. \quad (41)$$

Let us now discuss the role of the positron polarization in studying the effects of the contact interactions. From (9)–(11), it follows that, if the polarization configuration is chosen in such a way that $P_eP_{\bar{e}} < 0$, then $D > 1$ and $|P_{\rm eff}| > \max(|P_e|, |P_{\bar{e}}|)$. This means that an improvement of the sensitivity of observables to the contact interactions at a fixed luminosity could be expected on the basis of statistical arguments alone. At the same time, the inclusion of a positron polarization leads to an increase in the total systematic errors because of an uncertainty of the type $\delta P_{\bar{e}}/P_{\bar{e}}$. These two factors affect the sensitivity to observables differently, but the calculations show that it is improved in the majority of the cases. Table 4 presents the lower bounds on the parameter $\Lambda_{\alpha\beta}$ for two situations, that where only the electrons are polarized (the positrons are unpolarized) and that where both beams are polarized. In the majority of the cases, the presence of a positron polarization leads to an increase in the lower bound on $\Lambda_{\alpha\beta}$; only for some of them—namely, for the of production of lepton pairs at a luminosity of 500 fb^{-1} that have the RR and LL configurations and also for the process $e^+e^-_L \to \bar{b}b_L$—does the limiting value in question decrease. This occurs because, in the helicity cross sections, the systematic error induced by the factor $\delta P_{\bar{e}}/P_{\bar{e}}$ increases significantly in relation to the statistical uncertainty.

It is also instructive to compare, at various values of the parameter $\delta P_{\bar{e}}/P_{\bar{e}}$, the sensitivities in (27) for process (1) to the contact interactions for the above two cases, where the electron and positron beams are polarized, $\mathcal{S}(P_e, P_{\bar{e}})$, and where only the electron beam is polarized, $\mathcal{S}(P_e, 0)$. A comparison of these characteristics is illustrated graphically in Figs. 1–3 and in Figs. 4–6 in the form of the functional dependence of the ratio of the sensitivities on the quantity $\delta P_{\bar{e}}/P_{\bar{e}}$ at the luminosities of 50 and 500 fb^{-1}, respectively. It can be seen from Figs. 1–6 that, for $\delta P_{\bar{e}}/P_{\bar{e}} \approx \delta P_e/P_e = 0.5\%$, the advantage of the positron polarization manifests itself in the improvement of the sensitivity of the process up to 50%. With increasing $\delta P_{\bar{e}}/P_{\bar{e}}$, however, this ratio decreases and, at some values of $\delta P_{\bar{e}}/P_{\bar{e}}$, becomes less than unity. Hence, the advantage provided by the positron polarization disappears completely in this case. The region of $\delta P_{\bar{e}}/P_{\bar{e}}$ values where the inclusion of a positron polarization leads to the improvement of the sensitivity lies in the interval from 0.5% to a few tens of percent. Thus, an insignificant growth of the uncertainty in the positron polarization ($\delta P_{\bar{e}}/P_{\bar{e}} > 0.5\%$) annihilates the effect of improvement of the sensitivity. At the same time, the sensitivity of the cross section σ_{RL} is virtually independent of the parameter $\delta P_{\bar{e}}/P_{\bar{e}}$. From a comparison of the data in Figs. 1–3 with those in Figs. 4–6, we can deduce that, at the luminosity of 500 fb^{-1}, the role of systematic error becomes dominant. This is the reason why, at a high luminosity, the lower bound on the parameter $\Lambda_{\alpha\beta}$ becomes highly sensitive to the input parameters that determine the systematic error.

It should be noted that the data in Figs. 1–6 and in Tables 2 and 3 make it possible to set constraints on $\Lambda_{\alpha\beta}$ for any values of the parameter $\delta P_{\bar{e}}/P_{\bar{e}}$. The formula necessary for this has the form

$$\Lambda_{\alpha\beta}(P_e, P_{\bar{e}}) \approx \sqrt{\mathcal{S}(P_e, P_{\bar{e}})/\mathcal{S}(P_e, 0)}\,\Lambda_{\alpha\beta}(P_e, 0). \quad (42)$$

It was obtained by expanding the deviation $\Delta\sigma_{\alpha\beta}$ in the small parameter $s\eta_{\alpha\beta}/e^2$ and by retaining only linear terms. The linear approximation ensures a rather high precision of formula (42) in determining

Table 4. Model-independent constraints on the parameter $\Lambda_{\alpha\beta}$ at a 95% C.L. that were obtained from the helicity cross sections at $E_{\text{c.m.}} = 0.5$ TeV, $P_e = 0.9$, $\delta P_e/P_e = 0.5\%$, $P_{\bar{e}} = 0.6$, and $\delta P_{\bar{e}}/P_{\bar{e}} = 1.0\%$ [the arrows indicate the change in the sensitivity of observables in going over from unpolarized to polarized positrons: $(P_e, 0) \to (P_e, P_{\bar{e}})$]

Process	$\mathcal{L}_{\text{int}}$, fb^{-1}	Λ_{RR}, TeV	Λ_{LL}, TeV	Λ_{RL}, TeV	Λ_{LR}, TeV
$e^+e^- \to \mu^+\mu^-$	50	41.3 → 45.0	41.3 → 44.5	37.7 → 42.3	37.0 → 41.5
	500	59.4 → 58.4	58.4 → 56.2	59.5 → 63.0	58.1 → 61.4
$e^+e^- \to \bar{b}b$	50	44.9 → 53.2	44.6 → 46.9	42.6 → 48.9	34.2 → 37.6
	500	60.9 → 73.6	53.9 → 53.3	68.5 → 75.5	48.3 → 50.3
$e^+e^- \to \bar{c}c$	50	37.4 → 40.9	35.4 → 37.0	27.3 → 31.4	32.2 → 35.1
	500	45.0 → 46.9	40.1 → 40.2	39.8 → 43.2	41.8 → 43.0

the constraints on $\Lambda_{\alpha\beta}$. In particular, it is straightforward to reproduce Table 4 for $\delta P_{\bar{e}}/P_{\bar{e}} = 1\%$ with the aid of (42) and Figs. 1–6.

Finally, we address the problem of comparing the model-independent constraints obtained on the basis of the helicity cross sections with the corresponding estimates following from the analysis of observables that are traditionally measured in experiments and which are hereafter referred to as canonical observables. In what is concerned with the problem of choosing canonical observables, it is necessary to consider that the number of independent observables corresponds to the number of different spin configurations of the initial and final states of process (1), the latter number being determined by the helicity-conservation law. For massless initial and final fermions, there are only four such configurations. By way of example, we choose the independent observables as follows. For unpolarized e^+e^- beams ($P_e = P_{\bar{e}} = 0$), these are the scattering cross section (25) and the forward–backward asymmetry (26). The presence of a longitudinal polarization of the electron beam in the case of an unpolarized positron beam ($P_{\bar{e}} = 0$) makes it possible to supplement this list by including two polarization asymmetries in it. The first is the left–right asymmetry

$$A_{LR} = \frac{\sigma_L - \sigma_R}{\sigma_L + \sigma_R}, \tag{43}$$

where σ_L and σ_R are the cross sections for electrons having, respectively, a left- and a right-hand circular polarization in the case of unpolarized positrons. For the last observable in this list, we can take the polar-

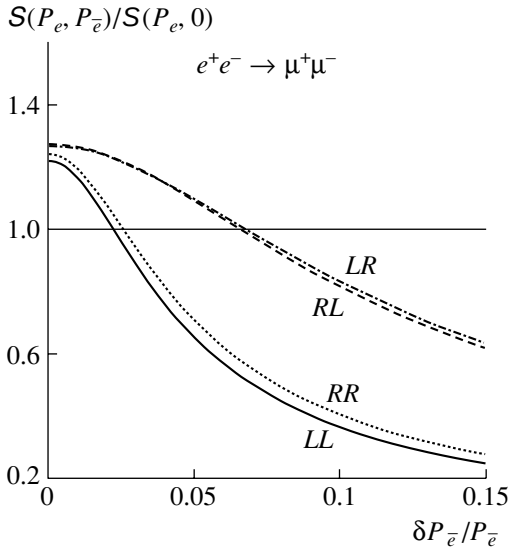

Fig. 1. Ratio $\mathcal{S}(P_e, P_{\bar{e}})/\mathcal{S}(P_e, 0)$ of the sensitivities of the helicity cross sections for the process $e^+e^- \to \mu^+\mu^-$ to the contact interactions as a function of $\delta P_{\bar{e}}/P_{\bar{e}}$ at $\mathcal{L}_{\text{int}} = 50\,\text{fb}^{-1}$, $P_e = 0.9$, $\delta P_e/P_e = 0.5\%$, and $P_{\bar{e}} = 0.6$. The corresponding helicity configurations are indicated on the curves.

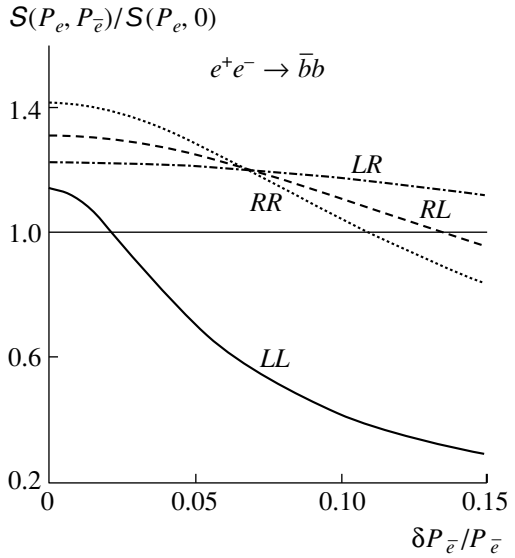

Fig. 2. As in Fig. 1, but for the process $e^+e^- \to \bar{b}b$.

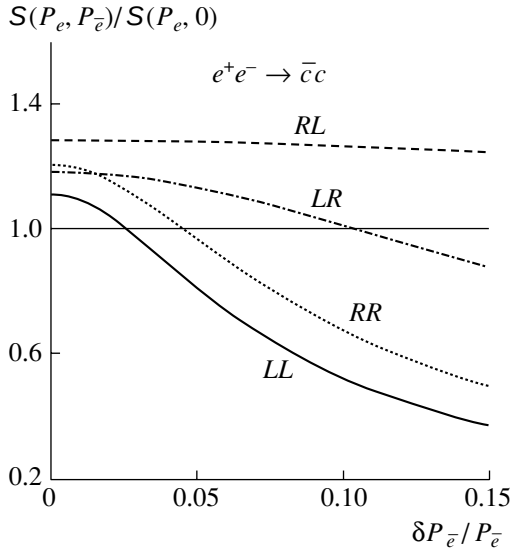

Fig. 3. As in Fig. 1, but for the process $e^+e^- \to \bar{c}c$.

ization forward–backward asymmetry

$$A_{FB}^{\rm pol} = \frac{(\sigma_L^F - \sigma_R^F) - (\sigma_L^B - \sigma_R^B)}{(\sigma_L^F + \sigma_R^F) + (\sigma_L^B + \sigma_R^B)}. \qquad (44)$$

Under the assumption of e–l universality in the lepton process (1), the number of independent observables is reduced by one owing to the relation $\mathcal{M}_{LR} = \mathcal{M}_{RL}$ between the relevant amplitudes. However, it is necessary to take into account the complete set of observables for the production of quark pairs.

It should be emphasized that, for linear colliders, there are presently no data on model-independent constraints on the contact interactions from the canonical observables in the general form. Indeed, such an analysis is nontrivial from the practical point of view, since each canonical observable depends on the entire set of parameters (there are four of them). We did not aim here at deriving a general solution to this problem. In order to obtain the required information, we can adopt, however, a traditional way that is described in the literature and which is based on considering the dependence of the canonical observables only on one parameter of the contact interactions, the remaining parameters then being set to zero. Obviously, the limits on $\Lambda_{\alpha\beta}$ from such an analysis will be greater than those that would follow from a general analysis, since the one-parameter dependence of observables completely rules out the possibility of an accidental cancellation of effects induced by different contact interactions. Nevertheless, such a possibility cannot be excluded either, since any of these could be realized in nature. For the canonical observables denoted in the following by $\mathcal{O}_i = \sigma,\ A_{FB},\ A_{LR}$, and $A_{LR,FB}$, the function χ^2 is constructed in the form

$$\chi^2 = \sum_i \left(\frac{\mathcal{O}_i - \mathcal{O}_i(\mathrm{SM})}{\delta\mathcal{O}_i(\mathrm{SM})} \right)^2, \qquad (45)$$

where the index i runs through the entire set of the observables and $\delta\mathcal{O}_i(\mathrm{SM})$ is the expected experimental error for each observable $\mathcal{O}_i(\mathrm{SM})$ in the Standard Model. The statistical uncertainties in the cross section and in the forward–backward asymmetry can be

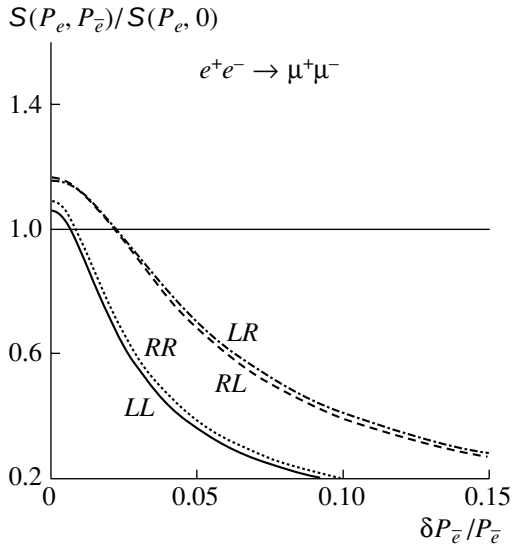

Fig. 4. As in Fig. 1, but for $\mathcal{L}_{\rm int} = 500\,\mathrm{fb}^{-1}$.

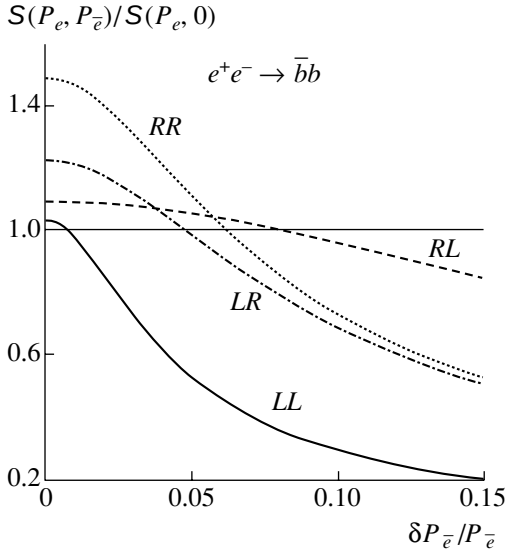

Fig. 5. As in Fig. 1, but for the process $e^+e^- \to \bar{b}b$ at $\mathcal{L}_{\rm int} = 500\,\mathrm{fb}^{-1}$.

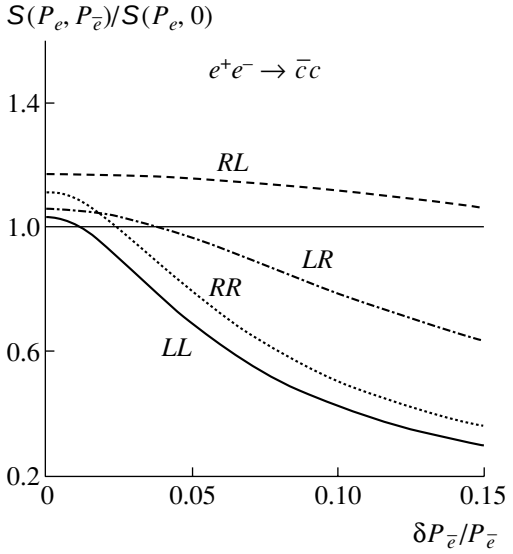

Fig. 6. As in Fig. 1, but for the process $e^+e^- \to \bar{c}c$ at $\mathcal{L}_{\rm int} = 500\,{\rm fb}^{-1}$.

represented in the form

$$\frac{\delta\sigma}{\sigma} = \frac{1}{\sqrt{N}}, \qquad \delta A_{FB} = \sqrt{\frac{1 - A_{FB}^2}{N}}, \qquad (46)$$

where $N = \epsilon\,\mathcal{L}_{\rm int}\,\sigma(P_e = P_{\bar{e}} = 0)$. The total error in σ, including the statistical and the systematic contribution, has the same form as the expression in (33) at $\delta^{\rm syst} = 0.5\%$. As is well known from [25], the systematic error in A_{FB} is extremely small because the corresponding contributions in the numerator and the denominator are canceled almost completely. For the left–right asymmetry A_{LR} (and for the left–right forward–backward asymmetry $A_{LR,FB}$ as well), the total experimental uncertainty, which includes the statistical and systematic errors in quadratures, is given by

$$\delta A_{LR} = \sqrt{\frac{1 - (P_{\rm eff} A_{LR})^2}{P_{\rm eff}^2 N_P} + A_{LR}^2 \left(\frac{\delta P_{\rm eff}}{P_{\rm eff}}\right)^2}, \quad (47)$$

where the equality $N_P = DN$ follows from the assumption that events are measured for the same exposure time at $P_e = 0.9$ and $P_{\bar{e}} = -0.6$ and at $P_e = -0.9$ and $P_{\bar{e}} = 0.6$. As above, it is additionally assumed that $\delta P_e/P_e = 0.5\%$ and $\delta P_{\bar{e}}/P_{\bar{e}} = 1\%$. The resulting constraints at a 95% C.L. are presented in Table 5. They should be compared with the constraints derived on the basis of the helicity cross sections (Table 4). We can see that the constraints on $\Lambda_{\alpha\beta}$ differ most strongly at a luminosity of 50 fb^{-1}, the respective difference being a few TeV to 10 TeV for the RR and LL configurations. For the off-diagonal helicity configurations LR and RL, this difference is even more pronounced and, in some cases, is as large as 15 TeV for the scale $\Lambda_{\alpha\beta}$. At the higher luminosity of 500 fb^{-1}, the distinctions between the limiting values of the scales Λ_{LL} and Λ_{RR} become less significant and, in some cases (for example, in the production of c-quark pairs), disappear completely. For the LR and RL configurations, this difference of $\Lambda_{\alpha\beta}$ values continues increasing and, for some processes, exceeds 20 TeV.

Table 5. Model-dependent constraints on the parameter $\Lambda_{\alpha\beta}$ (at a 95% C.L.) that were obtained from the canonical observables σ, A_{FB}, A_{LR}, and $A_{LR,FB}$ at $P_e = 0.9$, $\delta P_e/P_e = 0.5\%$, $P_{\bar{e}} = 0.6$, and $\delta P_{\bar{e}}/P_{\bar{e}} = 1.0\%$ by varying one parameter of the contact interactions, with the remaining parameters being set to zero

Process	$\mathcal{L}_{\rm int}$, fb^{-1}	Λ_{RR}, TeV	Λ_{LL}, TeV	Λ_{RL}, TeV	Λ_{LR}, TeV
$e^+e^- \to \mu^+\mu^-$	50	33.4	33.6	25.5	24.8
	500	49.7	48.9	38.4	37.6
$e^+e^- \to \bar{b}b$	50	42.2	38.1	39.1	27.3
	500	62.3	50.0	43.8	37.4
$e^+e^- \to \bar{c}c$	50	35.5	32.4	19.6	26.0
	500	46.2	40.1	24.8	31.2

4. CONCLUSIONS

Let us summarize our conclusions and list the most important results obtained from a model-independent analysis of the contact four-fermion interactions at linear electron–positron colliders employing longitudinally polarized beams.

(i) A general approach has been developed for separating the helicity cross sections for the process $e^+e^- \to \bar{f}f$ on the basis of new integrated observables constructed from the polarization cross sections σ_F and σ_B for fermion scattering into the forward and the backward hemisphere, respectively.

(ii) By using the properties of the helicity cross sections—that is the fact that they depend only on one parameter of the contact interactions—we have performed a model-independent analysis and set constraints on the parameters of the interactions being considered.

(iii) The constraints on the parameter $\Lambda_{\alpha\beta}$ have been investigated in detail as functions of the systematic errors introduced by the corresponding uncertainties in the longitudinal polarization of electrons and positrons. The regions of $\delta P_{\bar{e}}/P_{\bar{e}}$ have been found where the presence of a positron polarization leads to an improvement of the sensitivity of observables in

relation to that in the case where only the electron beam is polarized.

(iv) We have performed a comparative analysis of the constraints on the parameters $\Lambda_{\alpha\beta}$ from the new observables and from the canonical variables (σ, A_{FB}, A_{LR}, and $A_{LR,FB}$). A comparison of their sensitivities demonstrates a noticeable advantage of the former over the latter for the majority of the cases.

ACKNOWLEDGMENTS

I am grateful to A.A. Babich and N. Paver for stimulating discussions and enlightening comments.

REFERENCES

1. Gargamelle Collab. (F. J. Hasert *et al.*), Phys. Lett. B **46B**, 138 (1973).
2. J. Erler and P. Langacker, in *Proceedings of the 5th International Wein Symposium: A Conference on Physics Beyond the Standard Model (WEIN 98), Santa Fe, 1998*.
3. D. Abbaneo *et al.*, Preprint CERN-EP-2000-016 (2000).
4. A. Gurtu, *Talk at the XXX International Conference on High Energy Physics, Osaka, Japan, 2000*.
5. E. J. Eichten, K. D. Lane, and M. E. Peskin, Phys. Rev. Lett. **50**, 811 (1983).
6. R. J. Cashmoreet *et al.*, Phys. Rep. **122**, 275 (1985); R. Rückl, Phys. Lett. B **129B**, 363 (1983).
7. P. Haberl, F. Schrempp, and H.-U. Martyn, in *Proceedings of "Physics at HERA," Hamburg, 1991*, Vol .2, p. 1133.
8. H. Kroha, Phys. Rev. D **46**, 58 (1992).
9. K. Cheung, S. Godfrey, and J. A. Hewett, in *Proceedings of the 1996 DPF/DPB Summer Study on New Directions for High Energy Physics (Snowmass 96)*, Ed. by D. G. Cassel, L. Trindle Gennari, and R. H. Siemann (SLAC, Stanford, 1997), p. 989.
10. V. Barger, K. Cheung, K. Hagiwara, and D. Zeppenfeld, Phys. Rev. D **57**, 391 (1998).
11. V. Barger, K. Cheung, K. Hagiwara, and D. Zeppenfeld, Phys. Lett. B **404**, 147 (1997).
12. D. Zeppenfeld and K. Cheung, Preprint MADPH-98-1081 (1998).
13. A. A. Babich, A. A. Pankov, and N. Paver, Phys. Lett. B **452**, 355 (1999).
14. J. Kalinowski, R. Rückl, H. Spiesberger, and P. Zerwas, Phys. Lett. B **406**, 314 (1997).
15. T. G. Rizzo, Preprint SLAC-PUB-7982 (1998).
16. J. A. Valls, Preprint FERMILAB-Conf-97/135-E (1997).
17. P. Abreu *et al.*, Preprint CERN-EP/2000-068 (2000); K. Cieślik *et al.*, Preprint DELPHI 2000-038 CONF 356 (2000); Preprint DELPHI 2000-129 CONF 428 (2000); A. Behrmann *et al.*, Preprint DELPHI 2000-036 CONF 355 (2000); P. Abreu *et al.*, Eur. Phys. J. C **11**, 383 (2000); A. Behrmann *et al.*, Preprint DELPHI 99-58 CONF 247 (1999).
18. V. Barger, K. Cheung, P. D. Roy, and D. Zeppenfeld, Phys. Rev. D **57**, 3833 (1998).
19. V. Barger and K. Cheung, Phys. Lett. B **480**, 149 (2000).
20. V. Barger *et al.*, Phys. Lett. B **478**, 224 (2000).
21. A. A. Pankov and N. Paver, Phys. Lett. B **432**, 159 (1998).
22. A. A. Babich, P. Osland, A. A. Pankov, and N. Paver, Phys. Lett. B **476**, 95 (2000); **481**, 263 (2000).
23. P. Osland and A. A. Pankov, Phys. Lett. B **403**, 93 (1997); **406**, 328 (1997).
24. A. A. Pankov, Yad. Fiz. **63**, 940 (2000) [Phys. At. Nucl. **63**, 870 (2000)].
25. K. Flöttmann, Preprint DESY 95-064 (1995); K. Fujii and T. Omori, KEK preprint 95-127 (1995); T. Omori, KEK preprint 98-237 (1998).
26. A. Djouadi *et al.*, Z. Phys. C **56**, 289 (1992).
27. S. Riemann, FORTRAN program ZEFIT Version 4.2; D. Bardin *et al.*, Preprint DESY 99-070 (1999).
28. J.-M. Frère, V. A. Novikov, and M. I. Vysotsky, Phys. Lett. B **386**, 437 (1996).
29. C. Damerell and D. J. Jackson, in *Proceedings of the 1996 DPF/DPB Summer Study on New Directions for High Energy Physics (Snowmass 96)*, Ed. by D. G. Cassel, L. Trindle Gennari, and R. H. Siemann (SLAC, Stanford, 1997), p. 442.
30. M. Swartz, in *Proceedings of the 19th International Symposium on Lepton and Photon Interactions at High Energies (LP 99), Stanford, 1999*.
31. E. Accomando *et al.*, Phys. Rep. **299**, 1 (1998).
32. Particle Data Group (D. E. Groom *et al.*), Eur. Phys. J. C **15**, 191 (2000).

Translated by A. Isaakyan

Physics of Atomic Nuclei, Vol. 65, No. 3, 2002, pp. 534–538. Translated from Yadernaya Fizika, Vol. 65, No. 3, 2002, pp. 561–565.

ELEMENTARY PARTICLES AND FIELDS
Theory

Electroweak Pion–Nucleon Constant

G. A. Lobov

Institute of Theoretical and Experimental Physics,
Bol'shaya Cheremushkinskaya ul. 25, Moscow, 117259 Russia

Received April 18, 2001; in final form, July 18, 2001

Abstract—The parity-violating pion–nucleon coupling constant for the neutral currents of electroweak interaction is calculated by the method of QCD sum rules. In doing this, operators up to dimension 5 are retained in the operator-product expansion for the correlation function in an external pion field. That the value obtained for the pion–nucleon coupling constant is comparatively small stems from a partial cancellation between the leading perturbative and condensate contributions. This constant is compared with experimental data and with the results of calculations performed by other authors.

1. INTRODUCTION

The electroweak interactions of hadrons at low energies—in particular, parity-violating nuclear interactions—present problems that have received the least adequate study in electroweak theory [1]. In this theory, the electroweak interactions of hadrons at low energies are described by the sum of the products of neutral and charged currents [2]. Neutral currents are associated with Z-boson exchange between quarks, while charged currents are associated with the exchange of $W^{\pm}$ bosons. However, the contributions of neutral currents to hadronic reactions have not yet been observed experimentally. An upper limit on the pion–nucleon constant f for the neutral currents ($f \leq 2.2 \times 10^{-7}$) was obtained from the experimental investigation [3] of the P-odd circular polarization of photons in the transition from the 0^+ excited level to the 1^+ ground state in the ^{18}F nucleus. This limit on the constant f is at least one-half as great as the "best value" obtained from the analysis of a vast body of experimental data within the quark model of hadrons [4].

The electroweak nucleon–nucleon interaction is usually described in terms of the exchange of the extremely light mesons π, ρ, and ω between interacting nucleons [1, 5]. This approach was developed by analogy with the one-boson-exchange model of strong interactions between nucleons. In contrast to the case of strong interactions, diagrams for the electroweak nucleon–nucleon interaction involve only one strong-interaction vertex rather than two. The other vertex is determined by the electroweak interaction. It should be recalled that CP invariance rules out any exchange of a neutral pseudoscalar meson—in particular, the exchange of a π^0 meson. The point is that, in a CP-invariant theory, one cannot construct a P-odd and C-odd vertex because of the positive C parity of a neutral pseudoscalar meson. Thus, the interactions between nucleons in a CP-invariant theory of electroweak interactions can be mediated only by charged $\pi^{\pm}$ mesons. At the quark level, the electroweak vertex involving $\pi^{\pm}$-meson exchange is completely determined by Z-boson exchange between the quarks of a nucleon; that is, the electroweak vertex is determined completely by electroweak neutral currents. Since the pions are the lightest mesons, the nucleon–nucleon potential arising from the exchange of $\pi^{\pm}$ mesons is the most far-range potential among those caused by one-boson (ρ, ω) exchange.

The constants of the electroweak potentials arising from the exchange of the vector mesons ρ and ω can be reliably calculated within the quark model by using the formalism of vector-meson dominance [6]. These constants are about 10^{-7}–10^{-6}, and the respective potentials are short-range because of relatively large masses of the vector mesons in relation to the pseudoscalar-pion mass.

Thus, the values of the electroweak pion–nucleon constants deduced from a comprehensive analysis of P-odd effects [4] disagree with those obtained from a "direct" experiment with the ^{18}F nucleus [3].

The present study is devoted to consistently computing the electroweak pion–nucleon coupling constant on the basis of QCD sum rules [7, 8]. This method makes it possible to calculate the quantities characterizing the properties of nucleons in terms of quantities characterizing the QCD ground state. In particular, the nucleon mass [8] and the anomalous magnetic moments of nucleons [9] were evaluated by

1063-7788/02/6503-0534$22.00

this method. The QCD sum rules were successfully used in calculating the masses and leptonic decay widths of mesons. This method also yields various relations between a great many observables and makes it possible to predict some of them by using only a small number of parameters, which include, above all, vacuum expectation values of some quark and gluon operators.

In what follows, we calculate the electroweak pion–nucleon constant using the QCD sum rules. A detailed description of the method used can be found in [10, 11].

2. POLARIZATION OPERATOR

The basic quantity in our calculations is the polarization operator (two-point correlation function) in an external pion field. It is defined as

$$\Pi = i\int d^4x e^{ipx}\langle 0 \mid T\{\eta_p(x),\overline{\eta}_n(0)\} \mid 0\rangle_{\pi^+}, \quad (1)$$

where the currents η are the color-singlet products of three quark fields featuring quantum numbers of the proton and the neutron:

$$\eta_p = u^a C\gamma_\mu u^b \gamma_5\gamma_\mu d^c \varepsilon^{abc}, \quad (2)$$

$$\eta_n = d^a C\gamma_\mu d^b \gamma_5\gamma_\mu u^c \varepsilon^{abc}. \quad (3)$$

Here, u and d are quark fields; a, b, and c are color indices; and C is the charge-conjugation operator. The polarization operator (1) describes the transition $n \to p + \pi^-$ (or $p \to n + \pi^+$), since the current $\bar{\eta}_n$ creates a neutron, which interacts with the charged-pion field and which is then annihilated by the current η_p. In the calculation of the pion–nucleon coupling constant, a major contribution to the polarization operator (1) comes from the diagram where one of the quarks interacts with the quark–antiquark system (charged pion) and where the remaining two quarks undergo electroweak interaction mediated by the exchange of a neutral Z boson. The other diagrams, including those describing the interactions of the charged electroweak currents through the exchange of $W^\pm$ bosons, either make no contribution, or their contributions cancel one another.

This conclusion was deduced from a rather cumbersome analysis, which did not result in obtaining some explicit formula that would prove the cancellations in question. Nevertheless, the basic mechanism responsible for these cancellations could be revealed: the processes of emission or absorption of charged pions by one of the quarks in the nucleon competes with the exchange of W bosons between the quarks; therefore, the respective diagrams either are forbidden or cancel each other.

In the present study, we make use of the polarization operator (1) in an external pion field at zero pion 4-momentum. In order to calculate the contribution of the continuum to the polarization operator (1) at a nonvanishing pion 4-momentum, one has to use a double dispersion relation. In computing the constant of the electroweak interaction due to the exchange of pions between intranuclear nucleons, the pion 4-momentum is, however, close to zero.

3. OPERATOR PRODUCT EXPANSION AND CONDENSATES

According to the method of QCD sum rules, the polarization operator (1) in the Euclidean domain $p^2 < 0$, $|p| \sim 1$ GeV^2 is represented as an operator-product expansion in inverse powers of p^2, where the coefficients are expressed in terms of vacuum expectation values of various operators [10]; that is,

$$\Pi(p^2) = \sum_n C_n(p^2)\langle O_n\rangle. \quad (4)$$

This expansion is valid at high p^2. Given the numerical values of the vacuum expectation values of the condensates ($\langle O_n\rangle$), the behavior of the polarization operator at relatively large values of p can be determined from (4). The coefficients $C_n(p^2)$ in (4) can be calculated within QCD. As a rule, expressions of the type in (4) are extended up to values of $|p^2| \sim 1$ GeV^2. At smaller values of the momentum, all terms in the series in (4) are significant, so that the correlation function (1) cannot be evaluated by the method being discussed.

The first term of the operator-product expansion (1) is generally associated with the diagram for asymptotically free quarks. The second term takes into account the interactions of quarks and gluons by perturbation theory. All virtual particles in the respective diagrams carry high momenta; therefore, their propagators are adequately described within perturbation theory. All the propagators in the diagrams associated with the third term do not have high momenta—the momenta of some of these propagators are close to zero. These diagrams involve large-scale vacuum fluctuations, and their contribution is proportional to nonvanishing vacuum expectation values of quark and gluon fields. The diagrams contributing to the fourth term involve no virtual particles of high momentum. In this case, the whole momentum flows through an instanton (a small-scale vacuum fluctuation). The third and the fourth terms of the expansion in (4) can be dubbed a partly perturbative and a nonperturbative term, respectively [12]. Thus the electroweak pion–nucleon

coupling constant is determined by the vacuum expectation values

$$a = -(2\pi)^2\langle\overline{q}q\rangle = 0.55\ \text{GeV}, \quad (5)$$

$$\langle\overline{q}i\tau_j\gamma_5 q\rangle_\pi = \chi\cdot g\pi_j\langle\overline{q}q\rangle, \quad (6)$$

$$\langle\overline{q}i\gamma_5\tau_j\sigma\cdot Gq\rangle_\pi = m_0^\pi g\pi_j\langle\overline{q}q\rangle, \quad (7)$$

where G is the strength tensor of the gluon field in QCD [10]. The chiral-symmetry-breaking quark-condensate density $\langle\overline{q}q\rangle$ is presented in (5). Its minimum mass dimension is equal to three. The value of the quark condensate was derived from the analysis of the meson data that was performed in [3]. In (6) and (7), j is the pion isospin index field, while g is the coupling constant for the strong interaction between the pion and the quark. The coupling constant g can be estimated within the model assuming that the current quark becomes massive in the field of vacuum fluctuations and that the resulting constituent quark interacts with the pion field. An interaction of this type gives rise to the factor $m_q^2/p^2 \approx 0.1$ (m_q is the constituent quark mass), which modifies the quark propagator in the pion field.

The Goldberger–Treiman relation implies that

$$g = 2.8 \quad (8)$$

in the case of constituent quarks; this being so, the constant χ in (6) is

$$\chi \approx -5.7\ \text{GeV}^{-1}. \quad (9)$$

From (7), it follows that the numerical value of the quark–gluon condensate in the pion field is determined by the constant m_0^π. In the case of a constituent quark of mass $m_q \approx 0.35$ GeV, this constant and the constant m_0^2, which governs the numerical value of the quark–gluon condensate of dimension 5, are related as

$$m_0^\pi = 2m_0^2/m_q, \quad (10)$$

$$\langle\overline{q}g\pi\cdot Gq\rangle = -m_0^2\langle\overline{q}q\rangle, \quad (11)$$

provided that the pion field vanishes.

The numerical value of the constant m_0^2 in formula (11) was first derived in [13] from the condition ensuring the self-consistency of the sum rules for baryons. This constant was also determined in [14]; its numerical value is 0.4 GeV^2. From (10), we then obtain

$$m_0^\pi \approx 2.3\ \text{GeV}. \quad (12)$$

The electroweak pion–nucleon constant depends not only on the aforementioned quantities but also on the constant describing the coupling of the quark current to the nucleon. In accordance with [10], this constant will henceforth be set to

$$\beta^2 = 0.3\ \text{GeV}^6. \quad (13)$$

4. DISPERSION RELATIONS

The QCD sum rules are based on the dispersion relations that make it possible to relate the polarization operator (1) in the Euclidean domain (it can be found theoretically) to the imaginary part of this operator in the domain of timelike momenta (this imaginary part can be extracted from experimental data). If, in some domain of the values of p^2, the function in (1) can be expressed in terms of the parameters c_i and if its imaginary part $\text{Im}\Pi(p^2)$ in another domain can be expressed in terms of the observables a_j, then the equation

$$\Pi(s, c_i) = \frac{1}{\pi}\int_0^\infty \frac{\text{Im}\Pi(p^2, a_j)}{p^2 + s}dp^2 \quad (14)$$

relates c_i to a_j.

In the dispersion relation (14), we set $s \to \infty$. In this case, the left-hand side of Eq. (1) can be expressed in terms of the vacuum expectation values of quark and gluon fields [parameters c_i in (14)] by employing the operator-product expansion (4). On the other hand, a phenomenological formula for the correlation function (1) in an external pion field can be obtained in terms of the baryon fields by using the dispersion relation (14), with the proviso that the correlation function (1) can be saturated by the contributions of the lowest physical states. This being so, all other states can be approximated by the contribution of a continuum whose threshold w^2 is also to be determined from the sum rules.

If the left-hand and right-hand sides of Eq. (14) could be calculated exactly, then Eq. (14) would hold identically at an arbitrary value of s. However, both sides were calculated approximately. The left-hand side of Eq. (14) was calculated by using the operator-product expansion (4), the accuracy of such a calculation becoming higher with increasing s. On the contrary, the *nucleon pole plus continuum* approximation becomes more accurate with decreasing s. The basic idea is that there exists some region of s values where both approximations are valid, yielding a reasonably accurate result for the function $\Pi(s)$. However, a straightforward application of Eq. (14) involves some difficulties. The main problem is that the continuum (the domain of large $p^2 > 0$) can make a contribution commensurate with that of the nucleon pole. Therefore, the *nucleon pole plus continuum* approximation is ill-defined. This problem can be solved by applying the Borel transformation [7, 8] to both sides of Eq. (14).

5. BOREL TRANSFORMATION

The Borel transformation is applied to a function $f(s)$ satisfying Eq. (14) in order to suppress the contributions of excited states to the sum rules. It has the form

$$Bf(s) = \frac{s^{n+1}}{n!}\left(-\frac{d}{ds}\right)^n f(s) \qquad (15)$$
$$= \frac{1}{\pi}\int_0^\infty dp^2 \exp\left(-\frac{p^2}{M^2}\right)\mathrm{Im}f(p^2),$$
$$s = -p^2 \to \infty, \quad n \to \infty, \quad s/n = M^2,$$

where $Bf(s)$ is a function of $s/n = M^2$. Considering s/n to be finite, we arrive at the Borel transforms

$$Bf(s) = \overline{f}(M^2).$$

The procedure specified by (15) leads to a suppression of the contribution from the domain of large p^2 (continuum), but it enhances the pole contribution. Thus, we have to find an appropriate interval of M^2 values instead of an interval of p^2 values.

From (15), it follows that

$$B(s^k) = 0.$$
$$B(s+p^2)^{-1} = \exp\left(-\frac{p^2}{M^2}\right), \qquad (16)$$
$$B\left(\frac{1}{s^n}\right) = \frac{1}{(M^2)^{n-1}(n-1)!}.$$

The first equation in (16) is valid for all integral $k \geq 0$, whereby the problem of subtractions in the dispersion relations is solved. The second equation leads to a suppression of the contribution from the continuum in relation to the contribution of the nucleon pole, while the third equation ensures a suppression of higher order terms in the operator-product expansion (4) owing to the factorial in the denominator.

The sum rule used here to determine the pion–nucleon electroweak constant naturally involves the threshold w of the continuum and the Borel mass M, which are free parameters. The best fit gives the values

$$w^2 = 2\ \mathrm{GeV}^2, \qquad (17)$$
$$M^2 = 1.2\ \mathrm{GeV}^2, \qquad (18)$$

which determine the required pion–nucleon constant. The values in (17) and (18) ensure a controllable accuracy at a level of 20 to 30%.

6. PION–NUCLEON CONSTANT

Here, we omit standard technical details of our calculations, such as those that are associated with applying the dimensional regularization and the modified minimal-subtraction scheme and with taking into account anomalous dimensions. The resulting expression for the electroweak pion–nucleon constant as obtained on basis of QCD sum rules has the form

$$f = A\left\{\left[(4M^2-m^2)M^4E_3 \qquad (19)\right.\right.$$
$$-\left(2M^2-\frac{2}{3}m^2\right)\chi aM^2E_2$$
$$\left.-\left(M^2-\frac{1}{2}m^2\right)m_0^\pi aE_1\right]\left(1+\frac{4}{27}L^{-1}+\frac{m^2}{M^2}\right)$$
$$+(-20M^2+4m^2)M^4E_3$$
$$+(8M^2+2m^2)\chi aM^2E_2+(3M^2-m^2)m_0^\pi aE_1$$
$$+\exp\left(-\frac{w^2}{M^2}\right)\frac{w^4}{M^4}\left[(4M^2-m^2)\frac{1}{6}w^4\right.$$
$$\left.\left.-\left(2M^2-\frac{2}{3}m^2\right)\chi a\frac{1}{2}w^2-\left(M^2-\frac{1}{2}m^2\right)m_0^\pi a\right]\right\},$$

where χ and a are given by (9) and (5), respectively, and where

$$A = \frac{gG_\mathrm{F}\sin^2\theta_\mathrm{W}}{34\pi^2m^2\beta^2}M^4L^{-4/9}\exp\left(\frac{m^2}{M^2}\right). \qquad (20)$$

Here, $G_\mathrm{F} = 10^{-5}/m^2$ is the Fermi constant for the electroweak interactions; m is the nucleon mass; $\sin^2\theta_\mathrm{W} \approx 0.23$, where θ_W is the Weinberg angle. In (19),

$$L = 0.62\ln(10M) = 1.5, \qquad (21)$$
$$E_k = E_k(x) = 1-\exp(-x)\sum_0^k\frac{x^l}{l!}, \quad x = \frac{w^2}{M^2} \qquad (22)$$

arise upon taking into account anomalous dimensions and the contribution of the continuum [9, 10]. From (19) and (20), it follows that the constant f is proportional to $\sin^2\theta_\mathrm{W}$. This result is a consequence of the fact that the constant f is determined by the contribution of the neutral currents that are due to Z-boson exchange between quarks. The pion–nucleon constant

$$f = 3.4\times10^{-7} \qquad (23)$$

is obtained by substituting into (19)–(22) the numerical values of the parameters of the theory from the preceding sections. The nonperturbative terms in Eq. (19), which are proportional to χa, constitute about half the magnitude of the constant in (23).

The pion–nucleon electroweak coupling constant appears in the effective Lagrangian

$$L = \frac{f}{\sqrt{2}}\varepsilon_{3ik}\bar{N}\cdot\tau_i N\pi_k, \qquad (24)$$

which describes emission and absorption of charged pions by nucleons. The isovector structure of the interaction (24) implies the isospin selection rule $\Delta T = 1$.

7. CONCLUSION

The pion–nucleon electroweak coupling constant has been calculated on the basis of QCD sum rules. Previously, this method was successfully used to calculate various features of hadrons. The calculation of the coupling constant under consideration in [15] yielded a value that is more than an order of magnitude less than that obtained here. According to [15], this is due to incorrectly taking into account the p^2 dependence of the imaginary part of the polarization operator (14) [16]. Within the accuracy of the calculations, our value of the pion–nucleon coupling constant (23) is consistent both with the latest direct experimental limits on this constant [3] and with the results of a global fit to the entire body of experimental data on P-odd effects in nucleon–nucleon interactions [17].

From the theoretical standpoint, the conclusion that the contribution of the chiral-symmetry-breaking quark condensate $\langle\bar{q}q\rangle$ accounts for half of the pion–nucleon electroweak coupling constant is the most interesting result of our study. This explains the failure of all attempts at evaluating the pion–nucleon electroweak coupling constant within perturbation theory [6]. The accuracy of our calculation of the pion–nucleon electroweak coupling constant (23) (30% or better) can be deduced by estimating higher order terms of the operator-product expansion (condensates of dimension six) and the contribution of higher excited states.

ACKNOWLEDGMENTS

I am grateful to B.L. Ioffe for discussions and advice and to Yu.G. Abov and P.A. Krupchitsky for discussions on the experiments studying P-odd effects in nuclear physics.

This work was supported in part by the Russian Foundation for Basic Research (project no. 01-02-16024).

REFERENCES

1. G. A. Lobov, Nucl. Phys. A **577**, 449 (1994); E. M. Henley, *Symmetry Problems in Low-Energy Physics,* Ed. by H. Ejiri (World Sci., Singapore, 1995).
2. L. B. Okun, *Leptons and Quarks* (Nauka, Moscow, 1990; North-Holland, Amsterdam, 1984).
3. M. Bini *et al.,* Phys. Rev. C **38**, 1195 (1988).
4. B. Desplanque, J. F. Donoghue, and B. R. Holstein, Ann. Phys. (N.Y.) **124**, 449 (1980).
5. G. A. Lobov, *Time-Reversal Invariance and Parity Violation in Neutron Reactions,* Ed. by C. R. Gould (World Sci., Singapore, 1993).
6. B. Desplanque, Phys. Rep. **297**, 1 (1998).
7. M. A. Shifman, A. I. Vainshtein, and V. I. Zakharov, Nucl. Phys. B **147**, 385 (1979).
8. B. L. Ioffe, Nucl. Phys. B **188**, 317 (1981); Erratum **191**, 591 (1981).
9. B. L. Ioffe and A. V. Smilga, Nucl. Phys. B **252**, 109 (1984).
10. B. L. Ioffe, *Elementary-Particle Physics: Proceedings of XX LNPI Winter School* (Leningr. Inst. Yad. Fiz., Leningrad, 1985), p. 113.
11. G. A. Lobov, *Modern Problems in the Nuclear Physics and Chemistry of Condensed Matter: Proceedings of First Moscow International School in Physics at the Institute of Theoretical and Experimental Physics* (Red. Usp. Fiz. Nauk, Moscow, 1999), p. 81.
12. L. B. Okun', Usp. Fiz. Nauk **134**, 3 (1981) [Sov. Phys. Usp. **24**, 341 (1981)].
13. V. M. Belyaev and B. L. Ioffe, Zh. Éksp. Teor. Fiz. **83**, 876 (1982) [Sov. Phys. JETP **56**, 493 (1982)].
14. A. Manohar and H. Georgi, Nucl. Phys. B **234**, 189 (1984).
15. E. M. Henley, W.-Y. P. Hwang, and L. S. Kisslinger, Phys. Lett. B **367**, 21 (1996).
16. W.-Y. P. Hwang, private communication.
17. J. Lang *et al.,* Phys. Rev. C **34**, 1545 (1986); E. G. Adelberger and W. C. Haxton, Annu. Rev. Nucl. Part. Sci. **35**, 501 (1985).

Translated by R. Rogalyov

Physics of Atomic Nuclei, Vol. 65, No. 3, 2002, pp. 539–545. Translated from Yadernaya Fizika, Vol. 65, No. 3, 2002, pp. 566–572.

ELEMENTARY PARTICLES AND FIELDS
Theory

Determination of the Parameters of the Δ(1232) Resonance from Partial-Wave Analyses of Elastic πN Scattering

A. S. Omelaenko*

Kharkov Institute for Physics and Technology, Akademicheskaya ul. 1, Kharkov, 310108 Ukraine

Received November 1, 2000; in final form, February 15, 2001

Abstract—On the basis of data on the P_{33} amplitude from various partial-wave analyses of elastic πN scattering, the pole characteristics of the $\Delta(1232)$ resonance are determined within the resonance model. An approximate analytic formula that relates the residue to the background is obtained. Estimates confirm that the nonresonance part of the phase shift is small and differs significantly from the results of the calculations within the current algebra and the approach of effective Lagrangians. This contradiction is removed in a modified resonance-model version developed on the basis of taking into account the quadratic term in the expansion of the Jost function in a series at the pole point. It is shown that the coordinates of the pole and the phase shift of the residue change only slightly in relation to the results within the traditional model, but that the absolute value of the residue increases by about 20%.

1. INTRODUCTION

Although elastic πN scattering has been studied for a long time and is thought to be well understood, there is a significant scatter of the results for the absolute value and the phase shift of the residue at the pole of the P_{33}-wave amplitude in the $\Delta(1232)$-resonance region (Table 1, [1, 2]). In principle, this can be due to modifications in the experimental basis, its qualitative and quantitative improvements. Another reason behind this can be associated with the presence of a model ambiguity in the analytic description of the amplitude. This is manifested significantly in the extrapolation of the amplitude toward the pole point occurring beyond the physical region. As to the P_{33} amplitude itself, it is well described within the resonance model [3, 4], where an additional background contribution is taken into account along with the standard Breit–Wigner expression. From the results of the calculations presented in [4], it follows that the magnitude of this background is moderate and that the corresponding phase shift at the resonance point is about 3° to 4°. However, this estimate contradicts the results of the calculations within the current algebra and the approach of effective Lagrangians, where the background phase shift at the resonance proves to be about 15° [5, 6].

In order to clarify these questions, the resonance and the pole characteristics of the P_{33}-wave amplitude are calculated here within a realistic resonance model by using data from a few partial-wave analyses of elastic πN scattering. The relation between the residues of the total and the resonance amplitude is derived in an analytic form with allowance for the background, and the resonance model is modified by taking into account the second-order correction in the expansion of the Jost function in the vicinity of the pole of the amplitude.

2. AMPLITUDE OF THE P_{33} WAVE IN THE $\Delta(1232)$-RESONANCE REGION

2.1. Residue in the Resonance Model

In the region of the excitation of the first nucleon resonance, the description of the P_{33}-wave amplitude for πN scattering is simplified because this amplitude is elastic. In the resonance model, the relevant S-matrix element depending on the total energy W (in the c.m. frame) has the factorized form

$$S(W) = S_B(W)S_R(W), \tag{1}$$

where the quantities S_B and S_R correspond to the background and the resonance, respectively; in the physical region, they are determined by corresponding real phase shifts,

$$S = e^{2i\delta}, \quad S_B = e^{2i\delta_B}, \quad S_R = e^{2i\delta_R}. \tag{2}$$

Here, the rule of phase summation is

$$\delta(W) = \delta_B(W) + \delta_R(W). \tag{3}$$

In the complex plane of W, the quantities S_B and S_R are given by

$$S_B(W) = \frac{1 + iB(W)}{1 - iB(W)}, \tag{4a}$$

*e-mail: omelaenko@kipt.kharkov.ua

Table 1. Pole parameters of the P_{33}-wave amplitude [1]

Data	M_P, MeV	$\Gamma_P/2$, MeV	|res|, MeV	φ(res), deg
Cutkosky 80	1210 ± 1	53 ± 2	50 ± 1	-47 ± 1
Arndt 91	1210	50	52	-31
Hoehler 93	1209	50	50	-48
Arndt 95	1211	50	38	-22
Arndt 99a	1211	51	39	-23
Arndt 99b	1211	50	47	-47

Note: The symbols |res| and φ(res) stand for, respectively, the absolute value and the phase shift of the residue at the pole point $M_P - i\Gamma_P/2$ in the complex plane of the total energy W. The values in the two lower rows correspond to versions of the treatment of the data from the analysis reported in [2] (private communication of Arndt).

$$S_R(W) = \frac{W - M_R - i\Gamma(W)/2}{W - M_R + i\Gamma(W)/2}. \quad (4b)$$

It is assumed that the background function $B(W)$ introduced above and the width $\Gamma(W)$ satisfy the conditions $B(W) = B^*(W^*)$ and $\Gamma(W) = \Gamma^*(W^*)$, so that, in the physical region, $B(W)$ and $\Gamma(W)$ are real and are related to the phase shifts δ_B and δ_R as

$$\tan\delta_B(W) = B(W), \quad (5a)$$

$$\tan\delta_R(W) = \frac{\Gamma(W)/2}{M_R - W}, \quad (5b)$$

where M_R is the resonance mass. From Eq. (4b), it can be seen that, at the W values that satisfy the equation

$$W - M_R + i\Gamma(W) = 0, \quad (6)$$

the function S_R has a pole. According to scattering theory, the root of Eq. (6), $W_P = M_P - i\Gamma_P/2$, that lies in the fourth quadrant of the complex plane of W at positive values of M_P and Γ_P corresponds to a resonance. Considering that the expansion of the denominator on the right-hand side of Eq. (4b) in a series in powers of $(W - W_P)$ begins from the linear term and retaining only this term in the vicinity of the pole, we can recast (4b) into the form

$$S_R(W) \cong \frac{W - M_R - i\Gamma(W)/2}{(1 + i\Gamma'(W_P)/2)(W - W_P)}, \quad (7)$$

where $\Gamma'(W_P)$ is the value of the derivative $d\Gamma(W)/dW$ at the pole point. From Eqs. (6) and (7), we can obtain an exact formula for the residue:

$$\mathrm{res}(S_R) = \frac{-i\Gamma(W_P)}{1 + i\Gamma'(W_P)/2}. \quad (8)$$

We will now consider that the numerator on the right-hand side of (7) vanishes at the point $W_P^* = M_P + i\Gamma_P/2$, which is conjugate to the pole, and expand it in a series at this point. Retaining only the first term in this expansion and assuming that this approximation can be used at the pole as well, we find that, in the unipolar approximation, the resonance S-matrix element has the form

$$S_R(W) \cong \frac{1 - i\Gamma'(W_P^*)/2}{1 + i\Gamma'(W_P)/2} \frac{W - M_P - i\Gamma_P/2}{W - M_P + i\Gamma_P/2}, \quad (9)$$

whence we obtain an approximate expression for the residue:

$$\mathrm{res}(S_R) \cong -i\Gamma_P \frac{1 - i\Gamma'(W_P^*)/2}{1 + i\Gamma'(W_P)/2}. \quad (10)$$

For expression (10) to be correct, it is obviously necessary that the distance Γ_P between W_P^* and the pole not be overly large and that the energy dependence of the width $\Gamma(W)$ be sufficiently smooth. Comparing (8) and (10), we also obtain

$$\Gamma(W_P)/\Gamma_P \cong 1 - i\Gamma'(W_P^*)/2. \quad (11)$$

In particular, the equality $\Gamma(W_P) = \Gamma_P$ holds for an energy-independent width.

The residue of the amplitude $T \equiv (S-1)/2i$ is usually presented in analyses. It follows from (10) that the absolute value and the phase shift of the residue of the resonance amplitude are

$$|\mathrm{res}(T_R)| \cong \Gamma_P/2, \quad (12)$$

$$\varphi(\mathrm{res}(T_R)) = 2\varphi_0, \quad (13)$$

where

$$\varphi_0 \cong \arg(1 - i\Gamma'(W_P^*)/2) = -\arg(1 + i\Gamma'(W_P)/2). \quad (14)$$

From (13) and (14), it can be seen that the phase shift of the residue is equal to zero if the width is independent of energy.

In general, the approximate result for the residue of the amplitude with allowance for the background has the form (it should be noted that the presence of

a background does not affect the coordinates of the pole)

$$|\mathrm{res}(T)| \cong (\Gamma_P/2)|S_B(W_P)|, \quad (15)$$

$$\varphi(\mathrm{res}(T)) \cong 2\varphi_0 + \arg(S_B). \quad (16)$$

The second term on the right-hand side of (16) determines the contribution of the background to the phase shift of the residue.

2.2. Inclusion of the Second-Order Correction in the Expansion of the Jost Function

As a matter of fact, the above approximation is a starting point for constructing, in a standard way, the resonance model, where only the first term in the expansion of the Jost function in a power series in the vicinity of the pole point is taken into account (see, for example, [7]). By introducing the parameter c defined by the ratio of the coefficients of the second and the first term in this expansion, we can take into account the second-order correction on the right-hand side of (9) by making the substitution

$$\frac{W - M_P - i\Gamma_P/2}{W - M_P + i\Gamma_P/2}$$

$$\to \frac{W - M_P - i\Gamma_P/2 + c^*(W - M_P - i\Gamma_P/2)^2}{W - M_P + i\Gamma_P/2 + c(W - M_P + i\Gamma_P/2)^2}.$$

Upon going over to the model and introducing the energy-dependent width in (4b), there arises the additional factor

$$S_c(W) = \frac{1 + c^*(W - M_R - i\Gamma(W)/2)}{1 + c(W - M_R + i\Gamma(W)/2)}. \quad (17)$$

For the corresponding phase shift δ_c determined by the relation $S_c(W) = e^{2i\delta_c}$ to vanish as we approach the threshold, the constant c must be real. In this case, the modification of the model via the inclusion of the second-order term in the expansion of the Jost function generates, in the phase shift, the additional contribution given by

$$\tan\delta_c = -\frac{c\Gamma(W)/2}{1 + c(W - M_R)}. \quad (18)$$

Thus, the total phase shift is equal to the sum

$$\delta = \delta_B + \delta_R + \delta_c, \quad (19)$$

while the expressions for the absolute value of the residue and for its phase shift [(15) and (16), respectively] are modified to become

$$|\mathrm{res}(T)| \cong (\Gamma_P/2)|S_B(W_P)||1 - ic\Gamma(W_P)|, \quad (20)$$

$$\varphi(\mathrm{res}(T)) \cong 2\varphi_0 \quad (21)$$
$$+ \arg(S_B(W_P)) + \arg(1 - ic\Gamma(W_P)).$$

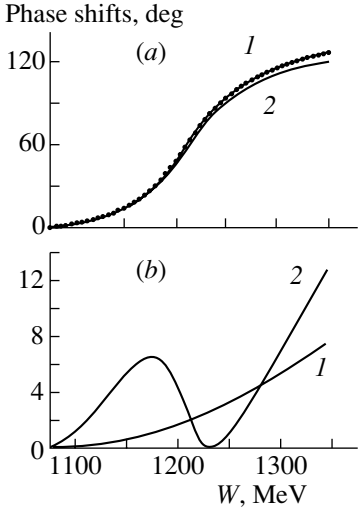

Fig. 1. Energy dependence of the total phase shift δ and of its resonance and background parts according to the calculations within the standard resonance model at $M_R = 1235.14$ MeV, $\Gamma_R = 123.36$ MeV, $r = 0.97520$ fm, and $a = 0.02822$ fm^3: (a) results of the calculations for δ and δ_R (curves *1* and *2*, respectively) and data of the SM99 partial-wave analysis (points); (b) results of the calculations for the background phase shift δ_B and for the difference of δ_R and the values of this quantity at $r = 0$ (curves *1* and *2*, respectively).

3. NUMERICAL CALCULATIONS

3.1. Resonance Model

The width was calculated here by the formula

$$\Gamma(W) = \Gamma_R(q/q_R)^3 R(W), \quad (22)$$

which takes into account the threshold dependence and which involves the c.m. particle momentum $q \equiv q(W)$; its value at $W = M_R$, q_R; the quantity $\Gamma_R = \Gamma(M_R)$; and the factor $R(W)$ correcting the energy dependence of the width,

$$R(W) = (1 + q_R^2 r^2)/(1 + q^2 r^2), \quad (23)$$

with r being a phenomenological parameter. The background was described with the aid of Eqs. (4a) and (5a), where $B(W)$ was parametrized as

$$B(W) = aq^3(W). \quad (24)$$

The inclusion of the additional factor $2M_R/(M_R + W)$ in expression (22) for the width leads to the relativistic version of the model, with the resonance amplitude being given by

$$T_R(W) = \frac{\Gamma(W)W_R}{M_R^2 - W^2 - i\Gamma(W)M_R}. \quad (25)$$

However, the calculations have revealed that, in this case, the results for the resonance and pole parameters remain virtually unchanged. For this reason, we will employ below only the nonrelativistic formulation of the model.

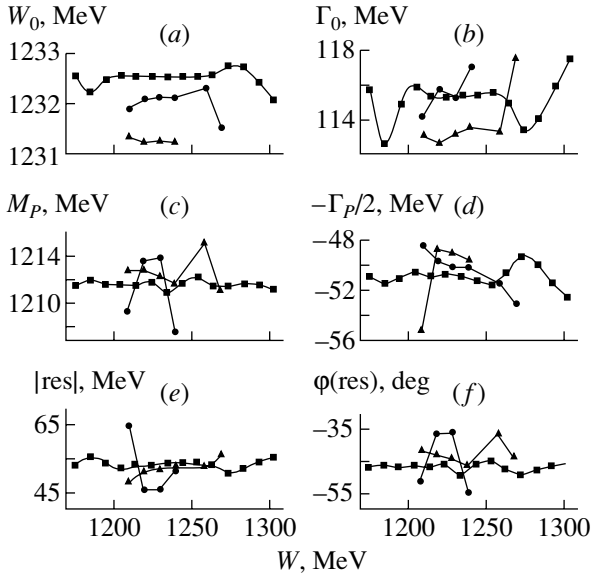

Fig. 2. Resonance and pole parameters according to the data of the (boxes) SM99, (triangles) SM99s, and (circles) KA84 partial-wave analyses in the energy intervals of widths 30, 60, and 80 MeV, respectively, their centers being plotted along the abscissa.

3.2. Fitting Data on the Phase Shift of the P_{33} Amplitude

The model parameters M_R, Γ_R, r, and a were determined from the data on the phase shift of the P_{33} wave in the region of W from the threshold to 1350 MeV that were obtained with a step of 5 MeV from the SAID system available through the Internet (http://said.phys.vt.edu). It includes the parametrized (SM99) and the energy-independent (SM99s) version of the partial-wave analysis reported in [2], its preceding versions SM90 [8] and SM95 [9], and the KP80 partial-wave analysis [10] and its smoothed version KA84. Upon fitting the parameters, the resonance model makes it possible to obtain a good description of the data on δ in all cases. By way of example, the result of a fit to data of the SM99 partial-wave analysis is presented in Fig. 1*a*. Figure 1*b* illustrates the role that the empirical parameter r plays in the formation of the resonance contribution. The background phase shift is positive, taking values of 2° to 3° at the resonance point.

The calculations were further performed for the resonance parameters M_0 (the position of the point where the phase shift takes the value of 90°) and $\Gamma_0 = 2/(d\delta/dW)|_{W=M_0}$ (the experimental width) and for the pole parameters—namely, the coordinates of the pole of the amplitude, the absolute value of the corresponding residue, and its phase shift $\varphi[\mathrm{res} \equiv \mathrm{res}(T)]$. The resonance and pole parameters for the SM99 partial-wave analysis and for solutions of other partial-wave analyses are quoted in Table 2. There, the values of χ^2 are of a rather arbitrary character because, as a rule, the errors in the phase-shift values are not presented in partial-wave analyses—in the calculations, the experimental points were arbitrarily assigned the error values of 0.25°. The SM99s (single energy) version, which was implemented for 16 energy values in such a way that a strong dependence on the experimental data that fell within the vicinity of each node was preserved, is the only partial-wave analysis presenting the error values. The value of $\chi^2 = 65$ was obtained from a fit to this solution, with the overwhelming contribution to it coming from the point at $W = 1180$ MeV. Upon the elimination of this point, χ^2 decreased to 27, but the results for the sought parameters changed only slightly. Unfortunately, there are only a few points in the central region, which is of greatest interest.

In order to estimate the effect exerted by individual groups of experimental points on the formation of the values of the sought parameters, fits were also performed for data from specific energy intervals. In principle, the results obtained in this way must be compatible if the experimental data are of a very high quality and if the model used in fitting is adequate. For the SM99, SM99s, and KA84 partial-wave analyses, this was so in some cases for energy intervals of widths 30, 60, and 80 MeV, respectively (Fig. 2). It can be seen that the region around 1210–1220 MeV is the most informative. For the SM99 solution, this test yielded the best result—at the center of the resonance distribution, the results for the experimental mass, the width, and all of the pole parameters showed the weakest dependence on the choice of input data interval, errors increasing away from the center of the distribution. For the energy-independent SM99s solution and the earlier KA84 solution, there are pronounced deviations in the central region that is shown in the graphs, the results losing physical significance beyond it. In view of this, the resonance and pole parameters were determined here on the basis of only data in the central region ($1180 < W < 1260$ MeV), since this region is the most appropriate for this purpose. In Table 2, the corresponding results are presented in the lower row for each of the analyses considered in the present study. It can be seen that, in some cases, these results differ from those obtained from a fit over the entire resonance region, especially for the phase shift of the residue.

3.3. Approximate Formula for the Residue

The approximate values calculated by formulas (14)–(16) for the absolute value and the phase shift of the residue within the standard resonance model are presented parenthetically in Table 2 under the precise

Table 2. Resonance and pole parameters of P_{33}-wave amplitude

Data	N	χ^2	M_0, MeV	Γ_0, MeV	M_P, MeV	$\Gamma_P/2$, MeV	|res|, MeV	φ(res), deg
KP80	27	19.0	1231.0	116.0	1209.2	50.4	52.4	−48.9
							(52.9)	(−49.9)
*	10	4.2	1230.9	115.4	1210.1	49.5	50.1	−46.2
KA84	55	54.0	1231.2	118.2	1208.7	51.4	53.7	−49.8
							(54.5)	(−51.1)
*	17	7.9	1231.2	116.8	1211.2	50.7	51.3	−43.2
SM90	55	0.25	1231.3	113.9	1210.6	49.9	51.8	−46.8
							(51.8)	(−46.9)
*	17	0.14	1231.3	114.0	1210.5	49.8	51.6	−46.9
SM95	55	0.18	1231.9	113.0	1211.6	50.1	52.4	−46.0
							(52.4)	(−46.2)
*	17	0.08	1232.0	113.2	1211.6	50.2	52.5	−46.2
SM99	55	0.15	1232.5	115.2	1211.5	50.8	53.1	−46.9
							(53.2)	(−47.1)
*	17	0.00	1232.5	115.4	1211.5	50.9	53.2	−47.0
SM99s	16	65.0	1232.1	114.7	1210.9	50.5	52.9	−48.0
							(53.6)	(−49.2)
SM99s, c	15	27.0	1232.1	115.0	1210.6	50.5	53.0	−48.6
*	5	0.82	1231.9	112.8	1212.9	48.3	47.6	−42.0

Note: N is the number of points; asterisks and the letter "c" correspond to data for $1180 < W < 1260$ MeV and data without the point at $W = 1180$ MeV, respectively; and the values in parentheses correspond to the calculations of the residue by formulas (14)–(16).

Table 3. Resonance and pole parameters of the P_{33}-wave amplitude within the modified resonance model

Data	M_0, MeV	Γ_0, MeV	M_P, MeV	$\Gamma_P/2$, MeV	|res|, MeV	φ(res), deg
KP80	1231.1	118.8	1206.7	52.2	57.0	−55.4
KA84	1231.4	120.8	1206.4	53.2	58.5	−56.1
SM99	1232.8	118.2	1209.1	53.6	60.7	−53.5
SM99s	1233.3	117.9	1210.4	55.2	64.7	−51.7

results and are in good agreement with them. Also, there is the possibility of obtaining, within a realistic model, an independent estimate of the background in the case where data on the pole parameters of the resonance are available. Indeed, formula (15) makes it possible to establish a relation between the relative value of the residue, y, and the background parameter a:

$$y \equiv \frac{|\mathrm{res}(T)|}{\Gamma_P/2} \cong \left|\frac{1+iaq^3(W_P)}{1-iaq^3(W_P)}\right|. \qquad (26)$$

Upon solving Eq. (26) for a, the background phase shift $\delta_B(W)$ can be calculated with the aid of (24) and (5a). In order to characterize the background, the results of such a calculation at $W = 1232$ MeV are presented in Fig. 3 versus y from various partial-wave analyses. It can be seen that the estimates of the background phase shift at the resonance are grouped around the values of $-15°$, $-3°$, and $+3°$. In order to obtain the value of $+15°$, which is characteristic of the approach of effective Lagrangians [4], one must have the value of $y \approx 1.32$, which would correspond to the absolute value of the residue of about 68 MeV. The contribution of the background to the phase shift

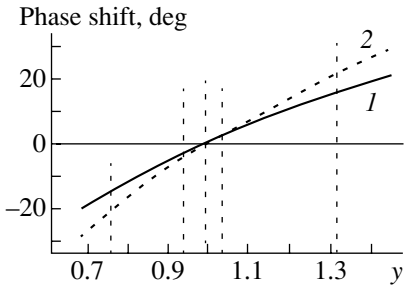

Fig. 3. Background phase shift δ_B at $W = 1232$ MeV (curve *1*) and contribution of the background to the phase shift of the residue (curve *2*) versus y. Vertical dashed lines correspond to ($y \approx 0.76$) Arndt 95, Arndt 99a data; ($y \approx 0.94$) Cutkosky 80, Arndt 99b data; ($y \approx 1.00$) Hoehler 93 data; ($y \approx 1.04$) SM90 data and the present estimate based on the SM99 data; and ($y \approx 1.32$) $\delta_B(1232) \approx 15°$.

of the residue also changes considerably with y (see curve *2* in Fig. 3).

3.4. Modified Resonance Model

Alternatively, the phase shift δ was described with the aid of formulas (17)–(21), which were derived within the model developed by taking into account the second-order term in the expansion of the Jost function and by introducing a free parameter c. As before, the background was described with the aid of (24); however, the empirical factor $R(W)$ (with the parameter r), which is typical of the standard model, was not introduced in expression (22) for the width. Hence, the modified model involves four adjustable parameters as before. A good description was obtained for data on δ from all of the partial-wave analyses considered here. By way of example, the result for the SM99 partial-wave analysis is presented in Fig. 4*a*. At the resonance point, we have $\delta_B \sim 23°$ in this case. However, the correction associated with the inclusion of the second-order term in the expansion of the Jost function is negative, and the total nonresonance phase shift approaches 15° (Fig. 4*b*). This is in agreement with the estimates obtained within the approach of effective Lagrangians [6]. By and large, the curve representing the nonresonance phase shift is in reasonable agreement with the estimate based on the current-algebra model [5] as well. The values of the resonance and pole parameters for the modified model are presented in Table 3. In relation to what we have in the standard resonance model, the coordinates of the pole exhibit moderate shifts that depend on the choice of analysis, while the absolute value of the residue appears to be about 20% greater. The phase shift of the residue increases somewhat. As to the experimental mass and width, the results for them are close, on the whole, to traditional values.

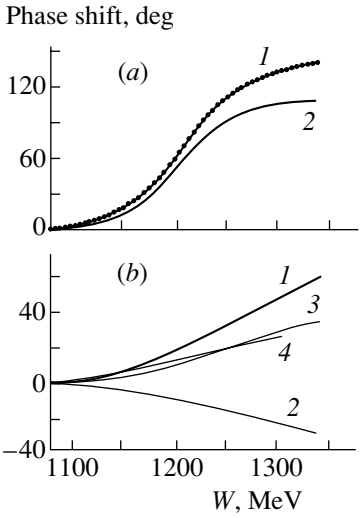

Fig. 4. Energy dependence of the total phase shift δ and of its resonance and background parts within the modified resonance model at $M_R = 1256.08$ MeV, $\Gamma_R = 222.44$ MeV, $a = 0.29143$ fm^3, and $c = 0.34821$ fm: (*a*) results for δ and δ_R (curves *1* and *2*, respectively) and data of the SM99 partial-wave analysis (points); (*b*) results for δ_B, δ_c, and $\delta_B + \delta_c$ (curves *1*, *2*, and *3*, respectively) and nonresonance phase shift borrowed from [3] (curve *4*).

4. CONCLUSIONS

The basic points of the present study and its conclusions concerning the P_{33}-wave amplitude for πN scattering can be briefly formulated as follows:

(i) As a matter of fact, the approximation considered in Section 2 is the starting point in constructing the resonance model on the basis of the expansion of the Jost function in the vicinity of the pole of the amplitude; the above test has demonstrated its applicability to calculating the pole parameters. For the absolute value and the phase shift of the residue, the analytic expressions (14)–(16) have been derived in this approximation. From these expressions, it follows, among other things, that the equality of the absolute values of the residue and the imaginary pole coordinate suggests the absence of background and that the resonance contribution to the phase shift of the residue is determined by the value of $d\Gamma(W)/dW$ at the pole point.

(ii) If the background is described by one parameter and if the residue and the pole coordinates are known, the background can be estimated on the basis of expression (15) without invoking information about $\Gamma(W)$ for this. Estimates of the background phase shift according to data from various partial-wave analyses exhibit a wide scatter—from $-15°$ to $+3°$ at the resonance point; however, values of about $+15°$, which are characteristic of the calculations

within the current algebra and the approach of effective Lagrangians [5, 6], cannot be obtained in this way.

(iii) A retrospective fit to the data from basic partial-wave analyses has revealed that the pole parameters have changed only slightly over the last two decades. This may indirectly suggest that advances in experiments studying the Δ(1232)-resonance region are not as pronounced as might have been expected.

(iv) The present calculations within the constrained energy intervals has enabled us to assess the "energy resolution" of various analyses. For example, a determination of the resonance and pole parameters on the basis of the SM99 analysis, which employs the most comprehensive sample of experimental data, is possible by using the data from the interval of width about 30 MeV. For other analyses, the minimal width of such an interval varies from 60 to 80 MeV, and the results for the pole parameters change significantly in response to its shift. This demonstrates that the region of the first resonance has not yet received adequately study, so that new systematic and precise measurements are required for performing a reliable analysis.

(v) A modified resonance-model version developed on the basis of retaining the quadratic term in the expansion of the Jost function at the pole point has been considered. A satisfactory description of data from partial-wave analyses has been obtained. The resulting estimate of the nonresonance phase shift complies well with the results of the calculations within the current algebra and the approach of effective Lagrangians. In relation to the results within the traditional model, the absolute value of the residue undergoes the most pronounced change (an increase of about 20%).

ACKNOWLEDGMENTS

I am grateful to I.I. Strakovsky for a discussion and enlightening comments and to R.A. Arndt for kindly placing the data on the residue at my disposal prior their publication. I also acknowledge the crucial importance of the SAID information system.

REFERENCES

1. Particle Data Group, Eur. Phys. J. C **15**, 725 (2000).
2. R. A. Arndt, R. L. Workman, I. I. Strakovsky, and M. M. Pavan, nucl-th/9807087; submitted to Phys. Rev. C.
3. F. Nichitiu, *Analiza de Fasa in Fizica Interactiilor Nucleare* (Editura Akademiei RSR, Bucharest, 1980; Mir, Moscow, 1983).
4. S. S. Vasan, Nucl. Phys. B **106**, 71 (1976).
5. M. G. Olsson, Phys. Rev. D **13**, 2502 (1976).
6. R. M. Davidson, N. S. Mukhopadhyay, and R. S. Wittman, Phys. Rev. D **43**, 71 (1991).
7. A. G. Sitenko, *Scattering Theory* (Vishcha Shkola, Kiev, 1975; Springer-Verlag, Berlin, 1991).
8. R. A. Arndt, L. Zhujun, L. D. Roper, *et al.*, Phys. Rev. D **43**, 2131 (1991).
9. R. A. Arndt, I. I. Strakovsky, R. L. Workman, and M. M. Pavan, Phys. Rev. C **52**, 2120 (1995).
10. R. Koch and E. Pietarinen, Nucl. Phys. A **336**, 331 (1980).

Translated by A. Isaakyan

Physics of Atomic Nuclei, Vol. 65, No. 3, 2002, pp. 546–551. From Yadernaya Fizika, Vol. 65, No. 3, 2002, pp. 573–578.

ELEMENTARY PARTICLES AND FIELDS
Theory

On the Nature of the Scalar $a_0(980)$ and $f_0(980)$ Mesons*

N. N. Achasov

Sobolev Institute of Mathematics, Siberian Division, Russian Academy of Sciences, Universitetskiĭ pr. 4, Novosibirsk, 630090 Russia

Received May 15, 2000

Abstract—A critical consideration of all unusual properties of the scalar $a_0(980)$ and $f_0(980)$ mesons is presented within the four-quark, two-quark, and molecular models. Arguments in favor of the four-quark model are given. Further experiments that could finally resolve this issue are discussed.

1. INTRODUCTION

The spherical neutral detector (SND) at the VEPP-2M e^+e^- collider in Novosibirsk discovered [1, 2] the electric dipole decays $\phi \to \gamma\pi^0\pi^0$ and $\phi \to \gamma\pi^0\eta$ in the region of soft (by strong-interaction standards) photons with energies of $\omega < 120\,\text{MeV}$—i.e., in the region of the scalar $a_0(980)$ and $f_0(980)$ mesons, $m_{\pi^0\pi^0} > 900\,\text{MeV}$ and $m_{\pi^0\eta} > 900\,\text{MeV}$ [$\phi \to \gamma f_0(980) \to \gamma\pi^0\pi^0$ and $\phi \to \gamma a_0(980) \to \gamma\pi^0\eta$]. The data yield

$$\text{Br}(\phi \to \gamma\pi^0\pi^0;\, m_{\pi^0\pi^0} > 900\,\text{MeV}) = (0.5 \pm 0.06 \pm 0.06) \times 10^{-4} \quad (1)$$

of the total

$$\text{Br}(\phi \to \gamma\pi^0\pi^0) = (1.14 \pm 0.10 \pm 0.12) \times 10^{-4},$$

$$\text{Br}(\phi \to \gamma\pi^0\eta;\, m_{\pi^0\eta} > 900\,\text{MeV}) \simeq 0.5 \times 10^{-4} \quad (2)$$

of the total

$$\text{Br}(\phi \to \gamma\pi^0\eta) = (0.83 \pm 023) \times 10^{-4}.$$

The cryogenic magnetic detector-2 (CMD-2) at the VEPP-2M e^+e^- collider in Novosibirsk confirmed these results [3].

A new preliminary SND analysis [4] of 1998 data with twice as large a data sample in relation to 1996 data [1] also confirms the results in (2).

The branching ratios in Eqs. (1) and (2) are huge for this photon-energy region and can probably be understood only if four-quark resonances are produced [5, 6]. Note that the $a_0(980)$ meson is produced in ϕ radiative decay as intensively as the η' meson containing strange quarks.

*This article was submitted by the author in English.

2. EVIDENCE FOR STRANGE QUARKS IN THE $f_0(980)$ AND $a_0(980)$ MESONS

To feel why the numbers in Eqs. (1) and (2) are huge, one can make a rough estimate. Let us assume that there is structural radiation without a resonance in the final state with the spectrum

$$\frac{d\Gamma(\phi \to \gamma\pi^0\pi^0(\eta))}{d\omega} \sim \frac{\alpha}{\pi}\delta_{\text{OZI}}\frac{1}{m_\phi^3}\omega^3,$$

where $\delta_{\text{OZI}} \sim 10^{-2}$ is a factor describing the suppression by the Okubo–Zweig–Iizuka (OZI) rule. Recall that the ω^3 law follows from gauge invariance. Indeed, the decay amplitude is proportional to the electromagnetic field $F_{\mu\nu}$ (in our case, to the electric field)—i.e., to the photon energy ω in the soft photon region.

Then, one obtains

$$\Gamma(\phi \to \gamma\pi^0\pi^0(\eta)) \sim \frac{1}{4}\frac{\alpha}{\pi}\delta_{\text{OZI}}\frac{\omega_0^4}{m_\phi^3} \simeq 10^{-6}\,\text{MeV};$$

i.e., $\text{Br}(\phi \to \gamma\pi^0\pi^0(\eta)) \sim 2 \times 10^{-7}$, where $\omega_0 = 120\,\text{MeV}$.

To understand why Eq. (2) points to the four-quark model is especially easy. Indeed, the ϕ meson is an isoscalar, virtually pure $s\bar{s}$ state that decays into the isovector hadron state $\pi^0\eta$ and the isovector photon. The isovector photon originates from the ρ meson, $\phi \to \rho\, a_0(980) \to \gamma\pi^0\eta$, whose structure in this energy region is familiar,

$$\rho \approx \frac{u\bar{u} - d\bar{d}}{\sqrt{2}}. \quad (3)$$

The structure of the $a_0(980)$ meson, from which the $\pi^0\eta$ system originates, is in general the following:

$$a_0(980) = c_1\frac{u\bar{u} - d\bar{d}}{\sqrt{2}} + c_2\frac{s\bar{s}(u\bar{u} - d\bar{d})}{\sqrt{2}} + \ldots. \quad (4)$$

1063-7788/02/6503-0546$22.00

With the first term in Eq. (4) taken to be dominant, there are no strange quarks in the intermediate state. Thus, we would have the decay suppressed by OZI rule with $\mathrm{Br}(\phi \to \gamma a_0(980) \to \gamma\pi^0\eta) \sim 10^{-6}$ owing to the real part of the decay amplitude [6]. The imaginary part of the decay amplitude, resulting from the K^+K^- intermediate state ($\phi \to \gamma K^+K^- \to \gamma a_0(980) \to \gamma\pi^0\eta$), violates the OZI rule and increases the branching ratio to 10^{-5} [5, 6].

The four-quark hypothesis is also supported by J/ψ decays. Indeed, we have

$$\mathrm{Br}(J/\psi \to a_2(1320)\,\rho) = (109 \pm 22) \times 10^{-4}\,[7], \tag{5}$$

while

$$\mathrm{Br}(J/\psi \to a_0(980)\,\rho) < 4.4 \times 10^{-4}\,[8]. \tag{6}$$

The suppression

$$\frac{B(J/\psi \to a_0(980)\,\rho)}{B(J/\psi \to a_2(1320)\,\rho)} < 0.04 \pm 0.008 \tag{7}$$

seems strange if one considers the $a_2(1320)$ and $a_0(980)$ states as tensor and scalar two-quark states from the same P-wave multiplet with the quark structure

$$a_0^0 = \frac{u\bar{u} - d\bar{d}}{\sqrt{2}}, \quad a_0^+ = u\bar{d}, \quad a_0^- = d\bar{u}, \tag{8}$$

while the four-quark nature of the $a_0(980)$ meson with the symbolic quark structure

$$a_0^0 = \frac{s\bar{s}(u\bar{u} - d\bar{d})}{\sqrt{2}}, \quad a_0^+ = s\bar{s}u\bar{d}, \quad a_0^- = s\bar{s}d\bar{u} \tag{9}$$

does not contradict the suppression in Eq. (7).

Moreover, it was predicted in [9] that, if the $a_0(980)$ meson is taken as a four-quark state from the lightest nonet of the MIT bag [10], its production rate should be suppressed in $\gamma\gamma$ collisions by a factor of ten in relation to the $a_0(980)$ meson taken as a two-quark P-wave state. The estimate obtained in [9] for the four-quark model was

$$\Gamma(a_0(980) \to \gamma\gamma) \sim 0.27\,\mathrm{keV}, \tag{10}$$

which was confirmed by the experiments reported in [11, 12]:

$$\Gamma(a_0 \to \gamma\gamma) = \frac{0.19 \pm 0.07^{+0.1}_{-0.07}}{B(a_0 \to \pi\eta)}\,\mathrm{keV}\ (\mathrm{Crystal\ Ball}), \tag{11}$$

$$\Gamma(a_0 \to \gamma\gamma) = \frac{0.28 \pm 0.04 \pm 0.1}{B(a_0 \to \pi\eta)}\,\mathrm{keV}\ (\mathrm{JADE}).$$

At the same time, it was anticipated [13, 14] in the two-quark model (8) that

$$\Gamma(a_0 \to \gamma\gamma) = (1.5\text{–}5.9)\Gamma(a_2 \to \gamma\gamma) = (1.5\text{–}5.9)(1.04 \pm 0.09)\,\mathrm{keV}. \tag{12}$$

The wide spread in the predictions is due to different reasonable guesses at the form of the potential.

As for the decay $\phi \to \gamma f_0(980) \to \gamma\pi^0\pi^0$, a more sophisticated analysis is required.

The structure of the $f_0(980)$ meson, from which the $\pi^0\pi^0$ system originates, is in general the following:

$$f_0(980) = \tilde{c}_0 gg + \tilde{c}_1\frac{u\bar{u} + d\bar{d}}{\sqrt{2}} + \tilde{c}_2 s\bar{s} + \tilde{c}_3\frac{s\bar{s}(u\bar{u} + d\bar{d})}{\sqrt{2}} + \ldots. \tag{13}$$

First, we discuss the possibility of treating the $f_0(980)$ meson as a quark–antiquark state.

The hypothesis that the $f_0(980)$ meson is the lowest two-quark P-wave scalar state with the quark structure

$$f_0 = \frac{u\bar{u} + d\bar{d}}{\sqrt{2}} \tag{14}$$

contradicts Eq. (1) in view of the OZI rule, in the same way as Eq. (8) contradicts Eq. (2) (see the above arguments).

Moreover, this hypothesis contradicts the following facts:

(i) a strong coupling to the $K\bar{K}$ channel [15, 6],

$$1 < R = \left|\frac{g_{f_0K^+K^-}}{g_{f_0\pi^+\pi^-}}\right|^2 \lesssim 8, \tag{15}$$

since Eq. (14) implies that $|g_{f_0K^+K^-}/g_{f_0\pi^+\pi^-}|^2 = \lambda/4 \simeq 1/8$, where λ characterizes strange-sea suppression;

(ii) a weak coupling to gluons [16],

$$\mathrm{Br}(J/\psi \to \gamma f_0(980) \to \gamma\pi\pi) < 1.4 \times 10^{-5}, \tag{16}$$

versus the expected one [17] for Eq. (14),

$$\mathrm{Br}(J/\psi \to \gamma f_0(980)) \gtrsim \frac{\mathrm{Br}(J/\psi \to \gamma f_2(1270))}{4} \simeq 3.4 \times 10^{-4}; \tag{17}$$

(iii) weak coupling to photons [18, 19],

$$\Gamma(f_0 \to \gamma\gamma) = 0.31 \pm 0.14 \pm 0.09\,\mathrm{keV}\ (\mathrm{Crystal\ Ball}), \tag{18}$$

$$\Gamma(f_0 \to \gamma\gamma) = 0.24 \pm 0.06 \pm 0.15\,\mathrm{keV}\ (\mathrm{MARK\ II}),$$

versus the expected one [13, 14] for Eq. (14),

$$\Gamma(f_0 \to \gamma\gamma) = (1.7\text{–}5.5)\Gamma(f_2 \to \gamma\gamma) = (1.7\text{–}5.5)(2.8 \pm 0.4)\,\mathrm{keV}; \tag{19}$$

(iv) the decays $J/\psi \to f_0(980)\omega$, $J/\psi \to f_0(980)\phi$, $J/\psi \to f_2(1270)\omega$, and $J/\psi \to f_2'(1525)\phi$ [7]:

$$\mathrm{Br}(J/\psi \to f_0(980)\omega) = (1.4 \pm 0.5) \times 10^{-4}, \quad (20)$$

$$\mathrm{Br}(J/\psi \to f_0(980)\phi) = (3.2 \pm 0.9) \times 10^{-4}, \quad (21)$$

$$\mathrm{Br}(J/\psi \to f_2(1270)\omega) = (4.3 \pm 0.6) \times 10^{-3}, \quad (22)$$

$$\mathrm{Br}(J/\psi \to f_2'(1525)\phi) = (8 \pm 4) \times 10^{-4}. \quad (23)$$

The suppression

$$\frac{\mathrm{Br}(J/\psi \to f_0(980)\,\omega)}{\mathrm{Br}(J/\psi \to f_2(1270)\,\omega)} = 0.033 \pm 0.013 \quad (24)$$

seems strange in the model under consideration, as well as Eq. (7) in the model (8).

The existence of the decay $J/\psi \to f_0(980)\,\phi$ of greater intensity than the decay $J/\psi \to f_0(980)\,\omega$ [compare Eqs. (20) and (21)] rules out the model specified by Eq. (14) since, in the case under discussion, the decay $J/\psi \to f_0(980)\,\phi$ must be suppressed in relation to the $J/\psi \to f_0(980)\,\omega$ decay by the OZI rule. Thus, Eq. (14) is excluded at a level of physical rigor.

Can one consider the $f_0(980)$ meson as an almost pure $s\bar{s}$ state? This is impossible without a gluon component. Indeed, it is anticipated for the scalar $s\bar{s}$ state from the lowest P-wave multiplet that [17]

$$\mathrm{Br}(J/\psi \to \gamma f_0(980)) \gtrsim \frac{\mathrm{Br}(J/\psi \to \gamma f_2'(1525))}{4} \simeq 1.6 \times 10^{-4}, \quad (25)$$

in contradiction to Eq. (16), which, in fact, requires the $f_0(980)$ meson to be the eighth component of the $SU_f(3)$ octet,

$$f_0(980) = \frac{u\bar{u} + d\bar{d} - 2s\bar{s}}{\sqrt{6}}. \quad (26)$$

This structure gives

$$\Gamma(f_0 \to \gamma\gamma) = \frac{3}{25}(1.7\text{–}5.5)\Gamma(f_2 \to \gamma\gamma) = (0.57\text{–}1.9)(1 \pm 0.14)\,\mathrm{keV}, \quad (27)$$

which is on the verge of conflict with Eq. (18).

In addition, it predicts

$$\mathrm{Br}(J/\psi \to f_0(980)\,\phi) = (2\lambda \approx 1) \cdot \mathrm{Br}(J/\psi \to f_0(980)\,\omega), \quad (28)$$

which is also on the verge of conflict with experimental data [compare Eq. (20) with Eq. (21)].

Equation (26) contradicts Eq. (15) for the prediction

$$R = \left|\frac{g_{f_0K^+K^-}}{g_{f_0\pi^+\pi^-}}\right|^2 = \frac{(\sqrt{\lambda} - 2)^2}{4} \simeq 0.4. \quad (29)$$

In addition, the mass degeneracy $m_{f_0} \simeq m_{a_0}$ is coincidental in this case if the a_0 meson is treated as the four-quark state or contradicts the light hypothesis (8).

The introduction of a gluon component gg in the structure of the $f_0(980)$ meson allows the puzzle of weak coupling to gluons [see (16)] to be easily resolved. Indeed, since [17]

$$\mathrm{Br}(R[q\bar{q}] \to gg) \simeq O(\alpha_s^2) \simeq 0.1\text{–}0.2, \quad \mathrm{Br}(R[gg] \to gg) \simeq O(1), \quad (30)$$

a minor ($\sin^2\alpha \leq 0.08$) dopant of gluonium,

$$f_0 = gg\sin\alpha + \left[\left(1/\sqrt{2}\right)(u\bar{u} + d\bar{d})\sin\beta + s\bar{s}\cos\beta\right]\cos\alpha, \quad (31)$$

$$\tan\alpha = -O(\alpha_s)\left(\sqrt{2}\sin\beta + \cos\beta\right),$$

makes it possible to satisfy Eqs. (15) and (16) and to obtain a weak coupling to photons,

$$\Gamma(f_0(980) \to \gamma\gamma) < 0.22\,\mathrm{keV} \quad (32)$$

at

$$-0.22 > \tan\beta > -0.52. \quad (33)$$

Thus, $\cos^2\beta > 0.8$ and the $f_0(980)$ meson is an almost pure $s\bar{s}$ state, as in [20]. This yields

$$0.1 < \frac{\mathrm{Br}(J/\psi \to f_0(980)\omega)}{\mathrm{Br}(J/\psi \to f_0(980)\phi)} = \frac{1}{\lambda}\tan^2\beta < 0.54. \quad (34)$$

As for the experimental value

$$\frac{\mathrm{Br}(J/\psi \to f_0(980)\omega)}{\mathrm{Br}(J/\psi \to f_0(980)\phi)} = 0.44 \pm 0.2, \quad (35)$$

it needs refinement.

The scenario with the $f_0(980)$ meson as in Eq. (31) and with the $a_0(980)$ meson as a two-quark state (8) runs into the following difficulties:

(i) It is impossible to explain the mass degeneracy of the f_0 and the a_0 meson.

(ii) It is possible to obtain only [5, 6]

$$\mathrm{Br}(\phi \to \gamma f_0 \to \gamma\pi^0\pi^0) \simeq 1.7 \times 10^{-5}, \quad \mathrm{Br}(\phi \to \gamma a_0 \to \gamma\pi^0\eta^0) \simeq 10^{-5}. \quad (36)$$

(iii) It is predicted that

$$\Gamma(f_0 \to \gamma\gamma) < 0.13 \times \Gamma(a_0 \to \gamma\gamma), \quad (37)$$

which is on the verge of conflict with the experimental data [compare Eqs. (11) and (18)].

(iv) It is also predicted that

$$\begin{aligned}&\mathrm{Br}(J/\psi \to a_0(980)\rho) \\ &= (3/\lambda \approx 6) \times \mathrm{Br}(J/\psi \to f_0(980)\phi),\end{aligned} \tag{38}$$

which has almost no chance [compare Eqs. (6) and (21)].

Note that the prediction independent of λ,

$$\begin{aligned}&\frac{\mathrm{Br}(J/\psi \to f_0(980)\phi)}{\mathrm{Br}(J/\psi \to f_2'(1525)\phi)} \\ &= \frac{\mathrm{Br}(J/\psi \to a_0(980)\rho)}{\mathrm{Br}(J/\psi \to a_2(1320)\rho)},\end{aligned} \tag{39}$$

is excluded by the central value in

$$\frac{\mathrm{Br}(J/\psi \to f_0(980)\phi)}{\mathrm{Br}(J/\psi \to f_2'(1525)\phi)} = 0.4 \pm 0.23, \tag{40}$$

obtained from Eqs. (21) and (23) [compare with Eq. (7)]. However, the experimental error is of course overly large. Even a twofold improvement in the accuracy of the measurement in Eq. (40) could be crucial for the scenario under discussion.

The prospects for the model of the $f_0(980)$ meson as the almost pure $s\bar{s}$ state (31) and the $a_0(980)$ meson as the four-quark state (9) with a coincidental mass degeneracy are rather poor, especially as the four-quark model with the symbolic structure

$$f_0 = \frac{s\bar{s}(u\bar{u} + d\bar{d})}{\sqrt{2}}\cos\theta + u\bar{u}d\bar{d}\sin\theta, \tag{41}$$

built around the MIT bag [10], reasonably justifies all unusual features of the $f_0(980)$ meson [15, 21].

Indeed, a strong coupling to the $K\bar{K}$ channel is resolved at $1/16 < \tan^2\theta < 1/2$ (see [15]). There is no problem of the a_0- and f_0-meson mass degeneracy for $\tan^2\theta < 1/3$. A weak coupling to photons was predicted in [9],

$$\Gamma(f_0(980) \to \gamma\gamma) \sim 0.27\,\mathrm{keV}. \tag{42}$$

There is also no problem with the suppression in (24).

But it should be explained how the problem of a weak coupling to gluons is resolved. Recall that, in the MIT-bag model, the $f_0(980)$ meson "consists" of pairs of color-singlet and colored pseudoscalar and vector two-quark mesons [10, 9, 15], including a pair of flavorless colored vector two-quark mesons. It is precisely this pair that converts into two gluons in the lowest order in α_s.

The width of the $f_0(980)$ meson with respect to decay into two gluons can be calculated by using a procedure similar to that for calculating the width of a four-quark state with respect to decay into two photons [9]. This yields

$$\begin{aligned}\Gamma(f_0 \to gg) = \frac{g_0^2}{16\pi m_{f_0}} \cdot 0.03 \left(\frac{\alpha_s \cdot 4\pi}{f_{\underline{V}}^2}\right)^2 \\ \times (1 + \tan\theta)^2\cos^2\theta,\end{aligned} \tag{43}$$

where $g_0^2/4\pi \approx 10$–20 GeV is the OZI-superallowed coupling constant; 0.03 is the fraction of the pair of the flavorless colored vector two-quark mesons in the $f_0(980)$-meson wave function, which is converted into two massless gluons; and $\alpha_s 4\pi/f_{\underline{V}}^2$ is the probability of the transition of the flavorless colored vector two-quark meson into the massless gluon, $\underline{V} \leftrightarrow g$ ($f_{\underline{V}}^2/4\pi = f_\rho^2/8\pi \approx 1$ since the spatial wave functions of the flavorless colored vector two-quark meson and the ρ meson are identical). Thus, we have

$$\Gamma(f_0 \to gg) \approx 15\alpha_s^2(1 + \tan\theta)^2\cos^2\theta\ \ (\mathrm{MeV}). \tag{44}$$

For $-1/\sqrt{2} < \tan\theta < -1/4$, one obtains a width that is at worst one order of magnitude less than in the case of a two-quark scalar meson [17] and which does not contradict Eq. (16).

If we use only planar diagrams, we can find, in the four-quark model, that

$$\begin{aligned}&\mathrm{Br}(J/\psi \to a_0^0(980)\rho^0) \approx \mathrm{Br}(J/\psi \to f_0(980)\omega) \\ &\approx 0.5\mathrm{Br}(J/\psi \to f_0(980)\phi),\end{aligned} \tag{45}$$

which does not contradict experimental data [see Eqs. (6), (20), and (21)].

Recall that almost all four-quark states of the MIT bag [10] are very broad owing to their decays through OZI-superallowed channels. That is why it is impossible to extract them from the background. Only in the rare cases near or under the thresholds of the OZI-superallowed decay channels should the "primitive" four-quark states emerge as narrow resonances. Such evidence for the MIT bag is probably provided by the $a_0(980)$ and $f_0(980)$ mesons as well as by the resonance–interference phenomena predicted in [9] and discovered at the thresholds of the reactions $\gamma\gamma \to \rho^0\rho^0$ and $\gamma\gamma \to \rho^+\rho^-$ (for an overview, see [21]).

A few words on the attractive molecular model, wherein the $a_0(980)$ and $f_0(980)$ mesons are the bound states of the $K\bar{K}$ system [22, 23], are in order. This model explains the mass degeneracy of the states and their strong coupling to the $K\bar{K}$ channel. In the molecular model, as in the four-quark model, there is no problem with the suppressions in (7) and (24). Note that Eq. (45) is also valid in the $K\bar{K}$-molecule model.

But its predictions for two-photon widths [14],

$$\Gamma(a_0(K\bar{K}) \to \gamma\gamma) = \Gamma(f_0(K\bar{K}) \to \gamma\gamma) \approx 0.6\,\text{keV}, \quad (46)$$

are on the verge of conflict with the data in (11) and (18). Moreover, the $K\bar{K}$-molecule widths should be less than the binding energy of $\epsilon \approx 20$ MeV. The current data [7], $\Gamma_{a_0} \simeq 50$–100 MeV and $\Gamma_{f_0} \simeq 40$–100 MeV, contradict this. The $K\bar{K}$-molecule model also predicts [24]

$$\text{Br}(\phi \to \gamma f_0 \to \gamma\pi\pi) \simeq \text{Br}(\phi \to \gamma a_0 \to \gamma\pi^0\eta) \simeq 10^{-5}, \quad (47)$$

which contradicts Eqs. (1) and (2).

Investigations of the production of $a_0(980)$ and $f_0(980)$ mesons in the reactions $\pi^- p \to \pi^0\eta n$ [25] and $\pi^- p \to \pi^0\pi^0 n$ [26] over a wide range of the 4-momentum transfer squared $[0 < -t < 1\,\text{GeV}^2]$ show that these states are compact like the ρ and other two-quark mesons but not extended like the molecules with form factors due to the wave functions. It seems that these experiments rule out the $K\bar{K}$-molecule model. As for the four-quark states, they are compact like the two-quark ones.

Finally, it is necessary to answer the traditional question of where the scalar two-quark states from the lowest P-wave multiplet with the quark structures (8) and (14) are. We believe that there is no problem with this now! All members of this multiplet are established [7]:

$$b_1(1235),\ I^G(J^{PC}) = 1^+(1^{+-}),\quad \Gamma_{b_1(1235)} \simeq 142\,\text{MeV}; \quad (48)$$

$$h_1(1170),\ I^G(J^{PC}) = 0^-(1^{+-}),\quad \Gamma_{h_1(1170)} \simeq 360\,\text{MeV};$$

$$a_1(1260),\ I^G(J^{PC}) = 1^-(1^{++}),\quad \Gamma_{a_1(1260)} = 250\text{–}600\,\text{MeV};$$

$$f_1(1285),\ I^G(J^{PC}) = 0^+(1^{++}),\quad \Gamma_{f_1(1285)} \simeq 24\,\text{MeV};$$

$$a_2(1320),\ I^G(J^{PC}) = 1^-(2^{++}),\quad \Gamma_{a_2(1320)} \simeq 107\,\text{MeV};$$

$$f_2(1270),\ I^G(J^{PC}) = 0^+(2^{++}),\quad \Gamma_{f_2(1270)} \simeq 185\,\text{MeV};$$

$$a_0(1450),\ I^G(J^{PC}) = 1^-(0^{++}),\quad \Gamma_{a_0(1450)} \simeq 265\,\text{MeV},\quad m_{a_0(1450)} = 1300\text{–}1500\,\text{MeV},\quad \Gamma_{a_0(1450)} = 100\text{–}300\,\text{MeV};$$

$$f_0(1370),\ I^G(J^{PC}) = 0^+(2^{++}),\quad \Gamma_{f_0(1370)} = 200\text{–}500\,\text{MeV},\quad m_{f_0(1370)} = 1200\text{–}1500\,\text{MeV}.$$

Of course, one cannot consider the scalar members of Eq. (48) as well established, and it is still necessary to reduce the experimental uncertainties in their masses and widths. Nevertheless, it will be obvious from Eq. (48) that forces responsible for the mass splitting in the P-wave multiplet are either small or compensate each other. That is why it is justified to expect the existence of the $a_0(\sim 1300)$ and $f_0(\sim 1300)$ states, and it seems beyond doubt that the $a_0(980)$ and $f_0(980)$ mesons do not fit into the set in (48).

The statement of the OPAL collaboration [27] that the inclusive production of $f_0(980)$ in hadronic Z^0 decay is consistent with the hypothesis in (14) is not conclusive because no calculation of the inclusive production of four-quark states has been performed thus far. From the general point of view, one can nevertheless expect both copious multiquark-state inclusive production and two-quark one, because, in either case, primary production is the multiproduction of vacuum $q\bar{q}$ pairs.

3. THEORETICAL GROUNDS FOR THE FOUR-QUARK MODEL

A few words on the theoretical grounds for the four-quark nature of the scalar $f_0(980)$ and $a_0(980)$ mesons are in order. It was shown in the context of the MIT bag [10] that the low-lying scalar four-quark nonet as a bound state of diquarks[1)] arises from the strong binding energy in such a configuration due to a hyperfine interaction Hamiltonian of the form

$$H_{\text{hf}} = -\Delta \sum_{i<j} \mathbf{s}_i \cdot \mathbf{s}_j \mathbf{F}_i \cdot \mathbf{F}_j, \quad \mathbf{s} = \boldsymbol{\sigma}/2, \quad \mathbf{F} = \boldsymbol{\lambda}/2,$$

which was obtained from single-gluon exchange in QCD.

The result is [10]

$$\sigma = C^0 = ud\bar{u}\bar{d},$$

$$\kappa^+ = C_{K^+} = ud\bar{d}\bar{s}, \quad \kappa^0 = C_{K^0} = ud\bar{u}\bar{s},$$

$$\kappa^- = C_{K^-} = ds\bar{u}\bar{d}, \quad \bar{\kappa}^0 = C_{\bar{K}^0} = us\bar{u}\bar{d},$$

$$f_0 = C^s = \frac{(us\bar{u}\bar{s} + ds\bar{d}\bar{s})}{\sqrt{2}},$$

$$a_0^+ = C^s_{\pi^+} = us\bar{d}\bar{s}, \quad a_0^0 = C^s_{\pi^0} = \frac{(us\bar{u}\bar{s} - ds\bar{d}\bar{s})}{\sqrt{2}},$$

$$a_0^- = C^s_{\pi^-} = ds\bar{u}\bar{s},$$

[1)] $T_a = \varepsilon_{abc}\bar{q}^b\bar{q}^c$ and $\bar{T}^a = \varepsilon^{abc}q_b q_c$. Note that similar diquarks bind up with quarks to form the baryon octet.

$$m_\sigma = 650\,\text{MeV}, \quad m_\kappa = 900\,\text{MeV},$$
$$m_{f_0} = m_{a_0} = 1100\,\text{MeV}.$$

Of course, the MIT bag model is rather rough, so that one can consider its prediction only as a guide. Since the σ and κ mesons lie considerably above their OZI-superallowed decay channels, their widths are on the order of 1 GeV. That is why information about them can be obtained only in a model-dependent way.

In the last few years, there has been a true renaissance in the treatments of $\pi\pi$ and πK scattering on the basis of phenomenological linear σ models (see, for example, [28–32]). It has been argued that corresponding σ mesons are quark–antiquark states. But, in fact, there is no difference in the formulation of the two-quark and the four-quark case at the Lagrangian level [33].

4. CONCLUSION

There are many reasons to consider the $a_0(980)$ and $f_0(980)$ mesons as four-quark states. In summary, we nevertheless emphasize once again that a further study of the decays $\phi \to \gamma f_0(980)$, $\gamma a_0(980)$; $J/\psi \to a_0(980)\,\rho$, $f_0(980)\,\omega$, $f_0(980)\,\phi$, $a_2(1320)\,\rho$, $f_2(1270)\,\omega$, $f_2'(1525)\,\phi$; $a_0(980) \to \gamma\gamma$; and $f_0(980) \to \gamma\gamma$ will make it possible to solve the puzzle of the nature of the $a_0(980)$ and the $f_0(980)$ meson or at least to rule out some of the scenarios discussed above.

ACKNOWLEDGMENTS

I am grateful to V.V. Gubin and G.N. Shestakov for stimulating discussions.

This work was supported in part by the INTAS (grant no. 94-3986).

REFERENCES

1. M. N. Achasov *et al.*, Phys. Lett. B **438**, 441 (1998).
2. M. N. Achasov *et al.*, Phys. Lett. B **440**, 442 (1998).
3. R. R. Akhmetshin *et al.*, Preprint No. 99-11 (Budker Institute of Nuclear Physics, Siberian Division, Russian Academy of Sciences, Novosibirsk, 1999); E. P. Solodov, *Talk at International Workshop on e^+e^- Collisions from ϕ to J/ψ, Budker Institute of Nuclear Physics, Novosibirsk, Russia, 1999.*
4. V. B. Golubev, *Talk at International Workshop on e^+e^- Collisions from ϕ to J/ψ, Budker Institute of Nuclear Physics, Novosibirsk, Russia, 1999*; http://www.inp.nsk.su/phipsi/golubev.ps
5. N. N. Achasov and V. N. Ivanchenko, Nucl. Phys. B **315**, 465 (1989).
6. N. N. Achasov and V. V. Gubin, Phys. Rev. D **56**, 4084 (1997).
7. Particle Data Group (C. Caso *et al.*), Eur. Phys. J. C **4**, 1 (1998).
8. L. Köpke and N. Wermmes, Phys. Rep. **174**, 67 (1989).
9. N. N. Achasov, S. A. Devyanin, and G. N. Shestakov, Phys. Lett. B **108B**, 134 (1982).
10. R. L. Jaffe, Phys. Rev. D **15**, 267, 281 (1977).
11. D. Antreasyan *et al.*, Phys. Rev. D **33**, 1847 (1986).
12. T. Oest *et al.*, Z. Phys. C **47**, 343 (1990).
13. V. M. Budnev and A. E. Kaloshin, Phys. Lett. B **86B**, 351 (1979).
14. T. Barnes, Phys. Lett. B **165B**, 434 (1985).
15. N. N. Achasov, S. A. Devyanin, and G. N. Shestakov, Usp. Fiz. Nauk **142**, 361 (1984) [Sov. Phys. Usp. **27**, 161 (1984)].
16. G. Eigen, in *Proceedings of the XXIV International Conference on High Energy Physics, Munich, 1988*, Ed. by R. Kotthaus and J. H. Kühn (Springer-Verlag, Berlin, 1989), p. 590.
17. M. B. Cakir and G. R. Farrar, Phys. Rev. D **50**, 3268 (1994); F. E. Close, G. R. Farrar, and Z. Li, Phys. Rev. D **55**, 5749 (1997).
18. H. Marsiske *et al.*, Phys. Rev. D **41**, 3324 (1990).
19. G. Gidal, in *Proceedings of the BNL Workshop on Glueballs "Hybrids and Exotic Hadrons," Upton, 1988,* p. 171.
20. N. A. Törnqvist, Phys. Rev. Lett. **49**, 624 (1982); Z. Phys. C **68**, 647 (1995).
21. N. N. Achasov and G. N. Shestakov, Usp. Fiz. Nauk **161** (6), 53 (1991) [Sov. Phys. Usp. **34**, 471 (1991)].
22. J. Weinstein and N. Isgur, Phys. Rev. D **27**, 588 (1983); Phys. Rev. D **41**, 2236 (1990).
23. F. E. Close, N. Isgur, and S. Kumano, Nucl. Phys. B **389**, 513 (1993).
24. N. N. Achasov, V. V. Gubin, and V. I. Shevchenko, Phys. Rev. D **56**, 203 (1997).
25. A. R. Dzierba, in *Proceedings of the Second Workshop on Physics and Detectors for DAΦNE'95, Frascati, 1995,* Ed. by R. Baldini *et al.*, Frascati Phys. Ser. **4**, 99 (1996); D. Alde *et al.*, hep-ex/9712009.
26. D. Alde *et al.*, Z. Phys. C **66**, 375 (1995).
27. K. Ackerstaff *et al.*, Eur. Phys. J. C **4**, 19 (1998).
28. N. N. Achasov and G. N. Shestakov, Phys. Rev. D **49**, 5779 (1994).
29. F. Sannino and J. Schechter, Phys. Rev. D **52**, 96 (1995).
30. N. A. Törnqvist, Z. Phys. C **68**, 647 (1995).
31. R. Delbourgo and M. D. Scadron, Mod. Phys. Lett. A **10**, 251 (1995).
32. S. Ishida, M. Y. Ishida, H. Takahashi, *et al.*, Prog. Theor. Phys. **95**, 745 (1996).
33. D. Black, A. H. Fariborz, F. Sannino, and J. Schechter, Phys. Rev. D **59**, 074026 (1999).

Physics of Atomic Nuclei, Vol. 65, No. 3, 2002, pp. 552–561. Translated from Yadernaya Fizika, Vol. 65, No. 3, 2002, pp. 579–588.

ELEMENTARY PARTICLES AND FIELDS
Theory

Effective Lagrangians and $I^G(J^{PC}) = 1^-(1^{-+})$ Exotic Resonance State in the VP and the PP Channel

N. N. Achasov* and **G. N. Shestakov****

Institute of Mathematics, Siberian Division, Russian Academy of Sciences, Universitetskiĭ pr. 4, Novosibirsk, 630090 Russia

Received October 13, 2000; in final form, April 13, 2001

Abstract—For $I^G(J^{PC}) = 1^-(1^{-+})$ exotic waves in the reactions $\rho\pi \to \rho\pi$, $\rho\pi \to \eta\pi$, $\rho\pi \to \eta'\pi$, and $\rho\pi \to (K^*\bar{K} + \bar{K}^*K)$ and in allied reactions, a model is constructed that satisfies the conditions of unitarity and analyticity and which employs, as an input, an "anomalous" nondiagonal $VPPP$ interaction relating the $\rho\pi$, $\eta\pi$, $\eta'\pi$, and $K^*\bar{K} + \bar{K}^*K$ channels. The possibility of obtaining, within this simple field-theoretical model, a resonance behavior of the $I^G(J^{PC}) = 1^-(1^{-+})$ amplitudes corresponding to the $\{10\} - \{\bar{10}\}$ and $\{8\}$ representations of the $SU(3)$ group and their mixing is demonstrated explicitly in the mass range 1.3–1.6 GeV, where data of present-day experiments suggest a rich exoticism. © *2002 MAIK "Nauka/Interperiodica".*

1. INTRODUCTION

Hints of states featuring the exotic quantum numbers of $I^G(J^{PC}) = 1^-(1^{-+})$ create an ever increasing agitation among both experimentalists and theorists [1–20]. In the range 1.3–1.6 GeV, they were found in the mass spectra of the $\eta\pi$, $\eta'\pi$, $\rho\pi$, $b_1\pi$, and $f_1\pi$ systems produced in high-energy π^-p collisions and in $N\bar{N}$ annihilation at rest [1–12].

Theoretical considerations on the spectrum of exotic resonance states and their decay modes are based primarily on the MIT bag model, the constituent-gluon model, the color-tube model, lattice calculations, and QCD sum rules, as well as on a number of quite general selection rules. With special emphasis on observed $J^{PC} = 1^{-+}$ phenomena, these constituent quark–gluon models and rules are discussed in [1–20], where the interested reader can also find comprehensive analyses of relevant experimental data and extensive lists of references. The resonance character of recorded signals and the most popular assumption of their hybrid ($q\bar{q}g$) nature form the subject of lively discussions and call for further refinements [1, 6, 7, 12, 14–20].

We note that the first argument in favor of the possible existence of an exotic $J^{PC} = 1^{-+}$ state that is associated with the $\eta\pi$ and $\rho\pi$ channels and which is a member of the $SU(3)$ 20-plet was obtained by the bootstrap method more than 35 years ago [21] (see also [22]).

Methods that produce information about exotic partial waves and which do not employ quark–gluon terms also include those of current algebra and of effective chiral Lagrangians. Suffice it to recall that a prediction was obtained within these approaches for isospin-2 $\pi\pi$ scattering length [23, 24]. Constructing, with the aid of effective chiral Lagrangians, expansions of amplitudes in power series in momenta, one can reveal, even in lower order terms, the presence of contributions featuring open exoticism. This brings about the question of whether at least some of these contributions, which are specified at low energies, are manifestations ("tails") of high-lying exotic resonances. For example, it is well known that, for $\pi\pi$-scattering channels involving σ and ρ resonances, the regions of a resonant and a low-energy behavior of scattering amplitudes can be matched consistently (in the sense of agreement with experimental data) by using an appropriately chosen scheme for unitarizing input chiral contributions and by respecting, to the highest possible degree, the requirements of analyticity [25–34]. In other words, these channels can be treated within model concepts demonstrating that the low-energy contributions computed with the aid of chiral Lagrangians can in principle transform, with increasing energy, into resonances that have parameters observed experimentally. In the present study, we continue following this way and construct a model that satisfies the requirements of unitarity and analyticity and which describes the $J^{PC} = 1^{-+}$ exotic wave in the reaction $\rho\pi \to \eta\pi$ and in allied reactions like $\rho\pi \to \eta'\pi$, $\eta\pi \to \eta\pi$, $\rho\pi \to \rho\pi$, and $\eta\pi \to (K^*\bar{K} + \bar{K}^*K)$ using, as inputs, exotic tree-level amplitudes

*e-mail: achasov@math.nsc.ru
**e-mail: shestako@math.nsc.ru

generated by the simplest anomalous effective interaction (that is, an interaction that involves the tensor $\epsilon_{\mu\nu\tau\kappa}$) of vector ($V$) and pseudoscalar ($P$) mesons. Such an interaction is induced by the Wess–Zumino anomalous chiral Lagrangian [35].

In the effective nonlinear chiral Lagrangian, the ordinary normal component, which contains the octet of pseudoscalar mesons, generates the amplitudes for $PP \to PP$ reactions in the tree approximation, the corresponding quantum numbers in the s channel being $J^{PC} = 0^{++}$ and 1^{--} [24]. In the next approximation, $J^{PC} = 1^{-+}$ exotic contributions appear in the $PP \to PP$ amplitudes owing to finite parts of one-loop diagrams. However, they prove to be nonzero only because of the violation of $SU(3)$ symmetry for the masses of pseudoscalar mesons. Resonances to which such contributions could be matched must possess quite strange a property—all constants of their coupling to the octet of pseudoscalar mesons are bound to vanish in the limit of $SU(3)$ symmetry. It would therefore be more natural to believe that $J^{PC} = 1^{-+}$ exotic resonances, if any, have a different origin. Within effective chiral Lagrangians, their generation may be due to the anomalous interaction of vector and pseudoscalar mesons [36–43]. This is indirectly supported by an analysis of the $PP \to PP$ amplitudes within the linear $SU(3) \times SU(3)$ σ model including only scalar and pseudoscalar mesons [28]. In this model, repulsive forces are operative in the $J^{PC} = 1^{-+}$ channel, so that no resonance states arise.

The ensuing exposition is organized as follows. In Section 2, the general properties of the amplitudes for $VP \to PP$ reactions involving the nonets of vector and pseudoscalar mesons are considered under the assumption of $SU(3)$ symmetry. In Section 3, we construct a simple model aimed at describing the p-wave (exotic) amplitudes for $VP \to VP$, $VP \to PP$, and $PP \to PP$ reactions that employs, as an input, a nondiagonal $VPPP$ interaction relating the $\rho\pi$, $\eta\pi$, $\eta'\pi$, and $K^*\bar{K} + \bar{K}^*K$ channels. In Section 4, it is demonstrated that, within this model, a resonance behavior of the $I^G(J^{PC}) = 1^-(1^{-+})$ amplitudes corresponding to the $\{10\} - \{\bar{10}\}$ and $\{8\}$ representations of the $SU(3)$ group and to their mixing can be obtained in the range 1.3–1.6 GeV. In quark–gluon terms, the $\{10\} - \{\bar{10}\}$ representation can be realized from the sector of $qq\bar{q}\bar{q}$ states, while the $\{8\}$ representation corresponding to $J^{PC} = 1^{-+}$ can in principle be associated with either $qq\bar{q}\bar{q}$ or $q\bar{q}g$ states. In the Appendix, we present an example where n-loop diagrams are calculated and summed in order to obtain unitarized amplitudes.

2. GENERAL PROPERTIES OF $VP \to PP$ AMPLITUDES

The Lorentz and $SU(3)$ structure of the amplitudes for $V_a(k) + P_b(q_1) \to P_c(q_2) + P_d(q_3)$ reactions, where V_a and P_a are members of the vector and the pseudoscalar meson octet in the Cartesian basis ($a = 1, ..., 8$)[1)] and k, q_1, q_2, and q_3 are the 4-momenta of the particles involved in the reaction being considered, has the form

$$M^{(\lambda)}_{ab;cd} = -i\epsilon_{\mu\nu\tau\kappa} e^{\mu}_{(\lambda)} q_1^{\nu} q_2^{\tau} q_3^{\kappa} [f_{abm} d_{mcd} A(s,t,u) + d_{abm} f_{mcd} B(s,t,u) + (u_{ab})_{cd} C(s,t,u)]. \quad (1)$$

Here, f_{abc} and d_{abc} are the standard structure constants of the $SU(3)$ group [44], $(u_{ab})_{cd} = f_{cam} d_{mbd} - d_{cam} f_{mbd}$ [45], $e^{\mu}_{(\lambda)}$ is the μ component of the vector characterizing the polarization of the V meson of helicity λ, $s = (k + q_1)^2$, $t = (k - q_2)^2$, and $u = (k - q_3)^2$; from Bose symmetry, it follows that the invariant amplitude $A(s,t,u)$ is antisymmetric under the substitution $t \leftrightarrow u$, while the invariant amplitudes $B(s,t,u)$ and $C(s,t,u)$ are symmetric. We note that expression (1) can be obtained in a standard way [45–48] by taking into account, along with $SU(3)$ symmetry, the requirements of P and C conservation.

The first and the second term in (1) correspond to the amplitudes for, respectively, $\{8_a\} \to \{8_s\}$ and $\{8_s\} \to \{8_a\}$ octet transitions (we denote these amplitudes by A_{as} and A_{sa}); as usual, $\{8_s\}$ and $\{8_a\}$ stand for the $SU(3)$ symmetric and antisymmetric octet representations contained in the representations $\{8\} \times \{8\}$. The third term in (1) describes transitions that proceed through the representations $\{10\}$ and $\{\bar{10}\}$ with amplitudes A_{10} and $A_{\bar{10}}$ having equal magnitudes and entering into (1) in the combination $A_{10} - A_{\bar{10}}$; in other words, this is the transition from the $\{10\} - \{\bar{10}\}$ VP 20-plet to the final $\{10\} + \{\bar{10}\}$ PP 20-plet. The amplitudes A_{as} and A_{sa} for the transitions between the self-adjoint representations are expanded in, respectively, the $J^{PC} = 2^{++}, 4^{++}, ...$ and the $J^{PC} = 1^{--}, 3^{--}, ...$ partial waves; therefore, they do not contain explicitly exotic contributions. The specific $\eta_8\pi$ final state is absent from the representation $\{8_a\}$, but it is present in the representations $\{8_s\}$, $\{10\}$, and $\{\bar{10}\}$ [21, 22, 49]. The $SU(3)$-exotic meson amplitudes A_{10} and $A_{\bar{10}}$ are expanded in the $J^P = 1^-, 3^-, ...$ partial waves. The isotriplet amplitudes from $A_{10} - A_{\bar{10}}$ correspond to the following two sets of reactions that differ in s-channel G parity: (i) $\rho\eta_8 \to \pi\pi$, $\rho\eta_8 \to K\bar{K}$, $\omega_8\pi \to \pi\pi$, and

[1)] $V_a = (\rho_1, \rho_2, \rho_3, K_4^*, K_5^*, K_6^*, K_7^*, \omega_8)$ and $P_a = (\pi_1, \pi_2, \pi_3, K_4, K_5, K_6, K_7, \eta_8)$.

$\omega_8\pi \to K\bar{K}$ and (ii) $\rho\pi \to \eta_8\pi$, $K^*\bar{K} \to \eta_8\pi$, and $\bar{K}^*K \to \eta_8\pi$. The partial amplitudes for the reactions from the first set possess the nonexotic quantum numbers $I^G(J^{PC}) = 1^+(1^{--}, 3^{--}, ...)$ and, hence, only a hidden $SU(3)$ exoticism. Reactions from the second set—in the following, we will be interested, among other things, precisely in these reactions—are purely exotic, since they involve the $I^G(J^{PC}) = 1^-(1^{-+}, 3^{-+}, ...)$ partial waves.

The amplitude for $V_a(k) + P_b(q_1) \to P_c(q_2) + P_d(q_3)$ reactions involving the $SU(3)$ singlets V_0 and P_0 can be represented in the form

$$N^{(\lambda)}_{ab;cd} = -i\epsilon_{\mu\nu\tau\kappa} e^{\mu}_{(\lambda)} q_1^{\nu} q_2^{\tau} q_3^{\kappa} [\delta_{a0} f_{bcd} D(s,t,u) + \delta_{b0} f_{acd} E(s,t,u) + \delta_{c0} f_{abd} F(s,t,u)], \quad (2)$$

where the Latin indices, which correspond to flavors, run through the values of $0, 1, ..., 8$ and where $V_0 = \omega_0$, $P_0 = \eta_0$, and $f_{ab0} = 0$. By isoscalar particles of specific masses, we mean the $\eta = \eta_8 \cos\theta_P - \eta_0 \sin\theta_P$ and $\eta' = \eta_8 \sin\theta_P + \eta_0 \cos\theta_P$ mesons characterized by the mixing angle of $\theta_P \approx -20^\circ$ [50, 51] and the ideally mixed mesons $\omega = \sqrt{1/3}\,\omega_8 + \sqrt{2/3}\,\omega_0$ and $\phi = \sqrt{2/3}\,\omega_8 - \sqrt{1/3}\,\omega_0$.

The amplitude in (2) describes transitions through octet intermediate states. The first two $SU(3)$ structures in (2) do not contribute to the production of $\eta\pi$ and $\eta'\pi$, because they correspond to transitions to the $\{8_a\}$ final states, which do not involve $\eta_8\pi$ states. The third $SU(3)$ structure in (2) describes the production of the $\eta\pi$ and $\eta'\pi$ systems owing to the singlet component in the wave functions for the η and η' mesons. Under the substitution $t \leftrightarrow u$, the invariant amplitudes $D(s,t,u)$ and $E(s,t,u)$ are symmetric, whereas the invariant amplitude $F(s,t,u)$ does not possess any specific symmetry. Thus, the first two terms in (2) are expanded in the $J^{PC} = 1^{--}, 3^{--}, ...$ partial waves, while the third term is expanded in the $J^{PC} = 1^{-+}, 2^{++}, 3^{-+}, 4^{++}, ...$ partial waves, the odd waves in the latter set $(1^{-+}, 3^{-+}, ...)$ being exotic. In principle, $VP \to PP$ channels featuring ω, ϕ, η, and η' mesons can be considered on the basis of expressions (1) and (2) in the most general form.

3. MODEL FOR THE $I^G(J^{PC}) = 1^-(1^{-+})$ WAVES IN $VP \to VP$, $VP \to PP$, AND $PP \to PP$ REACTIONS

Let us consider the $SU(3)$-invariant Lagrangian that describes contact $VPPP$ interaction and which, with respect to vector mesons, also possesses nonet symmetry. Specifically, we set

$$L(VPPP) = ih\,\epsilon_{\mu\nu\tau\kappa} \mathrm{tr}(\hat{V}^{\mu}\partial^{\nu}\hat{P}\partial^{\tau}\hat{P}\partial^{\kappa}\hat{P}) + i\sqrt{1/3}\,h'\,\epsilon_{\mu\nu\tau\kappa} \mathrm{tr}(\hat{V}^{\mu}\partial^{\nu}\hat{P}\partial^{\tau}\hat{P})\partial^{\kappa}\eta_0, \quad (3)$$

where h and h' are coupling constants, $\hat{P} = \sum_{a=1}^{8} \lambda_a P_a/\sqrt{2}$, $\hat{V}^{\mu} = \sum_{a=0}^{8} \lambda_a V_a^{\mu}/\sqrt{2}$, and λ_a are the Gell-Mann matrices [44]. Tree-level $VP \to PP$ amplitudes corresponding to the Lagrangian in (3) are specified by expressions (1) and (2) featuring the following set of invariant amplitudes (for the sake of brevity, their arguments are omitted): $(A, B, C, D) = h(0, 2, 1, \sqrt{6})$ and $(E, F) = h'(\sqrt{2/3}, -\sqrt{2/3})$. From the discussion in Section 2, it follows that the fact that the amplitudes C and F are nonzero implies that, for the inelastic reactions $\rho\pi \to \eta_8\pi$, $K^*\bar{K} \to \eta_8\pi$, and $\bar{K}^*K \to \eta_8\pi$, the Lagrangian in (3) generates the input $I^G(J^{PC}) = 1^-(1^{-+})$ exotic amplitudes corresponding to the $\{10\} - \{\bar{10}\}$ 20-plet of the $SU(3)$ group and that, for the reactions $\rho\pi \to \eta_0\pi$, $K^*\bar{K} \to \eta_0\pi$, and $\bar{K}^*K \to \eta_0\pi$, this Lagrangian generates amplitudes corresponding to the $\{8\}$ octet of the $SU(3)$ group. In higher orders, these amplitudes also induce $I^G(J^{PC}) = 1^-(1^{-+})$ exotic amplitudes for elastic processes like $\rho\pi \to \rho\pi$ and $\eta\pi \to \eta\pi$. In this connection, it is of interest to consider the following 4×4 set of mutually coupled amplitudes for the exotic channels of $VP \to VP$, $VP \leftrightarrow PP$, and $PP \to PP$ reactions:

$$T_{ij} = \begin{bmatrix} T(\rho\pi \to \rho\pi) & T(\rho\pi \to \eta\pi) & T(\rho\pi \to \eta'\pi) & T(\rho\pi \to K^*K) \\ T(\eta\pi \to \rho\pi) & T(\eta\pi \to \eta\pi) & T(\eta\pi \to \eta'\pi) & T(\eta\pi \to K^*K) \\ T(\eta'\pi \to \rho\pi) & T(\eta'\pi \to \eta\pi) & T(\eta'\pi \to \eta'\pi) & T(\eta'\pi \to K^*K) \\ T(K^*K \to \rho\pi) & T(K^*K \to \eta\pi) & T(K^*K \to \eta'\pi) & T(K^*K \to K^*K) \end{bmatrix}. \quad (4)$$

Here, $i, j = 1, 2, 3, 4$ number the $\rho\pi$, the $\eta\pi$, the $\eta'\pi$, and the K^*K channel, respectively; it goes without saying that, by the brief notation of K^*K, we mean $\bar{K}^*K$ and $K^*\bar{K}$. The corresponding matrix of coupling constants generated by the Lagrangian in (3) for the contact $VPPP$ interaction has the

form

$$h_{ij} = h \begin{bmatrix} 0 & \alpha & \beta & 0 \\ \alpha & 0 & 0 & \gamma \\ \beta & 0 & 0 & \delta \\ 0 & \gamma & \delta & 0 \end{bmatrix}, \qquad (5)$$

where

$$\alpha = \sqrt{\frac{1}{3}}\cos\theta_P - \frac{h'}{h}\sqrt{\frac{2}{3}}\sin\theta_P, \qquad (6)$$

$$\beta = \sqrt{\frac{1}{3}}\sin\theta_P + \frac{h'}{h}\sqrt{\frac{2}{3}}\cos\theta_P,$$

$$\gamma = \sqrt{\frac{2}{3}}\cos\theta_P + \frac{h'}{h}\sqrt{\frac{1}{3}}\sin\theta_P, \qquad (7)$$

$$\delta = \sqrt{\frac{2}{3}}\sin\theta_P - \frac{h'}{h}\sqrt{\frac{1}{3}}\cos\theta_P.$$

Below, we consider three natural limiting cases:

(I) $h' = 0$, all exotic amplitudes belong to the $\{10\} - \{\bar{10}\}$ representation of the $SU(3)$ group.

(II) $h = 0$, all exotic amplitudes belong to the octet representation of the $SU(3)$ group.

(III) $h' = h$, the input interaction (3) possesses an additional nonet symmetry in relation to pseudoscalar mesons.

In order to meet the condition of unitarity for coupled-channel amplitudes, we sum the chains of all s-channel loop diagrams of the type depicted in Fig. 1. This model-dependent field-theoretical method of unitarization has long since been well known in the literature (see, for example, [32, 52–55]). It should be noted that, for cases (I) and (II), the unitarized amplitudes for the entire set of processes in which we are interested can actually be constructed from the amplitudes for loop diagrams explicitly shown in Fig. 1. Indeed, it can be proven that, in all channels, the common ratio of the arising geometric progressions proves to be proportional to the sum of the diagrams in Figs. 1b–1e, loop diagrams of the types in Figs. 1f and 1g and in Figs. 1h and 1i playing the role of input contributions in the corresponding elastic channels (in just the same way as the contact diagram in Fig. 1a plays this role for the inelastic $\rho\pi \to \eta\pi$ channel). But in case (III), the situation is much more involved.

Prior to presenting the results of summation and of the calculation of loops, we deem it expedient to make two comments concerning the model used.

First, the contact contributions from $VPPP$ interaction in exotic channels could be modified by the contributions of tree diagrams involving the exchanges of V mesons that arise upon taking into account the anomalous Lagrangian for VVP interaction and the usual Lagrangian for VPP interaction. However, the resulting complication of the form of input exotic amplitudes does not in fact lead to any new possibilities (or degrees of freedom) for obtaining a resonance behavior of the total unitarized amplitudes—this merely encumbers the model with additional technical problems, rendering it much less transparent than the model exclusively relying on the Lagrangian in (3). By way of example, we indicate that, upon modifying the input exotic amplitudes, the above clear-cut way of unitarization would have to be replaced by one version of Padé approximation of another [27, 28], because it would become impossible to calculate and sum up higher loops directly.

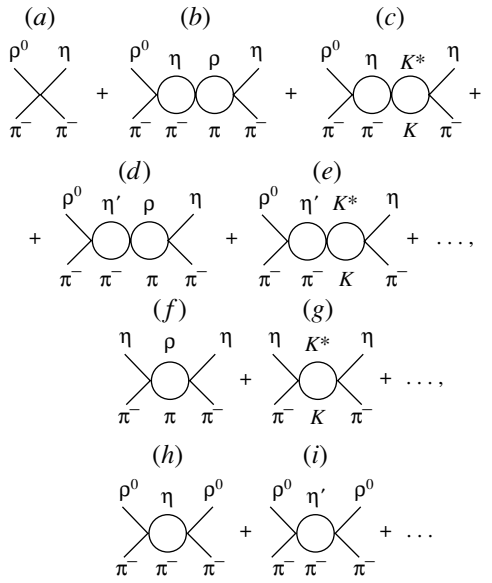

Fig. 1. Examples of the diagrams that are summed in order to obtain unitarized amplitudes.

Second, the effective coupling constant h appearing in the Lagrangian given by Eq. (3) is not unambiguously defined in a theory involving anomalous chiral Lagrangians (for a detailed discussion of this issue, see, for example, [36–43]). One can only state that it is quite modest in relation to the scale specified by the combination $2g_{\rho\pi\pi}g_{\omega\rho\pi}/m_\rho^2 \approx 284\ \mathrm{GeV}^{-3}$ [40, 43]. For this reason, we will consider the coupling constants h and h' as free parameters of the model in the region of their relatively small values.

Summation of the relevant diagrams can easily be performed with the aid of the matrix equation for auxiliary amplitudes $\tilde{T}_{ij}$. This equation, which is schematically depicted in Fig. 2, has the form

$$\tilde{T}_{ij} = h_{ij} + h_{im}\Pi_{mn}\tilde{T}_{nj}. \qquad (8)$$

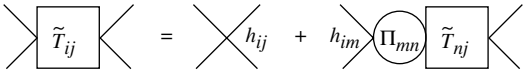

Fig. 2. Auxiliary equation for summation of chains of diagrams belonging to the types in Fig. 1.

The auxiliary amplitudes $\tilde{T}_{ij}$ are introduced at an intermediate stage of the calculations and correspond to the hypothetical situation where all particles involved in the reactions being studied are considered without taking their spins into account, but where these amplitudes are otherwise precise analogs of the physical amplitudes T_{ij} quoted in Eq. (4). In Eq. (8), the quantities h_{ij} are given by relations (5)–(7), while Π_{ij} is a diagonal matrix of loops; that is, $\Pi_{ij} = \delta_{ij}\Pi_j$, where Π_1, Π_2, Π_3, and Π_4 correspond to four independent s-channel loops featuring the $\rho\pi$, $\eta\pi$, $\eta'\pi$, and K^*K intermediate states, respectively, with the assumption that all particles are spinless still being retained. We note that, if all particles are spinless, h_{ij} and Π_{ij} in Eq. (8) are dimesionless just like the amplitudes $\tilde{T}_{ij}$ themselves. For the elements of the matrix $h_{im}\Pi_{mj} = h_{ij}\Pi_j$, it is convenient to introduce, with allowance for (5), the compact notation

$$h_{im}\Pi_{mj} = h_{ij}\Pi_j = h\begin{bmatrix} 0 & \alpha_2 & \beta_3 & 0 \\ \alpha_1 & 0 & 0 & \gamma_4 \\ \beta_1 & 0 & 0 & \delta_4 \\ 0 & \gamma_2 & \delta_3 & 0 \end{bmatrix}, \qquad (9)$$

where $\alpha_1 = \alpha\Pi_1$, $\beta_3 = \beta\Pi_3$, etc. Solving Eq. (8), we obtain

$$\tilde{T}_{ij} = [\,(\hat{1} - \hat{h}\hat{\Pi})^{-1}\,]_{im}\, h_{mj}, \qquad (10)$$

where $\hat{1}$ is an identity matrix and the matrix $\hat{h}\hat{\Pi}$ is specified by relation (9); we also have

$$\bar{D} = \det(\hat{1} - \hat{h}\hat{\Pi}) \qquad (11)$$
$$= 1 - h^2(\alpha_1\alpha_2 + \beta_1\beta_3 + \gamma_2\gamma_4 + \delta_3\delta_4) + h^4(\alpha_1\delta_4 - \beta_1\gamma_4)(\alpha_2\delta_3 - \beta_3\gamma_2).$$

By way of example, we present explicit expressions for the amplitudes of five reactions:

$$\tilde{T}(\rho\pi \to \rho\pi) = h^2[\alpha\alpha_2 + \beta\beta_3 - h^2(\alpha\delta_4 - \beta\gamma_4)(\alpha_2\delta_3 - \beta_3\gamma_2)]/\bar{D}, \qquad (12)$$

$$\tilde{T}(\rho\pi \to \eta\pi) = h\,[\alpha - h^2(\alpha\delta_3 - \beta_3\gamma)\delta_4]/\bar{D}, \quad (13)$$

$$\tilde{T}(\rho\pi \to \eta'\pi) = h\,[\beta + h^2(\alpha_2\delta - \beta\gamma_2)\gamma_4]/\bar{D}, \quad (14)$$

$$\tilde{T}(\rho\pi \to K^*K) = h^2[\alpha_2\gamma + \beta_3\delta]/\bar{D}, \qquad (15)$$

$$\tilde{T}(\eta\pi \to \eta\pi) = h^2[\alpha\alpha_1 + \gamma\gamma_4 - h^2(\alpha\delta_3 - \beta_3\gamma)(\alpha_1\delta_4 - \beta_1\gamma_4)]/\bar{D}. \qquad (16)$$

In cases (I) and (II), the relation $h^2(\alpha\delta - \beta\gamma) = 0$ holds [see Eqs. (5)–(7)], so that, in Eqs. (10)–(16), the terms proportional to the combination on the left-hand side of it drop out, with the result that all formulas are significantly simplified [for example, the numerator on the right-hand side of (13) reduces to $h\alpha$ since $h^2(\alpha\delta_3 - \beta_3\gamma) = h^2(\alpha\delta - \beta\gamma)\Pi_3$ according to (9)].

Let us now take into account the particle spins. We consider the following three processes:

$$\rho^0(k) + \pi^-(q_1) \to \rho^0(k') + \pi^-(q_1'), \qquad (17)$$

$$\rho^0(k) + \pi^-(q_1) \to \eta(q_2) + \pi^-(q_3), \qquad (18)$$

$$\eta(p) + \pi^-(q) \to \eta(q_2) + \pi^-(q_3). \qquad (19)$$

Suppose that $Q = k + q_1 = k' + q_1' = q_2 + q_3 = p + q$ and $s = Q^2$. By directly calculating, with the aid of the Lagrangian in (3), arbitrary terms in the summed series of diagrams (see Appendix), we find that the Lorentz structures in relevant physical amplitudes and their angular dependences are given by

$$T^{(\lambda',\lambda)}(\rho^0\pi^- \to \rho^0\pi^-) \qquad (20)$$
$$= \epsilon_{\mu'\nu'\tau'\sigma}e^{\mu'*}_{(\lambda')}q_1'^{\nu'}k'^{\tau'}\,\epsilon^{\sigma}{}_{\mu\nu\tau}e^{\mu}_{(\lambda)}q_1^{\nu}k^{\tau}\;\tilde{T}'(\rho\pi \to \rho\pi)$$
$$= (\delta_{\lambda,+1} + \delta_{\lambda,-1})(\delta_{\lambda',+1} + \delta_{\lambda',-1}) \times (s/2)|\mathbf{q}_1|^2(\lambda\lambda' + \cos\theta)\,\tilde{T}'(\rho\pi \to \rho\pi),$$

$$T^{(\lambda)}(\rho^0\pi^- \to \eta\pi^-) \qquad (21)$$
$$= \epsilon_{\mu\nu\tau\sigma}e^{\mu}_{(\lambda)}q_1^{\nu}q_2^{\tau}q_3^{\sigma}\;\tilde{T}'(\rho\pi \to \eta\pi)$$
$$= -(\delta_{\lambda,+1} + \delta_{\lambda,-1})i\sqrt{s/2}|\mathbf{q}_1||\mathbf{q}_3| \times \sin\theta\,\tilde{T}'(\rho\pi \to \eta\pi),$$

$$T(\eta\pi^- \to \eta\pi^-) = |\mathbf{q}|^2\cos\theta\,\tilde{T}'(\eta\pi \to \eta\pi), \qquad (22)$$

where λ (λ') is the helicity of the primary (final) ρ^0 meson and θ is the angle between the momenta of the primary and the final pion in the reaction c.m. frame. Needless to say, all the physical amplitudes T in Eqs. (20)–(22) are dimensionless. At the same time, it can be seen from (20)–(22) that the invariant amplitudes $\tilde{T}'$ have different dimensions in $VP \to VP$, $VP \to PP$, and $PP \to PP$ channels. These invariant amplitudes are directly obtained from the corresponding auxiliary amplitudes $\tilde{T}$ [see Eqs. (10)–(16)] by substituting, into the latter, the physical dimensional coupling constants h and h' from Lagrangian (3) and the p-wave loop integrals in the form

$$\Pi_i = \frac{1}{16\pi}\,\frac{2}{3}\,F_i \qquad (23)$$

$$\times \begin{cases} 4s, \ i = 1,4 \ \ (VP \text{ loops}), \\ 1, \ i = 2,3 \ \ (PP \text{ loops}), \end{cases}$$

where

$$F_i = C_{1i} + sC_{2i} + \frac{s^2}{\pi} \int\limits_{m_{i+}^2}^{\infty} \frac{[P_i(s')]^3 \, ds'}{\sqrt{s'}\, s'^2 (s' - s - i\varepsilon)} \tag{24}$$

$$= C_{1i} + sC_{2i} + \frac{(s - m_{i+}^2)^{3/2}(s - m_{i-}^2)^{3/2}}{8\pi s^2}$$
$$\times \left[\ln \left(\frac{\sqrt{s - m_{i-}^2} - \sqrt{s - m_{i+}^2}}{\sqrt{s - m_{i-}^2} + \sqrt{s - m_{i+}^2}} \right) + i\pi \right]$$
$$+ \frac{1}{4\pi} \left\{ \frac{1}{2m_{i+}m_{i-}} \ln \left(\frac{m_{i+} - m_{i-}}{m_{i+} + m_{i-}} \right) \right.$$
$$\times \left[\frac{m_{i+}^4 m_{i-}^4}{s^2} - \frac{3m_{i+}^2 m_{i-}^2}{2s}(m_{i+}^2 + m_{i-}^2) \right.$$
$$+ \frac{3}{8}(m_{i+}^4 + m_{i-}^4 + 6m_{i+}^2 m_{i-}^2)$$
$$\left. + \frac{s(m_{i+}^2 + m_{i-}^2)}{16 m_{i+}^2 m_{i-}^2}(m_{i+}^4 - 10 m_{i+}^2 m_{i-}^2 + m_{i-}^4) \right]$$
$$+ \frac{m_{i+}^2 m_{i-}^2}{2s} - \frac{5}{8}(m_{i+}^2 + m_{i-}^2)$$
$$\left. + \frac{s(3m_{i+}^4 + 3m_{i-}^4 + 38 m_{i+}^2 m_{i-}^2)}{48 m_{i+}^2 m_{i-}^2} \right\}.$$

Here, $P_i(s) = [(s - m_{i+}^2)(s - m_{i-}^2)/(4s)]^{1/2}$; m_{i+} and m_{i-} are, respectively, the sum and the difference of the particle masses in the ith channel; and C_{1i} and C_{2i} are subtraction constants. We note that expression (24) is valid for $s \geq m_{i+}^2$. In the regions $m_{i-}^2 < s < m_{i+}^2$ and $s \leq m_{i-}^2$, it changes form in accordance with an analytic continuation [56].

4. ANALYSIS OF POSSIBLE RESONANCE PHENOMENA

First of all, we note that the number of free parameters in the model can be reduced almost without adversely affecting its potential. In particular, we assume that $C_{11} = C_{14}$ and $C_{21} = C_{24}$ for VP loops and that $C_{12} = C_{13}$ and $C_{22} = C_{23}$ for PP loops. Moreover, the s dependence of the combinations $C_{1i} + sC_{2i}$ is not crucial in the vicinity of a possible resonance; for the important free parameters, one can therefore retain only the constants C_{11} and C_{12}, setting $C_{21} = C_{22} = 0$, which will be done in the majority of the versions considered below. The simplest way to grope for a possible resonance situation consists in finding a zero of $\mathrm{Re}(\bar{D})$ [see Eqs. (11)–(16)] at fixed values of h and h' and fixed $\sqrt{s}$—for example, at $\sqrt{s} = 1.43$ GeV. In doing this, the subtraction constants C_{11} and C_{12}, which are left to be free parameters, are not determined unambiguously. By way of example, we indicate that, in cases I and II, they are only bound to satisfy a relation of the type $C_{12} = (\xi_1 + \xi_2 C_{11})/(\xi_3 + \xi_4 C_{11})$, with ξ_i being known numbers. However, this ambiguity is not a drawback—on the contrary, it offers the possibility for varying C_{11}, whereby one can readily change the shape of resonance curves and the relationships between the cross sections for different channels.

According to the analysis performed in [36–40, 43], the region $|\tilde{h}| \leq 0.4$ is admissible for the quantity $\tilde{h} \equiv F_\pi^3 h$, where $F_\pi \approx 130$ MeV. In order to illustrate the existence of resonance phenomena in our toy model, we consider the values of $\tilde{h}$ (and of $\tilde{h}' \equiv F_\pi^3 h'$) in the vicinity of 0.1. It is worth noting that, actually, resonance phenomena are possible in the model over the entire region $|\tilde{h}| \leq 0.4$, but, as $|\tilde{h}|$ (or $|\tilde{h}'|$ or both) increases from 0.1 to 0.4, distinct enhancements of the resonance type are shifted in the reaction cross sections to the region $\sqrt{s} \approx 1$–1.3 GeV (it should be emphasized that the unitarized amplitudes greatly depend on the second and fourth powers of the coupling constants; therefore, they are highly sensitive to changes in $|\tilde{h}|$ and $|\tilde{h}'|$).

Figures 3 and 4 display typical energy dependences of the cross sections for the reactions $\rho^0\pi^- \to \rho^0\pi^-$, $\rho^0\pi^- \to \eta\pi^-$, $\rho^0\pi^- \to \eta'\pi^-$, and $\rho^0\pi^- \to K^{*0}K^-$ and of the phases of the amplitudes for the reactions $\rho\pi \to \rho\pi$ and $\rho\pi \to \eta\pi$ according to the predictions of the model for cases (I)–(III) (note that the amplitude for the inelastic process $\rho\pi \to \eta\pi$ was found apart from the sign). These figures, together with Tables 1 and 2, which give specific parameter values used in plotting the curves in the figures, illustrate resonance effects that are concentrated predominantly in the regions $\sqrt{s} \approx 1.3$–1.4 GeV and $\sqrt{s} \approx 1.5$–1.6 GeV, respectively. Among the aforementioned four channels, the $\rho\pi \to \eta\pi$ channel is dominant as a rule in case (I), where all the amplitudes being considered belong to the $\{10\} - \{\bar{10}\}$ representation. In case (II), where all the amplitudes belong to the octet representation, the channels $\rho\pi \to \rho\pi$ and $\rho\pi \to \eta'\pi$ play a leading role. In case (III), where $h' = h$ and where the input interaction (3) possesses a nonet symmetry, the cross sections for all channels, with the exception of that for the K^*K channel, are quite sizable, so that the general pattern is rather intricate.

Let us now compare the values found here for the cross sections (see Figs. 3 and 4) with the cross

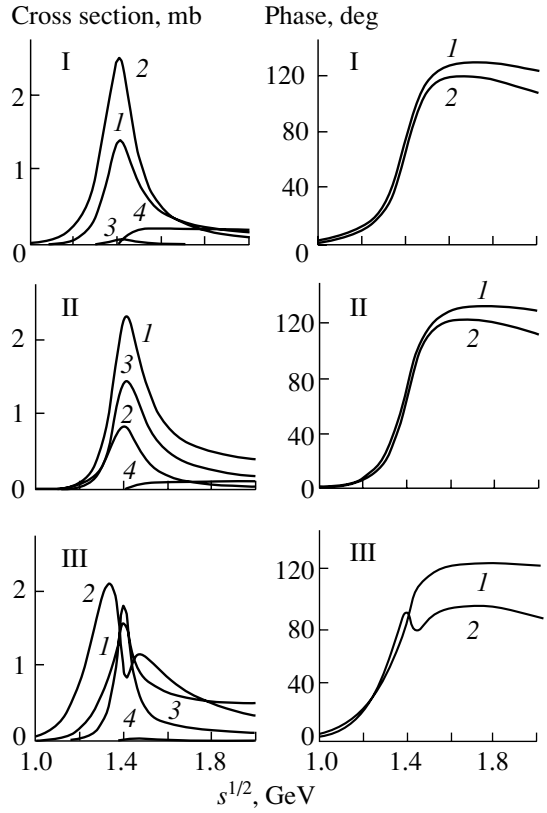

Fig. 3. Cross sections for the reactions (*1*) $\rho^0\pi^- \to \rho^0\pi^-$, (*2*) $\rho^0\pi^- \to \eta\pi^-$, (*3*) $\rho^0\pi^- \to \eta'\pi^-$, and (*4*) $\rho^0\pi^- \to K^{*0}K^-$ and phases of the amplitudes for the reactions (*1*) $\rho\pi \to \rho\pi$ and (*2*) $\rho\pi \to \eta\pi$ in cases (I)–(III). The values of the parameters were taken from Table 1.

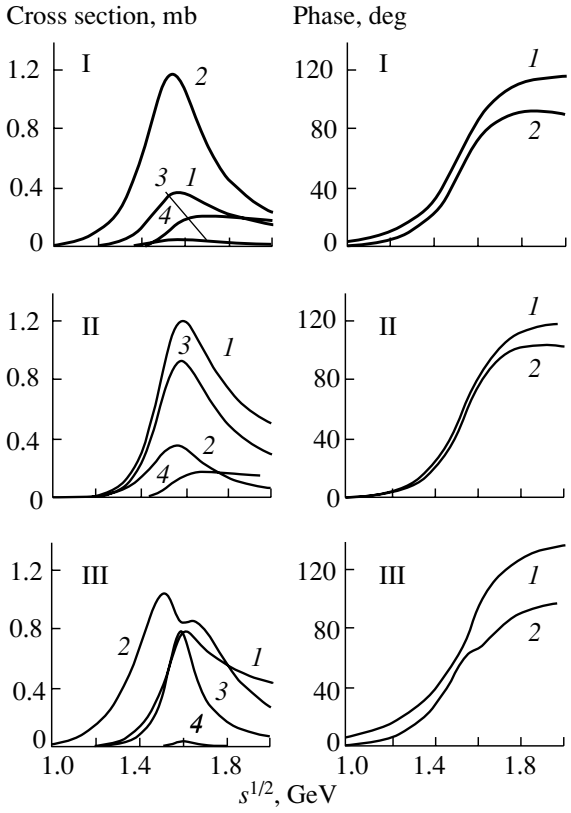

Fig. 4. As in Fig. 3, but for the parameter values borrowed from Table 2.

sections for the production of the $a_2(1320)$ resonance. By using data on the decay branching fractions from [1], we find that, at $\sqrt{s} = m_{a_2} = 1.32$ GeV, $\sigma(\rho^0\pi^- \to a_2 \to \rho^0\pi^-) \approx 5.7$ mb and $\sigma(\rho^0\pi^- \to a_2 \to \eta\pi^-) \approx 2.36$ mb. If we additionally take into account the relationship between the factor $(2J+1)/|\mathbf{k}|^2$ for $a_2(1320)$ and the $J = 1$ enhancement found for $\sqrt{s} \approx 1.3$–1.4 GeV or for $\sqrt{s} \approx 1.5$–1.6 GeV, it can be concluded that we are definitively dealing here with a resonance behavior of the $I^G(J^{PC}) = 1^-(1^{-+})$ exotic waves in the range $1.3 \le \sqrt{s} \le 1.6$ GeV, at least in the $\rho\pi$, $\eta\pi$, and $\eta'\pi$ channels.[2)]

It seems that the most pronounced manifestation of the $I^G(J^{PC}) = 1^-(1^{-+})$ exotic state in the range 1.3–1.4 GeV (or of states that are most often denoted by π_1) was observed in the $\eta\pi^0$ channel of the charge-exchange reaction $\pi^-p \to \eta\pi^0 n$ at energies of 32, 38, and 100 GeV [11]. The intensity of the π_1 signal at a maximum in this reaction proved to be only 3.5 times smaller than the corresponding intensity of the signal from the $a_2(1320)$ resonance. It is of paramount importance that, in this case, both $a_2(1320)$ and π_1 are produced through the same mechanism, that of Reggeized ρ-meson exchange, which is dominant at high energies. If π_1 is indeed a complicated structure of the $qq\bar{q}\bar{q}$ or $q\bar{q}g$ type, then the fact that the cross section for π_1 production in the charge-exchange reaction proved to be on the same order of magnitude as the cross section for the production of the "simple" $q\bar{q}$ resonance $a_2(1320)$ is strong evidence in favor of the resonance character of the observed exotic signal.

In the reaction $\pi^-p \to \eta\pi^-p$ at 37 GeV [3] and 18 GeV [12], the production of the π_1 state in the $\eta\pi^-$ channel proved to be suppressed in relation to the production of the $a_2(1320)$ resonance in proportion to 15 and 30, respectively. This may be due to a more complicated mechanism of this reaction as compared to the charge-exchange reaction. As a matter of fact, there are three competing natural-parity exchanges in the former case: Reggeized ρ exchange, Reggeized f_2 exchange, and Pomeron exchange. As is known from [57], the last two types of exchange are dominant

[2)] In the model considered here, the question of additional couplings between the resonance-type formations being discussed and the $b_1\pi$ and $f_1\pi$ channels remains open, but it is difficult to include these couplings in our scheme in a straightforward way.

Table 1. Values of the model parameters for the curves in Fig. 3 (C_{11} and C_{12} are given in GeV^2, while the remaining parameters are dimensionless)

Case	$F_\pi^3 h$	$F_\pi^3 h'$	C_{11}	C_{21}	C_{12}	C_{22}
I	0.10746	0	0.17	0	1.25	0
II	0	0.10746	0.34	0	0.67	0
III	0.10746	0.10746	0.49	0	0.50	0

Table 2. Values of the model parameters for the curves in Fig. 4 (C_{11} and C_{12} are given in GeV^2, while the remaining parameters are dimensionless)

Case	$F_\pi^3 h$	$F_\pi^3 h'$	C_{11}	C_{21}	C_{12}	C_{22}
I	0.10746	0	0.18	0	0.76	0
II	0	0.08417	0.33	0	0.78	0
III	0.10746	0.10746	0.11	0.11	0.11	0.11

in the case of $a_2^-(1320)$ production. We note that the π_1 state can be produced through Pomeron exchange only owing to the presence of an octet component in its wave function. If, however, this component is small—that is, if π_1 predominantly belongs to the $\{10\} - \{\bar{10}\}$ representation of the $SU(3)$ group—the production of π_1 through Pomeron exchange must be suppressed.

In high-energy photoproduction reactions, which are dominated by Reggeized one-pion exchange (for example, in the reaction $\gamma p \to \rho^0\pi^-\Delta^{++} \to \pi^+\pi^-\pi^-\Delta^{++}$ at low momentum transfers from the photon to the $\pi^+\pi^-\pi^-$ system), it is natural to expect that the Regge form factors normalized to unity at the pion pole will have close values for the cases of $a_2(1320)$ and π_1 production; therefore, the corresponding cross sections can in principle be on the same order of magnitude. Indeed, a sizable signal in the region around 1.7 GeV is observed in the reactions $\gamma p \to \rho^0\pi^-\Delta^{++} \to \pi^+\pi^-\pi^-\Delta^{++}$ and $\gamma p \to \rho^0\pi^+ n \to \pi^+\pi^-\pi^+ n$ along with a distinct $a_2(1320)$ peak [58]. However, this signal may be due, at least partly, to the contribution of the known resonance $\pi_2(1670)$ [58]. In this connection, we deem that large-statistics searches for the π_1 state (or states) in photoproduction reactions—such searches are planned in the physics program of the Jefferson Laboratory (see the relevant discussion in [6, 14, 15, 18–20])—are of crucial importance. In addition, one may hope to see commensurate cross sections for $a_2(1320)$ and for π_1 production via the one-pion-exchange mechanism in electroproduction reactions as well—for example, in $\gamma^* p \to \rho^0\pi^-\Delta^{++}$ and $\gamma^* p \to \rho^0\pi^+ n$. By combining data on the photoproduction and electroproduction of π_1 with data on π_1 decay into $\rho\pi$, it would become possible to verify, for the first time, the vector-dominance model for an exotic meson state. We note that a detailed investigation of the radiative decays of π_1 states into $\gamma\pi$ in π_1 production on nuclei via the one-photon-exchange mechanism is planned at CERN with the aid of the COMPASS spectrometer [59].

In summary, we conclude that our calculations appear to be yet another piece of evidence in favor of the existence of a manifestly exotic $I^G(J^{PC}) = 1^-(1^{-+})$ resonance in the range 1.3–1.6 GeV.

ACKNOWLEDGMENTS

This work was supported in part by a joint grant (no. IR-97-232) from INTAS and the Russian Foundation for Basic Research.

APPENDIX

By way of example, we will calculate, on the basis of the Lagrangian in (3), the contribution of the diagram featuring an arbitrary number of s-channel $\eta\pi$ and $\rho\pi$ loops to the $\rho^0\pi^- \to \rho^0\pi^-$ amplitude, which is given by (20). For the process

$$\rho^0(k) + \pi^-(q_1) \to \eta(\tilde{q}_1) + \pi^-(Q - \tilde{q}_1)$$
$$\to \rho(\tilde{k}_1) + \pi(Q - \tilde{k}_1) \to \eta(\tilde{q}_2) + \pi^-(Q - \tilde{q}_2)$$
$$\to \rho(\tilde{k}_2) + \pi(Q - \tilde{k}_2) \to \eta(\tilde{q}_3)$$
$$+ \pi^-(Q - \tilde{q}_3) \to \ldots \to \rho(\tilde{k}_n) + \pi(Q - \tilde{k}_n)$$
$$\to \eta(\tilde{q}_{n+1}) + \pi^-(Q - \tilde{q}_{n+1}) \to \rho^0(k') + \pi^-(q_1'),$$

where $\tilde{q}_i$ and $\tilde{k}_j$ are the variables of momentum integration in the loops involved and $Q = k + q_1 = k' + q_1'$ ($Q^2 = s$), we consider a diagram where there are $n+1$ s-channel $\eta\pi$ loops and n s-channel $\rho\pi$ loops, with n taking values of $0, 1, 2, \ldots$ (see, for example, the diagram in Fig. 1h). Further, we introduce the notation

$$\epsilon_{\mu\nu\tau\sigma} e^\mu_{(\lambda)} Q^\nu \tilde{q}_1^\tau k^\sigma = [e_{(\lambda)} Q \tilde{q}_1 k],$$
$$\epsilon_{\mu\nu\tau\sigma} e^{\mu *}_{(\lambda')} Q^\nu \tilde{q}_{n+1}^\tau k'^\sigma = [e^*_{(\lambda')} Q \tilde{q}_{n+1} k'],$$
$$\epsilon_{\mu_j\nu\tau\sigma} Q^\nu \tilde{q}_i^\tau \tilde{k}_j^\sigma = [Q\tilde{q}_i\tilde{k}_j]_{\mu_j},$$
$$\epsilon_{\mu_j\nu\tau_i\sigma_j} Q^\nu = [Q]_{\mu_j\tau_i\sigma_j},$$
$$l(\tilde{q}_i) = (\tilde{q}_i^2 - m_\eta^2)((Q - \tilde{q}_i)^2 - m_\pi^2),$$
$$l(\tilde{k}_j) = (\tilde{k}_j^2 - m_\rho^2)((Q - \tilde{k}_j)^2 - m_\pi^2).$$

The amplitude corresponding to the diagram in question can then be represented in the form

$$I_{2n+1}^{(\lambda',\lambda)} = -(h\alpha)^{2n+2}(-1)^n 2^n \left(\frac{i}{(2\pi)^4}\right)^{2n+1}$$

$$\times \int \ldots \int d\tilde{q}_1\, d\tilde{k}_1\, d\tilde{q}_2\, d\tilde{k}_2\, d\tilde{q}_3 \ldots d\tilde{k}_n\, d\tilde{q}_{n+1}$$
$$\times \frac{[\epsilon_{(\lambda)} Q\tilde{q}_1 k]}{l(\tilde{q}_1)} \frac{[Q\tilde{q}_1\tilde{k}_1]_{\mu_1}}{l(\tilde{k}_1)} \frac{[Q\tilde{q}_2\tilde{k}_1]^{\mu_1}}{l(\tilde{q}_2)} \frac{[Q\tilde{q}_2\tilde{k}_2]_{\mu_2}}{l(\tilde{k}_2)}$$
$$\times \frac{[Q\tilde{q}_3\tilde{k}_2]^{\mu_2}}{l(\tilde{q}_3)} \cdots \frac{[Q\tilde{q}_n\tilde{k}_n]_{\mu_n}}{l(\tilde{k}_n)}$$
$$\times \frac{[Q\tilde{q}_{n+1}\tilde{k}_n]^{\mu_n}}{l(\tilde{q}_{n+1})} [e^*_{(\lambda')} Q\tilde{q}_{n+1} k'].$$

The factor 2^n originates from identical contributions of $\rho^0\pi^-$ and $\rho^-\pi^0$ intermediate states. Upon integration followed by summation over intermediate indices, we obtain

$$I^{(\lambda',\lambda)}_{2n+1} = -(h\alpha)^{2n+2} \left(\frac{1}{16\pi}\frac{2}{3}F_2\right)^{n+1}$$
$$\times \left(-\frac{1}{16\pi}\frac{2}{3}\cdot 2F_1\right)^n (\epsilon_{\mu\nu\tau_1\sigma} e^{\mu}_{(\lambda)} Q^{\nu} k^{\sigma})$$
$$\times g^{\tau_1\tau'_1}[Q]_{\mu_1\tau'_1\sigma_1} g^{\mu_1\mu'_1} g^{\sigma_1\sigma'_1}[Q]_{\mu'_1\tau_2\sigma'_1}$$
$$\times g^{\tau_2\tau'_2}[Q]_{\mu_2\tau'_2\sigma_2} g^{\mu_2\mu'_2} g^{\sigma_2\sigma'_2}[Q]_{\mu'_2\tau_3\sigma'_2} \times$$
$$\cdots \times g^{\tau_n\tau'_n}[Q]_{\mu_n\tau'_n\sigma_n} g^{\mu_n\mu'_n} g^{\sigma_n\sigma'_n}[Q]_{\mu'_n\tau_{n+1}\sigma'_n}$$
$$\times g^{\tau_{n+1}\tau'_{n+1}} (\epsilon_{\mu'\nu'\tau_{n+1}\sigma'} e^{\mu'*}_{(\lambda')} Q^{\nu'} k'^{\sigma'})$$
$$= (h\alpha)^{2n+2} \left(\frac{1}{16\pi}\frac{2}{3}F_2\right)^{n+1} \left(\frac{1}{16\pi}\frac{2}{3}\cdot 4sF_1\right)^n$$
$$\times \epsilon_{\mu'\nu'\tau'\sigma} e^{\mu'*}_{(\lambda')} q'^{\nu'}_1 k'^{\tau'} \epsilon^{\sigma}{}_{\mu\nu\tau} e^{\mu}_{(\lambda)} q^{\nu}_1 k^{\tau}$$
$$= \epsilon_{\mu'\nu'\tau'\sigma} e^{\mu'*}_{(\lambda')} q'^{\nu'}_1 k'^{\tau'} \epsilon^{\sigma}{}_{\mu\nu\tau}$$
$$\times e^{\mu}_{(\lambda)} q^{\nu}_1 k^{\tau} (h\alpha)^{2n+2} \Pi^{n+1}_2 \Pi^n_1$$
$$= \epsilon_{\mu'\nu'\tau'\sigma} e^{\mu'*}_{(\lambda')} q'^{\nu'}_1 k'^{\tau'} \epsilon^{\sigma}{}_{\mu\nu\tau}$$
$$\times e^{\mu}_{(\lambda)} q^{\nu}_1 k^{\tau} [h^2 \alpha\alpha_2 (h^2\alpha_1\alpha_2)^n].$$

From this representation, it follows that the Lorentz structures of the initial and the final vertex of the diagram factorize and are independent of the number of loops and that the invariant amplitude $h^2\alpha\alpha_2\,(h^2\alpha_1\alpha_2)^n$ coincides with the nth term of the expansion of the invariant amplitude $\tilde{T}'(\rho\pi \to \rho\pi)$ from (20) in powers of $h^2\alpha_1\alpha_2$ [this can easily be proven with the aid of expressions (11) and (12)].

REFERENCES

1. Particle Data Group (C. Caso *et al.*), Eur. Phys. J. C **3**, 1, 394, 609 (1998).
2. D. Alde *et al.,* Phys. Lett. B **205**, 397 (1988).
3. G. M. Beladidze *et al.*, Phys. Lett. B **313**, 276 (1993).
4. H. Aoyagi *et al.*, Phys. Lett. B **314**, 246 (1993).
5. C. Amsler *et al.*, Phys. Lett. B **333**, 277 (1994).
6. G. S. Adams, Nucl. Phys. A **623**, 158c (1997).
7. A. Zaitsev, in *Hadron Spectroscopy*, Ed. by S.-U. Chung and H. J. Willutzki, AIP Conf. Proc. **432**, 461 (1998); T. Adams, in *Hadron Spectroscopy*, Ed. by S.-U. Chung and H. J. Willutzki, AIP Conf. Proc. **432**, 104 (1998); A. Ostrovidov, in *Hadron Spectroscopy*, Ed. by S.-U. Chung and H. J. Willutzki, AIP Conf. Proc. **432**, 263 (1998); W. Dünnweber *et al.*, in *Hadron Spectroscopy*, Ed. by S.-U. Chung and H. J. Willutzki, AIP Conf. Proc. **432**, 309 (1998); D. P. Weygand, in *Hadron Spectroscopy*, Ed. by S.-U. Chung and H. J. Willutzki, AIP Conf. Proc. **432**, 313 (1998); D. S. Brown, in *Hadron Spectroscopy*, Ed. by S.-U. Chung and H. J. Willutzki, AIP Conf. Proc. **432**, 318 (1998); D. Ryabchikov, in *Hadron Spectroscopy*, Ed. by S.-U. Chung and H. J. Willutzki, AIP Conf. Proc. **432**, 527 (1998); E. Klempt, in *Hadron Spectroscopy*, Ed. by S.-U. Chung and H. J. Willutzki, AIP Conf. Proc. **432**, 867 (1998).
8. D. R. Thompson *et al.*, Phys. Rev. Lett. **79**, 1630 (1997).
9. A. Abele *et al.*, Phys. Lett. B **423**, 175 (1998); **446**, 349 (1999).
10. G. S. Adams *et al.*, Phys. Rev. Lett. **81**, 5760 (1998).
11. D. Alde *et al.*, Yad. Fiz. **62**, 462 (1999) [Phys. At. Nucl. **62**, 421 (1999)].
12. S. U. Chung *et al.*, Phys. Rev. D **60**, 092001 (1999); S. U. Chung, Nucl. Phys. A **655**, 77c (1999).
13. F. E. Close and H. J. Lipkin, Phys. Lett. B **196**, 245 (1987); H. J. Lipkin, Phys. Lett. B **219**, 99 (1989).
14. P. R. Page, Phys. Lett. B **415**, 205 (1997); Nucl. Phys. A **663**, 585 (2000).
15. A. Afanasev and P. R. Page, Phys. Rev. D **57**, 6771 (1998).
16. A. Donnachie and P. R. Page, Phys. Rev. D **58**, 114012 (1998).
17. N. Isgur, Phys. Rev. D **60**, 114016 (1999).
18. T. Barnes, nucl-th/9907020.
19. A. V. Afanasev and A. P. Szczepaniak, Phys. Rev. D **61**, 114005 (2000).
20. S. Godfrey and J. Napolitano, Rev. Mod. Phys. **71**, 1411 (1999).
21. J. Schechter and S. Okubo, Phys. Rev. **135**, B1060 (1964).
22. B. W. Lee, S. Okubo, and J. Schechter, Phys. Rev. **135**, B219 (1964).
23. S. Weinberg, Phys. Rev. Lett. **17**, 616 (1966).
24. J. A. Cronin, Phys. Rev. **161**, 1483 (1967).
25. L. S. Brown and R. L. Goble, Phys. Rev. Lett. **20**, 346 (1968).
26. G. J. Gounaris and J. J. Sakurai, Phys. Rev. Lett. **21**, 244 (1968).
27. J. L. Basdewant and B. W. Lee, Phys. Rev. D **2**, 1680 (1970).
28. L.-H. Chan and R. W. Haymaker, Phys. Rev. D **10**, 4143 (1974).
29. W. Lin and B. D. Serot, Phys. Lett. B **233**, 23 (1989).
30. A. Dobado, M. J. Herrero, and T. N. Truong, Phys. Lett. B **235**, 134 (1990).

31. J. Gasser and U.-G. Meissner, Nucl. Phys. B **357**, 90 (1991).
32. N. N. Achasov and G. N. Shestakov, Phys. Rev. D **49**, 5779 (1994).
33. M. Harada, F. Sannino, and J. Schechter, Phys. Rev. D **54**, 1991 (1996).
34. D. G. Dumm, A. Pich, and J. Portoles, Phys. Rev. D **62**, 054014 (2000).
35. J. Wess and B. Zumino, Phys. Lett. B **37B**, 95 (1971).
36. Ö. Kaymakcalan, S. Rajeev, and J. Schechter, Phys. Rev. D **30**, 594 (1984).
37. H. Gomm, Ö. Kaymakcalan, and J. Schechter, Phys. Rev. D **30**, 2345 (1984).
38. Ö. Kaymakcalan and J. Schechter, Phys. Rev. D **31**, 1109 (1985).
39. J. Schechter, Phys. Rev. D **34**, 868 (1986).
40. P. Jain, R. Johnson, U.-G. Meissner, *et al.*, Phys. Rev. D **37**, 3252 (1988).
41. T. Fujiwara, T. Kugo, H. Terao, *et al.*, Prog. Theor. Phys. **73**, 926 (1985).
42. M. Bando, T. Kugo, and K. Yamawaki, Nucl. Phys. B **259**, 493 (1985); Phys. Rep. **164**, 217 (1988).
43. U.-G. Meissner, Phys. Rep. **161**, 213 (1988).
44. M. Gell-Mann, Phys. Rev. **125**, 1067 (1962).
45. V. I. Ogievetskiĭ and I. V. Polubarinov, Yad. Fiz. **4**, 853 (1966) [Sov. J. Nucl. Phys. **4**, 605 (1967)]; R. E. Cutkosky, Ann. Phys. (N.Y.) **23**, 415 (1963).
46. P. G. O. Freund, H. Ruegg, D. Speiser, and A. Moralis, Nuovo Cimento **25**, 307 (1962).
47. S. L. Glashow and J. J. Sakurai, Nuovo Cimento **25**, 337 (1962).
48. H. Ruegg, Nuovo Cimento A **41**, 576 (1966).
49. C. A. Levinson, H. J. Lipkin, and S. Meshkov, Nuovo Cimento **32**, 1376 (1964); H. J. Lipkin, in *High-Energy Physics and Elementary Particles* (IAEA, Vienna, 1965), p. 325.
50. F. J. Gilman and R. Kauffman, Phys. Rev. D **36**, 2761 (1987).
51. E. P. Venugopal and B. R. Holstein, Phys. Rev. D **57**, 4397 (1998).
52. F. Zachariasen, Phys. Rev. **121**, 1851 (1961); in *High-Energy Physics and Elementary Particles* (IAEA, Vienna, 1965), p. 823.
53. M. Gell-Mann and F. Zachariasen, Phys. Rev. **124**, 953 (1961).
54. W. Thirring, Phys. Rev. **126**, 1209 (1962); in *Theoretical Physics* (IAEA, Vienna, 1963), p. 451.
55. A. N. Kamal, Int. J. Mod. Phys. A **7**, 3515 (1992).
56. N. N. Achasov, S. A. Devyanin, and G. N. Shestakov, Yad. Fiz. **32**, 1098 (1980) [Sov. J. Nucl. Phys. **32**, 566 (1980)].
57. E. J. Sacharidis, Lett. Nuovo Cimento **25**, 193 (1979).
58. Y. Eisenberg *et al.*, Phys. Rev. Lett. **23**, 1322 (1969); G. T. Condo *et al.*, Phys. Rev. D **41**, 3317 (1990); **43**, 2787 (1991); **48**, 3045 (1993).
59. M. Moinester and S. U. Chung, hep-ex/0003008.

Translated by A. Isaakyan

Physics of Atomic Nuclei, Vol. 65, No. 3, 2002, pp. 562–566. Translated from Yadernaya Fizika, Vol. 65, No. 3, 2002, pp. 589–593.

ELEMENTARY PARTICLES AND FIELDS
Theory

Skyrmion in Nuclear Matter

U. T. Yakhshiev

Institute of Applied Physics, National University of Uzbekistan, Tashkent, Uzbekistan

Received November 10, 2000; in final form, March 26, 2001

Abstract—The properties of Skyrmions in finite nuclei are considered. The deformation effect is taken into account through the external-field-induced distortion of the profile function of a chiral field. The masses of classical Skyrmions and the distribution of their baryon number versus the Skyrmion position within a nucleus are discussed. © *2002 MAIK "Nauka/Interperiodica".*

The in-medium modification of the properties of nucleons is an interesting topical problem of low-energy hadron physics. Previously, the properties of a nucleon at the center of a finite nucleus or in infinite nuclear matter were analyzed within a modified Skyrme model [1]. More recent model extensions include the QCD scale anomaly in the approximation of infinite nuclear matter [2], where the effective Lagrangian was modified via the external-field-induced distortion of pion fields; that is, a pion–nucleus optical potential was introduced. The effective properties of a nucleon that were determined in this way were in qualitative agreement with experimental data and with the results of other authors. In particular, a nucleon in nuclear matter was found to be deformed. Since a spherically symmetric problem was considered, the deformation appeared to be only a breathing Skyrmion mode, a deviation of the shape of a Skyrmion from a spherical shape being beyond the scope of those studies.

In a number of studies devoted to exploring the properties of baryons whose baryon number is above unity ($B > 1$) [3], a deformation was introduced through a unit vector $\mathbf{n}$ in the so-called chiral ansatz U. Upon quantization, there then arises a rich spectrum of rotational soliton states, which can be treated as multi-Skyrmion systems. In those studies, the deformation was introduced in connection with the need for considering multi-Skyrmion systems as a discrete unit, and the case of unit baryon number ($B = 1$) reduces to the ordinary hedgehog ansatz [4].

Using the modified Skyrme Lagrangian in nuclear matter [1], we consider here the properties of a classical Skyrmion located out of the center of a finite nucleus. Since a finite nucleus has a nonuniform density, a Skyrmion is deformed, its properties being dependent on the distance R from the nuclear center. We aim at analyzing this dependence.

In the static form, the modified Skyrme Lagrangian in nuclear matter is given by [1]

$$\mathcal{L} = -\frac{F_\pi^2}{16}\alpha_p(\mathbf{r})\mathrm{tr}(\nabla U)(\nabla U^+) \qquad (1)$$
$$+\frac{1}{32e^2}\mathrm{tr}[L_i, L^j]^2 + \frac{F_\pi^2 m_\pi^2}{16}\alpha_s(\mathbf{r})\mathrm{tr}[U + U^+ - 2],$$

where $L_i = U^+\partial_i U$, F_π is the pion decay constant, e is a dimensionless parameter, and m_π is the pion mass. The medium functionals $\alpha_s(\mathbf{r})$ and $\alpha_p(\mathbf{r})$ are expressed in terms of functionals $\chi_s(\mathbf{r})$ and $\chi_p(\mathbf{r})$ that depend on the S- and P-wave pion–nucleus scattering lengths and scattering volumes and on the nuclear density $\rho(\mathbf{r})$:

$$\alpha_p(\mathbf{r}) = 1 - \chi_p(\mathbf{r}), \qquad \alpha_s(\mathbf{r}) = 1 + \frac{\chi_s(\mathbf{r})}{m_\pi^2}. \quad (2)$$

The nuclear effect is taken into account through these functionals. The chiral ansatz U has the hedgehog form $U(\mathbf{r}) = \exp\left[\frac{i\boldsymbol{\tau}\cdot\mathbf{r}}{|\mathbf{r}|}F(r)\right]$ for a Skyrmion located at the center of a nucleus [1]. When a Skyrmion is out of the nuclear center, the ansatz has the form

$$U(\mathbf{r}-\mathbf{R}) = \exp\left[\frac{i\boldsymbol{\tau}\cdot(\mathbf{r}-\mathbf{R})}{|\mathbf{r}-\mathbf{R}|}F(\mathbf{r}-\mathbf{R})\right], \quad (3)$$

where the profile function F depends not only on the absolute value of the radius vector but also on its direction. In this approach, a soliton is deformed, so that its shape deviates from a spherical shape. Since the deformation is induced by an external field distorting the profile of the pion fields, the ansatz in (3) is quite appropriate for analyzing the properties of a Skyrmion in finite nuclei.

In calculating the mass functional on the basis of Lagrangian (1), it is more convenient to use the reference frame whose origin coincides with the center of mass of the Skyrmion. This implies a transition

from the variable $\mathbf{r}$ to the variable $\mathbf{r}' = \mathbf{r} - \mathbf{R}$ in the expression for the mass functional

$$M(R) = -\int \mathcal{L}[U(\mathbf{r}-\mathbf{R}), \mathbf{r}]d^3\mathbf{r} \qquad (4)$$
$$= -\int \mathcal{L}[U(\mathbf{r}'), \mathbf{r}', \mathbf{R}]d^3\mathbf{r}'.$$

We will explore the properties of a Skyrmion in spherical nuclei. In this case, the Skyrmion mass depends only on the absolute value of the vector $\mathbf{R}$. The *Skyrmion plus nucleus* system then has a symmetry axis passing through the centers of the nucleus and the Skyrmion. We choose the direction of the z' axis along this symmetry axis, in which case the azimuthal (φ) dependence of the chiral-field profile function F is removed. Taking this fact into account, performing some algebraic manipulations, and introducing the notation $\mathrm{s} \equiv \sin(F)$, $\mathrm{c} \equiv \cos(F)$, and $\tilde{r} = eF_\pi r'$ (which is a dimensionless variable), we obtain the mass functional

$$M(R) = \frac{2\pi F_\pi}{e}\int_0^\infty d\tilde{r} \qquad (5)$$
$$\times \int_0^\pi \sin\theta d\theta \left\{ \frac{m_\pi^2}{4e^2F_\pi^2}\alpha_s(\tilde{r},\theta,R)(1-\mathrm{c})\tilde{r}^2 \right.$$
$$+ \frac{1}{8}[2\mathrm{s}^2 + (F_\theta(\tilde{r},\theta))^2 + \tilde{r}^2(F_{\tilde{r}}(\tilde{r},\theta))^2]\alpha_p(\tilde{r},\theta,R)$$
$$\left. + \frac{\mathrm{s}^2}{2}\left[\frac{\mathrm{s}^2}{\tilde{r}^2} + \frac{(F_\theta(\tilde{r},\theta))^2}{\tilde{r}^2} + 2(F_{\tilde{r}}(\tilde{r},\theta))^2\right]\right\},$$

where $F_{\tilde{r}}(\tilde{r},\theta)$ and $F_\theta(\tilde{r},\theta)$ are the derivatives with respect to the first and the second argument, respectively.

Obviously, the θ dependence appears in the profile function F because of a nonuniform density of a finite nucleus. To simplify this dependence, we break down the interval of the variable θ into N_θ sectors in such a way that the density and the corresponding medium functionals vary only slightly within a given sector $[i, i+1]$ ($i = \overline{0, N_\theta - 1}$). Since the profile function and its derivatives depend only slightly on the medium density [1], they can be considered to be independent of θ in a given sector $\theta_i < \theta < \theta_{i+1}$. Therefore, F and its derivatives can be approximated as

$$F(\tilde{r}, \theta_i < \theta < \theta_{i+1}) = F^i(\tilde{r}), \qquad (6)$$
$$F_{\tilde{r}}(\tilde{r}, \theta_i < \theta < \theta_{i+1}) = F^i_{\tilde{r}}(\tilde{r}),$$
$$F_\theta(\tilde{r}, \theta_i < \theta < \theta_{i+1}) = F^i_\theta(\tilde{r}).$$

In this approximation, the mass functional takes the form

$$M(R) = \frac{2\pi F_\pi}{e}\sum_{i=0}^{N_\theta-1}\int_0^\infty d\tilde{r}\left\{M_i^{(2)}A_i^{(2)}\right. \qquad (7)$$
$$\left. + A_i^{(4)}M_i^{(4)} + M_i^{(\chi^{SB})}A_i^{(\chi^{SB})}\right\},$$
$$M_i^{(2)} = \frac{1}{8}[2\mathrm{s}_i^2 + (F_\theta^i)^2 + \tilde{r}^2(F_{\tilde{r}}^i)^2],$$
$$A_i^{(2)} = \int_{\theta_i}^{\theta_{i+1}} d\theta \sin\theta\alpha_p(\tilde{r}, R, \theta),$$
$$M_i^{(4)} = \frac{\mathrm{s}_i^2}{2}\left[\frac{\mathrm{s}_i^2}{\tilde{r}^2} + \frac{(F_\theta^i)^2}{\tilde{r}^2} + 2(F_{\tilde{r}}^i)^2\right],$$
$$A_i^{(4)} = \int_{\theta_i}^{\theta_{i+1}} d\theta \sin\theta,$$
$$M_i^{(\chi^{SB})} = \frac{m_\pi^2}{4e^2F_\pi^2}(1-\mathrm{c}_i)\tilde{r}^2,$$
$$A_i^{(\chi^{SB})} = \int_{\theta_i}^{\theta_{i+1}} d\theta \sin\theta\alpha_s(\tilde{r}, R, \theta),$$

where θ_i and θ_{i+1} are the boundaries of the corresponding sector ($\theta_0 = 0$, $\theta_{N_\theta} = \pi$), $\mathrm{s}_i = \sin(F^i)$, and $\mathrm{c}_i = \cos(F^i)$.

Minimizing the mass functional in a certain sector $[i, i+1]$, we find that F^i satisfy the set of equations

$$\left[A_i^{(2)} + A_i^{(4)}\frac{8\mathrm{s}_i^2}{\tilde{r}^2}\right]F^i_{\tilde{r}\tilde{r}} + A^{(2)}_{\tilde{r},i}F^i_{\tilde{r}} + A_i^{(2)}\frac{2F^i_{\tilde{r}}}{\tilde{r}} \qquad (8)$$
$$- A_i^{(\chi^{SB})}\beta^2\mathrm{s}_i - \frac{\mathrm{s}_{2,i}}{\tilde{r}^2}\left[A_i^{(2)} + A_i^{(4)}\left(\frac{4\mathrm{s}_i^2}{\tilde{r}^2}\right.\right.$$
$$\left.\left. + \frac{2(F_\theta^i)^2}{\tilde{r}^2} - 4(F_{\tilde{r}}^i)^2\right)\right] = 0,$$

where $\mathrm{s}_{2,i} = \sin(2F^i)$ and

$$A^{(2)}_{\tilde{r},i} = \int_{a_i}^{b_i} d\theta\frac{\partial\alpha_p(\tilde{r}, R, \theta)}{\partial\tilde{r}}.$$

The boundary conditions for these equations,

$$F^i(0) = \pi, \qquad F^i(\infty) = 0, \qquad (9)$$

are determined from the condition that the soliton has a unit topological charge:

$$B = -\sum_{i=0}^{N_\theta-1}\frac{1}{\pi}\int_0^\infty A_i^{(4)}F^i_{\tilde{r}}\mathrm{s}_i^2 d\tilde{r} = 1. \qquad (10)$$

Applying the iteration method, we successively calculate the derivatives of the profile functions with respect to θ by using the results of preceding iterations:

$$F_\theta^i(\tilde{r}) = \frac{F^{i+1}(\tilde{r}) - F^i(\tilde{r})}{\theta_{i+1} - \theta_i}. \qquad (11)$$

Let us discuss the parametrization of the nuclear density and of the input parameters of the model. The medium functionals are taken in the form [1]

$$\chi_s(\tilde{r}, R, \theta) = -4\pi b_0 \left(1 + \frac{m_\pi}{M_N}\right) \rho(\tilde{r}, R, \theta),$$

$$\chi_p(\tilde{r}, R, \theta) = \frac{\kappa(\tilde{r}, R, \theta)}{1 + g_0' \kappa(\tilde{r}, R, \theta)},$$

$$\kappa(\tilde{r}, R, \theta) = \frac{4\pi c_0 \rho(\tilde{r}, R, \theta)}{1 + m_\pi / M_N},$$

where $M_N = 938$ MeV is the nucleon mass and $g_0' = 1/3$ is the Migdal parameter taking into account short-range correlations. The empirical parameters $b_0 = -0.024 m_\pi^{-1}$ and $c_0 = 0.21 m_\pi^{-3}$ were determined by fitting low-energy data on pion–nucleus scatterings [5].

Since we consider the properties of a Skyrmion in spherical nuclei, the density is parametrized as [6]

$$\rho(r) = \frac{2}{\pi^{3/2} r_0^3} \left[1 + \frac{Z-2}{3} \left(\frac{r}{r_0}\right)^2\right] \exp\left\{-\frac{r^2}{r_0^2}\right\} \quad (12)$$

$$\text{for } 4 < A < 20,$$

$$\rho(r) = \frac{\rho_0}{1 + \exp\left\{\dfrac{r - R'}{a}\right\}} \quad \text{for } A \geq 20,$$

where Z is the charge number of a nucleus, $\rho_0 = 0.5 m_\pi^{-3}$ is the normal nuclear density, $R' = 1.2 A^{-1/3}$ fm, and $a = 0.58$ fm. We consider the ^{16}O and ^{40}Ca nuclei, for which this density parametrization is fairly accurate. The parameter r_0 is equal to 1.76 fm for ^{16}O.

The input parameters of the model are set to the values of $F_\pi = 108$ MeV and $e = 4.84$, at which the nucleon mass and Δ in free space prove to be equal to the respective experimental values [4].

Figure 1 shows the Skyrmion mass as a function of the distance R from the center of the nucleus being considered. The solid curves represent the ratio of the intranuclear Skyrmion mass $M_S(R) \equiv M(R)$ [see Eq. (5)] at the distance R from the center of the nucleus to the free-space value $M_S(\rho = 0)$. The dashed curves correspond to the nuclear density divided by its value at the center of the nucleus, $\rho(R)/\rho(R = 0)$. As might have been expected, the effective Skyrmion mass is minimal at the center—it increases toward the nuclear surface, tending to its free-space value.

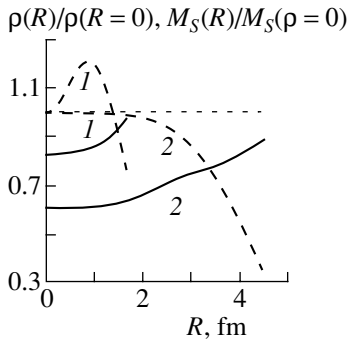

Fig. 1. Ratio of the effective Skyrmion mass $M_S(R)$ in a nucleus to its free value $M_S(\rho = 0)$ versus the distance R between the centers of the nucleus and the Skyrmion (solid curves) and nuclear density $\rho(R)$ divided by its value $\rho(R = 0)$ at the nuclear center (dashed curves). Curves *1* and *2* refer to the ^{16}O and the ^{40}Ca nucleus, respectively.

The solid curves *1* and *2* approach unity at large distances. This behavior is observed for a Skyrmion in a medium-mass (^{16}O) and a heavy (^{40}Ca) nucleus. Thus, the effective Skyrmion mass averaged over the entire nuclear volume differs from the free-space value not by about 40%, as in the case of infinite nuclear matter of density ρ_0 [1], but by a considerably smaller value.

For a Skyrmion in ^{16}O, Fig. 2 shows the distribution of the baryon-number density in the yz plane at the distance of $R = 0.5$ fm between the centers of the nucleus and the Skyrmion. Figure 2*b* shows the projection of the baryon number density onto the yz plane. The contour lines are the projections of constant values of the baryon-number density. For neighboring contours, the baryon-number density differs by 0.004. The arrow indicates the direction toward the nuclear center. The $y = z = 0$ point in Fig. 2 corresponds to the center of the Skyrmion (not to the nuclear center). It can be seen that the distribution is asymmetric; that is, the baryon number peaks out of the center of the Skyrmion ($\mathbf{r}' = 0$). Therefore, the Skyrmion is deformed in such a way that its shape becomes nonspherical. This deformation can be analyzed by examining the quadrupole moments of Skyrmions. The quadrupole moments of nucleons should be calculated but, in fact, they may be considered only upon quantizing the theory in question. Here, only the isoscalar and isovector quadrupole moments of Skyrmions in ^{40}Ca are shown in Fig. 3 by the solid and dashed curves, respectively. The maxima of these quantities are at a distance where the nuclear density decreases by about 5–8%. The isoscalar and isovector quadrupole moments change sign at large R; that is, the shape

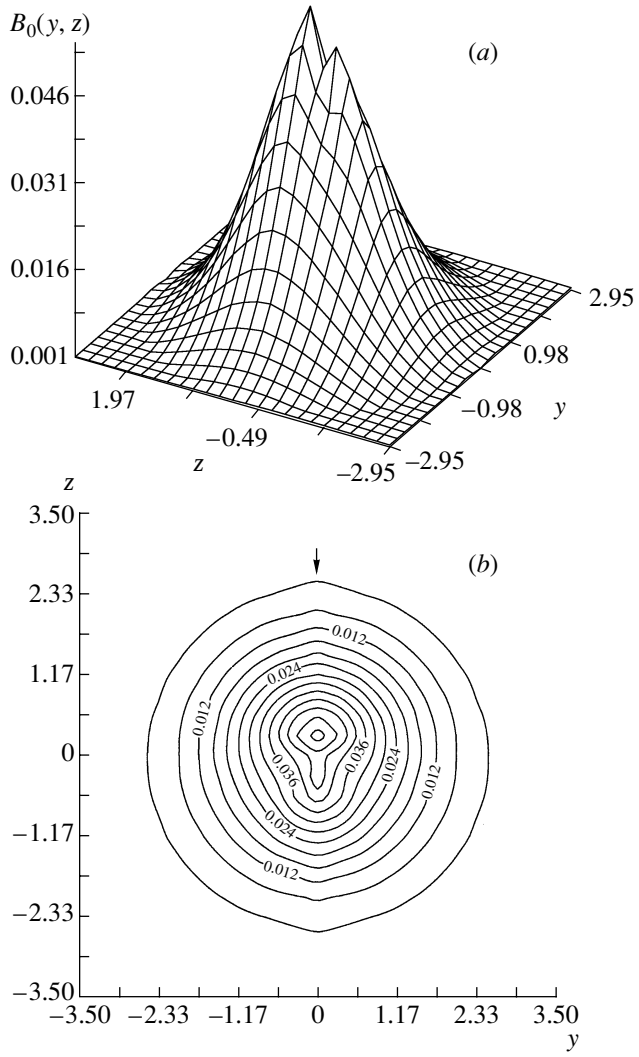

Fig. 2. (*a*) Baryon-number density $B_0 = -F_{\tilde{r}}\mathrm{s}^2/(2\pi^2\tilde{r}^2)$ in the yz plane and (*b*) its projection onto the yz plane with a step of 0.004 between contours for the Skyrmion in ^{16}O. The arrow indicates the direction toward the nuclear center. Here, $y = eF_\pi r'_y$ and $z = eF_\pi r'_z$ are dimensionless variables. The distance R between the centers of the nucleus and the Skyrmion is 0.5 fm.

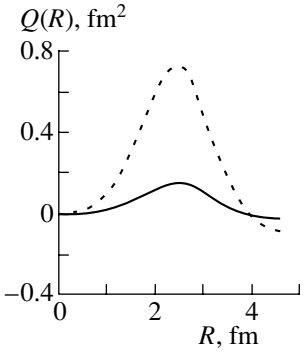

Fig. 3. Isoscalar ($Q_{I=0}$) and isovector ($Q_{I=1}$) quadrupole moments of a Skyrmion (solid and dashed curves, respectively) in ^{40}Ca versus the distance R from the nuclear center.

of quantized Skyrmions changes from a prolate to an oblate one, or vice versa.

In summary, we have considered the effective Lagrangian that takes into account the nuclear-matter effect on a chiral field. This has resulted in a deformed nonspherical state of Skyrmions in a nonuniform medium. The deformation is maximal at distances where the heavy-nucleus density decreases by about 5 to 8%. For a Skyrmion within the ^{40}Ca nucleus, this distance is about 2.5 fm. The effective Skyrmion mass in a nucleus decreases with increasing nuclear density, attaining a minimum at the nuclear center. The mean effective mass of a nucleon in a nucleus—it enables one to estimate the nuclear binding energy—can be calculated upon quantizing the theory. Such a quantization would also make it

possible to compare the properties of nucleons with experimental data.

ACKNOWLEDGMENTS

This work was supported by INTAS (grant no. YSF 00-51) and the Uzbek State Committee for Science and Technology.

REFERENCES

1. A. M. Rakhimov and U. T. Yakhshiev, Yad. Fiz. **62**, 1966 (1999) [Phys. At. Nucl. **62**, 1824 (1999)].
2. M. M. Musakhanov, A. M. Rakhimov, U. T. Yakhshiev, and Z. Kanokov, Yad. Fiz. **62**, 1988 (1999) [Phys. At. Nucl. **62**, 1845 (1999)]; A. M. Rakhimov, F. C. Khanna, U. T. Yakhshiev, and M. M. Musakhanov, Nucl. Phys. A **643**, 383 (1998).
3. V. B. Kopeliovich and B. E. Shtern, Pis'ma Zh. Éksp. Teor. Fiz. **45**, 165 (1987) [JETP Lett. **45**, 203 (1987)]; V. A. Nikolaev, Fiz. Élem. Chastits At. Yadra **20**, 401 (1989) [Sov. J. Part. Nucl. **20**, 173 (1989)]; V. A. Nikolaev and O. G. Tkachev, Fiz. Élem. Chastits At. Yadra **21**, 1499 (1990) [Sov. J. Part. Nucl. **21**, 643 (1990)].
4. G. S. Adkins, C. R. Nappi, and E. Witten, Nucl. Phys. B **228**, 552 (1983); G. S. Adkins and C. R. Nappi, Nucl. Phys. B **233**, 109 (1984); I. Zahed and G. E. Brown, Phys. Rep. **142**, 1 (1986).
5. T. E. O. Ericson and W. Weise, *Pions and Nuclei* (Clarendon, Oxford, 1988; Nauka, Moscow, 1991).
6. A. I. Akhiezer, A. G. Sitenko, and V. K. Tartakovskii, *Nuclear Electrodynamics* (Naukova Dumka, Kiev, 1989; Springer-Verlag, Berlin, 1994).

Translated by R. Tyapaev

Physics of Atomic Nuclei, Vol. 65, No. 3, 2002, pp. 567–572. Translated from Yadernaya Fizika, Vol. 65, No. 3, 2002, pp. 594–599.

ELEMENTARY PARTICLES AND FIELDS
Theory

Scale of Corrections to the t-Channel Pole Approximation in Quasielastic Pion Knockout from a Nucleon by High-Energy Electrons

V. G. Neudatchin, L. L. Sviridova, and N. P. Yudin*

Institute of Nuclear Physics, Moscow State University, Vorob'evy gory, Moscow, 119899 Russia

Received December 20, 2000

Abstract—An investigation of a dominant role of the simplest t-channel pole diagrams in pion electroproduction on nucleons for quasielastic-knockout kinematics at an electron energy of a few GeV is completed—namely, the competition between the t-channel pion and rho-meson pole amplitudes, on one hand, and the s-channel pole amplitude (tree diagram), on the other hand, is considered. When the virtual-photon mass is sufficiently large [$Q^2 > 2\,(\mathrm{GeV}/c)^2$], the last amplitude does not make significant contributions to relevant cross sections, either the longitudinal ($d\sigma_L/dt$) or the transverse ($d\sigma_T/dt$) one. At $Q^2 = 0.7\,(\mathrm{GeV}/c)^2$, the term associated with the interference between the t-channel pion-pole amplitude and the s-channel pole amplitude is still noticeable in the longitudinal cross section. The vertex functions $g_{\rho NN}(t)$ as obtained from the cross section for the quasielastic knockout of rho mesons and from the cross section for pion photoproduction are compared. Their disagreement must give impetus to a further development of the gauge-invariant theory of pion photoproduction. © *2002 MAIK "Nauka/Interperiodica".*

1. INTRODUCTION

The possibility of describing the electroproduction process $p(e, e'\pi^+)n$ at high energies of the knock-on pion in terms of the mechanism employing the pion pole in the t channel (see the diagrams in Fig. 1) has been discussed in the literature since the appearance of the study reported in [1]. Here, an important argument is that the cross section corresponding to the main competing mechanism associated with the nucleon pole in the s channel (tree diagram in Fig. 2) dies out in proportion to Q^{-4} with increasing virtual-photon 4-momentum q_μ ($Q^2 = -q^2$) in relation to the cross section for the t-channel pole mechanism [1]. In [1–6], the pole mechanism in question (Fig. 1) was calculated within light-front dynamics; this made it possible to find the form factor (wave function) for the πNN vertex from a comparison with experimental data.

In contrast to those studies, we considered the process $p(e, e'\pi^+)n$ in the laboratory frame [7, 8]; as a result, we were able to single out, in a natural way, the kinematical region where the recoil momenta of the final baryon are low and where the energies of the knock-on meson are high. By making use of crossing symmetry, one can introduce, in just the same way as in light-front dynamics, the concept of the pion wave function in the nucleon. If the pole diagram is dominant, a consideration in the laboratory frame makes it possible to extract the square of the pion wave function in the channel $p \to n + \pi^+$, $|\Psi_p^{n\pi}(k^2)|^2$, directly from experimental data on electroproduction [9]. This is done by following the same line of reasoning as in the nonrelativistic physics of the quasielastic knockout of nucleons from nuclei [10] and of electrons from atoms, molecules, and solid-state films [11], where these reactions furnished a vast body of radically new information.

In analyzing experimental data, we obtained three pieces of evidence for a dominant role of the pole mechanism—that is, for a minor role of the competing s-channel pole diagram.

First, we found that, in quasielastic-knockout kinematics, experimental data reported in [9, 12] lead to the same momentum distribution over a wide region of energies of the knock-on pion, but this is the result that is expected in the case where the pole mechanism is dominant.

Second, our results obtained in [7, 8] from an analysis of experimental data from [9, 12] revealed that the constant component in the momentum distribution—the background that characterizes qualitatively the distorting effect of the s-channel pole diagram on the momentum distribution—is very small (in the physics of direct nuclear reactions, a similar constant component in differential cross sections is associated with the compound-nucleus contribution).

Third, the momentum distribution $|\Psi_p^{n\pi}(k^2)|^2$ that we extracted from experimental data on pion electroproduction is in excellent agreement with that which

*e-mail: yudin@helene.npi.msu.su

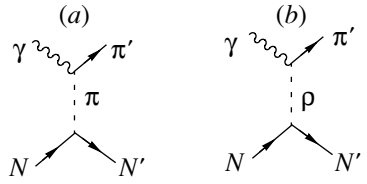

Fig. 1. t-channel pole diagram involving an intermediate virtual (a) pion or (b) rho meson.

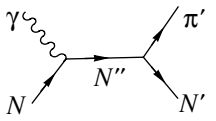

Fig. 2. s-channel pole (tree) diagram.

we obtained on the basis of the separable Afnan pion–nucleon potential for the P wave [13]. This potential in turn was determined from the phase shifts for pion–nucleon scattering, which are absolutely independent data.

Needless to say, all the above considerations must be supplemented with a formal analysis of the relative importance of the t-channel pole diagram and of the s-channel pole diagram under various kinematical conditions [in performing this analysis, it should be borne in mind, among other things, that the actual values of Q^2 in the experiments reported in [9, 12] fall within the range 1–3 $(\mathrm{GeV}/c)^2$]. Here, this is done both for longitudinal and for transverse virtual photons, a comparison with photoproduction data being drawn for the latter case. Naturally, allowances for the special features of all vertex functions—in particular, in the $NN\gamma$ and $NN\pi$ vertices of the s-channel pole diagram—are made here.

We will demonstrate that, in the case of longitudinal photons, the s-channel pole diagram is suppressed to a considerable extent in quasielastic-knockout kinematics (here, only the process $e + \pi^+ \to e' + \pi^+$, which is diagonal in the internal state of the knock-on pion, is operative). Of course, this is a spectacular feature of the pion-electroproduction reaction, and it justifies our previous results from [7, 8], which were mentioned above (for a preliminary qualitative discussion, the reader is referred to the review article [14]). However, the contribution of the interference between the t- and the s-channel pole diagram is nonnegligible at a comparatively small value of the photon-virtuality parameter [$Q^2 = 0.7\,(\mathrm{GeV}/c)^2$].

In the case of transverse photons characterized by a comparatively high virtuality [$Q^2 \geq 2\,(\mathrm{GeV}/c)^2$], the s-channel pole diagram is also suppressed, the aforementioned correction being small here.

For real photons, there is no such suppression, so that the s-channel pole diagram plays a significant role here. However, a comparative analysis of pion electroproduction and pion photoproduction on a nucleon makes it possible to extract quite reliably, from experimental data on the photoproduction process $p + \gamma \to \pi^+ + n$, the contribution of the pole diagram featuring a virtual rho meson (see Fig. 1b)—that is, to determine the momentum distribution of rho mesons in a nucleon over a broad range of momenta (in [8, 15], we were able to extract, within the pole approximation, the momentum distribution of rho mesons in a nucleon from experimental data on the process $e + p \to e' + \pi^+ + n$ [12] for transverse virtual photons γ_T^*, but this was done only for low momenta; we also outlined the way in which one can extract the momentum distribution of omega mesons from data of $e + p \to e' + \pi^0 + p$ quasielastic experiments). Here, we implement the simplest version of such an analysis, describing the final pion in the plane-wave approximation.

2. DESCRIPTION OF THE FORMALISM

Without going into details, we present the fundamentals of the theoretical formalism. The quantity obtained by integrating the differential cross section for pion electroproduction on a nucleon with respect to the azimuthal angle has the form [16]

$$\frac{d^3\sigma}{dW^2 dQ^2 dt} = \Gamma\left\{\varepsilon\frac{d\sigma_L}{dt} + \frac{d\sigma_T}{dt}\right\}, \qquad (1)$$

where

$$\Gamma = \frac{\alpha}{(4\pi)^2}\frac{W^2 - M^2}{Q^2 E_e^2 M^2}\frac{1}{1-\varepsilon} \qquad (2)$$

is the flux of virtual photons and

$$\varepsilon = \left[1 + \frac{2\mathbf{q}^2}{Q^2}\tan^2\frac{\theta_e}{2}\right]^{-1} \qquad (3)$$

is a parameter that determines the degree of longitudinal photon polarization. Here, M is the nucleon mass, E_e is the incident-electron energy, $(q_0, \mathbf{q}) = q_\mu$ is the photon 4-momentum, $Q^2 = -q^2$, $W^2 \equiv (p+q)^2 = (-Q^2 + M^2 + 2q_0 M)_{\mathrm{lab}}$ (p is the primary-nucleon momentum), θ_e is the electron scattering angle, $t \equiv (k' - q)^2$, and k' is the final-pion momentum.

The contributions of the longitudinal and the transverse cross section ($d\sigma_L/dt$ and $d\sigma_T/dt$, respectively) are separated by varying kinematical conditions.

The cross sections $d\sigma_{L,T}/dt$ can be represented in the form

$$\frac{d\sigma_L}{dt} = \frac{\overline{|J_{\lambda=0}|^2}}{32\pi W\,|\mathbf{q}|\,(W^2 - M^2)}, \qquad (4)$$

$$\frac{d\sigma_T}{dt} = \frac{\frac{1}{2}\left\{\overline{|J_{\lambda=1}|^2} + \overline{|J_{\lambda=-1}|^2}\right\}}{32\pi W\,|\mathbf{q}|\,(W^2 - M^2)},$$

where J_λ stands for the matrix elements of the hadronic current for longitudinal ($\lambda = 0$) and transverse ($\lambda = \pm 1$) photons,

$$J_\lambda = J^\mu e_{\lambda\mu}, \tag{5}$$

with $e_{\lambda\mu}$ being unit vectors of virtual-photon polarization that satisfy the transverseness condition $q^\mu e_{\lambda\mu} = 0$. The overbars in (4) denote averaging over spins.

A pion (Fig. 1a) or a rho meson (Fig. 1b) can appear in the reaction being considered as a virtual meson. For the process depicted in Fig. 1a (this is the case of an intermediate virtual pion), the matrix element of the current can be represented as

$$J_\lambda = ie\frac{\mathcal{M}(p \to n\pi)}{k^2 - m_\pi^2} F_\pi(Q^2)(k + k')e_\lambda, \tag{6}$$

where

$$\mathcal{M}(p \to n\pi) \tag{7}$$
$$= \sqrt{2} G_{\pi NN} g_{\pi NN}(k^2)\bar{u}(p')\gamma^5 u(p);$$

u are the Dirac spinors for the nucleons; p and p' are the momenta of, respectively, the primary and the final nucleon; k is the momentum of the virtual meson (a pion in the case being considered); e is the electron charge; $G^2_{\pi NN}/4\pi \approx 14$; $g_{\pi NN}(k^2) = (\Lambda_\pi^2 - m_\pi^2)/(\Lambda_\pi^2 + k^2)$ is the relevant vertex function; m_π is the pion mass; and $F_\pi(Q^2)$ is the pion form factor, which was set to the free-pion form factor

$$F_\pi(Q^2) = [1 + Q^2/0.5\ (\mathrm{GeV}/c)^2]^{-1}.$$

The matrix element of the current for the diagram in Fig. 1b (which involves an intermediate virtual rho meson) has the form

$$J_\lambda = e\frac{\mathcal{M}_\mu(p \to n\rho)}{k^2 - m_\rho^2}\left(-g^{\mu\nu} + \frac{k_\mu k_\nu}{m_\rho^2}\right) \tag{8}$$
$$\times\, \varepsilon^{\mu\nu\alpha\beta} e_{\lambda\nu} q_\alpha k_\beta \frac{g_{\rho\pi\gamma}}{m_\pi} F_{\rho\pi}(Q^2),$$

where $\mathcal{M}^\mu(p \to n\rho^+) = \sqrt{2} G_{\rho NN} g_{\rho NN}(k^2)\bar{u}(p') \times \Gamma^\mu u(p)$; $\Gamma^\mu = \gamma^\mu + (\kappa/2M)\sigma^{\mu\nu}k_\mu$; $\kappa = 6.1$ is the isovector magnetic moment of the nucleon; m_ρ is the rho-meson mass; $G^2_{\rho NN}/4\pi = 0.84$; $g_{\rho NN}(k^2) = (\Lambda_\rho^2 - m_\rho^2)/(\Lambda_\rho^2 + k^2)$ is the relevant meson–nucleon vertex function; $\varepsilon^{\mu\nu\alpha\beta}$ is a fully antisymmetric tensor; $g_{\rho\pi\gamma} = 0.0378/e$; and $F_{\rho\pi}(Q^2)$ is the form factor for the $\rho\pi\gamma$ transition, $F_{\rho\pi}(Q^2) = [1 + Q^2/\Lambda^2]^{-2}$ with $\Lambda = 3m_\rho$.

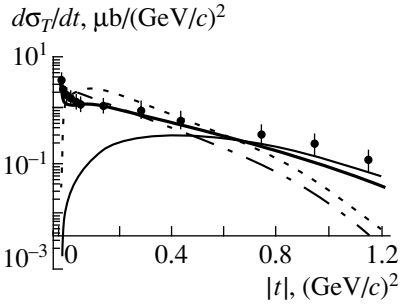

Fig. 3. Photoproduction cross section: (dashed curve) contribution of the pion pole, (thin solid curve) contribution of the rho-meson pole, (dash-dotted curve) contribution of the diagram in Fig. 2, and (thick solid curve) total contribution. The experimental data (points) were borrowed from [18].

For the s-channel pole diagram in Fig. 2, the matrix element J_λ is given by

$$J_\lambda = ie\sqrt{2} G_{\pi NN} g_{\pi NN}(k^2)\bar{u}(p')\gamma^5 \frac{(\hat{p} + \hat{q}) + M}{(p+q)^2 - M^2} \tag{9}$$
$$\times\, \gamma^\mu e_{\lambda\mu} u(p) F_{\gamma NN}(Q^2) F_{\pi NN}(W^2, Q^2),$$

where $\hat{p} = p_\mu \gamma^\mu$;

$$F_{\gamma NN}(Q^2) = (1 + Q^2/\Lambda_\gamma^2)^{-2} \tag{10}$$

is the electromagnetic form factor for the nucleon with $\Lambda_\gamma = 0.88$ GeV/c; and $F_{\pi NN}(W^2, Q^2)$ is the form factor for the πNN vertex for the s-channel pole diagram (a real pion and a real nucleon plus a virtual nucleon), the latter usually being taken in the form

$$F_{\pi NN}(W^2, Q^2) = \left(1 + \frac{W^2 + Q^2 - M^2}{\Lambda^2}\right)^{-2}. \tag{11}$$

As in [17], we set $F_{\pi NN}(W^2,\ Q^2) = 1$. At a $F_{\pi NN}(W^2, Q^2)$ value significantly differing from unity, the contribution of the s-channel pole diagram (Fig. 3, dash-dotted curve) to the photoproduction cross section is strongly suppressed, with the result that the experimental cross section could not be reproduced at low t.

The momentum distribution of a meson (its wave function) in a nucleon is in direct proportion to the form factor for the relevant meson–nucleon vertex. By way of example, we indicate that, for the virtual pion, the relation between the two quantities has the form [7, 14]

$$\overline{\left|\Psi_p^{n\pi}(k^2)\right|^2} = 2G^2_{\pi NN}\, g^2_{\pi NN}(k^2)\frac{|k^2|}{(k_0 - \epsilon_\mathbf{k})^2}, \tag{12}$$

where $\epsilon_\mathbf{k} = \sqrt{\mathbf{k}^2 + m_\pi^2}$, $|k_0| \ll \epsilon_\mathbf{k}$.

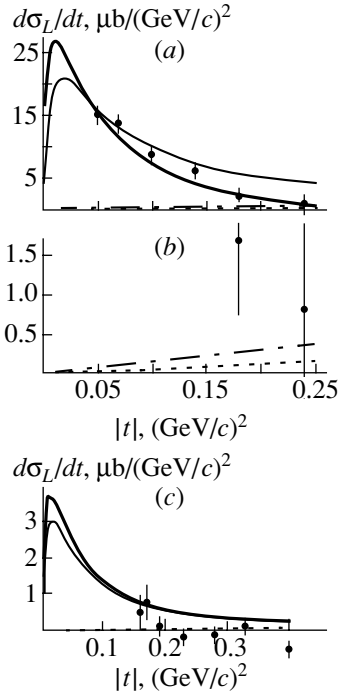

Fig. 4. (*a*) Contribution of pions to the longitudinal cross section for electroproduction at $Q^2 = 0.7$ (GeV/c)^2 and $W = 2.19$ GeV: (thin solid curve) contribution of the mechanism depicted in Fig. 1*a*, (dashed curve) contribution of the mechanism depicted in Fig. 1*b*, (dash-dotted curve) contribution of the mechanism depicted in Fig. 2, and (thick solid curve) total contribution. The interference terms are not shown. As a matter of fact, the difference of the values represented by the thin and thick solid curve is the contribution of interference terms. The experimental data shown by points were borrowed from [9, 12]. (*b*) As in Fig. 4*a*, but on a different scale (contribution of rho mesons and contribution of the diagram in Fig. 2). (*c*) Longitudinal cross section for electroproduction at $Q^2 = 3.32$ (GeV/c)^2 and $W = 2.65$ GeV. The notation is identical to that in Fig. 4*a*.

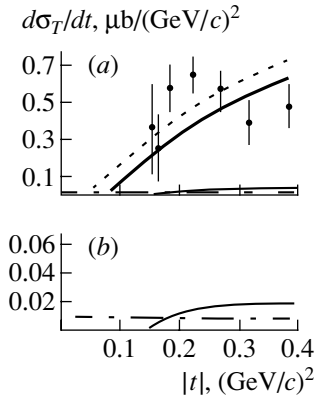

Fig. 5. (*a*) Contribution of rho mesons to the transverse cross section for electroproduction at $Q^2 = 3.32$ (GeV/c)^2 for $W = 2.65$ GeV. The notation is identical to that in Fig. 4. (*b*) As in Fig. 5*a*, but on a different scale (contribution of pions and contribution of the diagram in Fig. 2).

3. RESULTS OF THE CALCULATIONS AND DISCUSSION

First of all, we note a significant distinction between the structures of the currents J_λ for longitudinal and transverse photons [Eqs. (7), (8)]. We begin our discussion of the results by considering the longitudinal electroproduction cross section $d\sigma_L/dt$. The vertex function $g_{\pi NN}(k^2)$ was found here in the pole approximation [7] from the longitudinal cross section $d\sigma_L/dt$ determined experimentally at $Q^2 = 0.7$ (GeV/c)^2 in the region of quasielastic kinematics [9]. This approximation is justified if the contribution of the s-channel pole diagram to this cross section is small and if, in addition, the contribution of the pole diagram in Fig. 1*b* (the case of an intermediate rho meson) is insignificant in relation to the contribution of the analogous diagram involving an intermediate pion (Fig. 1*a*). This is indeed so (see Figs. 4*a*, 4*b*). Thus, the mechanism depicted in Fig. 1*a* makes a dominant contribution to the longitudinal cross section for pion electroproduction at $Q^2 = 0.7$ (GeV/c)^2. The diagrams in Figs. 1*b* and 2 yield corrections that improve the agreement with experimental data (the contribution from the interference between the mechanisms shown in Figs. 1*a* and 2 is especially important here). For $Q^2 \geq 2$ (GeV/c)^2, this factor is no longer operative (Fig. 4*c*).

The smallness of off-shell effects, which is ensured by the condition $|k| \ll |k'|$ [11], is one of the criteria of the validity of the pole approximation for quasielastic knockout. In this case, the condition of gauge invariance is also satisfied to a high precision since there occurs quasifree electron scattering on a meson ($e + \pi^+ \to e' + \pi^+$).

Let us now proceed to discuss the transverse cross section $d\sigma_T/dt$. From experimental data on $d\sigma_T/dt$ at $Q^2 = 3.3$ (GeV/c)^2, we found, in [8], the vertex function $g_{\rho NN}(k^2)$ in the pole approximation for momenta much lower than the meson mass, $k^2 \equiv |t| \ll m_\rho^2$. Using this function in calculating the cross section $d\sigma_T/dt$ and taking into account the contributions of the diagrams in Figs. 1 and 2, we now arrive at two conclusions. From a comparison of the t-channel pole diagrams in Figs. 1*a* and 1*b*, we can find that, at sufficiently large Q^2 [$Q^2 = 3.3$ (GeV/c)^2 in our case], the diagram in Fig. 1*b* with an intermediate rho meson is by far dominant (in contrast to what occurs for $d\sigma_L/dt$)—see Fig. 5. Further, a comparison of the contributions of the pole diagram in Fig. 1*b* and the s-channel pole diagram in Fig. 2 reveals that, at the above value of Q^2, the contribution of the latter is

insignificant (see Fig. 5). (By considering a process that is inclusive in the states of the final spectator baryon B, it was found in [1] that, with increasing Q^2, the contribution of the s-channel diagram to the cross section $d\sigma_T/dt$ decreases asymptotically in proportion to Q^{-4}.) It follows that the use of the pole approximation in determining the vertex function $g_{\rho NN}(k^2)$ was justified in this case as well.

Thus, a measurement of the transverse cross section $d\sigma_T/dt$ for the process $p(e,e'\pi^+)n$ at electron energies of about 10 GeV, transverse-photon virtualities in the region $Q^2 \geq 2\ (\mathrm{GeV}/c)^2$, and the recoil momenta of the final neutron in the region extending up to $\mathbf{k}^2 \approx 1\ (\mathrm{GeV}/c)^2$ would be the most direct way to determine experimentally the momentum distribution of rho mesons in a nucleon over a rather broad momentum range required for our purposes. No such experiments have been performed so far {the experimental data reported in [12] were obtained only for $k^2 = |t| \leq 0.4\ (\mathrm{GeV}/c)^2$, whereas the momentum distribution of rho mesons extends far beyond this region up to $k^2 = |t| \sim 1\ (\mathrm{GeV}/c)^2$}.

In view of this, it is advisable to address the question of the extent to which experimental data on pion photoproduction on a proton that were obtained for $k^2 = |t| \leq 2\ (\mathrm{GeV}/c)^2$ [18] can be used to extract the momentum distribution of rho mesons. The electro- and the photoproduction process differ drastically from each other in that the quasielastic-knockout situation is not realized in the case of photoproduction since a real photon cannot be absorbed by a free meson; therefore, the entire process can proceed only for a meson bound in a nucleon. This is the reason why the pole diagrams in Fig. 1 are not dominant here—that is, all three diagrams in Figs. 1a, 1b, and 2 are operative in the case being considered.

The momentum distribution of rho mesons can be determined by simultaneously taking into account the t-channel pole diagrams in Fig. 1 and the s-channel pole diagram in Fig. 2. In such a situation, there arises the question of gauge invariance. The simplest way is adopted in [17], where a common cutoff factor is introduced in order to multiply by it the gauge-invariant sum of the amplitudes for Figs. 1a and 2 for pointlike particles—this factor is taken in the form of the function $(t-m_\pi^2)P^\pi_{\mathrm{Regge}}(t,W)$, which modifies the pion pole $1/(t-m_\pi^2)$, transforming it into the Reggeized image $P^\pi_{\mathrm{Regge}}(t,W)$. In terms of our study, the common factor is question is equivalent to the form factor $g_{\pi NN}(t)$. The t-channel pole diagram involving a virtual rho meson (Fig. 1b) corresponds to an amplitude that is gauge-invariant as it is. The corresponding amplitude for pointlike particles is multiplied by $g_{\rho NN}(t)$ in our studies and by the expression $(t-m_\rho^2)P^\rho_{\mathrm{Regge}}(t,W)$ in [17].

The procedure for Reggeization according to [17] is quite natural for the pole diagrams in Fig. 1. But the diagram in Fig. 2 corresponds to a totally different physics. Here, we are dealing with a strongly excited nucleon; therefore, the approach being discussed is questionable in that case. The results that we obtained previously for the electroproduction process make it possible to test the correctness of the approach employed in [17].

The two cutoff factors are related by the equation

$$g^2_{мNN}(t) = (t-m_м^2)^2\left|P^м_{\mathrm{Regge}}\right|^2. \qquad (13)$$

The parameters of the function $P^м_{\mathrm{Regge}}(t,W)$ were fitted to experimental data at $E_\gamma = 5$ and 8 GeV. From (13), one can obtain the function $g_{мNN}(t)$ and the cutoff constant $\Lambda_м$. Satisfactory agreement between the two curves representing $g^2_{\rho NN}(t)$ $\{g^2_{\rho NN}(t) = \left[(\Lambda_\rho^2 - m_\rho^2)/(\Lambda_\rho^2 - t)\right]^2$ and $g^2_{\rho NN}(t) = (t-m_\rho^2)^2|P^\rho_{\mathrm{Regge}}|^2\}$ can be achieved by setting $\Lambda_\rho = 0.87\ \mathrm{GeV}/c$. Our previous result based on electroproduction data is $\Lambda_\rho = 1.4\ \mathrm{GeV}/c$ [8]. This is a significant discrepancy, which implies that the gauge-invariant theory of photoproduction requires a further refinement.

For $|t| \leq 1\ (\mathrm{GeV}/c)^2$, there is no such discrepancy; for pions, we obtained here $\Lambda_\pi = 0.7\ \mathrm{GeV}/c$, which is in agreement with our previous value [7].

4. CONCLUSION

We have completed our investigation of the role of the simplest pole diagrams in pion photo- and electroproduction on nucleons at energies of a few GeV. This has been done by considering formal aspects of the competition between the pole amplitudes represented by Figs. 1a and 1b and the tree amplitude represented by Fig. 2 under various kinematical conditions. We have arrived at the conclusion that, under the kinematical conditions of quasielastic meson knockout, in which case the virtual-photon mass is rather large ($[Q^2 \geq 2\ (\mathrm{GeV}/c)^2$], the tree diagram ($s$-channel pole diagram) is immaterial, as was assumed in our previous studies.

An analysis of the longitudinal cross section $d\sigma_L/dt$ at $Q^2 = 0.7\ (\mathrm{GeV}/c)^2$ has revealed that, at a photon mass squared on this order of magnitude—that is, at comparatively small values of it—the agreement with experimental data can be considerably improved by taking into account the interference between the pion pole amplitude and the tree amplitude. This, however, does not change our previous results

reported in [7, 8], which were based on the use of solely the t-channel pole amplitude. On the basis of our experience summarized above, we have briefly touched upon the pion-photoproduction reaction at energy of a few GeV. Here, $Q^2 = 0$ and the tree diagram plays a significant role; in view of this, the question of the gauge invariance of the total reaction amplitude becomes nontrivial. The values of the cutoff parameter Λ_ρ for the vertex function $g_{\rho NN}(t)$ that were obtained on the basis of experimental data on the quasielastic knockout of rho mesons appear to be sharply different from those determined with the aid of data on pion photoproduction. We believe that this will give impetus to a further development of the theory of meson photoproduction.

As a next step in a theoretical analysis of pion electro- and photoproduction, it would be desirable to go over from the plane-wave approximation to an approach where allowance is made for the final-state interaction between the knock-on pion and the spectator nucleon.

The concept of quasielastic knockout can naturally be extended to an investigation of the momentum distributions of sigma and eta mesons in a nucleon, but electron and photon beams are inappropriate for this; instead, one can harness pion beams of energy about a few GeV and record triple coincidences of a scattered pion with two decay particles from $\eta \to 2\gamma$ or $\sigma \to 2\pi$. However, such experiments are difficult.

ACKNOWLEDGMENTS

This work was supported by the Russian Foundation for Basic Research (project no. 00-02-16117).

REFERENCES

1. J. Speth and V. R. Zoller, Phys. Lett. B **351**, 533 (1995).
2. J. Speth and A. W. Tomas, Adv. Nucl. Phys. **268**, 263 (1997).
3. N. N. Nikolaev, J. Speth, and G. T. Garvey, Z. Phys. A **349**, 59 (1994).
4. A. Szczurek and J. Speth, Nucl. Phys. A **570**, 765 (1994).
5. A. Szczurek and J. Speth, Nucl. Phys. A **555**, 249 (1993).
6. A. Szczurek, V. Ulechenko, H. Holtman, and J. Speth, Nucl. Phys. A **624**, 495 (1997).
7. V. G. Neudatchin, N. P. Yudin, and L. L. Sviridova, Yad. Fiz. **60**, 2020 (1997) [Phys. At. Nucl. **60**, 1848 (1997)].
8. N. P. Yudin, V. G. Neudatchin, and L. L. Sviridova, Yad. Fiz. **61**, 1689 (1998) [Phys. At. Nucl. **61**, 1577 (1998)].
9. P. Brauel, T. Canzler, D. Cords, *et al.,* Z. Phys. C **3**, 101 (1979).
10. D. G. Ireland, G. van der Steenhoven, *et al.,* Phys. Rev. C **49**, 2182 (1994); M. Traini, Phys. Rev. C **55**, 160 (1997); J. Yahne *et al.,* Phys. Rev. C **48**, R964 (1993).
11. V. G. Neudachin, Yu. V. Popov, and Yu. F. Smirnov, Usp. Fiz. Nauk **169**, 1111 (1999); E. Weigold and I. E. McCarthy, *Electron Momentum Spectroscopy* (Kluwer, Dordrecht, 1999).
12. C. J. Bebek, C. N. Brown, S. D. Holmes, *et al.*, Phys. Rev. D **17**, 1693 (1978).
13. T. Y. Saito and I. R. Afnan, Few-Body Syst. **18**, 101 (1995).
14. V. G. Neudatchin, L. L. Sviridova, and N. P. Yudin, Yad. Fiz. **64**, 1680 (2001) [Phys. At. Nucl. **64**, 1600 (2001)].
15. N. P. Yudin, L. L. Sviridova, and V. G. Neudatchin, Yad. Fiz. **62**, 694 (1999) [Phys. At. Nucl. **62**, 645 (1999)].
16. V. Dmitrasinovich and F. Gross, Phys. Rev. C **40**, 2479 (1989); P. J. Mulders, Phys. Rep. **185**, 83 (1990); S. Boffi, C. Giusi, and F. D. Pacati, Phys. Rep. **226**, 1 (1993).
17. M. Guidal, J.-M. Laget, and M. Vanderhaeghen, Nucl. Phys. A **627**, 645 (1997).
18. A. M. Boyarski *et al.*, Phys. Rev. Lett. **20**, 300 (1968).

Translated by A. Isaakyan

Physics of Atomic Nuclei, Vol. 65, No. 3, 2002, pp. 573–580. Translated from Yadernaya Fizika, Vol. 65, No. 3, 2002, pp. 600–607.

ELEMENTARY PARTICLES AND FIELDS
Theory

Dependence of the Interferometric Sizes of the Pion Generation Volume on the Sizes of the Pion Wave Packet

M. Kh. Anikina*, A. I. Golokhvastov, and J. Lukstins*****

Joint Institute for Nuclear Research, Dubna, Moscow oblast, 141980 Russia

Received November 27, 2000

Abstract—The effect of the sizes of the initial pion wave packet on the results that the interference method yields for the sizes of the elements of the pion-generation volume is studied experimentally for central MgMg interactions at a momentum of 4.3 GeV/c per nucleon. © *2002 MAIK "Nauka/Interperiodica"*.

1. INTRODUCTION

Identical pions emitted from their generation volume—for example, from the region of a collision of two high-energy nuclei—are related by quantum-mechanical interference correlations, which are significant for pions having close momenta: $(p_1 - p_2) \sim \hbar/R$, where R is the size of the generation volume [1] (hereafter, we usually set $\hbar = 1$).

The distinction between the actual two-particle spectrum and the background spectrum where interference correlations are "switched off" in one way or another can contain information about the spatial sizes of the generation volume, about the duration of the pion-emission process [2–5] (for an overview, see [6–9]), about the velocity of the generation volume in a given reference frame [10, 11], and even about the sizes and relative velocities of various elements of this volume [12–14].

The notion of an "element" is introduced for an inhomogeneous generation volume (see Section 4) whose parts (elements) move at different velocities in different directions and emit pions into different regions of the momentum spectrum from different spacetime points. Such inhomogeneities, which are typical of the majority of multiparticle-production models, give no way to define the spacetime size of the whole generation volume; more precisely, the notion of the size of the whole volume is meaningless in this case.

For pions originating from central MgMg interactions at a momentum of 4.3 GeV/c per nucleon and belonging to restricted regions of their momentum spectrum, we explore here the possibility of determining the sizes of the quasi-steady-state elements of the pion generation volume. The problem consists in that the degree to which an element can be considered to be steady-state and probably its sizes depend on the degree of boundedness of the pion spectrum subjected to analysis. However, the use of soft (long-wave) pions could affect the results of measurements.

In other words, a bounded subensemble of pions chosen for an interference analysis is characterized by the initial wave packet, whose sizes are related to the degree of boundedness of the momentum spectrum of pions of the subensemble (see Section 2). In this study, we examine the effect of the sizes of the packet on the results that the interference method yields for the sizes of an element (Section 8).

2. INITIAL WAVE PACKET

The mean multiplicity of negative pions in nucleon–nucleon interaction at the energy considered here is $\langle n \rangle \sim 0.6$ [15]. Therefore, we can expect that π^- mesons from MgMg collisions ($\langle n \rangle \sim 9$) are produced almost independently of one another by different "single-particle sources" (that is, in different nucleon–nucleon interactions, pion–nucleon rescatterings and charge-exchange processes, and resonance decays) at different spacetime points of the generation volume.

For a single-particle source of a pion, we consider a reaction where the pion was produced or was significantly rescattered for the last time prior to leaving the generation volume, whereupon it can be thought to be free. Its momentum at the instant of detection coincides with that at the instant of emission, and the energy at the detection point coincides with the energy at the emission point. Further, we have $E^2 = \mathbf{p}^2 + m_\pi^2$.

The amplitude of the probability that an arbitrarily chosen pion is emitted at the 4-point $r = (t, \mathbf{r})$ of a

*e-mail: anikina@sunhe.jinr.ru
**e-mail: golokhv@sunhe.jinr.ru
***e-mail: jaris@sunhe.jinr.ru

single-particle source and has a 4-momentum $p = (E, \mathbf{p})$ is

$$\psi(r)\exp(ipr), \tag{1}$$

where $\psi(r)$ is the amplitude of the probability for the pion to be emitted at the point r and $\exp(ipr) = \exp[i(Et - \mathbf{p}\cdot\mathbf{r})]$ is the amplitude of the conditional probability for the pion occurring at the point r to have the momentum p [16].

Upon coherently averaging the amplitude in (1) over all possible emission points, we arrive at the amplitude of the probability for the pion emitted by the single-particle source in question to have the momentum p:

$$\varphi(p) = \int \psi(r)\exp(ipr)d^4r. \tag{2}$$

Upon the inverse Fourier transformation of this amplitude, we return to $\psi(r)$:

$$\psi(r) = (2\pi)^{-3}\int \varphi(p)\exp(-ipr)d^3\mathbf{p}. \tag{3}$$

Here, $\varphi(p)$ is the amplitude of the probability for the pion to have the momentum p and $\exp(-ipr)$ is the amplitude of the probability for the pion having the momentum p to occur at the point r [16]. The procedure specified by Eq. (3) is the averaging of the amplitude

$$\varphi(p)\exp(-ipr) \tag{4}$$

over all possible momenta of the single-particle source. The amplitudes $\psi(r)$ and $\varphi(p)$ are bijectively related to each other.

The density of the probability that the pion has the momentum p—that is, the 4-momentum spectrum of the single-particle source—is $W(p) = \varphi(p)\varphi^*(p)$. The density of the probability that the pion is emitted at the point r—that is, the spacetime form of a single-particle source—is $V(r) = \psi(r)\psi^*(r)$.

The root-mean-square deviations for the spatial function $V(r)$, $\Delta r_i = (\langle r_i^2\rangle - \langle r_i\rangle^2)^{1/2}$ and $\Delta t = (\langle t^2\rangle - \langle t\rangle^2)^{1/2}$, and the corresponding quantities for the momentum function $W(p)$, $\Delta p_i = (\langle p_i^2\rangle - \langle p_i\rangle^2)^{1/2}$ and $\Delta E = (\langle E^2\rangle - \langle E\rangle^2)^{1/2}$, satusfy the uncertainty relations $\Delta p_i \Delta r_i \geq 1/2$ and $\Delta E \Delta t \geq 1/2$. It is the mathematical property of the Fourier transformations (2) and (3). The uncertainty relations reduce to equalities for Gaussian distributions.

We emphasize that the amplitudes in (1)–(4) are not plane waves or wave packets that propagate from the emission point to a detector. Yet, one can state that $\psi(r)$ is the initial wave packet of a pion. However, all the preceding equalities become invalid as soon as it begins to diffuse (with the velocity approximately equal to that of pions diverging in various directions [17]). For example, Δr_i grows infinitely at a constant Δp_i.

The variances Δr_i and Δt in terms of the amplitudes are usually referred to as the sizes of a single-particle source—that is, the ambiguity in the position of the pion-emission 4-point (see [4, 18–20]). In terms of wave functions, they are called the sizes of the initial wave packet of a pion [9, 20–25]. In some cases, they are also called the coherence length and time [18, 21, 22, 26] or the correlation length and time [26, 27].

The effect of these sizes on the results that the interference method yields for the size of the pion-generation volume was studied within various theoretical models (see [4, 9, 18–27] and references therein). The results were different and even opposite, from an underestimation of the actual size of the generation volume to its overestimation.

In this study, we try to explore this effect experimentally using the dependence of the variances of the momentum spectra, Δp_i and ΔE, and, therefore, of the amplitude $\varphi(p)$ on the chosen pion subensemble [16, 28]. This choice also affects the amplitude $\psi(r)$ and, therefore, the sizes of the single-particle source (the sizes of the initial wave packet), Δr_i and Δt (see Section 8).

3. INTERFERENCE

If we shift the single-particle source $\psi(r)$ being considered by a 4-vector r_a (see [4, 19]), the amplitude of the probability for the pion to have the momentum p changes in such a way that, instead of (2), we arrive at ($x = r - r_a$)

$$\int \psi(r-r_a)\exp(ipr)d^4r = \exp(ipr_a) \tag{5}$$
$$\times \int \psi(x)\exp(ipx)d^4x = \varphi(p)\exp(ipr_a).$$

Let the centers of the single-particle sources for two arbitrarily chosen π^- mesons be at the points r_a and r_b, and let the possible emission points be distributed around them over r'_a and r'_b. The amplitude of the probability that the first and the second pion (with momenta p_1 and p_2, respectively) are emitted at the points r'_a and r'_b, respectively, is equal to the product of the single-particle amplitudes, because the pions are assumed to be produced independently:

$$A'_{ab} = \psi_a(r'_a - r_a)\psi_b(r'_b - r_b) \tag{6}$$
$$\times \exp[i(p_1 r'_a + p_2 r'_b)].$$

We average this amplitude over the shape of the source; that is, we integrate it with respect to r'_a and

r'_b. Since the integrals factorize and since the Fourier integral of the shifted function is given by (5), we obtain [4, 19]

$$A_{ab} = \varphi_a(p_1)\varphi_b(p_2)\exp[i(p_1 r_a + p_2 r_b)]. \quad (7)$$

Similarly, the probability amplitude for the first and the second π^- meson to be emitted by the sources with the centers at r_b and r_a, respectively, is

$$A_{ba} = \varphi_b(p_1)\varphi_a(p_2)\exp[i(p_1 r_b + p_2 r_a)]. \quad (8)$$

If the two possibilities are indistinguishable (see the discussion in [3]), the density of the probability of choosing two π^- mesons that have the momenta $\mathbf{p}_1$ and $\mathbf{p}_2$ and which are emitted by the sources with the centers at r_a and r_b is one-half of the squared modulus of the sum of these two amplitudes:

$$2W_{ab}(\mathbf{p}_1, \mathbf{p}_2) = |A_{ab} + A_{ba}|^2 \quad (9)$$
$$= |A_{ab}|^2 + |A_{ba}|^2 + 2\mathrm{Re}(A_{ab}A^*_{ba}).$$

If the possibilities are distinguishable (for example, if these two pions with different momenta are emitted in different nucleus–nucleus collisions, where the momentum-conservation law is satisfied independently), we must average the probabilities rather than the amplitudes:

$$2W^{\mathrm{off}}_{ab}(\mathbf{p}_1, \mathbf{p}_2) = |A_{ab}|^2 + |A_{ba}|^2. \quad (10)$$

This two-particle background spectrum, where correlations are switched off, is usually obtained in experiments precisely in this way, by mixing pions from different events [5] (see Section [7]).

The ratio of the probabilities in (9) and (10) (that is, the correlation function for these two pion-emission points) is

$$C_{ab}(\mathbf{p}_1, \mathbf{p}_2) = 1 + \frac{2\mathrm{Re}(A_{ab}A^*_{ba})}{|A_{ab}|^2 + |A_{ba}|^2}. \quad (11)$$

The numerator of the interference term in (11) is

$$2\mathrm{Re}\{\varphi_a(\mathbf{p}_1)\varphi_b(\mathbf{p}_2)\varphi^*_b(\mathbf{p}_1)\varphi^*_a(\mathbf{p}_2) \quad (12)$$
$$\times \exp[i(p_1 - p_2)(r_a - r_b)]\}.$$

Here, all amplitudes are the complex functions, and this expression cannot be simplified without additional assumptions.

4. HOMOGENEOUS GENERATION VOLUME

We consider the case of a homogeneous pion-generation volume—that is the case where all single-particle sources are identical:

$$\varphi_a(\mathbf{p}) = \varphi_b(\mathbf{p}) = \varphi(\mathbf{p}). \quad (13)$$

This condition is not valid for a generation volume whose elements move in different directions and emit pions from different point into different parts of the momentum spectrum.

Such an inhomogeneity is typical of almost all multiparticle-production models, such as cascade models with resonances that decay in flight; fireball models with diverging fireballs; hydrodynamic and thermodynamic models with an expanding volume; and multiperipheral, parton, and string models, where the momentum depends, for example, on the chain vertex or on the break point.

In MgMg interactions, the equality in (13) does not hold for the whole generation volume either—that is, for the complete ensemble of negative pions [12, 13]. However, it is likely valid, in some approximation, for an "individual" element of the volume—that is, for a subensemble of pions from a small region of the momentum spectrum where $\mathbf{p}_1 \approx \mathbf{p}_2$ [12, 13].

Hereafter, we adopt the assumption specified by Eq. (13), nourishing the hope that it is possible to separate such (virtually) homogeneous elements. In this case, the amplitudes $\varphi(\mathbf{p})$ in (12) are combined into the probabilities $\varphi(\mathbf{p})\varphi^*(\mathbf{p})$ and cancel with the denominator in (11):

$$C_{ab}(q) = 1 + \cos[(p_1 - p_2)(r_a - r_b)]. \quad (14)$$

In contrast to the original expression (11), this expression is Lorentz-invariant: it contains only differences of momenta but not the momenta themselves.

The function in (14) depends on the distance between the centers of one-particle sources. Under condition (13), the size and the shape of the sources are identical [see Eqs. (2), (3)], and any points located similarly with respect to the sources can be considered as centers [4]. The correlation function (14) is independent of the source sizes (the sizes of the initial wave packets) even if they exceed the distance between the source centers [see Eqs. (7)–(11)]. Of course, it is valid only if pions are indeed emitted independently and if they do not interact in the final state.

5. SHAPE OF THE GENERATION VOLUME

Given the shape of a homogeneous generation volume (homogeneous element)—that is, the space-time density of the distribution of the centers of pion sources, $\rho(r)$—we can calculate the total correlation function by averaging the two-point correlation function (14) over all possible positions of these two points ($q \equiv p_1 - p_2$):

$$C(q) = 1 \quad (15)$$
$$+ \int\int \rho(r_a)\rho(r_b)\cos[q(r_a - r_b)]d^4 r_a d^4 r_b.$$

The procedure of averaging probabilities rather than amplitudes assumes that different positions of the

point r_a (or r_b or both) result in different final states (see the discussion in [3]).

Considering that $\cos[q(r_a-r_b)] = \mathrm{Re}[\exp(iqr_a)\exp(-iqr_b)]$, we obtain

$$C(q) = 1 + \mathrm{Re}\left\{\int \rho(r_a)\exp(iqr_a)d^4r_a \times \int \rho(r_b)\exp(-iqr_b)d^4r_b\right\} = 1 + \left|\int \rho(r)\exp(iqr)d^4r\right|^2. \quad (16)$$

This is the basic relation of the interference method for determining the experimental sizes of the pion-generation volume.

Assuming that the spacetime shape of the generation volume in its rest frame is close to the Gaussian distribution

$$\rho(r) = \frac{1}{(2\pi)^2 R_h R_v R_\parallel T} \times \exp\left(-\frac{r_h^2}{2R_h^2} - \frac{r_v^2}{2R_v^2} - \frac{r_\parallel^2}{2R_\parallel^2} - \frac{t^2}{2T^2}\right), \quad (17)$$

we find from the square of the Fourier transform (16) that

$$C(q) = 1 + \exp\left(-q_h^2R_h^2 - q_v^2R_v^2 - q_\parallel^2R_\parallel^2 - q_0^2T^2\right), \quad (18)$$

where the symbol $\parallel$ and the subscripts h and v indicate, respectively, the longitudinal direction and the directions transverse to the beam and to each other (for example, a vertical and a horizontal direction); R_i is the root-mean-square scatter of pion-emission points; and T is the root-mean-square scatter of the pion-emission instants. By fitting this (or any other) approximation to the experimental correlation function, one can determine the sizes R_i and T of the generation volume.

Usually, the root-mean-square sizes of the generation volume that are determined by the interference method are weakly dependent on the choice of approximation. The Gaussian distribution is used because of its simplicity; only for this distribution can the projections be simultaneously factorized and combined in a natural way, for example, $q_\perp^2 \equiv q_h^2 + q_v^2$.

A few physical and methodological factors can distort the shape of the correlation peak [6–8]. Usually, this is "compensated" by introducing an additional free parameter λ:

$$C(q) = 1 + \lambda\exp\left(-q_\perp^2R_\perp^2 - q_\parallel^2R_\parallel^2 - q_0^2T^2\right). \quad (19)$$

In contrast to (14), expression (18) is not Lorentz-invariant, because the shape of the generation volume (17) is noninvariant. Moreover, there is no Lorentz-invariant probability-density function $\rho(r)$. The invariant function $\rho(r) = \rho(t^2-\mathbf{r}^2)$ cannot be normalized to unity, because 4-dimensional integrals of this function are divergent. In the literature, the correlation function is often approximated (since the appearance of Goldhaber's study [1]) by the invariant form

$$C(Q_{\mathrm{inv}}) = 1 + \lambda\exp(-Q_{\mathrm{inv}}^2S^2), \quad (20)$$

where $Q_{\mathrm{inv}}^2 \equiv \mathbf{q}^2-q_0^2$, but this form does not follow directly from the general formula (16). It can be obtained only in the "variable reference frame" that coincides with the c.m. frame of each successive pion pair, where $q_0 = 0$.

6. EXPERIMENTAL DATA

Films of experimental data for a 4π coverage were obtained at a 2-m streamer chamber in a magnetic field (SKM-200–GIBS [29]) by using a ^{24}Mg beam of momentum $p_{\mathrm{lab}} = 4.3$ GeV/c per nucleon from the Dubna synchrophasotron. The magnesium target of thickness 1.2 g/cm^2 was placed inside the sensitive volume of the chamber. The chamber was triggered only in the case of a central MgMg collision—that is, when stripping neutrons, protons, and other fragments of the beam nucleus missed the forward cone of angle about 2.4° to the beam (about 4 msr). This corresponds to a stripping-nucleon transverse momentum of about 180 MeV/c [29]. Antistripping counters were placed at a distance of 6 m from the target, with 2 m of a 0.9-T magnetic field behind; therefore, particles softer than stripping particles missed the counters almost always. The fraction of these central (more precisely, all-nucleon) interactions amounted to approximately 4×10^{-4} of all inelastic MgMg collisions.

The accuracies to which the pion momenta and angles were measured in the laboratory frame were, respectively, about 1% and 5 mrad [29], which corresponds to the accuracy in determining the relative momenta of two pions in the MgMg c.m. frame (2–6 MeV/c). Since the invariant relative momentum of two pions depends only on their effective mass, $Q_{\mathrm{inv}}^2 = M_{\pi\pi}^2-4m_\pi^2$, the accuracy of the present experiment can be estimated on the basis of the accuracy of the mass measurement in the decays of relativistic ($\sim 4A$ GeV/c) $^4_\Lambda$H hypernuclei ($^4_\Lambda\mathrm{H} \to {}^4\mathrm{He} + \pi^-$) at the same spectrometer [30]. The decay energy in that process (56 MeV) is close to the region of interest. The root-mean-square deviation of the effective masses measured in [30] from tabular values was approximately 3 MeV.

Multiple scattering in the target introduces an additional error of about 4 MeV/c in the relative momentum of two pions. Thus, the total root-mean-square error is less than the bin width that we used in the fit (10 MeV/c, see below). In turn, the bin width was significantly less than the width of the interference peak ($\sigma \sim 40$ MeV/c).

The analysis did not include pions such that the measurement error for them that was translated into their rest frame exceeded 10 MeV/c. Therefore, the maximum error in the relative momentum of two pions at the interference peak does not exceed a value of about 14 MeV/c. The loss of π^- mesons (about 10%) that was caused mainly by the absorption in the target and by a poor measurability of vertical tracks is localized in the target-rapidity region around -1.1 in the MgMg c.m. frame. The sample subjected to analysis comprises 120 000 pions from 14 000 events (470 000 pion pairs).

7. BACKGROUND ENSEMBLE AND FITTING

The ensemble of the events without correlations was constructed in the form of complete events rather than in the form of individual pion pairs. This background ensemble has the same multiplicity distribution as the actual ensemble, but the number of events in it is 30 times greater. For each multiplicity of π^- mesons (n), a background event was formed by n π^- mesons randomly chosen from different actual events containing the same number of π^- mesons. This procedure is very close to that used in [31] and differs from the procedure proposed in [32] in that the actual and the background spectrum are constructed by using the same event sample—they contain the same fraction of π^- mesons (and their pairs) from the events characterized by the same multiplicity of π^- mesons.

In the interference analysis, we used all pairs of π^- mesons that belonged both to the actual and to the background ensemble and which satisfied selection criteria ($|\mathbf{p}_1|, |\mathbf{p}_2| < p_{\mathrm{cut}}$, see Section 8).

The parameters of the generation volume were determined by the method of maximum likelihood, approximately in the same way as in [33, 34]. We plotted three-dimensional (or four-dimensional) histograms with respect to $q_\perp$ (or $|q_v|$ and $|q_h|$), as well as $|q_\parallel|$ and $|q_0|$, separately for actual and for background pairs with a step of 10 MeV/c (MeV) in the interval 0–80 MeV/c (MeV).

The number of pairs in each bin of the histogram for background pairs was divided by 30, which is the ratio of the number of background to the number of actual events. After that, the contents of each nonempty bin in the histogram for background pairs was multiplied by $C(q)$ (19) [or (18)] for a certain set of free parameters $R_\perp^2$ (or R_v^2 and R_h^2), $R_\parallel^2$, T^2, and λ. Assuming that the value obtained in this way is the mean value for the Poisson distribution, we calculated, for actual pairs, the probability for the number of pairs in the same bin of the histogram. The product of the probabilities for all bins was then maximized with respect to the above parameters by using the FUMILI code.

In contrast to [34], we did not use a normalization free parameter that would reduce the ratio of the numbers of actual and background pairs outside the interference peak to unity. In our method, this ratio is about 0.99 for $|\mathbf{q}| > 100$ MeV/c at all p_{cut}, because the excess of the number of actual events over the background at the peak is approximately 1% of all π^- pairs. When we analyze, however, the pion subensembles with extremely low p_{cut}, there are few pairs outside the peak, so that it is impossible to use a normalization free parameter; as a result, it becomes necessary to construct the background ensemble in the form of complete events rather than the form of individual pion pairs.

The histogram width of 80 MeV/c (MeV) includes almost entirely the informative part of the interference peak: the peak width at the bottom is about 100 MeV/c (MeV). At the same time, the histogram width is sufficiently small to permit a fit to pion subensembles with a broad and a narrow momentum spectra (for different p_{cut}) on the basis of approximately the same part of the peak. This may be of importance since the approximation in (18) was chosen quite arbitrarily. However, our result depends only slightly on the histogram width, at least within the interval 60–100 MeV/c (MeV).

In our analysis, we did not include π^- pairs (either actual or background ones) with $Q_{\mathrm{inv}} < 10$ MeV because, in this region, there can occur measurement errors that are associated with the confusion of tracks on different stereoscopic projections of the films. This also removes the problem of two-particle resolution of pions with very close momenta, the Gamow correction for the Coulomb interaction of pions [32] becoming negligible, because it is significant only in the region of small Q_{inv}. Nevertheless, we introduced this correction in the standard way [33]: we took each mixed pair with the weight $\eta'/[\exp(\eta') - 1]$, where $\eta' = 2\pi m_\pi \alpha / Q_{\mathrm{inv}}$ ($\alpha = 1/137$).

8. ELEMENT SIZE

The volume of pion generation in MgMg collisions is inhomogeneous; it expands both in the longitudinal [12] and in the transverse [13] direction with respect

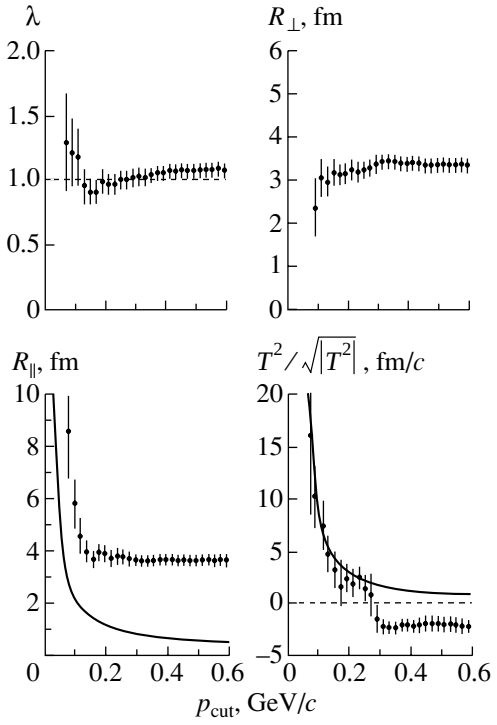

Fig. 1. Parameters of the generation-volume element versus the pion subensemble chosen for the interference analysis. The subensemble includes π^- mesons with momenta $|\mathbf{p}| < p_{\mathrm{cut}}$ in the MgMg c.m. frame. A fit employs the approximation in (19). The solid curves indicate the minimum sizes of the wave packet that were determined according to the relations $R_\parallel = \hbar/2\Delta p_\parallel$ and $T = \hbar/2\Delta E$, where $\Delta p_\parallel$ and ΔE are the experimental root-mean-square deviations for the pion spectrum at given p_{cut}.

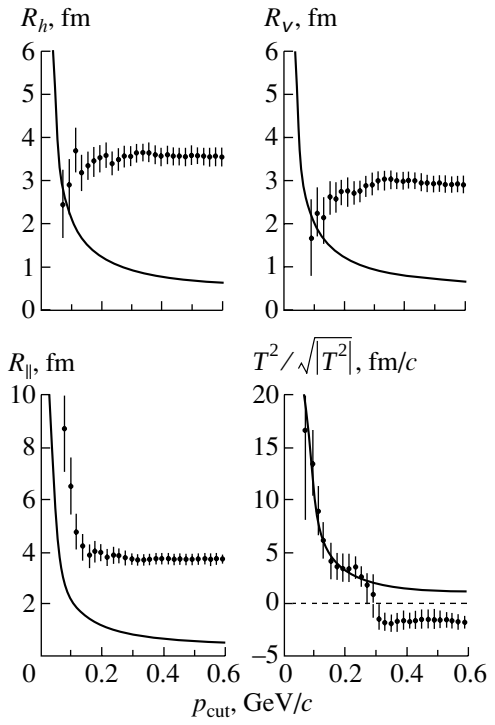

Fig. 2. Sizes of the generation-volume element versus the pion subensemble chosen for the interference analysis. The subensemble includes π^- mesons with momenta $|\mathbf{p}| < p_{\mathrm{cut}}$ in the MgMg c.m. frame. A fit employs the approximation in (18). The solid curves indicate the minimum sizes of the wave packet that are determined according to the relations $R_i = \hbar/2\Delta p_\parallel$ and $T = \hbar/2\Delta E$, where Δp_i and ΔE are the experimental root-mean-square deviations for the pion spectrum at given p_{cut}.

to the beam. Pions from different parts of the momentum spectrum correspond to different elements of the volume, which move relative to one another with relativistic velocities; therefore, the applicability condition for the basic formula (16) of the interference analysis is violated. Any attempt at performing such an analysis for the whole pion ensemble leads to an absurd result: the parameter T^2, which stands for the variance of the distribution of pion-emission instants, appears to be negative [12, 13].

Let us try to single out a rather homogeneous generation-volume element that is at rest in the MgMg c.m. frame and which emits pions into a bounded region of the momentum spectrum, $|\mathbf{p}| < p_{\mathrm{cut}}$. The result obtained by fitting the approximation in (19) to correlation functions for such bounded subensembles is displayed in Fig. 1 versus p_{cut}. It can be seen from Fig. 1 that the parameter T^2 becomes positive from $p_{\mathrm{cut}} < 250$ MeV/c. The boundary value of the element energy in [13] was chosen precisely in this way.

As we shrink the bounded region of the momentum spectrum, the pion subensemble becomes "purer," better satisfying the condition in (13); that is, it is described by the unique amplitude $\varphi(\mathbf{p})$. In this pure subensemble, one can single out, however, a subset that is characterized by a lower variance of the momentum spectrum and which therefore corresponds to a different amplitude $\varphi'(\mathbf{p})$ [16, 28]. In this case, $\varphi'(\mathbf{p}) = \varphi(\mathbf{p})$ for $|\mathbf{p}| < p_{\mathrm{cut}}$ and $\varphi'(\mathbf{p}) = 0$ for $|\mathbf{p}| > p_{\mathrm{cut}}$. The new function $\varphi'(\mathbf{p})$ is bijectively related to the new function $\psi'(r)$ through the Fourier transformation specified by Eqs. (2) and (3).

For this bounded subset of pions, no experiment would enable one to find out whether the new filtered function $\varphi'(\mathbf{p})$ is merely the projection of the function $\varphi(\mathbf{p})$ or whether it completely describes single-particle sources. In other words, it can be stated that, if our single-particle sources were actually described by the initial wave packet $\psi'(r)$ rather than by $\psi(r)$, we would obtain the same experimental results as those for the packet $\psi(r)$ in the case of $|\mathbf{p}| < p_{\mathrm{cut}}$. Slightly relaxing the interpretation, we can formulate

this as follows: without changing the initial wave packet, we just exactly simulate the situation where it is described by the amplitude $\psi'(r)$ rather than by $\psi(r)$.

To state it otherwise, the only physical meaning of the amplitude (wave function) is that its square is the probability. As to the probability for a pion to have a specific momentum depends on the subensemble with which we associated this pion. For example, the probability that the pion belonging to the $|\mathbf{p}| < p_{\rm cut}$ subensemble has a momentum in excess of $p_{\rm cut}$ is zero.

Thus, there arises the possibility of studying, on the basis of our experimental data, the effect of the sizes of the initial wave packet for a pion on the sizes of its generation volume that are determined by the interference method. For specific $p_{\rm cut}$ values, the curves in Fig. 1 show the lower bounds on the size of the wave packet. The curves are drawn through the points determined according to the relations $R_\parallel = \hbar/2\Delta p_\parallel$ and $T = \hbar/2\Delta E$, where $\Delta p_\parallel$ and ΔE are experimental root-mean-square deviations for the spectrum of pions belonging to the subensemble corresponding to given $p_{\rm cut}$. It is impossible to draw a similar curve for $R_\perp$, because $q_\perp$ has no definite direction.

Figure 2 displays the results of a complete four-dimensional fit to the data by using the approximation in (18) (with the preexponential factor λ). The behavior of this factor is not shown—it is identical to that in Fig. 1. Yet, Figs. 1 and 2 remain virtually unchanged upon setting $\lambda = 1$. The curves in Fig. 2 and the curves in Fig. 1 are obtained similarly, but the former feature transverse directions as well.

The errors in the figures are purely statistical, but the neighboring points are of course correlated, because they were obtained for nearly the same ensemble of pairs. The difference of the horizontal and the vertical size provides a measure of our systematic errors.

The dependence of the sizes of generation-volume elements on the chosen pion subensemble was studied in some other experiments as well (see, for example, [34–39] and references therein), but without any connection with the sizes of the wave packet: the variances of the momentum distribution in the subensembles were not presented there (see, however, [37]).

The use of a sharp boundary $p_{\rm cut}$ of the subensemble (though somewhat smoothed owing to finite statistics) could lead to the strong inequalities $R_i\Delta p_i \gg \hbar/2$ and $T\Delta E \gg \hbar/2$, which are insignificant for estimates [28]. However, the interference analysis for subensembles characterized by a smooth boundary for the case where a pion is included in the subensemble at random, with the probability $\exp(-\mathbf{p}^4/\sigma^4)$ (where σ is varied), leads to results that are close to preceding ones (they are not shown here). We used the fourth power (not of the second one) because, for a Gaussian distribution, the subensemble includes an overly great number of pions with high momenta, in which case there arise large errors.

Our results agree and simultaneously disagree with both groups of theoretical models. The behavior of the transverse sizes is closer to that in models where the finiteness of the wave-packet sizes results in underestimating the actual sizes of the generation volume. The behavior of the longitudinal size and the duration of the emission process seems to lend support to models where the squared sizes of the wave packet and of the generation volume are summed up. However, the statistical significance of these results is insufficient for drawing a definitive conclusion on this point.

The behavior of the time parameter in Figs. 1 and 2 casts some doubt on the possibility of measuring it by the interference method.

ACKNOWLEDGMENTS

We are grateful to R. Lednicky and V. L. Lyuboshitz for numerous discussions and critical comments.

REFERENCES

1. G. Goldhaber *et al.,* Phys. Rev. **120**, 300 (1960).
2. G. I. Kopylov and M. I. Podgoretskiĭ, Yad. Fiz. **15**, 392 (1972) [Sov. J. Nucl. Phys. **15**, 219 (1972)].
3. G. I. Kopylov and M. I. Podgoretskiĭ, Yad. Fiz. **18**, 656 (1973) [Sov. J. Nucl. Phys. **18**, 336 (1973)].
4. G. I. Kopylov and M. I. Podgoretskiĭ, Yad. Fiz. **19**, 434 (1974) [Sov. J. Nucl. Phys. **19**, 215 (1974)].
5. G. I. Kopylov, Phys. Lett. B **50B**, 472 (1974).
6. W. A. Zajc, Nevis Report No. 1384 (Columbia University, 1987).
7. M. I. Podgoretskiĭ, Fiz. Élem. Chastits At. Yadra **20**, 628 (1989) [Sov. J. Part. Nucl. **20**, 266 (1989)].
8. D. H. Boal *et al.,* Rev. Mod. Phys. **62**, 553 (1990).
9. U. A. Wiedemann and U. Heinz, Phys. Rep. **319**, 145 (1999).
10. R. Lednicky and V. L. Lyuboshits, Yad. Fiz. **35**, 1316 (1982) [Sov. J. Nucl. Phys. **35**, 770 (1982)].
11. M. I. Podgoretskiĭ, Yad. Fiz. **37**, 455 (1983) [Sov. J. Nucl. Phys. **37**, 272 (1983)].
12. M. Kh. Anikina *et al.,* Preprint No. E1-95-311, JINR (Joint Inst. Nuclear Research, Dubna, 1995).
13. M. Kh. Anikina *et al.,* Phys. Lett. B **397**, 30 (1997).
14. H. Appelshäuser *et al.,* Eur. Phys. J. C **2**, 661 (1998).
15. V. D. Aksinenko *et al.,* Nucl. Phys. A **348**, 518 (1980).
16. R. P. Feynman and A. R. Hibbs, *Quantum Mechanics and Path Integrals* (McGraw-Hill, New York, 1965; Mir, Moscow, 1968), Chap. 5.

17. A. Messiah, *Quantum Mechanics* (Interscience, New York, 1961; Nauka, Moscow, 1978), §VI.3.
18. R. Lednicky and V. L. Lyuboshitz, Heavy Ion Phys. **3**, 93 (1996).
19. R. Lednicky *et al.,* Phys. Rev. C **61**, 034901 (2000).
20. Yu. M. Sinyukov and A. Yu. Tolstykh, Z. Phys. C **61**, 593 (1994).
21. S. Pratt, Phys. Rev. D **33**, 72 (1986).
22. S. S. Padula *et al.,* Nucl. Phys. B **329**, 357 (1990).
23. H. Merlitz and D. Pelte, Z. Phys. A **357**, 175 (1997).
24. U. A. Wiedemann *et al.,* Phys. Rev. C **56**, 614 (1997).
25. J. Zimányi and T. Csörgő, Heavy Ion Phys. **9**, 241 (1999).
26. I. V. Andreev and R. M. Weiner, Phys. Lett. B **253**, 416 (1991).
27. I. V. Andreev *et al.,* Int. J. Mod. Phys. A **8**, 4577 (1993).
28. L. I. Mandel'shtam, *Full Collection of Works,* Vol. 5: *Lectures on Foundations of Quantum Mechanics* (Akad. Nauk SSSR, Leningrad, 1950), Lecture 5.
29. S. A. Avramenko *et al.*, Prib. Tekh. Éksp., No. 3, 27 (1999).
30. A. U. Abdurakhimov *et al.,* Nuovo Cimento A **102**, 645 (1989).
31. S. Y. Fung *et al.,* Phys. Rev. Lett. **41**, 1592 (1978).
32. M. Gyulassy *et al.,* Phys. Rev. C **20**, 2267 (1979).
33. W. A. Zajc *et al.,* Phys. Rev. C **29**, 2173 (1984).
34. A. D. Chacon *et al.,* Phys. Rev. C **43**, 2670 (1991).
35. D. Beavis *et al.,* Phys. Rev. C **34**, 757 (1986).
36. R. Bock *et al.,* Mod. Phys. Lett. A **3**, 1745 (1988).
37. W. B. Christie *et al.,* Phys. Rev. C **47**, 779 (1993).
38. T. Alber *et al.,* Z. Phys. C **66**, 77 (1995).
39. I. G. Bearden *et al.,* Phys. Rev. C **58**, 1656 (1998).

Translated by M. Kobrinsky

Physics of Atomic Nuclei, Vol. 65, No. 3, 2002, p. 581. Translated from Yadernaya Fizika, Vol. 65, No. 3, 2002, p. 608.

ERRATA

Erratum: "Final-State Interaction in Multichannel Quantum Systems and Pair Correlations of Nonidentical and Identical Particles at Low Relative Velocities"

[*Physics of Atomic Nuclei* 61, 2050–2063 (1998)]

R. Lednicky, V. V. Lyuboshitz, and V. L. Lyuboshitz

In Eqs. (66) and (68), the term

$$\frac{1}{2}\hat{k}\,\hat{d}_0\,\hat{k}$$

should be replaced by

$$\frac{1}{4}(\hat{k}^2\,\hat{d}_0\,+\hat{d}_0\,\hat{k}^2).$$

Equation (69) should read

$$\beta_l = \frac{\pi}{\mid a_l \mid}\cot\left(\frac{\pi}{\kappa_l \mid a_l \mid}\right) + \frac{2}{\mid a_l \mid}\left\{\ln(\kappa_l \mid a_l \mid) + \frac{1}{2}\left[\psi\left(\frac{1}{\kappa_l \mid a_l \mid}\right) + \psi\left(-\frac{1}{\kappa_l \mid a_l \mid}\right)\right]\right\}.$$

In footnote 4 on page 2061, the minus sign in the expression for β_l should be deleted.

1063-7788/02/6503-0581$22.00